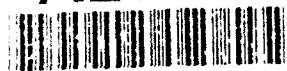


AD-A263 234



2

# TRENDS IN NON-CRYSTALLINE SOLIDS

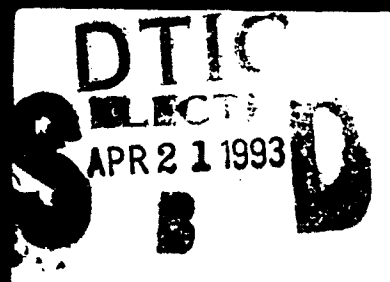
Proceedings of the  
Third International Workshop  
on Non-Crystalline Solids

Editors

A. Conde

C. F. Conde

M. Millán



World Scientific

AD NUMBER	DATE	DTIC ACCESSION NOTICE
1. REPORT IDENTIFYING INFORMATION		<b>REQUESTER:</b> 1. Put your mailing address on reverse of form. 2. Complete items 1 and 2. 3. Attach form to reports mailed to DTIC. 4. Use unclassified information only. 5. Do not order documents for items 3 and 4.
A. ORIGINATING AGENCY <i>University of South Florida</i>		
B. REPORT TITLE AND/OR NUMBER <i>THE NEW YORK JOURNAL OF MATHEMATICS</i>		
C. MONITOR REPORT NUMBER <i>1420 6/44 11/2</i>		
D. PREPARED UNDER CONTRACT NUMBER <i>DA-11-100-0000</i>		
2. DISTRIBUTION STATEMENT		<b>DTIC:</b> 1. Assign Accession Number 2. Classify and Grade

DTIC Form 50  
Apr 89

PREVIOUS EDITIONS ARE OBSOLETE

93-08510



98

**TRENDS IN  
NON-CRYSTALLINE  
SOLIDS**

Proceedings of the Third International Workshop on Non-Crystalline Solids

# TRENDS IN NON-CRYSTALLINE SOLIDS

Matalascañas (Costa de la Luz), Spain      5 – 8 November 1991

**Editors**

**A. Conde, C. F. Conde & M. Millán**

*Departamento de Física de la Materia Condensada  
Instituto de Ciencia de Materiales, C.S.I.C.  
Universidad de Sevilla*



**World Scientific**

*Singapore • New Jersey • London • Hong Kong*



*Published by*

World Scientific Publishing Co. Pte. Ltd.

P O Box 128, Farrer Road, Singapore 9128

*USA office:* Suite 1B, 1060 Main Street, River Edge, NJ 07661

*UK office:* 73 Lynton Mead, Totteridge, London N20 8DH

**TRENDS IN NON-CRYSTALLINE SOLIDS**

Copyright © 1992 by World Scientific Publishing Co. Pte. Ltd.

*All rights reserved. This book, or parts thereof, may not be reproduced in any form or by any means, electronic or mechanical, including photocopying, recording or any information storage and retrieval system now known or to be invented, without written permission from the Publisher.*



ISBN 981-02-1035-3

Printed in Singapore by Kim Hup Lee Printing Co. Pte. Ltd.

## INTERNATIONAL ADVISORY COMMITTEE

F.J. Baltá-Calleja (C.S.I.C., Madrid, Spain)  
R.W. Cahn (University of Cambridge, U.K.)  
J. Colmenero (Universidad del País Vasco, Spain)  
A. Conde (Universidad de Sevilla, Spain)  
J.M. Dubois (Université de Nancy I, France)  
E.W. Fischer (Max Plank Institut, Mainz, Germany)  
G. Herzer (Vacuumsmelze GmbH, Hanau, Germany)  
M.D. Ingram (University of Aberdeen, U.K.)  
J. Jäcke (Universität Konstanz, Germany)  
H. Matyja (Institute of Materials Science & Engineering, Warsaw, Poland)  
M.T. Mora (Universidad Autónoma de Barcelona, Spain)  
H.T. Savage (Instituto de Magnetismo Aplicado, Madrid, Spain)  
G.R. Strobl (Universität Freiburg, Germany)  
A. van den Beukel (Delft University of Technology, The Netherlands)  
H.G. Zachmann (Universität Hamburg, Germany)  
J. Zarzycki (Université de Montpellier II, France)

## LOCAL ORGANIZING COMMITTEE

Departamento de Física de la Materia Condensada, e  
Instituto de  CSIC.  
Universidad de Sevilla 

A. Conde (Chairman)  
C.F. Conde  
A. Criado  
J. Leal  
M. Millán

## SPONSORS

Ministerio de Educación y Ciencia

Junta de Andalucía (Consejerías de Presidencia y de Educación y Ciencia)

Universidad de Sevilla

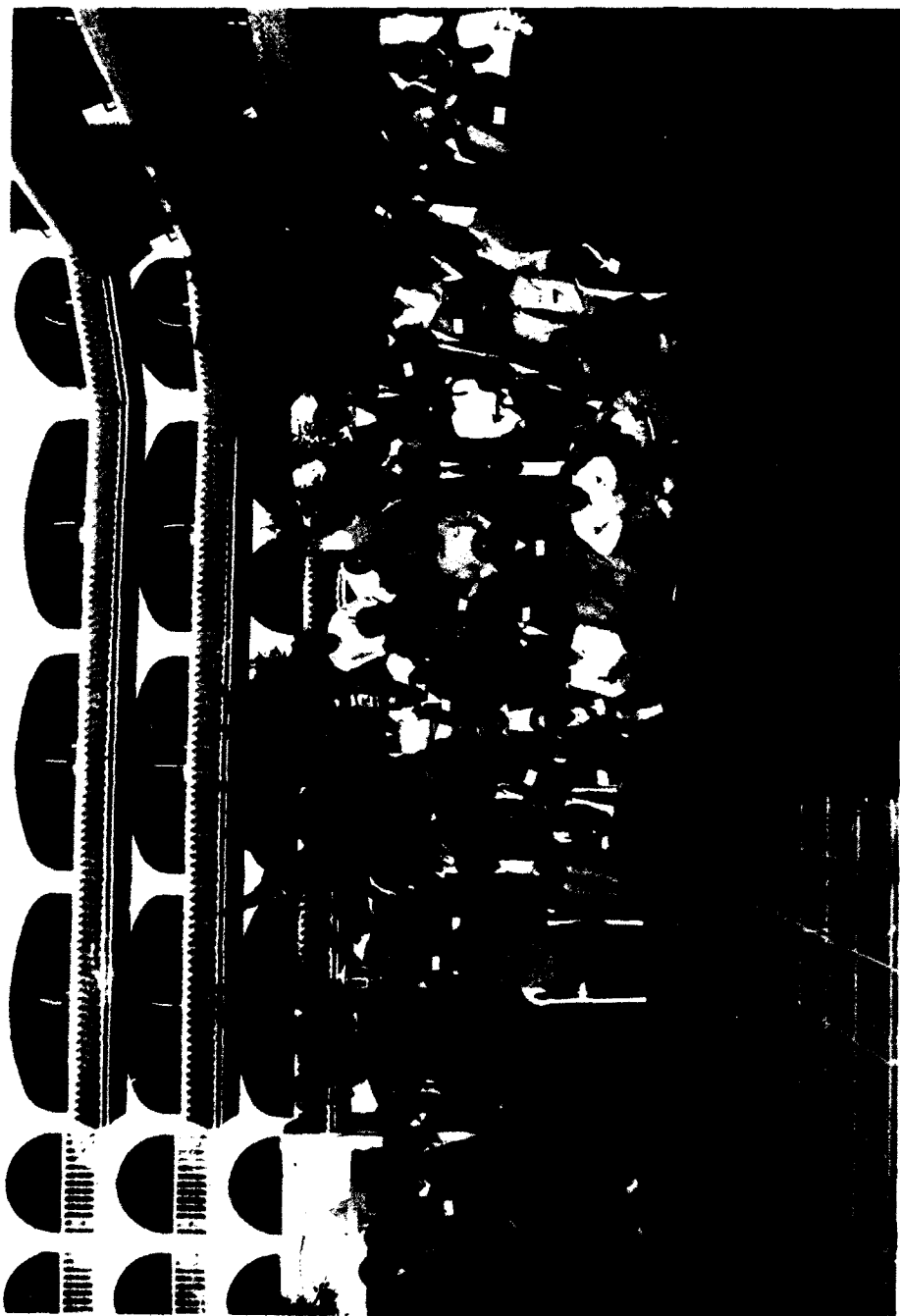
Consejo Superior de Investigaciones Científicas

Grupo Especializado de Física del Estado Sólido (R.S.E.F.)

U.S. Army Research, Development and Standardization Group (U.K.)

DTIC QUALITY INSPECTED 1

Accession For	
NTIS GRA&I	<input checked="checked" type="checkbox"/>
DTIC TAB	<input type="checkbox"/>
Unannounced	<input type="checkbox"/>
Justification	
By <i>perform 50</i>	
Distribution/	
Availability Codes	
Dist	Avail and/or Special
<i>A-1</i>	



## PREFACE

The Third International Workshop on Non-Crystalline Solids was held in Matalascañas (Costa de la Luz) near Sevilla, Spain, from November 5th to November 8th 1991, and was attended by some 85 scientists from 11 countries.

The three-day scientific program comprised 11 invited lectures and 69 contributions distributed among five oral sessions and three poster sessions. The presented papers covered a great variety of topics dealing with processing techniques and structure, crystallization, glass transition, relaxation and molecular motion, properties and applications of non-crystalline materials with emphasis on basics and focussed principally on metallic, chalcogenide and polymeric glasses, with only a sidelong glance at oxide glasses.

This book contains 11 review papers corresponding to the plenary talks and 64 papers selected from the contributions. The papers have been subjected to a refereeing procedure during and/or after the Workshop and revisions were made if necessary. The editors would like to thank the contributors for promptly preparing the manuscripts, the referees for their critical reading of the papers and the publishers for their advice and help during the planning and preparation of this book.

The Workshop would not have been possible without the dedicated help of many individuals. Particular merit goes to members of the Scientific Committee of this series of Workshops, Professors R. W. Cahn, E. W. Fischer and J. Zarzycki, who assisted in preparing the Conference program; and the invited speakers for their instructive overviews. Unfortunately, Dr. G. Herzer, Hanau, Germany, was ill and unable to attend.

We would also like to express our gratitude to the people and Institutions, listed elsewhere, who contributed to the success of the Workshop by their personal engagement in Committees or gave financial support.

x

Finally, it is a pleasure to announce that this series of Workshops, — the first held near Barcelona in 1986 and the second in San Sebastián in 1989 — will continue. The fourth will be held in 1994, organized by the “Instituto de Magnetismo Aplicado” of the Complutense University of Madrid, being chaired by Professors A. Hernando and M. Vázquez.

*Sevilla, March 1992*

A. Conde  
C. F. Conde  
M. Millán

## CONTENTS

Preface . . . . .	ix
-------------------	----

### I. PROCESSING TECHNIQUES AND STRUCTURE

#### Plenary Lectures

Mechanical Amorphisation of Ordered Intermetallic Phases . . . . .	3
<i>R. W. Cahn</i>	
Unconventional Methods for Obtaining Glasses and Amorphous Materials . . . . .	15
<i>J. Zarzycki</i>	
On the Nature of the Partially Crystalline State of Polymeric Solids . . . . .	37
<i>G. R. Strobl</i>	

#### Contributions

On the Amorphization of the Nd-Fe and Sm-Fe Systems by Mechanical Alloying . . . . .	57
<i>V. E. Martín, J. M. González, L. Schultz and K. Schnitzke</i>	
Microstructural Studies of Nanocrystalline and Amorphous Phase Formation by Milling Techniques . . . . .	61
<i>M. A. Morris</i>	
On the Sintering of Mixed Aerogels . . . . .	65
<i>M. Ramírez del Solar and L. Esquivias</i>	
Structural Modifications in Silica Xerogels Prepared using Sonocatalysis and an Additive . . . . .	69
<i>E. Blanco, N. de la Rosa-Fox and L. Esquivias</i>	
Fe-57 Mössbauer Study of Some (FeCo) <sub>75</sub> SiB Metallic Alloys . . . . .	73
<i>I. Orúe, J. M. Barandiarán, M. L. Fernández-Gubieda and F. Plazaola</i>	

The Structure and Optical Properties of Phosphate Glasses with Iron Ions . . . . .	77
<i>J. Wasylak</i>	
Recent Results in Neutron Scattering from Non-Crystalline Solids using a Pulsed Source . . . . .	81
<i>W. S. Howells</i>	
A New Approach to the Structural Study of Non Crystalline Polymers through Neutron Diffraction . . . . .	85
<i>J. J. del Val, B. Rosi, F. J. Davies and G. R. Mitchell</i>	
Neutron Scattering Study of the Chain Conformations in the Mixtures of Block Copolymers . . . . .	89
<i>A. D. Vilesov, G. A. Evmenenko and H. G. Zachmann</i>	
Neutron Scattering from Amorphous Hydrogenated Carbon . . . . .	93
<i>W. S. Howells, R. J. Newport, P. J. R. Honeybone and P. Revell</i>	
Study of Phase Separation in Amorphous PEN/PET Blends by Means of $^{13}\text{C}$ CP/MAS NMR . . . . .	97
<i>M. M. Guo and H. G. Zachmann</i>	
EXAFS and XANES Study of $\text{TiO}_2\text{-SiO}_2$ Gels and Glasses . . . . .	101
<i>J. Matos, L. Esquivias and C. Prieto</i>	

## II. CRYSTALLIZATION

### Plenary Lectures

Nanocrystalline Alloys Obtained by Crystallization of Metallic Glasses . . . . .	107
<i>H. Matyja and T. Kulik</i>	
Influence of the Crystallization on the Mechanical Properties of Glassy Polymers . . . . .	127
<i>F. J. Baltá-Calleja</i>	



## Contributions

Nanocrystalline Materials by Crystallization of Zr-based Metallic Glasses . . . . .	149
<i>U. Köster, T. Spassow and M. Sutton</i>	
Crystallization Kinetics in Nanocrystalline Materials . . . . .	153
<i>S. Suriñach, A. Otero, M. D. Baró, M. T. Clavaguera-Mora and N. Clavaguera</i>	
Magnetic and Structural Characterization of Nanocrystalline Fe-Cu-Nb-Si-B Alloys . . . . .	157
<i>M. Vázquez, P. Marín, J. González, A. Hernando and E. Pulido</i>	
The Effect of Adding Ti and Zr on the Crystallization Behaviour of Amorphous Fe-Cr-B Alloys . . . . .	161
<i>K. Ishii and B. Cantor</i>	
Thermal Stability and Quenching Rate in an FeSiB Glass . . . . .	165
<i>C. F. Conde and A. Conde</i>	
Crystallization Kinetics of an Fe <sub>75</sub> Co <sub>4</sub> Si <sub>3</sub> B <sub>18</sub> Alloy . . . . .	169
<i>M. Millán, J. Leal and A. Conde</i>	
Crystallization Process by Study of Resistivity through Controlled Joule Effect Heating . . . . .	173
<i>P. Rougier and R. Krishnan</i>	
Calorimetric Study of the Crystallization Processes of Amorphous CoP Alloys . . . . .	177
<i>F. Cebollada, J. M. González, S. Suriñach, M. D. Baró and M. T. Clavaguera-Mora</i>	
Crystallization Kinetics of Pd-Ni-P Amorphous Alloys . . . . .	181
<i>I. Tellería and J. M. Barandiarán</i>	
Electron Microscopy Study of Crystallization of a Ni <sub>68</sub> Cr <sub>14</sub> B <sub>18</sub> Glass . . . . .	185
<i>A. Criado, M. Millán and A. Conde</i>	
The Study of Crystallization of Glasses by Thermal Analysis . . . . .	189
<i>J. Málek and V. Smrčka</i>	

Crystallization of the $\text{Se}_{85}\text{Te}_{15}$ Glassy Alloy: Calorimetric and Morphological Study . . . . .	193
<i>M. D. Baró, Y. Calventus, S. Suriñach, M. T. Clavaguera-Mora and N. Clavaguera</i>	
The Glass Forming Ability in Cu-As-Se System . . . . .	197
<i>J. Málek and L. Tichý</i>	
Neutron Diffraction Study of Structural Changes Induced by Heat Treatment in Ge-Se Glasses . . . . .	201
<i>X. Torrelles, S. Bordas, M. T. Clavaguera-Mora and N. Clavaguera</i>	
Evidence of Two Amorphous Phases in Ge-Te-Sb Alloys . . . . .	205
<i>M. Belhadji, C. Vautier, P. Lebaudy and J. M. Saiter</i>	
Effects of Annealing on Amorphous $\text{Cu}_{0.03}\text{Ge}_{0.20}\text{Te}_{0.77}$ Alloy . . . . .	209
<i>M. Casas-Ruiz, R. A. Ligeró, J. Vázquez and R. Jiménez-Garay</i>	

### III. RELAXATION PROCESSES, GLASS TRANSITION AND MOLECULAR MOTIONS

#### Plenary Lectures

Structural Relaxation in Metallic Glasses . . . . .	215
<i>A. van den Beukel</i>	
Cooperativity of Molecular Motion in Liquids near the Glass Transition . . . . .	237
<i>J. Jäcke</i>	
Studies of Structure and Glass Transition in Liquid Crystalline Copolyesters by Means of Synchrotron Radiation and Related Methods . . . . .	245
<i>H. G. Zachmann and S. Thiel</i>	

#### Contributions

Electrical Resistivity and Young's Modulus Correlations during Structural Relaxation in Amorphous $\text{Fe}_{75}\text{TM}_{25}\text{B}_{20}$ (TM = Cr, Mn, Ni) . . . . .	257
<i>M. Baricco, G. Koebrugge, G. Riontino and J. Sietsma</i>	

Relaxation Behaviour of Curie Temperature of an Fe-based Glass . . .	261
<i>C. F. Conde and A. Conde</i>	
Positron Lifetime and X-Ray Diffraction Measurements during Structural Relaxation in Metallic Glasses $\text{Fe}_{78-x}\text{Co}_x\text{Si}_9\text{B}_{13}$ . . .	265
<i>J. Filipceki</i>	
An Improved Method for the Calculus of Activation Energy Spectra (AES) in the Analysis of Relaxation Experiments . . .	269
<i>F. L. Cumbreira, F. Guiberteau and A. Muñoz</i>	
Specific Heat Measurements of Ge Doped $\text{Te}_{0.15}\text{Se}_{0.85}$ Glasses in the Glass Transition Region . . .	273
<i>E. Illeková, M. T. Clavaguera-Mora, M. D. Baró and S. Surinách</i>	
Characterization of Se-based Chalcogenide Alloys by Measurement of Tg Variations . . .	277
<i>A. Hamou, J. M. Saiter, J. Bayard and J. Grenet</i>	
Is the Soft Potential Model Able to Explain the Glassy Anomalies? . .	281
<i>M. A. Ramos, L. Gil and U. Buchenau</i>	
Monte-Carlo Simulation of the Glass Transition in Dense Three-Dimensional Polymer Melts . . .	285
<i>J. Baschnagel, W. Paul, K. Binder and H. P. Wittmann</i>	
Glass Transition and Physical Aging in Amorphous Poly (Ethylene Terephthalate) . . .	289
<i>G. Vigier, J. Tatibouet and J. Pérez</i>	
X-Ray Diffraction in Glassy Polymers Around Tg . . .	293
<i>J. J. del Val, J. Colmenero, B. Rosi and G. R. Mitchell</i>	
Quasielastic Neutron Scattering Study of the Dynamics of the $\alpha$ -Relaxation in Polymers . . .	297
<i>J. Colmenero, A. Arbe, A. Alegría and B. Frick</i>	
Physical Aging and Dielectric Relaxation in a Polar Glassy Polymer . . .	301
<i>A. Alegría, E. Guerrica-Echevarría, I. Tellería and J. Colmenero</i>	

Temperature Dependence of Enthalpy Relaxation Parameters in a Fully Cured Epoxy Resin . . . . .	305
<i>S. Montserrat Ribas</i>	
Molecular Dynamics in PVAc Studied by Relaxation Techniques and Photon Correlation Spectroscopy . . . . .	309
<i>F. Alvarez, A. Alegría, J. M. Alberdi and J. Colmenero</i>	
Influence of the Stretching on the Molecular Dynamics of Glassy Poly(Vinyl Chloride) . . . . .	313
<i>A. Elícegui, J. J. del Val, J. Colmenero, V. Bellenger, J. Verdú, G. Martínez and J. L. Millán</i>	
Dynamic Mechanical Relaxations of an Amorphous Copolyester . . . .	317
<i>R. Benavente, J. M. Pereña, E. Pérez, A. Bello and V. Lorenzo</i>	
Dynamic Mechanical Behaviour of Vinyl Alcohol-Ethylene Copolymers . . . . .	321
<i>M. L. Cerrada, J. M. Pereña, R. Benavente, E. Pérez and A. Bello</i>	
Local Deformation Inhomogeneity in Dynamic Mechanical Behaviour of Block Copolymers . . . . .	325
<i>A. D. Vilesov, V. P. Volodin, I. V. Kenunen, N. Striebeck and H. G. Zachmann</i>	
Study of the Molecular Dynamics in PVME/PH Miscible Blends by means of Nuclear Magnetic Resonance . . . . .	329
<i>J. M. Alberdi, M. F. Lorenzo and J. Colmenero</i>	
Non-linear Creep and the Effect of Free Volume . . . . .	333
<i>J. Maia, A. M. Velho and A. C. Diogo</i>	
Determination of Trap Parameters in Polymers . . . . .	337
<i>J. Świątek and A. Mandowski</i>	

#### IV. PROPERTIES AND APPLICATIONS

##### Plenary Lectures

Non-Crystalline Aluminium Alloys: Fundamentals and Applications	343
<i>J. M. Dubois</i>	

Magnetoelastic Interactions in Amorphous Ferromagnets — Theory and Applications . . . . .	365
<i>H. T. Savage and M. Vázquez</i>	
Ionically Conducting Glasses . . . . .	385
<i>M. D. Ingram</i>	
<b>Contributions</b>	
Magnetic Properties of Ternary Co-B-C Melt Spun Alloys Amorphized over an Extended Concentration Range . . . . .	401
<i>M. Pont, R. Puzniak, K. V. Rao and A. Inoue</i>	
Magnetic Properties of Rapidly Quenched NdDyFeB Alloys . . . . .	405
<i>J. S. Muñoz, M. Pont and J. Reverter</i>	
Anisotropy Field Distribution in Amorphous Co-P Alloys . . . . .	409
<i>A. García-Arribas, J. Herreros and J. M. Barandiarán</i>	
Unidirectional Magnetic Anisotropy in the Fe <sub>80</sub> B <sub>20</sub> Metallic Glass . . . . .	413
<i>J. M. Riveiro, J. Flores and M. J. Bernal</i>	
Selection and Processing of Metallic Glass Materials for Fluxgate Applications . . . . .	417
<i>O. V. Nielsen, F. Primdahl, J. R. Petersen and B. Hernando</i>	
Bistable Behaviour in Stress-Annealed Non-Magnetostrictive Amorphous Wire . . . . .	421
<i>C. Gómez Polo, M. Vázquez, T. Reininger and H. Kronmüller</i>	
Large Barkhausen Effect and Coupling Factors in Iron Rich Amorphous Wires . . . . .	425
<i>J. D. M. Carey, M. D. Hickmott, H. T. Savage,</i> <i>C. Gómez-Polo, M. Vázquez, J. B. Blanco and J. González</i>	
Variation of the Magnetic Anisotropy of Amorphous Ribbons by Reduction in Thickness by Mechanical Polishing . . . . .	429
<i>M. Tejedor, J. A. García and J. Carrizo</i>	

Corrosion Behaviour of $\text{Fe}_{60}\text{Ni}_{20}\text{B}_{20}$ Amorphous Alloy and Partially Crystallized . . . . .	433
<i>A. R. Pierna, A. Lorenzo and J. González</i>	
On Current Controlled Negative Differential Resistance in Chalcogenide Glassy Semiconductors . . . . .	437
<i>M. Domínguez, E. Márquez, P. Villares and R. Jiménez-Garay</i>	
Electrical Conductivity in the Ionic Amorphous Solid $\text{As}_{42}\text{Se}_{41}\text{Ag}_{17}$ . . . . .	441
<i>M. Oliva, J. L. Rojas, E. Márquez, P. Villares and R. Jiménez-Garay</i>	
Optical Properties of $\alpha\text{-Ge}_{1-x}\text{Sb}_x$ Thin Films . . . . .	445
<i>J. M. del Pozo and L. Díaz</i>	
A. C. Conductivity of an Amorphous Niobium Phosphate . . . . .	449
<i>M. Cantero, M. Martínez-Lara, L. Moreno-Real, S. Bruque, C. Criado and J. R. Ramos-Barrado</i>	
Author index . . . . .	453

## **I. PROCESSING TECHNIQUES AND STRUCTURE**

## Mechanical Amorphisation of Ordered Intermetallic Phases

ROBERT W. CAHN

*Department of Materials Science and Metallurgy,  
University of Cambridge,  
Pembroke Street, Cambridge CB2 3QZ,  
England*

### ABSTRACT

The discovery that certain intermetallic phases can be amorphised by intense mechanical deformation was reported in 1983, and since then the technique has been applied to great variety of alloys. The favourite technique is ball-milling of powders, either mixtures of elements or ready-alloyed intermetallic phases. An alternative is intense rolling or wire-drawing of finely divided strips or wires of elementary metals in contact. The present state of knowledge is surveyed.

Various generalizations have been proposed concerning the factors that determine whether a particular intermetallic phase can be amorphised, mechanically or otherwise. A particular topic of current discussion is whether the essential precondition is the destruction of long-range order or whether, alternatively, the important thing is to expand the lattice (such expansion is an incidental byproduct of disordering). In this connection, the theoretical parallels between (solid-state) amorphisation and melting have received special consideration. These issues are briefly discussed in the paper, in the context of solid-state amorphisation reactions generally.

### 1. Introduction

There are four known ways of turning a crystalline solid into an amorphous one, without passing through the liquid state at any stage. These are irradiation, interdiffusion of elementary metals, pressure-induced vitrification and mechanical deformation. Collectively they are known as *solid-state amorphization reactions (SSAR)*. The main theme of this short survey is the fourth one, but to set the scene, a short account of the other three methods will be helpful.

#### 1.1 Amorphisation by Irradiation

Amorphisation of minerals, silicates in particular, by radiation has been known for a long time among mineralogists, and powdered rocks brought back from the moon's surface by the American astronauts showed thin amorphous layers at the surface of each mineral particle, caused by the



faint solar "wind", i.e., ion bombardment mostly by protons at keV energies, over millions of years. — Where metals are concerned, the first observation was of amorphisation of  $U_6Fe$  by fission fragment irradiation<sup>1</sup>, and since then, almost all observed cases of amorphisation by irradiation, whether with fission fragments, heavy ions or high-energy electrons, have referred to ordered intermetallic compounds. Some of the compounds listed, in reviews by Russell<sup>2</sup> and by Okamoto and Meshii<sup>3</sup>, as having been amorphised in this way are  $Co_2Ti$ ,  $CuTi$ ,  $Fe_2Ti$ ,  $Ni_6Nb_7$ ,  $NiTi$  and  $Zr_3Al$ ; a number of others, such as  $NiAl$ ,  $CuZn$ ,  $Fe_3Al$ , remained crystalline. More recently, Luzzi and Meshii (see overview<sup>4</sup>) performed a long, systematic series of experiments with high-voltage electron irradiation, notably of  $Cu_3Ti_2$ , and concluded that substantial loss of long-range order was a precondition of amorphisation. Another major study, by Okamoto *et al.*<sup>5</sup>, of  $Zr_3Al$  amorphised by bombardment with  $Kr^+$  ions, placed more emphasis on the lattice expansion which accompanies disordering rather than on the disordering *per se*, as the destabilising factor. This issue is further discussed below.

Relatively low temperatures (to prevent healing of damage and particularly of induced disorder), high doses and high dose rates were found to be necessary to achieve amorphisation. Opinions continue to diverge concerning the features that distinguish amorphisable from non-amorphisable compounds; an early view, that compounds with narrow or zero homogeneity range amorphise most easily, has proved to have too many exceptions.

### 1.2 Amorphisation by Interdiffusion

This process, sometimes called *chemically driven solid-state amorphization reaction*, has received an enormous amount of attention by metallurgists and metal physicists since the discovery in 1983, by Schwarz and Johnson<sup>6</sup>, that interdiffusion between thin multilayer films of lanthanum and gold in contact generated an amorphous zone in the interdiffusion zone. Gold was chosen because it is a "fast diffuser" (technically, an interstitial diffuser) in lanthanum, with the result that the diffusion rate of La in Au was certainly much slower than that of Au in La. Most subsequent research has shown that such diffusional asymmetry is important; in fact this asymmetry matters most in the resultant amorphous phase. A recent measurement, by Greer *et al.*<sup>7</sup>, with a Ni-Zr couple showed that at 573K, the diffusivity of Zr in the Ni-Zr amorphous phase is about a million times smaller than that of Ni. Diffusional asymmetry in a metallic glass implies a substantial difference in atomic radius of the constituent atoms.

It is this diffusional asymmetry which kinetically inhibits the nucleation and growth of the thermodynamically stable crystalline intermetallic compounds in the diffusion region; however, once the amorphous layer becomes thick enough, the stable intermetallic phase can no longer be kept at bay. For instance, in the Ni-Zr system the critical thickness at 300°C  $\approx$  100 nm<sup>8</sup>; when such a diffused couple is raised to a higher temperature, the intermetallic phase can expand at the cost of the amorphous layer<sup>9</sup>. — The diffusivity criterion is desirable but not sufficient; the amorphous phase must have a large negative heat of mixing, which ensures that it has a lower free energy than the initial mixture of two elementary metals. It appears to be assumed that if the competing intermetallic compound has a large negative heat of mixing, so will the corresponding metastable amorphous phase. — The diffusivity criterion has been described as "desirable" rather than "nec-

essary", because several groups (e.g., Ding *et al.*<sup>10</sup>) have recently shown amorphisation in metal combinations where no "fast" diffusion is observed.

One issue which is currently being debated is the effect of the gradually diminishing concentration gradient across the growing amorphous layer. It has been claimed<sup>11-13</sup> that the initial steep gradient reduces or suppresses the driving force for nucleation of the stable intermetallic phase, and that this suppression disappears as the gradient reduces. Others are not wholly convinced by the thermodynamic argument (Greer, *priv. comm.*). An alternative, kinetic treatment of the same problem — the competition between the metastable amorphous phase and the stable crystalline phase — has been proposed by Gusak and Nazarov<sup>14</sup>. The subtle kinetic and thermodynamic factors that govern the competition between amorphization and intermetallic phase formation have been extensively discussed by others also, for instance by Highmore<sup>15,16</sup> and by Greer<sup>17</sup>. It is however important to be clear that not only the crystalline stable phase, but also the metastable amorphous phase does in fact need to be heterogeneously nucleated, most readily at grain boundaries of the more slowly diffusing metal; if the zirconium layer is monocrystalline, no SSAR takes place<sup>18</sup>.

Clearly, the fact that a limiting thickness of amorphous layer exists suggests, at first sight, that amorphisation will be favoured if individual metal layers are made very thin. In fact, Lin and Spaepen<sup>19</sup> found that when they prepared Ni-Nb sandwiches with ultrathin (3 nm) evaporated layers, amorphisation took place without the need for subsequent heat-treatment! Contrariwise, Clemens<sup>20</sup> discovered that, whereas a multilayer of thick (20 nm) Ni and Ti films amorphised readily on annealing, no amorphous phase could be formed if the layers were only 1-2 nm thick, and he suggested that for very thin films, the interfaces are probably coherent and of low energy, whereas with thick layers, energetic incoherent interfaces are present and this favours amorphisation. Clearly, this thickness effect varies from one system to another.

Cahn has discussed the diffusion process in amorphous layers formed in this way, and has demonstrated, on the basis of recent experiments on Ni-Zr on the kinetics of amorphous layer growth, by Rubin and Schwarz<sup>21</sup>, that diffusion rates in amorphous alloys made by SSAR are different from the values in similar glasses made by rapid solidification. In the previously cited study by Ding *et al.*<sup>10</sup>, the rates of growth in Ni/Zr and Au/Zr couples differed only by about 10 times, whereas the diffusivity of Ni in Zr is about 10<sup>5</sup> times greater than that of Au in Zr.

Numerous kinds of metallic couple have been found to be subject to this form of SSAR. — The classic early overview of this form of amorphization is by Johnson<sup>22</sup>, while a very recent and up-to-date review (which also discusses mechanical amorphization) is by Schwarz *et al.*<sup>23</sup>. Two conferences have also been devoted to SSAR, including the mechanical version<sup>24,25</sup>.

### 1.3 Pressure-Induced Vitrification

This specialised technique is restricted to systems with a negative volume change on melting. In a renowned experiment, Mishima *et al.*<sup>26,27</sup> amorphised ice Ih by compressing to 10 kbar at 77K; SnI<sub>4</sub> is another species which was amorphised in this manner<sup>28</sup>. Schwarz *et al.*<sup>23</sup> suggested that metalloids such as Ge, Si, Sb and Bi might also behave like this, but that has yet to be established. However, pure Si has been amorphised by ball-milling.

## 2. Mechanically Aided Amorphisation

I suggest this name for procedures in which heavy deformation is used to reduce the thickness of the initial metals so that diffusion distances become small enough to allow amorphisation to proceed, as distinct from other procedures in which the deformation in itself causes an amorphous phase to form. In fact, the two approaches shade into each other.

The production of "ultrafine filamentary composites" by intense swaging, groove-rolling or wire-drawing was pioneered in the 1970s, notably by Bevk who wrote an excellent review about these materials<sup>29</sup>. (There was special interest in making such composites as superconductors.) In connection with our present concerns, it should be remembered that ultraheavy deformation greatly alters physical properties such as electrical conductivity and elastic stiffness, and thus the overall free energies of the starting phases are inevitably affected. As an example of this, Fig. 1 (from Bevk's review) shows the very large changes of Young's modulus due to wire drawing (and subsequent recrystallization annealing); small wire diameters here correspond to large wire-drawing strains. At that time, SSAR was unknown.

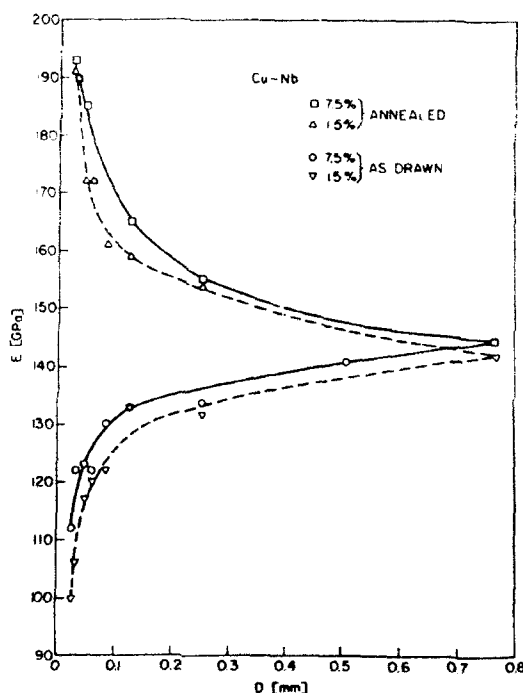


Fig. 1. Young's Modulus of Cu/Nb composites of two different compositions as a function of as-drawn wire diameter, before and after annealing. (Ref. 29)

Atzmon *et al.*<sup>30,31</sup> rolled stacks of alternating 20-200  $\mu\text{m}$  foils of Ni/Zr, Cu/Zr, Ni/Er and Cu/Er to very heavy reductions and then annealed them. They also experimented with rolled, mixed Ni and Zr powders held in a steel tube. In all cases an amorphous phase formed, but some elemental metals remained unaltered. Schultz<sup>32</sup> worked with similar Ni/Zr stacks; his amorphous phase had a composition different from that of the average of the stack, implying that the Zr had become exhausted before the Ni. In fact, it appears from an excellent review by Schultz<sup>33</sup> that he was the first to observe mechanically aided amorphisation.

An extensive series of experiments on cold-rolled multilayer stacks, done by Bordeaux and Yavari, 1987-90, has recently been reviewed by them<sup>34</sup>. They worked with the Ni/Nb, Ni/Zr (the universal favourite!), Cu/Zr, Cu/Ti and Fe/Ti. They were also able to amorphise an Al/Pt stack after heavy rolling<sup>35</sup>; this is a system with a strong negative heat of mixing but (in view of the near equality of atomic diameters) presumably little asymmetry of diffusivities. With the Ni/Zr system, they showed that most of the rolled stack was already amorphised immediately after rolling, before any annealing. This was confirmed by Martelli *et al.*<sup>36</sup>, who also demonstrated amorphous layers in Ni/Zr compressed stacks.

Bordeaux and Yavari made careful kinetic measurements of amorphisation rates, using XRD and DSC, and were able to show (in spite of difficulties occasioned by the fact that the as-rolled layer thicknesses had a broad Gaussian distribution) that amorphisation was much faster than in an inter-diffusion experiment in the absence of cold work. This comparison was also complicated by the fact that deformation causes local heating at the foil interfaces, which may transiently approach 100K as measured by thin foil thermocouples<sup>36</sup>. From their kinetic studies of the rate of thickness increase of the amorphous layers they deduced that the activation energies for Ni diffusion in the amorphous layers were much lower than those measured for undeformed multilayer stacks; this suggests that "holes", the form that deformation damage takes in a metallic glass, have accelerated diffusion; this is quite reasonable, since holes are known to be the main means of atomic transport in such glasses. — It may well be that the extreme defect concentrations (deduced from evidence such as that in Fig. 1) so much altered the balance of free energies and hence the driving force for amorphisation that this may also have contributed to the change in kinetics.

### 3. Mechanically Induced Amorphisation

In the last Section, several experiments were mentioned in which amorphised layers were observed immediately following heavy cold deformation, before any annealing had been done. Such processing constitutes *mechanically induced* (as opposed to *aided*) *amorphisation*. However, this term is usually applied to experiments in which a powder is mechanically milled (=ground). The powder can either be a prealloyed intermetallic phase, or else a mixture of elementary powders.

Milling is done by causing hard grinding media (balls), often of steel, to collide with each other, trapping powder particles between. Various geometries (rotary mills, vibratory mills, planetary mills) are used. Details of apparatus and its mode of operation are presented in a detailed overview by Koch<sup>37</sup>; the reader is referred to this very up-to-date and critical account.

The formation of amorphous phases by mechanical alloying of elemental metal powders was first reported in Russia<sup>38</sup>. Soon afterwards, Schwarz and Koch<sup>39</sup> prepared amorphous products by ball-milling Ni/Ti and Ni/Nb mixtures. There was then a rapid acceleration of research. A number of intermetallics could be milled to give amorphous products; so could appropriate mixtures of two intermetallics of different compositions in the same binary systems<sup>40</sup>. In fact, it now appears that in most instances, the end-product is the same, irrespective of whether the starting material is a mixture of elements, a single intermetallic phase or a mixture of two such phases. An exception to this found in  $\text{Mg}_{70}\text{Zn}_{30}$ , which can only be amorphised by grinding the intermetallic compound, not from the elements<sup>41</sup>. — A special case is the amorphisation of ball-milled pure Si, observed by Gaffet and Harmelin<sup>42</sup>. For details of the rather complex arguments adduced to reveal amorphisation, and the nature of the evidence that crystalline Si becomes unstable when the grain size is reduced below a critical level of  $\approx 3$  nm, the reader is referred to Koch's review<sup>37</sup>.

Fig. 2, from the review by Schwarz *et al.*<sup>23</sup>, shows the progressive disappearance of crystalline XRD lines and their replacement by an amorphous halo. Schwarz and Petrich<sup>43</sup>, by removing samples at intervals during milling and subjecting them to comparative DSC measurements, were able to deduce that initially, amorphisation kinetics are determined by interdiffusion; at a later stage, particles are separated by amorphous layers and attrition, creating fresh metal/metal contacts, determines kinetics.

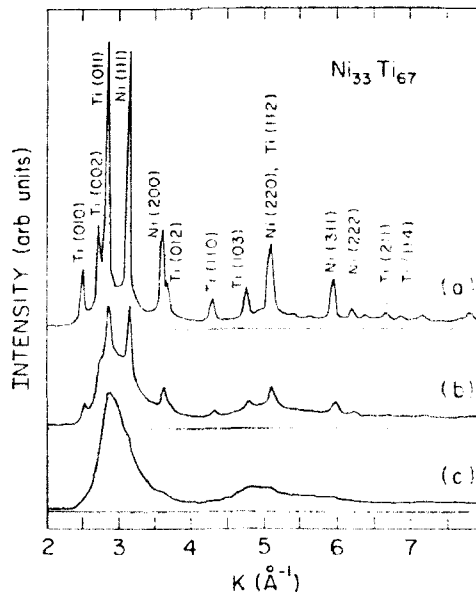


Fig. 2. XRD patterns as a function of  $K = 4\pi \sin\theta / \lambda$ , for a mixture of Ni and Ti powders, mechanically alloyed for (a) 2, (b) 5 and (c) 25 h. (From ref. 23).

Thus, it appears that mechanically aided and mechanically induced amorphisation, in spite of superficial differences, are really variants of a single process. In mechanically induced amorphisation, the temperature rises substantially for brief moments as particles collide. The estimation of the temperatures which may be reached is critically examined by Koch<sup>37</sup>.

Various recent researches have established that for a given system and composition, different results are obtained according to the nature and intensity of the ball-milling (in particular, according as planetary or vibrational mills are used). Gerasimov *et al.*<sup>44</sup> showed that with the Ti/Cu and Zr/Co systems, increasing ball energy led to a tendency towards a crystalline as opposed to an amorphous product. Thus, Weeber *et al.*<sup>45</sup>, working with our familiar friend the Ni/Zr system, found that with one kind of mill, Ni and Zr reacted directly to give an amorphous phase; with another kind of mill, a crystalline intermetallic phase was formed as an intermediate product. For a planetary mill, where there are two independently controllable rotation speeds, different regimes were found by Gaffet for the Ni/Zr system according to the combination of speeds; details of this, and other very recent studies of the different behaviour of different milling systems, can be found in Koch's review<sup>37</sup>.

Mechanically amorphised powders have been tested by a variety of methods to confirm their amorphous nature. The radial distribution function of amorphous NiTi is very similar, whether it has been made by melt-spinning or by mechanical milling. A range of Ni/Zr glasses was made by both these methods and the superconducting transition temperature, which is highly sensitive to atomic arrangement, turned out to be similar for the two groups of material<sup>33</sup> (Fig. 3). The small systematic deviation between the two groups of points was traced to the use of two distinct measurement techniques.

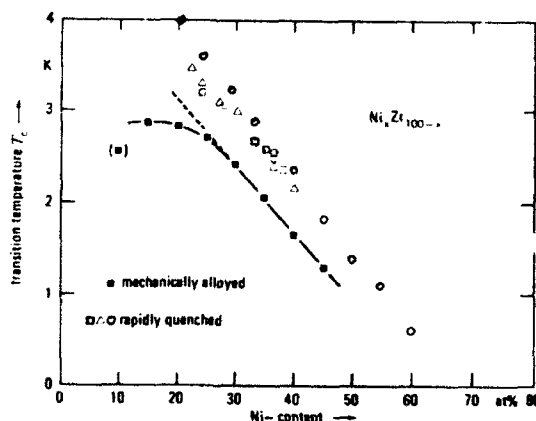


Fig. 3. Superconducting transition temperature of mechanically alloyed and melt-spun variants of amorphous  $Ni_xZr_{100-x}$  samples. (Ref. 33).

#### 4. Criteria for Mechanical Amorphisation.

The researches of Luzzi and Meshii<sup>4</sup> on the irradiation --induced amorphisation of  $\text{Cu}_3\text{Ti}$  were mentioned at the outset. They demonstrated that, in this phase, it was necessary for long-range (chemical) order to be substantially (not totally) destroyed before the amorphous phase could form. In an important study, Jang and Koch<sup>46</sup> were able to partially amorphise  $\text{Ni}_3\text{Al}$ ; before any amorphous phase formed, the Bragg LRO parameter had fallen to zero. Some milling time thereafter, part of the microstructure slipped from a nanocrystalline into an amorphous condition (Fig. 4).

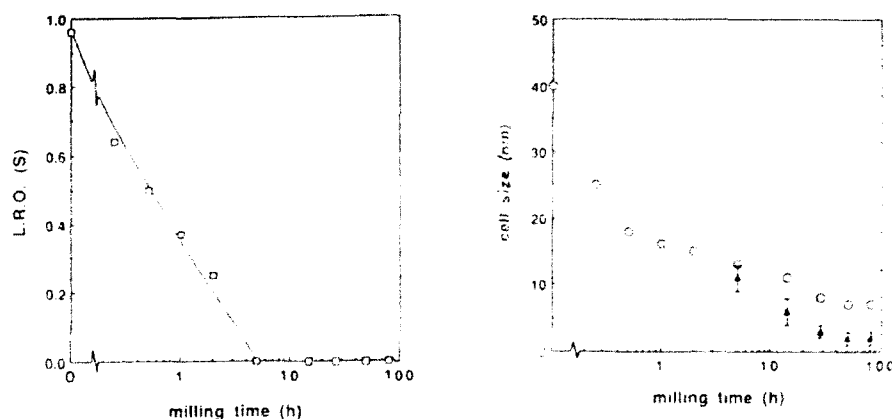


Fig. 4. Long-range order parameter and grain diameter of  $\text{Ni}_3\text{Al}$  as function of milling time. RHS: open symbols from XRD, closed symbols from TEM.<sup>46</sup>

This study showed that after long milling times, an alloy can enter a state where some of the structure is nanocrystalline while other parts have become truly amorphous. Even pure metals can reach the stage of nanocrystallinity; recently, Fecht *et al.*<sup>47</sup> ball-milled b.c.c and h.c.p. metals such as Fe, Cr, Co, Zr, Nb, and reduced all of them to a nanocrystalline condition (grain sizes in the range 9 - 13 nm), but no amorphous phase was formed. There is now a reliable calorimetric technique allowing nanocrystalline and amorphous phases to be distinguished<sup>48</sup>, but this not yet been applied to analyse the exact structure of ball-milled intermetallic phases such as  $\text{Ni}_3\text{Al}$ .

Gialanella *et al.*<sup>49</sup> recently examined in depth the disordering of  $\text{Ni}_3\text{Al}$  by milling. It was found that the lattice parameter continued to increase, substantially, after all LRO had disappeared. Lattice strain, enhanced defect concentrations and elastic mismatch no doubt contributed to this, but it is also probable that the gradual destruction of short-range order (following the disappearance of long-range order) also contributed. The fact that, to amorphise the alloy, milling has to continue well beyond the stage when LRO disappears, suggests that some or all of the factors listed are necessary to destabilise the crystalline lattice for this alloy.

An important new approach is due to Beke *et al.*<sup>50</sup>. They were able to

estimate from first principles the additional elastic mismatch energy stored in an ordered solid solution (compound) when its long-range chemical order is destroyed, whether mechanically or by irradiation; this depends, of course, among other things on the atomic sizes. They then further showed that if (a) the (virtual) critical disordering temperature is above the melting temperature and (b) the ratio of the elastic mismatch energy to the ordering energy is high enough. These criteria were tested on numerous systems (most of these had been disordered experimentally by irradiation rather than milling) and agreement was found throughout. This is the first carefully tested universal criterion for amorphisation via destruction of LRO that has yet been proposed.

### 5. Amorphisation and Melting

The resemblances and differences between solid-state amorphisation and melting — and for that matter, between both these processes and loss of long-range chemical order — have interested a number of investigators in recent years. Cahn and Johnson<sup>51</sup> in 1986 critically compared all three processes with special reference to the need for heterogeneous nucleation in all three. Since then, there have been developments in our understanding of melting as well as of amorphisation. Further, it is now quite clear that, in some alloys at least, chemical disordering above  $T_c$  is nucleated at antiphase domain boundaries (e.g., Leroux *et al.*<sup>52</sup>); in view of this fact, it is worth bearing in mind that intermetallic phases such as  $\text{Ni}_3\text{Al}$  which are ordered up to their melting temperatures *ipso facto* contain no antiphase domain boundaries, and so their mechanically induced disordering should be impeded on this account.

An important analysis was published recently by Wolf *et al.*<sup>53</sup>. They examine recent experimental, theoretical and computer simulation research related to melting and conclude that there are two types of melting, one involving heterogeneous nucleation (e.g., at free surfaces, grain boundaries, etc.) and one involving mechanical destabilisation of the crystalline lattice (the so-called shear instability first described long ago by Born). Wolf *et al.* then adduce reasons why loss of long-range chemical order is not in itself the prime cause of amorphisation; rather, the increase of unit cell volume which is always an incidental result of disordering (the more so, the higher the ordering energy) leads to a critical combination of volume and temperature at which the lattice becomes destabilised. The reader is referred to this stimulating paper for details of the involved argument.

Fecht and Johnson, who have analysed the thermodynamics of melting and of amorphisation in some detail<sup>54</sup>, have recently studied the amorphisation of  $\text{Fe}_2\text{Er}$  hydride powder particles, small enough so as not to contain any grain boundaries<sup>55</sup>. Thereby, premature heterogeneous nucleation of the amorphous phase is prevented, and the result is a  $\lambda$ -type specific heat anomaly when homogeneous amorphisation finally arrives on heating. This kind of melting is catastrophic, and resembles, as Fecht and Johnson point out, the (simulated) catastrophic melting of a crystal superheated well above the thermodynamic (i.e., heterogeneously nucleated) melting temperature. In the end, it may well be that the study of amorphisation will decisively enhance our understanding of the long-disputed nature of the melting transition.



## 6. Sonochemical Synthesis

This article has been wholly concerned with solid-state transitions, at least until melting reared its head in the last few lines. Since liquids *have* now appeared in this article, it will be as well to conclude with a mention of the most remarkable method which has yet been demonstrated to make a metallic glass.

Suslick, at the University of Illinois, is a noted exponent of the science of sonochemistry<sup>56</sup>, that is, the effecting of chemical change by appropriately directed ultrasonic energy...a form of mechano-chemistry. His team has now demonstrated<sup>57</sup> that it is possible to make fine amorphous iron powder by ultrasonic irradiation, at 0°C, of iron pentacarbonyl,  $\text{Fe}(\text{CO})_5$ , a liquid. The powder, of  $\approx 5 \mu\text{m}$  diameter and with a very large effective surface area, shows promise as a catalyst. This must be the ultimate in mechanical amorphisation.

## 7. References

1. J. Bloch, *J. Nucl. Mat.* **6** (1962) 203.
2. K.C. Russell, *Prog. Mat. Sci.* **28** (1985) 229.
3. P.R. Okamoto and M. Meshii, in *Science of Advanced Materials*, ed. H. Wiedersich and M. Meshii. (ASM International, Materials Park, Ohio, 1990), p. 33
4. D.E. Luzzi and M. Meshii, *J. Less-Comm. Met.* **140** (1988) 193.
5. P.R. Okamoto, L.E. Rehn, J. Pearson, R. Bhadra and M. Grimsditch, *J. Less-Comm. Met.* **140** (1988) 231.
6. R.B. Schwarz and W.L. Johnson, *Phys. Rev. Lett.* **51** (1983) 415.
7. A.L. Greer, K. Dyrbye, L.U. Aaen-Andersen, R.E. Somekh, J. Böttiger and J. Janting, *Mat. Res. Soc. Symp. Proc.* **187** (1990) 3.
8. S.B. Newcomb and K.N. Tu, *Appl. Phys. Lett.* **48** (1986) 1436.
9. W.J. Meng, C.W. Nieh, E. Ma, B. Fultz and W.L. Johnson, *Mater. Sci. Eng.* **97** (1988) 87.
10. F.-R. Ding, P.R. Okamoto and L.E. Rehn, *J. Mater. Res.* **4** (1989) 1444.
11. P.J. Desré and A.R. Yavari, *Phys. Rev. Lett.* **64** (1990) 1533.
12. P.J. Desré and A.R. Yavari, *J. Phys. France* **51** (1990) C4-11.
13. P.J. Desré, *Acta Metall. et Mater.* **39** (1991) 2309.
14. A.M. Gusak and A.V. Nazarov, *J. Phys. Condens. Matt.* (1992), in press.
15. R.J. Highmore, A.L. Greer, J.A. Leake and J.E. Evetts, *Mater. Lett.* **6** (1988) 401.
16. R.J. Highmore, *J. Phys. France (Colloques)* **51** (1990) C-37.
17. A.L. Greer, *Phil. Mag. B* **61** (1990) 525.
18. A.M. Vredenburg, J.F.M. Westendorp, F.W. Saris, N.M. van der Pers and Th. D. Keijser, *J. Mater. Res.* **1** (1986) 775.
19. C.-J. Lin and F. Spaepen, *Acta Metall.* **34** (1986) 1367.

20. B.M. Clemens, *Phys. Rev. B* **33** (1986) 7615.
21. J.B. Rubin and R.B. Schwarz, *Appl. Phys. Lett.* **55** (1989) 36.
22. W.L. Johnson, *Prog. Mat. Sci.* **30** (1986) 81.
23. R.B. Schwarz, J.B. Rubin and T.J. Tiainen, in *Science of Advanced Materials*, ed. H. Wiedersich and M. Meshii (ASM International, Materials Park, Ohio, 1990), p. 1.
24. *Solid State Amorphizing Transformations*, ed. R.B. Schwarz and W.L. Johnson. (Proc. Conf. at Los Alamos, August 1987). *J. Less-Comm. Met.*, **140** (1988), pp. 1-399.
25. *Multilayer Amorphisation by Solid-State-Reaction and Mechanical Alloying*, ed. A.R. Yavari and P. J. Desré. *Colloque No. 4, Suppl. au J. de Physique (France)*, **51** (1990), pp. C4-3 — C4-310.
26. O. Mishima, L.D. Calvert and E. Whalley, *Nature* **310** (1984) 393; *ibid* **314** (1985) 76.
27. E. Whalley, *J. Less-Comm. Met.* **140** (1988) 361.
28. Y. Fujii, M. Kowaka and A. Onodera, *J. Phys. C* **18** (1985) 789.
29. J. Bevk, *Ann. Rev. Mater. Sci.* **13** (1983) 319.
30. M. Atzmon, J.D. Verhoeven, E.D. Gibson and W.L. Johnson, *Appl. Phys. Lett.* **45** (1984) 1052.
31. M. Atzmon, K.M. Unruh and W.L. Johnson, *J. Appl. Phys.* **58** (1985) 3865.
32. L. Schultz, *Mat. Res. Soc. Symp. Proc.* **80** (1987) 97.
33. L. Schultz, in *New Materials by Mechanical Alloying Techniques*. E. Arzt and L. Schultz, eds. (DGM Informationsgesellschaft, Oberursel, 1989), pp. 53-72.
34. F. Bordeaux and A.R. Yavari, *J. Phys. France*, **51** (1990) C4-249.
35. F. Bordeaux and A.R. Yavari, *J. Appl. Phys.* **67** (1990) 2385.
36. S. Martelli, G. Mazzone, A. Montone and M. Vittori Antisari, *J. Phys. France* **51** (1990) C4-241.
37. C.C. Koch, in *Processing of Metals and Alloys*, ed. R.W. Cahn. (VCH, Weinheim, 1991), pp. 193-245.
38. A. Ye. Yermakov, Ye. Ye. Yurchikov and V.A. Barinov, *Phys. Met. Metall.* **52** (1981) 90; *ibid* **54** (1982) 935.
39. R.B. Schwarz and C.C. Koch, *Appl. Phys. Lett.* **49** (1983) 146.
40. P.Y. Lee, J. Jang and C.C. Koch, *J. Less-Comm. Met.* **140** (1988) 73.
41. A. Calka and A.P. Radlinski, *Mat. Sci. Eng. A* **118** (1989) 131.
42. E. Gaffet and M. Harmelin, *J. Less-Comm. Met.* **157** (1990) 210.
43. R.B. Schwarz and R.R. Petrich, *J. Less-Comm. Met.* **140** (1988) 171.
44. K.B. Gerasimov, A.A. Gusev, E. Yu. Ivanov and V.V. Boldyrev, *J. Mater. Sci.* **26** (1991), in press.
45. A.W. Weeber, W.J. Haag, A.J.H. Wester and H. Bakker, *J. Less-Comm. Metals* **140** (1988) 119.
46. J.S.C. Jang and C.C. Koch, *J. Mater. Res.* **5** (1990) 498.

47. H.J. Fecht, E.Hellstern, Z. Fu and W.L. Johnson, *Met. Trans. A* **21A** (1990) 2333.
48. L.C. Chen and F. Spaepen, *Nature* **336** (1988) 366; *J. Appl. Phys.* **69** (1991) 679.
49. S. Gialanella, S.B. Newcomb and R.W. Cahn, in *Ordering and Disordering in Alloys*, ed. A.R. Yavari. (Elsevier Applied Science, London, 1992), in press.
50. D.L. Beke, P.I. Loeff and H. Bakker, *Acta Metall et Mater.* **39** (1991) 1259, 1267.
51. R.W. Cahn and W.L. Johnson, *J. Mater. Res.* **1** (1986) 724.
52. C. Leroux, A. Loiseau, M.C. Cadeville, D. Broddin and G. van Tendeloo, *J. Phys: Condens. Matt.* **2** (1990) 3479.
53. D. Wolf, P.R. Okamoto, S. Yip, J.F. Lutsko and M. Kluge, *J.Mater. Res.* **5** (1990) 286.
54. H. Fecht and W.L. Johnson, *Nature* **334** (1988) 50.
55. H.J. Fecht and W.L. Johnson, *Mater. Sci. Eng. A* **133** (1991) 427.
56. K.S. Suslick, *Scient. Amer.* **260** (1989) 80.
57. K.S. Suslick, S.-B. Choe, A.A. Cichowlas and M.W. Grinstaff, *Nature* **353** (1991) 414.

UNCONVENTIONAL METHODS FOR OBTAINING GLASSES  
AND  
AMORPHOUS MATERIALS

J. ZARZYCKI

*Laboratory of Science of Vitreous Materials, UA 1119  
University of Montpellier 2, (France).*

ABSTRACT

Glasses and amorphous solids may be obtained by various techniques starting from the liquid or solid state. These methods are briefly described here and their fields of application, as well as eventual influences on resulting final products, discussed.

1. Introduction : Glasses and "Amorphous Solids"

Glasses were originally defined as non-crystalline solids obtained by quench of liquids sufficiently rapid to by-pass crystallization.

It was, however, progressively realized that this is not the only method by which non-crystalline materials could be obtained and many "amorphous" thin layers were produced by condensing a vapour on a cold substrate. It is now recognized that many routes exist by which liquid, gas or solid phases may be converted into non-crystalline materials. There is still some confusion in the respective definitions of the various terms "glassy", "amorphous" and "non-crystalline". We shall define *glasses* as that subgroup of non-crystalline materials which display glass transition phenomenon, the remainder being catalogued as "amorphous".<sup>1</sup> This classification is, however, by no means universally adopted and some authors prefer to consider the term "amorphous" as synonymous with "non-crystalline" and define glasses as amorphous materials which display the  $T_g$  transition.

## 2. Formation of Non-Crystalline Solids

Following Turnbull<sup>2</sup> it may be considered that the procedure for forming non-crystalline materials in general consists of three steps :

In the first step the material is *energized* by melting, evaporation, dissolution or irradiation. (In the recently discovered method for forming amorphous alloys by solid state diffusion, the energization consists in the creation of new solid surfaces).

In the second step the material is *deenergized* by quenching, condensation or establishing a contact between dissimilar surfaces. This step offers a thermodynamic opportunity for forming the non-crystalline material.

The third step, which immediately follows the second, is a further deenergization in which the non-crystalline form is *kinetically trapped* and brought down to ambient temperature.

There is no theoretical proof that the lowest energy state of a three-dimensional material must be crystalline, but experimental evidence shows that in solid state crystalline or quasi-crystalline arrangements are more stable than the non-crystalline arrangements, which form below a configuration freezing point or transition point  $T_g$  for glasses.

The non-crystalline solid formation thus appears to be *kinetically* preferred to crystallization.

The kinetically favored path in a structural evolution is generally the one which involves the least reconstruction. The formation of non-crystalline solids will preferentially occur in the cases where crystallization requires important remodelling of atomic configuration (reconstructive processes).

The appearance of crystallization indicates either that the thermodynamic factors override the process or that the crystal growth was not thermally activated i.e. was not quench suppressible.

The following general types of methods are at our disposal<sup>3</sup> :

- melt quenching
- vapour quenching
- crystalline solid disordering (other than melting)

- interdiffusion and sintering
- electrolysis
- pyrolysis
- reactions in solution.

### 3. Melt quenching

The usual way of obtaining a glass is by quenching a melt obtained by fusion of one or several crystalline substances. When the rate of temperature decrease is sufficient to by-pass crystallization, the disordered state of the liquid is retained in the solid state.

Intrinsic glass-forming tendency is strongly correlated with scaled glass temperature  $T_{rg} = T_g/T_c$  where  $T_c$  is the thermodynamic crystallisation point and increases with  $T_{rg}$ . The nucleation speed  $I$  of the crystalline phase increases rapidly below a certain temperature  $T_0$  i.e. below a "threshold undercooling"  $\Delta T_r^\circ = (T_c - T_0)/T_c$ .

For  $\text{SiO}_2$ ,  $\text{B}_2\text{O}_3$  etc,  $T_{rg} \sim 0.7$  to  $0.8$ , while for metal melts  $T_{rg} \sim 0.4$  to  $0.6$  with  $\Delta T_r^\circ \sim 0.2$  to  $0.3$ . Calculations show<sup>4,5</sup> that nucleation would be insuppressible when  $T_{rg} = 0$ , suppressible at quench rates  $\sim 10^6 \text{ Ks}^{-1}$  for  $T_{rg} = 0.5$  and inobservable for  $T_{rg} > 0.7$ .

Crystallization is then further restrained by kinetic resistance to crystal growth which proceeds with a speed  $u$ .

A suitable combination of  $I$  and  $u$  gives an *intrinsic* glass-forming tendency (IGFT) and thus determines a minimum cooling rate necessary to convert a given volume of melt into glass.

IGFT is strongly affected by the presence of foreign particles (contaminants) which act as heterogeneous nucleation centers.

While the quench in air is most usual, the quench in a liquid (water, mercury or liquid nitrogen) may be used to achieve higher cooling rates. The quenching rate is, however, quickly limited in practice (up to  $10^{-2} \text{ }^\circ\text{C/s}$ ) by the formation of an insulating vapour layer at the glass-liquid interface (calefaction effect).

To achieve higher cooling rates it is necessary to use a contact with a *solid* of high thermal conductivity, generally a metal such as copper.

The "splat cooling" technique invented by Duwez<sup>6</sup> consists in projecting a droplet of a melt by the action of a pressure shock wave which propulses the sample towards a curved Cu-plate. The glass is obtained in the form of thin flakes of a few  $\mu\text{m}$  thickness resulting from a high speed conduction cooling ( $10^6 - 10^9 \text{ Ks}^{-1}$ ).

In another device, due to Piotrowsky<sup>7</sup>, the molten drop expelled from a crucible is smashed between two metallic plates, one of which is electronically triggered via a photocell by the drop itself. The advantage of this device is that it produces plates of uniform thickness devoid of holes as in Duwez device but quenching speeds are somewhat lower ( $10^5 \text{ Ks}^{-1}$ ).

Devices using laser sources for melting were recently developed.

The quality of the contact between the liquid and the solid substrate controls the effective cooling rate as shown by Ruhl<sup>8</sup>.

The calculation of limiting cooling speeds in splat cooling was done by Bletry<sup>9</sup>.

The cooling of a molten drop between two rapidly rotating steel rollers was first used by Zarzycki and Naudin<sup>10</sup> to produce flakes of  $\text{B}_2\text{O}_3 - \text{PbO} - \text{Al}_2\text{O}_3$  glasses for unmixing kinetics studies. Chen and Miller<sup>11</sup> developed a similar device for obtaining metallic glasses which was also used by Suzuki and Anthony<sup>12</sup> to examine various binary systems of refractory oxides, some of which formed glasses.

All the preceding devices produce small samples suitable only for laboratory examination of structure. To make continuous ribbons of metallic glasses Chen and Miller<sup>13</sup> used a metallic (Cu-Be) wheel spinning at 300-1800 rpm. The liquid stream impinges onto the *inside* of torus-like convex surface of the wheel. The quenched ribbon slips out of the wheel under the action of the centrifugal force. Ribbons 0.5 mm wide, 20  $\mu\text{m}$  thick, and up to 100 m in length, were produced.

The technique was further improved by quenching the melt on the *outside* of the spinning wheel. The liquid is spread in the form of continuous film with quench rates  $10^6 - 10^8 \text{ Ks}^{-1}$ . Modern devices enable ribbons up to several dm wide to be produced.

In splat cooling techniques one dimension (the thickness) of the splat or of the ribbon is kept small in order to speed up the heat

exchange. It is also possible to subdivide the melt into droplets small enough to achieve high cooling rate by radiation. In the method of laser spin-melting<sup>14</sup> small droplets are produced by spinning at 8.000 - 30.000 rpm the target in the form of a rod the extremity of which is heated by a power CO<sub>2</sub>-laser. Cooling rates of 500  $\mu$ m droplets were estimated at 4000°C/s. Various refractory oxides and their mixtures (Al<sub>2</sub>O<sub>3</sub>, Ga<sub>2</sub>O<sub>3</sub>, La<sub>2</sub>O<sub>3</sub>, Nb<sub>2</sub>O<sub>3</sub>, Ta<sub>2</sub>O<sub>5</sub>, etc.) were obtained in partly non-crystalline form.

#### 4. Vapour quenching

The formation of non-crystalline solids may also be achieved by the deposition of one or several components in vapour state onto a substrate. The vapour may be produced by heating a suitable compound and deposited as such without further modification (nonreactive deposition) or a chemical reaction may intervene (reactive deposition). In general the faster the rate of cooling or of deposition the further the non-crystalline solid departs from equilibrium. In the deposition methods the cold substrate causes the atoms to be "frozen" in random positions ; the higher its temperature the higher the mobility of the atoms and less structural defects are produced - but if substrate temperature is too high the material crystallizes (devitrifies).

In these methods the volume changes and the deenergization rates are orders of magnitude greater than in melt quenching. This leads to higher probabilities that crystallization will be by-passed.

Thus the scope of materials which can be successfully brought into non-crystalline state is much greater than in the melt quenching.

These processes are typically used for producing thin films for electronic and optical applications. Reactive deposition, however, may also be used to produce bulk glasses difficult to obtain from the melt or when hyperpure materials are needed (e.g. blanks for optical fibres).

The typical methods are :

- thermal evaporation
- sputtering
- glow-discharge decomposition
- chemical vapour deposition (CVD)



#### *4.1 Thermal evaporation*

The method consists of producing a vapour in vacuum and condensing it onto the specimen. The various techniques differ according to the heating method employed to evaporate the substance : electric resistance heating, electron beam heating or high-frequency heating. The operation takes place in a residual atmosphere ( $10^{-4}$  to  $10^{-7}$  torr) and the vapour pressure of the depositing material is kept below  $10^{-2}$  torr. Single metals can be readily evaporated in this way. For multicomponent systems several separate sources may be used or a metal alloy rapidly evaporated using the "flash" technique.

#### *4.2 Sputtering*

In this method the specimen to be coated and the solid source are both contained in a closed vessel in a low pressure gas atmosphere (generally Ar). A high d.c. voltage of a few kV is used to produce a glow discharge, with the specimen as anode and the source as cathode. This produces  $\text{Ar}^+$  ions which are driven towards the cathode and eject (sputter) the atoms from the cathode. Part of these will condense on the specimen forming a uniform, generally non-crystalline film of a composition close to that of the source materials. Industrial devices use alternating voltages of 13 MHz and capacitive coupling which enables both metallic and dielectric materials to be used as targets. In "magnetron sputtering" magnetic fields increase the path of the ions and thus their collision frequency which results in a better sputter yield.

#### *4.3 Glow-discharge decomposition*

In this process chemical reaction is initiated in the gas phase by supplying sufficient activation energy in the form of an rf glow discharge.

The method became extremely important following the discovery of Spear and Le Comber<sup>15</sup> that by using this technique certain amorphous semi-

conductors may be substitutionally doped to control their electronic properties.

Hydrogenated amorphous silicon  $a\text{-(SiH}_x\text{)}$  is obtained from silane  $\text{SiH}_4$  and may give n-type or p-type semiconductors by adding respectively  $\text{PH}_3$  or  $\text{B}_2\text{H}_3$  to the initial gas. The rates of deposition are of the order of  $1\text{--}10 \text{ \AA s}^{-1}$ .

4.4 *Chemical Vapour Deposition (CVD)* involves a heterogeneous reaction and deposition from organometallic or metal halide vapours on a heated solid substrate. Hydrides are often used.

For example, passing gas mixtures such as  $\text{SiH}_4$ ,  $\text{PH}_3$  and  $\text{O}_2$  or  $\text{SiCl}_4$ ,  $\text{POCl}_3$  and  $\text{O}_2$  over a heated Si surface at temperatures below  $1000^\circ\text{C}$ ,  $\text{SiO}_2\text{--P}_2\text{O}_5$  glass layers are formed.

Thermally activated homogeneous oxydation of mixtures of metal halide vapours is used to obtain bulk glass of high purity and quality by vapour deposition techniques. Metal halides ( $\text{SiCl}_4$ ,  $\text{GeCl}_4$ ,  $\text{TiCl}_4$ ,  $\text{BCl}_3$ ,  $\text{POCl}_3$ ) are generally used as starting compounds and also  $\text{SiH}_4$  and organometallics e.g.  $(\text{CH}_3)_3\text{B}$ . At temperatures above  $1500^\circ\text{C}$  homogeneous oxydation reaction predominates and without a catalyzing surface a finely divided glass particulate material called "soot" is obtained.

When collecting soot on a target heated at a sufficiently high temperature ( $\approx 1800^\circ\text{C}$  for  $\text{SiO}_2$ ) sintering and conversion into solid bubble-free glass occur. By this means very large glass "boules" (over 500 Kg) were obtained for  $\text{SiO}_2$  either in pure form or with additions ( $\text{TiO}_2$ ,  $\text{Al}_2\text{O}_3$ ,  $\text{B}_2\text{O}_3$ );<sup>16,17</sup>

Lowering the soot deposition temperature to less than  $1500^\circ\text{C}$  helps to retain the more volatile components (e.g.  $\text{B}_2\text{O}_3$ ); this results in a porous silica body which can then be sintered in a separate step at a higher temperature<sup>18</sup>. Deposition methods based on these principles are used to prepare preforms for glass optical fibres.

## 5. Solid state methods

Non-crystalline solids may be obtained from crystals without passing through the fusion stage. There are several ways of destroying a regular crystal lattice.

### 5.1 Radiation damage

Collision of atoms of a crystal with energetic particles produces lattice defects ; the effect is cumulative and the process may end in the formation of a non-crystalline solid. Fast neutrons have a low probability of collision but each collision produces a large number of defects ; charged particles have a higher probability of collision but produce less displacements. The transfer of the kinetic energy of the particle to the neighbouring atoms produces "thermal spikes" of the order of several thousand K for  $10^{-10}$  -  $10^{-11}$  s which extend to regions of the order of  $10^4$  atoms and may produce local melting followed by an ultrafast quench.

Exposure of various ceramic materials to neutron doses of the order of  $3 \times 10^{20}$  neutrons/cm<sup>2</sup> renders these materials amorphous (metamictized).

### 5.2 Mechanical disordering

#### 5.2.1 Effects of intense shock waves

Powerful pressure shock waves of several hundred kbar generated during explosions may produce amorphization of crystals without their melting. The external boundaries of the original crystal are conserved and show the absence of flow but the crystalline lattice is destroyed. Such glasses are called *diaplectic* or *thetomorphic*.

Shock pressures are produced in the laboratory by explosions propelling a projectile (striking plate) which produces on impact with the specimen a pressure pulse of several hundred kbar of a few  $\mu$ s duration. Methods of calculating pressures and temperatures thus generated were given by Wackerle<sup>19</sup> and Gibbons and Ahrens<sup>20</sup>. In natural events (meteoritic impacts) much higher pressures are expected, reaching several Mbar. This may induce partial or total fusion and even vaporization of the sample.

Another use of the shock waves which should lead to important applications in the field of metallic glasses is the *explosive compaction* of metallic glass particles into homogeneous cylinders or disks. Such bulk pieces cannot be obtained by sintering without inducing crystallization whereas shockwave treatment preserves the

amorphous character of the material.

#### 5.2.2. *Slow mechanical actions*

The effects of shearing under prolonged mechanical grinding of a crystal can progressively destroy the crystalline order and lead to the formation of a non-crystalline solid. The *mechanical alloying* processes make use of "ball-milling" in attrition devices. The mechanical action which produces disorganization is combined with diffusional effects. These methods are the object of active studies.

Amorphous alloys such as Au-La, Ni-Zr, Cu-Zr, Ni-Hf, Ni-Nb and Ni-Ti formed by amorphization from layers or by "ball-milling" could also be quenched from the liquid state. The solid-state amorphized materials are thermodynamically more stable than when phase-separated into their pure crystalline components but less stable than in their crystalline intermetallic compound form. Hence the essential condition is that these compounds do not nucleate. Furthermore the rate of interdiffusion must be rapid and different for both components.

### 6. Diffusion effects

Interdiffusion effects can be employed to produce non-crystalline materials. Using multilayers formed of superposed crystalline metallic thin films, Johnson et al.<sup>21</sup> have shown the possibility of producing amorphous interlayers when pure metals characterized by a large negative heat of mixing are brought into contact under suitable kinetic conditions.

The subject of mechanical and interdiffusion amorphization will be treated in detail in another contribution to this Workshop<sup>22</sup>.

### 7. Electrochemical methods - Anodic oxydation

Amorphous oxide layers can be grown on the surface of a metal or semiconductor by making it the anode in an electrolytic cell in a variety of aqueous electrolytes. Al, Zr, Nb and especially Ta, will oxydize when a current is passed through the cell under sufficient overvoltage and a glass layer is formed up to several thousand Å thick<sup>23</sup>.

## 8. Pyrolysis

In this type of method a suitable compound (the precursor) is subjected to controlled thermal decomposition, the residue being the product to be synthesized.

As far as non-crystalline materials are concerned, pyrolysis is used in the synthesis of glass-like carbons.

## 9. Solution methods ; "sol-gel" processing of glasses

In polymer technology non-crystalline or partly crystalline materials ("plastics") are currently obtained in a direct way using methods of organic chemistry.

There exists, however, a whole set of methods in which *inorganic* glasses may be synthesized using methods of solution chemistry.

"Sol-gel" processes belong to this latter group of syntheses: they are based on the possibility of forming the disordered network of the glass, not directly at high temperatures from the melt, but at low temperatures from suitable compounds by chemical polymerization in a liquid phase. In this way a *gel* is first formed from which glass may be obtained by successive elimination of the interstitial liquid and collapse of the resulting solid residue by sintering.

As the sintering operation is carried out at temperatures much *lower* than those required for the melting of glass-forming components, practically in the vicinity of the transition temperature, the process is particularly attractive for the production of those glasses which require high melting temperatures (e.g.  $\text{SiO}_2$  glass can be made at  $1200^\circ\text{C}$  instead of at  $2000^\circ\text{C}$ ).

The second important characteristic of the process is that final homogeneity is directly obtained in solution *on a molecular scale*. This can be compared to the difficulties of obtaining homogeneous glasses in the classic way, particularly when one of the components is more volatile or when the resulting melts possess a high viscosity which hinders efficient mixing of the constituents. (In some cases it

is then necessary to remelt the original batch several times to reach the necessary compositional uniformity). This in turn increases the likelihood of contamination from crucible walls, particularly at high temperatures, or during repeated crushing procedures.

In the sol-gel route the glass may, in principle, be obtained with a degree of purity which depends only on the starting ingredients as the low temperature of the sintering process reduces the risk of contamination.

A substantially lower elaboration temperature, excellent homogeneity obtained directly on molecular level, and a high degree of purity, are the main advantages classically recognized for the sol-gel process.

Industrial applications are at present confined to the field of thin coatings and fibers. However, bulk glass may be obtained provided the gel is prepared in *monolithic* form, i.e. prevented from cracking during drying.

The "precursor-based" synthesis of glasses, ceramics and composites is, at the present time, one of the most rapidly progressing fields of Materials Science and Engineering and has already been treated in more detail in the First Workshop of this series<sup>24</sup>.

#### 10. Effects of the modes of formation on the structure and properties of glasses.

The preceding methods permitted the field of glass formation to be extended and a whole series of new non-crystalline solids to be obtained. In cases where the same material can be prepared in different ways, the essential question is whether the structure and properties of these materials differ according to the mode of formation.

There have been quite a number of investigations and even specialized conferences devoted to this topic<sup>25,26</sup>. Systematic comparative studies are, however, limited to semiconductors, (Si, Ge, As<sub>2</sub>S<sub>3</sub>, Si-H<sub>x</sub>), a few oxides (e.g. SiO<sub>2</sub>, GeO<sub>2</sub>) and several metallic alloys (e.g. Co-Zr, Ni-Ti).

Non-crystalline solids which can be formed only by condensation method generally crystallize when reheated without presenting a glass-melt  $T_g$  transition - they should thus be catalogued as *amorphous*.

Some of them, however, e.g. As<sup>12</sup>, do show  $T_g$  point before crystallization and should therefore be considered as *glassy*.

Stephens<sup>28</sup> compared the properties of vapour-deposited a-Se with those of melt-quenched Se glass. Figure 1 shows the results obtained for heat capacity from DSC studies. The glass-transition temperature  $T_g$  increased by about 10°C when the temperature of the cooled substrate was increased from -150°C to +5°C. After anneal the  $T_g$  was found to be the same as for well relaxed melt-quenched samples.

Phases condensed from vapour may display greater disorder (topological and compositional) but their basic structures are generally similar to the materials obtained by quench of liquid phases.

The specific volumes of non-crystalline elemental semiconductors a-Si and a-Ge formed by condensation, irradiation or melt quenching procedures were compared. The specific volumes varied considerably with the method of preparation but, when deposited on warm substrates or well annealed, the limiting volumes were identical or comparable to within 2% of the corresponding diamond cubic crystal<sup>29</sup>. Raman spectrum of rf-sputtered a-Si showed a continuous variation with deposition temperature<sup>30</sup> and differed from that of a CVD specimen (Fig.2).

Conversely, no difference in Raman spectrum was detected between an a-Si specimen formed by CVD or by quench following a laser pulse<sup>31</sup> (Fig.3).

Calorimetric studies have shown<sup>32</sup> that the excess specific heat of a-Ge over the corresponding crystalline value differed for electro-deposited and vapour deposited films (Fig.4). The indices of refraction of a-Si films produced by ion-implantation of crystalline Si were measured in the two metastable states : as implanted or thermally stabilized<sup>33</sup>, (Fig.5). They were shown to depend both on the mass of the incident amorphizing ions and the subsequent annealing temperature. It is in the case of electronic properties that the largest differences are observed in thin layers of semiconductors. The deposition conditions depend here on many experimental parameters, some of them imposed by the method and others which must imperatively be kept constant to ensure reproducibility of the results.

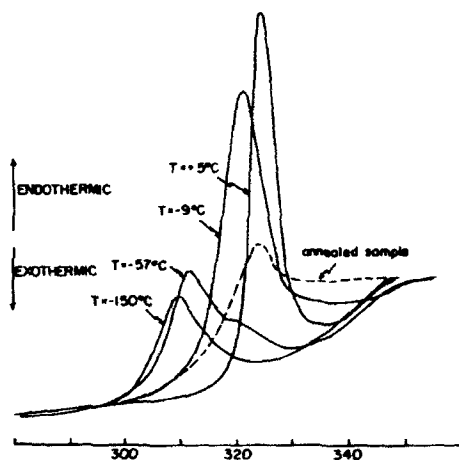


Fig.1 - Heat capacity curves obtained from differential scanning calorimetry at a scan rate= $20^\circ/\text{min}$  for Se thin films thermally evaporated onto substrates kept at temperatures indicated (After<sup>28</sup>).

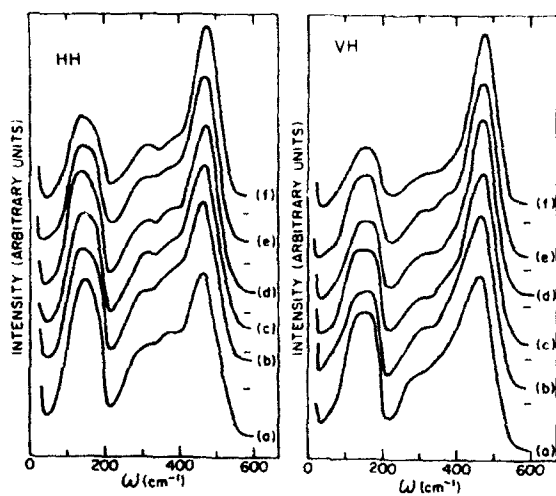


Fig.2 - Raman HH and VH spectra at 300°K of rf-sputtered amorphous -Si at a)  $30^\circ\text{C}$  b)  $200^\circ\text{C}$  c)  $400^\circ\text{C}$  d)  $500^\circ\text{C}$  e)  $560^\circ\text{C}$  compared to f) CVD a-Si at  $525^\circ\text{C}$  (After 30)



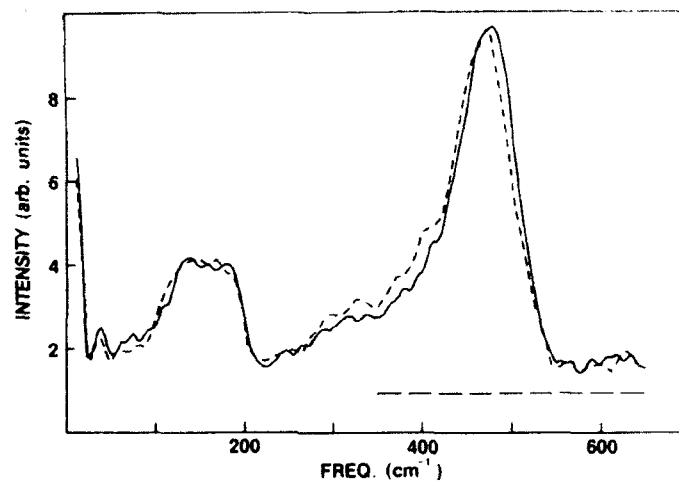


Fig.3 - Raman spectra of amorphous Si obtained by CVD (solid curve) and by liquid quench after a 700 ps laser pulse (dashed curve) (From<sup>33</sup>).

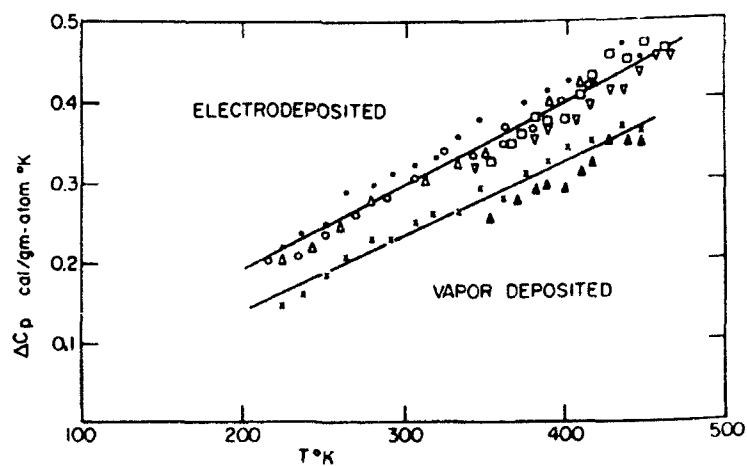


Fig.4 - The excess specific heat of amorphous Ge over the corresponding crystalline value for thin films obtained by electrodeposition (upper line) or by thermal evaporation (lower line) (After<sup>32</sup>).

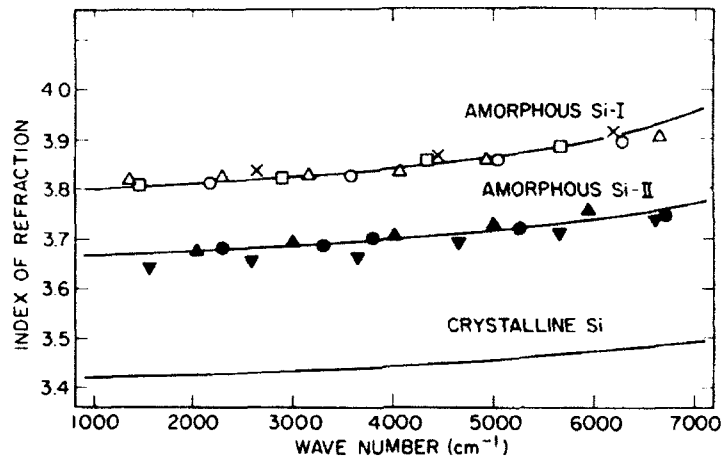


Fig.5 - Infrared refractive indices at  $4000\text{ cm}^{-1}$  of crystalline and amorphous Si obtained by ion implantation in two metastable states : Si-I as implanted and Si II, thermally stabilized (From 33).

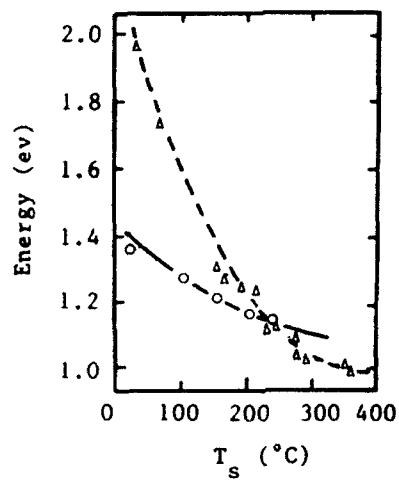


Fig.6 - Optical gap versus substrate temperature of hydrogenated a-Si thin films obtained by CVD ( $\Delta$ ) and rf plasma (o) (From 34).

In the case of amorphous hydrogenated silicon, the structural differences point to different Si-H bonding configurations, dangling bonds, weak bonds, etc. which influence the optical gap and localized states<sup>34</sup>, (Fig.6).

It should be noted that the species in vapour may not have the same composition as the source ; crystalline  $\text{As}_2\text{S}_3$  emits on heating  $\text{As}_4\text{S}_4$  molecules which condense in a layer bonded by Van der Waals forces and only subsequent annealing brings on polymerization. On the other hand, Mössbauer spectroscopy revealed a precipitous drop in concentration of homopolar S-S bonds in Te-doped  $\text{As}_2\text{S}_3$  glass with the temperature of liquid quench<sup>35</sup>. This was ascribed to the presence of  $\text{S}_8$  rings which form in glasses quenched from temperatures below 700°C. (Fig.7). No such effect was, however, detected in  $\text{As}_2\text{Se}_3$  glass.

The case of  $\text{SiO}_2$  glass which has been prepared by many different methods is particularly interesting. High density forms (e.g. shock-loaded) and low density forms (e.g. CVD) may be distinguished. Structural differences consist in variable proportion of network rings<sup>36</sup> and point defects (E centers) according to the method of preparation, the faster quench of deposition methods leading to more "open" structures.

Fig.9 shows the IR spectra of sputter-deposited and melt-quenched  $\text{GeO}_2$ <sup>37</sup>.  $^{29}\text{Si}$  MASNMR studies have shown that in vitreous  $\text{SiO}_2$  the Si-O-Si bond angles distribution varies with the method of preparation, this was attributed to different -OH contents<sup>38</sup>.

Mechanical alloying and interdiffusion methods favor the compositions in the vicinity of intermetallic compounds while in liquid quench methods the deep eutectic compositions are preferred.

The structure and properties of solid state amorphized alloys were revealed to be very similar to those formed by melt quenching. For example, the X-ray pattern, the enthalpy and kinetics of crystallization of amorphous (Ni-Ti) alloys formed by "ball-milling" were found virtually identical with those of melt-quenched glassy alloys of the same compositions. Fig.10 shows the comparison between the radial distribution functions of  $\text{Ni}_{40}\text{Ti}_{60}$  alloys obtained by mechanical alloying or liquid quenching<sup>39</sup>.

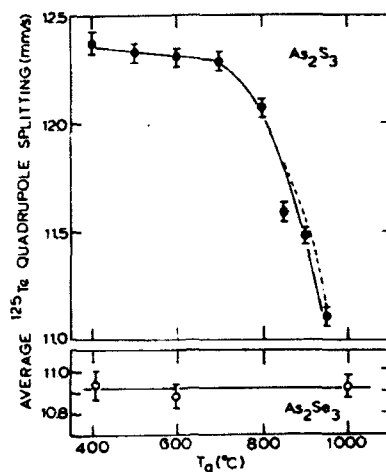


Fig.7 - Average quadrupole splitting obtained by Mössbauer spectroscopy for glassy  $\text{As}_2\text{S}_3$  (top) and  $\text{As}_2\text{Se}_3$  (bottom) liquid-quenched from temperature  $T$  indicated. (The samples were doped with traces of  $^{125}\text{Te}$  or  $^{128}\text{Te}$ )<sup>4</sup> (From<sup>35</sup>).

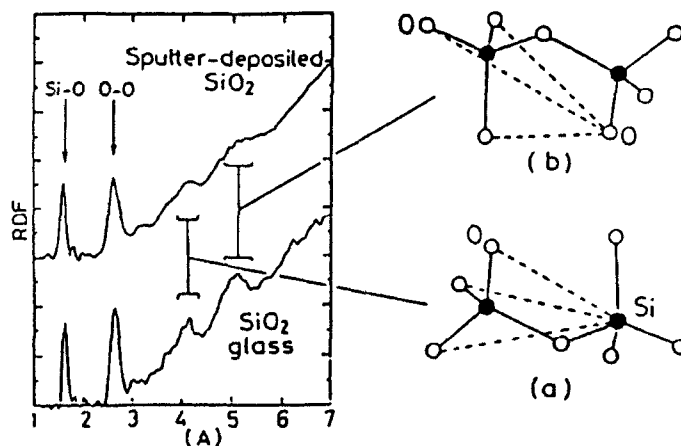


Fig.8 - Radial distribution functions obtained by neutron diffraction of sputter-deposited (top) and melt-quenched  $\text{SiO}_2$  (below). The schematic Figures (a) and (b) show respectively the second-order Si-O and O-O distances between adjacent  $\text{SiO}_4$  tetrahedra contributing to peaks at 4 Å at 5 Å, indicative of the degree of disorder. (From<sup>37</sup>).

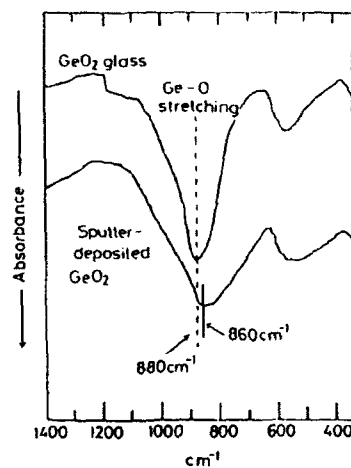


Fig.9 - Infrared absorption spectra of melt-quenched (top) and sputter-deposited GeO<sub>2</sub> (bottom). (From<sup>37</sup>).

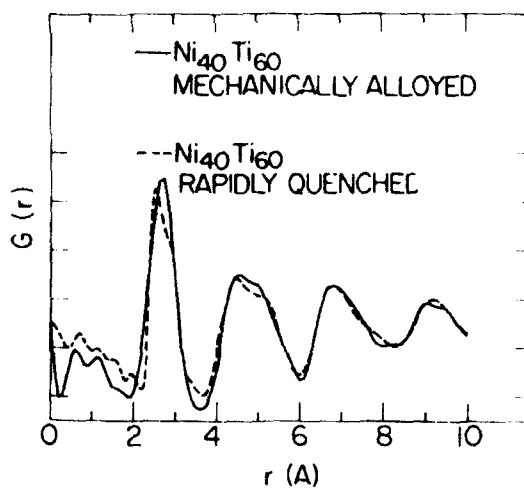


Fig.10 - Reduced atomic pair distribution functions of non-crystalline Ni<sub>40</sub>Ti<sub>60</sub> obtained by mechanical alloying (solid curve) and rapid quenching technique (dashed curve) (After<sup>39</sup>).

Sol-gel methods lead to glasses which have identical properties as the glasses obtained from the melt if the eventual variation of the chemical composition is taken into account. In some cases increased speed of devitrification was observed ; it can be ascribed to a higher OH content which induces heterogeneous nucleation<sup>40,41</sup>.

No conclusive differences in unmixing phenomena in gel-derived glasses were observed , provided the chemical composition is kept constant.

#### 11. Conclusion

Various methods of obtaining non-crystalline solids, glasses and amorphous materials from liquid, gas or solid states, extended the formation range and permitted new non-crystalline materials to be obtained.

When the same material is formed by different methods, structural differences may be detected ; they generally vanish on annealing.

Applications of these new methods are very important in the field of thin films and here the electronic properties are particularly sensitive to preparation conditions.

To ensure reproducibility of results it is imperative to control usually numerous experimental parameters.

#### 12. References

1. J.Zarzycki, *Glasses and the Vitreous State* (Cambridge University Press, Cambridge, 1991) pp.8-10
2. D.Turnbull, *Undercooled Alloy Phases*, ed. E.W.Collings and C.C.Koch. (Metallurgical Soc., Warrendale, Pa, 1986) pp.3-22.
3. J.Zarzycki in *Materials Science and Technology*, eds.R.W.Cahn, P.Haasen, E.Y.Kramer, Vol.9, ed.J.Zarzycki,(VCH, Weinheim,1991) pp.93-117.
4. D.Turnbull, *Cont.Phys.* 10, (1969),473.
5. D.Turnbull in *Physics of Non-Crystalline Solids*,ed.J.A.Prins, (North Holland, Amsterdam,1964)pp.41-56.
6. P.Duwez, R.H.Willens and W.Klement jr., *J.Appl.Phys.* 31(1960) 1136-1173.

7. P. Pietrokowski, *Rev. Sci. Instr.*, 34 (1963) 445.
8. C. Ruhl, *Mat. Sci. Eng.* 1, (1967) 313-320.
9. J. Blettry, *J. Phys. D-6*, (1973) 256-275.
10. J. Zarzycki and F. Naudin, *Phys. Chem. Glasses*, 8, (1967) 11-18.
11. H. S. Chen and C. E. Miller, *Rev. Sci. Instrum.*, 41 (1970), 1237.
12. T. Suzuki and A. Anthony, *Mat. Res. Bull.*, 9, (1974) 745-754.
13. H. S. Chen and C. E. Miller, *Mat. Res. Bull.*, 11, (1976), 49-54.
14. L. E. Topol, D. H. Hengsteinberg, M. Blander, R. A. Happe, N. L. Richardson and L. S. Nelson, *J. Non-Cryst. Sol.*, 12, (1973) 377-390.
15. W. E. Spear and P. G. Le Comber, *Sol. St. Comm.*, 17 (1975) 1193.
16. R. H. Dalton, M. E. Nordberg, *U.S. Patent*, 2239551 April 21 (1941).
17. M. E. Nordberg, *U.S. Patent*, 2326059 August 3 (1943).
18. P. C. Schultz, *U.S. Patent*, 3859073 January 7, (1975).
19. J. Wackerle, *J. Appl. Phys.*, 33 (1962) 922-937.
20. R. V. Gibbons and J. J. Ahrens, *J. Geophys. Res.*, 76 (1971) 5489-5498.
21. W. L. Johnson, W. L. Dolgin and M. Van Rossum in *Glass-Current Issues*, eds. A. F. Wright and J. Dupuy, (Martinus Nijhoff Publ. 1985) 172-187.
22. R. W. Cahn, *Mechanical Amorphisation of Ordered Intermetallic Phases*, this Workshop.
23. L. Young, *Anodic oxide films*, (Academic Press, N.Y. 1961).
24. J. Zarzycki in *Current Topics on Non-Crystalline Solids*, eds. M. D. Baró and N. Clavaguera, (World Scientific, Singapore, 1986) pp. 161-174.
25. *Effects of modes of formation on the structure of glass.* *Proc. 1<sup>st</sup> Conf., Nashville TN.*, eds. R. A. Weeks, D. L. Kinser and G. Kordas. *J. Non-Cryst. Sol.* 71, (1985) pp. 1-456.
26. *Ibid. Proc. 2<sup>nd</sup> Conf. Nashville TN*, eds. R. A. Weeks and D. L. Kinser. (Trans. Tech. Publ., Aedemansdorf, 1987). *Diffusion and Defect Data* 53-54, (1987) 1-512.
27. J. P. De Neufville and H. K. Rockstadt in *Amorphous and Liquid Semiconductors*, eds. J. Stuke and W. Brenig (Taylor and Francis, London, 1974) pp. 419-424.
28. R. B. Stephens, *J. Appl. Phys.*, 49, (1978) 5855-5864.

29. M.H.Brodsky, D.Kaplan and J.F.Ziegler, *Appl.Phys.Lett.*, 21, (1972), 305-307.
30. J.S.Lannin, L.J.Pilione, S.T.Khirsagar, R.Messier and R.C.Ross *Phys.Rev.B.*, 26, (1982) 3506-3509.
31. N.Maley, J.S.Lannin and A.G.Cullis, *Phys.Rev.Lett.*, 53, (1984) 1571-1573.
32. H.S.Chen and D.Turnbull, *J.Appl.Phys.*, 40, (1969) 4214-4215.
33. C.N.Waddell, W.G.Spitzer, J.E.Fredrickson, G.K.Hubler and T.A.Kennedy, *J.Appl.Phys.*, 55, (1984) 4361-4366.
34. Z.Ding and G.Han, *Diffusion and Defect Data* 53-54 (1987) 43-54.
35. I.Zitkovsky and P.Boolchand, (*ibid.*) p.167-172.
36. F.L.Galeener, (*ibid*) pp.305-314.
37. K.Suzuki, (*ibid*) pp.233-244.
38. R.Aujila, R.Dupree, I.Frarnan and D.Holland, (*ibid*) pp.99-104.
39. R.B.Schwarz, P.R.Petrich and C.K.Saw, *J.Non-Cryst.Sol.*, 76, (1985) 281-302.
40. S.P.Mukherjee, J.Zarzycki, J.M.Badie and J.P.Traverse, *J.Non-Cryst.Sol.*, 20, (1976) 455-458.
41. J.Zarzycki in "*Nucleation and Crystallization of Glasses*", Eds.J.H.Simmons, D.R.Uhlmann and G.H.Beall, *Advances in Ceramics Vol.4* (The American Ceramic Soc., Columbus, O., 1982) pp.204-217.



ON THE NATURE OF THE PARTIALLY  
CRYSTALLINE STATE OF POLYMERIC SOLIDS

G.R. STROBL

*Fakultaet fuer Physik*

*Universitaet Freiburg*

*7800 Freiburg*

*Federal Republic of Germany*

ABSTRACT

Polymer crystallization is controlled by kinetical factors rather than by equilibrium thermodynamics. After cooling from the melt partially crystalline structures built of stacks of crystallites and intervening disordered regions are formed. The transformation usually proceeds by the growth of spherulites and, in special cases, by a continuous crystallization mode. Crystallites exhibit a pronounced surface melting. For chemically perturbed chains stacks are built up consecutively during cooling via the insertion of additional crystallites. The state of order and the segmental mobility in the disordered regions are different from a pure melt. The processes contributing to the formation of the partially crystalline state were studied by small angle X-ray scattering, Raman-spectroscopy and quasielastic neutron-scattering.

1. Introduction

For chains with a regular chemical constitution formation of crystals is principally possible. These macromolecular crystals are generally built up by chains in a helical low-energy conformation with a uniform orientation of the helix axes. In order to form the crystalline equilibrium state all chains have to be extended over their full length. Starting from a highly entangled melt of coiled macromolecules this ideal crystalline state is never reached. Cooling a melt below the equilibrium melting point generally leads to structures which are only in parts crystalline. One observes layer-like crystallites which are separated by disordered regions, thus setting up a lamellar two-phase structure<sup>1</sup>. Structure formation is controlled by crystallization kinetics rather than by equilibrium thermodynamics. The structure which develops at a given temperature is that with the highest

growth rate, rather than that with the lowest free energy. As a consequence, structure parameters like the crystallite thickness depend on the chosen crystallization temperature. Structures are only metastable and change completely, if a sample is heated above the original crystallization temperature.

In most cases crystallization starts at nuclei and proceeds by the growth of spherulites. In the special case of crystallization in cold-drawn fibers an alternative continuous crystallization mode is observed<sup>2,3</sup> which is reminiscent of the process of spinodal decomposition. After completion of the isothermal transformation, crystallization continues further upon cooling. Two processes contribute to this further enhancement of the crystallinity: a continuous shift of the crystalline-amorphous interface, which reduces the thickness of the amorphous layers<sup>4</sup>, and the formation of additional thin crystallites, which become inserted into the already existing stack<sup>5</sup>. Both processes are essentially reversible with temperature.

The article discusses the character and properties of the different processes contributing to the formation of the partially crystalline state, and sketches the present state of understanding. A number of relevant experiments, previous and new ones, are described, in particular

- ( i ) small angle X-ray scattering (SAXS) experiments, performed to study the kinetics of structure formation<sup>2</sup> and the continuous structure change with temperature<sup>4,5</sup>.
- ( ii ) Raman spectroscopic measurements<sup>6</sup>, which yield the conformational distribution in the partially crystalline state and provide evidence for the occurrence of transition regions at the surface of the crystallites,
- ( iii ) quasielastic neutron scattering experiments, which provide evidence for a peculiar character of the segmental motion in the disordered regions, being different from a pure melt.

## 2. Crystallization by Nucleation and Growth

### 2.1. General observations

Starting from the isotropic melt, a sufficient amount of supercooling below the equilibrium melting point  $T_m(\infty)$  is necessary in order to initiate crystallization with reasonable crystallization rates. Spherulites are then observed which grow with constant radial speed. The spherulites have a complex internal

structure and are composed of crystalline-amorphous stacks.

Spherulites expand through the lateral growth of the crystallites. Fig. 1 sketches the situation given for an individual crystallite. Growth occurs only in lateral direction by an attachment of chain sequences straightened over a length corresponding to the crystallite thickness  $l$ . Growth in chain direction is largely suppressed by the presence of folds and entanglements at the crystallite surface. A thickening of crystals requires a replacement of whole chain sequences within the crystallites and therefore proceeds, if at all, only slowly ( $dl/dt \sim lgt$ , observed for polymers with low or moderate molecular weight; thickening is completely suppressed for polymers with chemical perturbations, like branched polyethylene?).

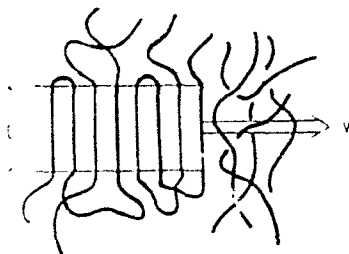


Fig. 1. Structure and growth front of a polymer crystallite.

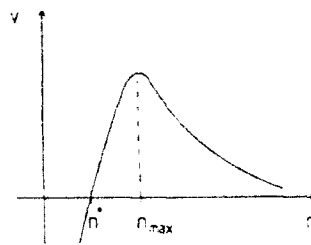


Fig. 2. Dependence of crystallization/melting rate on the sequence length.

Crystallite thicknesses  $l$  and growth rates  $v$  change strongly with temperature. Studies were performed on numerous systems. The behaviour is essentially uniform and can be described by the following characteristic dependencies:

$$l \sim \frac{C_1}{T_m(x) - T} + C_2 \quad (1)$$

$$v \sim \exp - \frac{C_3}{T_m(x) - T} \quad (2)$$

According to Eq. 1 chains become more and more extended on approaching the equilibrium melting point. However, at the same time crystallization rates

decrease drastically. Hence, growth of extended chain crystals at temperatures near  $T_m(\infty)$  is practically impossible.

## 2.2. Kinetics of lateral growth

The microscopic steps associated with lateral growth are under discussion since the beginning of crystallization studies on polymers. General agreement has not been reached so far. Quite clear, however, is the selection rule which determines the thickness of the growing crystallites: the lamellae which form at a given crystallization temperature are those with the largest growth rate. Analysis can be based upon this kinetic criterium.

Generally, crystal growth rates are determined by the thermodynamic driving force and relevant relaxation times. Dealing with crystallites of finite thickness one has first to inquire after their melting point. For Gibbs free energies  $g_a$  and  $g_c$  for a monomer in the melt and crystal respectively, and a surface free energy  $\sigma$ , the equilibrium condition at the melting point of crystallites composed of sequences of  $n^*$  monomers,  $T_m(n^*)$ , becomes

$$g_c n^* - 2\sigma = g_a n^* \quad (3)$$

Near to the equilibrium melting point  $T_m(n^* \rightarrow \infty)$  the Gibbs free energy difference increases linearly with temperature

$$g_a - g_c = \frac{\Delta h}{T_m(\infty)} (T_m(\infty) - T) \quad (4)$$

( $\Delta h$  denotes the melting enthalpy). Insertion of Eq. 4 in Eq. 3 gives the well known result

$$T_m(n^*) = T_m(\infty) - \frac{2\sigma T_m(\infty)}{\Delta h} \frac{1}{n^*} \quad (5)$$

Eq. 5 describes the melting point reduction resulting from the small thickness of the crystallites.

Clearly, crystals growing at a given crystallization temperature  $T_c$  have to be thicker than the crystals in equilibrium with the melt at this temperature:

$$n > \frac{2 \sigma T_m(\infty)}{\Delta h} \frac{1}{T_m(\infty) - T_c} = n^* \quad \text{or} \quad (6)$$

$$n = n^*(T_c) + \delta n. \quad (7)$$

The overlength  $\delta n$  determines the thermodynamic driving force and therefore the growth rate.

In linear approximation the velocity of the phase boundary can be generally written as

$$v = \frac{a}{\tau} \frac{f}{kT}, \quad (8)$$

where  $f$  denotes the driving force

$$f = (g_a - g_c) \delta n \quad (9),$$

and ' $a$ ' the monomer diameter.  $\tau^{-1}$  describes the equilibrium rate of sequence attachment, which is equal to the rate of sequence detachment at a stationary boundary. The experimental observations indicate an exponential dependence of  $\tau^{-1}$  on the sequence length  $n$ :

$$\tau^{-1}(n) = \tau_0^{-1} \exp - \alpha n. \quad (10)$$

The elementary monomer jump rate  $\tau_0^{-1}$  and the parameter  $\alpha$  are only weakly temperature dependent.

Insertion of Eq. 10 and Eq. 9 into Eq. 8 gives the dependence of the growth rate  $v$  on the overlength  $\delta n$ :

$$v(\delta n) = \frac{a}{\tau_0} \frac{g_a - g_c}{kT} \exp - \alpha n^* \cdot \delta n \cdot \exp - \alpha \delta n. \quad (11)$$

Fig. 2 shows this dependence in a schematic drawing. Crystals grow for  $n > n^*$ , and melt for  $n < n^*$ . The growth rate has its maximum at

$$n_{\max} = n^* + 1/\alpha \quad (12),$$

where it becomes

$$v = \frac{a}{e \alpha \tau_0} \frac{\Delta g}{k T} \exp - \alpha n^* \quad (13).$$

Choosing a fixed crystallization temperature, the large majority of crystallites will grow with the thickness and growth rate at the maximum as given by Eqs. 12, 13. Insertion of Eq. 5 yields for the dependence of the crystallite thickness  $l_{\max} = a n_{\max}$  and the growth rate  $v$  on the supercooling  $\Delta T = T_m(\infty) - T_c$  the relations

$$l_{\max} = \frac{a 2 \sigma T_m(\infty)}{\Delta h} \cdot \frac{1}{\Delta T} + \frac{1}{\alpha} \quad (14)$$

and

$$v \sim \frac{a}{\tau_0} \frac{\Delta T}{T_m(\infty)} \exp - \frac{C}{\Delta T} \quad (15),$$

in agreement with the experimental results (Eqs. 1, 2).

Up to this point the situation seems clear. What remains, is an understanding of the exponential dependence of the equilibrium attachment rate on the sequence length (Eq. 10). The temperature dependence of the structure is mainly determined by this property. Its origin is still under discussion. There is the original suggestion by Hoffman and Lauritzen which provided the basis for some detailed theories<sup>8</sup>. These authors interpret Eq. 10 as being indicative for a secondary nucleation at the growth face. A smooth growth face is assumed, onto which complete layers are added after nucleation steps. This secondary nucleation requires an activation energy proportional to the sequence length and therefore would explain Eq. 10. There exists, however, an alternative explanation. Experimental evidence for atomically smooth growth faces in crystallizing polymer melts is lacking. As pointed out by Sadler<sup>9</sup>, growth faces of polymer

crystals could be rough. If this is true, normal growth rather than layer growth occurs<sup>10</sup>. For normal growth conditions the dependence expressed by Eq. 10 finds a straightforward simple answer: before a sequence, which lies coiled in the melt, can be incorporated into the growing crystal, it has to be stretched, and all intervening entanglements with other chains have to be removed. This requires an activation entropy proportional to the sequence length. Expressed in other words: only a fraction  $\sim \exp - \alpha n$  in the melt shows the proper conformation required for an attachment.

Hence, if normal growth onto rough growth faces occurs in polymer crystallization, the observed growth kinetics and the resulting temperature dependent structure formation finds a simple explanation.

### 3. Continuous Crystallization Mode

If crystallization is conducted starting from an oriented melt or glass, a process different from nucleation and growth has been observed in a number of cases<sup>2,3</sup>. Studies in the electron microscope or by X-ray scattering suggest a continuous transition from the amorphous to the partially crystalline state. Density fluctuations appear all over the sample and grow continuously in amplitude up to the final state given by the crystalline-amorphous layer structure. Throughout the transformation the sample remains homogeneous. The observations indicate occurrence of a special mode of crystallization.

An example is given in Figs. 3,4. The study<sup>2</sup> deals with the crystallization process initiated by annealing a glassy oriented fibre of polyethyleneterephthalate (PET) at temperatures slightly above the glass transition. Fig. 3 shows as a result of a SAXS-experiment the evolution of the structure factor  $I(s)$  with time ( $s$  denotes the scattering vector  $s = 4\pi \sin \theta / \lambda$ ). Two different ranges show up: for scattering vectors  $s < s_c = 0.95 \text{ nm}^{-1}$  intensities increase with time, for  $s > s_c$  they decrease. As shown by Fig. 4, kinetics follow an exponential law,  $I \sim \exp Rt$ , with positive or negative rate constants  $R$  for  $s < s_c$  or  $s > s_c$  respectively.

The observed scattering curves reflect the introduction of density fluctuations into the originally homogeneous sample. The experiment shows, that long wavelength fluctuations have the tendency to grow, and short wavelength fluctuations to decay. The structure which develops is primarily determined by those fluctuation waves which have the largest growth rates. This maximum

occurs at  $s \approx 0.6 \text{ nm}^{-1}$ . As a consequence the resulting structure will exhibit a quasi-periodicity in the order of 10 nm.

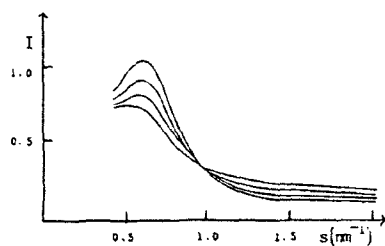


*Fig. 3. Crystallization of PET starting from the oriented glassy state. Evolution of structure factor with time.*

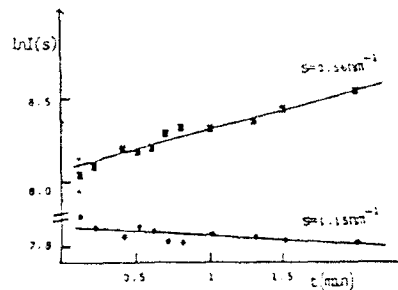


*Fig. 4. Exponential growth or decay of scattering intensities.*

The location of the growth rate maximum and therefore of the long-spacing  $L$  change with the crystallization temperature. As demonstrated by

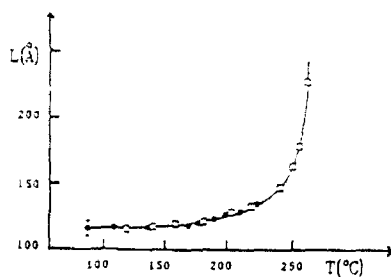


*Fig. 5. Crystallization of oriented PET. Long spacing in dependence on the crystallization temperature.*

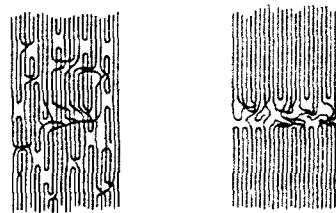


*Fig. 6. Clustering of conformational defects annealing an amorphous polymer fiber.*

Fig. 5,  $L$  shifts to larger values with increasing temperature. The dependence can be described in good approximation by

$$L \sim (T_s - T)^{-1/2} \quad (16),$$



where  $T_s$  is located near to the equilibrium melting point  $T_m(x)$  of polyethyleneterephthalate.

The observed kinetics is reminiscent of a well-known process occurring in a different system: the spinodal decomposition of binary mixtures. Here the phase separation initiated by a temperature jump from the homogeneous phase into the two phase-region below the spinodal can proceed via a specific unmixing process, as described by the theory of Cahn and Hilliard<sup>11</sup>. Theory shows that concentration fluctuations with wavelengths above a critical value become intrinsically unstable. As a consequence phase separation sets in without any activation. The structure pattern is dominated in its initial stages by the concentration wave with the largest growth rate. Its wavelength shifts to higher values on approaching the spinodal curve. All these characteristics are also found for the continuous mode of polymer crystallization. It looks therefore appealing to try to transfer the mechanism of spinodal decomposition to the case of polymer crystallization.

Of course, from the chemical point of view, one is dealing with a one-component system. However, the monomers which constitute the polymer chain can greatly differ in their mobilities and flexibilities and hence their potential to crystallize within the given limited time. For example, chain parts contributing to an entanglement essentially act as crosslinks which cannot be incorporated into a crystal. Other unfavorable conformations with long times of relaxation are sharp folds or chain torsions. These conformational defects are not fixed at certain monomers, but can move along the chain. Considering these properties, a process of defect clustering can be envisaged which continuously builds up two phases, crystalline regions free of defects, and amorphous regions where all the defects become concentrated. Fig. 6, taken from a work of Fischer and Goddar<sup>12</sup>, illustrates this idea. Clustering processes can only take place if the defects move along the chains. Preorientation of chains in the amorphous state apparently leads to a high axial mobility and thus promotes the continuous crystallization mode.

#### 4. Surface Crystallization and Melting

After the completion of the transformation process at the chosen temperature crystallization continues further upon cooling. One observes a continuous decrease of the thickness of the amorphous layers and a corresponding increase of the crystallite thickness, i.e. a shift of the interface towards the disordered regions. A reverse process, i.e. a surface melting, occurs during heating. As long as the sample is not heated above the original crystallization temperature the changes in the layer thicknesses are largely reversible. The observations suggest the existence of a local equilibrium between the crystalline and the disordered phase.

Direct evidence for this process has been provided by SAXS-experiments on polyethylene<sup>4</sup>. Fig. 7 shows the normalized one-dimensional electron-density autocorrelation function

$$\gamma_1(x) = \langle \Delta\rho(x' + x) \Delta\rho(x') \rangle / \langle \Delta\rho^2 \rangle \quad (17)$$

derived by Fourier transformation from SAXS-curves<sup>13</sup> measured during cooling (left) and successive heating (right) of a sample. The average thickness of the

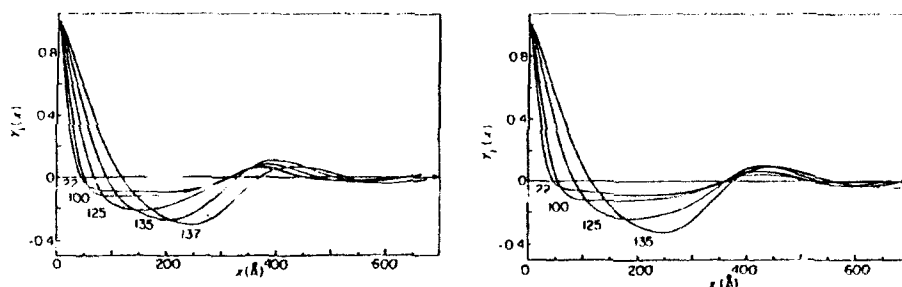
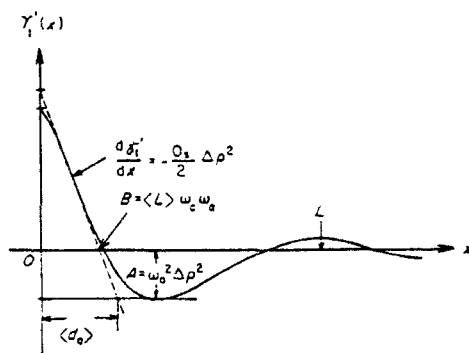


Fig. 7. Linear PE, crystallized at  $T = 125^\circ \text{C}$ . Correlation functions obtained during cooling (left) and heating (right).

amorphous layers,  $\langle d_a \rangle$ , is given by the base length of the 'triangle' at the origin, as indicated in the schematic drawing in Fig. 8 ( $\gamma_1' = \gamma_1 \cdot \langle \Delta\rho^2 \rangle$ ). Fig. 9

shows the temperature dependence of  $\langle d_a \rangle$ . One observes a large, essentially reversible change.



**Fig. 8.** General shape of electron density correlation function of a crystalline-amorphous layer structure. ( $\omega_c/\omega_a$ : fraction of crystalline/amorphous phase;  $\Delta\rho = \rho_c - \rho_a$ : electron density difference;  $O_s$ : specific interface;  $L$ : long spacing).

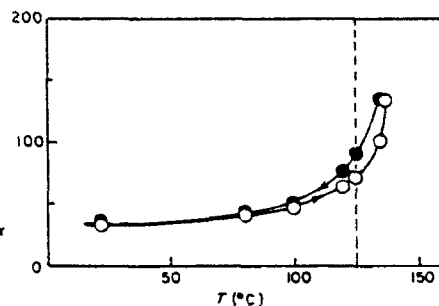


**Fig. 9.** Linear PE, crystallized at  $T = 125^\circ\text{C}$ . Temperature dependence of the average thickness of the amorphous layers during cooling and heating.

Further support and additional insights come from Raman-spectroscopic investigations on polyethylene<sup>6</sup>. Basically the Raman spectrum is sensitive to the chain conformation, being essentially determined by the trans-gauche ratio. An additional feature, a factor group splitting of the bands due to intermolecular interactions within a unit cell, shows up in the orthorhombic crystallites. Spectra measured in the partially crystalline state can be decomposed into contributions of the different coexisting phases. The mass fractions in the different states then follow directly from the weights of the respective spectral components. As it turns out, spectra cannot be decomposed in only two components corresponding to crystalline and a melt-like phase. There is clear evidence for the occurrence of a third, intermediate phase, associated with transition regions.

Fig. 10 shows as an example Raman spectra measured in the range of the C-C-stretching vibrations (left) and the CH<sub>2</sub>-twisting vibrations (right) for different temperatures upon cooling a sample of high molecular weight polyethy-

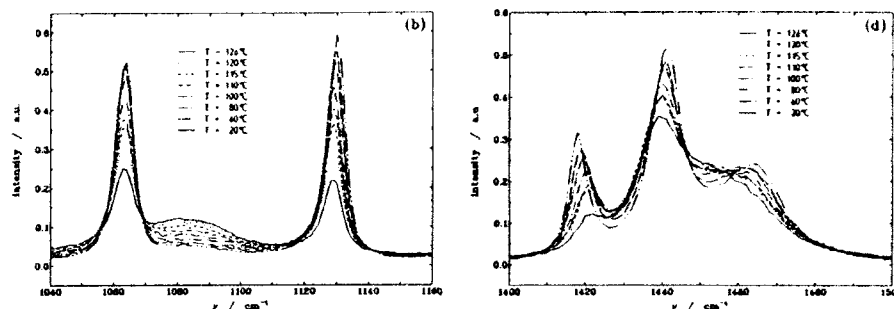


Fig.10. Linear PE, crystallized at  $T = 126^\circ \text{C}$ . Raman spectra measured during cooling in the frequency ranges of the CC-stretching vibrations (left) and the CH<sub>2</sub>-bending vibrations (right).

lene. Pronounced changes are observed. Fig. 11 gives the result of the data evaluation: one notes a decrease of the melt-like fraction, an increase in the crystalline fraction, and a rather constant value for the fraction of methylene units in the intermediate phase. The results suggest a continuous shift of the interface, together with the transition region, as indicated in Fig. 12.

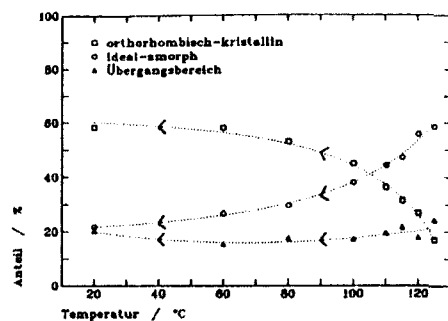


Fig.11. Linear PE. Temperature dependence of the crystalline (□), the disordered (Δ) and the intermediate fraction (○).

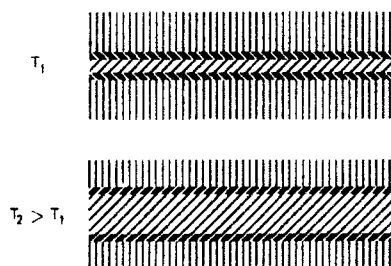


Fig.12. Surface melting in a partially crystalline polymer.

The observed surface crystallization and melting is indicative for a specific state of order in the disordered regions, different from that of a pure polymer melt. An ideal two-phase structure, set up of crystalline and truly melt-like regions, would not lead to any surface melting. In fact, the disordered regions are composed of loops, which are fixed with their ends in the crystallites, and show a high concentration of entanglements, which are not resolvable. Hence, the mean chemical potential of the units in this phase differs from that of a pure melt and changes with the thickness of the disordered layer. There have been a number of theoretical discussions of the process<sup>14, 15, 16</sup>. Melting curves were calculated, as they follow for various models. A discrimination between the different models seems at present unfeasible.

So far theories deal separately with the process of the primary crystallization, as described in chapter 2, and the surface crystallization and melting. This is certainly unsatisfactory. A proper theory of polymer crystallization has to account for both processes in one common treatment. The crystallites and the disordered regions with their specific microscopic structure are formed simultaneously. A treatment of the crystallization kinetics therefore should not be based on the analysis of the lateral growth of an individual crystallite. One should deal instead from the begin with the crystallization of a stack of crystallites and disordered regions. Up to now no attempts in this direction exist.

#### 5. Stack formation by insertion of crystallites

The continuous crystallinity change associated with surface melting is also reflected in a broadening of the melting peak. Fig. 13 shows the thermogram obtained with a differential scanning calorimeter for a sample of linear polyethylene.

Especially broad melting ranges are observed for polymers which include a small amount of noncrystallizable units, like short-chain branches or chemically different co-units. Fig. 14 presents as an example the melting curve of a commercial low density polyethylene (LDPE), which has 3.3% of short chain branches. The melting curve is rather broad and exhibits a pronounced fine structure. The fine structure reflects the thermal history and is for this sample directly related to the previous step-wise cooling. The behaviour suggests a

successive formation of groups of additional crystallites during cooling.

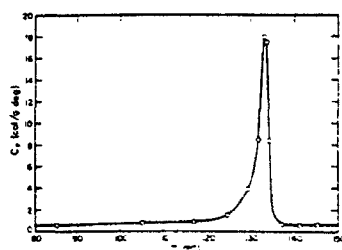


Fig. 13. DSC-thermogram of linear PE.

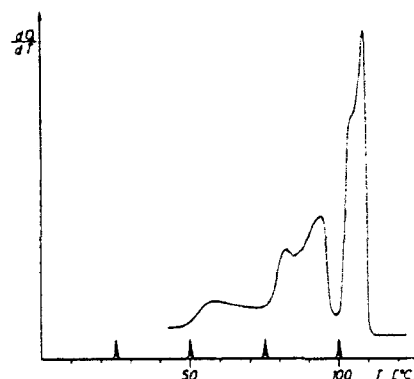


Fig. 14. DSC-thermogram of a LDPE-sample, which was cooled in steps (115→100→75→50→25°C)

A detailed picture of this crystallization process, which is typical for polymers with perturbations in the chemical composition, was derived from electron microscopic investigations and SAXS-experiments. The principle is sketched in Figs. 15 and 16. During the lateral growth of a crystallite all noncrystallizable units, and also entanglements, which cannot be resolved, are transported to the surface.

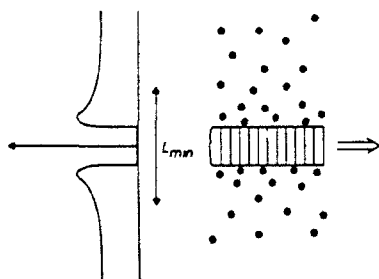


Fig. 15. Surface enrichment of noncrystallizable units during lateral growth of a crystallite.

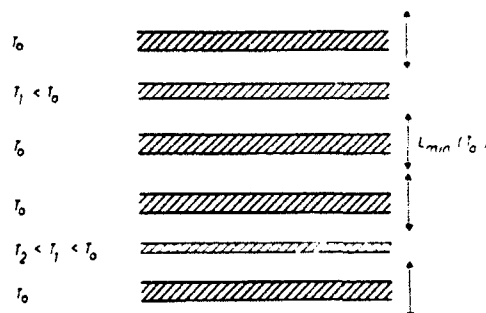


Fig. 16. Stack formation by consecutive insertion of crystallites. Primary structure at  $T_0$ , and changes with cooling to  $T_1$  and  $T_2$ .

The zone with an enhanced concentration of the noncrystalline units,

setting up together with the crystallite a layer of thickness  $L_{\min}$ , cannot be entered by any other growing lamella. After completion of the primary crystallization at the temperature chosen at the begin,  $T_0$ , the distances between adjacent crystallites therefore will vary between  $L_{\min}$  and an upper limit  $L_{\max} \approx 2 L_{\min}$  (for larger distances an additional lamella will develop in between). Cooling the sample leads to the formation of additional crystallites. This insertion process will begin in the most thick amorphous regions and will then proceed, at lower temperatures, to the thinner ones. The controlling parameter determining the temperature, at which a crystallite forms within a disordered layer, is the local concentration of noncrystallizable units. As described by van t'Hoff's law, an increase in this concentration results in a melting point depression. Crystals which appear at lower temperatures will be generally thinner and include more defects. Essential for this model is the assumption of a non-uniform distribution of the non-crystallizable units, being higher in the thinner amorphous layers. A necessary prerequisite for this property is a complete suppression of transport of the non-crystallizable units through the crystallites, so that an equilibration of the concentrations is prevented.

The model has been suggested by direct electron microscopic investigations and temperature dependent SAXS-experiments. Fig. 17 presents the

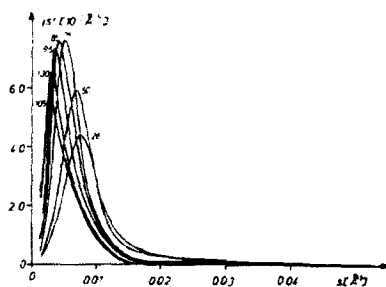


Fig. 17. SAXS curves measured for LDPE during cooling.

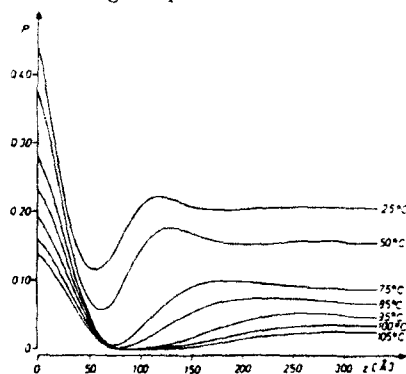


Fig. 18. Correlation functions  $P(z)$  derived from the curves in Fig. 17.

SAXS-curves measured during cooling, Fig. 18 gives the derived correlation functions  $P(z)$ .  $P(z)$  describes the probability, that both ends of a rod with length

$z$  are located in crystalline regions.  $P(z)$  increases upon cooling for all values of  $z$ , which is indicative for a successive addition of crystallites, without a reorganisation of the already existing stack. The properties of the crystallites added within a temperature range follow from the respective changes in  $P(z)$ . One finds a continuous decrease of the thickness of the formed crystallites from 60 Å (at 100°C) to 40 Å (at 40°C).

#### 6. Segmental motion in the disordered region:

The peculiar character of the disordered phase became apparent in a study of the segmental motion in polyethylene using quasielastic neutron scattering. Here only a summary of relevant results is given. A complete report is presented elsewhere<sup>17</sup>.

A major point of interest of the study has been the effect of the crystallization conditions and the type of the sample on the segmental mobility. Experiments were performed on a high molecular weight linear polyethylene ( $M > 10^6$ ) and a LDPE-sample. Measurements were conducted on the backscattering inelastic spectrometer IN10 at the Institute Laue-Langevin in Grenoble.

Scattering on polyethylene is incoherent. A quantity of special interest is the elastic incoherent structure factor (EISF)  $S(q, \omega = 0)$ . For the two-phase systems under study the EISF is given by

$$S(q, \omega=0) = \alpha \exp -\langle u^2 \rangle_0 q^2/3 + (1-\alpha) \exp -(\langle u^2 \rangle_0 + \langle u^2 \rangle_r) q^2/3 \quad (18)$$

Here  $\alpha$  describes the crystallinity,  $\langle u^2 \rangle_0$  and  $\langle u^2 \rangle_r$  denote the mean-squared displacements associated with vibrations (in the crystallites and the amorphous region) and with the diffusive motion in the amorphous regions. Precisely speaking,  $\langle u^2 \rangle_r$  describes the displacement within times  $t < 3 \cdot 10^{-8}$ s, as a consequence of the limited energy resolution of the spectrometer.

Figs. 19,20,21 show some selected results. Fig. 19 presents the temperature dependence of the EISF, measured for the linear polyethylene at different scattering vectors  $q$  after an isothermal crystallization from the melt (at  $T = 125^\circ\text{C}$ ). One notes a deviation from the normal linear decrease already at low temperatures, which occurs in two steps.



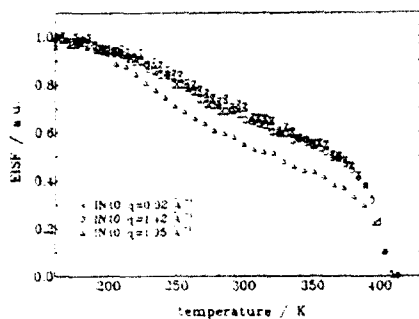


Fig.19. Linear PE ( $M > 10^6$ ), crystallized from melt.  $T$ -dependence of EISF, measured at different  $q$ 's (IN10).

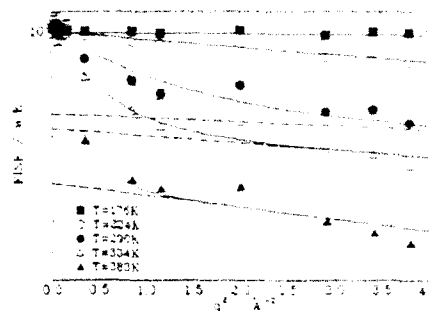


Fig.20. Linear PE ( $M > 10^6$ ), crystallized from melt.  $q$ -dependence of EISF. Fits based on Eq. 18.

Fig. 20 shows, for the same sample, the  $q$ -dependence of the EISF at different temperatures, with curves fitted on the data on the basis of Eq.18. The crystallinity values  $\alpha$  derived from the fitting procedures were in good agreement with crystallinities obtained by Raman-spectroscopy. The values obtained for the mean squared displacements  $\langle u^2 \rangle_1$  are presented in Fig. 21, together with the results obtained for two other samples, the same linear polyethylene after a crystallization from solution, and an LDPE-sample.

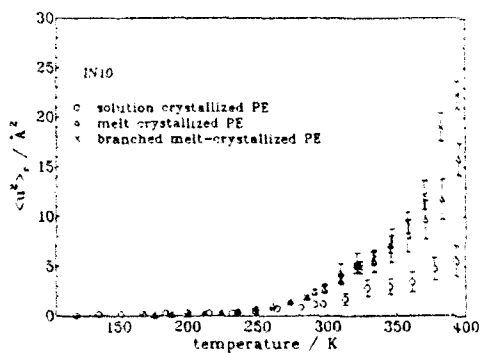


Fig.21. Different PE samples.  $T$ -dependence of diffusive displacements in the amorphous phase.

There is a clear difference in mobility between the three samples. The lowest mobility, and therefore the strongest restriction of the motion, is found for the solution-crystallized linear PE. The highest mobility exists for the branched sample. There appears to be a general difference in mobility between melt- and solution crystallized samples, with the lower mobility for the solution crystallized sample. Segmental motion increases in two steps. It sets in around 250K, which corresponds to the glass transition of a pure polyethylene melt. The second increase begins around 320K, the temperature where surface melting starts. The curves demonstrate, that the increase in the thickness of the amorphous layer, following from the surface melting, leads directly to a higher mobility. For the branched sample, the increase in thickness with temperature is larger, since whole crystallites melt. The experiment thus provides evidence for a direct relation between the crystallite thickness and the segmental mobility. This can be regarded as the origin of the thickness dependence of the chemical potential, assumed in all discussions of surface melting.

## 7. Conclusion

The partially crystalline state of polymeric solids is controlled by the kinetics of transformation. Isothermal crystallization after cooling from the melt leads to a layer structure composed of crystallites and intervening amorphous regions. The structure which is formed is that with the highest growth rate. The amorphous phase is different from a pure melt. The segmental mobility is restricted due to the fixing of parts of the chains in the adjacent crystallites and the presence of unresolvable entanglements. The thickness of the amorphous layers decreases upon cooling. This process of surface crystallization, and the reverse process of surface melting on heating a sample, is indicative for a special state of order in the amorphous layers. For polymers with perturbations in the chemical structure stacks of crystallites are built up consecutively during cooling via an insertion mechanism. The range of crystallization and melting in this case becomes very broad. The segmental mobility in the disordered regions changes with the crystallization conditions and the type of the sample. The mobility is directly related to the thickness of the amorphous layers.

## References

1. B. Wunderlich, *Macromolecular Physics I, II, III* (Academic Press, New York, 1973).
2. R. Günther, *Dissertation* (Mainz, 1981)
3. J. Petermann, J.M. Schultz, R.M. Gohil, R.W. Hendricks and J.S. Lin, *J. Polym. Sci., Polym. Phys. Ed.* **20** (1982) 523.
4. Y. Tanabe, G.R. Strobl and E.W. Fischer, *Polymer* **27** (1986) 1147.
5. G. Strobl, M.J. Schneider and I.G. Voigt-Martin, *J. Polym. Sci., Polym. Phys. Ed.* **18** (1980) 1361.
6. R. Mutter, W. Stille and G. Strobl, *J. Polym. Sci., Polym. Phys. Ed.*, submitted 1991.
7. G. Strobl, T. Engelke, E. Maderek and G. Urban, *Polymer* **24** (1983) 1585.
8. J.D. Hoffmann, G.T. Davis and J.I. Lauritzen, in *Treaties on Solid State Chemistry* **3**, ed. N.B. Hannay (Plenum Press, New York, 1976).  
J.D. Hoffmann and R.L. Miller, *Macromolecules* **21** (1988) 3038.  
R.L. Miller and J.D. Hoffmann, *Polymer* **32** (1991) 963.
9. D.M. Sadler, *Polymer* **24** (1983) 1401.  
D.M. Sadler and G.H. Gilmer, *Phys. Rev. Lett.* **56** (1986) 2708.  
D.M. Sadler, *Nature* **326** (1987) 175.
10. A.A. Chernov, *Modern Crystallography III. Crystal growth* (Springer, Berlin, 1984).
11. J.W. Cahn: *Trans. Metall. Soc. AIME* **242**, 166 (1968).  
J.E. Hilliard, in *Phase Transformations*, ed. H.L. Anderson (American Society for Metals, Metals Park, OH, 1970).
12. E.W. Fischer and H. Goddar, *J. Polym. Sci.* **16** (1969) 4405.
13. G. Strobl and M. Schneider, *J. Polym. Sci.* **18** (1980) 1343.
14. E.W. Fischer, *Kolloid Z. u. Z. Polym.* **218** (1967) 97.
15. H.G. Zachmann, *Kolloid Z. u. Z. Polym.* **231** (1969) 504.
16. J. Rieger, M.L. Mansfield, *Macromolecules* **22** (1989) 3810.
17. G. Hohlweg, B. Holzer, G. Strobl and B. Stühn, *Macromolecules*, submitted (1992)
18. M. Bee, *Quasielastic Neutron Scattering* (Adam Hilger, Bristol, 1988).

## ON THE AMORPHIZATION OF THE Nd-Fe AND Sm-Fe SYSTEMS BY MECHANICAL ALLOYING

V.E. Martín, J.M. González  
*Instituto de Ciencia de Materiales - CSIC.  
Serrano 144. 28006 Madrid, Spain*

and

L. Schultz, K. Schnitzke  
*Siemens AG, Research Laboratories.  
Erlangen, Germany*

### ABSTRACT

In this work we have studied of the formation of amorphous phases in the Nd-Fe and Sm-Fe systems when the samples are prepared by the mechanical alloying technique. Also, the products formed upon heat treatments are identified.

### 1. Introduction

During the last few years new rare-earth-containing, Fe-rich phases with interesting hard magnetic properties have been prepared by the mechanical alloying technique. Examples of this are the Nd-Fe-B and Sm-Fe-TM (TM: early transition metal) systems<sup>1-2</sup>. In what follows we report on the characterization of mechanically alloyed samples of the binary Nd-Fe and Sm-Fe systems, aiming at the study of the phases formed during the milling process and upon heat treatments. The interest in this study is related to the detailed knowledge of microstructural features present in more complicated systems, like ternary ones mentioned above.

### 2. Experimental techniques

Samples of nominal composition  $R_xFe_{100-x}$  ( $5 \leq x \leq 30$ ,  $R = Nd, Sm$ ) were prepared by means of a planetary high-energy ball mill, starting from pure element powders. The powders were mixed under a pure argon atmosphere and sealed in a stainless steel container together with stainless steel balls. The milling was performed during 64 hours at the highest intensity available.

Samples characterization was carried out by X-ray diffraction (XRD) in a Siemens D500 diffractometer using  $Cu-K\alpha$  radiation. The thermal analysis was performed by means of a differential scanning calorimeter under Ar atmosphere, at a heating rate of  $40^\circ C/min$  up to  $730^\circ C$ . Magnetic characterization of as-milled samples was carried out at room temperature on pressed powder cylinders using a

vibrating sample magnetometer (VSM) based on a superconducting coil (7.5 T).

### 3. Results

In Fig.1 we present X-ray diffractograms corresponding to some of the compositions obtained in the Sm-Fe system. Two peaks can be observed corresponding to the  $\alpha$ -Fe phase, with particle size around 20 nm (The particle size was calculated from the Scherrer expression,  $d = 0.9 \lambda / \Delta\theta \cos\theta^3$ ). Moreover, a halo centered around 32 degrees ( $2\theta$ ) is apparent. The intensity of this halo decreases with decreasing Sm content, and vanishes for the  $\text{Sm}_5\text{Fe}_{95}$  sample. Figure 2 shows the compositional dependence of the ratio of the intensity of the halo and that corresponding to the principal peak of the  $\alpha$ -Fe phase.

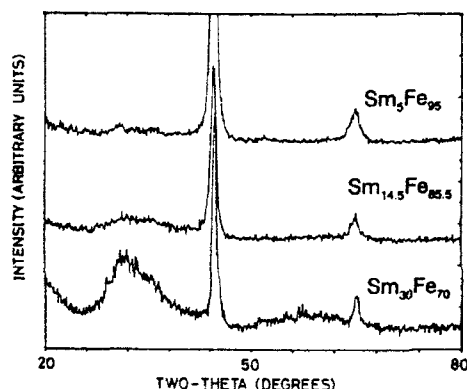


Fig.1 X-ray diffractograms of as-milled Sm-Fe samples.

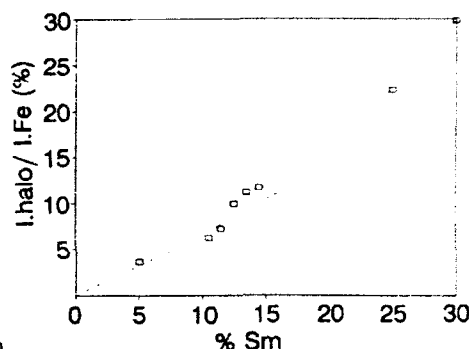


Fig.2 Compositional dependence of the ratio of the intensity of the halo to the intensity of the main  $\alpha$ -Fe peak, measured in the Sm-Fe samples.

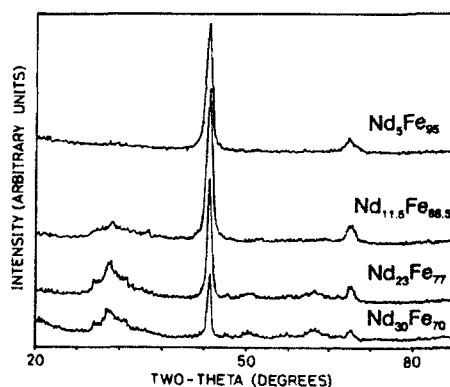


Fig.3 X-ray diffractograms of as-milled Nd-Fe samples.

In the case of the as-milled Nd-Fe system, the X-ray diffractograms (see Fig.3) show again the presence of  $\alpha$ -Fe peaks. In this case, the calculated particle size varies from 20 nm for the  $\text{Nd}_5\text{Fe}_{95}$  composition up to 35 nm for the  $\text{Nd}_{30}\text{Fe}_{70}$ . On the other hand, widened superimposed Nd peaks are visible without any evidence of a diffuse halo.

The study of the thermal stability performed in Sm-Fe samples showed two different features. For

compositions between 5 and 14.5% Sm, a small exothermic peak centered around 650°C is observed, whose intensity increases with the Sm content. Also the onset of an endothermic peak is observed at 680°C. By means of X-ray diffraction we identified this process as corresponding to the formation of the  $\text{Sm}_2\text{Fe}_{17}$  phase. On the other hand, for compositions with  $x=25$  and 30% Sm two different processes were observed. The first one, an exothermic process observed at 490°C, is related to the formation of the  $\text{SmFe}_2$  phase (see Fig.4, for the  $\text{Sm}_{30}\text{Fe}_{70}$  composition). A second endothermic process appears at 715°C. X-ray diffraction results allow the identification of this process as corresponding to the transformation of  $\text{SmFe}_2$  in  $\text{SmFe}_3$  phase.

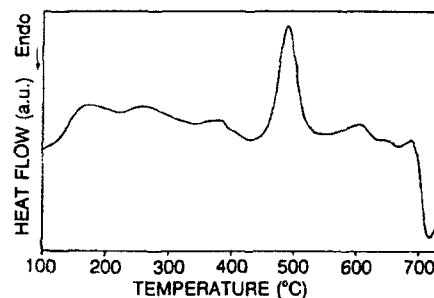


Fig.4 DSC of the sample with nominal composition  $\text{Sm}_{30}\text{Fe}_{70}$  (40°C/min)

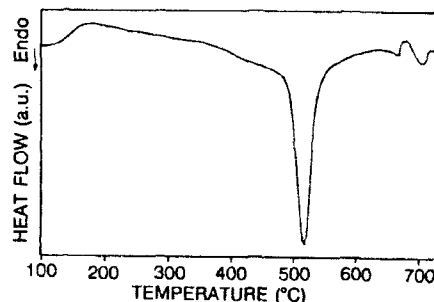


Fig.5 DSC of the sample with nominal composition  $\text{Nd}_{23}\text{Fe}_{77}$  (40°C/min).

In the case of the Nd-Fe system, an irreversible endothermic peak for all the samples was observed (at temperatures ranging, for decreasing Nd content, from 514°C up to 560°C). This peak corresponds to the formation of the  $\text{Nd}_2\text{Fe}_{17}$  phase, as shown by X-ray diffractograms performed in samples annealed at temperatures below and above the endothermic peak temperature (see Fig.5, for the  $\text{Nd}_{23}\text{Fe}_{77}$  composition).

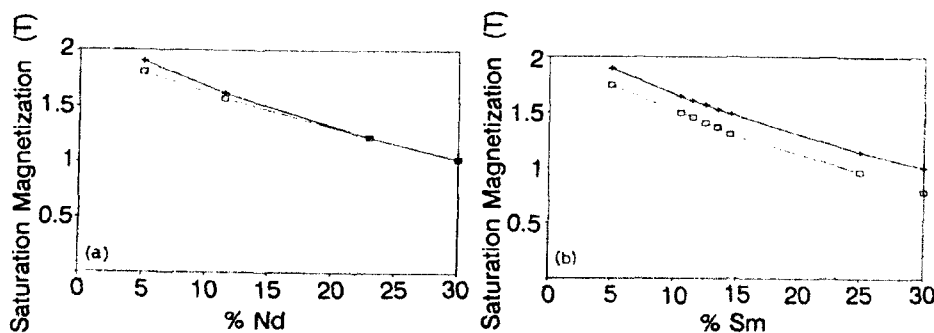


Fig.6 Comparison of the compositional dependence of the saturation magnetization of samples of the same nominal composition measured before (+) and after (□) 64h milling.  
a) Nd-Fe system, b) Sm-Fe system.

Finally, as-milled material of both systems was magnetically characterized. Fig.6 shows the compositional dependence of the saturation magnetization of unmilled and "as-milled" samples with the same nominal Fe content. The behaviour of both systems is clearly different. In the case of the Nd-Fe system, no significant differences between both sets of samples are apparent, whereas in the case of the Sm-Fe system, the saturation magnetization of the milled samples is always smaller than the saturation magnetization measured in the unmilled powders. The difference between both kinds of samples increases with the Sm content.

#### 4. Discussion

We suggest that, considering our XRD results, the as-milled Sm-Fe samples consist of a mixture of  $\alpha$ -Fe and a Sm-Fe amorphous phase. The proportion of this amorphous phase increases with the increase in Sm content as evidenced by the increasing ratio of the intensities of the main diffraction peak (halo) of both phases (Fig.2). The presence of this amorphous phase can be also inferred from the magnetic measurements as involved in the differences between the saturation magnetization of unmilled and as-milled samples (no other crystalline phases were detected by XRD). Finally, the exothermic peak observed in the DSC thermograms of all samples could be related to the crystallization of the amorphous Sm-Fe phase.

A different behaviour was observed in the case of the Nd-Fe system. X-ray diffractograms and magnetic measurements seem to indicate that the as-milled material is a mixture of Nd and Fe, without any evidence of the formation of Nd-Fe alloys upon milling. In the DSC thermograms only an endothermic peak appears, being related to the formation of the 2:17 phase.

The different behaviour of the two systems is attributed to different thermodynamics. According to Miedema calculations<sup>4</sup>, the Sm-Fe system shows a negative heat of mixing (-2 KJ/mole) which allows partial amorphization, whereas Nd-Fe has a slightly positive heat of formation (+1 KJ/mole) preventing alloying under the given milling conditions<sup>5</sup>. The two-phase Sm-Fe powder (amorphous +  $\alpha$ -Fe) formed after mechanical alloying provides a unique precursor for the formation of hard magnetic  $\text{Sm}_2\text{Fe}_{17}\text{N}_x$  samples after crystallization and nitrogenation<sup>2</sup>.

#### 5. References

1. L. Schultz, J. Wecker, and E. Hellstern. *J.Appl.Phys.* **61**, 3583 (1987)
2. K. Schnitzke, L. Schultz, J. Wecker, and M. Katter. *Appl. Phys. Lett.* **57**, 26 (1990)
3. L.V. Azároff and M.J. Buerger. "The powder method in X-Ray crystallography". Ed. Mc Graw-Hill (1958) pag. 254
4. A.K. Niessen, F.R. de Boer, P.F. de Châtel, W.C.M. Mattens, and A.R. Miedema. *CALPHAD* **7**, 51 (1983)
5. L. Schultz, and J. Wecker. *Mater. Sci. Eng.* **99**, 127 (1988).

## MICROSTRUCTURAL STUDIES OF NANOCRYSTALLINE AND AMORPHOUS PHASE FORMATION BY MILLING TECHNIQUES

M.A.MORRIS

Institute of Structural Metallurgy,  
University of Neuchâtel, Switzerland

### **Abstract**

The ball-milling technique has been used to characterise the formation of amorphous or intermetallic phases for the systems  $\text{Cr}_2\text{Nb}$  and  $\text{Al}_3\text{Fe}$ . It appears that chemical order cannot be obtained by the highly energetic milling process within the time necessary to reach homogeneous chemical compositions. This leads to the formation of metastable phases and to partial amorphisation of the powders.

### **Introduction**

Mechanical alloying by ball-milling offers a unique possibility of preparing nanocrystalline powders of different alloy systems. The process has been used, followed by high temperature consolidation, to produce dispersion strengthened copper base alloys (1) and Ni-Ti alloys (2) with grain sizes in the nanocrystalline range. On the other hand the milling process has been shown to produce metastable and/or amorphous phases in competition with intermetallic compounds due to the local atomic disorder caused by the high energy impact of the balls with the powders.(3,4).As intermetallic phases have crystallographic structures which are quite complex, it appears necessary to evaluate the possible formation of the compound by this technique in the case of each particular system

The aim of the present study has been to characterise the different phases obtained prior to or instead of the intermetallic compounds during the milling process in the case of the two systems  $\text{Al}_3\text{Fe}$  and  $\text{Cr}_2\text{Nb}$ . The former is a line compound while the latter can form over a range of compositions. In the case of the  $\text{Al}_3\text{Fe}$  the formation of the compound by ball-milling will therefore be determined by the exact stoichiometric composition of the powders being achieved during the milling process while this restriction will be less important in the case of the  $\text{Cr}_2\text{Nb}$  compound. For this reason, two different compositions of elemental powders have been studied in the case of the  $\text{Al}_3\text{Fe}$  system, namely Al-20 at% Fe and Al-25 at% Fe. In the case of the  $\text{Cr}_2\text{Nb}$  system the composition of the elemental powders was Cr-34 at% Nb. Ball milling was carried out in a Pulverisette 7 instrument with hardened steel containers and balls. The details have been given elsewhere (1,3). In all cases the powders were milled for different periods of time between 5 and 80 hours. The evolution of the milled microstructures has been followed by transmission and scanning electron microscopy together with x-ray diffraction of the powders.

### **Results and discussion**

#### **Milled powders**

Mixing of the chromium and niobium powders as a function of milling time occurred by the formation of layered structures within the powders, as shown in Figure 1. The composition



of the layers varied with increasing milling time such that after 15 hours the average composition of the two elements had been reached in most layers. At this stage, however, the hexagonal Laves phase (which according to the equilibrium phase diagram is only stable above 1600°C) formed. This phase, however, disappeared on further milling for 20 or 25 hours, confirming it to be a metastable phase. Figure 2 shows the X-ray diffraction spectra obtained from these milled powders. Milling of the powders for up to 60 hours resulted in partial amorphization of the system but never on the formation of the stable cubic  $\text{Cr}_2\text{Nb}$  intermetallic compound. TEM examination of the 60 hours milled powders confirmed the presence of an amorphous matrix in which small crystallites were embedded. This is shown in Figure 3.

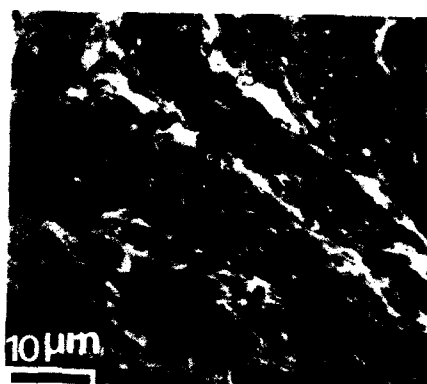


Fig. 1. Layered structure formed in the Cr-Nb milled powders.

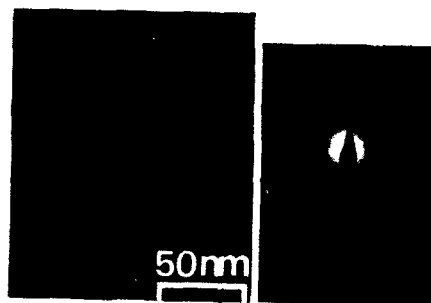


Fig. 3. TEM Dark field image and diffraction pattern obtained from the Cr-Nb powders after 60 hours milling.

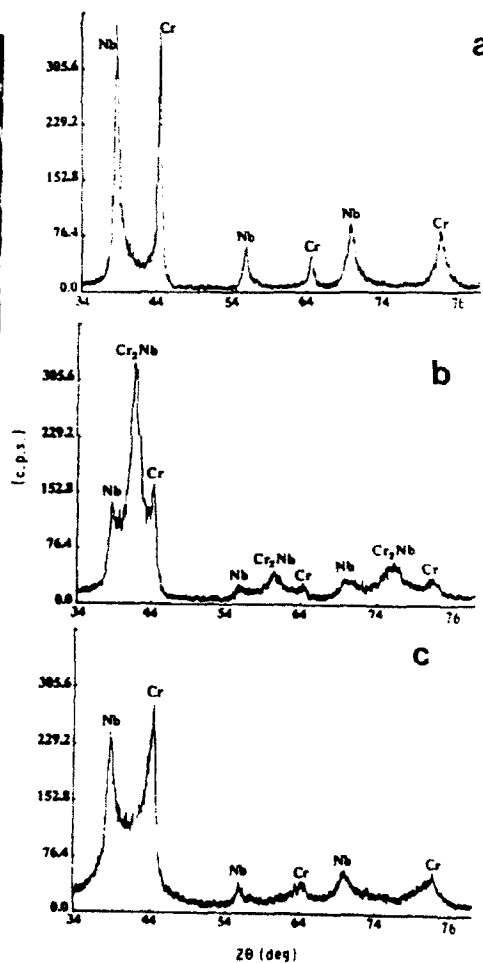


Fig. 2. X-ray diffraction spectra obtained from the Cr-Nb milled powders a) 5 hours, b) 15 hours and c) 25 hours.

The behaviour of the aluminium and iron powders was slightly different. Mixing of the elements did not occur by formation of layered structures, instead it occurred locally from outside of the particles such that the distribution of iron (seen white in figure 4) within the aluminium powders became finer with increasing milling time. The X-ray spectra obtained from these powders showed that formation of the stable  $\text{Al}_3\text{Fe}$  intermetallic phase never occurred by milling. As seen in Figure 5 for the Al-20 %Fe powders the aluminium and iron peaks present up to 20-30 hours milling disappeared after 40 hours and the presence of an amorphous phase was then detected. Observation of the powders by TEM showed that only

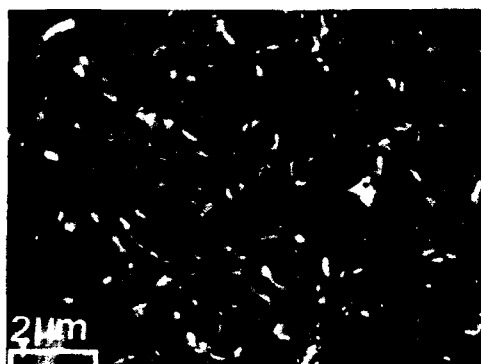


Fig. 4. Iron distribution (white) observed within the Al-Fe milled powders.



Fig. 6. TEM dark field image and diffraction pattern obtained from the Al-20%Fe powders milled for 40 hours. Note the white crystallites emmbedded in the amorphous matrix

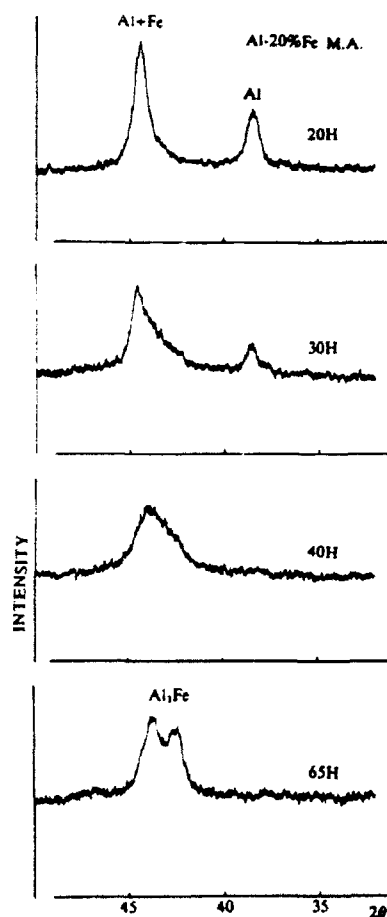


Fig. 5. X-ray spectra obtained from the Al-Fe milled powders. Note the round peak after 40 hours characteristic of partial amorphization as seen in figure 6.

partial amorphization had occurred as some crystallites were seen within the amorphous matrix. Figure 6 shows an example and we note that the crystal size ranges between 5-10 nm. On further milling up to 65 hours, the appearance of a new  $\text{Al}_3\text{Fe}$  distorted phase was detected. Similar behaviour was obtained for the powders with composition 25%Fe, but the distorted  $\text{Al}_3\text{Fe}$  phase appeared after only 40 hours milling and partial amorphization was not previously observed.

#### Annealed Powders

Annealing of the powders was carried out as a means of simulating the exposure of the powders to the high temperatures of the consolidation processes. In the case of the  $\text{Cr}_2\text{Nb}$  system, annealing of the 15 hours milled powders at  $1100^\circ\text{C}$  produced the formation of the stable cubic Laves phase. This phase did, however, disappear if the annealed powders were re-milled for a further 10 hours. The appearance of the intermetallic  $\text{Cr}_2\text{Nb}$  phase by annealing the powders confirms that chemical homogeneity was achieved. Therefore the disappearance of this phase on further milling was explained as being due to the chemical disorder produced by the excess defects created by the deformation process. Similar atomic disorder has been assumed to be responsible for the formation of the metastable hexagonal phase after milling for 15 hours and also for the lack of formation of the stable cubic phase by milling alone.

Annealing of the aluminium-iron powders milled for 40 hours produced the formation of the stable  $\text{Al}_3\text{Fe}$  intermetallic phase. However, some of the superlattice peaks of the ordered structure were not present in the x-ray diffraction spectrum. Electron diffraction analysis of this structure was carried out by TEM from the material obtained after consolidation of the powders by hot compaction at  $500^\circ\text{C}$ . The structure was confirmed to be the monoclinic  $\text{Al}_3\text{Fe}$  with lattice parameters  $a = 1.548 \text{ nm}$ ,  $b = 0.808 \text{ nm}$  and  $c = 1.247 \text{ nm}$ . However this structure was faulted by extensive twinning and this explained the lack of some superlattice peaks in the x-ray diagrams of the annealed or consolidated powders. Also this can explain that such complex structure could not form by milling alone as much atomic disorder is introduced by the process. Instead a distorted version of the  $\text{Al}_3\text{Fe}$  phase was obtained with the same average chemical composition as the stable monoclinic structure but with a higher level of atomic disorder.

#### Conclusions

For the two systems compared in the present study, the intermetallic compounds cannot form by the milling process alone. The technique produces such atomic mobility through the creation of defects that chemical order is not possible within the times required to achieve homogeneous chemical composition. This leads to the formation of metastable phases or even partial amorphization of the powders. Annealing or high temperature consolidation of the powders does, however, lead to the formation of nanocrystalline structures of the intermetallic compounds.

#### References

1. M.A. Morris and D.G. Morris, *Mat. Science and Eng.* **A111**, (1989), 219.
2. D.G. Morris and M.A. Morris, *Mat. Science and Eng.* **A110**, (1989), 139.
3. M.A. Morris, *J. Mater. Science*, **26**, (1990), 1157.
4. M.A. Morris and D.G. Morris, *J. Mater. Science*, **26**, (1991), 4687.

## ON THE SINTERING OF MIXED AEROGELS

M. RAMIREZ-DEL-SOLAR AND L. ESQUIVIAS

*Department of Structure and Properties of the Materials.*

*University of Cádiz. Apdo. 40*

*Puerto Real (11510), Cádiz (SPAIN).*

### ABSTRACT

Mixed  $\text{TiO}_2$ - $\text{SiO}_2$  sonogels and classic gels were dried on hypercritical conditions and submitted to a halogen treatment for dehydroxilation. The resulting porous aerogels were partially densified at several temperatures. In this work we use Small Angle X-Ray Scattering technique to study the evolution of the ultrastructure on sintering both kind of aerogels. The analysis of the scattering intensity profile indicates that the texture of these gels leads to deviations of the limiting slopes from the Porod's law which differs depending on the nature of the initial gel.

### 1. Introduction

Sol-gel techniques are being very actively studied from 80's onward and its scope for processing of non-crystalline materials become more and more wider. Despite objections raised to the sol-gel route as conventional method<sup>1</sup>, there is no doubt that it is competitive for building vitreous structures of certain mixed oxides (as  $\text{TiO}_2$ - $\text{SiO}_2$ ) due to the numerous troubles that their preparation from the oxides melt presents.

In order to tailor the process for this composition a complete study of the ultrastructural evolution from the initial colloidal solution to the final dense material must be done. On the basis of previous analyses during gelation<sup>2</sup> and after hypercritical drying<sup>3,4</sup> we carried out a first approach to the sintering process of  $\text{TiO}_2$ - $\text{SiO}_2$  aerogels.

### 2. Experimental

The sonogels method was used for the elaboration of a mixed gel (henceforth designed as S) with nominal composition  $0.05\text{TiO}_2$ - $0.95\text{SiO}_2$ . In this procedure, a solventless  $\text{Si}(\text{OEt})_4$ : $\text{H}_2\text{O}$  mixture, with molar ratio 1:4, was

submitted to intense ultrasonic radiation which initiates the hydrolysis of the silicon alkoxide as described in ref [3]. Once the resulting sonosol was cooled to 0°C, the adequate volume of a solution containing the titanium precursor  $\text{Ti}(\text{OBu}^n)_4$  (TBOT) was added drop by drop to obtain the desired composition. In this solution [TBOT]:[AcOH]:[BuOH] 1:1.5:3.5, the reactivity of titanium alkoxide was decreased by chelation with acetic acid<sup>5</sup>. For comparison, a classic silica sol was prepared under stirring in alcoholic (EtOH) dilution and doped with the same  $\text{TiO}_2$  amount (C sample).

The homogeneous liquids were poured in glass hermetic containers at 50°C until gelation. Hypercritical drying of the wet gels in an autoclave ( $p=190$  bar and  $T=300^\circ\text{C}$ ) leads to monolithic pieces of aerogels. Oxidation of the remaining organic groups for 5 hours and dehydration by means of chlorination for 8 hours were accomplished at 500°C. Partial densification of the samples was achieved after successive heat treatments for 5 hours/step at 780 and 870°C.

The microstructural evolution of both aerogels was studied using a synchrotron radiation Small Angle X-Ray Scattering (SAXS) experimental facility (LURE, Orsay), which provides a very intense beam with point-like cross-section. Bulk densities were measured by mercury volumetry.

### 3. Results and discussion

The intensities scattered by the S sample at each stage are plotted in figure 1a, in double logarithmic scale, as a function of the scattering vector  $q=(4\pi/\lambda)\sin(\theta/2)$ ,  $\lambda$  being the x-ray wavelength (1,46Å) and  $\theta$  the scattering angle. At smallest scattering vectors, curves present a saturation regime characteristic of a system with very homogeneous aggregates that is a peculiar feature of sonoaerogels<sup>6,7</sup>. For the experimental q-range a plateau is not reached by the C sample (Fig.1b). With increasing scattering angles a power law applies that is related with the topology of the network structure:  $I(q)\propto q^{-\alpha}$ .

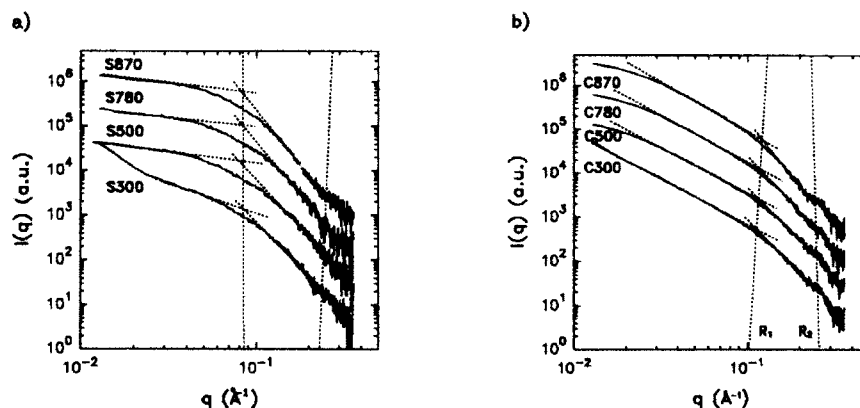


Figure 1.- Log-Log plots of the intensities scattered by samples a) S and b) C at the different stages of the heat treatment. (Curves are presented with a constant vertical displacement).

The two-phase media model described by Porod<sup>8</sup> is often used to evaluate the scattering patterns from aerogels. According to Porod's law  $\alpha=4$  for systems with well-defined sharp interfaces solid matrix-pores,  $\alpha<4$  if a fractal rough surface is present and decays with  $\alpha>4$  are typically attributed to "fuzzy" pore-matrix boundaries due to strong electronic density fluctuations. The most noticeable feature of the scattering profiles in figure 1 is the presence of two decay regimes which extend in a very narrow  $q$ -range as we might expect for quite monodispersed systems<sup>9,10</sup>. The crossover points, related to the cluster ( $R_1=\pi/q_1$ ) and elementary entities size ( $R_2=\pi/q_2$ ), enable us to assume an hierarchical two aggregation level model to describe these aerogels structure<sup>10,11</sup>. A third level could be considered for C samples, more polydispersed as it has been demonstrated by  $N_2$ -adsorption<sup>10</sup>, because of the inhomogeneity pointed out at larger distances (lower  $q$ ). Despite of the slopes ( $\alpha_0$ ) exhibited in this region, mass-fractal term can not be used for such a narrow domain<sup>11</sup>. Slopes ( $\alpha_1$ ) calculated in the Porod's regime (Table I) indicate that in both mixed aerogels oxidation and chemical dehydroxylation treatments provoke surface changes, probably related with the removal of OH and OR coverage.

**Table I.** Microstructural parameters of 0.05TiO<sub>2</sub>0.95SiO<sub>2</sub> aerogels calculated from SAXS and density measurements.

	$d_a$ (g/cm <sup>3</sup> )	$\phi_s$	V/S (Å)	$\alpha_0$	$\alpha_1$	k	N
C300	0.37	0.18	55.7	2.16	3.65	2.4	2.4
C500	0.37	0.18	45.0	2.19	3.64	2.2	2.0
C780	0.49	0.24	41.6	2.27	4.11	2.1	2.2
C870	0.90	0.45	30.5	2.45	4.52	2.0	3.6
S300	0.58	0.27	25.7	---	3.97	2.7	5.1
S500	0.55	0.25	27.1	---	3.70	2.8	5.2
S780	0.67	0.31	30.3	---	4.08	2.8	6.7
S870	0.89	0.41	29.3	---	4.50	2.8	9.5

As it has been proposed by de la Rosa-Fox et al<sup>9</sup> we can also estimate the similarity ratio ( $k=R_1/R_2$ ) of the hierarchical aggregation assumed and the cluster index ( $N_{mod}=\phi_s k^3$ ), where the solid volume fraction  $\phi_s=\rho_a/\rho_s$  was calculated from bulk ( $\rho_a$ ) and skeletal<sup>4</sup> ( $\rho_s(C)=2.02$  and  $\rho_s(S)=2.17$ ) densities determined from mercury volumetry and Wide

Angle X-Ray Scattering experiments<sup>4</sup>, respectively. The thermal evolution of these parameters signify a much more important increase of the sono-aerogel packing index during consolidation. This result is in accordance with the linear shrinkage observed above 500°C which is much more important than the one in the C sample<sup>3</sup>.

The evaluation of the integrated intensity :

$$Q_0 = \int_0^\infty I(q) q^2 dq \quad (1)$$

where the experimental intensities were corrected from Porod's law deviations<sup>12</sup>, allows the estimation of the surface/volume ratio from the equation<sup>8</sup>:

$$\lim[1/q^4] = \frac{Q_0}{\pi \phi (1-\phi)} \frac{S}{V} \quad (2)$$

where  $\lim[1/q^4]$  has been taken as the extrapolated  $1/q^4 = A + Bq^4$  to  $q=0$  from the high  $q$ -region.  $V/S$  values presented in table I denote that while in the classic aerogel cluster (or pores) size decrease on heating, there is only a slight increase in the sonogel serie.

These results point to a different evolution of the aggregates on the first sintering stages due to the textural divergences between the starting aerogels since sintering is a process of densification driven by interfacial energy. So, collapse of large pores in *C* sample with almost constant *N* leads to smaller "primary" clusters. In this way lenghts obtained from Porod's analysis could be related either to pores or clusters size. Small pores of *S* sample induce a significant shrinkage and coalescence of elementary particles causes increasing packing indexes and slightly larger clusters.

#### 4. Conclusion

Mixed titania-silica aerogels can be described on the basis of an hierarchical model with two or three level depending on the nature of the precursor gel. Densification occurs via viscous flow and is very much affected by the textural features. Coalescence of small sonogel particles leads to larger and more compact clusters while collapse of classic gel mesopores increases the size of the elementary entities aggregates.

#### 5. Acknowledgements

We would like to thank Dr. de la Rosa-Fox for many helpful discussions.

#### References

- 1 E.D.Zanotto in *Sixth International Workshop on Glasses and Ceramics from Gels* Ed.L.Esquivias (Universidad de Cádiz, Cadix, 1991) FO1.
- 2 M.Ramírez-del-Solar, L.Esquivias, A.F.Craievich and J.Zarzycki, *idem ref.1*, AP43.
- 3 M.Ramírez-del-Solar, N.de la Rosa-Fox, L.Esquivias and J.Zarzycki, *J.Non-Cryst Solids* **121** (1990) 84.
- 4 J.M.Ruiz-Rube, M.Ramírez-del-Solar, N.de la Rosa-Fox and L.Esquivias in *Basic Features of the Glassy State*, eds. J.Colmenero and A.Alegria (Pergamon Press, Singapore, 1990) p.68.
- 5 S.Doeuff, M.Henry, C.Sanchez and J.Livage, *J.Non-Cryst. Solids* **89** (1987) 206.
- 6 N.de la Rosa-Fox, L.Esquivias, A.F.Craievich and J.Zarzycki, *idem ref.3*, p. 211.
- 7 N.de la Rosa-Fox, L.Esquivias, A.F.Craievich and J.Zarzycki, *Rivista della Staz. Sper. Vetro* **I-20 (5)** (1990) 67.
- 8 G.Porod in *Small Angle X-Ray Scattering* eds. O.Glatter and O.Kratky (Academic Press, London, 1982) Ch.2-VI.
- 9 N.de la Rosa-Fox and L.Esquivias, *idem ref.1*, BO5.
- 10 J.J.Calvino, M.A.Cauqui, G.Cifredo, L.Esquivias, J.A.Pérez, M.Ramírez-del-Solar and J.M.Rodríguez-Izquierdo (In preparation).
- 11 J.Zarzycki, *idem ref. 3*, p.110.
- 12 W.Ruland, *J.Appl. Cryst.* **4** (1971) 70.

## STRUCTURAL MODIFICATIONS IN SILICA XEROGELS PREPARED USING SONOCATALYSIS AND AN ADDITIVE

E. Blanco, N. de la Rosa-Fox and L. Esquivias  
Department of Structure and Properties of the Materials, University of Cádiz.  
Apdo. 40 - Puerto Real(11510), Cádiz (SPAIN).

### ABSTRACT

Monolithic silica glasses are obtained at 1000°C by using sonocatalysis and a chemical additive from the gel produced in tetraethoxysilane hydrolysis. Transmission Electron Microscopy and nitrogen physisorption techniques are used in samples characterization during the densification steps.

### 1.- Introduction

The sol-gel method presents a great potential in obtaining complex shaped glasses<sup>1</sup>, and other advanced materials<sup>2,3</sup>. The addition of an additive in the sol stage allows for an easier way of interstitial liquid to be removed from the pores in the resulting gel<sup>4,5</sup>. The densification process can be described by a hierarchical structure evolution of quasi-spherical shaped<sup>6</sup>. The vitreous silica obtaining without the need of reaching the melting point is one of the most important advantages of the sol-gel route. Recently, this point has been questioned because a long heat-treatment is necessary to sinter the gel. Nucleation can be started which helps the devitrification process<sup>7</sup>. The presented results refer to the possibility of obtaining monolithic silica glass using the sol-gel method by means of sonocatalysis.

### 2.- Experimental

#### 2.1 Xerogels preparation.

Silica xerogels were prepared from tetraethoxysilane (TEOS) hydrolysed by HNO<sub>3</sub> acid water (pH=1) and formamide (NH<sub>2</sub>-COH) as additive in a molar ratio 1:10:7 respectively. This formamide molar ratio leads to a denser packing and better defined pore interfaces in aged and dried gels<sup>8</sup>.



Gels known as "sonogels" have been prepared by the application of high power ultrasounds (HPU) at 20 kHz and 600 w, to the liquid mixture. A calibration

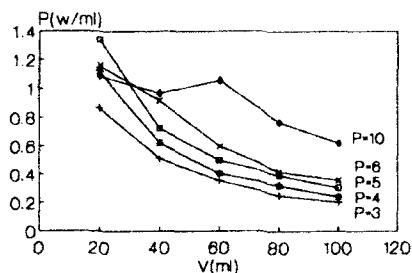


Fig. 1: Power supplied vs. liquid volume for different power levels.

of the High Ultrasonic Processor was made by the measure of temperature increase produced in several water volumes, with different output control setting, P(a.u.), selected in the processor. Graphs of the temperature vs time have a linear region which slopes are proportional to the power that has been supplied to each liquid volume. Then it is possible to plot the power supplied to different liquid volumes when a level of power is selected as is shown in Fig.1.

Two different ultrasound energies were applied to the samples: a low ultrasonic dose (0.1 kJ), submitting under ultrasound 30 cm<sup>3</sup> of solution for 100s and a high ultrasonic dose (0.3 kJ) to 30 cm<sup>3</sup> for 300 s. Both treatments at a power level of 5 (fig.1). A solventless hydrosol procedure was also used where acidic water is dripped on a mixture of TEOS-Formamide submitted to a magnetic stirring.

In all cases, the sols obtained were introduced into hermetically closed polyethylene containers. The gelification process took place at 40°C. After seven days of aging, samples were dried at 40°C until the shrinkage liquid was completely evaporated.

## 2.2 Densification process.

The first densification step is a 24 hour treatment at 100°C in an electric stove. During this process monolithic xerogels undergo an important shrinkage. Then samples were heated up to 200°C and treated at this temperature for twelve hours. At this point all the formamide has left the sample structure<sup>6</sup>.

After that, samples were heated up to 1000°C and held at this temperature for thirty minutes. Heating speed was, in all cases, 1°C/min. The bulk density of the samples, measured by Hg volumetry was 2.1 g/cm<sup>3</sup>.

## 2.3 Nitrogen physisorption measurements.

The pore analysis of the samples was carried out in a high vacuum system with nitrogen gas as adsorbate. Firstly the samples are degassed to empty the pores, after which equilibrium volumes of nitrogen adsorbed and desorbed as a function of the relative pressure are obtained<sup>6</sup>.

## 2.4 TEM measurements.

Transmission electron micrographs and microelectron diffraction of the samples treated at 1000°C for 30 minutes have been performed using the Cádiz

University Electron Microscopy facility.

### 3.- Results and discussion.

Fig. 2 shows a nitrogen physisorption isotherm that corresponds to type IV of IUPAC classification with hysteresis loop. The shape of the hysteresis allows to describe pore structures. The loop shapes found in these samples is in agreement with a model of agglomerates of approximately uniform spheres in almost regular array. In this way, a model of big clusters or aggregates built by elementary spherical particles explains the xerogel evolution on heating<sup>6</sup>.

Densification of these gels is a sintering process by which the pores are eliminated and the material is converted into glass. It tends to reduce the interfacial surface eliminating the pores, the collapse of which is governed by Newtonian viscous flow<sup>9</sup>. The transmission electron micrograph in Fig. 3 shows two quasi-spherical clusters (80 nm radius) formed by small particles ( $\approx 2$  nm). It is also possible to see the neck between them, the particle-neck size ratio reveals a high mechanical strength of the solid phase and so monolithic pieces can be obtained.

Electron microdiffraction in Fig. 4 (left) shows the glassy state in the low ultrasonic dose sample. However, devitrification appears in the high ultrasonic dose one as can be seen in Fig. 4 (right). This is due to the shape of the cluster surface, which depends on the ultrasonic dose<sup>10</sup>. That is, a high ultrasonic dose promotes a rough pore-matrix interface, hence this sample has more nucleation sites for the crystal to grow.

### 4.- Conclusions

Xerogel densification is produced by the viscous flow of the quasi-spherical aggregates built by small particles, giving rise to a packing of the solid phase with a rupture stress near the vitreous silica theoretical one.

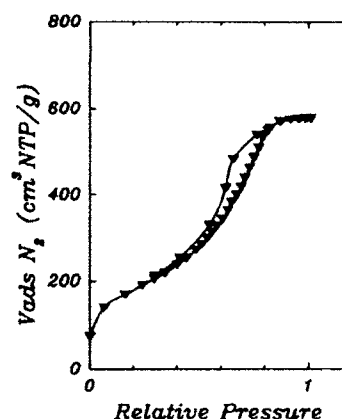


Figure 2: Nitrogen physisorption isotherm of a high dose ultrasound silica xerogel heat-treated at 400°C for one hour.

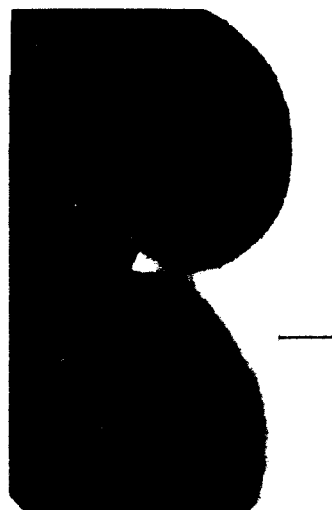


Figure 3: Transmission Electron Micrograph of a solventless sample treated at 1000°C for thirty minutes. (bar 40 nm).

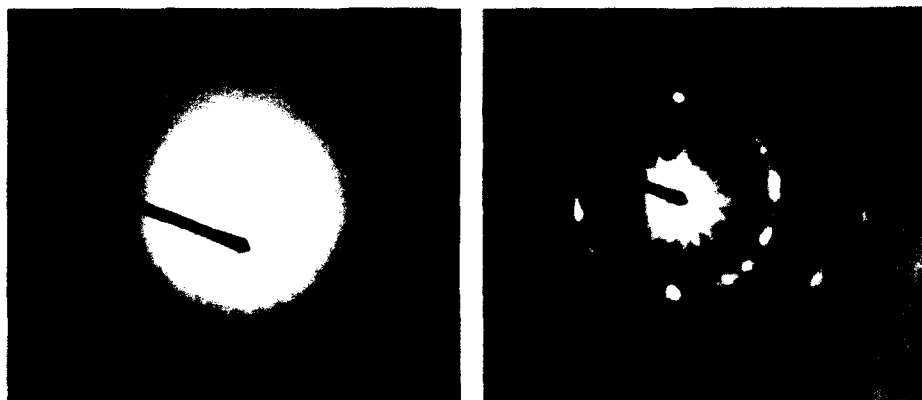


Figure 4: Electron microdiffraction of samples heat-treated at 1000°C for thirty minutes.

Monolithic vitreous silica can be obtained by the sol-gel processing at a lower temperature than its melting point. A high ultrasonic dose favours sample crystallisation.

#### Acknowledgements

Authors are greatfull to Mr. J. González for his assistance in the electron microscopy facility.

#### References.

- 1) R.D. Shoup in *"Ultrastructure Processing of Advanced Ceramics"*, eds. J.D. Mackenzie and D.R. Ulrich (Wiley, N.Y., 1988) p. 347.
- 2) E.M. Rabinovich et al. *J. Non-Cryst. Solids*, 63, (1984) 155.
- 3) M.Yamane, J.B. Caldwell and D.T. Moore in *"Better Ceramics Through Chemistry II"*, eds. C.J. Brinker, D.E. Clark and D.R. Ulrich (Mat. Res. Soc., Pittsburgh, 1986) p. 765.
- 4) L.L. Hench in *"Science of Ceramic Chemical Processing"* eds. L.L. Hench and D.R. Ulrich, (Wiley, New York, 1986) p. 52.
- 5) G. Orcel, J. Phalippou and L.L. Hench, *J. Non-Cryst. Solids*, 104, (1988) 170.
- 6) E. Blanco, N. de la Rosa-Fox, L. Esquivias and A.F. Craievich in VI Int. Workshop on Glasses and Ceramics from Gels, Seville (1991), BP3.
- 7) E.D. Zanotto, idem as (6), FO1.
- 8) E. Blanco, M. Ramirez-del-Solar, N. de la Rosa-Fox and A.F. Craievich, idem as (6), BP4.
- 9) J. Zarzycki in *"Glasses and the vitreous state"* Camb. Univ. Press (1991) p. 472.
- 10) N. de la Rosa-Fox and L. Esquivias, idem as (6), BO5.

## Fe-57 MÖSSBAUER STUDY OF SOME (FeCo)<sub>75</sub>SiB METALLIC ALLOYS

I.Orúe, J.M.Barandiarán, M.L.Fernández-Gubieda, F.Plazaola.  
Dpto. Electricidad y Electrónica, Facultad de Ciencias, UPV/EHU  
Apdo. 644, 48080 Bilbao

**ABSTRACT:** We report <sup>57</sup>Fe Mössbauer Spectroscopy measurements on (Fe<sub>94</sub>Co<sub>6</sub>)<sub>75</sub>Si<sub>x</sub>B<sub>25-x</sub> and (Fe<sub>50</sub>Co<sub>50</sub>)<sub>75</sub>Si<sub>x</sub>B<sub>25-x</sub> metallic glasses. The Isomer Shift (IS) in both samples shows an increase with the substitution of B by Si. We also report Mössbauer measurements on the Co rich side of (Fe<sub>x</sub>Co<sub>1-x</sub>)<sub>75</sub>Si<sub>15</sub>B<sub>10</sub> metallic alloys in the composition range  $0 \leq x \leq 0.15$ . Although the magnetostriction changes from negative to positive values in the measured compositional range, the IS remains constant at a value of 0.18 mm/s.

### Introduction

Co-rich amorphous alloys have been proved to be a subject of much interest both from a technical and fundamental point of view <sup>1-5</sup>. The alloys with a low amount of Iron or other metals have nearly zero magnetostriction at room temperature <sup>1</sup>. In the case of the (Fe<sub>x</sub>Co<sub>1-x</sub>)<sub>75</sub>Si<sub>15</sub>B<sub>10</sub> alloy series the magnetostriction at room temperature goes from negative values in the case of Co<sub>75</sub>Si<sub>15</sub>B<sub>10</sub> sample up to positive values passing through zero in the case of (Fe<sub>6</sub>Co<sub>94</sub>)<sub>75</sub>Si<sub>15</sub>B<sub>10</sub> sample <sup>2</sup>. Since magnetostriction is supposed to be sensitive to changes in the Short Range Order both Chemical and Topological, it is clear that addition of low quantities of Fe to a Co-based amorphous matrix should cause microstructure changes.

It has been suggested that the existence of two kinds of structural units formed by four metallic atoms may explain the saturation magnetostriction behaviour of the alloys in the Co rich side. One of the structural units, formed by four Co ions, could be the source of the negative  $\lambda_s$  in the parent Co<sub>75</sub>Si<sub>15</sub>B<sub>10</sub> composition, and the other one, formed by 3Co ions and 1Fe ion could be the cause of positive magnetostriction <sup>4</sup>.

In this work, we have proceeded to measure these amorphous alloys by Mössbauer

Spectroscopy. Thus, we have got information about the closest environment of the Fe-ion, mainly through two parameters: the Isomer Shift (IS), a measure of the electronic density in the Fe nucleus and the Magnetic Hyperfine Field ( $B_{hf}$ ) at the Fe nucleus.

On the other hand, very recent Mössbauer measurements on  $(Fe_xCo_{1-x})SiB$  alloys series show different hyperfine parameters behaviour at both sides of the alloys with  $x=0.8$ . Therefore, we have study by Mössbauer Spectroscopy two series of metallic glasses with a fixed concentration of Fe and Co, the first one below  $x=0.8$  and the second one above this value.

### Experimental results

The samples were prepared by standard melt spinning technique, using wheel surface speeds up to 40 m/s. The amorphous nature of the ribbons so obtained has been checked by X-ray diffraction. The fitting of the experimental data was performed assuming a distribution of hyperfine fields at Iron nucleus sites 5.

Three systems of amorphous alloys based in  $(FeCo)_{75}SiB$  composition have been prepared. In two of them the relative abundance of Iron and Cobalt has been fixed, being variable the relative concentration of the metalloids Si and B involved in the samples. These two systems are  $(Fe_{50}Co_{50})_{75}Si_xB_{25-x}$  and  $(Fe_{94}Co_6)_{75}Si_xB_{25-x}$ . Measuring such alloys systems by Mössbauer Spectroscopy we have studied the influence on the hyperfine parameters of the Silicon by Boron replacement in a sample with a 25% content of metalloids. The third series corresponds to the Co-rich side of the  $(Fe_xCo_{1-x})_{75}Si_{15}B_{10}$  metallic alloys in the composition range  $0 \leq x \leq 0.15$ . Due to the low Fe content of the Co rich amorphous alloys, it was necessary to use iron enriched on the  $^{57}Fe$  isotope to prepare the samples for the Mössbauer measurements.

On the one hand, from the analysis of the two systems of amorphous alloys with varying the Si-B ratio, we observe that the hyperfine field has not been affected by the exchange of Silicon by Boron. Besides, figure 1 shows  $B_{hf}$  is greater in the  $(Fe_{50}Co_{50})_{75}Si_xB_{25-x}$  alloys than in the  $(Fe_{94}Co_6)_{75}Si_xB_{25-x}$  ones. However, IS increases linearly with Silicon concentration in both series of alloys (fig. 1b). On the other hand, the Mössbauer Spectra of Co rich metallic glasses shows that  $B_{hf}$  as well as IS remain constant in the range  $0 < x \leq 0.15$  (fig. 2). Moreover, the hyperfine field distribution obtained in the Co rich samples is narrower than the distributions of other samples with larger Fe content (fig. 3).

### Discussion

The IS increase with Si content, shown in figure 1, has been observed in FeCoSiB and FeSiB, metallic glasses changing at the same time both metallic content and metalloid ratios<sup>6,7</sup>. Figure 1 shows both the dependence of the IS with the Fe-Co ratio and the same IS linear increase with Si content in the two series. The slope of both lines is .0037 mm/s per %Si. This observed increase of the IS means an increase in the 3d electron density or a decrease in the 4s electron density or both<sup>8</sup>. Such equal slopes in both measured samples with Si content indicates the same electron transference per Si atom in both series, whichever Fe-Co ratio is. Moreover, it indicates the higher tendency of Si, with one p-electron more than B in its outer shell, for giving up electrons to Fe 3d band.

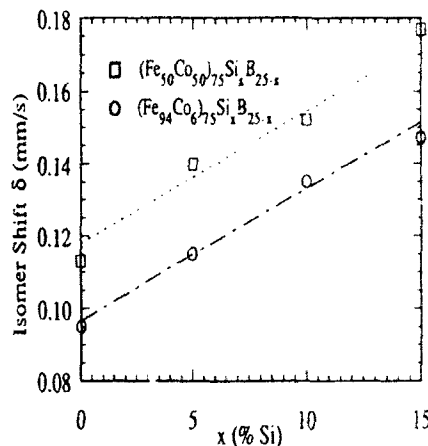


Fig. 1. Isomer Shift versus Si concentration

The IS behaviour in the Co-rich metallic glasses shown in figure 2 is quite different to the observed behaviour of the alloy series  $(Fe_xCo_{1-x})_{80}B_{20}$  amorphous alloys<sup>9</sup> and to the IS behaviour of the alloy series  $(Fe_xCo_{1-x})_{75}Si_{15}B_{10}$  in the Fe rich side<sup>10</sup>. Unlike the measured constant value of IS in the Co rich side samples, the two other systems show an increase of IS with Co content in the alloy. Nevertheless, the IS measured in the  $(Fe_{50}Co_{50})_{75}Si_{15}B_{10}$  metallic alloy and the value obtained in the Co rich side agree. This shows a clear saturation of IS with the increase of Co content in this alloy series. It is interesting to notice that the measured hyperfine field of this Co rich side of the alloy series remains constant at the value of  $24.6 \pm 0.2$  T. This behaviour may indicate the Fe atoms that substitute for the Co ones in the Co rich side of the alloy locate in the nearest neighbourhood of Co atoms. In other words, Fe atoms do not locate in the nearest neighbourhood of another Fe atoms. Therefore, the obtained results seem to support the structural units interpretation of this alloy series magnetostriction on the Co rich side.

The hyperfine field distribution of the two samples, shown in figure 3 supports the above suggestion. Figure 3 shows clearly the narrowing of the hyperfine field distribution respect to samples with larger Fe contents, indicating a stronger Short Range Order in the alloys with low Fe content.

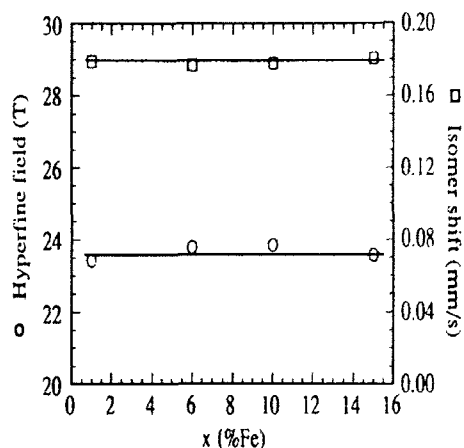


Fig. 2.  $B_{hf}$  and IS versus  $x$  (Fe-Co ratio) in the  $(Fe_xCo_{1-x})_{75}Si_{15}B_{10}$  alloys.

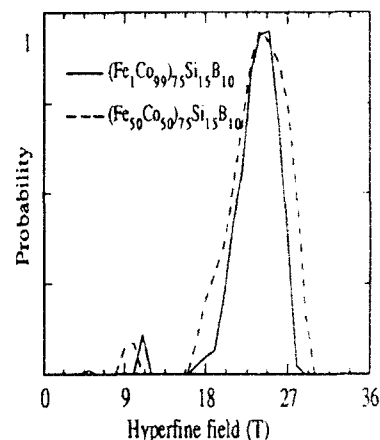


Fig. 3. Hyperfine field ( $B_{hf}$ ) distributions for  $(Fe_1Co_{99})_{75}Si_{15}B_{10}$  and  $(Fe_{50}Co_{50})_{75}Si_{15}B_{10}$ .

### Acknowledgments

This work has been supported by the Basque Government under grant PGV 8923.

### References

1. R.C.O'Handley and M.O.Sullivan, J.Appl. Phys. **52** (1981) 1841.
2. V.Madurga, M.Vázquez, A.Hernando & O.V.Nielsen, Solid State Com. **52** (1984) 701-703.
3. R.C. O'Handley, Phys. Rev. B **18** (1978) 930.
4. A.Hernando, V.Madurga, J.M.Barandiarán & O.V.Nielsen, SolidState Com. **54** (1985) 1059-1063.
5. R.A.Brand, J.Lauer, D.M.Herlach, J Phys. F: Met.Phys. **13** (1983) 675.
6. M.L.Fdez-Gubieda, Thesis. Universidad del Pais Vasco (1991)
7. J.M.Barandiarán, M.L.Fdez-Gubieda, F.Plazaola, O.V.Nielsen, Journal de Physique **49** (1988) C8-1367
8. L.R.Walker, G.K.Wertheim and V.Jaccarino, Phys.Rev.Letters **6** (1961) 98.
9. S. Dey, P. Deppe, M.Rosenberg, F.E.Luborsky and J.L.Walter, J.Appl.Phys. **52** (1981) 1805
10. M.L.Fdez-Gubieda, J.M.Barandiarán, F.Plazaola, J.Magn. and Magn. Mat (In press)

THE STRUCTURE AND OPTICAL PROPERTIES  
OF PHOSPHATE GLASSES WITH IRON IONS

J. WASYLAK

*University of Mining and Metallurgy,*

*Department of Glass*

*30 Mickiewicza St., 30-059 K r a k o w , Poland*

ABSTRACT

Phosphate glasses were melted under appropriate conditions with iron ions in order to obtain glasses with  $\text{Fe}^{2+}$  and  $\text{Fe}^{3+}$  ions. The structure of the obtained glasses was determined using Raman spectra. The electrical properties of phosphate glasses with transition metals elements were already determined earlier [1]. The present study refers to some physico chemical properties, especially light transmittance. The analysis of Raman spectra of the examined glasses has revealed the presence of metaphosphate and ortophosphate groups in the glass. Phosphate glasses with  $\text{Fe}^{2+}$  ions exhibit maximum light transmittance in the range 400 - 700 nm, and an almost complete absorption in the range 900 - 1100 nm, in contrast to glass containing  $\text{Fe}^{3+}$ . Retaining the  $\text{Fe}^{2+}$  ions in the glass is in practice possible only in the phosphate glass. This property of the glass qualifies it to be used for optical filters.

1. Experimental

The synthesis of glasses was carried out in corundum crucibles in an electric furnace. The melting temperature was 1200°C. During synthesis the oxidizing or reducing atmosphere was used depending on the glass composition. The melted glasses were cast in air and next annealed at a temperature determined from the DTA curve.



## 2. Results and discussion

Investigations were carried out on glasses from the system  $\text{Ba}(\text{PO}_3)_2 - \text{MgO} - (\text{ZnO})$  with an addition of 1 wt % of iron oxides.

Fig.1 shows Raman spectra typical for the examined phosphate glasses.

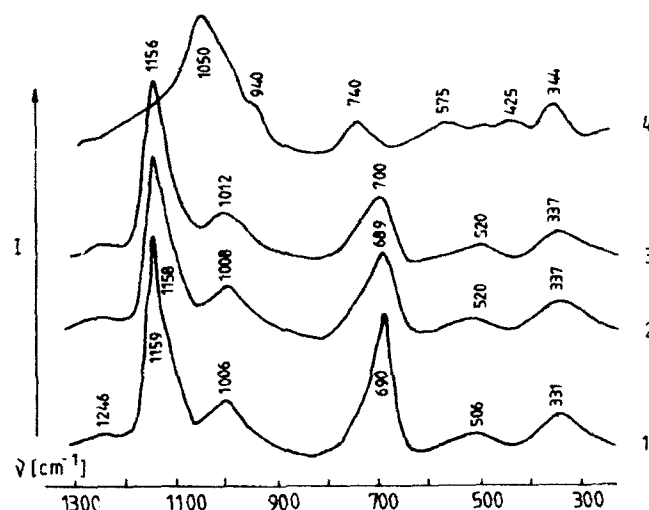


Fig.1. Raman spectra of phosphate glasses with iron oxides

- |  |   |
|--|---|
| 1. $\text{Ba}(\text{PO}_3)_2$              | 2. $\text{Ba}(\text{PO}_3)_2 - \text{MgO}$                  |
| 3. $\text{Ba}(\text{PO}_3)_2 - \text{ZnO}$ | 4. $\text{Ba}(\text{PO}_3)_2 - \text{MgO} \cdot \text{ZnO}$ |

When examining Raman spectrum of glassy  $\text{Ba}(\text{PO}_3)_2$  it has been found that it contains bands characteristic for the chain-like structure of metaphosphate which are evidence that fragments of the structure of crystalline barium metaphosphate, i.e. fragments of the  $[(\text{PO}_3)_2]_\infty$  have been retained [2,3]. The bands in Raman spectrum of glassy  $\text{Ba}(\text{PO}_3)_2$  have been assigned to the vibration of the following groups:

- |   |  |
|---|--|
| $690 \text{ cm}^{-1} - \nu_s(\text{POP})$ ,                   | $1060 \text{ cm}^{-1} - \nu_{as}(\text{POP})$ ,                  |
| $1159 \text{ cm}^{-1} - \nu_s(\text{O}^-\text{P}=\text{O})$ , | $1246 \text{ cm}^{-1} - \nu_{as}(\text{O}^-\text{P}=\text{O})$ . |

The band appearing at about  $50\text{ cm}^{-1}$  occurs in all phosphate glasses and it derives from the movements of the metaphosphate groups around the metal cation [4]. The band situated at about  $330\text{ cm}^{-1}$  derives from the few pyrophosphate groups present in metaphosphate glass and it is referred to as deformation vibrations of the  $\text{PO}_3$  groups. The broad band situated at about  $500\text{ cm}^{-1}$  represents various types of deformation vibration of the chain  $(\text{PO}_3)_n$ .

When analyzing in succession Raman spectra of glasses in the system  $\text{Ba}(\text{PO}_3)_2\text{-MgO}$ ,  $\text{Ba}(\text{PO}_3)_2\text{-ZnO}$  and  $\text{Ba}(\text{PO}_3)_2\text{-MgO-ZnO}$  (Fig.1), in all examined samples the presence of bands situated within the ranges:  $330\text{-}340$ ,  $500\text{-}550$ ,  $680\text{-}740$ ,  $1000\text{-}1050$ ,  $1140\text{-}1160$ ,  $1240\text{-}1260\text{ cm}^{-1}$  was observed. These bands have been assigned to vibrations revealed earlier in the metaphosphate chain with the band of the symmetric tensile vibrations of the  $\text{O}^-\text{P}\text{O}^-$  groups overlapping the weaker band at about  $1100\text{ cm}^{-1}$ , which may derive from asymmetric tensile vibrations of the  $\text{PO}_3$  group in the  $\text{P}_2\text{O}_7^{4-}$  ion. This is connected with a change of the glass structure from the metaphosphate type to that of pyrophosphate type (at  $\text{Mg}(\text{ZnO})$  content above 20 mole %). At a content of the Mg and Zn oxides equal to about 40 % mole there appear in the Raman spectra the orthophosphate groups  $\nu(\text{PO}_4)-425\text{ cm}^{-1}$ ,  $\nu_5(\text{PO}_4)-940\text{ cm}^{-1}$ .

When discussing the properties of the examined glasses particular attention has been given to light transmittance (fig.2) taking into consideration the effect of certain oxides on the shade of the colour, i.e. the quantitative ratio  $\text{Fe}^{2+}:\text{Fe}^{3+}$  in the glass.

The curve for light transmittance of glass containing  $\text{FeO}$  shows one maximum for the absorption of visible light within the range of infrared rays, about  $1.1\text{ }\mu\text{m}$  in length, whereas in the visible range it exhibits transmittance for blue rays. The curve for light transmittance of glass containing  $\text{Fe}_2\text{O}_3$  does not show any maximum in the visible

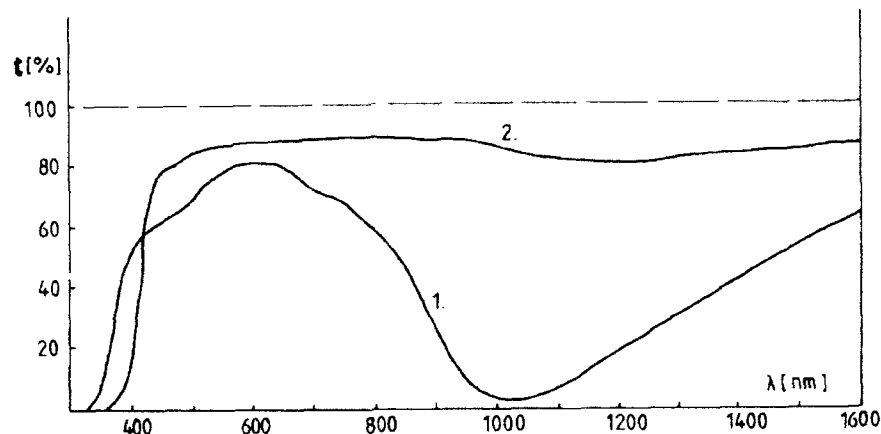


Fig.2. Light transmittance curves for phosphate glasses containing iron compounds: 1 - glass containing FeO, 2-containing  $\text{Fe}_2\text{O}_3$  (thickness of the samples : 3 mm)

part of the spectrum, and it exhibits greatest transmittance in the range from about 550 nm up to infrared. When examining the effect of the oxides of the MO group on the colour shade of phosphate glasses containing iron ions, it has been found that ZnO and MgO favour the shifting of the equilibrium towards the  $\text{Fe}^{2+}$  ions. Other properties of the examined glass have also been determined, the values of which fall within the following intervals: density -  $3.67 \pm 3.94 \text{ g/cm}^3$ , refractive index -  $1.588 \pm 1.622$ , coefficient of thermal expansion -  $136 \pm 108 \cdot 10^{-7} \text{K}^{-1}$ .

### 3. References

1. J. Wasylak, J. Koprowski, E. Czerwosz, *J. Phys.* **43**(12) (1982) 247
2. I. C. Gremier, A. Martin, A. Durif, e.a; *Bull. Soc. Mineral Crystallogr.* **XC24** (1967) 1165.
3. A. N. Lazarev, *Kolebatelnyye spektry i strojenije silikatov* (Nauka, Leningrad, 1968), p.320.
4. P. J. Miller, *J. Chem. Phys.* **71**(2) (1979) 997.

## RECENT RESULTS IN NEUTRON SCATTERING FROM NON-CRYSTALLINE SOLIDS USING A PULSED SOURCE

W S Howells

*ISIS Science Division, Rutherford Appleton Laboratory,  
Chilton, Didcot, OX11 0QX, UK*

### ABSTRACT

The advantages and unique properties of a pulsed source are illustrated with results obtained on the ISIS Facility. Diffraction experiments are illustrated with results on conducting glasses, mechanical amorphization, and carbon 60 Fullerene. Quasi-elastic and inelastic experiments have been carried out on, for example, the liquid-glass transition and vitreous silica.

### 1. Introduction

At the previous conference in this series, the advantages and unique properties of a pulsed neutron source were described and illustrated with results obtained on the ISIS Facility at the Rutherford Appleton Laboratory <sup>1</sup>. Since then much experience has been gained and new instruments installed, so this paper seeks to update the situation with new results using the techniques of diffraction, quasielastic scattering and inelastic scattering. Descriptions of the instruments can be found elsewhere <sup>2</sup> and a wide range of recent results is described in the ISIS annual reports <sup>3</sup>.

### 2. Diffraction results

The main advantages of a pulsed source diffractometer are as follows: a wide range of momentum transfer  $Q$  from typically 0.1 to 100 Å<sup>-1</sup> – the latter providing good resolution in the real-space radial distribution functions; the availability of high energy, short wavelength, neutrons together with low scattering angles minimises the inelastic (Placzek) corrections (this is being exploited to great advantage by the new diffractometer SANDALS); the resolution in  $Q$ -space for large scattering angles is good especially for high  $Q$ -values; and the fixed scattering angles allow novel experiments such as orientated samples and magnetic fields.

#### 2.1. Conducting glasses

A characteristic feature of the doped conducting glasses is the appearance in the structure factor  $S(Q)$  of a peak at low  $Q$ -values (typically about 1 Å<sup>-1</sup>) as the

concentration of the dopant is increased. This is particularly true of the silver halide doped borate glasses and especially with silver iodide <sup>4</sup>. An explanation for this pre-peak has been the subject of much debate. Recent molecular dynamics calculations whilst agreeing with the measured  $S(Q)$  for the higher  $Q$ -values is unable to solve the problem at low- $Q$  <sup>5</sup> (this is in general a problem area for molecular dynamics). However recent Reverse Monte Carlo calculations <sup>6</sup> on AgI-AgPO<sub>3</sub> glasses have shown that the PO network, when expanded by AgI doping, keeps its connectivity but contains large holes which are filled by the salt. It is the low-density PO network that gives rise to the low- $Q$  peak.

## 2.2 Mechanical amorphization

This is another area in which good  $Q$ -resolution is essential, this time in order to establish that Bragg peaks from a crystalline phase are present. Poor  $Q$ -resolution may be a problem on many reactor based diffractometers especially when the instrument is designed for disordered systems and so has a resolution  $\Delta Q/Q$  of about 2%. In order to identify crystalline peaks a resolution of about 0.5% in  $\Delta Q/Q$  is necessary and this is available at high scattering angles on LAD.

## 2.3 Orientated samples

The technique for measuring orientated flat samples on LAD was first applied to conducting polymer films <sup>7</sup>. This has now been extended to studies on amorphous metallic glasses in which the structure has been compared between three orthogonal directions in the ribbon. No differences have been observed - in disagreement with previously published results.

## 2.4 C60 Fullerene

The new diffractometer SANDALS was recently used to determine the room temperature structure factor of C60 <sup>8</sup>. The  $S(Q)$  was measured out to a  $Q$ -value of  $100\text{\AA}^{-1}$  to give the best real-space resolution currently available on a neutron diffractometer. Despite this the first peak in the  $g(r)$  corresponding to the nearest neighbour distance does not show any splitting but its shape is best described by two peaks at distances of 1.38 & 1.46Å (see figure 1). The former is the bond linking two six-member rings and the latter joins a six to a five-member ring. In the high- $r$  region, the structure is in good agreement with a model based on a bcc lattice.

## 3. Quasielastic results

The high resolution quasielastic spectrometer IRIS has been used to study the liquid-glass transition in two systems: propylene carbonate <sup>9</sup> and iso-propanol <sup>10</sup>. Propylene carbonate can be regarded as a model material for studies of the dynamics around the glass transition due to its simple molecular structure and its extreme 'fragility' according to Angell's classification system. The relaxation time

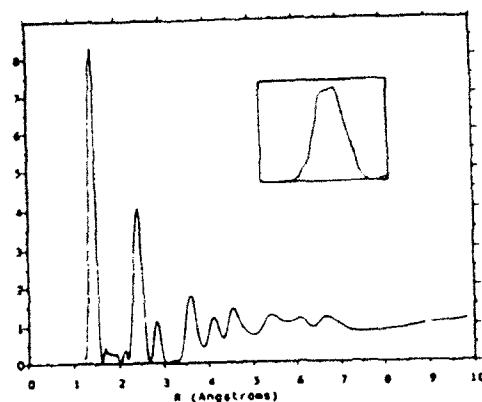


Figure 1. Radial pair distribution function for C<sub>60</sub> Fullerene. Inset shows the first peak expanded.

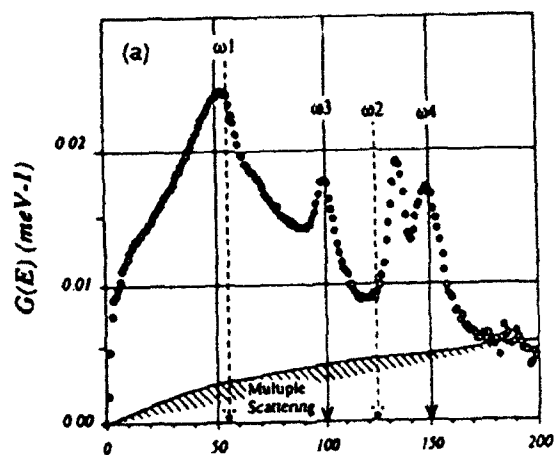


Figure 2. Generalized vibrational density of states  $G(E)$  for vitreous silica measured on MARI with 230 meV incident energy.

determined from the quasielastic peak width should, according to mode coupling theory, vanish at the critical temperature  $T_c$  as  $\tau \sim (T - T_c)^{-\alpha}$  when approaching  $T_c$  from above. Fits to the data give  $\alpha=2.3$  and  $T_c=188\text{K}$ , whereas viscosity data gave 2.3 and 197K respectively and the glass transition temperature is 160K.

#### 4. Inelastic results

A new spectrometer MARI has recently been commissioned on ISIS. This spectrometer was designed to have a very good energy resolution (about 1% of the incident energy) and continuous scattering angle coverage. This enables good quality measurements to be made of  $S(Q, \omega)$  for non-crystalline materials such as vitreous silica,  $\text{SiO}_2$ . The generalized vibrational density of state  $G(E)$  measured with an incident energy of 200 meV is shown in Figure 2<sup>11</sup>. The corresponding one obtained using 130 meV shows possible weak peaks at 63 meV and 77 meV. These are the D1 and D2 modes observed in Raman experiments and correspond to 4-ring and 3-ring modes, respectively. The excellent energy resolution of MARI is about one half of the width of the ring modes observed in the Raman spectrum and is therefore sufficient to observe these modes. The intensity is very weak and of the order 1% of the total area under the  $G(E)$ . If these rings exist they must therefore be at a low concentration.

#### 6. References

1. W. S. Howells, in *Basic features of the glassy state*, ed. J. Colmenero & A. Alegria (World Scientific, 1990) p57.
2. ISIS User Guide, Rutherford Appleton Laboratory report RAL-88-030.
3. ISIS Annual Report 1991, Rutherford Appleton Laboratory report RAL-91-050.
4. L. Borjesson, M. Elmroth & W. S. Howells, in *Basic features of the glassy state*, ed. J. Colmenero & A. Alegria (World Scientific, 1990) p93.
5. M. C. Abramo, G. Pizzimenti & A. Consolo, *Phil Mag* **64** (1991)
6. L. Borjesson, R.L. McGreevy & W. S. Howells, *Phil Mag* (1991) in press.
7. G. R. Mitchell, F. J. Davis, R. Cywinski & W. S. Howells, *J Phys C* **21** (1988) L411
8. A. K. Soper, W. I. F. David & W. S. Howells, to be published.
9. L. Borjesson & W. S. Howells, *Journal of Non-crystalline solids* **131** (1991) 53
10. P. Zetterstrom, U. Dahlborg, W. S. Howells & C. J. Carlile, in *Recent Developments in the Physics of Fluids*, ed. W. S. Howells & A. K. Soper (Adam Hilger, in press)
11. M. Arai, A. C. Hannon, A. D. Taylor, A.C. Wright, R.N. Sinclair & D.L. Price, proceedings of VII International Conference on the Physics of Non-Crystalline Solids, Cambridge, 1991.

## A NEW APPROACH TO THE STRUCTURAL STUDY OF NON CRYSTALLINE POLYMERS THROUGH NEUTRON DIFFRACTION

J. J. del Val

Departamento de Física de Materiales, Univ. País Vasco. Apdo. 1072,  
20080 San Sebastián, SPAIN.

B. Rosi, F. J. Davies and G. R. Mitchell

J. J. Thomson Physical Laboratory, Univ. Reading, Whiteknights,  
Reading RG6 2AF, U. K.

### ABSTRACT

We present a novel approach to the local structure of non crystalline polymers using a selective deuteration of the polymer chains in order to reveal their different and complex interactions. We have used samples of glassy polystyrene where the side group and the polymer backbone have been selectively deuterated. Neutron Diffraction data were obtained using SANDALS instrument at ISIS. The obtained patterns may be in part directly analyzed and it is possible to determine some partial structure factor correlations which relate to specific sites (e. g. polymer backbone-polymer backbone). These specific correlations are tested and compared to scattering functions obtained by computer built models. This powerful technique has considerable potential in the study of complex macromolecular materials.

### 1. Introduction.

The local structure of glassy polymers, expressed in terms of spatial and orientational correlations between chain segments, is still unknown in many respects and different models are still considered and debated. Investigations on the local organisations are made difficult by the great variety of structural units and of chain conformations<sup>1</sup>. This is further complicated when the polymer under study is constituted by large side chains.

Neutron scattering can be a particularly useful diffraction technique in that it can reduce these problems. Not only does it provide a very large amount of information by extending the explored Q range to values much higher than the typical X-ray scattering experiments but it also allows to simplify the structural complexity with the use of isotopic substitution. One of the major obstacles to the power of the technique for the study of polymeric materials lies in the presence of inelasticity effects, particularly severe in hydrogenous materials, which contaminate the experimental results.

The objective of this study was to combine the method of isotopic substitution with the exploitation of the particular features of the new SANDALS spectrometer installed at the pulsed neutron facility ISIS (U. K.) to obtain novel structural information on the structure of hydrogenated amorphous polymers.

### 2. Experimental.

We have performed our experiment on a series of partially deuterated samples of atactic Poly(Styrene) (PS), i. e. totally deuterated (D8), deuterated in the side phenyls



(D5), deuterated in the backbone (D3) and totally hydrogenated (D0).

The experiment made direct usage of the minimization of the inelasticity effects offered by the spectrometer SANDALS<sup>2</sup>.

The data were calibrated and corrected using standard procedures. The resulted structure factors for the four specimens showed interesting differences, particularly in the intensity of the so called polymerization peak ( $\sim 0.75\text{\AA}$ ) (see Fig. 1).

### 3. Analysis.

Fig. 1 shows the experimental Q-weighted structure factors obtained in the low Q region for the four samples studied (the data were reliable up to  $30\text{\AA}^{-1}$ ). Particular interest lies in the behaviour of the polymerization peak with varying H/D contrast. This peak is an interchain peak previously observed with X-ray scattering, which is not present in the corresponding monomer and which has been attributed to correlations between "superchains" constituted of stacks of side phenyl groups, which pack in a random coil fashion without any significant longer range order<sup>3</sup>.

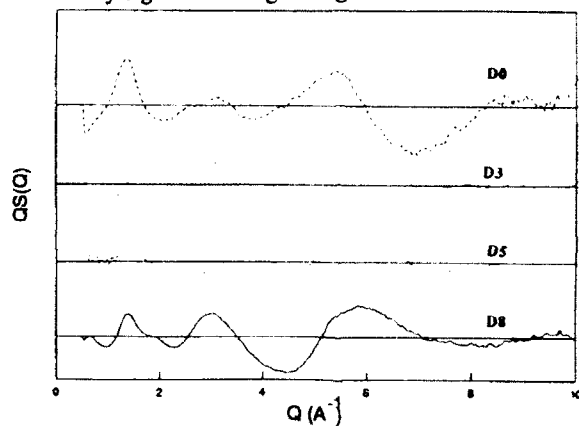


Fig. 1- Experimental Q-weighted structure factor for the four samples studied.

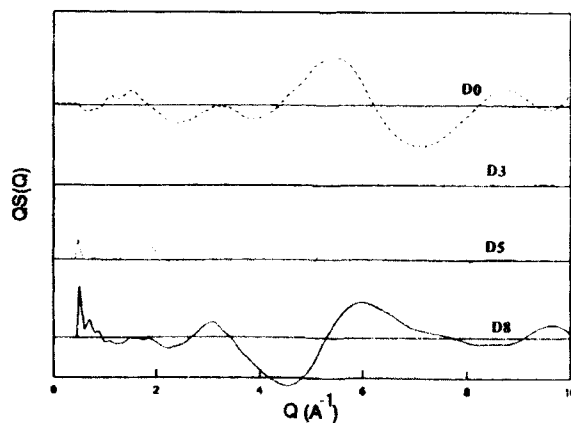


Fig. 2- Q-weighted structure factor obtained from modelling for the four samples studied.

The data were firstly analysed with a many chains model built with the "Amorphous Builder" facility of the molecular modeling system Quanta, distributed by Polygen Corp. This builds the disordered structure by growth in a box, subject to periodic boundary conditions and to statistical constraints on the allowed values for the bonds torsional angles. The growth was performed on a 200  $C_8H_8$  units chain and it was carried on the proper bulk density. The model gives a qualitatively good overall fit of the experimental data for every sample, but does not predict the interchain polymerisation peak, as Fig. 2 shows. This is probably due to the excessive random character of the model.

The alternative procedure consisted in constructing appropriate linear combinations of the experimental total scattering functions to obtain partial structure factors related to specific sites. In particular two functions could be isolated:  $S_{BR}(Q)$ , corresponding to correlations between Hydrogens in the backbone and Hydrogens in the side phenyl ring and  $S_{BB}(Q)$ , related to some of the correlations between backbone elements, i.e., H-H and C-H interactions. Other partial functions could not be obtained due to the non-selective character of the deuteration.  $S_{BB}(Q)$ , shown in Fig. 3 is of particular interest here.

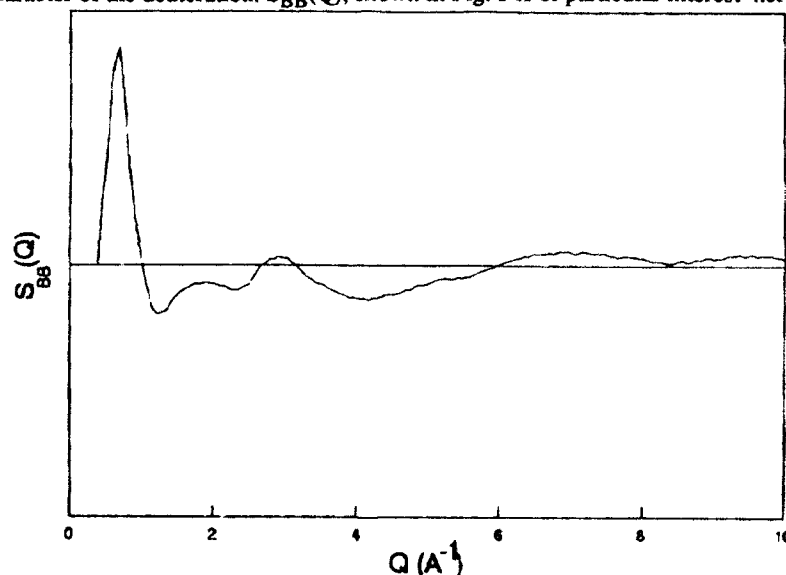


Fig.3- Experimental structure factor corresponding to correlations between backbone elements in PS.

Fig. 4 shows a comparison between the corresponding Fourier-transform  $g_{BB}(r)$  and the total  $g(r)$  obtained from the scattering pattern of  $D_8$ . As can be seen, the interchain peak at  $\sim 12\text{\AA}$  is a very broad feature in  $g_{BB}(r)$ , but it cannot be easily seen in the total  $g(r)$ , which is dominated by a  $5\text{\AA}$  periodicity. This shows that the partial RDF, which relates to particular sites interactions, contains informations that is much more specific and therefore easier to unravel.

#### 4. Conclusions

With this work we have explored the feasibility of a new approach to the study of local structure in amorphous polymers, which couples the use of a particularly suited diffractometer for the investigation of hydrogenous system with the application of the

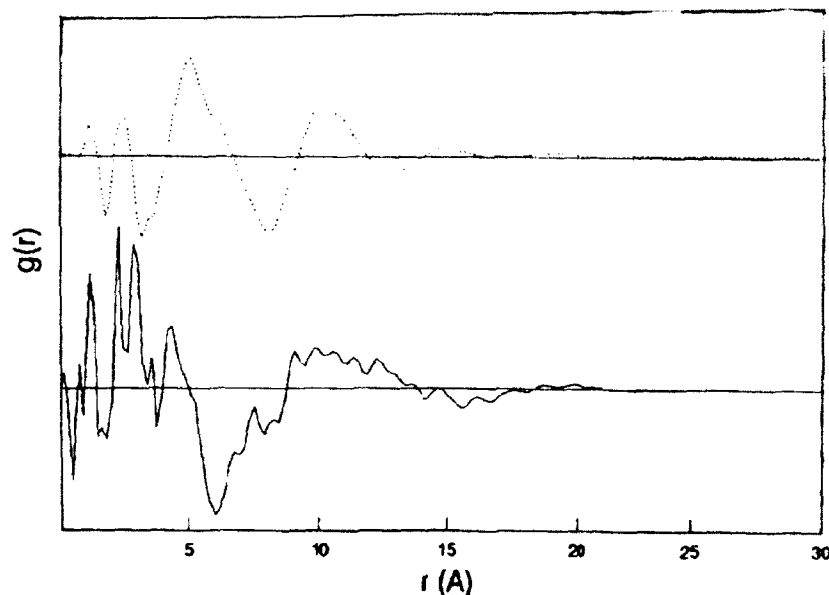


Fig.4- Comparison between Fourier transforms  $g(r)$  and  $g_{BB}(r)$  obtained from the scattering pattern of D8 and from  $S_{BB}(Q)$  respectively.

method of selective deuteration.

The use of SANDALS gives the possibility of obtaining quality scattering data from Hydrogen-containing systems. The method of selective deuteration gives a collection of independent data that must be simultaneously matched by statistical models, thereby providing a very severe test to the chosen models.

Whereas available dense many chains models make it possible to model the total scattering from the samples of interest, partial correlation functions relating to specific structural sites can be obtained and used to derive unique information on the structure of complex systems.

This approach is applicable to a wide range of polymeric systems.

## 5. Acknowledgements

This work forms part of the Courtaulds Polymer Science Prize Programme at the University of Reading and of an Acciones Integradas Programme with Universidad del País Vasco, San Sebastián, Spain, supported by the British Council, it was also supported by the Science and Engineering Research Council. We acknowledge Dr. A. K. Soper (ISIS) for his help with the experiment and with the data reduction and Dr. M. Stapleton of Polygen Corp. for his assistance in the "Amorphous Builder" calculations.

## 6. References

1. G. R. Mitchell, in *Comprehensive Polymer Science*, eds. G. Allen, J. C. Bevington, C. Booth and C. Price (Pergamon Press, London 1989).
2. B. Rosi and G. R. Mitchell, *Polym. Commun.* submitted.
3. G. R. Mitchell and A. H. Windle, *Polymer* **25** (1984) 906.

NEUTRON SCATTERING STUDY OF THE CHAIN CONFORMATIONS  
IN THE MIXTURES OF BLOCK COPOLYMERS

A.D.VILESOV\*

Institute of Macromolecular Compounds  
Academy of Sciences, St. Petersburg, Russia  
\*Present address: Institute of Technical and Macromolecular  
Chemistry, University of Hamburg, Germany

G.A.EVMENENKO

Nuclei Physics Institute, Academy of Sciences  
St. Petersburg, Russia

H.G.ZACHMANN

Institute of Technical and Macromolecular Chemistry  
University of Hamburg, Germany

ABSTRACT

The conformations of polybutadiene blocks in the binary mixtures of polystyrene-polybutadiene (PS-PB) lamellae-forming two-block copolymers (BC) were studied. The radius of giration of the long chains was measured about the normal to the interface by small angle neutron scattering (SANS). It turned out to be dependent on the concentration of the surrounding short chains. For every composition of the mixture the long chains were contracted in the lateral directions compared to their unperturbed dimensions.

1. Introduction

The conformations of the chains in homodisperse BC forming lamellae domain structures were studied in detail by SANS<sup>1, 2, 3</sup>. In the present work we studied by SANS the conformations of BC chains in the binary mixture of PS-PB BC of different molecular weight. For that kind of mixtures there was observed that they form perfect domain structures in a wide range of polydispersity and composition<sup>4</sup>. Recently there was developed a mean-field theory of the structures formed by chains of two different molecular weights<sup>5</sup>. According to that theory the domain consists of two sublayers

(Fig.1.). In the lower sublayer the conformation of the part of the long chain does not differ much from that of surrounding short ones. But in the upper sublayer the conformation of the another part of the long chain is

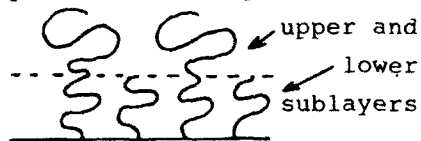


Fig.1. Structure of domain. perturbed due to spreading in the lateral directions. For both sublayers the lateral dimensions of the chains should be  $\sim N^{1/2}$ ,  $N$ -number of segments. We put the problem to estimate the value of lateral spreading of the long chain for different concentrations of the surrounding short ones.

## 2. Experimental section

There were synthesised by Dr.L.V.Vinogradova the following BC:

Tabl.1.	BC	$M_n 10^{-3}$ of PS, g/mol	$M_n 10^{-3}$ of PB, g/mol
1.	PS-PB	68	38
2.	PS-PB	184	119
3.	PS-PB <sub>D</sub>	120	146

PB<sub>D</sub> - deuterated PB. BC 1 and 2 were mixed in the ratios 2:1 and 5:1 by the numbers of the chains. Films were obtained by casting in toluene solutions. It was estimated that BC 1,2,3 and their mixtures formed common lamellae structures. Lamellae faces were oriented parallel to the surface of the film. The SANS experiments were carried out at the SANS diffractometer "Membrana"<sup>6</sup>. The films were oriented normal to the beam. Every scattering experiment was carried out by making two measurements: first the background with hydrogenated sample, second its mixture with 3 % wt. of BC 3. The signal of interest was obtained by subtracting these two signals. The intensity of the scattered radiation was expressed in the form:  $I(Q) = I_0 \exp(-Q^2 R_x^2)$ , where  $Q = 4\pi/\lambda \sin \theta$ ,  $2\theta$  - scattering angle,  $\lambda = 2.3 \text{ \AA}$  - average wave length of the incident beam,  $R_x$  - x-component of the

radius of giration of the chain. X is perpendicular to the beam. There was measured the  $R_x$  of  $PB_D$  block. The experimental observations were interpreted using the Guinier representation (Fig.2.).

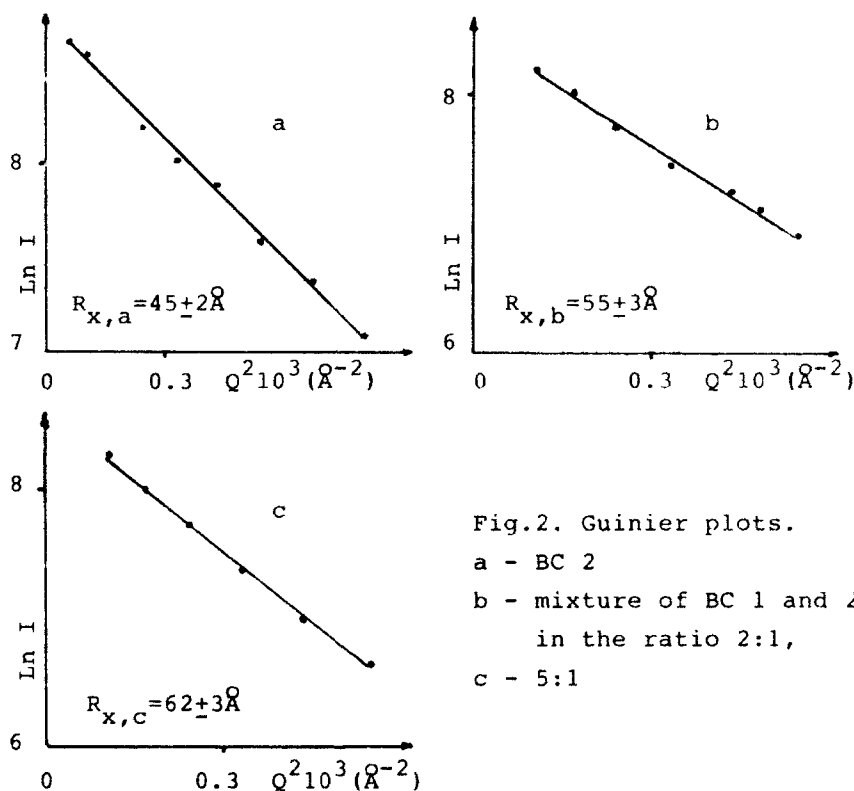


Fig.2. Guinier plots.

- a - BC 2
- b - mixture of BC 1 and 2  
in the ratio 2:1,
- c - 5:1

The calculated value of unperturbed  $R_x$  for  $PB_D$  block is  $76 \text{\AA}$ . The  $R_x$  of the long chain can be expressed in the form  $R_{x,i}^2 = u_{x,i}^2 + l_{x,i}^2$ ,  $u_{x,i}$ ,  $l_{x,i}$  - are the radii of giration of the parts of the chain in the upper and lower sub-layers correspondingly,  $i=a,b,c$  (Fig.2.). The values  $l_{x,i} = 23 \text{\AA}$  are the same for  $i=a,b,c$ . Consequently one can obtain (in  $\text{\AA}$ ):  $u_{x,a} = 39$ ,  $u_{x,b} = 50$ ,  $u_{x,c} = 57$ .

The calculated value of unperturbed upper part of the chain is  ${}_uR_x = 69\text{\AA}$ .

### 3. Conclusions

The effect of lateral contraction of the chain in domain structure is rather strong.

The surrounding by the chains of smaller molecular weight does not cause considerable expansion of the chain. Its dimension is even less than unperturbed one.

These results are not in agreement with the theories which predict unperturbed lateral chain dimension for the structures formed by homodisperse chains and increased dimension for the structures formed in the mixtures.

Acknowledgment: One of the authors (A.V.) thanks Deutsche Forschungsgemeinschaft for financial support.

### 4. References

1. G.Hadziioannou, C.Picot, A.Skoulios, M.-L.Ionescu, A.Mathis, R.Duplessix, Y.Gallot and J.-P.Lingelser, *Macromolecules*, **15**(1982)263.
2. E.L.Aero, A.D.Vilesov and M.M.Agamalyan, Preprint Nucl. Phys.Inst.Acad.Sci.USSR **791**(Leningrad,1982).
3. H.Hasegawa, T.Hashimoto, H.Kawai, T.P.Lodge, E.J.Amis, C.J.Glinka and C.C.Han, *Macromolecules*, **18**(1985)67.
4. G.Hadziioannou and A.Skoulios, *Macromolecules*, **15**(1982)267.
5. T.M.Birshtein, Yu.V.Liatskaya and E.B.Zhulina, *Polymer*, **31**(1990)2185.
6. M.M.Agamalyan, G.M.Drabkin and V.I.Sbitnev, *Physics Reports*, **168**(1988)265.

## NEUTRON SCATTERING FROM AMORPHOUS HYDROGENATED CARBON

W S Howells

*ISIS Science Division, Rutherford Appleton Laboratory,  
Chilton, Didcot, OX11 0QX, UK.*

R J Newport, P J R Honeybone

*Physics Laboratory, University of Kent,  
Canterbury, CT2 7NR, UK.*

and

P Revell

*Ion Tech Ltd, Teddington, TW11 0LT, UK.*

### ABSTRACT

An extensive study of amorphous hydrogenated carbon, a-C:H (often referred to as diamond-like carbon by virtue of its unique mechanical and optical attributes) has been conducted using the facilities at the ISIS pulsed neutron source. Diffraction data is able to resolve directly the contributions from the principal C-C bond types and to provide evidence for the existence of molecular hydrogen. Inelastic incoherent neutron scattering has been used in an attempt to study in more detail the nature of the hydrogen environment. These experiments have also provided further evidence for the presence of molecular hydrogen.

### 1. Introduction

Amorphous hydrogenated carbon (a-C:H) is of considerable technological interest because of its hardness, density and resistance to chemical attack. These properties, along with optical properties, such as optical gap and refractive index, may be varied by changing the deposition parameters, which has led to a large number of potential applications.

The structural understanding of this complex material has been slow to develop, primarily because of the large number of possible carbon bonding environments. Current structural models suggest clusters of  $sp^2$  carbon are connected by chains of hydrogenated  $sp^3$  carbon. In the studies described here, neutron diffraction has been employed to determine the atomic structure and



incoherent inelastic neutron scattering has been used to focus on the hydrogen vibrations. Since there is a direct relationship between the observed intensity and the eigenvector of the vibration (unlike infra-red and Raman spectroscopy, where complex matrix elements are present), it is possible to model the dominant hydrogen bonding environment in a direct way.

## 2. Experimental

The amorphous hydrogenated carbon used in these experiments was produced using a saddle field ion beam source <sup>1</sup>. A Carlo-Erba CHN combustion analyser was used to determine the composition of the sample and the densities were determined using a residual volume technique. Three samples were prepared containing 29%, 32% and 35% hydrogen.

The neutron scattering data were collected at the ISIS pulsed neutron facility. The diffraction experiments were on LAD, the Liquids & Amorphous materials diffractometer and the inelastic experiments on TFXA and MARI spectrometers. Full details of the instruments can be found elsewhere <sup>2</sup>.

## 3. Diffraction results

A pulsed neutron diffraction instrument such as LAD is well suited for measuring hydrogenous materials such as a-C:H. The high Q values accessible provide high real space resolution in the radial distribution functions. Furthermore, the combination of high incident neutron energy and low scattering angles minimise the inelastic, Placzek, corrections. The total radial distribution function for one of the samples is shown in Figure 1 and there are two features of interest. Firstly, due to the good resolution there is now the possibility of showing that the 1.54Å (*diamond-like*, sp<sup>3</sup>) bond is predominant but that the 1.4Å (*graphitic*, sp<sup>2</sup>) bond is present in significant amounts. Secondly, there is a feature between 0.7 and 0.8Å and this we have attributed to molecular hydrogen, H<sub>2</sub>, within the bulk of the film. This is confirmed by computer modelling using the Reverse Monte Carlo technique <sup>3</sup>.

## 4. Inelastic results

The inelastic spectrum obtained on TFXA in the low energy transfer region is shown in Figure 2. The rotation mode of molecular H<sub>2</sub> is at an energy of about 15 meV and the measured spectrum exhibits a double peak, which is consistent with an asymmetric hydrogen environment. The deduced bond length is less than that for gaseous hydrogen which suggests an effective high pressure for the hydrogen in a-C:H <sup>4</sup>.

Analysis of the higher energy region of the spectrum <sup>5</sup> has concentrated on the C-H modes. Infra-red spectroscopy has shown the presence of many hydrogen

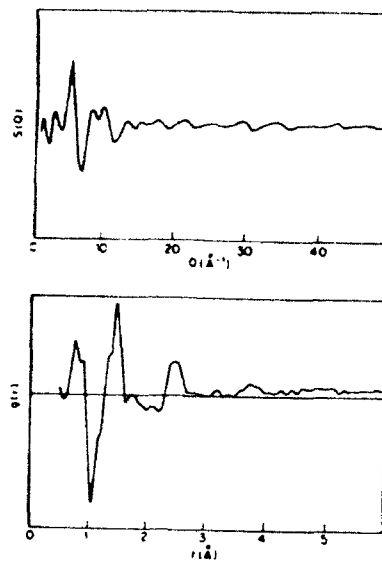


Figure 1. Structure factor (top) and radial pair distribution function (bottom) for a-C:H.

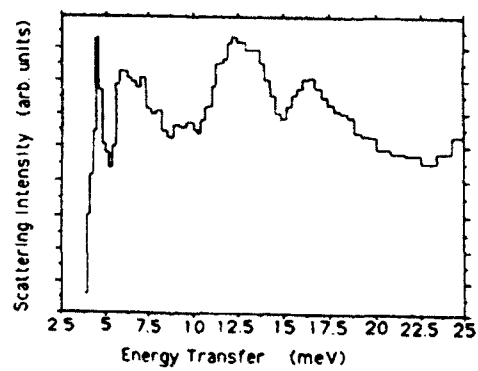


Figure 2. Low energy inelastic spectrum measured from a-C:H on TFXA.

bonding environments, each with a set of vibrational frequencies which are then used as a basis for constructing models. The model vibrations are obtained from individual internal coordinates, each of which is assigned a force constant. These force constants are fitted to the observed frequencies and then to the observed spectrum. Using a model for a combination of CH and CH<sub>2</sub> groups, it has been possible to explain almost all of the observed intensity.

We find that the hydrogen in all the samples is seen to be predominantly incorporated in CH<sub>2</sub> groups with at least two thirds of all hydrogen bonded in this way. It is striking that there appears to be no direct relationship between the hydrogen content and CH:CH<sub>2</sub> ratio. It is likely that a combination of saturation of unsaturated bonds together with the availability of hydrogenated carbon sites is responsible for this. Finally, it is interesting to note that the fraction of carbon that is unhydrogenated closely mirrors the carbon atomic fraction. Diffraction data is required to understand the nature of the bonding of this carbon, although further computer modelling will probably be required to illuminate the clustering of CH and CH<sub>2</sub>.

## 5. Conclusion

The hydrogen bonding environment in a-C:H has been extensively studied by means of neutron diffraction and inelastic neutron scattering. Molecular hydrogen has been detected and the ratio of CH to CH<sub>2</sub> groups has been determined. It is hoped that a complete analysis of the neutron data, coupled with computer modelling will give further information on the hydrogen bonding environment. In particular, it is important to know the extent of non-hydrogenated carbon clustering and whether it includes sp<sup>3</sup> or just sp<sup>2</sup> carbon.

## 6. References

1. J. Franks, *Vacuum* **34** (1984) 259
2. ISIS User Guide, *Rutherford Appleton Laboratory report* RAL-88-030.
3. R. J. Newport, P. J. R. Honeybone, S. P. Cottrell, J. Franks, P. Revell, R. J. Cernik and W. S. Howells, *Surface & Coatings Technology* **47** (1991) 668
4. P. J. R. Honeybone, R. J. Newport, W. S. Howells, J. Tomkinson & S. M. Bennington *Chem Phys Lett* **180** (1991) 145
5. P. J. R. Honeybone, R. J. Newport, W. S. Howells & J. Franks, *Proceedings of Diamond Films '91, Nice 1991* (to be published)

STUDY OF PHASE SEPERATION IN AMORPHOUS PEN/PET BLENDS BY  
MEANS OF  $^{13}\text{C}$  CP/MAS NMR

M.M. GUO, H.G. ZACHMANN

Institut für Technische und Makromolekulare Chemie,  
University of Hamburg, Bundesstr.45, 2000 Hamburg 13, Germany

ABSTRACT

The CP/MAS NMR spectra with no dipolar decoupling and delay decoupling of four blends, in which one component is deuterated, were measured and compared with the normal CP/MAS/DD spectra. It is shown that by applying these new methods, information on miscibility is obtained even in the case of identical chemical shift and relaxation time of the two components.

CP/MAS/DD (cross polarization/magic angle spinning/dipolar decoupling)  $^{13}\text{C}$  NMR has been demonstrated to be a valuable tool for the characterization of polymer-polymer miscibility<sup>1</sup>). In general, the mostly used methods are : 1) Measurement of perturbation in the isotropic chemical shift; 2) Inter-molecular CP in a mixture of deuterated and protonated materials; 3) Determination of the proton relaxation times.

For some polymer blends, such as blends of poly(ethylene naphthalene-2,6-dicarboxylate)(PEN) and poly(ethylene terephthalate)(PET) which are investigated in this paper, the chemical shifts and even the proton relaxation times of the components are the same. Therefore it is not possible to use the above mentioned methods to get information on miscibility. In the following, we want show that delay decoupling and no decoupling CP/MAS NMR methods yield information about the miscibility in this systems.

### Experimental part

Details on the polymer synthesis are given elsewhere<sup>2)</sup>. The samples were dissolved in hexafluoroisopropanol and coprecipitated by ethanol.

The NMR experiments were performed at room temperature on a Bruker MSL 300 NMR spectrometer operating at 75 MHz. The sample spinning frequency was 4.5 kHz. Spin sidebands were suppressed by using the pulse sequence TOSS.

### Results and discussion

Fig. 1 shows the  $^{13}\text{C}$  CP/MAS/DD NMR spectra of precipitated amorphous PEN, PET, and the blend PEN/PET(50/50). The chemical shift data are listed in Table 1. From the spectra and the data we can find that the chemical shift of the homopolymers PEN and PET as well as their blends are almost the same. The measured proton spin lattice relaxation times in rotation frame are 7.75, 7.70, 7.55 ms for PEN, PET, and the blend PET/PEN(50/50),

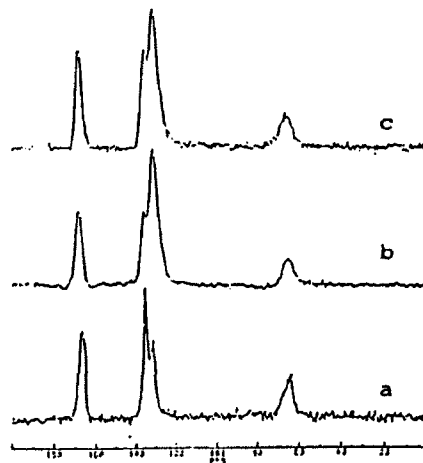


Fig. 1  $^{13}\text{C}$  CP/MAS/DD NMR spectra of a) PET; b) PEN; c) blends of PEN/PET(50/50)

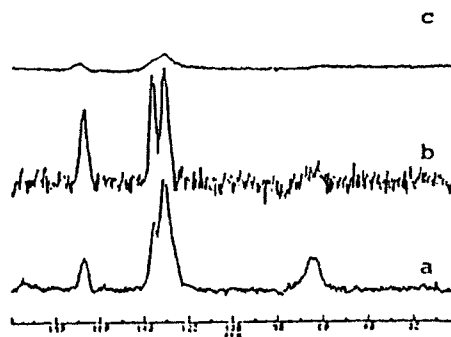


Fig. 2  $^{13}\text{C}$  CP/MAS Spectra of 50 PEN/50 PET-d<sub>8</sub> blend. a), full decoupling; b), delayed decoupling; c), no decoupling.

Table 1  $^{13}\text{C}$  CP/MAS/DD NMR chemical shifts of PEN, PET, and blends of PET and PEN

	PET	PEN	PEN/PET(50/50)
C=O	166.39	167.60	167.46
Aromatic C	135.34	135.58	135.23
	131.42	130.94	130.83
CH <sub>2</sub>	63.17	63.89	63.74

respectively. Therefore, it is difficult to get information on the miscibility by using these NMR methods.

We think there are two other methods which can be used to study the miscibility of polymers even when the chemical shift and the proton relaxation time of the components are the same:

1) Measurement of  $^{13}\text{C}$  CP/MAS NMR spectrum without dipolar decoupling. In this case high resolution Cross Polarization (CP) carbon signals from proton chains are not observed<sup>3</sup>). Magic Angle Spinning by itself, however, is sufficient to produce high resolution CP signals from deuterated chains and the quaternary-carbons in protonated polymer.

2) Measurement of  $^{13}\text{C}$  CP/MAS NMR spectrum with delayed decoupling. Following the cross polarization time, an extra delay,  $T_{\text{DD}}$ , is applied before data acquisition. This delay, normally 50-100  $\mu\text{s}$ , allows those carbon atoms to dephase which have strong coupling to protons. The contributions from deuterated carbons are, of course, unaffected by the delay.

Some  $^{13}\text{C}$  CP/MAS spectra, obtained under a variety of dipolar decoupling condition, are shown in Figs. 2,3,4, respectively. From the figures, we can see that for 50 PEN/50 PEN-co-PHB- $\text{d}_{14}$ (80:20) blend, the intermolecular CP between the deuterated carbons in PEN-co-PHB- $\text{d}_{14}$ (80:20) and

the protons in PEN are observed in the case of delayed decoupling and of no decoupling  $^{13}\text{C}$  CP/MAS spectra. This means that the average distances between deuterated-carbons in PEN-co-PHB- $\text{d}_{14}$ (80:20) and protons in PEN are on the order of 10 Å or less, i.e. the system is sufficiently miscible on a molecular scale. As for the other two blends, the intermolecular CP is not observed, the blends are not miscible. This is consistent with other results obtained in our group<sup>4</sup>).

Acknowledgment: One of the authors M.G. thanks the Alexander von Humboldt Foundation for a fellowship

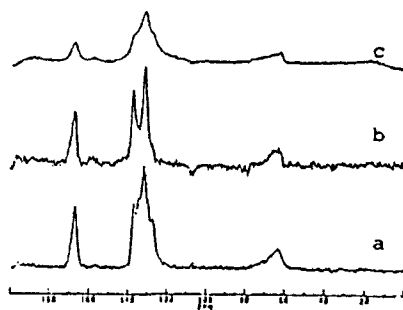


Fig. 3  $^{13}\text{C}$  CP/MAS Spectra of 50 PEN/50 PEN-co-PHB- $\text{d}_{14}$ (80:20) blend. a), full decoupling; b), delayed decoupling; c), no decoupling.

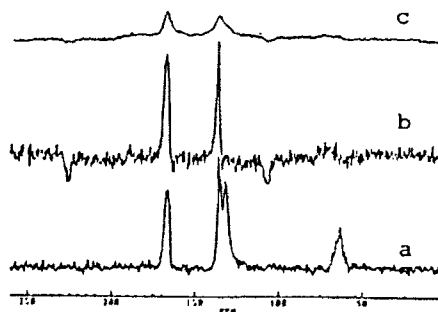


Fig. 4  $^{13}\text{C}$  CP/MAS Spectra of 50 PET/50 PEN-co-PHB- $\text{d}_{14}$ (80:20) blend. a), full decoupling; b), delayed decoupling; c), no decoupling.

#### Reference

1. T. Yu, and Mingming Guo, *Prog. Polym.Sci.* **15** (1990) 825
2. W.Wu, D.Wiswe, H.G.Zachmann, K.Hahn, *Polymer*, **26** (1985) 655
3. J.Schaefer, M.D.Sefcik and E.O.Stejskal, R.A.Mckay, *Macromolecules*, **14** (1981) 188
4. J.Nowacki, C. Schultz, and H.G.Zachmann, *Polymer*, in press.

EXAFS AND XANES STUDY OF  $\text{TiO}_2$ - $\text{SiO}_2$  GELS AND GLASSES

JESUS MATOS, LUIS ESQUIVIAS

*Departamento de Estructura y Propiedades de los Materiales.**Universidad de Cádiz. Apartado 40, Puerto Real. 11510 Cádiz.*

and

CARLOS PRIETO

*Instituto de Ciencia de Materiales de Madrid, (C.S.I.C.).**Facultad de Ciencias (C-4) Universidad Autónoma, 28049 Madrid. Spain*

## ABSTRACT

The first and second neighbours arrangement around Ti atoms were studied in gels and glasses of the  $x\text{TiO}_2$ -(1-x) $\text{SiO}_2$  system with  $x = 5$  and  $x = 10$  from X-ray Absorption Near Edge Structure (XANES) and Extended X-ray Absorption Fine Structure (EXAFS) performed at the K-edge of Ti at room temperature with synchrotron radiation by fluorescence detection.

From the comparison of XANES spectra with those of  $\text{SrTiO}_3$  and rutile  $\text{TiO}_2$  and anatase point out an octahedral environment of Ti can be inferred where the octahedra are distorted as in the case of  $\text{TiO}_2$ .

EXAFS spectra give information about the coordination spheres. In the cases under study first and second ones are suitable for discussion. The EXAFS Fourier Transform (FT) signal gives an approximate distance of  $1.95 \pm 0.05 \text{ \AA}$  for the dry gel Ti-O bond length and a 3% shorter in the glass. Some differences are observed at second neighbour scale, which concern to Ti-O-Si and Ti-O-Ti distances, according to the heat-treatment.

## 1. Introduction.

Gels are biphased materials, synthesized from precursors in the liquid state, formed by a solid backbone and a interstitial liquid which manipulation permits to obtain advanced glasses and other new materials<sup>1</sup>. Glasses can be prepared by densification of the solid matrix by heat-treatment once the liquid is removed.

One of the outstanding features commonly attributed to the sol-gel processing of multicomponent materials is the high degree of homogeneity on a molecular scale. When the precursors are alkoxides they are hydrolyzed and the solid phase results from the subsequent polycondensation process. In this case homogeneity can only be satisfactorily reached when their respective hydrolysis and polycondensation reactions occur in a synchronized manner. The purpose of this work is to know: a) in simultaneous processing of various alkoxides with different hydrolysis rate, whether sonocatalysis<sup>1</sup> can be used to increase the



microhomogeneity and b) at what extent the glass atomic short-range order is different from the gel one.

## 2. Experimental

Aerogels<sup>2</sup> were prepared from Tetraethoxysilane and Tetrabutylortotitanate as it has been already described<sup>3</sup>, with  $[H_2O]/[TEOS] = 4$  using AcOH to control the TBOT hydrolysis with  $[AcOH]/[Ti] = 5.5$ . From now on, "xAn" refers to a sample with a x%  $TiO_2$  nominal content, prepared using ultrasound (A=S) to mix the two phase alkoxide-water system, or employing ethanol (A=C) as common solvent, and heat-treated at a temperature of  $(10 \times n)^\circ C$  according to a process previously described<sup>4</sup>. n=d is used to refer those samples which were continuously heated at  $10^\circ C/min$  up to  $1100^\circ C$  and n=e indicates that AcOH was not used in the preparation.

Experiments were carried out on the beamline EXAFS-III at D.C.I. storage ring (Orsay, France) operating as in ref<sup>5</sup> by fluorescence yield detection. Energy resolution was estimated to be about 2 eV by the Cu foil 3d near edge feature. The energy calibration was monitored using the Ti foil sample and was set as 4965 eV at the first maximum of the derivative spectrum. EXAFS spectra were performed over a range of 800 eV above the Ti K-edge.

## 3. Analysis of the results

For all the XANES spectra (Fig.1) a Victoreen law, extrapolated from the low energy region, has been subtracted and then the normalization performed.

The threshold energy of all the samples is the same as in the  $TiO_2$  oxides, this means that most of the Ti ions are Ti (IV). Nevertheless, the 5S107 sample has the feature at 4970 eV, which corresponds to the 1s-3d electronic transition, higher than the other samples and slightly displaced to lower energies (2eV) which can indicate that an amount of Ti (III) is present. This effect has been previously reported<sup>6</sup> by comparison between  $TiO_2$  and  $Ti_2O_3$ , and between two kinds of silicates of  $Ti^{4+}$  and  $Ti^{3+}$ .

On the other side, the features position and height at 4985 and 5000 eV for the samples 1, 2, 3 and 4 are very similar to the anatase one, this means that the

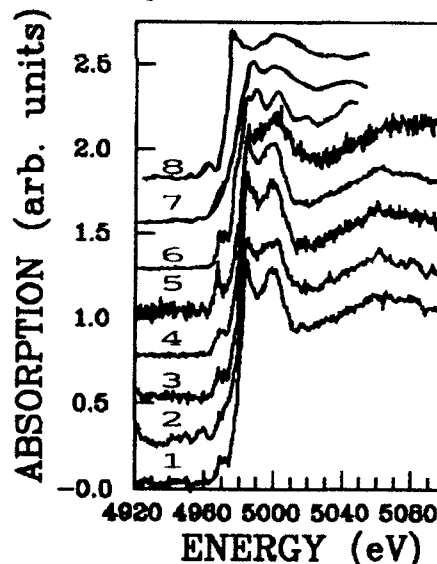


Figure 1. XANES spectra: 1- 10Cd, 2- 10Sd, 3- 5S30e, 4-5S30, 5-5S107, 6-  $TiO_2$  rutile, 7-  $TiO_2$  anatase, 8-  $SrTiO_3$ .

similar to the anatase one, this means that the Ti ions have an octahedral oxygen and these octahedra are hardly distorted. The XANES spectra shape for the 5S107 sample is rather different because the position and relative intensity are not the same as in the other samples. Its position is more similar to that of  $\text{SrTiO}_3$ , where there is only one distance Ti-O because the oxygen octhedrum is just a regular one.

To evaluate the neighbour's position around the absorber atoms, the well known EXAFS expresion<sup>7</sup> was used. This expression describes the EXAFS oscillations for a Gaussian distribution of neighbours around the central atom, in the single scattering theory and in the plane-wave approximation, as a function of  $N_j$  (average coordination number for the gaussian distribution of distances centered at the  $R_j$  value),  $\sigma_j$  (Debye-Waller contribution) and  $\Gamma_j$  (related to the photoelectron mean free path) between other parameters.

The FT of the  $k^3\chi(k)$  weighted signals (in these cases were calculated with a Hanning window from 3.5 to 14  $\text{\AA}^{-1}$  above the edge, Fig. 2) is the Radial Distribution Function around the Ti atoms with a shift caused by the backscattering phase that may be evaluated<sup>8</sup>. Fig 2a shows that in the C and S preparations the Ti ions coordination are almost the same but the existence of

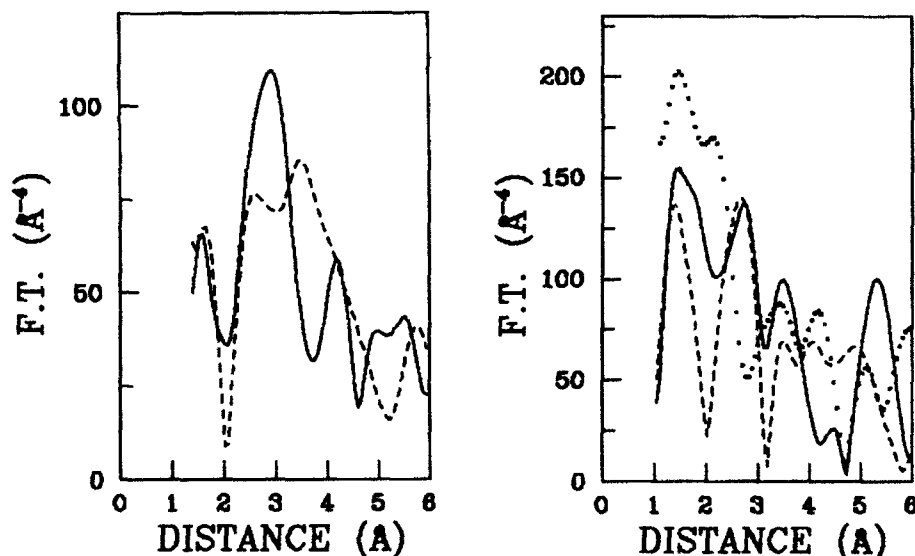


Figure 2. FT magnitude of the  $k^3$  weighted EXAFS signal a) 10Cd (cont.) and 10Sd (dashed), b) 5Sa (cont.), 5S30 (dashed) and 5S107 (dotted).

two well defined RDF peaks at the second neighbours level indicates that ultrasounds affect the short-range order. It can be observed on Fig. 2b that 5S-samples first peak magnitude, which account for the oxygen contribution to the EXAFS signal, is bigger for the 5S30 one. It is probably associated with a higher

$\sigma_i$  (Table I).

Their structural parameters were obtained fitting the aforementioned theoretical expression<sup>7</sup> to the filtered data. It was carried out by means of an interactive process in the  $k$  and  $R$  spaces in which the backscattering amplitude and phase functions were taken as the reported ones by McKale et al.<sup>8</sup>.

A FT filtering was used to extract the EXAFS contribution of the first coordination sphere from about 1.0 to 2.0 Å. The oxygen EXAFS contributions were simulated taking into account only one distance from the Ti to the oxygen ions, fixing the coordination number to 6 and the  $\Gamma$  value to 1.5 Å<sup>2</sup> as in other Ti oxides. It can be noted that the Ti-O distance is going down with the temperature treatment as it has been observed for the Si-O distances. This is caused by OH on the in the solid-air interphase which induce elongation in the adjacent bonds, slightly affecting the short-range order and backbone density, lower than the bulk glass<sup>9</sup>.

TABLE I Ti-O bond parameters deduced from EXAFS analysis			
	R(Å)	$\sigma(\text{Å}^2)$	$\Delta E_0(\text{eV})$
5Sa	1.95	0.093	3.0
5S30	1.94	0.100	10.0
5S107	1.89	0.088	7.8

#### 4. Conclusion

The Ti coordination is not affected by the method of preparation, in all cases they are hexacoordinated forming very distorted octahedra, but it does influence the short-range order at the scale of second neighbours.

The elimination of the OH interphase coverage makes that the Ti-O bond length decreases during sintering.

#### 5. References

1. *Sixth International Workshop on Glasses and Ceramics from Gels* ed. L. Esquivias. (Universidad de Cádiz, Cadix, 1991)
2. M. Prassas, J. Phalipou and J. Zarzycki, *J. Mat Sci.* **19** (1984) 1656.
3. M. Ramírez-del Solar, N. de la Rosa-Fox, L. Esquivias and J. Zarzycki, *J. Non-Cryst. Solids* **121** (1990) 84.
4. N. de la Rosa-Fox, L. Esquivias and J. Zarzycki, *Rev. Phys. Ap.* **C4**-233
5. D. Gómez-Vela, L. Esquivias and C. Prieto, submitted to *Phys. Stat. Sol.*
6. G.A. Waychunas, *J. de Phys.* **C8** (1986) 841.
7. K. Teo, *EXAFS: Basic Principles and Data Analysis in Inorganic Chemistry Concepts* **9** (Springer Verlag, Berlin, 1986).
8. A.G. McKale, B. W. Veal, A. P. Paulikas, S. K. Chan and G. S. Knapp, *J. Am. Chem. Soc.* **110** (1986) 3763.
9. J.M. Ruiz-Rube, M. Ramírez del Solar, N. de la Rosa Fox and L. Esquivias in *Basic Features of the Glassy State*, ed. J. Colmenero and A. Alegría (Pergamon Press, Singapore, 1990) p. 68.

## II. CRYSTALLIZATION

**NANOCRYSTALLINE ALLOYS OBTAINED BY CRYSTALLIZATION  
OF METALLIC GLASSES**

**H. MATYJA and T. KULIK**

Institute of Materials Science and Engineering  
Warsaw University of Technology  
Narbutta 85, 02-524 Warsaw  
Poland

**ABSTRACT**

Nanocrystalline materials can be created by crystallization of metallic glasses using special heat treatment e.g. flash annealing or by conventional annealing of glasses with appropriate composition. This ultrafine structure can result in novel and/or enhanced properties.

It was found that nanocrystalline structure can be created by conventional furnace annealing only in alloys with special composition, e.g. in Fe-Si-B alloys containing at least two alloying elements: Cu and Nb or Cu and Ta. Flash annealing results in substantial grain refinement of crystallization products and makes possible creation of ultrafine structure with grain diameter less than 30-40 nm in all Fe- and Co-based glasses studied in this work exhibiting primary crystallization.

**1. Introduction**

Nanocrystalline materials can be created by conventional annealing of metallic glasses with appropriate composition [1,10] or by crystallization of glasses using special heat treatment - flash annealing [2,3]. This ultrafine structure can result in novel and/or enhanced properties.

The aim of this work is to study the influence of composition and heat treatment of amorphous alloys on their structure.

New Fe-based alloys with nanocrystalline grain structure, exhibiting outstanding soft magnetic properties were recently reported by Yoshizawa et al. [1]. The ultrafine grain structure was obtained by appropriate conventional heat treatment of amorphous Fe-Cu-Nb-Si-B alloys [4]. The reasons for such effect of combined

addition of Cu and Nb on the structure of partially crystallized Fe-Si-B alloys are still not fully understood [5,6,7,8]. Small addition of copper are known [9] to increase number of quenched-in nucleation sites for  $\alpha$ -Fe primary crystals in Fe-B glasses. Addition of early transition metals like zirconium and niobium stabilize the glass and shift the temperature of the second crystallization step (the crystallization into boride) to higher temperatures.

The extraordinary magnetic properties of nanocrystalline ferromagnets are related to vanishing magnetocrystalline anisotropy in these materials. For Fe-based alloys the average anisotropy approaches zero when grain diameter  $D \leq 15$  nm, as was theoretically estimated by Herzer [11]. On the other hand, magnetic properties are also dependent on the alloy composition. Therefore, it is essential to know the influence of alloy composition on the microstructure of Fe-based glasses on their structure and magnetic properties after crystallization.

Nanocrystalline structures can be obtained in much wider range of compositions by using special heat treatment e.g. flash annealing. In this method introduced in early 1980s [12], the sample is heated directly by the pulse current passing through, allowing to achieve heating rates up to  $10^6$  K/sec. The sample can be placed in different protecting environments resulting in various cooling rates. The main advantage of this method is a possibility to reach temperatures much higher than the glass transition temperature  $T_g$  without crystallizing metallic glasses. During pulse heating the crystallization temperature  $T_x$  can be higher by 300-400 K than  $T_x$  observed using conventional heating [13].

There are some suggestions that if the annealing is done above the glass transition temperature, the nature of the crystallization process can be different [14]. This effect was primarily attributed to the change in the mechanism of nucleation from heterogeneous below  $T_g$  to homogeneous above  $T_g$ . High temperature and very short pulse time provide condition for formation of huge number of nuclei. Fast cooling should disable considerable growth and formation of some grains in expense of others.

By using flash annealing for crystallization of metallic glasses we succeeded in obtaining nanocrystalline structures in Fe-B system [15], in Fe-B-Si [16] and in Co-B-Si systems [3].

## 2. Experimental methods

Fe-based amorphous ribbons (4 mm wide and 20  $\mu\text{m}$  thick), with the compositions shown in Table 1, were prepared in air by the single-roller chill block melt spinning method. They showed no evidence of crystallinity in X-ray diffraction patterns.

The alloys were investigated by a differential scanning calorimetry (DSC) with a heating rate 10 K/min. The crystallization temperatures, as well as the enthalpies of crystallization, were determined. The values of activation energy were calculated according to Kissinger [17].

Controlled crystallization was performed in Perkin-Elmer DSC-2 unit applying continuous heating from room temperature  $T_r$  to  $T_{\text{max}}$ , followed by cooling down to  $T_r$  with maximum available cooling rate  $\sim 320$  K/min). The maximum temperature of heating  $T_{\text{max}}$  chosen for each alloy individually, exceeded the first calorimetric peak temperature  $T_1$  and was lower than the onset temperature of the second stage of crystallization.

Crystallization products were studied using X-ray diffractometry (Co- $K_\alpha$  radiation) and transmission electron microscopy (TEM).

Flash annealing has been performed using the experimental arrangement described previously [18] and applying zone cooling procedure [2] presented in Figure 1. Electric current of 20 A (resulting in the current density of 280 MA/m<sup>2</sup>) and pulse length in the range 25 to 35 ms was applied. Immersion of one end of the sample in liquid nitrogen (Fig. 1) creates temperature gradient over the sample length (equal to 100 mm). After such treatment the lower part of the sample remained amorphous. Crystallization started at some distance "l" above the level of liquid nitrogen and proceeded with the increase of "l". It results with the broad spectrum of microstructures in each sample.

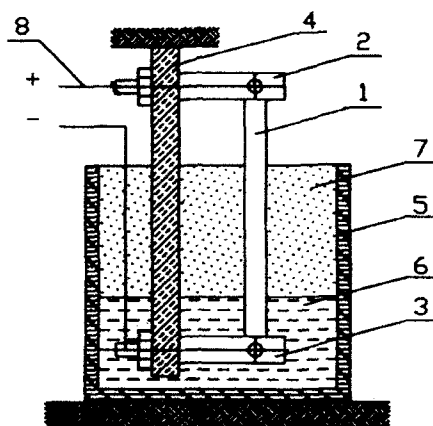


Fig. 1. The set up for holding and cooling a ribbon sample during flash annealing: 1 - sample, 2,3 - brass grips, 4 - holder isolating the grips, 5 - container of liquid nitrogen, 6 - liquid nitrogen, 7 - nitrogen vapour, 8 - current pulse supply

### 3. Nanoncrystallization of Fe-B-Si glasses by addition of special alloying elements

DSC curves for studied Fe-B-Si glasses are shown in Figure 2. The values of crystallization onset temperature  $T_x$ , the first peak temperature  $T_1$  and the second peak temperature  $T_2$  for given alloys are shown in Table 1. The values of activation energy  $E$  and crystallization enthalpy  $H$  for both stages of crystallization are presented in Table 2.

The alloy A can be regarded as the reference one. The influence of Cu, Nb and Ta additions on crystallization process of Fe-B-Si glasses can be established by comparing the appropriate results (thermal data, microstructures etc.) obtained for B, C, D and E alloys with those of alloy A.



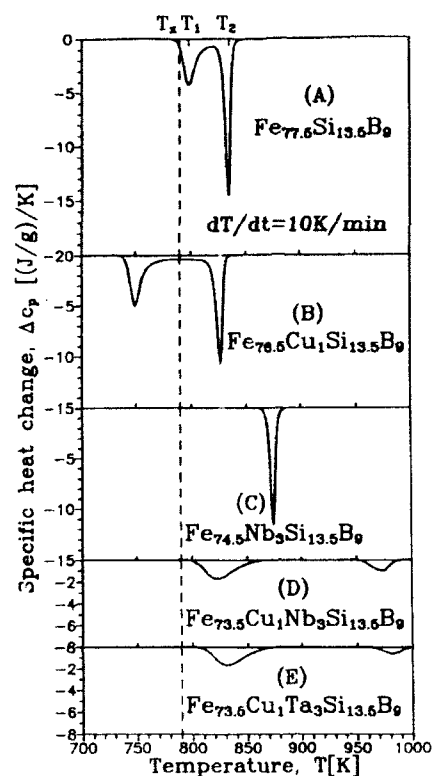


Fig. 2. DSC plots during continuous heating from room temperature to 1000 K at a constant heating rate  $dT/dt = 10$  K/min.

Table 1 Compositions and values of crystallization temperatures [K] ( $T_x$  - crystallization onset temperature;  $T_1$  and  $T_2$  - DSC peak temperatures of the first and the second stage of crystallization)

Alloy	Composition	$T_x$	$T_1$	$T_2$	$T_1 - T_2$
A	$\text{Fe}_{77.5}\text{Si}_{13.5}\text{B}_9$	790	799	835	36
B	$\text{Fe}_{76.5}\text{Cu}_1\text{Si}_{13.5}\text{B}_9$	741	749	826	77
C	$\text{Fe}_{74.5}\text{Nb}_3\text{Si}_{13.5}\text{B}_9$	869	875		
D	$\text{Fe}_{73.5}\text{Cu}_1\text{Nb}_3\text{Si}_{13.5}\text{B}_9$	803	822	972	150
E	$\text{Fe}_{73.5}\text{Cu}_1\text{Ta}_3\text{Si}_{13.5}\text{B}_9$	810	830	981	151

Table 2. Activation energy ( $E_{a1}$  and  $E_{a2}$ ) in kJ/mol and crystallization enthalpy ( $H_1$  and  $H_2$ ) in J/g for the first and the second stage of crystallization.

Alloy	$E_{a1}$	$E_{a2}$	$H_1$	$H_2$	$H_1+H_2$
A	295 $\pm$ 9	287 $\pm$ 8	62.5	99.5	162.4
B	235 $\pm$ 8	252 $\pm$ 11	78.8	87.9	166.7
C	347 $\pm$ 8		70.7		70.7
D	321 $\pm$ 8	456 $\pm$ 19	26.6	9.6	36.2
E	331 $\pm$ 16	460 $\pm$ 12	26.5	5.9	32.4

The addition of Cu and Nb or Ta very strongly affects the shape of DSC thermograms. Both peaks related to the two stages of crystallization are very flat and wide. This is probably caused by stored surface energy of large grain boundaries area in nanocrystalline alloys where further growth of  $\alpha$ -Fe(Si) crystals is retarded by amorphous matrix. The amorphous matrix surrounding  $\alpha$ -Fe-(Si) crystals is stabilized by addition of niobium or tantalum and increased content of boron due to the primary crystallization of  $\alpha$ -Fe(Si) crystals.

Microstructures of the alloys after the first stage of crystallization are shown in Figures 3 and 4. Ultrafine grain structure is revealed only by the alloys D and E. The reference alloy A, as well as the alloys B and C, containing only one alloying element (Cu or Nb), exhibits much coarser structure. The values of average grain diameter  $D$  of the studied glasses after the first stage of crystallization, enclosed in Table 3, amount from  $\sim 11$  nm for the alloy D up to  $\sim 300$  nm for the reference alloy A. There is also some correlation between the average grain diameter  $D$  and crystallization enthalpy  $H$ .

The above results clearly show, that the microstructure of the Fe-Si-B-based glasses after the first stage of crystallization is very strongly dependent on the alloy composition. Moreover, it is evident that nanocrystalline structure can be formed only in alloys with special compositions.

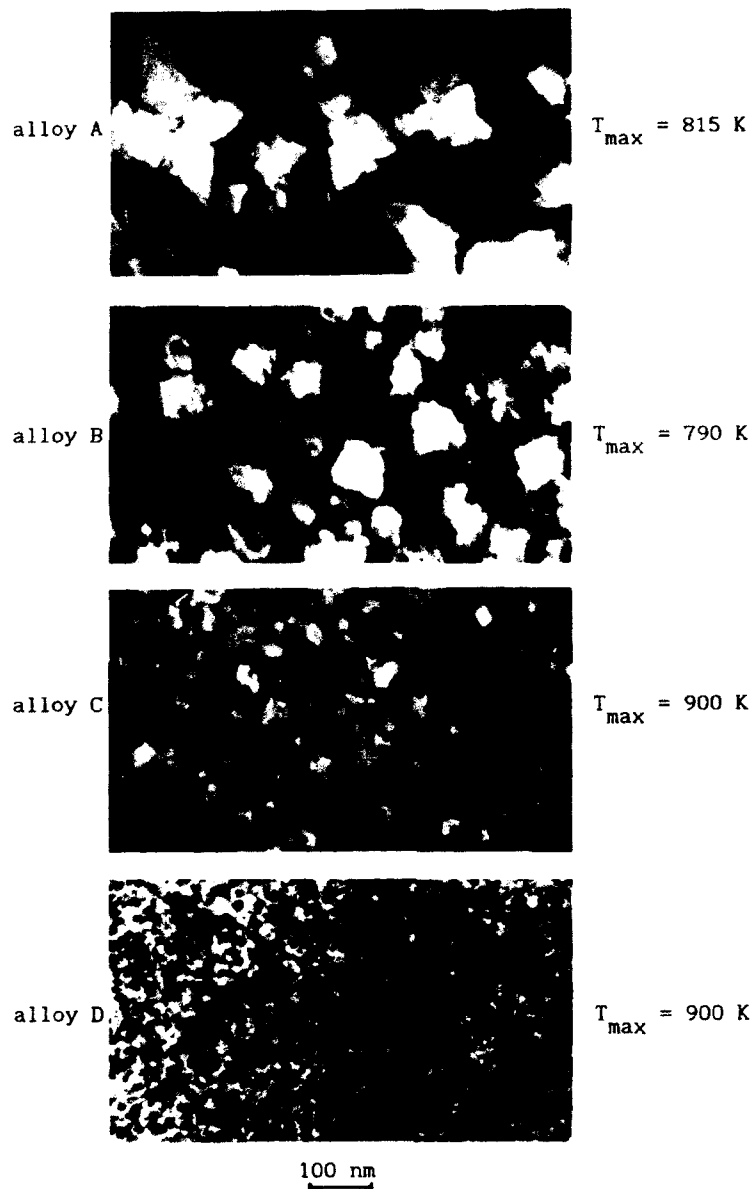


Fig. 3. Bright-field electron micrographs of the A, B, C and D alloys after the first stage of crystallization realized during continuous heating from room temperature to  $T_{\max}$  at a heating rate 10 K/min.

Table 3. Average grain diameter  $D$  [nm] and standard deviation  $\sigma$  after the first stage of crystallization realized in DSC unit during continuous heating from room temperature to  $T_{\max}$  [K].

Alloy	$D$	$\sigma$	$T_{\max}$
A	~300		815
B	71.1	22.4	790
C	23.3	12.1	900
D	11.1	4.5	900
E	11.4	4.7	900
D	5.4	2.5	822

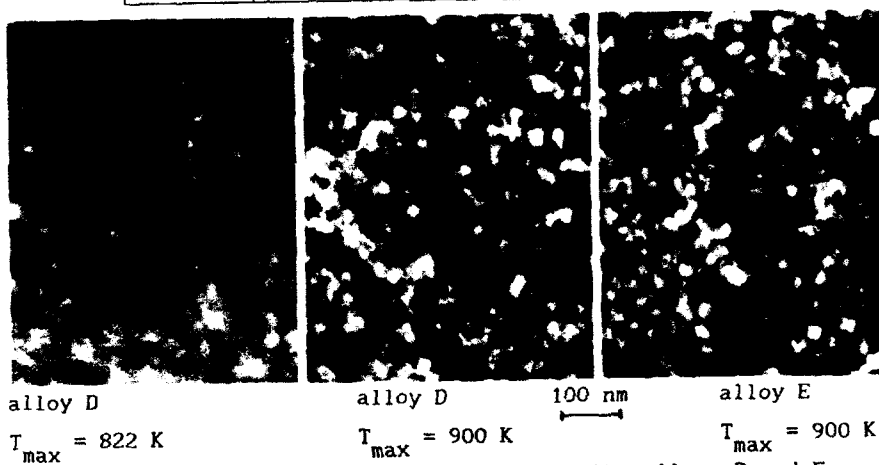


Fig. 4. Bright-field electron micrographs of the alloys D and E after the first step of crystallization realized during continuous heating from room temperature to  $T_{\max}$  at a rate 10 K/min.

The continuous heating applied in this study appears to be as good as isothermal annealing, which was the only method applied for nanocrystallization of Fe-based glasses so far.

On X-ray diffraction patterns (Fig. 5) for all the studied glasses one can see very broad ( $2\theta = 46-58^\circ$ ) and weak peak associated with the amorphous phase, still remaining after the first stage of crystallization and relatively strong peaks related to crystalline

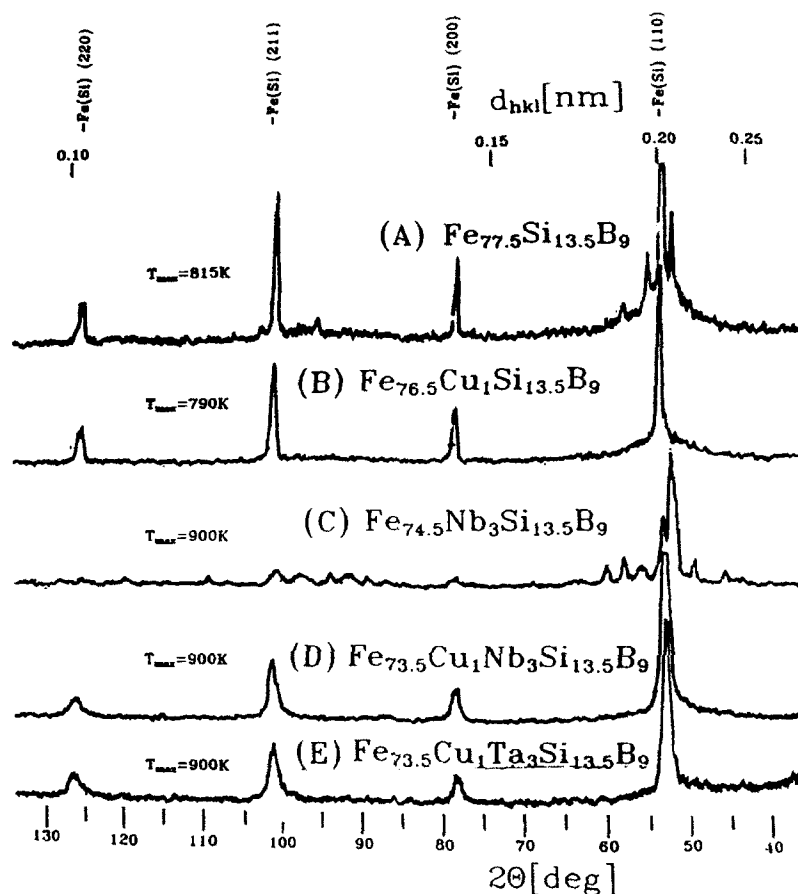


Fig. 5. The X-ray diffraction patterns of the studied alloys after the first stage of crystallization realized during continuous heating from room temperature to  $T_{\max}$  at a constant heating rate 10 K/min.

phases. Single crystalline phase was observed only for the alloys (B, D and E) containing copper. This phase was identified as  $\alpha$ -Fe(Si) with lattice parameter  $\sim 0.284$  nm, which is considerably lower than that (0.2866 nm) for pure  $\alpha$ -Fe. In the reference alloy A and in alloy C besides very strong peaks related to  $\alpha$ -Fe(Si) much weaker reflections are present, which probably come from tetragonal  $\text{Fe}_3\text{B}$  phase.

#### 4. Nanocrystallization of Fe-B-Si glasses by flash annealing

The effect of temperature gradient over the ribbon length during flash annealing with the applied procedure of zone cooling is seen in Figures 6 and 7. Change in the X-ray diffraction patterns with the

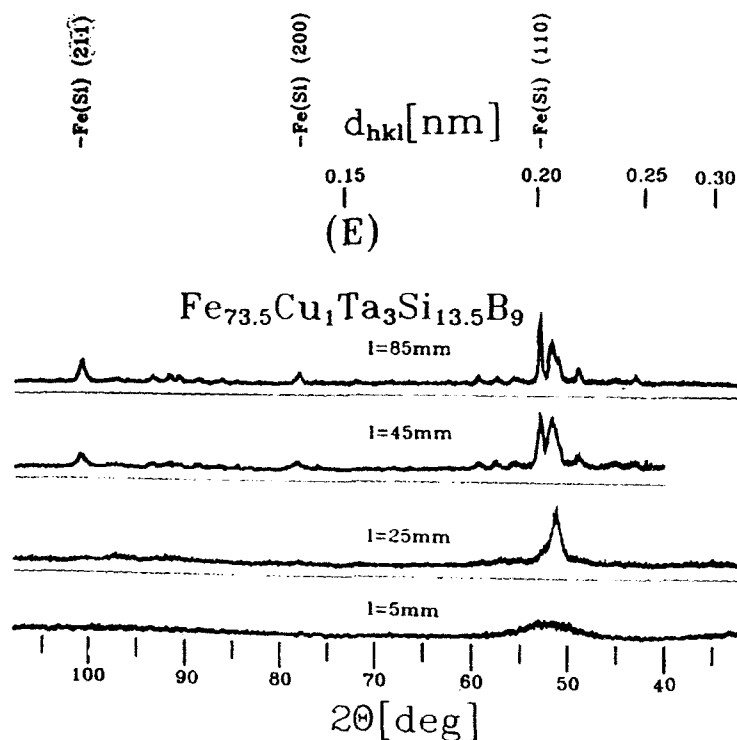


Fig. 6. Change in the X-ray diffraction patterns with the distance  $l$  above the liquid nitrogen level of the E alloy after flash annealing ( $t = 28$  ms).

distance  $l$  above the liquid nitrogen surface after flash annealing of the alloy E is presented in Figure 4. Bright-field electron micrographs of this alloy, partially corresponding to X-ray patterns shown in Figure 6, are presented in Figure 7. Similar spectrum of microstructures, from amorphous through partially crystalline up to fully crystalline with coarsened grains, has been observed in all samples.

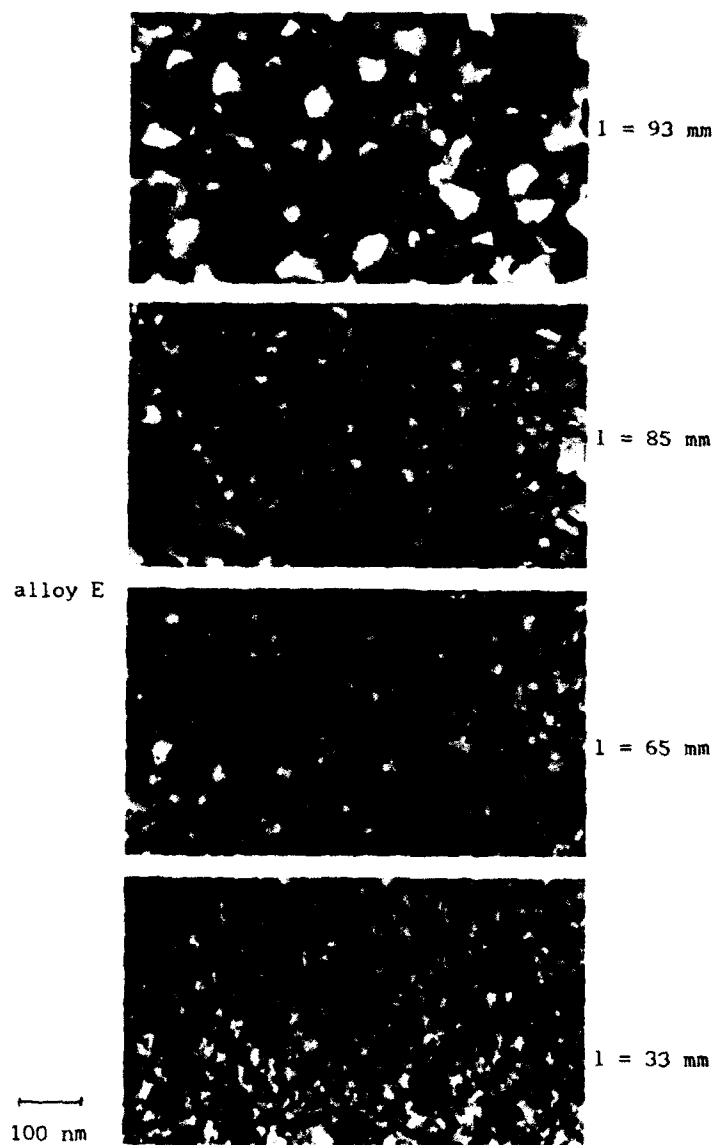


Fig. 7. Change of the microstructures of the alloy E with the distance  $l$  above the liquid nitrogen level after flash annealing ( $t = 28$  ms).

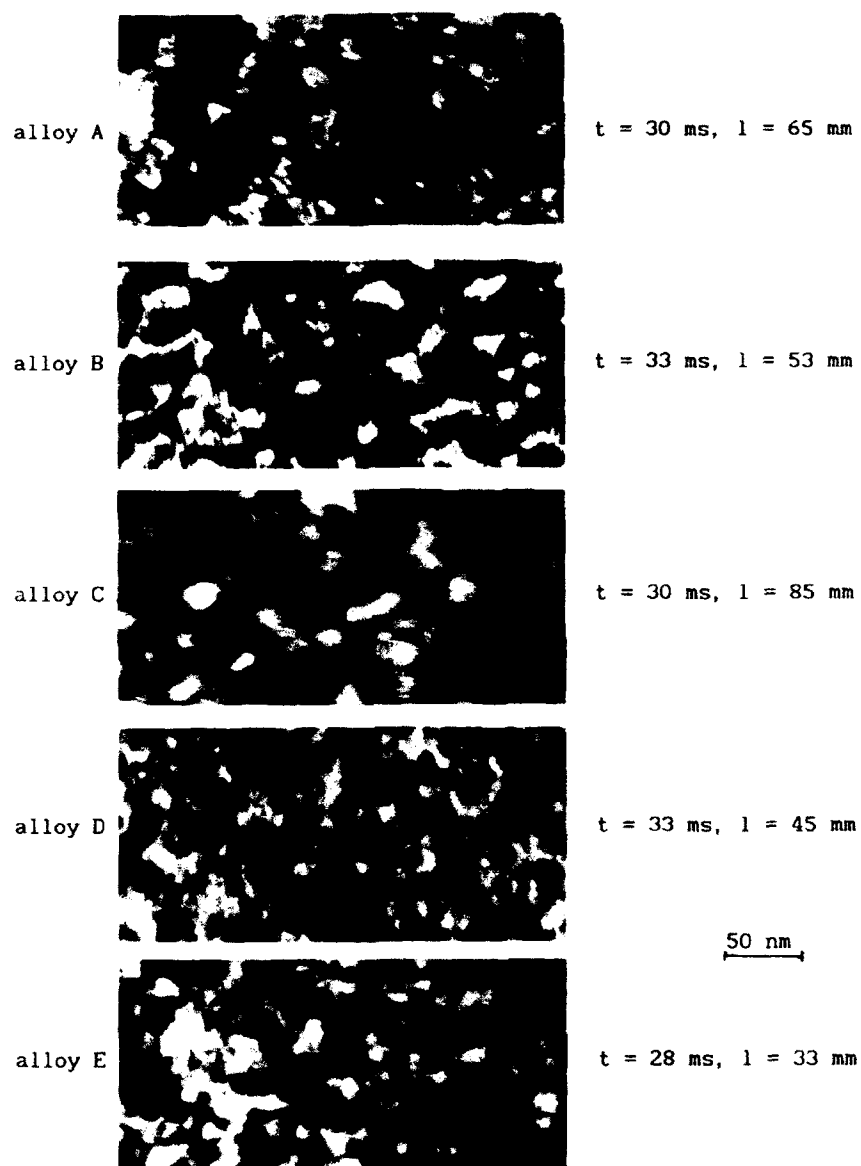


Fig. 8. Bright-field electron micrographs of the alloys after the first step of crystallization caused by flash annealing;  $t$  - pulse duration,  $l$  - distance above the liquid nitrogen level.



Microstructures of the studied alloys after the first stage of crystallization realized by flash annealing are shown in Figure 8. In this state all the alloys exhibit very fine grain structure and the difference between the particular alloys is insignificant. The values of average grain diameter, collected in Table 4, amount from ~ 13 nm

Table 4 . Average grain diameter  $D$  [nm] and standard deviation  $\sigma$  after the first stage of crystallization caused by conventional annealing [6] and by flash annealing.

Alloy	Conventional annealing		Flash annealing	
	$D$	$\sigma$	$D$	$\sigma$
A	~300		24.0	11.9
B	71.1	22.4	22.6	9.7
C	23.3	12.1	21.9	7.7
D	11.1	4.5	13.2	4.4
E	11.4	4.7	15.9	6.5

to ~ 24 nm for D and A flash annealed alloys, respectively. Comparing the values of average grain size for the alloys after flash annealing and conventional annealing, it is easy to notice the benefits associated with application of flash annealing for formation of nanocrystalline structure. The most remarkable effect of this non-conventional treatment on microstructure was observed for A and B alloys. Instead of large ~ 300 nm long dendrites, observed for the alloy after conventional annealing, equiaxed grains with average diameter equal to 24 nm are formed during flash annealing. Microstructures of the B alloy after conventional and flash annealing are presented in Figure 9.

The effect of flash annealing on the nanocrystallization process is probably associated with increased nucleation rate at high temperature (higher than the glass transition temperature  $T_g$ ) and with limited grain growth during very short heating and cooling time.

All results presented in Figures 7, 8, 9 and in Table 4 clearly show that flash annealing unusually decreases the influence of alloy

composition on the microstructure after crystallization.

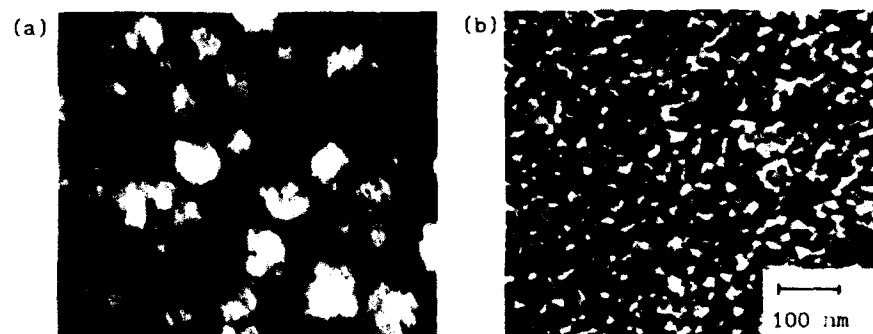


Fig. 9. Bright-field electron micrographs of the alloy B after:  
 (a) crystallization realized during continuous heating from room temperature to  $T_{\max} = 790$  K at a rate 10 K/min;  
 (b) flash annealing, with pulse duration  $t = 33$  ms, observed area was 50 mm above the liquid nitrogen level.

Table 5. Crystalline phases detected by x-ray and electron diffraction after the first stage of crystallization caused by conventional and flash annealing ( $\text{Fe}_3\text{B}$  - tetragonal structure).

Alloy	Conventional annealing	Flash annealing
A	$\alpha\text{-Fe}(\text{Si}) + \text{Fe}_3\text{B}$	$\alpha\text{-Fe}(\text{Si})$
B	$\alpha\text{-Fe}(\text{Si})$	$\alpha\text{-Fe}(\text{Si})$
C	$\text{Fe}_3\text{B} + \alpha\text{-Fe}(\text{Si})$	$\text{Fe}_3\text{B}$
D	$\alpha\text{-Fe}(\text{Si})$	$\alpha\text{-Fe}(\text{Si})$
E	$\alpha\text{-Fe}(\text{Si})$	$\text{Fe}_3\text{B}$

Crystalline phases observed in the studied glasses after the first stage of crystallization caused by conventional crystallization and flash annealing are listed in Table 5. The most striking effect of annealing method on crystallization product has been found for the alloy E. Instead of  $\alpha\text{-Fe}(\text{Si})$  phase, observed after the conventional annealing, tetragonal  $\text{Fe}_3\text{B}$  phase has been detected after flash annealing of the alloy E. The  $\alpha\text{-Fe}(\text{Si})$  also appeared in that alloy, but after flash annealing at higher temperature.

### 5. Nanocrystallization of Co-Si-B glasses by flash annealing

To answer the questions whether the refinement of microstructure is possible for other than Fe-B-Si-based metallic glasses and whether the refinement is dependent on the basic mode of crystallization (primary, eutectic and polymorphous) we have studied two Co-B-Si alloys: -  $\text{Co}_{78}\text{B}_{11}\text{Si}_{11}$  crystallizing primarily and  $\text{Co}_{70.5}\text{B}_{14.75}\text{Si}_{14.75}$  crystallizing polymorphously.

Microstructures of  $\text{Co}_{78}\text{B}_{11}\text{Si}_{11}$  alloy after the first stage of crystallization caused by conventional ( $T = 700\text{--}820\text{ K}$ ,  $\tau = 30\text{ min}$ ) and flash annealing are shown in Fig. 10. In both cases, the same two phases have been detected: primary crystals of hexagonal  $\alpha$ -Co-like phase and amorphous matrix still remaining after the first stage of crystallization. After the furnace annealing (Fig. 10a) elongated randomly oriented crystals ( $\sim 150\text{ nm}$  long and  $\sim 50\text{ nm}$  thick) have been observed. After the flash annealing crystals of the same phase are equiaxed and much smaller with diameter not exceeding  $40\text{ nm}$ . One can also notice substantial difference in volume fraction of amorphous phase. After flash annealing the amorphous phase is hardly seen between grains of crystalline phase.

Microstructures of  $\text{Co}_{70.5}\text{B}_{14.5}\text{Si}_{14.5}$  alloy after polymorphous crystallization by conventional - and flash annealing are shown in Fig. 11. In both cases the entire volume of amorphous ribbon polymorphously crystallized to the metastable  $\text{Co}_{17}\text{B}_{0.5}\text{Si}_{0.5}$  phase. At boundaries of large polyhedral grains, small grains, which are probably the product of partial decomposition of this phase, are visible. The microstructures shown in Figures 11a and 11b differ only in grain size. Likewise for primary also for polymorphously crystallizing glass, flash annealing results in much finer structure than the conventional annealing does. However very fine nanocrystalline structure has been created only in the glass exhibiting primary crystallization i.e.  $\text{Co}_{78}\text{B}_{11}\text{Si}_{11}$ .

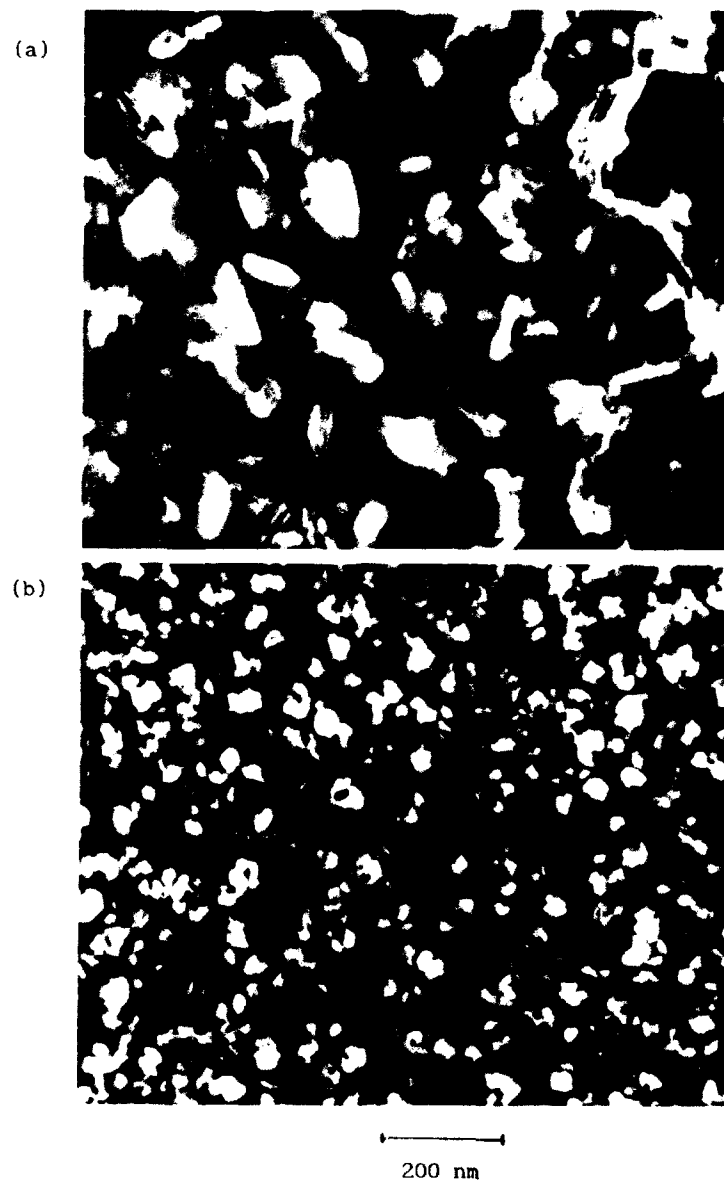


Fig. 10. Bright-field electron micrographs of  $\text{Co}_{78}\text{B}_{11}\text{Si}_{11}$  alloy after the first crystallization step caused by: (a) conventional annealing ( $T_{\text{max}} = 700 \text{ K}$ ,  $t = 30 \text{ min}$ ) and (b) flash annealing ( $t = 90 \text{ ms}$ ,  $l = 15 \text{ mm}$  above the liquid nitrogen level).

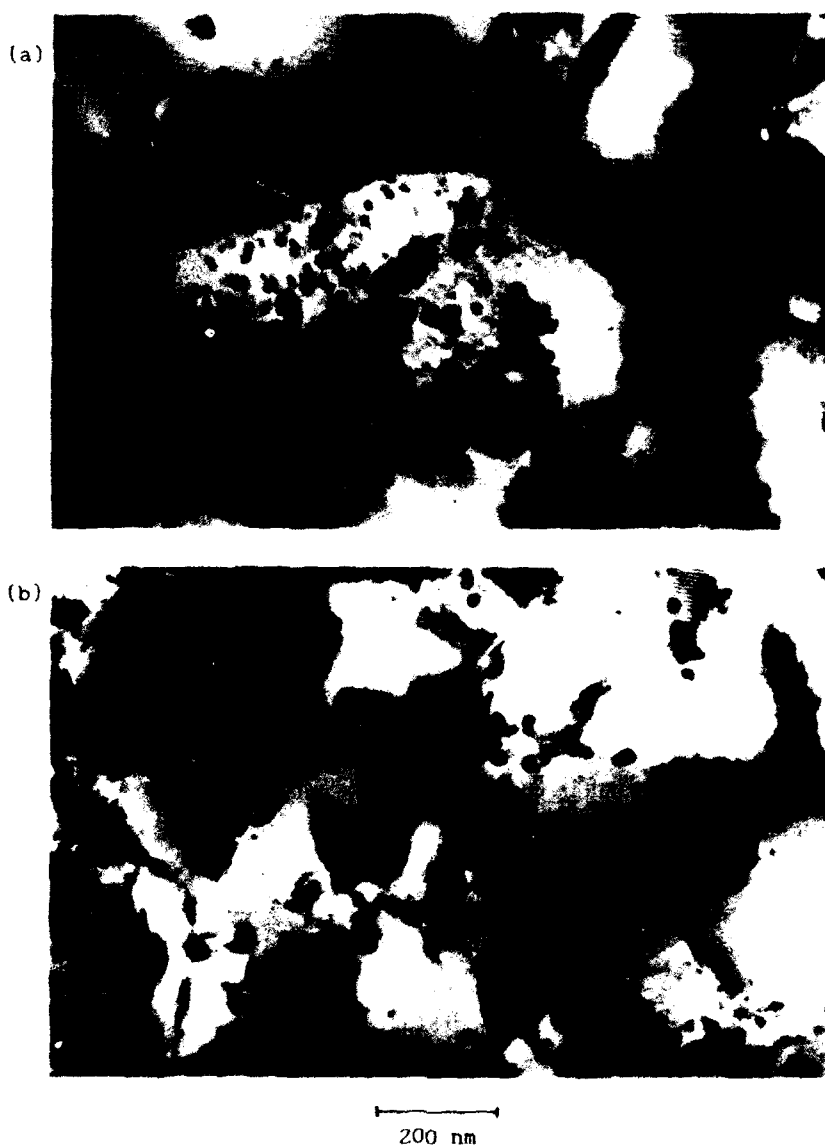


Fig. 11. Bright-field electron micrographs of  $\text{Co}_{70.5}\text{B}_{14.5}\text{Si}_{14.5}$  alloy after polymorphous crystallization caused by: (a) conventional annealing ( $T_{\text{max}} = 820 \text{ K}$ ,  $t = 30 \text{ min}$ ), and (b) flash annealing ( $t = 80 \text{ ms}$ ,  $l = 50 \text{ mm}$  above the liquid nitrogen level).

## 6. Conclusions

1. Microstructures of the Fe-Si-B-based glasses after the first stage of crystallization strongly depend on the alloy composition. Nanocrystalline structure can be created by controlled conventional crystallization only in alloys with special composition, e.g. in Fe-Si-B alloys containing at least two alloying elements: Cu and Nb or Ta.
2. Enthalpies for the first and the second stage of the crystallization for glasses containing Cu and Nb or Ta are about five times smaller than the crystallization enthalpy for Fe-B-Si glass. This is probably caused by stored energy of large grain boundary area in nanocrystalline alloys, where further growth of  $\alpha$ -Fe(Si) crystals is stabilized by addition of Nb or Ta.
3. Ultrafine structure with average grain diameter less than 24 nm can be obtained also in Fe- and Co-based glasses studied in this work by appropriate flash annealing where very short pulse time provides conditions for formation of large number of nuclei and fast cooling retards growth of just formed crystals. Therefore, this non-conventional heat treatment makes possible nanocrystallization in much wider composition range.
4. Nanocrystalline structure can be formed by flash annealing in glasses exhibiting primary crystallization and not in glasses exhibiting polymorphous crystallization. This effect can be explained as follows. Polymorphous crystallization is diffusionless, very rapid process characterized by relatively high growth rate of crystals with the same composition as decomposing amorphous matrix. Even flash annealing, with as short pulse time as 0.1 s, appears to be not enough fast heat treatment to prevent excess growth in polymorphously crystallizing glass. On the other hand, primary crystallization involves long range volume diffusion, which is responsible for relatively low rate of crystal growth. In this case flash annealing followed by rapid quenching is an effective method of substantial refinement of microstructure.

## 7. References

1. Y.Yoshizawa, S.Oguma and K.Yamauchi, *J. Appl. Phys.* **64** (1988) 6044.
2. H.Matyja and A.Załuska, *Phil. Mag.* **B61** (1990) 701.
3. T.Kulik, D.Bucka and H.Matyja, to be published.
4. T.Kulik, to be published.
5. T.H.Nok, M.B.Lee, H.J.Kim and I.K.Kong, *J. Appl. Phys.* **67** (9) (1990) 5568.
6. P.Duhaj, P.Švec, D.Janičkovič and I.Matko, *Mat. Sci. Eng. A J* **33** (1991) 398.
7. U.Köster, V.Skünemann, M.Blank-Bewersdorff, S.Brauer, M.Suttou and G.B.Stephenson, *Mat. Sci. Eng. A J* **33** (1991) 611.
8. K.Hono, A.Inoue and T.Sakurai, *Appl. Phys. Lett.* **58** (19) (1991) 2180.
9. U.Köster, R.Abel and M.Blanke, *Glastechnische Berichte K* **56** (1983) 584.
10. Y.Yoshizawa, K.Yamauchi, T.Yamane and H.Sugihara, *J. Appl. Phys.* **64** (1988) 6047.
11. G.G.Herzer, *IEEE Trans. Magn.* **25** (1989) 3327.
12. A.Załuska and H.Matyja, *J. Mater. Sci. Lett.* **2** (1983) 729.
13. A.Załuska and H.Matyja, *Int. J. Rapid Solidific.* **2** (1987) 205.
14. U.Köster, *Z. Metallkde* **75** (1984) 691.
15. A.Załuska, L.Załuski and A.Witek, *Mat. Sci. Eng. A* **122** (1989) 251.
16. T.Kulik, T.Horubała and H.Matyja, to be published.
17. H.E.Kissinger, *J. Res. NBS* **57** (1956) 217.
18. T.Kulik, B.Lisowski and H.Matyja, *Int. J. Rapid Solidific.* **4** (1989) 287.

## Acknowledgements

The financial support by Maria Skłodowska-Curie Joint Fund II is gratefully acknowledged.

INFLUENCE OF THE CRYSTALLIZATION ON THE MECHANICAL  
PROPERTIES OF GLASSY POLYMERS

F.J. BALTA CALLEJA  
Instituto de Estructura de la Materia , C.S.I.C.  
Serrano 119, 28016 Madrid, Spain

ABSTRACT

After a short introduction concerning the hardness microstructure correlation in case of low crystallinity polymers having a  $T_g$ -value above room temperature some of the more recent results on poly(ethylene terephthalate) samples prepared in the glassy state are presented. The effects of physical aging and of nucleating agents upon crystallization behaviour are discussed. The kinetics of crystallization from the glassy state studied in real time by measuring the microhardness (H) for different crystallization temperatures is reported. Results are discussed in terms of the Avrami equation. New precrystallization phenomena, evidenced by the presence of a small maximum in H as a function of annealing temperature, are observed at temperatures higher than  $T_g$ .

1. INTRODUCTION

In recent years investigations of the microhardness properties of various polymers have emerged as a physical method which can offer a fundamental knowledge on changes in the morphology of polymeric systems<sup>1,2)</sup>. Most of the studies on microhardness make reference to highly crystalline polymer materials having glass transition temperatures well below room temperature<sup>3-8)</sup>. A few investigations on the microhardness of low crystallinity materials and glassy polymers are also available<sup>9,10)</sup>. In particular, we have recently shown<sup>11)</sup> that the microhardness of poly(ethylene terephthalate) (PET) can offer a useful information concerning the various morphologies obtained



during primary crystallization (involving an incomplete spherulitic growth) and secondary crystallization, i.e. after spherulitic growth is completed. The obtained results were quantitatively discussed in the light of three structural factors: a) The volume fraction occupied by spherulites. b) The value of crystallinity within the lamellar stacks. c) The average thickness of the crystals.

The mechanism of crystallization of PET from the glassy state, on the other hand, has been amply investigated by several authors. The kinetics of crystallization from the glassy state was studied by Keller et al.<sup>12)</sup> and Zachmann and Stuart<sup>13)</sup> by measuring the density changes during crystallization and by Elsner et al. using time resolved small angle X-ray scattering<sup>14,15)</sup>. Günter and Zachmann examined the effect of catalysts on the kinetics of crystallization<sup>16)</sup>. Finally, Asano et al.<sup>17)</sup> have recently analyzed the influence of catalysts on the rate of crystallization and on the crystalline lattice distortions in PET by means of X-ray diffraction.

In the present study the mechanism of crystallization of PET from the glassy state is examined by measuring the microhardness "in situ" during crystallization at different temperatures. It is shown that the effect of nucleating agents and of physical aging upon the crystallization behaviour from the glassy state are of primary importance. The occurrence of new precrystallization phenomena observed at temperatures higher than  $T_g$  in physically aged PET is also reported.

## 2. EXPERIMENTAL DETAILS

Samples of amorphous PET containing manganese acetate as catalyst were melt-pressed in the form of 200 $\mu$ m thick films. The molecular weight determined by viscometry was

found to be 33.000. Two types of samples were investigated: a) Samples containing sodium montanate as crystal nucleating agent. b) Samples without nucleating agent. The glassy polymers were investigated: i) immediately after quenching in ice-water (initial sample) and ii) after one year of storage at room temperature.

Microindentation hardness was measured using a square based diamond. A loading cycle of 0.1min and a load of 0.5N were used. The microhardness value (in Pa) was derived from the residual projected impression using the equation<sup>18)</sup>:

$$H = Kp/d^2 \quad (1)$$

where  $d$  is the mean diagonal length of the indentation in  $m$ ,  $p$  the applied force in  $N$ , and  $K$  a geometrical factor equal to 1.854. The temperature dependence was determined in the range of room temperature up to  $140^\circ C$ . The hardness was measured during heating of the sample every  $3-4^\circ C$  up to  $140^\circ C$ . The isothermal crystallization of PET was measured at different constant temperatures in the  $90-117^\circ C$  range as a function of time every 45sec using a hot stage with a heat-controller designed by Prof. T. Yoshida, Dr. T. Asano and Mr. K. Mizuno at Shizuoka University. The surface temperature of the samples was calibrated with organic compounds of known melting point.

### 3. RESULTS

DSC scans of the glassy samples after immediate quenching show a typical step corresponding to the glass transition temperature near  $T_g \sim 70^\circ C$ . On the other hand, the  $T_g$  temperature in the aged material is revealed by the presence of a small endothermic peak which corresponds to a relaxation of the glass towards equilibrium<sup>19)</sup>.

Figs. 1a and 2a show the kinetics of the micro hardness variation during crystallization of the physically aged material as a function of time for different temperatures. Fig. 1 shows the H-data for the material without nucleating agent and Fig. 2 presents the microhardness data for the material with nucleating agent. The data shown in Figs. 1a and 2a give, in addition, the microhardness variation, measured at constant temperatures, until the time for which primary crystallization is completed. Furthermore, there is a main feature which distinguishes the data of Fig. 1a and 2a. In Fig. 2a one clearly observes during crystallization of PET with nucleating agent at 95 and 100°C two well-defined regions corresponding respectively to a first rapid crystallization and to a second slower crystallization rate. These two regions are not identified for temperatures of crystallization  $T_C < 95^\circ\text{C}$  and  $T_C > 100^\circ\text{C}$ . In addition, for the samples with nucleating agent (Fig. 2a) the final leveling-off value of H increases from  $H_M \sim 100\text{MPa}$  for  $T_C = 90^\circ\text{C}$  up to  $H_M \sim 160\text{MPa}$  for  $T_C = 105^\circ\text{C}$ . However, in the samples without nucleating agent (Fig. 1a) one just observes one single rapid rate of H-increase at each crystallization temperature. In this case the final leveling-off value of H is the same for all crystallization temperatures.

Most interesting is the fact that the initial hardness variation with time (Fig. 1b) for the material without nucleating agent shows a hardness maximum after 8-9 minutes when measured in the range of 105-110°C, just before the onset of primary crystallization. For the material with nucleating agent this maximum in hardness as a function of time appears at lower temperatures (90-95°C) and after longer annealing times (12-25 minutes) (Fig. 2b). On the other hand, for crystallization temperatures of  $T_C = 100^\circ\text{C}$  and  $105^\circ\text{C}$  solidification is so fast that it does

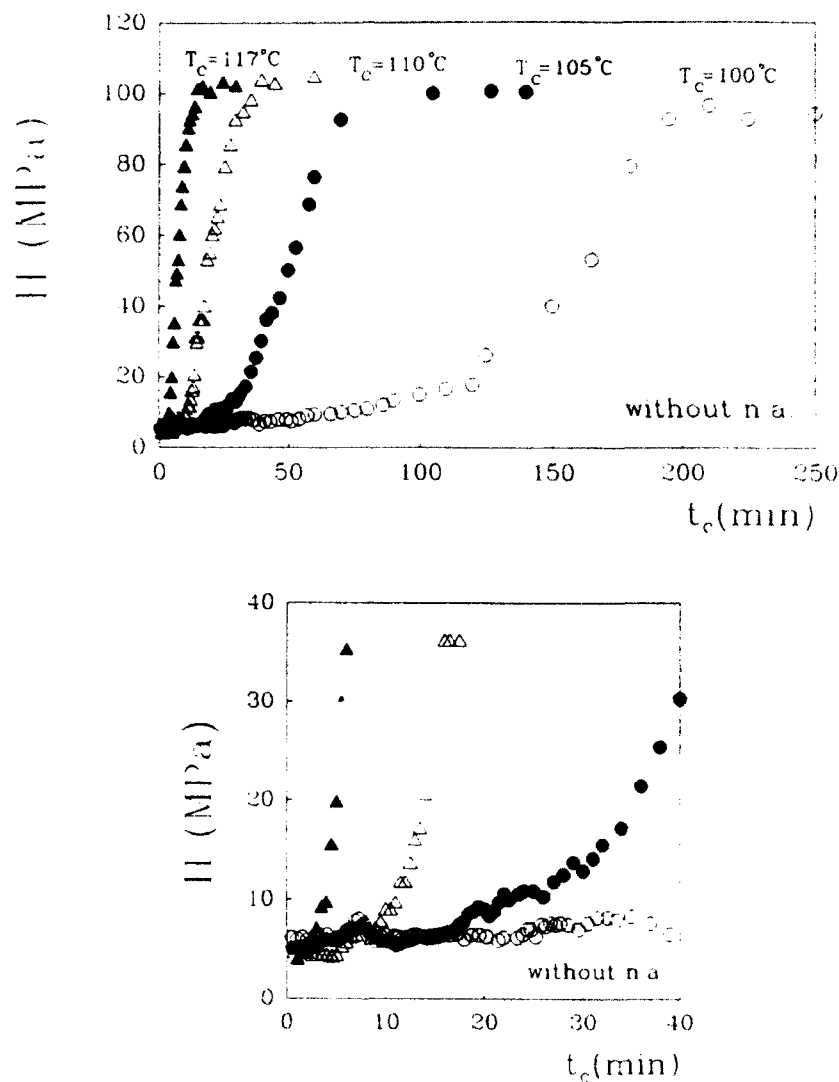


Figure 1

a) Variation of the microhardness for physically aged PET samples without nucleating agent as a function of crystallization time ( $t_c$ ) for different crystallization temperatures ( $T_c$ ). b) Microhardness variation as a function of time for the first steps of crystallization.

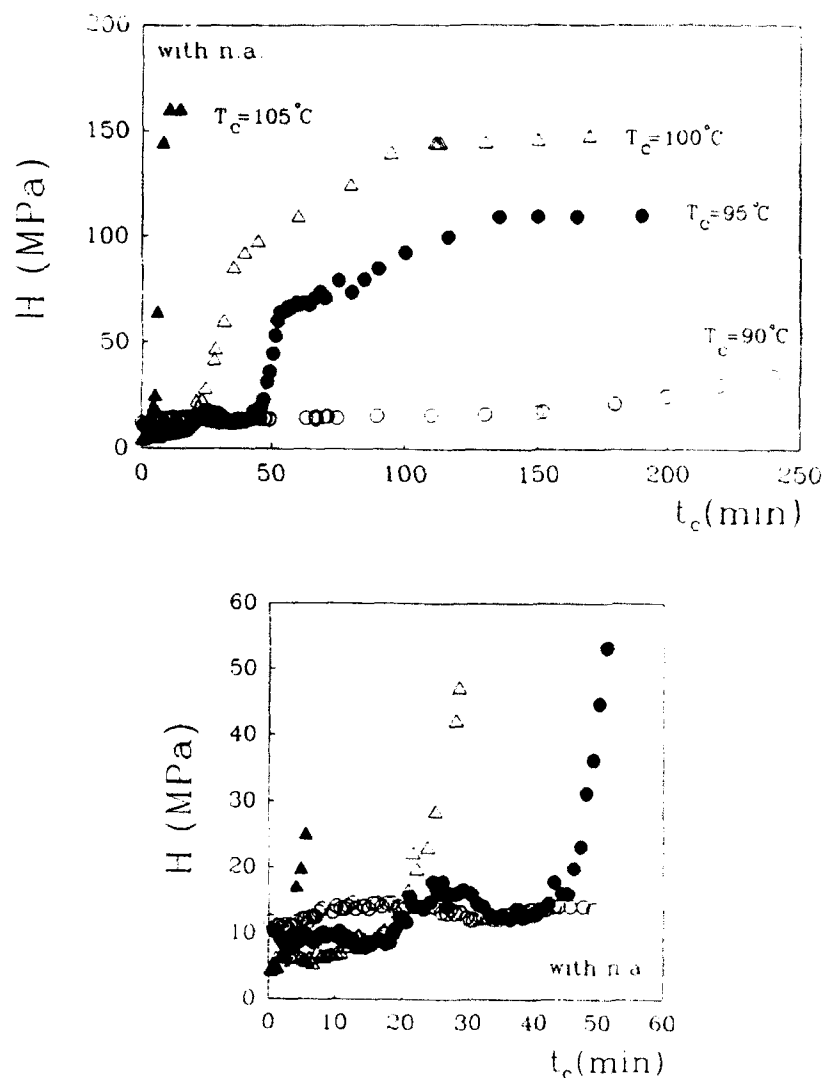


Figure 2

a) Variation of the microhardness for physically aged PET samples with nucleating agent as a function of crystallization time ( $t_c$ ) for different crystallization temperatures ( $T_c$ ). b) Microhardness variation as a function of time for the first steps of crystallization.

not let this precrystallization transition to be seen. The above time dependent transition suggests the occurrence of a molecular ordering giving rise to a hardening effect which vanishes after 5-15 minutes, depending on temperature and on the presence of nucleating agent. In contrast, the samples immediately solidified after quenching do not show the existence of such a precrystallization state as evidenced in Fig. 3.

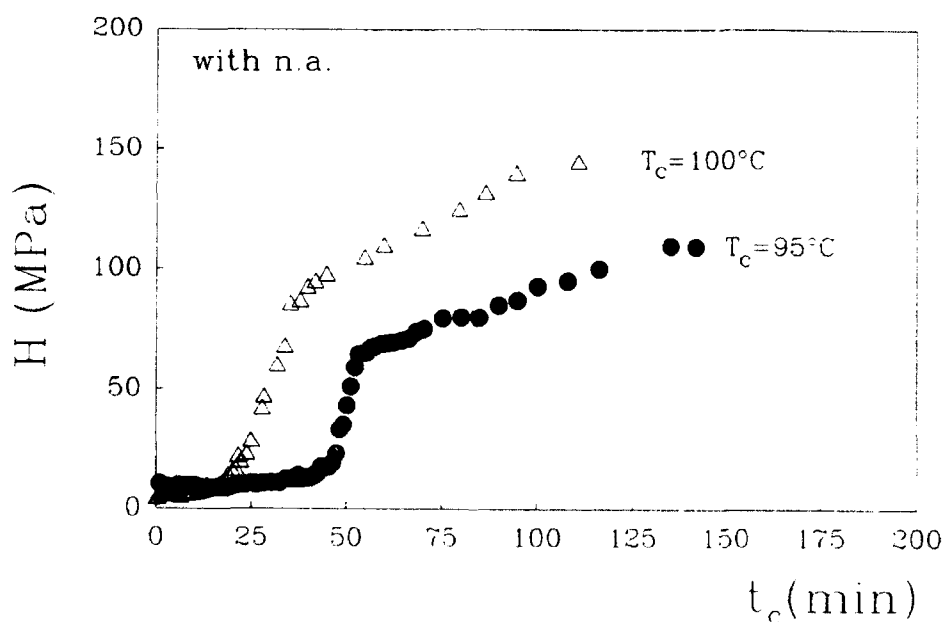


Figure 3  
Measured microhardness variation for fresh PET samples with nucleating agent immediately measured after quenching as a function of crystallization time,  $t_c$ , for two different crystallization temperatures.

Fig. 4a shows the variation of  $H$  as a function of temperature for quenched amorphous PET without (top) and with (bottom) nucleating agent before and after physical aging. One can distinguish two regions of behaviour: One for  $T > T_g$  and the other one for  $T < T_g$ .

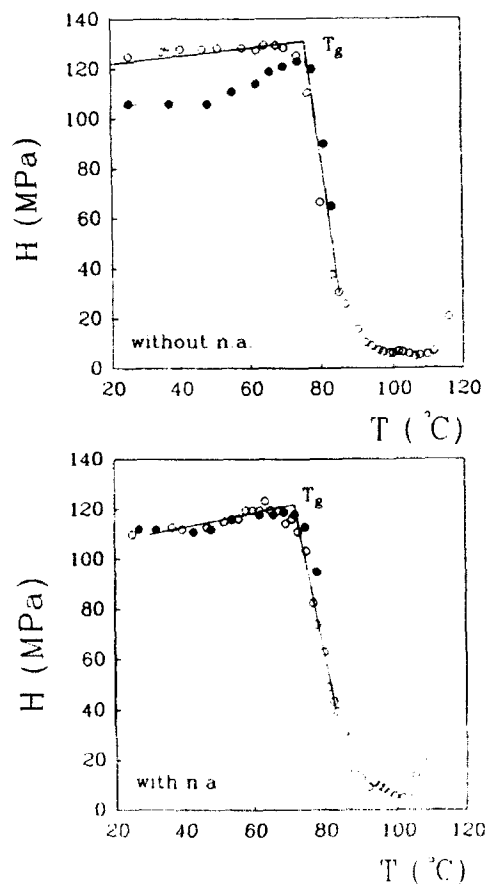


Figure 4  
Variation of the microhardness,  $H$ , for PET samples without (a) and with (b) nucleating agent as a function of temperature. Open symbols: physically aged materials. Solids symbols: materials immediately measured after quenching in ice water.

In the high temperature region ( $T > T_g$ ), in addition to the softening range centered at about 100°C we observe the small hardness maximum (Fig. 4a) which, according to the data of Figs. 1b and 2b, conspicuously characterizes a precrystallization transition. Fig. 4b illustrates a similar softening behavior for physically aged PET containing a nucleating agent. In this case, owing to the increase of the crystallization temperature the H-maximum corresponding to the precrystallization transition is shifted to  $T = 100-105^\circ\text{C}$ .

Finally, in the low temperature region ( $T < T_g$ ) one observes that samples without nucleating agent clearly show, larger microhardness values after a longer storage time at room temperature than the freshly prepared samples (Fig. 4a). On the other hand, the hardness values for the fresh samples containing nucleating agent immediately obtained after quenching are equal to the H-values obtained after one year storage time (Fig. 4b).

#### 4. DISCUSSION

##### 4.1 Precrystallization phenomena in physically aged materials ( $T > T_g$ )

The study of molecular transition relaxation phenomena in amorphous polymers beyond  $T_g$  has been the object of intense activity<sup>20</sup>). This has led to the concept of the existence of a liquid-liquid ( $T_{ll}$ ) transition which has been observed by a variety of physical methods. In attempting to detect such relaxation phenomena we have followed the microhardness variation of PET as a function of time at temperatures well above  $T_g$ . One could expect, in principle, that the set up of segmental motions at these temperatures would give rise to distinct softening phenomena capable to be detected by microhardness.



Instead, what we observe for physically aged PET in Figs. 1b and 2b is a local maximum in hardness measured at 105-110°C for the material without nucleating agent and at 90-95°C for PET with nucleating agent.

These results suggest that at this transition there is a restriction of segmental motions involving an internal liquid crystalline or "paracrystalline" molecular ordering giving rise, in turn, to a hardening effect. This hardening of the material vanishes after 5-7 minutes for physically aged PET without nucleating agent and after 20-35 minutes for physically aged PET with nucleating agent. Since this transition can be visualized as a precrystallization phenomenon involving larger segmental motions it is reasonable the result that the transition takes place at lower temperatures for the material with nucleating agent. Accordingly, the time at which the transition takes place is larger for PET with nucleating agent because the temperatures at which the precrystallization transition occurs is lower. In addition, the amplitude of the transition is larger (10-25min) for the PET with nucleating agent (~5min) than for the material without nucleating agent. In other words, it seems that the presence of the nucleating agent enhances the lifetime of these precrystallization states involving a local molecular order which induces the detected hardening. In case of high crystallization temperatures (higher than 110°C for aged PET without nucleating agent, and higher than 95°C for aged PET with nucleating agent) the crystallization rate is so fast that the precrystallization transition cannot be seen. On the other hand, for the lowest temperatures investigated the precrystallization transition is not either detected because, the mobility of the molecules is probably not sufficiently high to initiate the first crystallization steps. Finally, it is to be noted that in the freshly

prepared samples none of these precrystallization phenomena are observed (Fig. 3). In other words, a compact molecular arrangement near to the equilibrium state of the fluid and a reduced segmental mobility (after long periods of physical aging) are required for the onset of the precrystallization effects observed.

In Fig. 4 one can now, further, appreciate the precrystallization transition in the plot of  $H$  as a function of temperature for the aged PET samples with and without nucleating agent. Despite the large softening phenomenon occurring just above  $T_g$  the microhardness value does not totally vanish. Just before the onset of crystallization, one observes a small hardness maximum yielding  $H$ -values which are comparable to those found at room temperature for short chain paraffinic compounds<sup>21</sup>). This finding further supports the concept of a "liquid crystalline" like state before  $T_c$ .

#### 4.2 Influence of the nucleating agent on physical aging ( $T < T_g$ )

The results shown in Fig. 4a indicate, similarly as we have observed in previous investigations<sup>9</sup>), that the hardness values obtained below  $T_g$  clearly depend on the physical aging of the samples. Physical aging below  $T_g$  is connected to local molecular motions (conformational changes) involving ordering or parallelism of benzene rings of PET and reducing segmental mobility. Physical aging can be, thus, visualized as a slow "nucleation mechanism" below  $T_g$  which is accompanied by a hardening of the material. Beyond  $T_g$  the hardness values show a unique variation with a loss of memory of the previous aging effects.

Most interesting is the observation that the hardness value below  $T_g$  is larger for the materials with nucleating agent than for the samples without nucleating agent and equals the hardness of the aged material (Fig.4b). This result suggests that, the presence of nucleating particles within the polymer induces a similar hardening effect as that occurring in the material after physical aging. The effect of aging is, thus, hidden by the agent.

#### 4.3 Isothermal crystallization of PET

It is well known that the increase of crystallinity with time at a constant crystallization temperature follows the Avrami equation<sup>22)</sup>:

$$\alpha(t) = \alpha_c [1 - \exp(-Gt^n)] \quad (2)$$

where  $\alpha(t)$  is the degree of crystallinity at time  $t$ ,  $\alpha_c$  is the final degree of crystallinity,  $G$  is the Avrami constant which is proportional to the number of nucleating sites and  $n$  is the Avrami exponent which determines the type of crystallization which is taking place. Since in previous investigations<sup>11)</sup> the increase in the H-value of PET during primary crystallization was shown to be directly proportional to the increase of crystallinity, one may expect that the rise in the H-values will follow a similar relationship as a function of time

$$H(t) = H_m + (H_M - H_m) [1 - \exp(-Gt^n)] \quad (3)$$

where  $H_m$  and  $H_M$  represent the lowest and highest H-values obtained during the crystallization process respectively.

In Fig. 5  $\log\{-\ln[1 - (H(t) - H_m)/(H_M - H_m)]\}$  is plotted as a function of  $\log(t)$  for the different crystallization

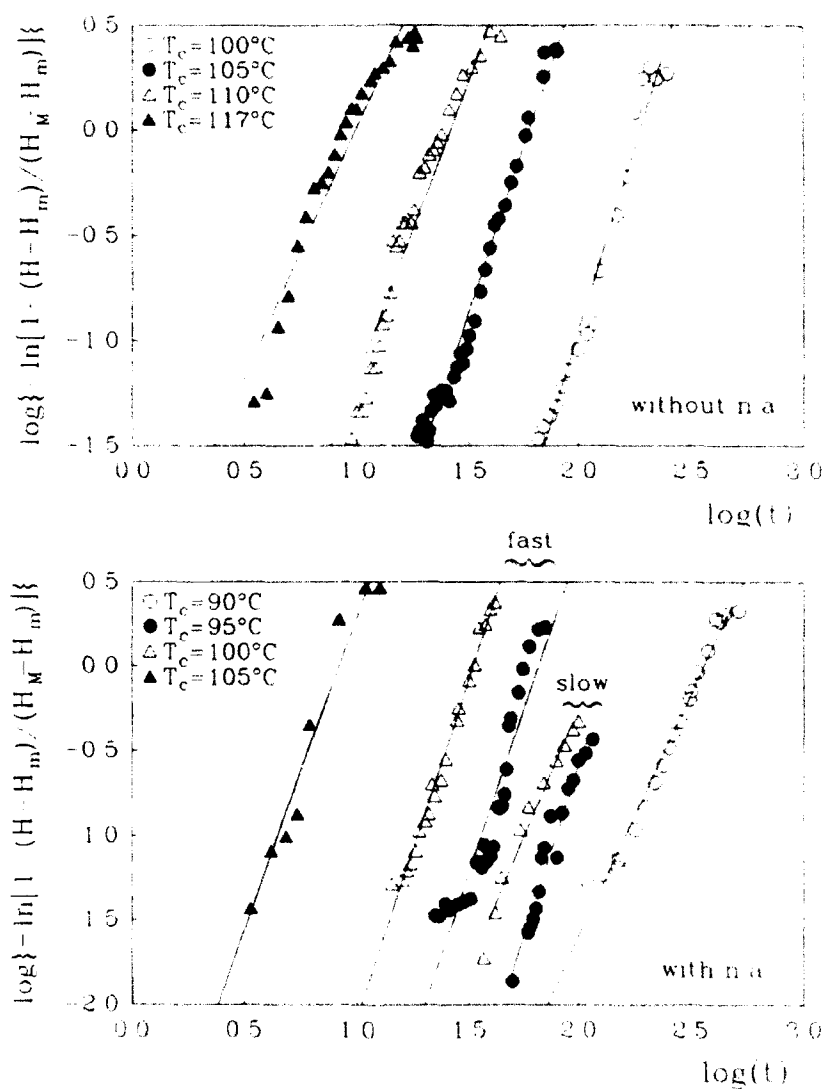


Figure 5  
Variation of  $\log\{-\ln[1-(H-H_m)/(H_M-H_m)]\}$  as a function of  $\log(t)$  for PET samples without (a) and with (b) nucleating agent for different crystallization temperatures.

temperatures and for the samples with and without nucleating agent. From the evaluation of such curves one obtains directly the  $n$  and  $G$  values from the slope and from the intercept of the straight line respectively. Fig. 5a shows the data obtained for the samples without nucleating agent. A value of about 3 in the Avrami exponent is observed for all the temperatures investigated (see table 1). The obtained value of  $n=3$  supports the concept of a three-dimensional spherulitic growth with a fixed number of nuclei born at  $t=0$  (homogeneous nucleation). On the other hand, for samples with nucleating agent (Fig. 5b) one observes two regions corresponding to an independent contribution of a slow and a fast crystallization rate to the  $H$ -variation obtained in Fig. 2a. There is a first region characterized by a rapid increase of the  $H$ -values with an Avrami exponent  $n=3$  and a second region also with  $n=3$ . These two regions can be interpreted in terms of a simultaneous crystallization from  $t=0$  due to two independent modes: i) A fast crystallization mode starting from the nuclei provided by the nucleating agent which appear at  $t=0$  within the sample. The spherulites grow from these nuclei up to a limited value when the nucleating agent is saturated. At this stage, the spherulites do not fill yet the whole volume of the sample. ii) A slow homogeneous crystallization mode starting spontaneously from self nuclei which is superposed to the fast crystallization mode.

It is to be noted that the nucleating agent does not change the Avrami exponent. However, it provides a much larger number of nuclei (proportional to  $G$ ) than the number of self nuclei appearing within the amorphous material (See table 1). Therefore, the crystallization for the sample with nucleating agent starts immediately at  $t=0$  and shows a faster crystallization rate than the sample without agent.

**Table 1.-** Experimental values for the crystallization temperatures,  $T_c$ , Avrami exponent,  $n$ , and Avrami constant,  $G$ , for different PET samples investigated

Samples	$T_c(^{\circ}\text{C})$	$n$		$G$	
without n.a.	100	3.3		$1.22 \times 10^{-8}$	
	105	3.1		$2.98 \times 10^{-6}$	
	110	2.9		$1.02 \times 10^{-4}$	
	117	2.7		$4.90 \times 10^{-3}$	
with n.a.	90	2.8		$4.90 \times 10^{-8}$	
	95	3.0	3.3	$5.5 \times 10^{-5}$	$2.3 \times 10^{-8}$
	100	3.2	3.0	$1.2 \times 10^{-5}$	$5.9 \times 10^{-7}$
	105	3.3		$2.44 \times 10^{-4}$	

For temperatures lower than  $T_c=95^{\circ}\text{C}$  and higher than  $T_c=100^{\circ}\text{C}$  only one slope is observed with an Avrami exponent equal to  $n=3$ . This means that in these cases there exists an homogeneous nucleation corresponding to a slow crystallization mode. At low temperatures ( $T_c=90^{\circ}\text{C}$ ) the nuclei appear within the sample because the time required to crystallize is very large ( $t_c=300$  min) and nuclei can be formed from the amorphous polymer. In this case the fast crystallization process is not observed because the crystallization temperature is too low. On the other hand, for temperatures larger than  $100^{\circ}\text{C}$  ( $T_c=105^{\circ}\text{C}$ ) there appears also one single region of crystallization. (Figs. 2a and 5b). This is because the temperature of crystallization is very high and the crystallization proceeds so rapidly that it seems reasonable to associate it to the fast mode.

Finally, the Avrami constant,  $G$ , increases with temperature of crystallization (table 1) indicating that the number of crystallization nuclei increases with increasing crystallization temperature.

From the change of  $H$ , the half-time of crystallization,  $\tau_{1/2}$ , can be determined. This value represents the time required to obtain one half the maximum  $H$ -value. In Fig. 6  $\tau_{1/2}$  is represented as a function of crystallization temperature for all the samples investigated. As can be observed the nucleating agent reduces the half-time of crystallization considerably at a given crystallization temperature.

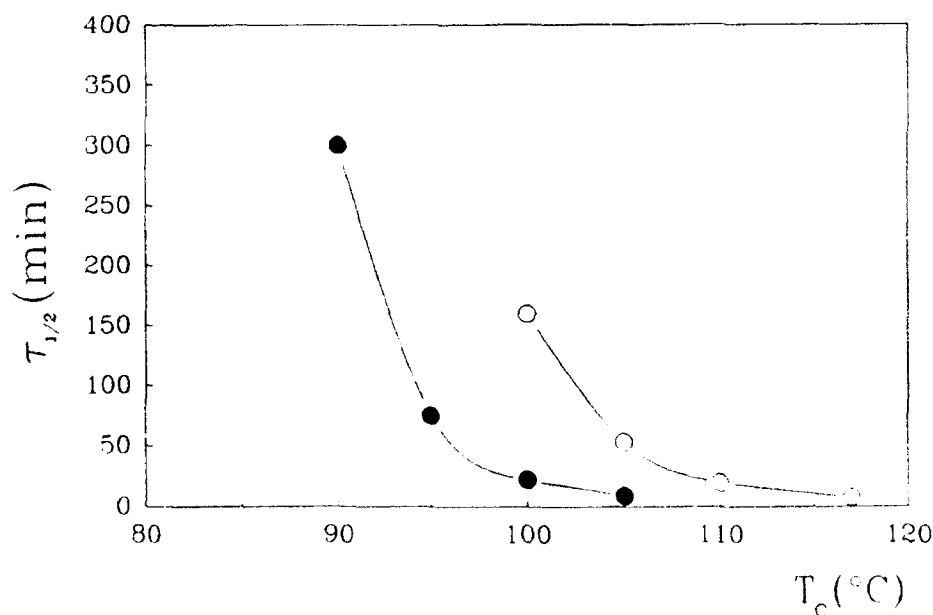


Figure 6  
Variation of the half-time of crystallization,  $\tau_{1/2}$ , as a function of crystallization temperature,  $T_c$ , for the investigated PET samples.

#### 4.4 Influence of crystallization temperature on the limiting value of Hardness

For samples of PET crystallized without nucleating agent the crystallinity obtained at the end of crystallization (table 2) is slightly larger than  $\alpha=0.22$ . This indicates that for these samples primary crystallization is completed<sup>11)</sup> (volume fraction of spherulites  $\phi=1$ ) leading to a constant microhardness value for each crystallization temperature. From table 2 and Fig. 1a one also sees that the time,  $t_c$ , needed to reach the leveling off value  $H_M$  drastically decreases with increasing  $T_c$ . It is noteworthy that for these samples without nucleating agent the final  $H_M$ -value is the same (100MPa) for all crystallization temperatures. This result is consistent with the final value obtained of  $H \approx 220$ MPa for the semicrystalline solidified sample measured at room temperature. The latter H-value is equal to the sum of  $H_a=120$ MPa (hardness of the glassy material) and  $H_M=100$ MPa.

However, for the samples with nucleating agent (Fig. 2) the crystallinity value at the end of the crystallization process depends on  $T_c$ . Here the value of  $\alpha$  increases from  $\alpha=0.179$  ( $\phi=0.81$ ) for the sample crystallized at  $T_c=90^\circ\text{C}$  up to  $\alpha=0.22$  ( $\phi=1$ ) for the sample crystallized at  $T_c=105^\circ\text{C}$ . Since, for the PET samples with nucleating agent after primary crystallization  $\phi < 1$ , one concludes that the material is not fully occupied by spherulites. Consequently, the final  $H_M$ -value is a function of the volume fraction of spherulites. As a result, the maximum H-value obtained for the PET samples with nucleating agent, measured at room temperature is a linear function of the volume fraction occupied by spherulites,  $\phi$ , as shown in Fig. 7. This linear dependence between  $H_M$  and  $\phi$  is similar to the correlation found between these two quantities in a preceding study<sup>11)</sup>.



**Table 2.-** Experimental values for the crystallization temperatures,  $T_c$ , crystallization time to reach the limiting H-value,  $t_c$ , density,  $\rho$ , crystallinity,  $\alpha$ , and volume fraction of occupied by spherulites.

Samples	$T_c(^{\circ}\text{C})$	$t_c(\text{min})$	$\rho(\text{g/cm}^3)$	$\alpha$	$\phi$
without n.a.	100	240	1.3691	0.224	1
	105	120	1.3727	0.249	1
	110	60	1.3738	0.257	1
	117	25	1.3746	0.262	1
with n.a.	90	480	1.3627	0.179	0.81
	95	180	1.3660	0.195	0.89
	100	150	1.3683	0.210	0.97
	105	15	1.3693	0.225	1

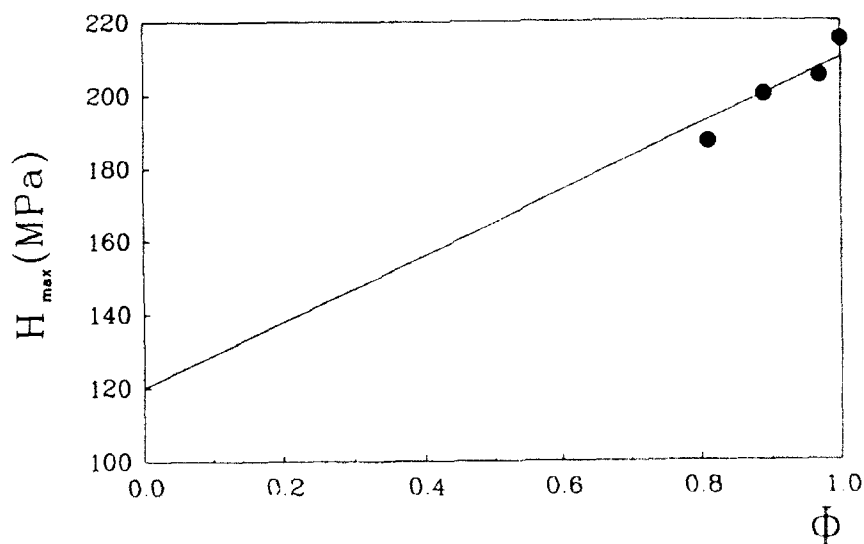


**Figure 7**  
Variation of the limiting microhardness value at the end of the primary crystallization process, measured at room temperature, as a function of the volume fraction occupied by the spherulites,  $\phi$ .

Most striking is the fact that for samples with nucleating agent (Fig. 2) with  $\Phi=1$  and  $\alpha=0.21-0.22$  ( $T_C \approx 100-105^\circ\text{C}$ ), the limiting  $H_M$ -value is much larger than for the samples without nucleating agent (Fig. 1). This result might be connected with a hardening effect of the material at high temperatures due to the influence of the nucleating agent. In a previous work the influence of the nucleating agent in reducing the level of lattice distortion in the spherulites was pointed out<sup>17)</sup>. This would explain why the samples with nucleating agent, having more nuclei yield a higher H-value than the samples without nucleating agent.

Comparison of the H-data from Fig. 7 for the samples with nucleating agent measured at room temperature with the  $H_M$  limiting values obtained at high temperatures in Fig. 2 -if one assumes that  $H_a = \text{const}$  at room temperature- shows that the hardness of the spherulites ( $H_{\text{sph}}$ ) is larger at high temperatures than at room temperature. From this result one concludes that the microhardness of the spherulites must suffer a decrease after solidification at room temperature. One may think that this decrease is partly due to a material relaxation during cooling which contributes to a softening of the spherulites at room temperature. On the other hand, the lower  $H_a$ -values obtained for the aged polymer with nucleating agent (110MPa) (Fig. 4a), in contrast with  $H_a \approx 120\text{MPa}$  for the polymer without nucleating (Fig. 4b) agent, might also contribute to the observed smaller values of H at room temperature for the former samples.

## 5. CONCLUSIONS

During primary crystallization of PET, at least, the following transitions can be distinguished using the microhardness technique:

- a) A pre-glass transition, also known as physical aging, which shows a hardening below  $T_g$  after long storage time. This transition involves local molecular ordering and parallelization of benzene rings of neighboring molecules.
- b) A glass transition giving rise to a well defined softening behaviour involving local segmental motions.
- c) A precrystallization effect observed in the aged material, which shows up as a time and temperature dependent hardening of the material. This effect probably involves long segmental motions and yields a "paracrystalline" or "liquid crystalline" state which is not stable and disappears before the onset of the crystallization
- d) Triclinic crystallization giving rise to a true final hardening of the material which can be: i) a fast process if crystallization starts from the nucleating agent or ii) a slow process if self nucleation takes place.

## 6. ACKNOWLEDGEMENTS

This work forms part of a wider study carried out in collaboration with Dr. J.C. Santa Cruz and Dr. T. Asano, Shizuoka University.

## 7. REFERENCES

- 1. F.J. Baltá Calleja, *Advances in Polym. Sci.* **66**, 117 (1985)
- 2. Y. Deslandes, E. Alva Rosa, F. Brise, T. Meneghini, *J. Mater. Sci.*, **26**, 2769 (1991)
- 3. J. Bowman, M. Bevis, *Colloid & Polym. Sci.* **255**, 954 (1977)
- 4. R.J. Crawford, *Polym. Testing* **1**, 37 (1982)
- 5. B. Darlix, B. Monasse, P. Montmitonnet, *Polym. Testing*, **6**, 107 (1986)

6. B. Martín, J.M. Pereña, J.M. Pastor, J.A. de Saja, J. Mater. Sci. Lett. 5, 1027 (1986)
7. F.J. Baltá Calleja, J. Martínez Salazar, T. Asano, J. Mater. Sci. Lett. 7, 165 (1988)
8. F.J. Baltá Calleja, H.G. Kilian, Colloid and Polymer Sci. 266, 29 (1988)
9. F. Ania, J. Martínez Salazar, F.J. Baltá Calleja, J. Materials Sci. 24, 2934 (1989)
10. R.H. Ion, H.M. Pollock, C. Roques-Cames, J. Mater. Sci. 25, 1444 (1990)
11. C. Santa Cruz, F.J. Baltá Calleja, H.G. Zachmann, N. Striebeck T. Asano. J. Polym. Sci. Polym. Phys. Ed. B29, 819 (1991)
12. A. Keller, G.R. Lester, L.B. Morgan, F.D. Hartley. E.W. Lord, Phil. Trans. R. Soc. A247, 1, 13, 23 (1954)
13. H.G. Zachmann, H.A. Stuart. Makromolekulare Chem. 41, 131 (1960)
14. G. Elsner, M.H.J. Koch, J. Bordas, H.G. Zachmann, Makromol. Chem. 181, 1263 (1981)
15. G. Elsner, C. Rickel, H.G. Zachmann, Adv. Polym. Sci. 67, 1 (1985)
16. B. Günter, H.G. Zachmann, Polymer, 24, 1008 (1983)
17. T. Asano, A. Zdeick-Pickuth, H.G. Zachmann, J. Mater. Sci. 24, 1967 (1989)
18. F.J. Baltá Calleja, J. Martínez Salazar, D.R. Rueda. Encycl. Polym. Sci. and Eng. Wiley-Interscience, 6, 614 (1986)
19. J.N. Hay, 23 Europhys. Conf. Macromol. Phys. Stockholm, Europhys. Conf. Abst. 15b, L9 (1991)
20. R.F. Boyer, Polymer Yearbook, p233 (1988)
21. F. Ania, H.G. Kilian, F.J. Baltá Calleja, J. Mater. Sci. Lett. 5, 1183 (1986)
22. B. Wunderlich, "Macromolecular Physics" Vol.2 Academic Press New York, S. Francisco, London, p.131 (1976)

## NANOCRYSTALLINE MATERIALS BY CRYSTALLIZATION OF ZR-BASED METALLIC GLASSES

U. KÖSTER

Dept.Chem.Eng., University of Dortmund, Dortmund, F.R. Germany,

T. SPASSOW

Dept.Chem., Kliment-Ohridski-University, Sofia, Bulgaria

and

M. SUTTON

Dept.Phys., McGill-University, Montréal, Canada H3A 2T8.

### ABSTRACT

Crystallization of intertransition-metal glasses with 67 at.% Zr been studied by means of transmission electron microscopy as well as time resolved x-ray diffraction. Above the glass transition temperatures in all these glasses the very fast crystallization of a metastable fcc phase (e.g.,  $\text{CoZr}_2$ :  $a = 12.2 \text{ \AA}$ ) was observed thus leading to nanocrystalline microstructures. In  $\text{Co}_{33}\text{Zr}_{67}$  this metastable compound transforms during further annealing first into another metastable phase with hexagonal structure ( $a = 8.76 \text{ \AA}$ ;  $c = 19.5 \text{ \AA}$ ). Analysis of the grain diameter versus annealing times in partially crystallized glasses as well as nanocrystalline microstructures identifies clearly polymorphous crystallization prior to any grain growth of the nanocrystalline fcc phase.

### INTRODUCTION

Crystallization of metallic glasses proceeds by nucleation and growth processes. Thus controlling these processes enables tailor-made microstructures, e.g. nanocrystalline materials. In metal-metalloid glasses below the glass transition nucleation is heterogeneous and crystallization is controlled by diffusion; above the glass transition crystallization is controlled by viscous flow and nucleation occurs by a transient type homogeneous reaction. The smallest grain size in metal-metalloid glasses which was formed by polymorphous crystallization, e.g. in  $\text{Fe}_{65}\text{Ni}_{10}\text{B}_{25}$ , was found to be only  $0.1 \text{ }\mu\text{m}$ ; primary crystallization of particular glasses, e.g. FINEMET, can lead to much smaller grain sizes, even to nanocrystalline microstructures [1]. Nanocrystalline microstructures, however, are known to be formed even by polymorphous crystallization in zirconium-based transition metal glasses [2,3,4,5]. The aim of this paper is to investigate in more detail the crystallization of such zirconium-based transition metal glasses above their glass transition temperatures.

## EXPERIMENTAL

Ribbons of binary as well as ternary  $\text{TM}_{33}\text{Zr}_{67}$  glasses ( $\text{TM} = \text{Fe, Co, Ni}$ ) were prepared by melt-spinning onto a copper wheel (diameter 250 mm) in a helium atmosphere of 400 mbar. Microstructures with the smallest grain size can be crystallized only at temperatures above the glass transition temperature, but still far below the "nose" in the TTT-diagram. Close to the glass transition temperature, however, crystallization in most metallic glasses is known to proceed so rapidly that partially crystallized microstructures could not be obtained. To ensure crystallization only during the isothermal annealing and not during heating up, the samples had to be annealed using rapid heating methods, e.g. by electrical current pulses. This pulse-heating technique was combined with *in situ* resistivity measurements and time-resolved x-ray diffraction using synchrotron radiation, on time scales as milliseconds [1,5]. The microstructure at various stages of the crystallization was studied by TEM. Only the middle part of a ribbon, which do not exhibit any temperature gradient during the pulse heating, was used for TEM. Specimen were thinned by electrolytic jet polishing using an electrolyte of 3 parts methanol, 1 part glycerine and 1 part  $\text{HNO}_3$  followed by ion beam milling.

## RESULTS AND DISCUSSION

In all  $(\text{Ni, Co, Fe})_{33}\text{Zr}_{67}$  glasses investigated at temperatures below the glass transition nucleation of the tetragonal equilibrium phase was observed to proceed by a transient type homogeneous reaction. Above the glass transition temperature, however, the very fast crystallization of a metastable fcc phase (e.g.,  $\text{CoZr}_2$ :  $a = 12.2 \text{ \AA}$ ) was found thus leading to a nanocrystalline microstructures. These metastable fcc phases transform during further annealing into the stable equilibrium tetragonal phase. Only in  $\text{Co}_{33}\text{Zr}_{67}$  (see fig. 1) this metastable fcc phase transforms during further annealing first into another metastable phase with hexagonal structure ( $a = 8.76 \text{ \AA}$ ;  $c = 19.5 \text{ \AA}$ ). Kinetics of these transformation reactions were studied in detail by quantitative metallography as well as by time-resolved x-ray diffraction, thus leading to time-temperature-transformation diagrams as shown for  $\text{Co}_{33}\text{Zr}_{67}$  in fig. 2.

In  $\text{Ni}_{33}\text{Zr}_{67}$  glasses [5] the lines for 5% crystallized volume for the metastable fcc phase ( $a = 12.6 \text{ \AA}$ ) as well as the stable bct phase as obtained from fitting the time-resolved x-ray data have a slope corresponding to an activation energy of 290 and 260 kJ/mole for the fcc and bct phase, respectively. The 95% line for the bct phase gives an activation energy of 193 kJ/mole, suggesting that the growth process has a lower activation energy than the nucleation.

The thermal stability of binary  $\text{TMZr}_2$ -glasses as well as their nanocrystalline microstructures has been found to increase in the sequence:  $\text{Ni} \rightarrow \text{Co} \rightarrow \text{Fe}$  and is closely related to the filling of the d-band. The nanocrystalline fcc  $\text{FeZr}_2$  phase

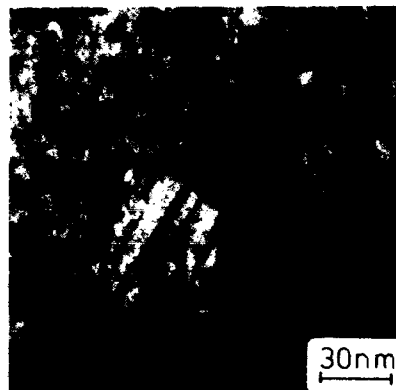


Fig. 1:  
Transformation of the nanocrystalline metastable fcc  $\text{CoZr}_2$  into the much coarser metastable hexagonal phase.

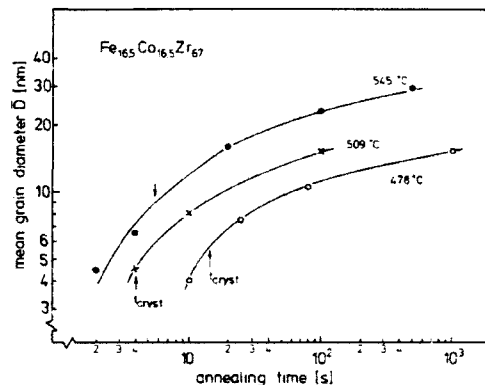


Fig. 3:  
Grain growth in partially crystallized as well as nanocrystalline fcc  $(\text{Fe,Co})\text{Zr}_2$ .

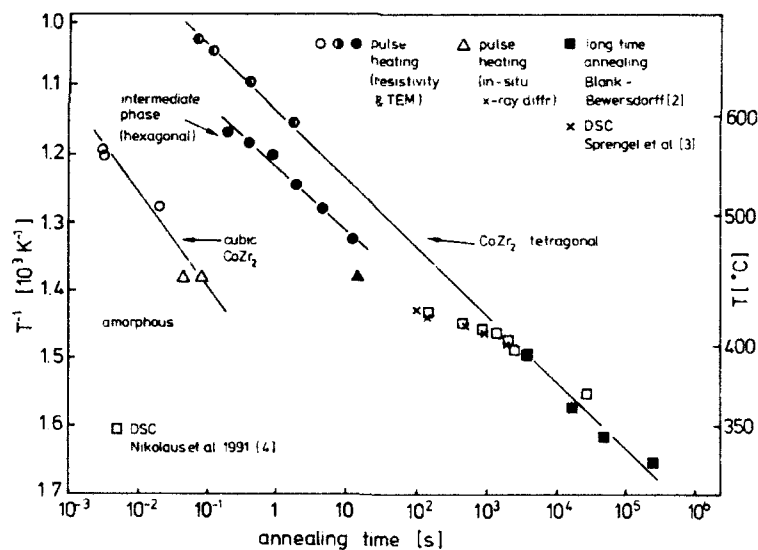


Fig. 2: Time-temperature-transformation diagram for  $\text{Co}_{33}\text{Zr}_{67}$  glasses

( $a = 12.2 \text{ \AA}$ ) transforms much slower than the other metastable fcc  $\text{TMZr}_2$  compounds, i.e. only at very high temperatures or after very long annealing. Therefore, this glass and even better the ternary  $\text{Fe}_{16.5}\text{Co}_{16.5}\text{Zr}_{67}$  glass can be

used to study crystallization and coarsening of the nanocrystalline phase during annealing in detail. As shown in fig. 3 the mean crystal diameter can be described best by the following equation:

$$D = 2 \cdot u_{\text{cryst}} \cdot t \quad \text{for } t < t_{\text{cryst}}$$

$$D = 2 \cdot u_{\text{cryst}} \cdot t_{\text{cryst}} + c_{\text{gg}} \cdot (t - t_{\text{cryst}})^{1/3} \quad \text{for } t > t_{\text{cryst}}$$

where  $u_{\text{cryst}}$  is the crystal growth rate during polymorphic crystallization,  $t_{\text{cryst}}$  the time for complete crystallization and  $c_{\text{gg}}$  a constant for the grain growth. It is of interest that the finest fully crystalline microstructure in this alloy can be formed only at an intermediate crystallization temperature.

It was not clear whether the nanocrystalline metastable fcc phase is always a precursor to the formation of the equilibrium phase, at all temperatures and even below the glass transition temperature. This would lead to the question, whether these rapidly quenched alloys are real glasses or extremely fine nanocrystalline microstructures which undergo only some grain growth prior to the transformation into the more stable tetragonal or hexagonal phases. As shown above the grain growth analysis indicates strongly that prior to any grain coarsening there is polymorphic crystallization with linear growth rates for the fcc phase.

So far we do not know whether the formation of nanocrystalline microstructures in the  $\text{TM}_{33}\text{Zr}_{67}$  glasses is unique. There is some evidence that the formation of nanocrystalline microstructures is limited to a narrow concentration band. In Ti-based glasses hydrogen additions have been found to lead to a dramatic reduction in grain size [6]. Further systematic work on the influence of the Zr-content as well as of hydrogen additions on the crystallization is underway.

## REFERENCES

1. U.Köster, U.Schünemann, M.Blank-Bewersdorff, S.Brauer, M.Sutton, G.B.Stephenson, Mater.Sci.Eng. **A133** (1991), 611;
2. M.Blank-Bewersdorff, *Kristallisationsverhalten von Zirkon-Basis Gläsern*, Fortschritt-Berichte VDI, Reihe 5: Nr.139, VDI-Verlag Düsseldorf 1987;
3. W.Sprengel, W.Dörner, H.Mehrer, Z.Metallkde. **81** (1990), 467;
4. N.M.Nikolaus, H.R.Sinning, F.Haessner, Mat.Sci.Eng., in press;
5. S.Brauer, J.O.Ström-Olsen, M.Sutton, Y.S.Yang, A.Zaluska, G.B.Stephenson, U.Köster, Phys.Rev., in press
6. D.Menzel, A.Niklas, U.Köster, Mater.Sci.Eng. **A133** (1991), 312.



## CRYSTALLIZATION KINETICS IN NANOCRYSTALLINE MATERIALS

S. SURINACH, A. OTERO, M. D. BARÓ, M. T. CLAVAGUERA-MORA

*Física de Materials, Departament de Física,  
Universitat Autònoma de Barcelona, 08193 Bellaterra, Spain*

and

N. CLAVAGUERA

*Departament d'Estructura i Constituents de la Matèria, Facultat de Física,  
Universitat de Barcelona, Diagonal 647, 08028 Barcelona, Spain*

## ABSTRACT

The crystallization behaviour of  $\text{Fe}_{73.5}\text{Cu}_1\text{Nb}_3\text{Si}_{13.5}\text{B}_9$  ribbons obtained by planar flow casting is studied by differential scanning calorimetry, X-ray diffraction and transmission electron microscopy. From the crystallization kinetics results, the lower part of experimental heating rate-temperature and time-temperature transformation curves are deduced.

## 1. Introduction

During the last decades metallic glasses have been intensively studied for their physical as well as technically applicable properties, but it was known that their excellent magnetic properties were irreparably lost upon crystallization. The discovery of a new ferromagnetic iron-based class of metallic glasses brings about amorphous materials which exhibit outstanding magnetic properties after partial crystallization<sup>1</sup>. An example of such new materials is  $\text{Fe}_{73.5}\text{Cu}_1\text{Nb}_3\text{Si}_{13.5}\text{B}_9$ . The samples were cast initially as amorphous ribbons, and by subsequent annealing above the crystallization temperature a homogeneous ultrafine grain structure of  $\alpha$ -Fe(Si) with a typical diameter of 10-20 nm and random texture was created within the amorphous matrix. The hysteresis loop, magnetostriction and domain structure of the as cast material and the nanocrystalline structure have been investigated and, in the later, a change of sign of the magnetostriction constant was found varying with the external field<sup>2</sup>. Mössbauer studies of the nanocrystalline structure<sup>3</sup> lead to the conclusion that it corresponds to fine grains of  $\text{Fe}_{1-x}\text{Si}_x$  ( $0.18 \leq x \leq 0.23$ ) alloys with the  $\text{DO}_3$  structure. Further studies have shown that on increasing the annealing temperature both the grain size and the coercivity increased<sup>4</sup>. The aim of the present work is to report detailed information on the crystallization behaviour of this primary crystallizing metallic glass.

## 2. Experimental and results

The alloys studied were kindly supplied in ribbon form by Dr. G. Herzer of Vakuumschmelze GmbH. The study has been performed by differential scanning calorimetry (DSC), X-ray diffraction (XRD) and transmission electron microscopy (TEM).

Figure 1 shows the DSC curves for the as-quenched ribbon and for a ribbon thermally relaxed. Curve (A) corresponds to the as-quenched ribbon and has been obtained when heating at 40 K/min. The ferro-paramagnetic transformation is observed as a peak at the Curie temperature  $T_C = 589$  K. Further a broad exothermic process occurs which is related to the relaxation of the as-quenched glass. On heating up to 800 K and cooling to room temperature the sample is thermally relaxed. Therefore, for a thermally relaxed sample, as shown in curve (B), the broad exothermic transformation is no longer present and the Curie temperature of the relaxed glass is shifted to a higher temperature ( $T_C = 611$  K) due to the reduction of the free volume. In both samples, the crystallization occurs in two steps as seen in the DSC curves. The first step begins at about 800 K and ends at about 934 K and is followed by a second step which ends at about 1000 K.

To elucidate the nature of the phases formed in the crystallization process, samples heated at 40 K/min up to several temperatures, indicated by arrows in Figure 1, have been analyzed by XRD and TEM. Figure 2 shows the evolution of the XRD pattern at those temperatures. The as-quenched sample has an amorphous structure, which evolves with increasing temperature. After completion of the first crystallization step (point d in Figure 1), a diffraction pattern (curve d in Figure 2) is obtained which corresponds to the presence of  $\alpha$ -Fe(Si) with a cell parameter of  $a=0.285$  nm. New Bragg peaks appear on further heating and they develop until full crystallization. The precise nature of this complex diffraction pattern is not yet determined. TEM images show when heating up to 825 K primary crystals with a mean size of about 10 nm and they increase in size on further heating. In the fully crystalline sample the presence of eutectic-like microstructures in lamellar form is apparent.

To explain the calorimetric behaviour during crystallization, we assume that each crystallization step is due to a rate of reaction given by

$$dx/dt = k(T)f(x) \quad (1)$$

where  $k(T)$  is the rate constant normally with an Arrhenius behaviour

$$k(T) = k_0 \exp(-E/RT) \quad (2)$$

$E$  being the apparent activation energy,  $k_0$  the pre-exponential factor and  $f(x)$  is a function that reflects the limiting mechanism of crystallization.

An utility of the study of the crystallization kinetics is the determination of the Temperature-Heating Rate-Transformation (T-HR-T) curves and the Time-Temperature-Transformation (T-T-T) curves for this metallic glass. Such diagrams are very powerful to predict the transformation that may occur when heat-treating the metallic glass. The T-HR-T curves give the loci of the points where a certain degree of crystallization has been achieved for each temperature, as a function of the heating rate used in the experiment<sup>5</sup>. To obtain the T-HR-T curves we proceed by integrating equation (1) at a constant heating rate, namely

$$\int_0^x \frac{dx}{k_0 f(x)} = \frac{1}{\beta} \int_0^T \exp(-E/RT) dT \quad (3)$$

It should be stressed that in general the extent of crystallization,  $x$ , is not itself a state function of temperature and time like its derivative,  $dx/dt$ , but for a process starting with an amorphous sample and heating at a constant rate, equation (3) gives the extent of crystallization as a function of temperature and heating rate, that is,  $x = x(T, \beta)$ . As a consequence, assuming a fixed value of  $x$ , equation (3) can be represented in a diagram that shows the temperature versus the heating rate used to obtain that fixed value of  $x$ .

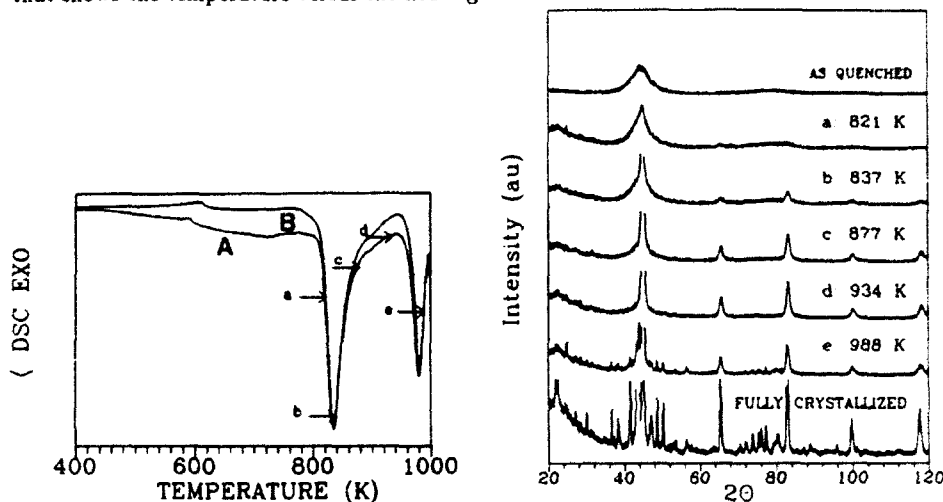


Fig.1.- (left) DSC curves for the as-quenched ribbon (A) and for a ribbon thermally relaxed (B).

Fig.2.- (right) XRD patterns for ribbons heated up to different temperatures (see Fig. 1).

The resulting T-HR-T curves for various values of  $x$ , for the first crystallization step, are shown in Figure 3. Also shown in this figure are the experimental points. Since crystallization is an activated process, the crystallization rate has an exponential form and time spent at temperatures below the critical one necessary to get an appreciable crystalline fraction is to a large degree lost. In this respect, as seen in this figure, the plateau region is normally the most useful in practical applications because it combines the attainment of the desired proportion of crystallized sample with a moderate energy cost. Another property of the T-HR-T curves is that they can be used to indicate how far in temperature one has to go when heating the glassy sample to get a partially crystalline material.

Under isothermal conditions, the integrated form of the kinetic equation (1) is

$$\int_0^x \frac{dx}{k_0 f(x)} = t \exp(-E/RT) \quad (4)$$

With the same remarks as before for the integration of equation (3), the explicit form of  $x = x(T, t)$  has been obtained and the T-T-T curves have been constructed. They are

presented in Figure 4. It is interesting to note that, for annealing times of about 1 hour, the first crystallization step begins to occur at about 770 K (500°C) and ends at about 830 K (550°C). These results can be correlated with the fact that the soft magnetic properties of this metallic glass become excellent after annealing for 1 hour at 510–550°C<sup>4</sup>.

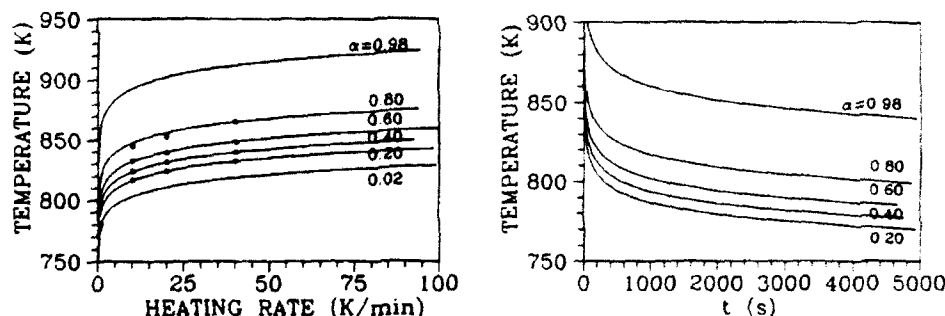


Fig.3.- (left) Temperature-Heating Rate-Transformation (T-HR-T) curves.

Fig.4.- (right) Time-Temperature-Transformation (T-T-T) curves.

### 3. Conclusions

The crystallization behaviour of  $\text{Fe}_{73.5}\text{Cu}_1\text{Nb}_3\text{Si}_{13.5}\text{B}_9$  ribbons obtained by planar flow casting has been studied by DSC, XRD and TEM. From the crystallization kinetics results the lower part of experimental heating rate-temperature and time-temperature transformation curves are deduced. Further we can conclude that excellent soft magnetic properties can also be obtained by heating the metallic glass up to about 850 K (580 °C) with heating rates in the range 20 to 80 K/min.

### 4. Acknowledgements

The authors wish to acknowledge gratefully Mr. X. Alcobé from the "Serveis Científico-Tècnics" of the University of Barcelona for the X-ray diffraction measurements. This work was supported by the CICYT (project No. MAT90-0454).

### 5. References

1. Y.Yoshizawa, S.Oguma and K.Yamauchi, *J. Appl. Phys.* **64** (1988) 6044
2. R.Grössinger, R.Heszke, A.Hernando, O.Mayerhofer, K.H.Müller, Ch.Pollak, E.Pulido, G.Rivero and J.Schneider, *IEEE Trans. Mag.* **26** (1990) 1403
3. J.Jiang, T.Zemcik, F.Aubertin and U.Gonser, *J.Mater. Sci. Lett.* **10**(1991) 763
4. G.Herzer, *IEEE Trans. Mag.* **26**(1990) 1397
5. S.Suriñach, M.D.Baró, J.A.Diego, N.Clavaguera and M.T.Clavaguera-Mora, *Acta metall. mater.*(1991) in press.

## MAGNETIC AND STRUCTURAL CHARACTERISATION OF NANOCRYSTALLINE Fe-Cu-Nb-Si-B ALLOYS.

M.Vázquez and P.Marín

*Instituto de Ciencia de Materiales, Serrano 144. 28006 Madrid*

J.González

*Dpto de Física de Materiales Fac.Químicas. 20009 San Sebastián*

A. Hernando and E.Pulido

*Instituto de Magnetismo Aplicado. RENFE-U.C.M. 28230 Madrid*

### ABSTRACT

Magnetic and structural characterization of  $\text{Fe}_{73.5}\text{Cu}_1\text{Nb}_3\text{Si}_{13.5}\text{B}_9$  and  $\text{Fe}_{73.5}\text{Cu}_1\text{Nb}_3\text{Si}_{16.5}\text{B}_6$  alloys has been performed after various isochronal and isothermal treatments. The softest magnetic behavior is found after thermal treatment during around 30 min at 540°C when carried out in conventional furnace. The current annealing technique has been successfully used to reproduce very similar results as those obtained by heating in a furnace. Nucleation and stabilization of nanocrystalline microstructure is responsible for such very soft magnetic behavior.

### 1. Introduction

The microstructure of amorphous alloys obtained by rapid quenching from the melt is characterised by the lack of long range order. Nevertheless, randomly oriented short range ordered units with size up to around 10-20 Å can be present. As a consequence of the absence of magnetocrystalline anisotropy, these materials magnetically behave as very soft. Macroscopic magnetic behavior is then determined by the intrinsic magnetoelastic anisotropies arising from the coupling between internal stresses and magnetization through the magnetostriction constant. After annealing at elevated enough temperature, the amorphous microstructure deteriorates as a consequence of the nucleation and growth of crystallites. The inhomogeneous distribution of crystallites as well as the appearance of non-vanishing macroscopic magnetocrystalline anisotropy then give rise to a magnetic hardening of the material.

However, as recently shown, thermal treatments above the crystallization temperature performed in some Fe-rich amorphous alloys containing small additions of Cu and Nb results in a striking magnetic softening of the material. This effect has been ascribed to the nucleation of  $\alpha$ -Fe Si fine grains with typical grain size in the range of tens of nanometers<sup>1,2</sup>. Such stable and homogeneous microstructure seems

to be related to the presence of Cu and Nb atoms which promote nucleation of grains and hinder their growth, respectively. According to the random anisotropy model, this soft magnetic behavior is a consequence of the small grain size created by annealing<sup>3</sup> which gives rise to a still minute macroscopic magnetocrystalline anisotropy and also to a reduction of internal stresses and effective magnetostriction.

The aim of the present work has been to present new results concerning the influence of various thermal treatments above the crystallization temperature on the hysteresis loops and their typical parameters. Particular emphasis is laid on the variations of coercive field.

## 2. Experimental techniques

Amorphous alloy ribbons obtained by melt-spinning technique and with nominal compositions  $\text{Fe}_{73.5}\text{Cu}_1\text{Nb}_3\text{Si}_{13.5}\text{B}_9$  (S1) and  $\text{Fe}_{73.5}\text{Cu}_1\text{Nb}_3\text{Si}_{16.5}\text{B}_6$  (S2) were kindly provided by Dr. G. Herzer of Vacuumschmelze GmbH, Hanau. Thermal treatments were performed by means of a conventional field-free furnace in argon atmosphere. Treatments were carried out either isochronally (1h) in the range of temperatures from 460 to 640°C, or isothermally (540 or 620°C) for different annealing times (up to 4h). Alternatively, samples were annealed by the current annealing technique which is based on the heating by the Joule effect produced when an electrical current flows along the sample<sup>4</sup>. In this case, isochronal treatments (1 min) were performed for different current densities flowing along the samples up to a maximum value of 51  $\text{Amm}^{-2}$ . This alternative technique has been successfully used to induce magnetic anisotropies in amorphous alloys. Its main advantage is the short annealing time necessary to get similar results as those obtained when annealing in furnaces for much longer times.

Hysteresis loops of the samples have been obtained by conventional low frequency induction and by extraction methods. Crystallization of the samples was followed with the help of a DSC-7 Perkin Elmer calorimeter at a heating rate of 8  $\text{Kmin}^{-1}$ . Also, X-ray diffraction studies were performed on samples after thermal treatments.

## 3. Experimental results and discussion.

Fig.1 shows the evolution of coercive field,  $H_c$ , for samples S1 and S2 as a function of annealing temperature for isochronal treatments (1h). Similar behavior is observed for both samples with minimum values around 530 and 560°C for S2 and S1, respectively. A drastic increase of  $H_c$  is obtained at 640°C for S1 and at 620°C for S2. In order to get further information about the dependence of  $H_c$  on annealing parameters, isothermal treatments were performed at 540°C and 620°C (see figures

2a and 2b). Values of  $H_c$  for S2 are slightly larger than those for S1 after annealing at 540°C. After a drastic initial reduction of coercive fields for annealing times around 20 to 30 min, their values are relatively stabilized for longer annealing time. The X-ray data after treatments for different annealing times show typical  $\alpha$ -Fe peaks, with decreasing breadth for longer annealing time. Also, from the analysis of the lines profile we can deduce a slightly larger grain size for the sample S2. That would give rise to larger magnetocrystalline anisotropy contribution to  $H_c$  although its magnetoelastic contribution is reduced in comparison (note that after annealing, magnetostriction of S2 takes smaller values than that of S1<sup>5</sup>). This consideration is valid in all the range of annealing temperatures between 500 and 600°C where  $H_c$  for S2 is larger than that of S1 (see Fig.1).

As regards the data obtained by differential scanning calorimetry, it has been found that crystallization peak is broadened in comparison to that of conventional amorphous alloys. It seems to indicate that crystallization kinetics is actually modified by the presence of Cu and Nb atoms.

On the other hand, a further crystallization of the materials occurs when annealing at 620°C for S1 but is delayed around 20°C for S2. This second step of crystallization should be correlated either to an increase of size of  $\alpha$ -Fe grains or

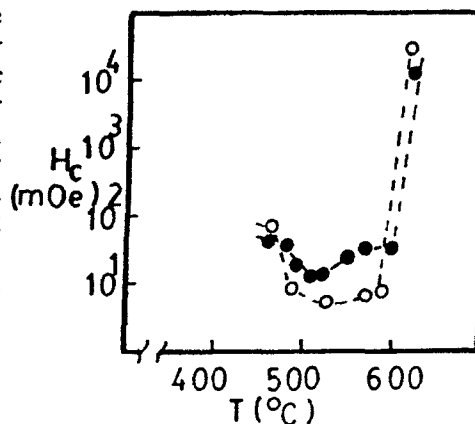


FIG 1. Dependence of coercive field for samples S1 (○) and S2 (●) as a function of annealing temperature. Annealing time was 1h in all the treatments.

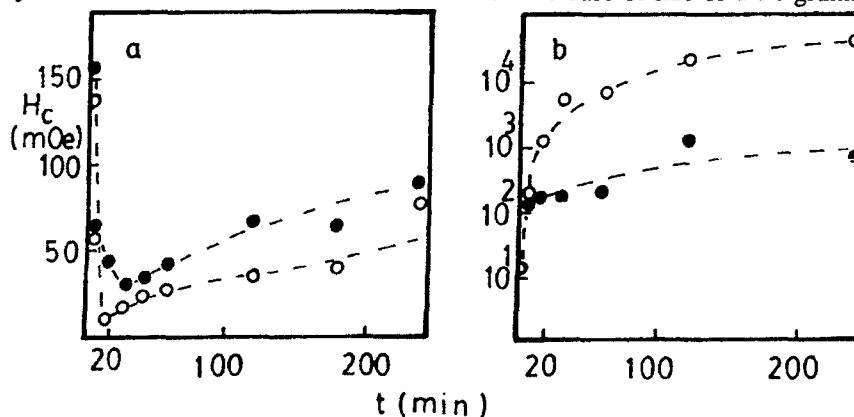


Fig.2 Coercive field of samples S1 (○) and S2 (●) after annealing at 540°C (a) and 620°C (b) for a range of annealing time.

to the nucleation of new phases. This point can not be clearly distinguished from our present X-ray data.

Fig.3 shows the modifications of the coercive field for sample S2 after 1 min current annealing at different current densities. Evolution of  $H_c$  is very similar to that obtained when treatments are performed with the help of a conventional furnace. The decrease of  $H_c$  when annealing between 35 and 47  $\text{Amm}^{-2}$  can be associated to the appearance of a nanocrystalline microstructure, while the final increase would correspond to the second crystallization observed when annealing in the furnace. Moreover, the dependence of saturation magnetization after current annealing is shown in Fig.4 as a function of the current density through the sample (Note that a higher current density corresponds to a higher temperature). The Curie point is modified as a consequence of the nucleation of new magnetic phases in comparison with the initial amorphous one as deduced from Fig.4. Also, the saturation magnetization at room temperature is slightly modified upon annealing. An initial decrease corresponding to nanocrystallization is followed by a final increase associated with the onset in the further crystallization.

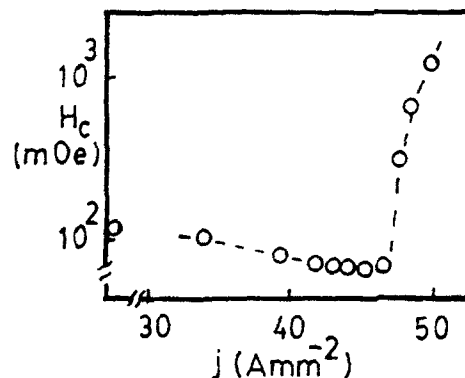


Fig 3. Dependence of coercive field of sample S2 for isochronal (1 min) treatments as a function of current density flowing along the sample.

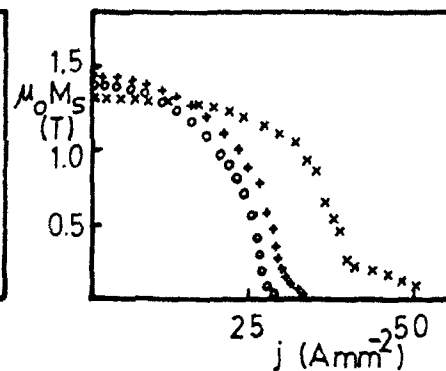


Fig 4. Evolution of saturation magnetization with current density along the sample S2 for as-cast state (O) and after 1 min current annealing at  $j=39$  (+) and  $50 \text{ Amm}^{-2}$  (\*).

This work has been supported by the C.I.C.Y.T. under project MAT 89/0508.

#### 4. References

- 1.- Y. Yoshizawa, S. Oguma and K. Yamauchi J. Appl. Phys. 64(1988) 6044
- 2.- G. Herzer IEEE Trans. Magn. 26 (1990)1397
- 3.- G. Herzer Mat. Sci. and Engin. A133(1991)1
- 4.- M. Vázquez, J. González and A. Hernando J. Magn. Magn. Mat. 53(1986)323
- 5.- G. Herzer. Proc. Int. Symposium on 3-d Transition-Semi Metal Thin Films, Magnetism and Processing. Sendai(1991) (in press)



## The Effect of Adding Ti and Zr on the Crystallization Behaviour of Amorphous Fe-Cr-B Alloys

K Ishii\* and B Cantor

*Oxford Centre for Advanced Materials and Composites,  
Department of Materials, University of Oxford,  
Parks Road, Oxford OX1 3PH, UK*

*\*On leave from Kawasaki Steel Corporation*

### ABSTRACT

The crystallization behaviour of  $\text{Fe}_{82-x}\text{Cr}_{18}\text{M}_x\text{B}_y$  ( $\text{M}=\text{Ti}$  or  $\text{Zr}$ ,  $x=0\sim 8$ ,  $y=5\sim 20$ ) amorphous alloy ribbons prepared by melt spinning have been investigated by a combination of differential scanning calorimetry and transmission electron microscopy.

### 1. Introduction

Amorphous alloys have many desirable properties, but they have metastable atomic structures and can crystallize easily at high temperature. Therefore it is important to develop new amorphous alloys that have higher crystallization temperatures. It has been reported that amorphous alloys containing Zr have high crystallization temperatures<sup>1)</sup>, and a similar effect is expected with Ti. However, there is no detailed information about such Zr and Ti containing amorphous alloys. In this work the crystallization behaviour of  $\text{Fe}_{82-x}\text{Cr}_{18}\text{M}_x\text{B}_y$  ( $\text{M}=\text{Ti}$  or  $\text{Zr}$ ,  $x=0\sim 8$ ,  $y=5\sim 20$ ) amorphous alloys have been investigated by a combination of differential scanning calorimetry (DSC) and transmission electron microscopy (TEM).

### 2. Experiments

The amorphous alloy ribbons were prepared by melt spinning, and were typically 1~3mm wide and 30~60 $\mu\text{m}$  thick. Crystallization kinetics were monitored with a Dupont 2000 thermal analyzer/910 DSC during continuous heating at 5 K/min from 200°C to 716°C, and isothermal heating in the range 440°C to 655°C. TEM examination was carried out in a Philips CM12 to determine the microstructures of the as-melt spun and heat treated ribbons.

### 3. Results

#### 3.1 Continuous heating DSC

Fig.1 shows typical continuous heating DSC traces for three of the Ti containing alloys together with corresponding phases determined by TEM. In general, the crystallization behaviour was similar to amorphous  $\text{Fe-B}^{2)}$  and  $\text{Fe}_{70}\text{Cr}_{18}\text{Mo}_2\text{B}_{10}^{3)}$ . As-melt spun  $\text{Fe}_{70}\text{Cr}_{18}\text{Ti}_2\text{B}_{10}$  consisted of an amorphous matrix with micron sized particles of bcc ferrite. The amorphous matrix crystallized with one exothermic peak to form a fine scale mixture of bcc ferrite grains and  $(\text{Fe,Cr})_3\text{B}$  boride particles. As-melt spun  $\text{Fe}_{65}\text{Cr}_{18}\text{Ti}_2\text{B}_{15}$  and  $\text{Fe}_{60}\text{Cr}_{18}\text{Ti}_2\text{B}_{20}$  exhibited fully amorphous structures. Amorphous  $\text{Fe}_{60}\text{Cr}_{18}\text{Ti}_2\text{B}_{20}$  crystallized with one

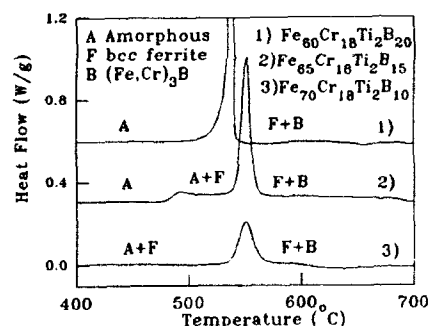


Fig.1 Typical DSC traces during continuous heating at 5 K/min.

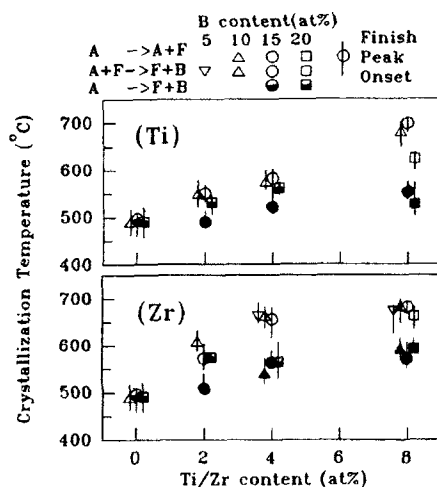


Fig.3 Influence of Ti and Zr content on crystallization temperature.

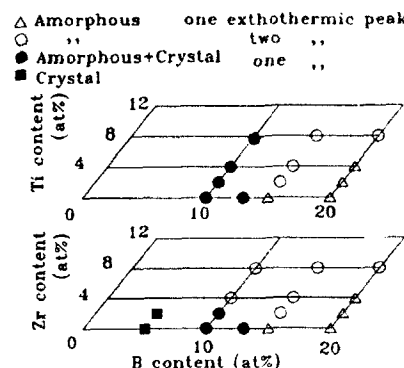


Fig.2 Phase diagrams for FeCr(Ti/Zr)B

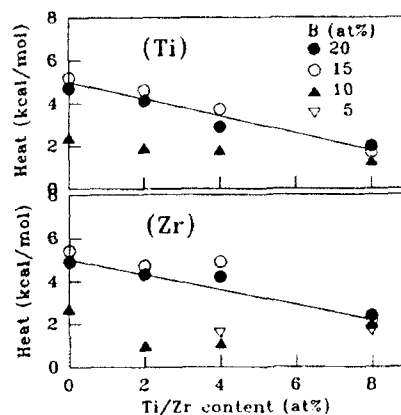


Fig.4 Influence of Ti and Zr content on heat of crystallization

exothermic peak to form a mixture of bcc ferrite grains and  $(\text{Fe,Cr})_3\text{B}$  boride particles directly. Amorphous  $\text{Fe}_{85}\text{Cr}_{15}\text{Ti}_2\text{B}_{15}$  crystallized with two exothermic peaks, the first one forming bcc ferrite particles in an amorphous matrix similar to as-melt spun  $\text{Fe}_{70}\text{Cr}_{18}\text{Ti}_2\text{B}_{10}$ , and the second one forming a mixture of bcc ferrite grains and  $(\text{Fe,Cr})_3\text{B}$  particles, similar to heat treated  $\text{Fe}_{70}\text{Cr}_{18}\text{Ti}_2\text{B}_{10}$ . Fig.2 shows phase diagrams for the full range of Zr and Ti containing alloys, indicating the as-melt spun and heat treated structures. Alloys containing Zr were amorphous over a wider range of compositions than alloys containing Ti. With increasing B content and decreasing Ti and Zr content, the crystallization behaviour changed from two exothermic peaks to one. Fig.3 shows that the crystallization temperature increased with increasing Ti or Zr content, with a greater effect of Zr than Ti. Fig.4 shows that the heat of crystallization decreased with increasing Ti or Zr content.

### 3.2 Isothermal DSC

Fig.5 shows typical isothermal DSC traces for  $\text{Fe}_{65}\text{Cr}_{18}\text{Ti}_2\text{B}_{15}$ . The exothermic peaks in Fig.5 correspond to the second peak during continuous heating in Fig.1. Fig.6 shows that the incubation time for the onset of crystallization in  $\text{Fe}_{65}\text{Cr}_{18}\text{Ti}_2\text{B}_{15}$  obeyed the Arrhenius law with an incubation activation energy of 5.7 eV. Similar Arrhenius behaviour for the onset of crystallization was found in many of the other amorphous alloys, with incubation activation energies in the range from 3~7 eV.

The kinetics of crystallization can often be expressed by the John-Mehl-Avrami equation<sup>6</sup>:

$$Y = 1 - \exp(-Kt^n) \quad (1) \quad \text{where } Y \text{ is the crystalline volume fraction, } K \text{ is a rate constant which depends on the crystal nucleation and growth rates, } t \text{ is the time and } n \text{ is the Avrami exponent which depends on the crystallization mechanism.}$$

Fig.7 shows Avrami plots of  $\ln[-\ln(1-Y)]$  vs  $\ln t$  for  $\text{Fe}_{65}\text{Cr}_{18}\text{Ti}_2\text{B}_{15}$ , with  $t$  measured from the onset of crystallization and  $Y$  taken as the corresponding heat evolved in Fig.5. The results in Fig.7 show good agreement with the Johnson-Mehl-Avrami eq(1) with an Avrami exponent of 3, indicating a crystallization process of 3-d spherical growth on pre-existing crystal nuclei dispersed throughout the bulk of the amorphous alloy. Similar Avrami behaviour was found in many of the other amorphous alloys.

$K$  in eq(1) can be written as:

$$K = (4\pi/3)NG_0^3 \exp(-3Q/RT) \quad (2)$$

where  $N$  is the density of crystal nuclei,  $G_0$  is a crystal growth constant,  $Q$  is the activation energy for growth,  $R$  is the gas constant and  $T$  is the temperature. Combining eqs(1) and (2) gives:

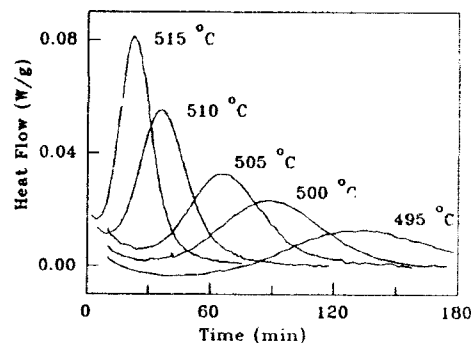


Fig.5 Isothermal DSC traces for  $\text{Fe}_{65}\text{Cr}_{18}\text{Ti}_2\text{B}_{15}$ .

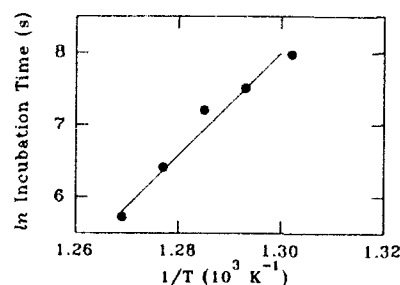


Fig.6 Incubation time for the onset of crystallization as a function of temperature for  $\text{Fe}_{65}\text{Cr}_{18}\text{Ti}_2\text{B}_{15}$ .

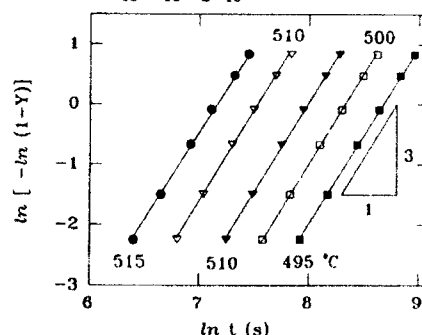


Fig.7 Avrami plots of  $\ln[-\ln(1-Y)]$  vs  $\ln t$  for  $\text{Fe}_{65}\text{Cr}_{18}\text{Ti}_2\text{B}_{15}$ .

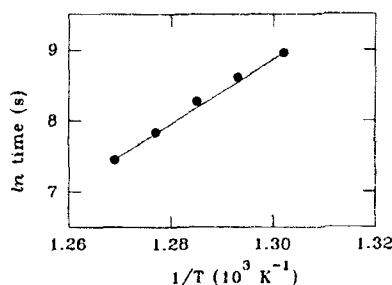


Fig.8 Time for 90% crystallization as a function of temperature for  $\text{Fe}_{65}\text{Cr}_{18}\text{Ti}_2\text{B}_{15}$ .

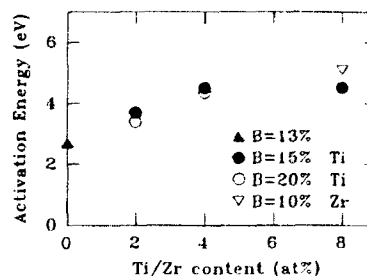


Fig.9 Influence of Ti and Zr content on the activation energy for crystal growth.

$$\ln t = \ln[-\ln(1-Y)] - \ln(4\pi NG/3) + 3Q/RT \quad (3)$$

Fig.8 shows the time for 90% crystallization in  $\text{Fe}_{65}\text{Cr}_{18}\text{Ti}_2\text{B}_{15}$  as a function of temperature, giving good agreement with eq(3) with an activation energy for crystal growth of 3.7eV. Similar behaviour was found in many of the other amorphous alloys, with an activation energy for crystal growth which increased with increasing Ti or Zr content, as shown in Fig.9.

#### 4. Conclusions

The crystallization behaviour of  $\text{Fe}_{82-x-y}\text{Cr}_{18}\text{M}_x\text{B}_y$  ( $\text{M}=\text{Ti}$  or  $\text{Zr}$ ,  $x=0\sim 8$ ,  $y=5\sim 20$ ) amorphous alloy ribbons prepared by melt spinning have been investigated by a combination of DSC and TEM. The main conclusions are as follows:

- 1) Alloys containing Zr are amorphous over a wider range of compositions than alloys containing Ti.
- 2) In continuous heating DSC, the crystallization temperature increases and the heat of crystallization decreases with increasing Ti or Zr content.
- 3) In isothermal DSC, the incubation time for the onset of crystallization obeys the Arrhenius law, with an incubation energy in the range 3~7eV. The crystallization process often obeys the Johnson-Mehr-Avrami law with an Avrami exponent of 3. The activation energy for crystal growth is in the range 2~5eV, and increases with increasing Ti or Zr content.

#### Acknowledgment

We would like to thank Professor Sir Peter Hirsch for providing laboratory space.

#### Reference

1. J.A.Leake and J.E.Rout, *Mater.Sci.Eng.* **97**(1988)325
2. W.T.Kim, K.Clay, C.Small and B.Cantor, *J.Non-Crys. Solids.* **127**(1991)273
3. V.Herold and U.Koster in *Rapidly Quenched Materials III* ed B.Cantor (Metal Society, London, 1978) Vol.1 p.364
4. J.W.Christian, *The Theory of Transformations in Metals and Alloys*, (Pergamon Press, Oxford, 1975)

## THERMAL STABILITY AND QUENCHING RATE IN AN FeSiB GLASS

C.F. Conde and A. Conde

*Departamento de Física de la Materia Condensada*

*Instituto de Ciencia de Materiales. C.S.I.C.*

*Universidad de Sevilla*

### ABSTRACT

Curie temperature and crystallization kinetics were studied for a metallic glass FeSiB produced at three different quenching rates.  $T_c$  decreases with increasing quenching rate; crystallization onset and activation energy for crystallization values also increase with the ribbon thickness.

### 1. Introduction

There is a great deal of evidence that the quenching rate has a strong influence on the physical properties of rapidly quenched materials (1-5). In fact, there is no unique glass structure for a given composition since  $T_g$  and the glass structure are both cooling-rate dependent. Thermal evolution of the structure of the glass, either structural relaxation or devitrification transformation, can be related to atomic rearrangements with changes of both chemical and topological short-range orders. So the different amorphous structures produced by varying quenching rate will exhibit differences in their structural evolution.

In this paper the behaviour of an FeBSi glass is described in connection with the above mentioned feature, specially in regard to thermal stability.

### 2. Experimental

Metallic glass with a nominal  $\text{Fe}_{79}\text{B}_{12}\text{Si}_9$  composition was prepared by the melt-spinning technique, from a master alloy of this composition. Ribbons 10 mm wide and 32, 34 and 40  $\mu\text{m}$  thick were produced from the alloy by means of varying gas (Ar) injection pressure of the melt on the rotating wheel.

Differential scanning calorimetry (DSC) and thermomagnetic gravimetry (TMG), on

Perkin-Elmer DSC-7 and TG-7 devices under Ar atmosphere, were used for the characterization of Curie temperature, thermal stability and crystallization kinetics of the three alloys. Calibration of both temperature and enthalpy scales of DSC and temperature scale of TG units were checked by using the usual standards.

Experiments at a constant heating rate were performed by heating the sample at the maximum available rate (320 K/min) from room-temperature to 100 K below the crystallization onset in order to minimize unwanted annealing.

### 3. Results

Fig. 1 shows, the DSC records at 10 K/min for the studied glasses. As can be observed, on heating no evidence of the glass transition is found but two exothermic peaks are present in all the records. For each glass, the temperature interval between the two exothermic peaks increases slightly when the heating rate rises (2,5-40 K/min). Crystallization enthalpy of the first exotherm relative to that the second one also increases upon increasing heating rate.

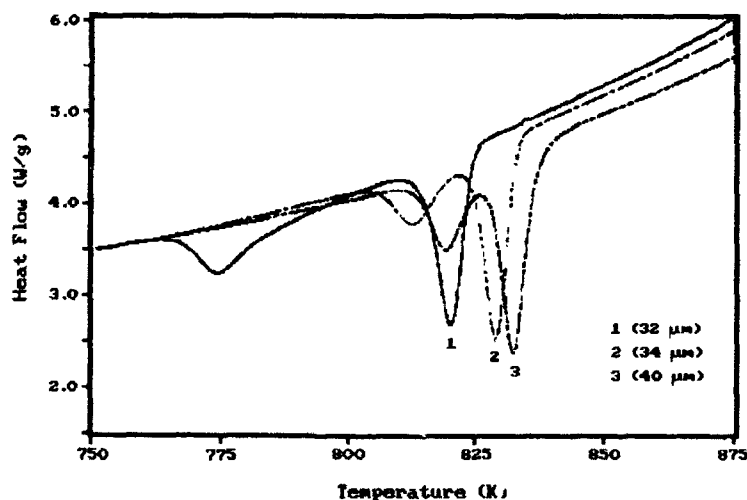


Fig. 1

By comparing the three curves of the Fig. 1, the crystallization onset is significantly displaced to higher temperatures with increasing thickness. Also, the temperature interval

between the two exotherms decreases with increasing thickness

The TMG records of the three glasses are shown in Fig. 2. One can observe that the ferromagnetic Curie temperature increases with increasing thickness. As  $T_c$  measures in some way the exchange interaction, it is obvious to suppose that short range order should influence  $T_c$ .

The crystallization onset is revealed in TMG records from the formation of a ferromagnetic crystalline phase. Curie temperature measured on partially crystallized samples (up to the first exotherm) indicated an  $\alpha$ -Fe type phase. Thermal evolution of the sample magnetization, revealed in the TMG curves, also shows the temperature range up to full crystallization. The different shape for the high temperature zone of the records, corresponding to the ferromagnetic-paramagnetic transition of the crystalline phase, should probably be related to structural differences of the  $\alpha$ -Fe type crystals.

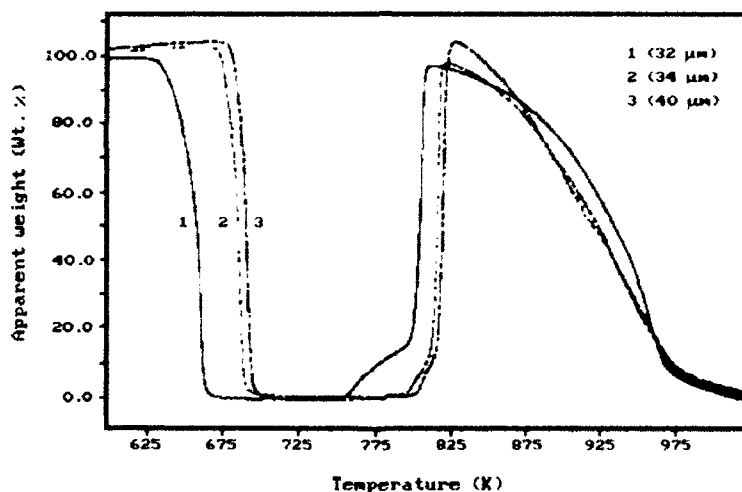


Fig. 2

Kinetic analysis of the non-isothermal DSC data were carried out by the Kissinger's peak shift method (6) the resulting values for the activation energy of the first peak is slightly higher than that for the second one (table 1). By comparing values obtained for the three glasses one observes a slight increase of the activation energy with increasing the thickness of ribbons.

Table 1. Characteristics of the glasses

Thickness ( $\mu\text{m}$ )	32	34	40
T Curie (K)	660	685	688
T onset (K)	763	803	812
T <sub>p1</sub> (K)	772	810	817
T <sub>p2</sub> (K)	818	827	831
$\Delta H$ (kJ/mol)	105	112	114
Ea <sub>1</sub> (kJ/mol)	350.3	369	370
Ea <sub>2</sub> (kJ/mol)	335.4	341.9	342.5

In conclusion, it has been demonstrated that the quenching rate affects both Curie temperature and thermal stability of the glass. Curie temperature decreases with increased quenching rate according to the usual behaviour of metallic glasses. Thermal stability, related to the crystallization onset temperature and activation energy values, should decrease with increasing heating rate. However, it should be noted that the most significant differences refer to the 32  $\mu\text{m}$  ribbon in relation to the other two, whereas ribbons of 34 and 40  $\mu\text{m}$  show less difference in their characteristic parameters. This feature is not easily understood and more work will be necessary.

#### 4. Acknowledgments

We thank J. Bigot, A. Dezellus and S. Peynot, CNRS-CECM (Vitry, France) for their help in the sample preparation.

Work supported by the CICYT of the Spanish Government (Project MAT88-301) and by the Junta de Andalucía.

#### 5. References

1. F.E. Luborsky and H.H. Liebermann. *J. Appl. Phys.* **51** (1980) 796.
2. A.L. Greer. *J. Mat. Sci.* **17** (1982) 1117.
3. U. Köster, U. Herold and H.G. Hillenbrand. *Scr. Metall.* **17** (1983) 867.
4. C. Hargitai, M-Hossó, C. Kopasz, G. Márki, I. Nagy and T. Tarnóczy. In S. Steeb and H. Warlimont (eds). *Rapidly Quenched Metals*, North Holland, Amsterdam (1985) p-87.
5. T. Tarnóczy and A. Lovas. *Mat. Sci. Eng.* **97** (1988) 509.
6. H.E. Kissinger. *Anal. Chem.* **29** (1957) 1702.



## CRYSTALLIZATION KINETICS OF AN $\text{Fe}_{75}\text{Co}_4\text{Si}_3\text{B}_{18}$ ALLOY

M. Millán, J. Leal and A. Conde

*Departamento de Física de la Materia Condensada.  
Instituto de Ciencia de Materiales. C.S.I.C.- Universidad de Sevilla. Spain.*

### ABSTRACT

Devitrification kinetics of an  $\text{Fe}_{75}\text{Co}_4\text{Si}_3\text{B}_{18}$  alloy has been studied by calorimetric DSC methods. The crystallization onset occurs at 775 K and non-isothermal DSC records show up to four exotherms. Kinetic analysis was derived from non-isothermal data while the main exotherm from those of isothermal. Microstructural study reveals a primary precipitation of  $\alpha$ -Fe followed by the formation of a  $\text{Fe}_3\text{B}$  phase, final products of the crystallization being  $\alpha$ -Fe and  $\text{Fe}_2\text{B}$  type phases.

### 1. Introduction.

The Johnson-Mehl-Avrami (JMA) equation (1) has been used extensively to analyse the crystallization kinetics of metallic glasses. In this equation the Avrami exponent reflects the nucleation and/or growth characteristics of the transformation. If the JMA analysis is valid, the value of  $n$  should not change with either the volume fraction transformed or the temperature of transformation. Calka and Radlinski (2) has shown that a more sensitive approach is to plot the first derivative of the Avrami plot against the volume fraction transformed, which effectively gives the local value of  $n$  (2-4). This plot can highlight changes in reaction kinetics during the transformation. In this paper, the technique suggested by Calka and Radlinski is applied to an iron-based metallic glass.

### 2. Experimental

Ribbons of the alloy were prepared by the melt-spinning technique, in vacuum, from a master alloy with the nominal composition cited above. Differential scanning calorimetry was performed on a Perkin-Elmer DSC-2C connected to a 3600 thermal analysis data station. Both, temperature and enthalpy calibration were checked by lead and  $\text{K}_2\text{SO}_4$  standards. To reduce

annealing effects, samples were heated at 320 K/min from room temperature to 100 K below the onset temperature in non-isothermal and to the annealing temperature for the isothermal records. For microstructural characterization, samples were thinned by ion beam (Ar) techniques. TEM observations were performed on a Hitachi H800 operated at 200 kV.

### 3. Results

DSC records at a constant heating rate (Fig. 1) show three peaks, the first of them resulting in two overlapped exotherms but some differences are apparent in the different heating rate records. So the ratio enthalpy of the two overlapped peaks is inverted when the heating rate raises.

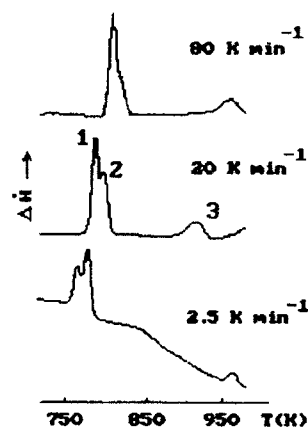


Fig. 1

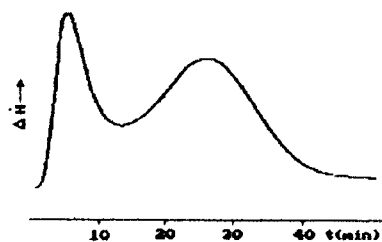


Fig. 2

Fig. 2 shows an isothermal record and, as can be observed, only two overlapped peaks are revealed. The activation energy of each crystallization stage was evaluated (Fig. 3) by the Kissinger's peak shift method (5). Table 1 shows the characteristic temperature (at 10 K/min), enthalpy and activation energy of the different peaks.

The isothermal kinetics of the transformation was analysed in terms of the JMA equation, after deconvolution of the two overlapped maxima. Fig. 4 shows the Avrami  $\ln(-\ln)$  plots for different isothermal runs of the first and the second peaks, respectively. For

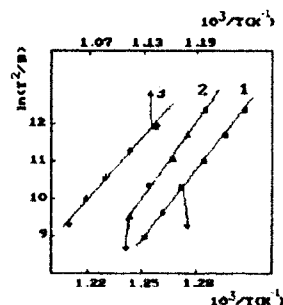


Fig. 3

Table 1

Peak	1	2	3	4 <sup>(*)</sup>
$T_p(K)$	779	790	896	967
$\Delta H(J/g)$	166		47	20
$E_a(eV/at)$	5.3	5.8	2.3	

(\*) at 2.5 K/min

the first peak (Fig. 4.a) the experimental points can be fitted by two linear steps. Avrami index value is 2.5 for the initial step decreasing at high  $x$  values. The effect is more appreciable for the highest annealing temperatures. For the second peak a linear fit with  $n=3.0$  is found. These values should suggest (6) a three-dimensional diffusion controlled growth with a nucleation rate decreasing for high values of  $x$  for the first stage of the transformation. For the second stage the value  $n=3.0$  should indicate an interface controlled growth.

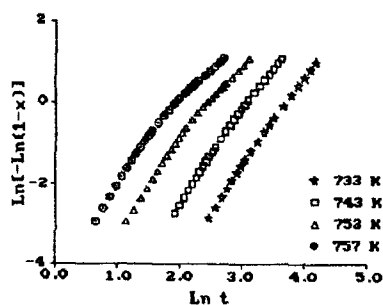


Fig. 4.a

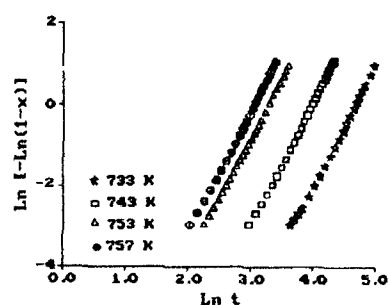


Fig. 4.b

It is clear that the experimentally determined Avrami index could be expected to be a constant only in some limiting cases. Either the growth morphology or the nucleation rate, or both, may change as the crystallization process proceeds. The variation of  $n$  with the volume fraction transformed was analysed by plotting the log time derivative of  $\ln[-\ln(1-x)]$  against volume fraction transformed at each temperature for the two crystallization peaks (2-4). Fig. 5 illustrates the variation of the modified Avrami index with  $x$ . For the first stage, plots of Fig. 5.a show a decreasing of the  $n_{loc}$  value when  $x$  rises. As can be observed, as the annealing temperature rises the decreasing of  $n$  begins at lower values of  $x$  to reach final values closer to  $n=1.5$ . This feature should indicate that the nucleation process is exhausted and the rate decreases to a zero value. Fig. 5.b shows the behaviour of  $n_{loc}$  for the second

crystallization stage, similar for all the isothermal crystallization temperatures:  $n_{loc}$  remains constant at 3.0 over most of the transformation. Deviations at low  $x$  should reflect the effects of the experimental difficulty in determining the start of the transformation, affecting mainly the low values of  $x$ . Deviations at high  $x$  should be caused by impingement affecting the three-dimensional growth.

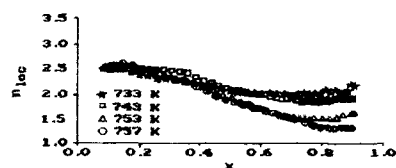


Fig. 5.a

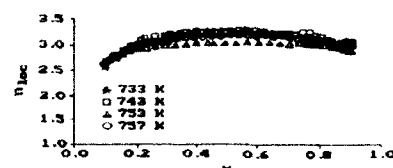


Fig. 5.b

The microstructure of the partially crystallized samples show the dendritic forms usually found for the precipitation of  $\alpha$ -Fe in Fe-B glasses and also other crystals of varied morphology. Electron diffraction patterns reveal the existence of  $\alpha$ -Fe and tetragonal  $Fe_3B$  type phases, along with remaining amorphous matrix. Fully crystallized samples show the usual polygonal forms and the existence of many planar defects. Electron diffraction reveals  $\alpha$ -Fe and  $Fe_2B$  type phases as final products of the transformation.

#### 4. Acknowledgements

This work was supported by the CICYT of the Spanish Government (Project MAT88-301) and by the Junta de Andalucía.

#### 5. References

1. J. Burke. "The Kinetics of Phase Transformations in Metals". Pergamon, London (1965).
2. A. Calka and A.P. Radlinski. Mat. Sci. Engng. 97 (1988) 241.
3. M.A. Gibson and G.W. Delamore. J. Mat. Sci. 22 (1987) 4550.
4. M. Millán and A. Conde. J. Mat. Sci. 26 (1991) 2133.
5. H.E. Kissinger. Analyt. Chem. 29 (1957) 1702.
6. V.R.V. Ramanan and G. Fish. J. Appl. Phys. 53 (1982) 2273.

# CRYSTALLIZATION PROCESS BY STUDY OF RESISTIVITY THROUGH CONTROLLED JOULE EFFECT HEATING

P. Rougier and R. Krishnan

Laboratoire de magnétisme et Matériaux Magnétiques, C.N.R.S. F-92195 Meudon

We have developed a new method of studying the crystallization process in melt-quenched amorphous magnetic alloys which consists of monitoring the resistivity while the amorphous sample (ribbon) is traversed by a current whose intensity is increased in a programmed way with time up to the or above the crystallization point. We report our results on  $\text{Fe}_{80-x}\text{Ni}_x\text{B}_{12}\text{Si}_8$  alloys with  $0 \leq x \leq 80$ , prepared by melt spinning technique. In this technique one studies the change in the resistivity ( $R$ ) as a function of electric power ( $P$ ), and steps are observed each time a phase transition occurs. Our analysis indicate that the samples with  $x=20, 40$  and  $70$  are key compositions. At the time of vitrification the following local units are suggested to be present (either individually or as a mixture), a)  $\text{Ni}_3\text{B}$ , b)  $\text{Ni}_3\text{Fe}$ , c)  $\text{Fe}_3\text{B}$ . For  $x=18$  and  $36$ , if one considers the units (a) and (b) indicated above there remains 44 % of Fe in excess. On the contrary for  $x=69$ , the crystalline phases are distributed between  $\text{Ni}_{36}\text{B}_{12}$  (or  $\text{Ni}_3\text{B}$ ), and  $\text{Ni}_{33}\text{Fe}_{11}$  (or  $\text{Ni}_3\text{Fe}$ ) and no excess of metal atoms appear.

## 1. Introduction

Crystallization process in amorphous alloys have been studied in detail in the past years, though it seems that no relation has been established between this process and the local units present in the amorphous phase. Some authors have related the local structure of amorphous Fe-Ni-B alloys to the first crystalline phase that appears<sup>1</sup>. Such an approach was thought not to be appropriate, considering the atomic rearrangements that take place during the crystallization process<sup>2</sup>. We describe in this paper a simple technique of studying the resistivity as a function of progressively increasing current density and show that an analysis of the results on a wide range of compositions in a particular system could bring very important information on the amorphous structural state. Raj et al<sup>3</sup> have indicated that no consensus exists about the local structure in Fe-Ni based amorphous alloys. Consequently we have chosen for this present study the amorphous system  $\text{Fe}_{80-x}\text{Ni}_x\text{B}_{12}\text{Si}_8$  in which we have considered the local units which are generally invoked namely,  $\text{Fe}_3\text{B}$ ,  $\text{Ni}_3\text{B}$ ,  $\text{Fe}_2\text{B}$ ,  $\text{Ni}_2\text{B}$ ,  $(\text{FeNi})_3\text{B}$  and  $(\text{FeNi}_3)\text{B}$ . These units are considered only from the chemical combination point of view and not on topological basis.

It has been recognized that the local order in an amorphous alloy has a memory of that in its crystalline counterpart. For alloys rich in Fe, Dubois et al<sup>4,5</sup> have shown the existence of crystallites of  $\alpha\text{-Fe}$  b.c.c. For Ni based alloys with less than 5 at% of Fe we have observed the presence of f.c.c. Ni crystallites<sup>6</sup>. As regards Si it has been generally admitted that it could either replace Fe substitutionally or enter into solid solution. We have based our discussion on the models proposed by Gaskell<sup>7</sup> and Machizaud<sup>8</sup>.

## 2. Experimental Details

The amorphous  $\text{Fe}_{80-x}\text{Ni}_x\text{B}_{12}\text{Si}_8$  system with  $0 < x < 80$  at.% was studied where  $x$  was increased generally in steps of 5 at.% and in certain ranges 2 and 1 at.%. As regards the metallic atoms our compositions cover combinations such as,  $(\text{Fe}_3\text{Ni})_{80}$ ,  $(\text{FeNi})_{80}$  and  $(\text{FeNi}_3)_{80}$ . It was important that we study for our experiments the alloys characteristic of crystallized Fe-Ni alloys. The samples were prepared by the single roller melt spinning

method using starting materials of purity better than 99.9 %. The exact composition of the samples was determined by the electron probe micro analysis.

The resistivity was measured by the technique called "Controlled Joule Effect Analysis" (CJEA), which has been described before by us in detail <sup>9,10</sup>. Briefly this technique consists of monitoring the resistivity of the ribbon continuously while the intensity of the current sent through this is progressively increased at a programmed rate. The current intensity increases heating the sample by the Joule effect, leading to crystallization. An analogic system enables us to calculate the power  $P = V \cdot I$  and the resistance  $R = V/I$ , where  $V$  is the potential and  $I$  the current through the ribbon sample. A X-Y recorder is employed to get the tracing of the variation of  $R$  as a function of  $P$ . The rate increase of current has been standardized at 2.5 mA/sec. The experiments were carried out in argon atmosphere.

### 3. Experimental Results

The  $R = f(P)$  curves reflect the structural evolution related to the crystallization. The resistance of the sample at each instant arises on the one hand from the nature and the fraction of the precipitated phases and on the other hand from their conductivity and its temperature dependence. For want of space the results for all the samples cannot be presented here. Therefore only the most interesting and typical ones are shown.

Three dominants can be observed related to three composition regions for which the process of crystallization present some similarities and which are as follows:

I.  $0 \leq x \leq 20$ ; II.  $20 \leq x \leq 40$ ; III.  $40 \leq x \leq 80$ . Fig. 1 a to c show the results for  $x = 20, 40$  and  $70$  respectively. In the region III for  $\text{Fe}_{10}\text{Ni}_{70}\text{B}_{12}\text{Si}_8$  (Fig. 1 c), and the neighbouring compositions, one observes a relatively small drop in the resistivity when the crystallization sets in. Curiously in this region the crystallization continues followed by an increase in  $R$ . This particularity already has repercussions on either side of this composition. From an analysis of the above results we have attempted to justify theoretically the three experimental "key compositions" for  $x = 20, 40$  and  $70$ .

### 4. Discussion and Interpretation

The nature of the local units in an amorphous alloy depends on the chemical composition and it is also known that they constitute the seeds for the crystallization. Consequently, the crystallization and especially its evolution as observed in the  $R = f(P)$  curves have been supposed to be related to the local units. So we have deduced that the singularity connected with the key compositions arise from a change in the nature of these local units. We have attempted to justify theoretically these key compositions as follows. All the local units that have been mentioned in the literature have been considered and then it has been supposed that these units have an order of formation at the instant of solidification. We have also considered the availability of the various metal atoms to form these units.

Considering 100 atoms of the alloy, only one combination gives rise to the theoretical key compositions for  $x = 18, 36$ , and  $69$  in close agreement with the experimental data. The combinations are as follows: (1) first formation of  $\text{Ni}_3\text{B}$ , followed by, depending on the availability of the remaining atoms, (2) the formation of  $\text{Ni}_3\text{Fe}$  and again depending on the remaining atoms the formation of (3)  $\text{Fe}_3\text{B}$ . The well known repulsion between Si and B atoms has been taken into account in order to suppose that Si atoms distribute themselves between Fe and Ni. Under these conditions and considering the rather Si content we have not accounted for it.

The key compositions that appeared from our crystallization experiments have the following particularities:

- a) the alloy with  $x = 18$  could be distributed as  $\text{Ni}_{18}\text{B}_6$  and  $\text{Fe}_{18}\text{B}_6$  in other words,  $\text{Ni}_3\text{B}$  and  $\text{Fe}_3\text{B}$  in the same proportion. There remains 44 at.% of Fe in excess
- b) the alloy with  $x = 36$  could be distributed as  $\text{Ni}_{36}\text{B}_{12}$  ( $\text{Ni}_3\text{B}$ ), with the disappearance of  $\text{Fe}_3\text{B}$  units. There remains 44 at.% of Fe in excess.
- c) the alloy with  $x = 69$  could be distributed as  $\text{Ni}_{36}\text{B}_{12}$ ,  $\text{Ni}_3\text{B}$ , and  $\text{Ni}_{33}\text{Fe}_{11}$ ,  $\text{Ni}_3\text{Fe}$  (these two latter compositions are in high proportion and are not combined to B). This

composition is unique in the sense that there is no excess of atoms as in the previous cases.

Fig. 2 shows schematically the distribution of 100 atoms of the alloy as a function of  $x$  (Ni/Fe ratio) and it also describes how the local units and the excess of atoms evolve. Let us describe a typical example by illustrating the results for the alloy  $\text{Fe}_{35}\text{Ni}_{45}\text{B}_{12}\text{Si}_8$ . Forty eight atoms of the alloy namely, 36 Ni and 12 B, form the structural units  $\text{Ni}_3\text{B}$ , twelve atoms of the alloy namely, 9 Ni and 3 Fe, form  $\text{Ni}_3\text{Fe}$  and finally 32 Fe atoms remain in excess due to the lack of B and Ni atoms. Other important conclusions that can be drawn are as follows.

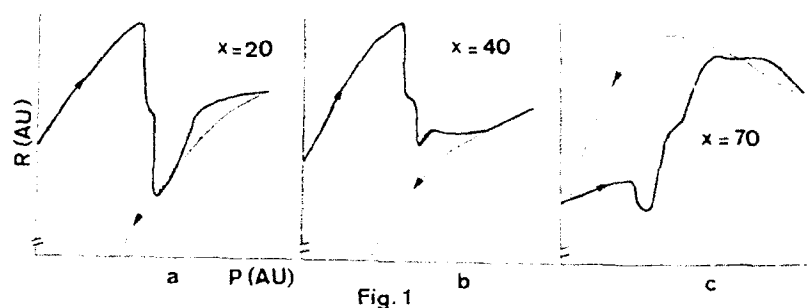


Fig. 1 The variation of the resistivity ( $R$ ) with power ( $P$ ) for  $x$  (a) 20, (b) 40 and (c) 70

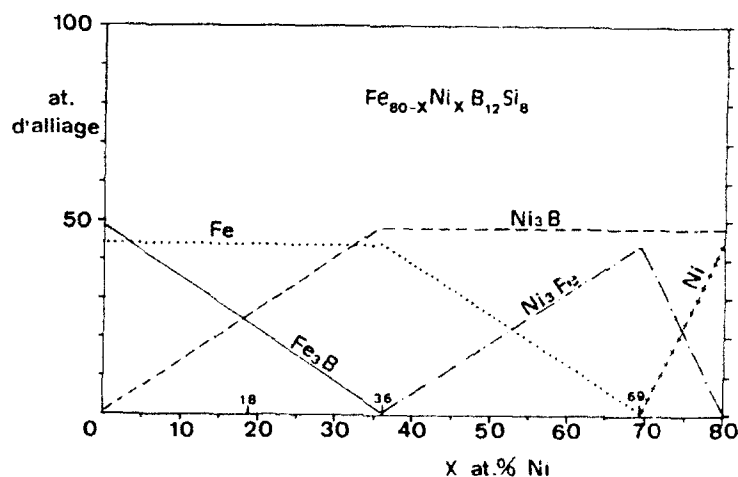


Fig. 2 The variation of the local units and metal atoms "in excess" as a function of Ni concentration ( $x$ )

## 5. Conclusions

We have developed a technique of macroscopic nature (CJEA) which enables us to study the crystallization process. We have shown the presence of composition regions for which the crystallization process is similar. Starting from a concept of an order of formation of structural units at the time of crystallization, the results have been analyzed. The drop in the resistivity generally accompanying the crystallization appears to be related to the presence of an "excess of metal atoms". This concept could also help to rethink of the various phenomena observed such as ageing, relaxation, and in certain cases an increase in the magnetization caused by very small additions of Mn and so on. Finally we qualify  $\text{Fe}_{11}\text{Ni}_{69}\text{B}_{12}\text{Si}_8$  as a perfect glassy alloy because there is no excess of metal atoms. Of course more work is needed to be able to relate the structural units present at the time of crystallization to the amorphous structure.

## 6. References

1. Glassy Metals, Ed. H. Beck and H.J. Guntherrodt, Springer, Berlin, p. ; H. Warlimont and P. Wordelik, Rapidly Quenched Metals, Ed. S. Steeb, H. Warlimont, Elsevier Pub. Amsterdam, p 619 1985
2. G.L. Whittle, Rapidly Quenched Metals, Ed. S. Steeb and H. Warlimont, Elsevier Pub. Amsterdam, p 545 1985
3. P. Raj and N. Satyamoorthy, J. Phys. F: Met Phys. 18 113 1988
4. J.M. Dubois and G. Le Caer, J. Phys. Coll. 43 C9 67 1982
5. J.M. Dubois, G. Le Caer and S.J. Guedes de Lima, Proc. Int. Conf. Met. Semicond. Glasses, Hyderabad, India, Trans. Tech. Pub. Switzerland, p 1986
6. R. Krishnan, M. Dancygier and P. Rougier, IEEE. Trans. Mag. MAG-20 1370 1984
7. P.H. Gaskell, Glassy Metals, Ed. H. Beck and H.J. Guntherrodt, Springer, Berlin, p 5-47, 1983 ; Proc. Int. Conf. Met. Semicond. Glasses, Hyderabad, India, Trans. Tech. Pub. Switzerland, p 1986
8. F. J. Machizaud, J. de Phys. Coll. C 9 43 9 1982
9. P. Rougier and R. Krishnan, J. de Phys. Coll C 6 46 417 1985
10. P. Rougier and R. Krishnan, IEEE Trans. Mag. MAG 23 1987
11. C. Djega-Mariadassou and P. Rougier, et al Hyper. Int. 45 343 1959
12. P. Rougier, Thesis, Doctorat d'Université de Paris, Paris University, 1990



## CALORIMETRIC STUDY OF THE CRYSTALLIZATION PROCESSES OF AMORPHOUS CoP ALLOYS

F. Cebollada and J.M. González

*Instituto de Ciencia de Materiales - CSIC. Serrano 144.  
28006 Madrid, Spain.*

S. Suriñach, M.D. Baró, M.T. Clavaguera-Mora

*Física de Materials, Dept. de Física. Univ. Autònoma de Barcelona  
08193 Bellaterra, Barcelona, Spain.*

### ABSTRACT

The activation energies for the crystallization processes of alloys of composition  $\text{Co}_{100-x}\text{P}_x$  ( $10 < x < 26$ ) have been obtained from DSC continuous heating scans. Microstructure of the crystallization products has been studied through SEM and X-ray diffraction. The influence of the compositional inhomogeneities on the calorimetric measurements has been studied.

### 1. Introduction

The amorphous system  $\text{Co}_{100-x}\text{P}_x$  has been the object of several studies, from the point of view of either its magnetic or structural properties<sup>1-4</sup>. Crystallization processes of this system are usually described as composed of two stages, a primary crystallization process followed by a eutectoid decomposition, thus obtaining in some cases a very fine microstructure with grain sizes in the order of 5 nm<sup>1</sup>. The transformation kinetics of these stages have been studied through indirect measurements by means of the evolution of physical magnitudes (e.g. coercive force, ferromagnetic resonance absorption lines and resistivity) that are sensitive to the structural variation (crystallization) produced during isothermal annealings<sup>2-4</sup>.

We present in this work a calorimetric study for compositions in the range  $10 < x < 26$ , performed through continuous heating scans that have allowed us to obtain results concerning the activation energy and the transformation enthalpy for both stages taking place during crystallization. The microstructure of the final crystallization products have been observed by means of SEM and X-ray analysis. The effects on the calorimetric measurements of the compositional inhomogeneity present when coming close to the edges of the samples have also been studied.

### 2. Samples and Experimental Techniques

$\text{Co}_{100-x}\text{P}_x$  ( $10 < x < 26$ ) samples have been obtained by electrodeposition on Cu

substrates by using a standard bath<sup>5</sup> at a temperature of 80°C and electrolytic current densities ranging from 50 mA cm<sup>-2</sup> to 600 mA cm<sup>-2</sup>. The samples are 50 mm long and 10 mm wide, its thickness being of approximately 50 μm for most of them except for those obtained with very low currents, which are of the order of 10 μm. Calorimetric studies have been performed under Ar atmosphere at different scanning rates on a DSC-7 calorimeter. SEM observations have been carried out by working at 8 KV and X-ray diffractograms have been performed with α-Cu radiation at 0.1°(2θ)/min. The composition of the samples has been studied by plasma absorption spectrometry.

### 3. Results

Continuous heating DSC curves (at constant heating rate) of all samples have been performed, all of them showing the existence of two peaks that are not always completely resolvable. Fig.1 shows the DSC curves (at 10°C min<sup>-1</sup>) of three samples of compositions with low ( $x = 12.5$ ), medium ( $x = 20.5$ ) and high ( $x = 26$ ) phosphorus content. Fig.2 shows the temperature of the maximum (for scanning rate of 40°C min<sup>-1</sup>) of each peak as a function of the composition. For compositions close to the eutectic both peaks are superimposed, for those far from the eutectic both peaks are clearly resolved. The crystallization enthalpy is, independently of composition, of the order of 60 J/g for both processes (when both peaks are not resolvable the global enthalpy is of approximately 120 J/g).

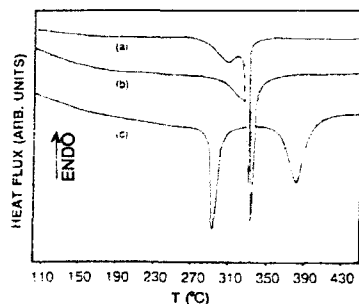


Fig.1. DSC curves of samples with high (a), medium (b) and low (c) P content.

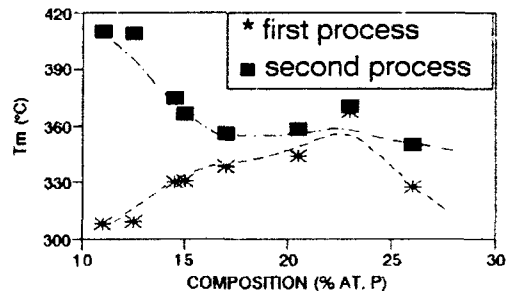


Fig.2. Temperature for the maximum of the crystallization peaks as a function of composition (40°C min<sup>-1</sup>).

The crystallization kinetics of amorphous alloys is usually ruled by a nucleation and growth process and the crystallized fraction  $\alpha$  can be expressed as

$$d\alpha/dt = k(T) f(\alpha) \quad (1)$$

where  $k(T)$  is assumed to have an Arrhenius behaviour

$$k(T) = A \exp(-E/KT) \quad (2)$$

E being the activation energy of the process, K the Boltzmann constant, T the absolute temperature and A a frequency factor. By measuring the temperature of the maximum  $T_m$  for each peak and process (when resolvable) at different scanning rates (10, 20, 40 and 80°C min<sup>-1</sup>) we have obtained the corresponding activation energies and frequency factors through the Kissinger plots<sup>6</sup> (table 1).

Table 1. Activation energies and frequency factors for both processes as a function of composition.

Composition (% at. P)	1 <sup>st</sup> Process		2 <sup>nd</sup> Process	
	E (eV)	A (s <sup>-1</sup> )	E (eV)	A (s <sup>-1</sup> )
26.0	1.8	6x10 <sup>13</sup>	1.9	9x10 <sup>13</sup>
20.5	---	-----	1.8	8x10 <sup>12</sup>
17.0	2.3	4x10 <sup>17</sup>	1.9	7x10 <sup>13</sup>
16.5	2.1	8x10 <sup>16</sup>	1.9	7x10 <sup>12</sup>
15.0	2.4	6x10 <sup>18</sup>	---	-----
13.5	1.8	4x10 <sup>14</sup>	2.0	2x10 <sup>13</sup>
12.5	2.2	5x10 <sup>17</sup>	1.9	4x10 <sup>12</sup>
12.0	1.8	5x10 <sup>14</sup>	2.0	2x10 <sup>13</sup>
11.0	2.1	6x10 <sup>16</sup>	2.0	1x10 <sup>13</sup>

X-ray diffractograms of samples with P content close or lower than the eutectic performed after completion of the first peak indicate the presence of Co plus an amorphous halo, meanwhile after completion of the second peak a mixture of Co plus Co<sub>2</sub>P can be observed. SEM observation of fresh fractures of these samples show the presence of a homogeneous microstructure composed of almost equiaxed crystals with sizes of the order of tenths of microns (fig.3). For samples with higher P content, the final crystallization product also shows the presence of Co plus Co<sub>2</sub>P, this one showing a strong texture with the [001] axis perpendicular to the sample plane. The dimension of the Co<sub>2</sub>P crystals along such direction has been evaluated by using the Scherrer expression, being of the order of 20 nm.



Fig.3. SEM micrograph of crystallization product of sample with x=12.5.

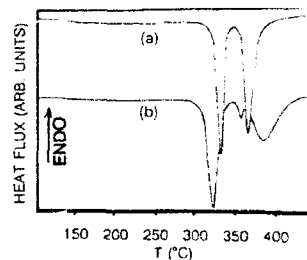


Fig.4. DSC curves of the central (a) and edge (b) regions of sample with x=15.

In order to study the effects of the compositional inhomogeneities<sup>7</sup> at the edges of the samples on the calorimetric measurements, a piece (5 mm long) of a sample with x=15 has been divided into four approximately equal pieces corresponding to

two central and two edge zones respectively. The DSC curves (at  $40^{\circ}\text{C min}^{-1}$ ) of the pieces including the edges present three processes: the first and third processes take place at temperatures that correspond to the processes of a sample with higher Co content meanwhile the second one occurs at a temperature that is very close to that of the sample with  $x=20$  as shown in figure 4.

#### 4. Discussion

Continuous heating DSC curves have allowed us to study separately the processes that conform the crystallization of this system, as well as their activation energies and frequency factors. The activation energy of the first process has an average value of 2.1 eV and a frequency factor higher than  $10^{14}\text{s}^{-1}$ . The second process has lower activation energy (approximately 1.9 eV) and a frequency factor of the order of  $10^{12}\text{s}^{-1}$  which suggests that it is due to a single atom diffusion mechanism. Although having an activation energy that remains almost constant independently of composition, this (second) process changes when moving from compositions with P content lower than that of the eutectic towards those with higher P content, as shown by the difference in the  $\text{Co}_2\text{P}$  texture. The almost equiaxed crystals that can be observed by SEM suggest that the crystallization process takes place through a nucleation and growth process. These crystallites are already observable after the completion of the first process, which seems to be responsible for the final microstructure. Some conclusion can be drawn regarding the previously reported<sup>7</sup> higher Co content at the edges of these samples. The comparison between the thermograms of central and edge regions indicates that the composition of the edges is not homogeneous but is made up of a mixture of two phases, one with composition close to the eutectic and another one with higher Co content.

#### 5. References

1. H. Bestgen, in *Rapidly Quenched Metals*, eds. S. Steeb and H. Warlimont (Elsevier Science Publishers B.V., Amsterdam, 1985).
2. R. Sonnenberg and G. Dietz, in *Rapidly Quenched Metals*, eds. S. Steeb and H. Warlimont (Elsevier Science Publishers B.V., Amsterdam, 1985).
3. J.M. Riveiro, M.C. Sánchez-Trujillo and G. Rivero, *IEEE Trans. on Mag. Mag-20(5)* (1984) 1376.
4. J. Dubowik and R. Gontarz, *J. Magn. Magn. Mat.* **62** (1986) 197.
5. A. Brenner, D.F. Couch and E. K. Williams, *J. Res. Nat. Bur. Stand.* **44** (1950) 109.
6. H.E. Kissinger, *An. Chem.* **29(11)** (1957) 1702.
7. F. Cebollada, V.E. Martín, M. Vázquez, F. Carmona, G. Rivero and J.M. González, in *Basic Features of the Glassy State*, eds. J. Colmenero and A. Alegría (World Scientific, Singapore, 1990).

## CRYSTALLIZATION KINETICS OF Pd-Ni-P AMORPHOUS ALLOYS

I. Tellería

Departamento de Física de Materiales, Universidad del País Vasco UPV/EHU  
Facultad de Química, Apdo. 1072, 20080 San Sebastián, Spain

and

J.M. Barandiarán

Departamento de Electricidad y Electrónica, Universidad del País Vasco UPV/EHU  
Facultad de Ciencias, Apdo. 644, 48080 Bilbao, Spain

## ABSTRACT

Crystallization kinetics of glassy  $\text{Pd}_{100-3x}\text{Ni}_{2x}\text{P}_x$  (where  $x$  takes values of 14, 16 and 23) has been studied by Differential Scanning Calorimetry under non isothermal treatments. Thermograms show a simple peaked crystallization exotherm for  $x=23$ , two crystallization stages for  $x=16$  and three crystallization stages for  $x=14$ . The crystallization processes have been analyzed by using the Kissinger's method. In all the cases, the first peak was better fitted by a Vogel-Fulcher type rate constant. Moreover, crystallization heat was studied showing that the crystallization enthalpy v.s. crystallization temperature also follows a Vogel-Fulcher law.

## INTRODUCTION

Crystallization process in metallic glasses is a topic of considerable interest. Technologically the subject is of importance since the properties of a glass can be changed significantly by the onset of crystallization, and the utilization of the glass is thus limited by the conditions of time and temperature at which crystallization occurs.

We present in this communication results from a systematic study of the crystallization kinetics in Pd-Ni-P glasses using Differential Scanning Calorimetry (DSC).

## EXPERIMENTAL

In this work a series of amorphous samples of nominal composition  $\text{Pd}_{100-3x}\text{Ni}_{2x}\text{P}_x$ , where  $x$  is 14, 16 and 23, was studied.

DSC measurements were performed on a Perkin-Elmer DSC 4, mass specimens around 2 mg were annealed in aluminium containers under a pure nitrogen atmosphere.

Heating rates of 1, 2, 5, 10, 20, 40, and 80 K/min were used and the starting temperature was 520 K for all runs. Samples were heated up to that temperature at 320 K/min from room temperature. The temperature scale was previously calibrated from the melting endotherms of pure  $K_2SO_4$  and zinc.

### RESULTS AND ANALYSIS

Different types of crystallization behaviour were exhibited upon heating depending on the glass composition. Figure 1 shows DSC thermograms obtained at a heating rate of 20 K/min from the three type ribbons.

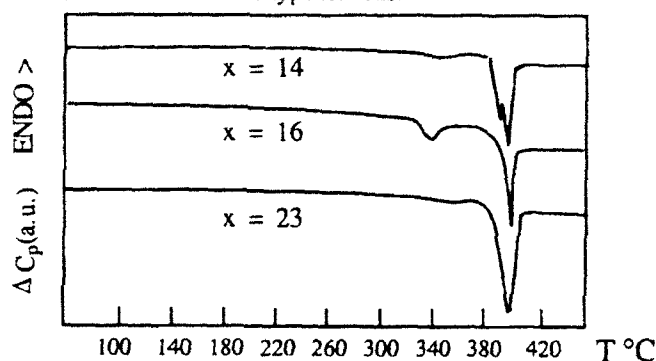


Figure 1. Typical DSC curves for  $Pd_{100-3x}Ni_{2x}P_x$  alloys obtained at a heating rate of 20 K/min

The kinetics of the transformation was analyzed in terms of the Avrami equation

$$\xi(t) = 1 - \exp \left[ - (Kt)^n \right]$$

obtaining the transformed fraction  $\xi$  at a time  $t$  and for a constant temperature  $T$ . Here  $K=K(T)$  is the rate constant of the crystallization process and  $n$  is the Avrami index. The alloy fraction transformed by heating at a constant rate  $R$  can be determined from an easily derived<sup>1)</sup> non-isothermal equation

$$\xi(T) = 1 - \exp \left\{ - \left( \frac{1}{R} \int_{T_1}^T K(T) dT \right)^n \right\} \quad (1)$$

The rate constant  $K(T)$  depends on a number of parameters<sup>2)</sup>; nevertheless, viscosity is the most important factor in the temperature range at which crystallization occurs, then

$$K(T) \equiv \frac{C}{\eta(T)}$$

If one considers a Vogel-Fulcher expression for the viscosity

$$\eta(T) \propto \exp\left(\frac{1}{\alpha_f(T-T_0)}\right)$$

where  $\alpha_f$  is the free volume expansion coefficient, and  $T_0$  is the temperature at which the free volume vanishes, the rate constant  $K(T)$  becomes

$$K(T) \equiv K_0 \exp\left(\frac{1}{\alpha_f(T-T_0)}\right) \quad (2)$$

By introducing expression (2) into expression (1) one reaches

$$\frac{1}{n} \ln \ln \left(\frac{1}{1-\xi}\right) = \ln \frac{K_0 \alpha_f}{R} + 2 \ln (T-T_0) - \frac{1}{\alpha_f(T-T_0)} + \ln (1-2\alpha_f(T-T_0)) \quad (3)$$

Expression (3) can be applied at the temperature  $T_x$ , at which  $d\xi/dT$  is maximum. At this temperature,  $\xi(T_x)$  is a constant ( $\xi(T_x) \approx 0.62$ ) independently of the heating rate<sup>3</sup>). By so doing we obtain

$$\ln \frac{(T_x - T_0)^2}{R} = \frac{1}{\alpha_f(T_x - T_0)} + \ln (1-2\alpha_f(T_x - T_0)) + \text{constant} \quad (4)$$

In order to obtain the Vogel-Fulcher parameters to the expression (4)  $\alpha_f$  and  $T_0$  we have used a computer program which fits the temperature  $T_x$  at different heating rates. Figure 2a is a typical Kissinger plot ( $\ln T_x^2/R$  vs  $1/T_x$ ) of experimental points and theoretical fitting. A slight curvature is apparent in this plot indicating some systematic deviation from an Arrhenius behaviour and it can be taken as an evidence for a Vogel-Fulcher behavior. The values of  $\alpha_f$  and  $T_0$  obtained are shown in Table

Sample	$\alpha_f(K^{-1})$	$T_0(K)$
Pd <sub>58</sub> Ni <sub>28</sub> P <sub>14</sub>	3 10 <sup>-4</sup>	452
Pd <sub>52</sub> Ni <sub>32</sub> P <sub>16</sub>	2.8 10 <sup>-4</sup>	452
Pd <sub>31</sub> Ni <sub>46</sub> P <sub>23</sub>	2.4 10 <sup>-4</sup>	452

Figure 2b shows a linear behaviour of crystallization enthalpy ( $\Delta H$ ) when temperature  $T_x$  was varied. As can be seen  $\Delta H=0$  when  $T_x=450$  K, which coincides with the  $T_0$  value obtained by analyzing the crystallization process. This agreement can be explained by the proportionality of  $\Delta H$  and free volume, and in free volume theories this magnitude varies with temperature as follows  $V \propto (T-T_0)$ .

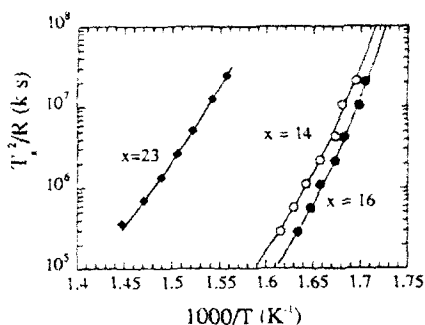


Figure 2a. Kissinger plot for the first crystallization peak

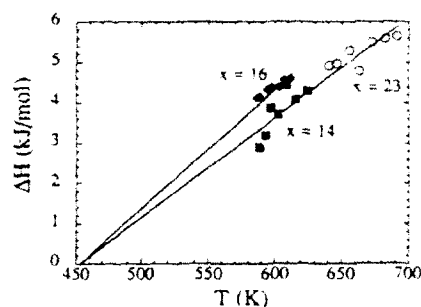


Figure 2b. Change of the crystallization enthalpy as a function of crystallization temperature

### CONCLUSIONS

The crystallization processes on the Pd-Ni-P glassy system show a clear non-Arrhenius temperature dependence which can be well described assuming the rate constant of crystallization to be proportional to the supercooled liquid viscosity, i.e. to follow a Vogel-Fulcher law. The temperature dependence of the increment of enthalpy of crystallization is also consistent with this description. These results confirm previous work on very different metallic glasses, suggesting that the free volume framework is adequate to describe the crystallization process of metallic glasses.

On the other hand, the free-volume parameters here obtained agree with those reported<sup>4)</sup> for viscosity. However, only a slight dependence of these parameters on composition was observed in the present system.

### ACKNOWLEDGMENTS

One of the authors (I.T.) wish to thank Guipuzkoako Foru Aldundia for partial financial support.

### REFERENCES

- 1.- J. Colmenero and J.M. Barandiarán, *J. Non-Cryst. Solids* **30**, 263 (1979).
- 2.- H.A. Davis, *Phys. Chem. Glasses* **17**, 159 (1976)
- 3.- J. Colmenero J. Ilarraz and J.M. Barandiarán, *Thermochim. Acta* **35**, 381 (1980)
- 4.- L.W. Koebugge, J. Sietsma and A. van der Beukel, *J. Non-Cryst. Solids*, **117/118**, 609 (1990).



## ELECTRON MICROSCOPY STUDY OF CRYSTALLIZATION OF A $\text{Ni}_{68}\text{Cr}_{14}\text{B}_{18}$ GLASS.

A. Criado, M. Millán and A. Conde.  
*Dpto. de Física de la Materia Condensada*  
*Instituto de Ciencia de Materiales. C.S.I.C.*  
*Universidad de Sevilla. Spain.*

### ABSTRACT

Devitrification of the  $\text{Ni}_{68}\text{Cr}_{14}\text{B}_{18}$  glass consist of two stages, evidenced as two overlapped exotherms in isothermal DSC records. The crystallization onset (at 10K/min) is 690 K. Electron microscopy reveals a precipitation of small crystallites of Ni followed by the formation of  $\text{Ni}_4\text{B}_3$  and  $\text{Ni}_7\text{B}_3$  type phases. For samples crystallized inside the microscope, crystallization starts at the border and gives  $\text{Ni}_4\text{B}_3$  and  $\text{Ni}_7\text{B}_3$ , preceeding the precipitation of Ni crystallites inside.

### 1. Introduction

Thermal stability and crystallization mechanisms of amorphous alloys strongly depend upon their chemical composition and the addition of a third element to a binary metal-metalloid glass generally increases thermal stability. In Ni-B metallic glasses, crystallization usually starts from the free surface without almost any nucleation in the bulk<sup>1</sup>.

In this paper we report an electron microscopy study of the amorphous to crystal transformation of a Ni-based glass containig Cr. Previously, a calorimetric study including crystallization kinetics analysis was reported<sup>2</sup>.

### 2. Experimental

Metglass ribbon (MBF80) of a nominal composition  $\text{Ni}_{68}\text{Cr}_{14}\text{B}_{18}(\text{C})$  was supplied by Allied Chemicals Co. (USA). Samples for electron microscopy were thinned by electropolishing in an usual perchloric and acetic bath or by ion-beam techniques using a dual ion mill device operated with argon. TEM study was performed in a Hitachi H800 microscope operated at 200 kV. Two types of samples were studied: partially or fully crystallized inside the calorimeter

chamber prior to thinning and amorphous to be crystallized after thinning inside the microscope.

### 3. Results

As previously reported<sup>2</sup> alloy crystallizes in two stages revealed as two overlapped exotherms in Isothermal DSC records. However, the enthalpy involved in the first one is

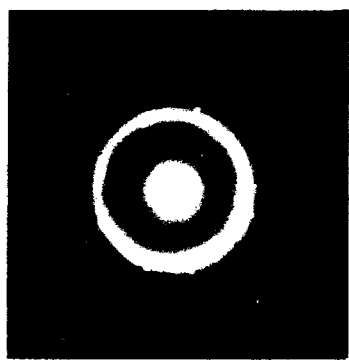


Fig. 1

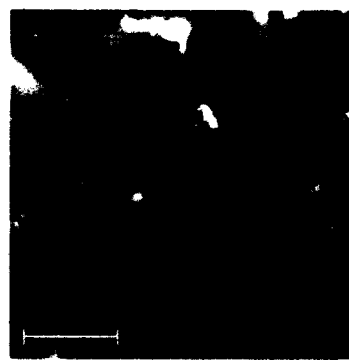


Fig. 2. (Bar = 1500 Å)

considerably lower than that of the second and it is not clearly defined in non-isothermal records. The crystallization onset occurs at  $690 \pm 1$  K (at 10 K/min.), the overall enthalpy being 4.6 kJ/mol.

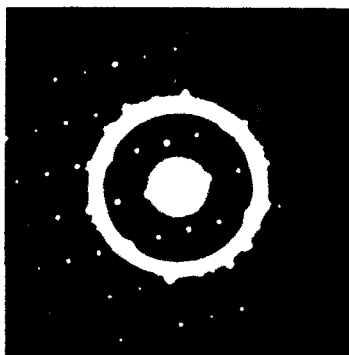


Fig. 3



Fig. 4

For partially crystallized (up to 707 K) samples a high number of small size crystallites are homogeneously distributed throughout the amorphous matrix, identified as  $\text{Ni}(\text{Cr})$  cubic phase by electron diffraction patterns (Fig. 1). The small fraction of precipitated crystals should explain the low enthalpy involved in this stage. This is an usual feature in the crystallization of Ni-based metallic glasses. This initial precipitation is immediately followed by the formation of a lower number of larger crystals (Fig. 2), identified by electron diffraction and dark field images as a  $\text{Ni}_4\text{B}_3$  orthorhombic phase (Fig. 3). Also, some crystals of a hexagonal  $\text{Ni}_7\text{B}_3$  phase<sup>3</sup> (Fig. 4) were identified.

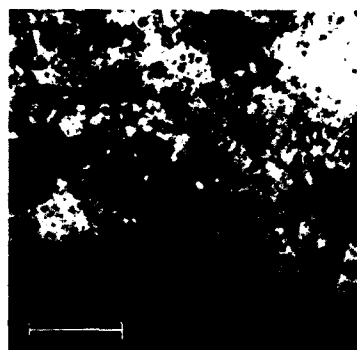


Fig. 5. (Bar = 7000 Å)



Fig. 6. (Bar = 1500 Å)

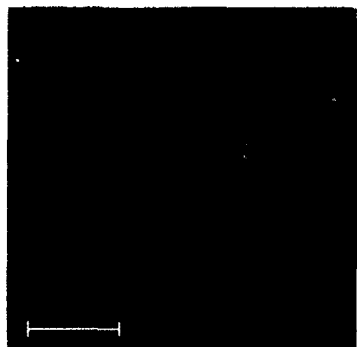


Fig. 7. (Bar = 3500 Å)

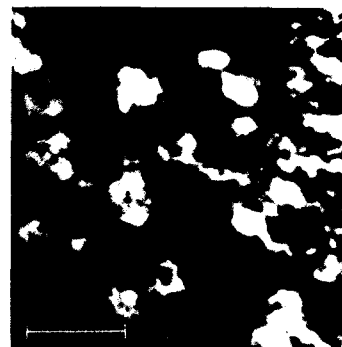


Fig. 8. (Bar = 2000 Å)

Fully crystallized samples contain small Ni crystals and larger crystals of the two phases (Fig. 5) cited above, but it seems that the  $\text{Ni}_7\text{B}_3$  type phase gradually transforms to  $\text{Ni}_4\text{B}_3$ .

Crystallization inside the microscope gives the same crystalline phases as final products of the crystallization but differences in morphology are observed. In these samples, crystallization begins at about 670 K on the edge and the crystallization front (Fig. 6) advances inside the sample. Electron diffraction on the crystallized band reveals the presence of both  $\text{Ni}_3\text{B}_2$  and  $\text{Ni}_3\text{B}$  type phases. At about 760 K, a precipitation of Ni crystallites is observed inside the untransformed zones (Fig. 7). This precipitation is followed by the formation of larger crystals of the two boride phases. Finally, as a combined result of the two mechanisms: advance of the front and transformation of the inside zone, the sample becomes fully crystallized (Fig. 8).

In spite of the final crystalline phases being the same for the two types of samples studied, differences in resulting grain morphologies are significative. On the other hand, transformation of thinned samples inside the microscope allows the observation that surface crystallization preceeds the precipitation of crystals in the bulk.

#### 4. Acknowledgments

This work was supported by the CICYT of the Spanish Government (Project MAT88-301) and by the Junta de Andalucía.

#### 5. References.

1. U. Köster. *Z. Metallkd.* **75** (1984) 691.
2. A. Criado, M. Millán, A. Conde and R. Márquez. *Magnetic Properties of Amorphous Metals*. (Elsevier Science Publishers, 1987), p. 291.
3. B. Punge-Witteler and U. Köster. *Mat. Sci. and Engng.* **97** (1988) 343.

## THE STUDY OF CRYSTALLIZATION OF GLASSES BY THERMAL ANALYSIS

J. MÁLEK and V. SMRČKA

*Joint Laboratory of Solid State Chemistry of the Czechoslovak Academy of Sciences  
and Institute of Chemical Tech., Čs. Legit sq. 565, PARDUBICE 532 10  
(Czechoslovakia)*

### ABSTRACT

A simple test of applicability of the Johnson-Mehl-Avrami (JMA) model is suggested. It is shown that two parametric model allows more quantitative description of the crystallization kinetics of  $(\text{GeS}_2)_{0.3}(\text{Sb}_2\text{S}_3)_{0.7}$  glass.

### 1. INTRODUCTION

In the last years many papers have been published on the determination of the kinetic parameters of crystallization processes from differential scanning calorimetry (DSC) data. For the description of these processes the JMA model is frequently used. Nevertheless it was shown<sup>1-3</sup> that in some cases this model cannot be successfully used for a quantitative description of experimental data. It is also without any doubt that the kinetic model should not be assumed *a priori* but it should be determined experimentally. The aim of this contribution is to propose a simple method allowing to verify the applicability of the JMA model. This method is tested using DSC crystallization data of  $(\text{GeS}_2)_{0.3}(\text{Sb}_2\text{S}_3)_{0.7}$  glass.

### 2. THEORY

The exothermal heat flow ( $H'$ ) corresponding to the crystallization process as measured by DSC technique can be expressed by the following equation<sup>4</sup>:

$$H' = \Delta H_c A e^{-x} f(\alpha) \quad (1)$$

where  $\Delta H_c$  is the crystallization heat and  $x = E/RT$  is the reduced activation energy. The symbols  $A$ ,  $E$ ,  $T$ ,  $\alpha$  have their usual meaning of preexponential factor, activation energy, temperature and degree of crystallization, respectively. The form of kinetic term  $f(\alpha)$  depends on the mechanism of the crystallization process and for the JMA model it can be expressed by the following equation:

$$f(\alpha) = n(1 - \alpha) [-\ln(1 - \alpha)]^{1-1/n}. \quad (2)$$

Now we can introduce<sup>5</sup> the  $z(\alpha)$  function defined as follows:

$$z(\alpha) = \pi(x) H' T / \beta \quad (3)$$

where  $\beta$  is the heating rate and  $\pi(x)$  is an approximation of temperature integral in the form<sup>6</sup>:

$$\pi(x) = \frac{x^3 + 18x^2 + 88x + 96}{x^4 + 20x^3 + 120x^2 + 240x + 120} \quad (4)$$

The function  $z(\alpha)$  can easily be obtained by transformation of DSC data according to Eq.3. It can be shown<sup>5,7</sup> that  $z(\alpha)$  curve has a maximum  $\alpha_p^\infty = 0.632$  for the JMA model. It is very important that  $\alpha_p^\infty$  does not depend on the kinetic exponent and it is practically invariant with respect to the value of the activation energy used to calculate  $\pi(x)$  term. Therefore, the  $\alpha_p^\infty$  value can be used as a test of applicability of the JMA model. If it differs more than 1% from the theoretical value (i.e.  $\alpha_p^\infty < 0.625$  or  $\alpha_p^\infty > 0.64$ ) then the JMA model can hardly be used to obtain a good fit of experimental data.

### 3. EXPERIMENTAL

The synthesis of glassy  $(\text{GeS}_2)_{0.3}(\text{Sb}_2\text{S}_3)_{0.7}$  sample was carried out in a conventional way<sup>7</sup> using 5N purity elements as starting material. The bulk glass was crushed into a powder and then sieved to particle size of 70 - 90  $\mu\text{m}$ . All experiment were performed on powder samples of about 10 mg in sealed Al pans, using Perkin-Elmer DSC-7 instrument. The sample was rapidly heated in the DSC holder up to 523 K (above  $T_g$ ) at heating rate 320 K/min, and after 3 min the DSC scan was started using the selected heating rate (2 - 20 K/min).

### 4. RESULTS AND DISCUSSION

Fig.1 shows the experimental DSC curves (points), normalized for sample weight, corresponding to the crystallization of  $\text{Sb}_2\text{S}_3$  phase in  $(\text{GeS}_2)_{0.3}(\text{Sb}_2\text{S}_3)_{0.7}$  glass at heating rates 5, 10 and 20 K/min. The activation energy of the crystallization process calculated by standard methods<sup>8-10</sup> is  $E = 251 \pm 10$  kJ/mol. The maximum of  $z(\alpha)$  function, calculated using this value of activation energy, was found to be  $\alpha_p^\infty = 0.57 \pm 0.01$ . Therefore, it seems that the JMA model is not suitable in this case. The kinetic parameters calculated using the method described recently<sup>7</sup> are summarized in Table I. The theoretical curves (dashed lines) corresponding to these kinetic parameters

are compared in Fig.1. It is evident that there are differences especially in the leading edge of DSC peaks.

The JMA model function derived on the basis of physical-geometrical assumptions of regularly shaped bodies evidently can hardly describe real heterogeneous system. In that case is very problematic to find a physical meaning of kinetic exponent  $n$ . An alternative approach can be based, however, on any function satisfying the need of a simple Eq.1 without demanding the correlation to a real mechanism of the process. From this point of view the two parametric Šesták-Berggren (SB) model<sup>11</sup>:  $f(\alpha) = \alpha^m(1 - \alpha^n)$  can be find useful. The kinetic parameters calculated<sup>7</sup> for the SB model are summarized in Table I.

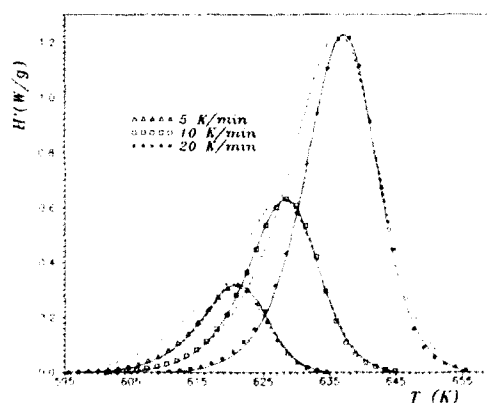


Fig.1

Experimental (points) DSC crystallization data of  $(\text{GeS}_2)_{0.3}(\text{Sb}_2\text{S}_3)_{0.7}$  glass for three different heating rates. Calculated curves corresponding to the JMA and SB model are shown by dashed and full lines, respectively

Table I  
Calculated kinetic parameters

Parameter	JMA model	SB model
m	-	1.31 +/- 0.07
n	1.47 +/- 0.04	1.0 +/- 0.1
ln A (1/s)	43.7 +/- 0.1	44.8 +/- 0.1
$\Delta H_c$ (J/g)	69 +/- 2	52 +/- 5

It is without any doubts that the SB equation allows quantitative description of the crystallization process as demonstrated by a good agreement between both experi-

mental and calculated<sup>7</sup> curves (full lines in Fig.1) for all heating rates. There is also a very good agreement between the calculated value of crystallization enthalpy ( $\Delta H_c$ ) for the SB model and experimentally determined one  $\Delta H_c = 52 \pm 1$  J/g.

## 5. CONCLUSIONS

It was shown that the  $\alpha_p^\infty$  value can be used as a simple test of applicability of the JMA model. If the  $\alpha_p^\infty$  is lower than 0.632 predicted by theory then empirical SB model could give more quantitative results. The calculated kinetic parameters can be used to predict the behavior of the system under e.g. isothermal conditions. Nevertheless, it should be stressed that the kinetic parameters calculated cannot say anything definitive about the real mechanism of the crystallization process. From this point of view, more attention should be paid to the morphological studies of the crystal growth.

## 6. ACKNOWLEDGEMENT

The authors gratefully acknowledge financial support for this work from the Czechoslovak Academy of Sciences (Grant No. 42901).

## 7. REFERENCES

1. L. Tichý, P. Nagels, *phys. stat. solidi A* **87** (1988) 769.
2. J. Málek, J. Klikorka, *J. Thermal. Anal.* **32** (1987) 1883.
3. J. Málek, *J. Non-Cryst. Solids* **107** (1989) 323.
4. J. Šesták, *Thermophysical properties of solids* (Elsevier, Amsterdam 1984).
5. J. M. Criado, J. Málek, A. Ortega, *Thermochim. Acta* **147** (1989) 337.
6. G. I. Senum, R. T. Yang, *J. Thermal. Anal.* **11** (1977) 445.
7. J. Málek, V. Smrčka, *Thermochim. Acta* **186** (1991) 153.
8. H. E. Kissinger, *Anal. Chem.* **29** (1957) 1702.
9. T. Ozawa, *J. Thermal. Anal.* **2** (1979) 301.
10. H. L. Friedman, *J. Polym. Sci. C* **6** (1964) 183.
11. J. Šesták, G. Berggren, *Thermochim. Acta* **3** (1971) 1.



## CRYSTALLIZATION OF THE $\text{Se}_{85}\text{Te}_{15}$ GLASSY ALLOY: CALORIMETRIC AND MORPHOLOGICAL STUDY

M. D. BARÓ, Y. CALVENTUS, S. SURINACH, M. T. CLAVAGUERA-MORA

*Física de Materials, Departament de Física,  
Universitat Autònoma de Barcelona, 08193 Bellaterra, Spain*

and

N. CLAVAGUERA

*Departament d'Estructura i Constituents de la Matèria, Facultat de Física,  
Universitat de Barcelona, Diagonal 647, 08028 Barcelona, Spain*

### ABSTRACT

The crystallization behaviour of  $\text{Se}_{85}\text{Te}_{15}$  was studied by differential scanning calorimetry, X-ray diffraction, optical and scanning electron microscopy. Crystallization takes place by nucleation and growth of individual crystals. The morphological analysis allowed to determine the nucleation and crystal growth rates and the activation energy for each process. The results obtained from the morphological studies are in agreement with the calorimetric ones.

### 1. Introduction

Chalcogenide semiconducting glasses, containing a large proportion of chalcogen atoms (S, Se or Te), are attractive materials due to their unusual optical properties. Recently, it has been pointed out that Se-Te alloys have some advantages over amorphous Se as far as their use in xerography is concerned<sup>1</sup>. In the technical applications the thermal stability of chalcogenide glasses is a problem of fundamental interest because the useful operating temperature range will be determined by the structural changes and eventual crystallization occurring at the operating temperature. Besides, the crystallization mechanisms are of importance because the glassy state may be used as a homogeneous state from which suitable crystalline phases, morphologies and distributions may be obtained by controlled crystallization. In this paper we report on the crystallization behaviour of bulk  $\text{Se}_{85}\text{Te}_{15}$  air-quenched glass investigated by differential scanning calorimetry (DSC), X-ray diffraction (XRD), optical microscopy (OM) and scanning electron microscopy (SEM). By the coupling of these techniques, nucleation rates, growth velocities and the activation energies for nucleation and crystal growth can be determined.

## 2. Experimental results and analysis

The evolution as a function of temperature of the XRD patterns shows that the emerging crystalline phase reflections correspond to h.c.p. Se(Te). On increasing temperature the peaks become more narrow and sharper till crystallization is completed. From the SEM micrographs we can observe randomly distributed spherulitic crystals in the bulk of the samples. The lamellae possess typical thicknesses of about  $0.3 \mu\text{m}$ . Direct analysis of the optical micrographs allowed us to determine crystal sizes and number densities, as well as the fraction of crystallized material, using standard quantitative metallographic methods. From the largest crystal size, the growth rates of the bulk crystals were evaluated and are shown in Figure 1. It should be noted that the growth rate observed remains constant at each temperature, with an increasing growth rate at higher temperature. The constant growth rates at each temperature presented in Figure 1 suggest a polymorphic crystallization mechanism of a single phase. The temperature dependence could be described by an Arrhenius relationship with an activation energy of  $154 \text{ kJ/mol}$ . The number of crystals per unit volume was calculated as  $N_v = N_a/\bar{\Phi}$ , where  $N_a$  is the number of crystals per unit area on the micrograph and  $\bar{\Phi}$  the average crystal size<sup>2</sup>. The variation of crystal number density with annealing time and temperature is presented in Figure 2. For nucleation, constant rates are seen only after an initial incubation period which decreases in value at higher temperatures. The temperature dependence could be explained by an Arrhenius behaviour with an activation energy for the nucleation of  $111 \text{ kJ/mol}$ . In a similar way the volume fraction of crystallized material was determined and the S-shaped curve indicates that the isothermal transformation is governed by the mechanisms of nucleation and growth. As the crystallization process proceeds by nucleation and growth, the Johnson-Mehl-Avrami-Erofe'ev (JMAE) model was assumed. From DSC measurements<sup>3</sup> the value obtained for the apparent activation energy is  $114 \text{ J/mol}$ , the best fit for the exponent in JMAE equation is 1.8 and the preexponential factor  $4.8 \cdot 10^{12} \text{ s}^{-1}$ .

## 3. Discussion

Further examination of the agreement between the experimental results obtained by the microstructural analysis and the calorimetric study can be undertaken by the use of the classical growth rate equation as a function of the different quantities determining the process. This is:

$$u = \frac{fkT}{3\pi a_0^2 \eta} [1 - \exp(-\Delta G/RT)] \quad (1)$$

where  $a_0$  is the atomic diameter,  $\eta$  the viscosity,  $\Delta G$  the Gibbs free energy difference between the liquid and the crystal, and  $f$  the fraction of sites at the crystal-liquid interface where atoms may preferentially be added and removed. Assuming a viscosity as a function of temperature given by  $\eta = \eta_0 \exp(B/(T - T_0))$ , the values of the growth rate observed experimentally are well reproduced<sup>4</sup>. Further, extrapolating the equation (1) at higher temperatures, the behaviour shown in Figure 3 is obtained. That is, at the temperatures at which the microstructural analysis was performed, the apparent activation energy of crystal growth is  $150 \text{ kJ/mol}$  but at the temperatures where the crystallization by heating at scan rates in the range  $1.25$  to  $40 \text{ K/min}$  occurs, that is around  $410 \text{ K}$ , the apparent

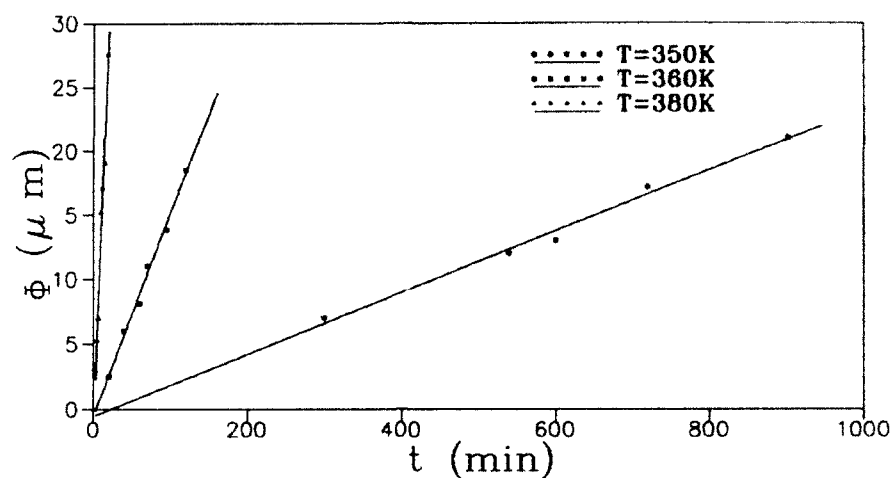


Fig. 1.- Growth of crystals (maximum diameter  $\Phi$ ) versus time  $t$  in isothermal annealings for  $\text{Se}_{85}\text{Te}_{15}$ .

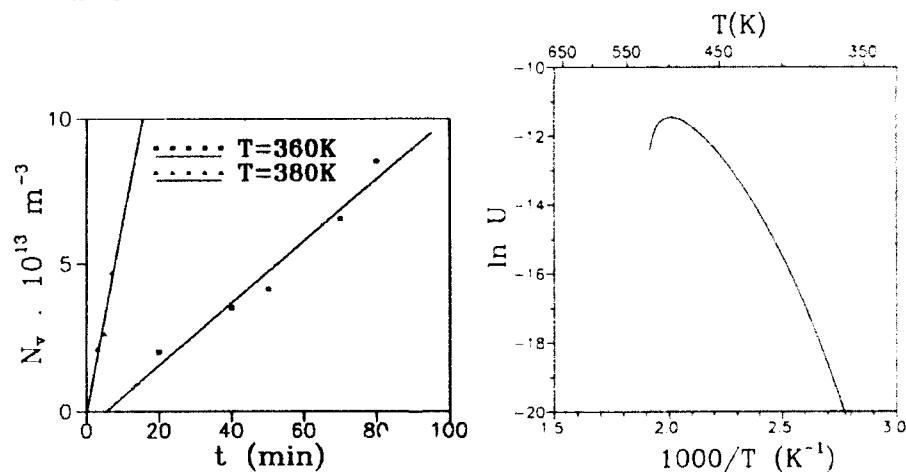


Fig. 2. (left)- Number of nuclei  $N_v$  per unit volume versus time in isothermal annealings for  $\text{Se}_{85}\text{Te}_{15}$ .

Fig. 3. (right)- Temperature dependence of the growth rate.

activation energy is 120 kJ/mol. It is not possible to use the classical nucleation theory to explain the experimental nucleation rates observed, because no incubation time is predicted by such theory. However, if the JMAE model is applied, the value of the kinetic exponent may be deduced from the microscopical analysis results. The value obtained agrees with that expected for a constant nucleation rate and two-dimensional phase-boundary limited crystal growth. The detailed analysis of the calorimetric results shows that, at low values of the transformed fraction  $\alpha$ , a value of 2.8 is obtained but in almost the whole interval the value is 1.8. The explanation comes from the fact that heterogeneous superficial nucleation is also present in the samples and interferes with the bulk uniform nucleation.

#### 4. Conclusions

The coupling of microstructural and calorimetric analyses of the crystallization in  $\text{Se}_{85}\text{Te}_{15}$  allowed to get a detailed picture of the process. A uniform bulk nucleation, which needs an incubation time to proceed, is obtained. Heterogeneous nucleation is also present. The first stages of the crystallization proceed by nucleation and two-dimensional growth in lamellae of  $\sim 0.3 \mu\text{m}$  thickness arranged into spherulite particles. The apparent activation energy of the crystallization process at temperatures of the order of 410 K is 114 kJ/mol, while the extrapolated value of the apparent activation energy of crystal growth at these temperatures is 120 kJ/mol, and the apparent activation energy of uniform bulk nucleation at 350-380 K is 111 kJ/mol. The comparison between the microstructural analysis and the calorimetric studies can be done for the first stages of the crystallization. Otherwise the calorimetric studies lead to the mean crystallization behaviour which is not a simple extrapolation of the results obtained by the microstructural analysis.

#### 5. Acknowledgements

The authors wish to acknowledge gratefully Mr. X. Alcobé from the "Serveis Científico-Tècnics" of the University of Barcelona for the X-ray diffraction measurements. The research reported in this paper was supported by the CICYT (project No. MAT90-0454) and by the CIRIT (AR 90-3641).

#### 6. References

1. H. Yang, W. Wang and S. Min, *J. Non-Cryst. Solids* **80** (1986) 503.
2. J.W. Cahn and J. Nutting, *Trans. metall. Soc. A.I.M.E.* **215** (1959) 526.
3. Y. Calventus, M. D. Baró, S. Suriñach, S. Bordas, M. T. Clavaguera-Mora and N. Clavaguera, *Anal. Fis.* **B 86** (1990) 134.
4. M. T. Clavaguera-Mora, S. Suriñach, M. D. Baró, S. Bordas and N. Clavaguera, *J. Thermal Anal.* **37** (1991) 1261.

## THE GLASS FORMING ABILITY IN Cu - As - Se SYSTEM

J. MÁLEK and L. TICHÝ

*Joint Laboratory of Solid State Chemistry of the Czechoslovak Academy of Sciences  
and Institute of Chemical Technology, Čs. Legií 565, 532 10 PARDUBICE  
(Czechoslovakia).*

### ABSTRACT

The crystallization behaviour of  $\text{Cu}_x(\text{As}_{0.4}\text{Se}_{0.6})_{1-x}$  glasses (for  $0 < x \leq 0.239$ ) is studied by X-ray diffraction (XRD), differential scanning calorimetry (DSC), scanning electron microscopy (SEM) and energy dispersive analysis of X-rays (EDX).

The crystalline phase formed in the glass as well as the corresponding kinetic parameters characterizing the crystallization process were determined. The glass forming ability criterions are discussed.

### 1. INTRODUCTION

The study of the properties of Cu-As-Se glasses is of considerable interest because the mean coordination number (CN) increases with an increase of copper content ( $\text{CN}_{\text{Cu}} = 4$ ,  $\text{CN}_{\text{Se}} = 2$ ) up to values of  $\text{CN} > 3$ .<sup>1</sup> Simultaneously with an increase of copper content the sign of correlation energy changes from negative to positive one<sup>1</sup>. Hence, the Cu-As-Se matrix (for some chemical compositions) has some characteristic similarities to the tetrahedrally coordinated solids.<sup>2,3</sup>

Our interest in the present study is mainly focused to the study of the glass transition ( $T_g$ ) and devitrification processes of Cu-As-Se glasses. The results obtained allow us to formulate the glass forming ability (GFA) criterion which, as we believe, has a general validity and can be applied to any glass forming system.

### 2. EXPERIMENTAL

The syntheses of the amorphous samples of  $\text{Cu}_x(\text{As}_{0.4}\text{Se}_{0.6})_{1-x}$  composition ( $x = 0.0217, 0.0543, 0.065, 0.076, 0.1304$  and  $0.239$ ) were carried out in evacuated ( $p \sim 10^{-4}$  Pa) quartz ampoules with 5N purity elements as starting materials. The ampoules were heated in a rotary furnace at  $900^\circ\text{C}$  for 10 hours and then water quenched. The glassy nature of the material was confirmed by XRD.

The DSC measurements were performed with Perkin-Elmer DTA-1700/TADS instrument operating in the heat flux DSC mode. Crushed samples were sealed in small quartz ampoules fitting the platinum measuring cups. The partially devitrified samples obtained by isothermal annealing were also studied by the XRD, SEM and EDX methods.

### 3. RESULTS AND DISCUSSION

The DSC thermograms of  $\text{Cu}_x(\text{As}_{0.4}\text{Se}_{0.6})_{1-x}$  glasses of  $0.0217 \leq x \leq 0.239$  compositions are shown in Fig.1. The small endotherm near 460 K corresponds to the  $T_g$ . The compositional dependence of  $T_g$  is plotted in Fig.2 (points).

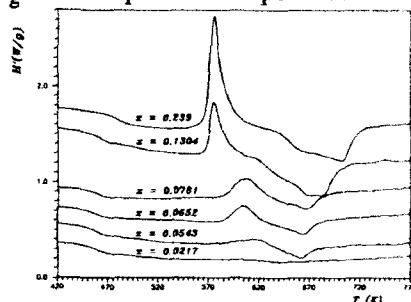


Fig. 1  
The DSC thermograms for  $\text{Cu}_x(\text{As}_{0.4}\text{Se}_{0.6})_{1-x}$  glasses normalized for sample weight (heating rate 20 K/min)

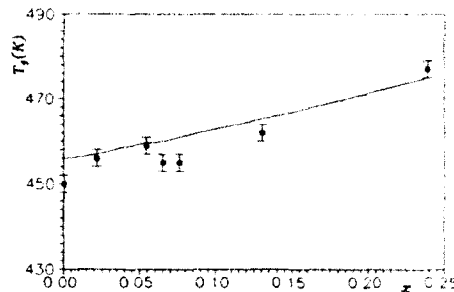


Fig. 2  
The compositional dependence of the  $T_g$  (points).  
The full line was calculated using Eq.1.

These values were determined by integral method<sup>4</sup> for heating rate 20 K/min. It is very important that despite a considerable increase of CN with increasing content of Cu in glassy matrix, the  $T_g$  values are nearly invariant with  $x$ . Therefore, the Tanaka's  $T_g$  vs. CN correlation<sup>5</sup> seems not to be acceptable in this case. It was found, however, that the values of  $T_g$  in Cu-As-Se system can be well correlated with CN and average atomization enthalpy of the glass  $H_A$  using a modified DeNeufville-Rockstad's approach<sup>6</sup>

$$T_g(x) = \frac{C}{32.2 k_B} \cdot \frac{H_A(x)}{CN(x)} \quad (1)$$

where  $C = (\text{CN} + 0.5)/2$  and  $k_B$  is the Boltzman constant. The compositional dependence of  $T_g$  calculated according to Eq.1 is shown in Fig.2 by full line.

The crystallization processes are indicated by the exothermal peaks which appear on the DSC thermograms (Fig.1) for  $x > 0.0217$ . The exothermal heat flow ( $H'$ ) corresponding to the crystallization process can be well approximated<sup>7</sup> by Eq.2

$$H' = \Delta H_{cr} \cdot K(T) \alpha^m (1 - \alpha)^n \quad (2)$$

where  $\Delta H_{cr}$  is the crystallization heat,  $\alpha \in (0, 1)$  is the degree of crystallization and  $K(T) = A \exp(-E/RT)$  is the crystallization rate constant. The kinetic parameters  $A$ ,  $E$ ,  $m$  and  $n$  were calculated by the evaluation procedure described recently<sup>8</sup>. The results for three selected glasses are summarized in Table I. It was experimentally confirmed that these kinetic parameters are invariant with respect to the heating rate in the range: 2 - 20 K/min. The experimental data (points) measured at 10 K/min together with DSC curves calculated using Eq.2 are shown in Fig.3. Taking into account experimental errors both experimental and calculated data are in acceptable agreement.

It was confirmed both by XRD and EDX techniques that the crystalline phase formed during the crystallization process probably corresponds to  $\text{CuAsSe}_2$  compound.

**Table I**Kinetic parameters for the crystallization of  $\text{Cu}_x(\text{As}_{0.4}\text{Se}_{0.6})_{1-x}$  glasses

x	m	n	E (kJ/mol)	ln A (s)	$\Delta H(\text{J/g})$
0.0652	0.8	1.0	140	25.5	-11
0.1304	0.8	1.0	124	24.0	-16
0.239	0.9	1.3	122	24.2	-18

The melting endotherm observed in DSC thermograms (Fig. 1) has somewhat complicated structure for glasses with higher content of Cu, i.e.  $x \geq 0.1304$ . Unfortunately, there is no available phase diagram of  $\text{As}_2\text{S}_3$  - Cu as far as we know. Nevertheless, considering the phase diagram<sup>9</sup> of  $\text{As}_2\text{S}_3$  -  $\text{CuSe}_2$  system it seems that the first endotherm can be explained by a peritectic reaction at 653 K and the second one by peritectic decomposition of  $\text{CuAsSe}_2$  compound at 723 K.

A correlation between the characteristic temperatures obtained from DSC data and the GFA has been anticipated<sup>7</sup>. There are two basic concepts how to determine the GFA criterion. First approach<sup>10</sup> takes into account the temperature of melting or solidification and the second one attempts to estimate the GFA from  $T_g$  and crystallization effects on DSC curves for reheating of already prepared glassy samples. The first approach, however, often fails in eutectic or peritectic systems. Therefore it seems that the second concept of the GFA is more convenient for Cu-As-Se system. Saad and Poulain<sup>11</sup> defined the GFA criterion as follows:

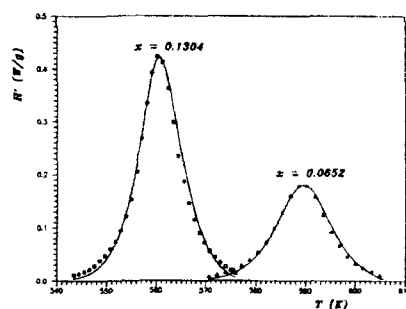


**Fig. 3**  
Experimental (points) and calculated (full lines) crystallization peaks  $\text{Cu}_x(\text{As}_{0.4}\text{Se}_{0.6})_{1-x}$  glasses (heating rate 10 K/min).

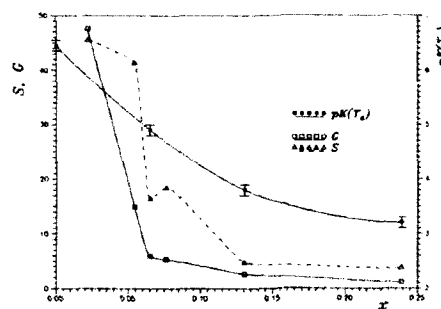


**Fig. 4**  
The compositional dependences of the GFA criteria  $S$ ,  $G$  and  $pK(T_g)$  for  $\text{Cu}_x(\text{As}_{0.4}\text{Se}_{0.6})_{1-x}$  glasses. The value of  $pK(T_g)$  for  $x = 0$  was calculated using data from Ref. 14

$$S = (T_p - T_0)(T_p - T_g)/T_g \quad (3)$$

where  $T_0$  and  $T_p$  correspond to the onset and maximum of crystallization peak, respectively. Similarly we can define a new GFA criterion:

$$G = (T_g - T_p) c_p^* / \Delta H_{cr} \quad (4)$$

where  $c_p^*$  is the heat capacity of undercooled melt. The greater the value of  $G$  and  $S$  criteria the better glass forming ability is approached. The compositional depend-

ences of the S and G criteria are presented in Fig.4. Both these dependences decrease rapidly for low copper content (except for some irregularities observed in the S(x) dependence) and for  $x \geq 0.1304$  remain practically unchanged.

Recently it was shown<sup>12, 13</sup> that the GFA can be well estimated on the basis of the crystallization rate constant at  $T_g$ . The value of  $K(T_g)$  can be calculated using the kinetic parameters summarized in Table I. The compositional dependence of  $pK(T_g) = -\log [K(T_g)]$  is plotted in Fig.4. The course of this dependence is similar like that for the S and G criterion although there is not such a sharp decrease for low values of x.

#### 4. CONCLUSIONS

The results of this study show that the  $T_g$  is only slightly dependent on composition glasses. The compositional dependence of  $T_g$  can be described by modified DeNeufville-Rockstad approach as a function of the coordination number and the atomization enthalpy. It was confirmed that during the crystallization of  $\text{Cu}_x(\text{As}_{0.4}\text{Se}_{0.6})_{1-x}$  glasses the  $\text{CuAsSe}_2$  phase is probably formed. The crystallization kinetics is described by a four parameter model. The calculated kinetic parameters were used for the estimation of the GFA criterion in the Cu-As-Se system. A new empirical criterion is also proposed. The compositional trend of this criterion is comparable with other parameters used for the description of the glass forming ability.

#### 5. ACKNOWLEDGEMENTS

The authors are indebted to Dr. L. Beneš and Dr. R. Novotný for their help with XRD and EDX measurements. The financial support of the Czechoslovak Academy of Sciences under grant number 42901 is much appreciated.

#### 6. REFERENCES

1. J. Hautala, S. Yamasaki, P.C. Taylor, *J. Non-Cryst. Solids* **114** (1989) 85.
2. K.S. Liang, A. Bienstock, C.W. Bates, *Phys. Rev.* **B10** (1974) 1528.
3. Z. U. Borisova, *Glassy Semiconductors* (Plenum Press, New York, 1981) p. 321.
4. M.J. Richardson, N.G. Savill, *Polymer* **16** (1975) 753.
5. K. Tanaka, *Solid State Commun* **54** (1985) 867.
6. J.P. DeNeufville and H.K. Rockstad, in *Amorphous and Liquid Semiconductors*, eds. J. Stuke and W. Brenig (Taylor and Francis, London 1974) p.419.
7. J. Šesták, *Thermophysical properties of solids* (Elsevier, Amsterdam 1984).
8. J. Málek, V. Smrčka, *Thermochim. Acta* **186** (1991) 153.
9. A. S. Khvorostenko et al., *Izv. Akad. Nauk SSSR, Neorg. Mater.* **8** (1972) 73.
10. A. Hrubý, *Czech. J. Phys.* **B22** (1972) 1187.
11. M. Saad, M. Poulain, *Mat. Sci. Forum* **19-20** (1987) 11.
12. S. Suriñach, M.D. Baro, M.T. Clavaguera-Mora, N. Clavaguera, *Fluid. Phase Equilib.* **20** (1985) 341.
13. J. Málek, *J. Non-Cryst. Solids* **107** (1989) 323.
14. D.W. Henderson, D.G. Ast, *J. Non-Cryst. Solids* **64** (1984) 43.



## NEUTRON DIFFRACTION STUDY OF STRUCTURAL CHANGES INDUCED BY HEAT TREATMENT IN Ge-Se GLASSES

X. TORRELLES

*Institut Laue-Langevin, 156X, 380442-Grenoble, France*

S. BORDAS, M. T. CLAVAGUERA-MORA

*Física de Materials, Departament de Física,  
Universitat Autònoma de Barcelona, 08193 Bellaterra, Spain*

and

N. CLAVAGUERA

*Departament d'Estructura i Constituents de la Matèria, Facultat de Física,  
Universitat de Barcelona, Diagonal 647, 08028 Barcelona, Spain*

### ABSTRACT

Glasses of  $\text{Ge}_x\text{Se}_{1-x}$  with  $x = 0.15, 0.20$  and  $0.25$  were prepared by melt quenching. The structural changes induced by heat treatment were analyzed with the instruments D1B and D2B at the Institute Laue-Langevin in Grenoble. For the three glasses a metastable crystalline phase appeared on heating. From the structural results, characteristic temperatures, tentative cell parameters and the crystallization behaviour of the metastable phase have been deduced.

### 1. Introduction

In order to investigate the thermal stability and crystallization behaviour of many glassy alloys, kinetic studies have been done using various techniques such as differential scanning calorimetry, transmission electron microscopy and electrical resistivity measurements. However, there have been very few systematic experiments by neutron diffraction, though this technique is one of the most direct methods to study the structural change of materials.

The work presented here is devoted to the evolution of the neutron scattering curves during thermal cycling of  $\text{Ge}_{15}\text{Se}_{85}$ ,  $\text{Ge}_{20}\text{Se}_{80}$  and  $\text{Ge}_{25}\text{Se}_{75}$  air-quenched glasses in order to study the formation of metastable phases, as previously reported<sup>1</sup>, and their crystallization kinetics.

### 2. Experimental details

Glasses of the three compositions were prepared by melt quenching in air. The structural changes induced by heat treatment were measured by neutron scattering experi-

ments performed on the high resolution diffractometer D1B at the Institute Laue-Langevin in Grenoble using a wavelength of 1.28 and 2.52 Å. Diffraction spectra were recorded for 5 min each during thermal cycling under Ar atmosphere between room temperature and 750 K. Such a time-resolved neutron experiment allows any structural transformation in the sample to be followed accurately.

### 3. Results

Figure 1 presents the evolution of the diffractograms of  $\text{Ge}_{20}\text{Se}_{80}$  glass subjected to the following thermal cycle: heating at a constant rate of 0.4 K/min up to 750 K, isothermal treatment and cooling down to room temperature. On heating, at a certain temperature  $T_c$ , an orthorhombic metastable phase appears in the diffractogram whose Bragg peaks first increases and then decreases on heating above a metastable liquidus temperature,  $T_{ml}$ . During the isothermal treatment there is no evident evolution of the intensities of the diffraction peaks. On cooling the intensity of the Bragg peaks increase showing that the melted fraction of the sample crystallizes again. The values of  $T_c$  and  $T_{ml}$  for the three compositions are shown in Table 1. The values of  $T_{ml}$  increase with the Ge content and remain in the range 600-730 K, that is at temperatures lower than those of the stable liquidus temperature.

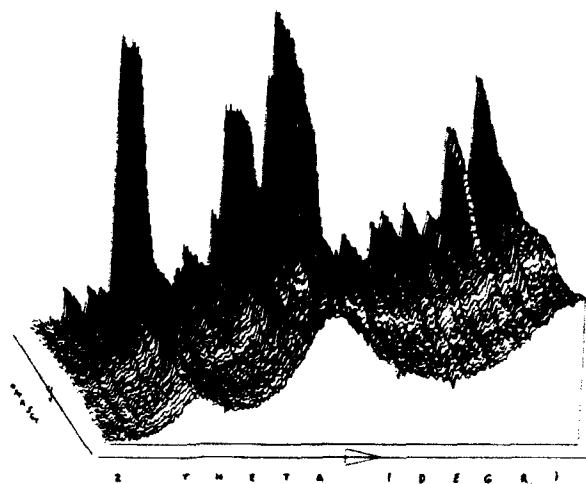


Fig. 1.- Thermal evolution of the diffractograms of  $\text{Ge}_{20}\text{Se}_{80}$

The crystalline phases present were identified using the D1B spectra ( $10^\circ < 2\theta < 90^\circ$ ) combined with XRD spectra and also, to get more precision and a greater  $2\theta$  scan, with the D2B spectra ( $2\theta < 150^\circ$ ). The more evident results on the existence of a metastable phase were found with the composition  $\text{Ge}_{20}\text{Se}_{80}$ . This sample was annealed for two days at a temperature of 575 K in order to increase the fraction of crystalline metastable phase. These spectra were treated with the calculation arsenal of the ILL and some extra considerations: mainly taking into account the great similitude between the calculated spectrum of

crystalline GeSe<sub>2</sub> and that obtained for the metastable phase and the fact that stable GeSe<sub>2</sub> is monoclinic (space group P2<sub>1</sub>/c) with  $b = 90.65^\circ$ . After some trials, the metastable phase was supposed to be orthorhombic (space group P222). This enables to fit correctly the D2B spectrum with the following parameters:  $a = 6.986 \text{ \AA}$ ;  $b = 17.808 \text{ \AA}$ ;  $c = 12.076 \text{ \AA}$  for the orthorhombic phase which coexist with the hexagonal Se phase. The crystallization kinetics have been studied through the neutron diffraction measurements under continuous heating regime. The crystalline fraction of a sample at a temperature  $T$  can be written as

$$x(T) = I_p(T)/I_{total}(T) \quad (1)$$

where  $I_p(T)$  is the sum of the intensities of all the Bragg peaks measured at a temperature  $T$ , and  $I_{total}(T)$  is the sum of total intensity measured in the whole spectrum at that temperature.

The analysis of the crystallization kinetics have been done using the Johnson-Mehl-Avrami-Erofe'ev model which is often applied satisfactorily to most chalcogenide glasses. That is:

$$dx/dt = k_0 \exp(-E/RT)n(1-x)[- \ln(1-x)]^{(n-1)/n} \quad (2)$$

where  $k_0$  is the pre-exponential factor,  $E$  is the activation energy of the process and  $n$  is the kinetic exponent.

In figure 2 is shown the best fit of this model with the experimental data and in Table 1 are given the corresponding parameters. The values of the activation energy are similar to those reported for Se rich glasses in the Ge-Sb-Se system<sup>3</sup>. As can be seen, the kinetic exponent  $n$  varies between 0.5 and 1.2 which may indicate that the crystallization is limited by the diffusion process and the crystal growth is one- or two-dimensional. The optical microscopic observation of a sample of composition Ge<sub>20</sub>Se<sub>80</sub> after partial crystallization shows that the crystal growth is basically unidimensional. This result confirms the previous assumptions.

#### 4. Conclusions

The structural evolution by thermal cycling of Se rich Ge-Se glasses has been followed by neutron diffraction. The temperatures of the beginning of crystallization and of melting of a metastable phase at a heating rate of 0.4 K/min have been obtained. Even at such a low heating rate the samples do not crystallize completely before melting, but a metastable phase is formed which on cooling the melt coexists with the stable hexagonal Se phase.

Long annealing (2 days) at a temperature below the metastable melting temperature allows to obtain a crystalline sample with a large amount of the metastable phase. Tentative cell parameters were obtained by fitting the D2B spectrum of the long annealed sample.

The crystallization behaviour of the metastable phase has been followed in its initial steps and the Johnson-Mehl-Avrami-Erofe'ev model has been used to reproduce its behaviour. The values of the kinetic exponent are between 0.5 and 1.2 which may indicate one- or two-dimensional growth limited by diffusion. This result seems to agree with the morphology of the crystal observed by optical microscopy.

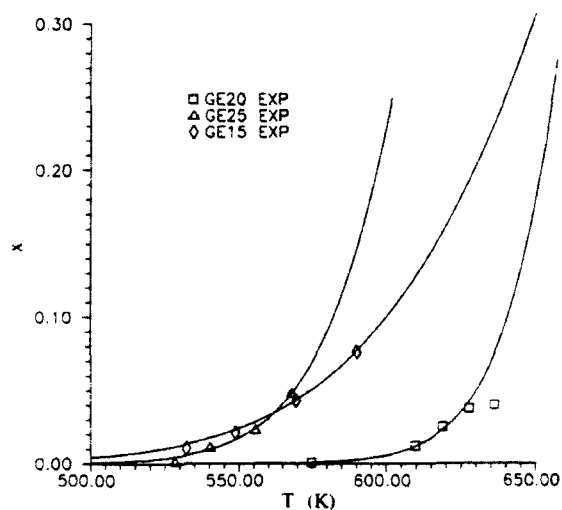


Fig. 2.- Comparison between experimental and calculated crystallized fraction according to data of Table 1.

Table 1.- Values for  $T_c$ ,  $T_{ml}$  and kinetic parameters obtained for the samples studied.

% Ge	$T_c$ (K)	$T_{ml}$ (K)	$E$ (kJ)	$\ln(k_0)$ $k_0$ in $s^{-1}$	$n$
15	520	600	150	17.0	0.5
20	584	662	180	24.0	1.2
25	552	725	200	29.8	0.7

##### 5. Acknowledgements

The ILL is acknowledged for the neutron facilities accorded. Dr. J. Rodriguez is acknowledged for its active participation in the experimental task and further discussions. This work has been supported by CICYT under project No. MAT-907/91.

##### 6. References

1. R. Azoulay, H. Thibierge and A. Brenac, *J. Non-Cryst. Solids* **18** (1975) 33.
2. G. Dittmar and H. Schäfer, *Acta Cryst.* **b32** (1976) 2726.
3. S. Bordas, M.T. Clavaguera-Mora and N. Clavaguera, *J. Non-Cryst. Solids* **119** (1990) 232.

## EVIDENCE OF TWO AMORPHOUS PHASES IN GE-TE-SB ALLOYS

M. BELHADJI\*,

C. VAUTIER, P. LEBAUDY and J.M. SAITER

*Laboratoire d'Etude et de Caractérisation  
des Composés Amorphes et des Polymères  
U.F.R. Sciences, BP 118,  
76134 Mt St Aignan Cédex, France*

### ABSTRACT

The  $\text{Ge}_{15.5-x}\text{Te}_{84.5}\text{Sb}_x$  ( $0.5 < x < 2.5$ ) amorphous alloys studied by differential scanning calorimetry show two glass transition temperatures followed two crystallization temperatures. This behaviour is probably due to the presence of two phases in the amorphous materials. Whatever the composition, the first crystallization corresponds to that of tellurium in the hexagonal form. The second correspond essentially to the crystallization of GeTe.

### 1. Introduction

In a previous paper [1] we have determined the ranges of composition where it was possible to obtain bulk amorphous Ge-Te-Sb alloys by quenching from the melt. Only a small range of composition around  $\text{Ge}_{15}\text{Te}_{82}\text{Sb}_3$  ternary eutectic and  $\text{Ge}_{15}\text{Te}_{85}$  binary eutectic complies with this characteristic.

Among these compounds some of them exhibit two glass transition temperatures followed by two crystallization temperatures. This paper deals with the study of  $\text{Ge}_{15.5-x}\text{Te}_{84.5}\text{Sb}_x$  ( $0.5 < x < 2.5$ ) alloys which exhibit such a behaviour. The studied compositions correspond to the transitory ternary peritectics displayed by Legendre et al. [2].

### 2. Experimental

The preparation of the samples takes place in two steps. First, the three elements (99.999% purity) in suitable quantity are introduced into a quartz ampoule and sealed in a vacuum of  $10^{-5}$  Pa. Then the ampoules were placed in an horizontally rotating oven and annealed at  $1000^\circ\text{C}$  for 3 hours. Finally, they were air quenched. The composition of the bulk alloys was checked by atomic absorption spectrometer (Perkin Elmer 2380).

The ingots were ground down to a fine powder and placed in a capillary tube sealed under vacuum. The samples were annealed up to  $1000^\circ\text{C}$  and quenched in cold water. The amorphicity of the sample is checked by X-ray diffraction (fig. 1). The thermograms were recorded using a Setaram DSC92 at sufficiently high heating rates (10 K/min.).

\* Permanent adress : Université Es-Senia, ORAN, Algérie

### 3. Results

Figure 1a shows the typical thermograms obtained for the studied compositions. Four characteristic phenomena appear in the studied temperature range. The first one ( $T_{g1}$ ) and the second one ( $T_{g2}$ ) which are clearly shown in figure 1b correspond to the glass transition temperatures; their values are reported in table I. They are followed by two peaks more or less separated, depending on the Sb concentration. They correspond to the crystallization of two phases. The values of these temperatures, denoted  $T_{C1}$  and  $T_{C2}$ , are reported in table I for the different compositions. Except for the second glass transition temperature  $T_{g2}$ , the other characteristic temperatures decrease as the amount of antimony increases.

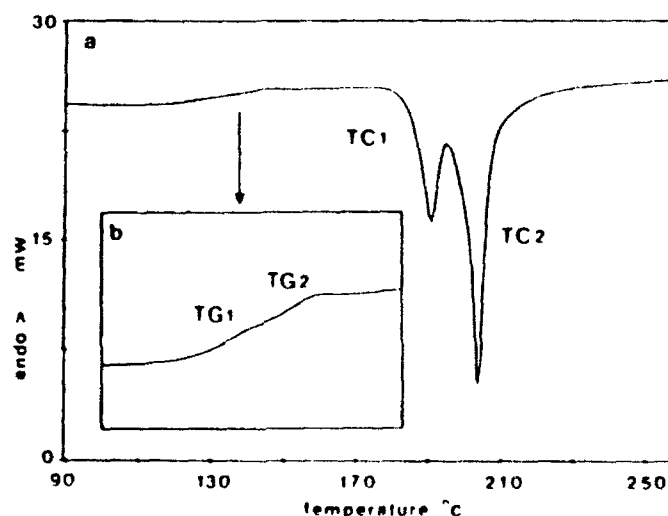


Figure 1: a) Typical thermogram, b) detail of the glass transition region

x	0.5	1.0	1.5	2.5
$T_{g1}$ (°C)	120	116	114	108
$T_{g2}$ (°C)	144	148	150	132
$T_{C1}$ (°C)	174	166	168	160
$T_{C2}$ (°C)	212	206	200	189

Table I: Glass transition and crystallization temperatures

#### 4. Discussion

The Te-based amorphous alloys exhibit either one  $T_g$  and two  $T_c$  as in  $(\text{GeSe}_2)_{60}(\text{GeTe})_{20}(\text{Sb}_2\text{Te}_3)_{20}$  [3], or two  $T_g$  and two  $T_c$  as in  $\text{Al}_{23}\text{Te}_{87}$  [4] and in  $\text{Si}_x\text{Te}_{1-x}$  [5-6]. However, in this last case the second glass transition appears after an annealing at a temperature near the first crystallization one. This may be explained by the fact that the first crystallization modifies the amorphous phase, generally Te precipitates so that the remaining amorphous phase contains less Te atoms and the environment of the other atoms is modified. A further annealing above  $T_{c1}$  enables the determination of the glass transition temperature of this second amorphous phase and the temperature  $T_{c2}$  corresponds to the crystallization of this second phase.

In the case of  $\text{Se}_{60}\text{Ge}_{20}\text{Sb}_{20}$  [7] both glass transition temperatures  $T_{g1}$  and  $T_{g2}$  appear before any crystallization. After the first crystallization at  $T_{c1}$  and a cooling at room temperature a further annealing lets  $T_{g2}$  unchanged and enables the determination of the second crystallization temperature. These results and X-ray analysis lead to the assumption that the as-prepared material contains two amorphous phases:  $\text{Sb}_2\text{Se}_3$  and  $\text{GeSe}_2$ .

In our case, both glass transition temperatures ( $T_{g1}$  and  $T_{g2}$ ) are followed by two exothermic peaks ( $T_{c1}$  and  $T_{c2}$ ). A first annealing at a temperature near  $T_{c1}$  leads to the precipitation of tellurium, in its hexagonal form, as in the other Te-based amorphous alloys (Fig. 2a). A rapid cooling at room temperature and a further annealing above  $T_{c2}$  leads to the following observations:

i) The glass transition temperature  $T_{g2}$  may be only detected at high annealing rate ( $50 \text{ K min}^{-1}$ ), in agreement with other authors [7]. The observed values of  $T_{g2}$  are slightly higher than before the first annealing, which is probably due to a kinetic effect.

ii) The crystallization temperature  $T_{c2}$  remains unchanged but is preceded by a small endothermic peak which is until now unexplained.

iii) The X-ray diffraction diagrams (fig. 2b) show an additional Te precipitation accompanying by the GeTe precipitation. Following Moss [8], this is probably due to the fact that the residual glass prior to the GeTe crystallization contains more than 50 at.% of Te.

iv) The X-ray diffraction diagrams (except perhaps the 0.5 at.% one) do not exhibit any ray corresponding to known Sb-based compounds. It is possible, as suggested by Moss [8], that the Sb atoms are concentrated into the GeTe crystals and, due to the low concentration of Sb, is not visible by X-ray diffraction.

#### 5. Conclusion

It is obvious that the as-prepared  $\text{Ge}_{15.5-x}\text{Te}_{84.5}\text{Sb}_x$  alloys contain two amorphous phases characterized by the two transition temperatures. However, the values of these temperatures do not correspond to that of known amorphous alloys.

During the first crystallization we only observe Te precipitation which leads to the impoverishment of one or both amorphous phases. Probably one because  $T_{g2}$  remains practically constant after the first annealing at  $T_{c1}$ . The second amorphous phase could have the approximative composition of GeTe which crystallize at  $T_{c2}$ .

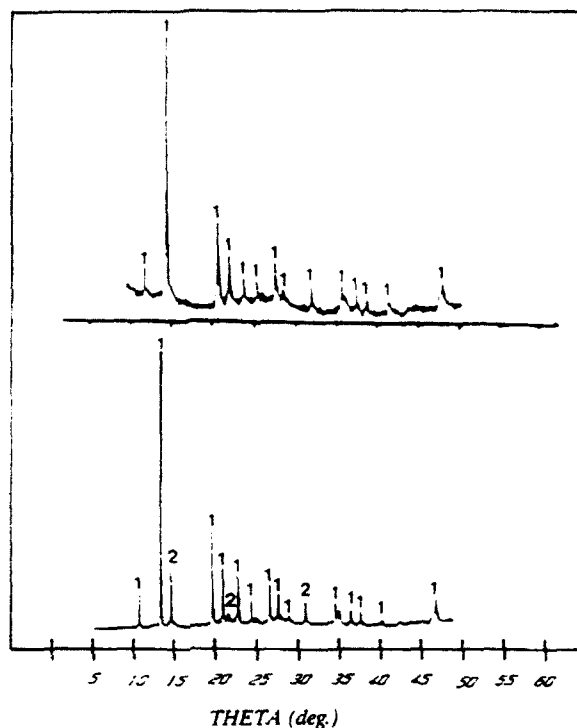


Figure 2 : X-ray diffraction diagrams.

a) after annealing near Tc1

b) after annealing above Tc2

1:Te ; 2:GeTe

We are continuing experimentattion by means of EXAFS in order to try to determine the nature of both amorphous phases

#### 6. References :

- [1] Ph. Lebaudy, J.M. Saiter, J. Grenet, M. Belhadji and C. Vautier, *Mat. Sci. and Eng.*, A132 (1991) 273.
- [2] B. Legendre, Chay Hancheng, M. Bordas and M.T. Clavaguera-Mora, *Thermochimica Acta*, 78 (1984) 141.
- [3] S. Surinach, M.D. Baro, M.T. Clavaguera-Mora, N. Clavaguera, *J. Non-Crystalline Solids*, 58 (1983) 209.
- [4] J. Colmenero and J.M. Barandiaran, *J. Non-Crystalline Solids*, 30 (1979) 263.
- [5] S. Asokan, G. Partansarathy and E.S.R. Gopal, *J. Mat. Sci. Letters*, 4 (1985) 50.
- [6] S. Asokan, G. Partansarathy and E.S.R. Gopal, *J. Non-Crystalline Solids*, 86 (1986) 48.
- [7] N. Afify, *J. Non-Crystalline Solids*, 126 (1990) 130.
- [8] S.C. Moss and J.P de Neufville, *Mat. Research Bul.*, 7 (1972) 423.



# EFFECTS OF ANNEALING ON AMORPHOUS $\text{Cu}_{0.83}\text{Ge}_{0.20}\text{Te}_{0.77}$ ALLOY.

M. Casas-Ruiz, R.A. Ligeró, J. Vázquez and R. Jiménez-Garay.

Facultad de Ciencias. Universidad de Cádiz.

Aptdo. 40. Puerto Real. Cádiz. Spain.

## ABSTRACT

Isothermal pre-anneal treatment was applied to a quenched  $\text{Cu}_{0.83}\text{Ge}_{0.20}\text{Te}_{0.77}$  alloy. By non-isothermal crystallizing in a DSC the set of kinetic parameters was obtained using the Augis-Bennet technique. It was found that the Avrami exponent  $n$ , decreased and tended to 2, with the increase of pre-anneal time.

## 1.- INTRODUCTION

The crystallization kinetics of glass-forming materials is controlled by nucleation and growth mechanisms which, with a few exceptions, are characterized by an activation energy  $E$ , and a kinetic exponent  $n$ , according to the Johnson-Mehl-Avrami (JMA) law<sup>1-2</sup>. These parameters can be determined by differential scanning calorimetry.

Two basic methods can be used, isothermal and continuous heating crystallization. Although the conclusions derived from the above mentioned JMA theoretical model have been strictly deduced for isothermal experiments, they can be applied, under certain restrictions and within a wide temperature range, to the data obtained by non-isothermal experiments.

## 2.- THEORETICAL BACKGROUND.

The theoretical basis for interpreting DSC results is provided by the formal theory of transformation kinetics as developed by Johnson and Mehl<sup>1</sup> and Avrami<sup>2</sup>. In its basic form the theory describes the evolution with time,  $t$ , of the transformed volume fraction  $x$ :

$$x = 1 - \exp[-(Kt)^n] \quad (1)$$

where  $n$  is a dimensionless exponent which is related to the morphology of crystal growth, and  $K$  the rate constant. The temperature dependence of  $K$  (at least within

narrow temperature ranges) can be expressed by the Arrhenius equation

$$K = K_0 \exp(-E/RT) \quad (2)$$

where  $K_0$  is an effective frequency factor,  $E$  the effective activation energy for the overall process,  $R$  the gas constant and  $T$  the absolute temperature.

The crystallization rate is obtained by differentiating the expression (1) with respect to time, bearing in mind the fact that, in the non-isothermal process, the reaction rate constant is a function of time through the Arrhenian temperature dependence<sup>3</sup>:

$$\frac{dx}{dt} = n(Kt)^{n-1} \left[ t \frac{dK}{dt} + K \right] (1-x) \quad (3)$$

The maximum crystallization rate is found by setting  $d^2x/dt^2=0$ , whence for  $[E(T_p-T_0)/RT_p^2] > 1$ <sup>3</sup>:

$$\left( \frac{K_p(T_p-T_0)}{\beta} \right)^n = 1 \quad (4)$$

A linear relationship is obtained by expressing the equation (4) in logarithmic form

$$\ln \frac{T_p-T_0}{\beta} = \frac{E}{RT_p} - \ln K_0 \quad (5)$$

from which  $E$  and  $K_0$  may be calculated.

The Avrami exponent  $n$ , is obtained by introducing the expression (4) into the equation (3):

$$n = \frac{\left( \frac{dx}{dt} \right)_p RT_p^2}{0.37 EK_p(T_p-T_0)} \quad (6)$$

### 3. EXPERIMENTAL

Quenched samples were prepared by melting weighted amounts of the elements (5N purity) in evacuated and sealed quartz ampoules. The molten alloys were held at 1373 K for 72 hours in a rotary furnace to ensure homogeneity and subsequently quenched in liquid nitrogen.

The calorimetric measurements were carried out in a Rigaku Thermoflex DSC, under purified He atmosphere.

The as-quenched samples were subjected to an annealing treatment at 453K respectively for 20 (ann-1), 60 (ann-2) and 100 (ann-3) minutes.

The crystallizing experiments were carried out by continuous heating at rates of 2, 4, 8, 16 and 32 K/min.

### 4. RESULTS AND DISCUSSION.

In order to study the crystallization kinetics, the above mentioned method was used. The plots of  $\ln[(T_p - T_0)/\beta]$  versus  $1/T_p$  are shown in Fig. 1. Table 1 shows the values of the kinetic parameters obtained in each case. It may be observed that the Avrami exponent decreases from 3.6 to 2.2 with the increase of pre-anneal time and this means that the crystallization occurs by different mechanisms: three-

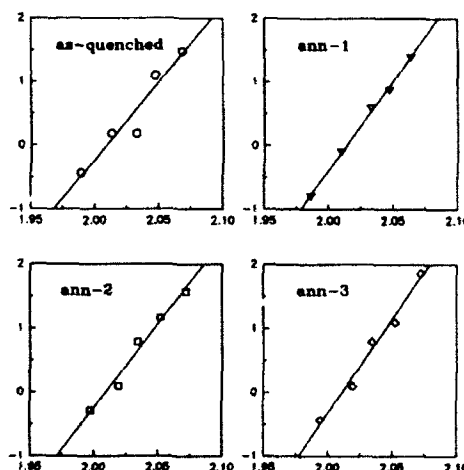


Fig. 1.  $\ln[(T_p - T_0)/\beta]$  versus  $1/T_p$  ( $10^3 \text{ K}^{-1}$ ) plots.

dimensional nucleation and growth for the as-quenched sample and two-dimensional for the ann-3 sample<sup>4,5</sup>. The effect can be explained by the pre-existing nuclei resulting from pre-annealing. In the pre-anneal treatment the density of pre-existing nuclei increases with the pre-annealed time, so that in the crystallization process, the nucleation rate would be slowed decreasing the values of the Avrami exponent<sup>6</sup>.

The values of the crystallization activation energies are very similar, which

means that the energy barrier which the glassy material must go through in order to attain the crystalline state is practically the same. On the other hand, the values of the frequency factors (which measure the probability of molecular collisions effective for the formation of the activated complexes, in each case) are also very similar, thus implying an equal crystallizing ability for the as-quenched and pre-annealed samples.

	as-quenched	ann-1	ann-2	ann-3
n	3.6	2.8	2.8	2.2
E (Kcal/mol)	48.3	55.6	51.8	58.5
$K_0$ ( $s^{-1}$ )	$3.3 \cdot 10^9$	$6.1 \cdot 10^{22}$	$1.1 \cdot 10^{21}$	$1.1 \cdot 10^{24}$

Table 1. Kinetic parameters calculated by Augis-Bennet technique<sup>3</sup>.

## 5.- CONCLUSIONS

The crystallization mechanism varies from three-dimensional growth to two-dimensional nucleation and growth according to the anneal treatment.

Pre-anneal treatment decreases the values of Avrami exponents in the crystallization processes.

The activation energies and frequency factors remains essentially independent of the treatment.

## REFERENCES

1. W.A. Johnson and R.F. Mehl, *Trans. Am. Inst. Min. Met. Eng.*, 135 (1939) 416.
2. M. Avrami, *J. Chem. Phys.* 7 (1939) 1103; 8 (1940) 212; 9 (1941) 177.
3. J.A. Augis and J.E. Bennet, *J. Thermal Anal.*, 13 (1978) 283.
4. J.W. Christian, *"The Theory Of Transformations in Metal and Alloys"*, 2nd edn., Pergamon, New York, 1975.
5. C.N.R. Rao and K.J. Rao, *"Phase Transition in Solids"*, McGraw-Hill, 1978.
6. W.F. Miao, J.T. Wang, S.L. Li and B.Z. Ding, *J. Non-Cryst. Sol.*, 117/118 (1990) 230.

### **III. RELAXATION PROCESSES, GLASS TRANSITION AND MOLECULAR MOTIONS**

## STRUCTURAL RELAXATION IN METALLIC GLASSES

A. van den Beukel

Delft University of Technology, Laboratory of Metallurgy  
Rotterdamseweg 137, 2628 AL Delft, The Netherlands

## ABSTRACT

Prior to crystallisation, in metallic glasses a change in many physical properties has been observed, which must be due to atomic rearrangements within the amorphous state. This phenomenon is called "structural relaxation". In this paper the experimental data is analysed in terms of a model of the underlying physical processes.

Two types of processes can be distinguished: 1. Those which are reversible with temperature and ascribed to chemical short range ordering (CSRO). 2. Irreversible processes which are due to the annealing out of excess free volume (TSRO). CSRO comes first and consists of a series of processes with a wide spectrum of activation energies. It is followed by TSRO, a process with well defined kinetics and a single value of the activation energy. There are also strong indications that in the "CSRO range" of as-quenched specimens irreversible processes (as yet unidentified) play a part.

In the description of TSRO it is important to distinguish between two types of physical properties: 1. Properties which are related to the average free volume, like density, electrical resistivity and elastic constants. 2. Properties which are connected with atomic mobility and therefore "defect controlled", like viscosity and diffusivity. The description of the behaviour of these properties makes it necessary to introduce two types of defects: Flow defects (concentration  $c_f$ ) for the description of viscosity and diffusion defects (concentration  $c_d$ ) for the description of diffusivity. A consistent description of the experimental data is obtained when it is assumed that  $c_d \sim c_f^{1/2}$ . The physical basis of this relation is as yet not understood.

Finally it is shown that the glass transition in metallic glasses can be quantitatively understood when it is described as a free volume related kinetic phenomenon.

## 1. Introduction

Metallic glasses are produced by rapid quenching from the liquid state. The amorphous state frozen in is unstable and upon warming up transforms into the stable crystalline state at the crystallization temperature  $T_c$  which depends somewhat on the heating rate. In common metallic glasses,  $T_c$  is somewhere between 600 and 800 K. Crystallization can be detected by X-ray diffraction and is visible in DSC-scans as a rather sharp exothermal peak.

Prior to crystallization, however, in metallic glasses a change in many physical properties has been observed. For instance, the density increases by about 0.1 %, the elastic constants increase by about 10 % and the viscosity increases by several orders of magnitude (for an overview see ref. 1). These observed changes in physical properties must be due to atomic rearrangements in the amorphous state and this process has been generally called "structural relaxation".

It was first suggested by Egami<sup>1</sup> that in structural relaxation two sub-processes should be distinguished. First, the as-quenched metallic glass will contain an amount of "free volume", defined as the volume difference between the actual and the "ideal" amorphous structure. The excess amount of free volume will anneal out during annealing at

temperatures below  $T_c$  if the atoms have a sufficiently large mobility. This process, which is comparable to the annealing out of excess vacancies in quenched crystalline materials, is called Topological Short Range Ordering (TSRO). Second, as metallic glasses always contain more than one chemical component, the relative positions of the various kinds of atoms with respect to each other must define, as in crystalline alloys, a kind of short range order. The degree of quenched-in short range order will be low and upon low temperature annealing the degree of order will increase. This process has been called Chemical Short Range Ordering (CSRO).

In this paper it will be shown how these concepts can be visualized and put on a quantitative basis by an analysis of experimental data on the change of physical properties of metallic glasses during structural relaxation.

## 2. Experimental data and analysis

### 2.1 Viscosity

At not too high stresses, metallic glasses show a Newtonian viscous behaviour. During structural relaxation, the viscosity increases linearly with time, as was first shown by Taub and Spaepen<sup>3</sup> on amorphous  $\text{Pd}_{82}\text{Si}_{18}$ . This behaviour was interpreted by Spaepen<sup>4</sup> in terms of the free volume model. The atomic mobility, responsible for viscous flow, was thought to be due to "flow defects" (concentration  $c_f$ ), which move with an activation energy  $E_f$ . For this mechanism, Spaepen derived the following expression for the viscosity.

$$\eta = \frac{kT\Omega}{c_f(\gamma_0 v_0)^2 k_f} \sim \frac{T \exp(E_f/RT)}{c_f(\gamma_0 v_0)^2} \quad (1)$$

where  $k_f \sim \exp(-E_f/RT)$  is the jump frequency of a flow defect;  $\gamma_0$  is the shear strain per jump;  $v_0$  is the volume of the defects;  $\Omega$  is the atomic volume;  $k$ ,  $R$  and  $T$  have their usual meaning.

The relation between the flow defect concentration  $c_f$  and the average free volume per atomic volume  $v_f$  has been derived by Turnbull and Cohen<sup>5,6</sup>. They assumed that an atomic jump is only possible if the local free volume per atom exceeds a critical value  $v^*$ . From this, and the distribution function of free volume over the atomic sites,  $p(v)dv =$

$$\frac{\gamma}{v_f} \exp\left(-\frac{\gamma v}{v_f}\right) dv \quad (\text{with } \gamma \text{ a constant}), \text{ it follows}$$

$$c_f = \exp(-x^{-1}) \quad (2)$$

where  $x = \frac{v_f}{\gamma v^*}$  is the so called reduced free volume.

During structural relaxation, free volume anneals out, resulting in a decrease of  $x$  and  $c_f$ . As it is generally observed that during this process the viscosity increases linearly with time, we have from equation (1):

$$\frac{dc_f^{-1}}{dt} = C \quad (3)$$

where  $C$  is a constant, and therefore

$$c_f^{-1} = c_{f0}^{-1} + Ct \quad (4)$$

with the temperature dependent reaction constant

$$C = C_0 \exp(-E_f/RT) \quad (5)$$

Equations (3) to (5) describe the annealing out of flow defects as a function of temperature and time. Note that, according to equation (3), this process follows second order kinetics, as  $\dot{c}_f \sim c_f^{-2}$ .

The activation energy describing the temperature dependence of  $\eta$  (equation (1) and of flow defect annealing (equation (5)) has been taken the same. However, from experimental data to be discussed further on, they appeared to be different. The reason for this discrepancy was sought <sup>7</sup> in a temperature dependence of  $\gamma_0 v_0$  and this idea was supported by measurements of this quantity by Taub <sup>8</sup> through stress relaxation experiments. The results of these measurements could be described by <sup>7</sup>

$$\gamma_0 v_0 \sim \exp(-E'/RT) \quad (6)$$

Combining this with (1), we finally have

$$\eta \sim T c_f^{-1} \exp(E_\eta/RT) \quad (7)$$

with  $E_\eta = E_f + 2E'$  and, from (3), (5) and (7):

$$\dot{\eta} \sim \exp(2E'/RT) \quad (8)$$

These equations have been tested in ref. 7 on an extensive set of data on the viscosity of Fe<sub>40</sub>Ni<sub>40</sub>B<sub>20</sub>. Three parameters are required:  $c_{f0}$ ,  $C_0$  and  $E_f$ . The set of parameters yielding the best results was given by

$$\begin{aligned} c_{f0} &= 3.2 \cdot 10^{-6} \\ C_0 &= 1.63 \cdot 10^{25} \text{ s}^{-1} \\ E_f &= 250 \text{ kJ mol}^{-1} \end{aligned} \quad (9)$$



It was shown in ref. 7 that with this set of parameters a satisfactory description of all experimental data could be obtained. The main results can be briefly summarized as follows:

1.  $\dot{\eta}(T)$  is well described by equation (8) with  $E' = 27 \text{ kJ mol}^{-1}$ . This value agrees well with that obtained from Taub's <sup>8</sup> results on  $\gamma_0 v_0$  vs  $T$ , as described by equation (6).

2. In a wide range of temperatures and times,  $\eta(T, t)$  is well described by equation (7). As shown in figure 1, a plot of  $\ln(\eta c_f T^{-1})$  vs  $T^{-1}$  yields a single straight line for all the

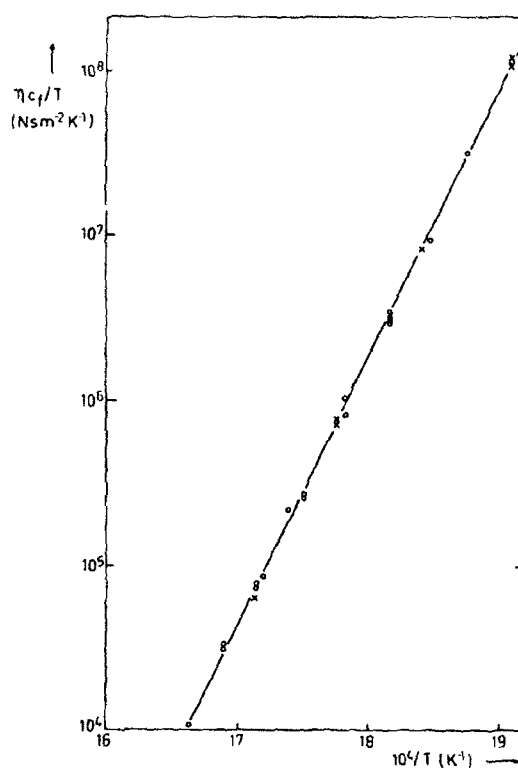


Figure 1. "Masterplot" of  $\eta c_f T$  vs  $T^{-1}$  (for an explanation see text). From ref. 7.

data, which covers a change in  $\eta$  by 4 orders of magnitude. The activation energy derived from the slope of this line corresponds to  $E_\eta = E_f + 2 E' = 304 \text{ kJ mol}^{-1}$ , as expected. The time dependence of  $\eta$  is hidden in  $c_f(t)$  and was calculated from equation (4) with the parameters given in (9).

## 2.2 Other Physical Properties

In analysing the effect of the annealing out of free volume on the physical properties, it is important to distinguish between two kinds of properties: 1. Those which are directly connected with atomic transport like the viscosity (discussed in section 2.1), and the diffusion coefficient (to be discussed in section 2.3). These properties are directly related with  $c_f$ , the concentration of flow defects, the carriers of atomic mobility as defined by equation (2). 2. Properties which are directly related with the amount of (reduced) free volume,  $v_f$  or  $x$ . The most obvious example of this kind is the volume of the specimen (or the length, or the density). In this case the change in volume due to the annealing out of free volume, will be proportional to the change in free volume:  $\Delta V \sim \Delta x$ . For other bulk properties, like the electrical resistivity and the elastic constants, we shall assume that this is true as well, and test this assumption later on by an analysis of the experimental data. So, in general, the change of this kind of properties due to the annealing out of free volume can be represented by

$$\Delta P = A_p \Delta x \quad (10)$$

where  $A_p$  is a constant.

The kinetics of the decay of free volume was determined from the viscosity data with equations (2), (4), (5) and (9), so  $\Delta x$  can be calculated as a function of annealing time and temperature. As an example, in figure 2 the observed isothermal change of the electrical resistivity of as-quenched specimens of  $\text{Fe}_{40}\text{Ni}_{40}\text{B}_{20}$  at the temperatures indicated is

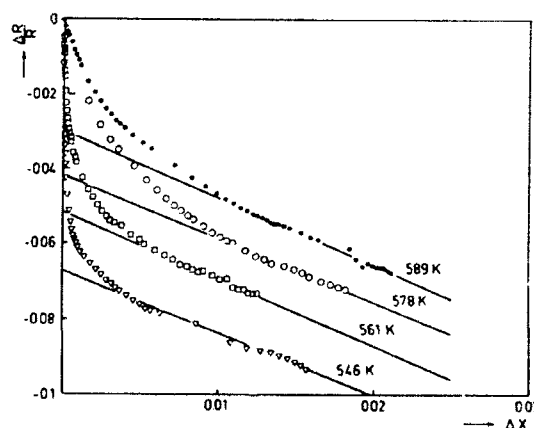


Figure 2. Relative decrease of electrical resistance of as-quenched  $\text{Fe}_{40}\text{Ni}_{40}\text{B}_{20}$  at the temperatures indicated, as a function of the calculated change in free volume. From ref. 9.

plotted versus the calculated  $\Delta x$  (from ref. 9). It is seen that, after an initial transient, at all temperatures the linear relationship predicted by equation (10) is correct. This means that the final part of structural relaxation is satisfactorily described in terms of the free volume

model with a single value of the activation energy ( $250 \text{ kJ mol}^{-1}$ ). Data on the elastic modulus <sup>10</sup>, the Curie temperature <sup>11</sup> and the specimen length <sup>12</sup> were analysed in the same way and yielded the same result.

The initial part of the relaxation, to be determined from the intercept of the straight lines in figure 2 with the ordinate, increases with decreasing annealing temperature. This effect is ascribed to chemical short range ordering (CSRO) and has been analysed in detail in references 13 and 14. The saturation of the effect is due to the fact that equilibrium short range order has been attained. This is in agreement with the observation that the decrease in resistivity is larger at the lower temperatures, because the degree of equilibrium short range order will increase with decreasing temperature. From the analysis of the CSRO part of the relaxation <sup>1,13</sup>, we only mention that CSRO, in contrast to TSRO, covers a wide, block shaped spectrum of activation energies ( $130 - 250 \text{ kJ mol}^{-1}$ ). The results were analysed in terms of the activation energy spectrum (AES) model of Gibbs and coworkers <sup>14</sup>.

As equilibrium short range order is a reversible function of temperature, the property changes due to structural relaxation in the CSRO range must show a reversible behaviour with temperature. As an example, this is demonstrated in figure 3. Here  $\Delta v^2$

( $v$  = longitudinal velocity of sound;  $v^2$  is proportional to Young's modulus) of  $\text{Fe}_{40}\text{Ni}_{40}\text{B}_{20}$  is plotted vs annealing time at 578 K for two specimens which had been preannealed at 503 K for  $10^4$  s (figure 3a) and  $10^6$  s (figure 3b) respectively (taken from ref. 10). The TSRO contribution, as calculated from equations (2), (4), (5), (9) and (10) is indicated by T and in both cases describes the final part of the relaxation very well. The remaining part is ascribed to CSRO and indicated by C. The CSRO part in figure 3a goes through a minimum, whereas in figure 3b it falls continuously until it saturates. The explanation is as follows. During the preanneal of  $10^4$  s at 503 K, only the lower energy part of the activation energy spectrum attains equilibrium order, yielding an increase of  $v^2$ . Upon further annealing at 578 K, this part disorders again, yielding a decrease of  $v^2$  (figure 3a). Beyond the minimum, the higher energy part of the activation energy spectrum, which had not yet attained equilibrium order during the preanneal, orders, yielding an increase of  $v^2$  until equilibrium order is attained. The latter part is absent in figure 3b, which means that the preannealing time  $t_p = 10^6$  s at 503 K was sufficiently long to reach equilibrium order for the whole spectrum.

The foregoing discussion also implies that the depth of the minimum in figure 3 will increase with increasing  $t_p$ , until it saturates when  $t_p$  is long enough to reach equilibrium order during the preanneal. This behaviour is demonstrated in figure 4, observed in  $\text{Pd}_{40}\text{Ni}_{40}\text{P}_{20}$  by Koebrugge <sup>15</sup>. The reversibility of CSRO is also demonstrated in figure 5, taken from Kokmeyer et al. <sup>16</sup>. Here a  $\text{Fe}_{40}\text{Ni}_{40}\text{B}_{20}$  specimen was cycled between two temperatures, 525 K and 600 K, and  $\Delta v^2$  was measured as a function of time. After correction for the calculated TSRO contribution, the resulting changes due to CSRO are reversible indeed (they are plotted here as a function of the activation energy in the spectrum, which can be obtained from the annealing times by use of the AES model).

The analysis up till now showed that the change of electrical resistivity, elastic modulus and length due to structural relaxation consists of two parts: a CSRO and a TSRO contribution. In all three cases the sign of the property change due to the two processes is the same (resp. negative, positive and negative). This means that on an isothermal of an as-quenched specimen the transition from CSRO to TSRO is not clearly visible. An example is given in figure 6, representing a set of  $v^2$ -isothermals of as-quenched  $\text{Fe}_{40}\text{Ni}_{40}\text{B}_{20}$  at the temperatures indicated <sup>10</sup>. The drawn curves labeled T and C are the result of the analysis

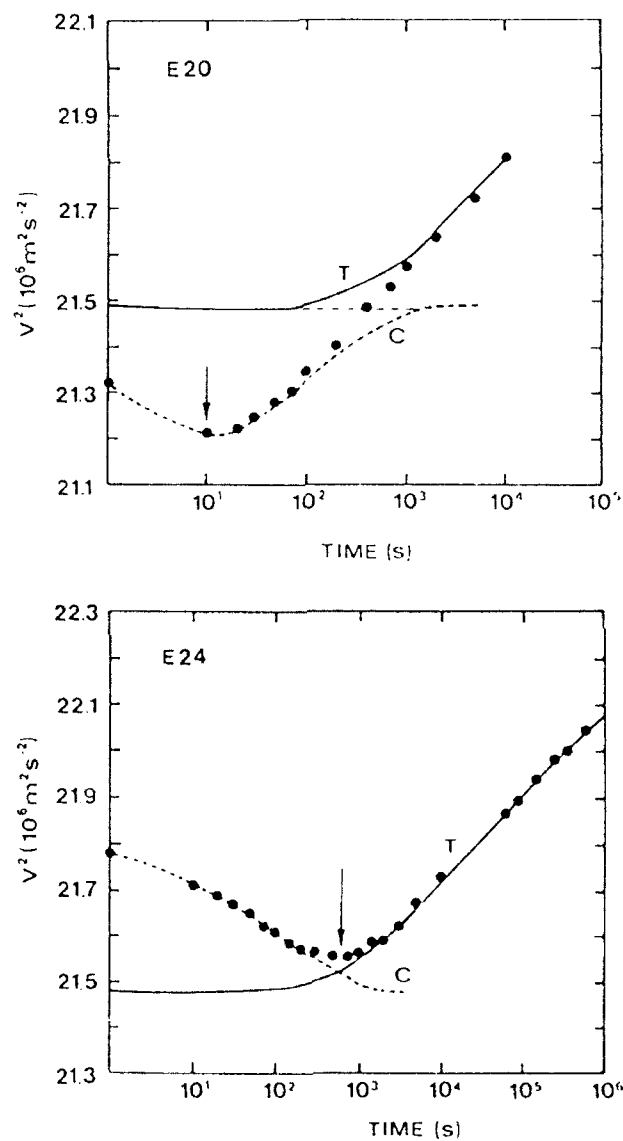


Figure 3. Change of  $v^2$  in  $\text{Fe}_{40}\text{Ni}_{40}\text{B}_{20}$  as a function of time at 578 K, after preannealing for  $10^4$  s (a) and  $10^6$  s (b) at 503 K. Drawn curves T: Calculated TSRO contributions. From ref. 10.

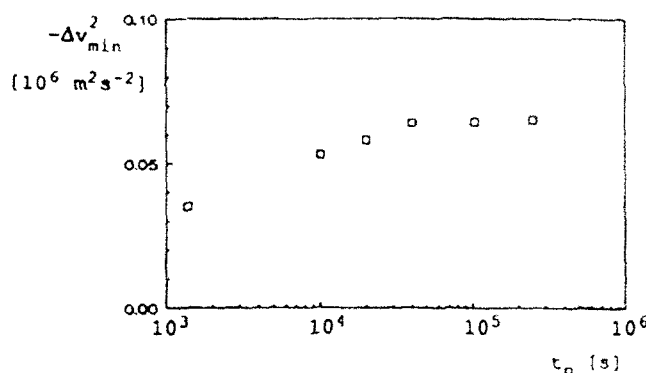


Figure 4. Depth of the minimum as in figure 3 as a function of preannealing time for  $\text{Pd}_{40}\text{Ni}_{40}\text{P}_{20}$ . From ref. 15.

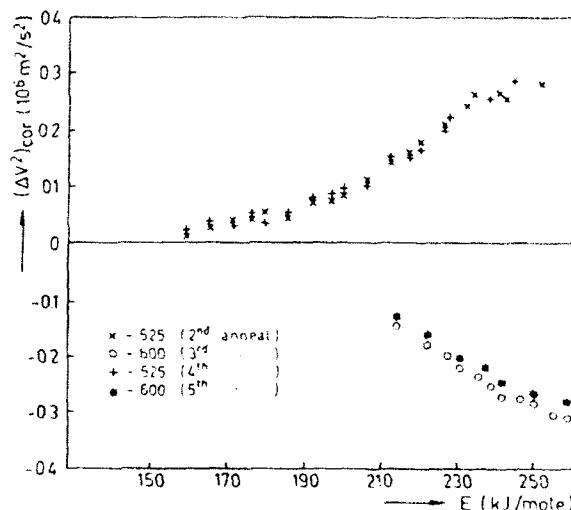


Figure 5. Reversible behaviour of  $\Delta v^2$  in  $\text{Fe}_{40}\text{Ni}_{40}\text{B}_{20}$  upon cycling between 525 and 600 K. The calculated TSRO part has been subtracted. From ref. 16.

described before; the transition is not clearly marked by the data points themselves. There is, however, up till now one physical property which behaves differently in this respect: the positron life time  $\tau$ . Figure 7 (from ref. 17), shows the isothermal change of  $\tau$  in  $\text{Fe}_{40}\text{Ni}_{40}\text{B}_{20}$  at 550 K. On the time axis,  $\tau_{fv}$  represents the time where the CSRO-TSRO transition was expected as a result of the analysis of modulus and resistivity data discussed earlier. It is seen that the maximum of the isothermal (C) corresponds well to  $\tau_{fv}$ , which means that in this case positron life time increases by CSRO and decreases by TSRO, which yields a clear marking of the transition.

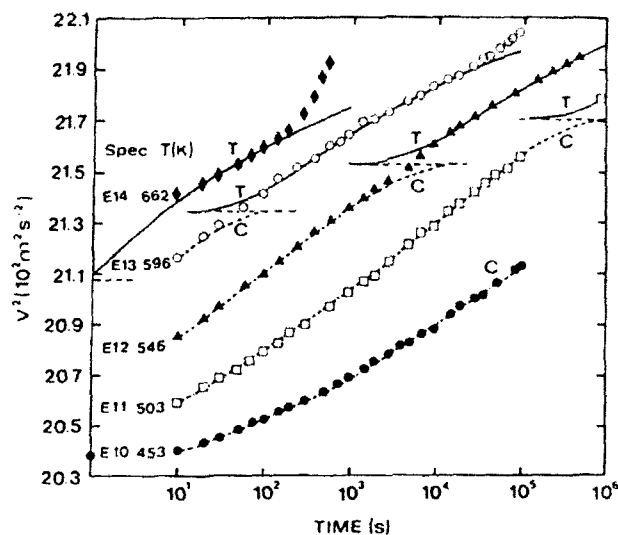


Figure 6. Change in  $v^2$  of as-quenched  $\text{Fe}_{40}\text{Ni}_{40}\text{B}_{20}$  as a function of time at the temperatures indicated. Drawn curves T: Calculated TSRO contribution. From ref. 10.

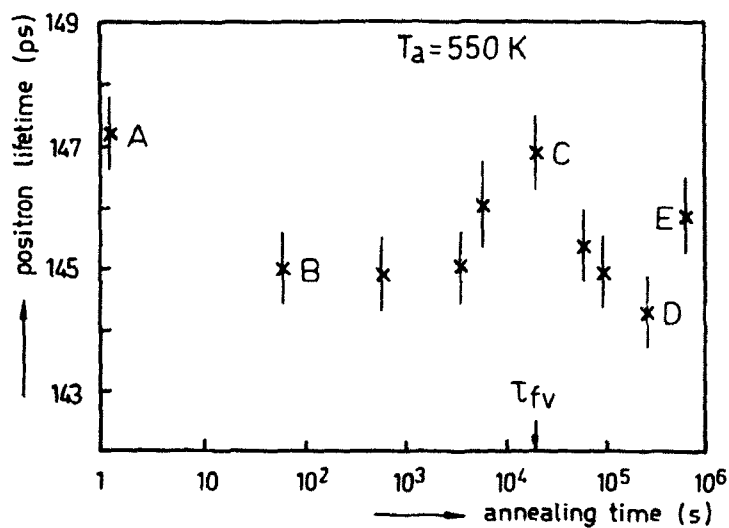


Figure 7. Change of positron life time in as-quenched  $\text{Fe}_{40}\text{Ni}_{40}\text{B}_{20}$  at 550K as a function of time.  $\tau_{fv}$ : Calculated CSRO-TSRO transition time. From ref. 17.

Recent experimental data on the change of resistivity during structural relaxation obtained by Kokmeyer et al.<sup>16</sup> and Koebrugge<sup>15</sup> indicate that the picture presented so far is too simple. The analysis of the TSRO part remains unchanged, but there are strong indications that in the processes preceding TSRO (the "CSRO range"), in as-quenched specimens, apart from reversible chemical ordering, an irreversible component also plays a part. In the pictures presented in this paper also two indications can be found for a greater complexity. First, in figure 7, the "CSRO range" ABC contains a falling part (AB) and a rising part (BC), which means that in this range at least two types of processes play a part with contributions of opposite sign to the change of positron life time. Second, in figure 5 the reversible effect is observed only in the activation energy range 170 - 250 kJ mol<sup>-1</sup>, which is smaller than the 130 - 250 kJ mol<sup>-1</sup> obtained from as-quenched isotherms. Further indications for irreversible processes in the pre-TSRO range were reported by Huizer et al.<sup>12</sup> from length measurements. The separation between the reversible and irreversible processes in this range has not yet been performed in a completely satisfactory way.

The results discussed so far can be summarized as follows:

1. The final part of structural relaxation can be described in terms of TSRO, the annealing out of free volume (equations (2) - (5)). This is true both for the viscosity, which depends on the flow defect concentration  $c_f$ , as for properties which are related to free volume itself, like length, electrical resistivity and elastic constants. The process is characterized by a well defined activation energy.
2. In the pre-TSRO range, reversible processes can be distinguished which are ascribed to chemical short range ordering (CSRO). The activation energy range of these processes in Fe<sub>40</sub>Ni<sub>40</sub>B<sub>20</sub> is about 170 - 250 kJ mol<sup>-1</sup>.
3. There are strong indications that in the pre-TSRO range (activation energy spectrum 130 - 250 kJ mol<sup>-1</sup>), as yet unidentified irreversible processes play a part.
4. In general, the sign of the property changes in the TSRO and the pre-TSRO range is the same. The exception is positron life time, which shows a maximum at the transition, the position of which is consistent with the results of the analysis carried out on other properties.

### 2.3. Diffusion Related Properties

#### 2.3.1. The Diffusion Coefficient

The description of diffusion behaviour of amorphous materials seems, at first sight, simple. As the atomic mobility in viscous flow is carried by the flow defects, there seems to be no reason why the atomic mobility in diffusion should not be governed by the same defects as well. In that case, the product of the viscosity  $\eta$  and the diffusion coefficient  $D$  should be constant, the well known Stokes-Einstein relation, the validity of which has been widely tested in fluids.

However, in analysing the extensive data of Horvath and Mehrer<sup>18</sup> of <sup>59</sup>Fe tracer diffusion in amorphous Fe<sub>40</sub>Ni<sub>40</sub>B<sub>20</sub>, Van den Beukel<sup>19,20</sup>, showed that the SE-relation does not hold. Instead it was found that, at constant temperature, the diffusion data from ref. 18, combined with the viscosity data from ref. 7, led to the result that, with a good precision, the relation  $\eta D^2 = \text{constant}$  was valid. This is illustrated in figure 8. From this it was concluded that diffusion in amorphous Fe<sub>40</sub>Ni<sub>40</sub>B<sub>20</sub> is carried by "diffusion defects", the concentration of which,  $c_d$ , is related to the concentration  $c_f$  as  $c_d \sim c_f^{1/2}$ . For the diffusion coefficient we then have

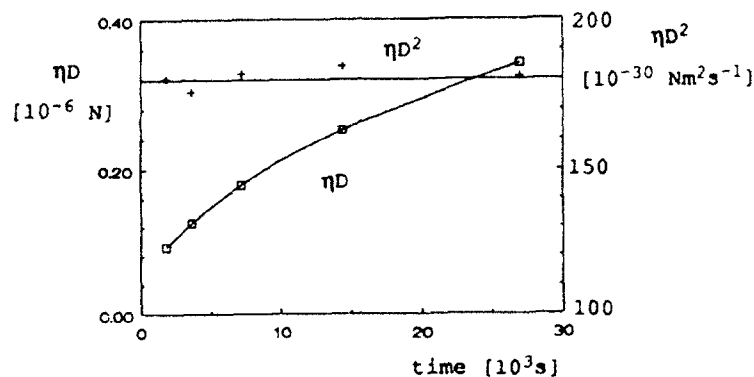


Figure 8.  $\eta D$  and  $\eta D^2$  of as-quenched  $\text{Fe}_4\text{Ni}_{40}\text{B}_{20}$  at 593K as a function of time. From ref. 20.

$$D = D_0 c_f^{1/2} \exp(-E_f/RT) \quad (11)$$

where  $D_0$  is a constant and where it was assumed, in accordance with the experimental data (see later on), that the activation energy for diffusion defects and flow defects is the same.

The evaluation of the diffusion data of Horvath and Mehrer<sup>18</sup> will be based on equation (11), whereas the time dependence of  $c_f$  in this expression will be described by equations (4) and (5). It must be realised here that the values of  $D$  after a time  $t$  at a temperature  $T$ , as presented by Horvath and Mehrer<sup>18</sup> are average values in the time interval  $(0, t)$ . From (11), (4) and (5) we then have

$$D(t) = \bar{D}(0, t) = \frac{2 D_0 c_{f0}^{1/2} \exp(-E_f/RT)}{\alpha t} [(1 + \alpha t)^{1/2} - 1] \quad (12)$$

where

$$\alpha = C_0 c_{f0} \exp(-E_f/RT) \quad (13)$$

It is emphasized that, for a comparison with experimental data, we have only one adaptable parameter left, namely  $D_0$ , which acts as a scaling factor. The other parameters,  $C_0$ ,  $c_{f0}$  and  $E_f$ , are taken from the observations on viscosity and represented in equation (9).

In table 1, all the data of Horvath and Mehrer<sup>18</sup> on as-quenched specimens are represented. In the table the values of  $D_c$ , as calculated from equation (12) with  $D_0 = 2.96 \cdot 10^4 \text{ m}^2 \text{ s}^{-1}$  are represented, and also the ratio  $r = D_c/D$  is given. The agreement between  $D_c$  and  $D$  is excellent in view of the estimated accuracy of the experimental diffusion coefficients. It is noted that the agreement covers a range of  $D$  values differing by a factor of  $10^4$ . An analogous analysis of Horvath and Mehrer's data on preannealed specimens yielded less satisfactory results. An explanation for this discrepancy is presented elsewhere<sup>21</sup>.



Table 1. Experimental ( $D$ , ref. 18) and calculated ( $D_c$ ) values of the diffusion coefficient of  $^{59}\text{Fe}$  tracers in as-quenched amorphous  $\text{Fe}_{40}\text{Ni}_{40}\text{B}_{20}$

$T(\text{K})$	$t(\text{h})$	$D(10^{-22} \text{ m}^2 \text{ s}^{-1})$	$D_c(10^{-22} \text{ m}^2 \text{ s}^{-1})$	$r$
533	1320	0.036	0.032	0.92
553	792	0.125	0.126	1.01
571	590	0.41	0.35	0.86
593	1	19.6	18.5	0.94
"	2	14.0	14.0	1.0
"	4	10.2	10.4	1.02
"	8	7.3	7.64	1.05
"	15	5.3	5.70	1.08
"	25	4.6	4.48	0.98
612	2	36.9	33.8	0.92
"	6	19.7	20.2	1.02
"	18	13.7	11.9	0.87
613	1	47.2	48.5	1.02
"	2	33.5	35.3	1.05
"	4	23.8	25.5	1.07
631	2	57.7	73.8	1.28
643	1	123	163	1.33

Recently, Duine <sup>22</sup> performed measurements on the diffusion of Au in amorphous  $\text{Pd}_{40}\text{Ni}_{40}\text{P}_{20}$ . The gold atoms were ion implanted in the glass at energies of 20 keV, and their penetration profile as a function of annealing temperature and time was measured by the Rutherford Back Scattering (RBS) technique. A typical result is shown in figure 9, from which the diffusion coefficient as a function of time can be determined. The first results confirmed the validity of equation (12).

### 2.3.2. Diffusion Controlled Processes

In section 2.2, it was argued that part of structural relaxation is due to chemical short range ordering (CSRO). The main characteristic of this process is the reversibility with temperature. It was shown that the effect on the change of physical properties due to CSRO can be isolated from the total effect observed.

As chemical ordering is considered to be a diffusion process, it is expected that the kinetics will depend on the concentration of diffusion defects. More specifically, it is expected that the rate of ordering will be proportional to  $c_d \sim c_f^{1/2}$ . In order to verify this,

the following experiment has been carried out <sup>23</sup>. A specimen of  $\text{Fe}_{40}\text{Ni}_{40}\text{B}_{20}$  was first annealed at 600 K for a time long enough to establish equilibrium order at that temperature. Subsequently, the specimen was annealed at 550 K and the change of the elastic modulus (again expressed as  $\Delta v^2$ ) was measured as a function of time. From the measured  $\Delta v^2$ , the calculated contribution of TSRO was subtracted, as outlined in section 2.2. The resulting  $\Delta v^2(t)$  is then due to CSRO only, and is represented in figure 10a (circles). As expected, the curve saturates when equilibrium order at 550 K is attained.

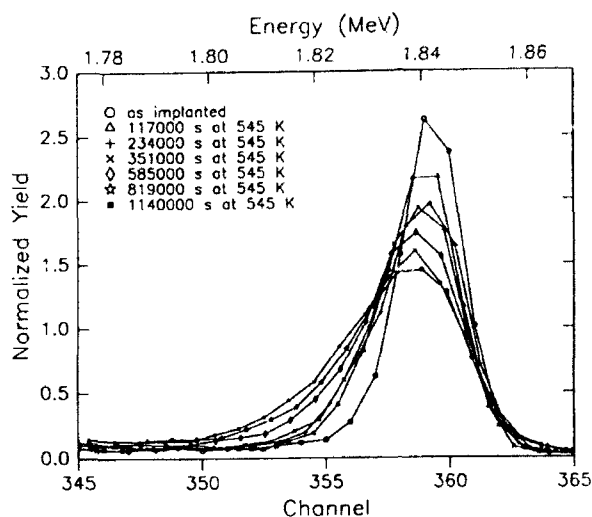


Figure 9. Concentration profiles of implanted Au atoms in  $\text{Pd}_{40}\text{Ni}_{40}\text{P}_{20}$  as measured with RBS after various subsequent annealings. From ref. 22.

Subsequently, the specimen was annealed again at 600 K for a period long enough to lower the flow defect concentration substantially, in the present example by a factor of 17 (as calculated from equations (2), (5) and (9)). Finally, the specimen was annealed again at 550 K and  $\Delta v^2(t)$  was measured. After subtracting the calculated TSRO contribution, the result is presented in figure 10a (triangles). It is clearly seen that the rate of CSRO is slowed down compared to the first anneal at 550 K. The time shift between the two curves in figure 10a is by a factor of 4, which is about  $(17)^{1/2}$ . This is in agreement with the expectation that the rate of CSRO is proportional to  $c_f^{1/2}$ . This can also be demonstrated by

plotting the results of figure 10a as  $\Delta v^2$  vs  $c_f^{1/2} t$ , which is done in figure 10b. The two

curves now coincide. Further experiments of the kind just described confirmed the idea. Recently, Koebrugge<sup>15</sup> repeated the experiments on amorphous  $\text{Pd}_{40}\text{Ni}_{40}\text{P}_{20}$ , with the same results.

Another diffusion controlled process is anelastic relaxation. This is the phenomenon that a material, upon loading in the elastic range, shows, after an instantaneous elastic strain, a time dependent strain, which is called "anelastic" because it is reversible upon unloading. The effect is caused by the fact that the atoms move into positions of lower energy with respect to the applied stress. This yields an extra elastic strain which takes some time, because the required atomic rearrangements take place by diffusion. The process is also often called "stress induced ordering" (SIO).

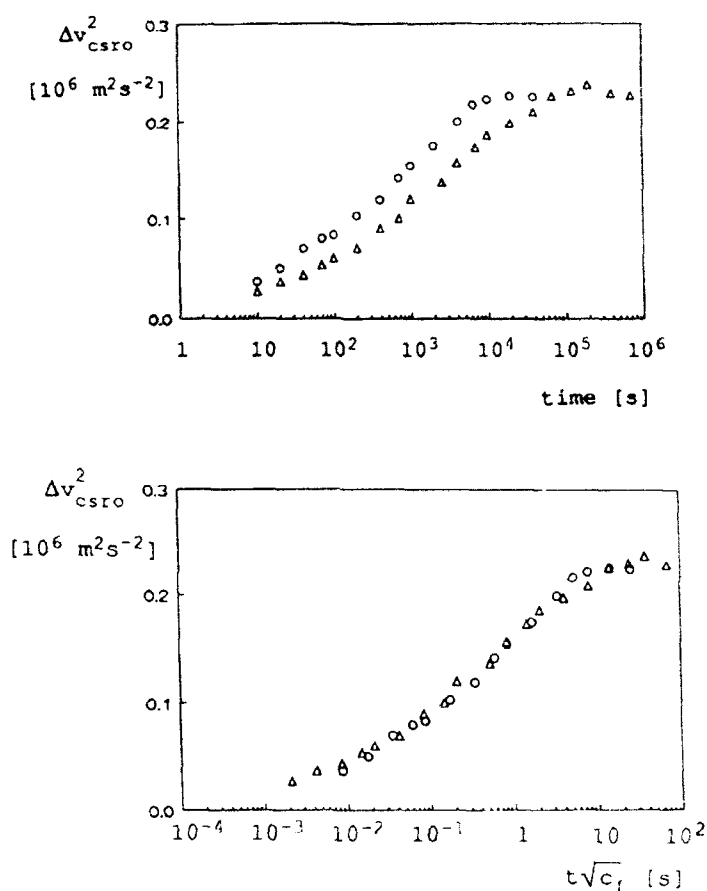


Figure 10. Reversible part of  $\Delta v^2$  in  $\text{Fe}_{40}\text{Ni}_{40}\text{B}_{20}$  at 550K for two different flow defect concentrations, plotted as a function of time (a) and of  $c_f^{1/2} t$  (b). From ref. 15.

The first attempt to study the influence of flow defect concentration on the rate of SIO was made by Leusink<sup>24</sup>. From experiments analogous to those just described on chemical ordering it was concluded that the rate of SIO is proportional to the flow defect concentration  $c_f$ . The experimental results of Leusink were reanalysed by Koebrugge<sup>15,25</sup> and extended with new experiments with an improved accuracy. The conclusion was that the rate of SIO is proportional to  $c_f^{1/2}$ . One of the results is presented in figure 11a, b. In figure 11a, the anelastic strain vs time is given as measured upon loading (even numbers)

and subsequent unloading (odd numbers) for  $\text{Fe}_{40}\text{Ni}_{40}\text{B}_{20}$  at 578 K. In the sequence 2 to 7, the flow defect concentration decreases continuously, and the retarding effect on the SIO kinetics is clearly visible. In figure 11b the same data are plotted vs  $t c_f^{1/2}$ , which yields

coincidence of both the loading and unloading curves within the experimental accuracy. In conclusion: available data both on the diffusion coefficient and the rate of chemical and stress induced ordering consistently shows that the rate of diffusion is proportional to  $c_f^{1/2}$ . The physical meaning of this amazing result is as yet unclear.

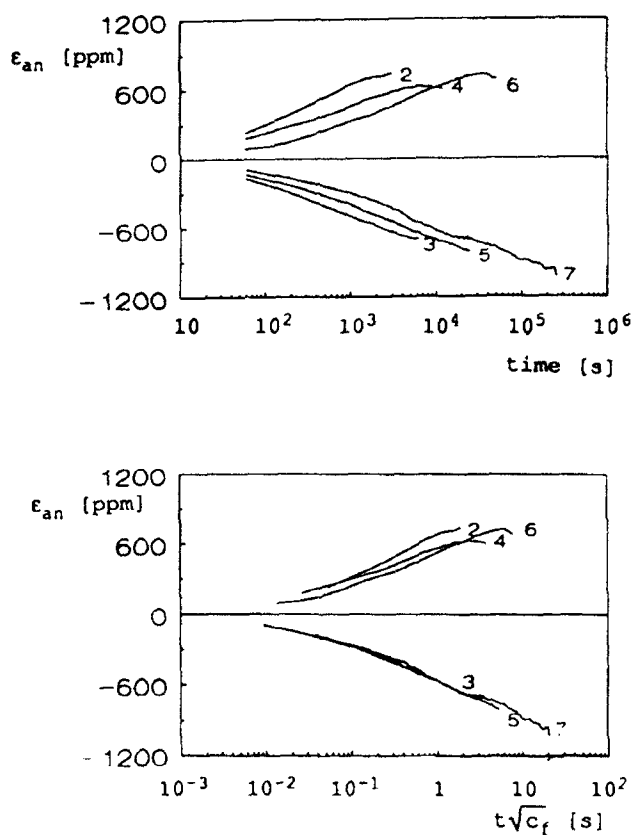


Figure 11. Anelastic strain of  $\text{Fe}_{40}\text{Ni}_{40}\text{B}_{20}$  at 578K upon loading (even numbers) and unloading (odd numbers), plotted vs time (a) and  $c_f^{1/2}t$  (b). From ref. 25.

#### 2.4. Free Volume In Equilibrium

In the foregoing, the annealing out of free volume (and thus of flow defects) was described by equation (3). According to this equation,  $\frac{dc_f}{dt} \sim c_f^2$ , which means that the

annealing out stops only when  $c_f = 0$ . From equation (7) it then follows that the viscosity would approach infinity. This is in conflict with experimental observations (e.g. refs. 26 and 27), which show that at high temperatures, in the vicinity of the glass transition temperature  $T_g$ , the viscosity approaches to a finite, temperature dependent equilibrium value  $\eta_e$ . From equation (7) it then follows that the flow defect concentration must attain a temperature dependent equilibrium value  $c_{fe}$ . Therefore, equation (3) must be modified in a way to yield the correct solution  $c_f = c_{fe}$  for infinite time.

In the literature<sup>26</sup>, several possible modifications of equation (3) have been proposed. We shall select here only one of them because, as will be pointed out later on, this one yields the best agreement with experimental data. It is:

$$\frac{dc_f}{dt} = -C c_f (c_f - c_{fe}) \quad (14)$$

which for  $c_{fe} \ll c_f$  reduces to (3). The solution is:

$$1 - \frac{c_{fe}}{c_f} = (1 - \frac{c_{fe}}{c_{fo}}) \exp [-C c_{fe} t] \quad (15)$$

which for  $c_{fe} \ll c_f$  reduces to (4).

For the viscosity we have, from equation (7)

$$\eta = \eta_0 c_f^{-1} \exp (E_\eta/RT) \quad (16)$$

For infinite time  $\eta$  approaches to

$$\eta_e = \eta_0 c_{fe}^{-1} \exp (E_\eta/RT) \quad (17)$$

In a limited temperature range around  $T_g$ , according to Cohen and Grest<sup>28</sup>, the equilibrium value of the reduced free volume can be approximately described by

$$x_e = \frac{T - T_0}{B} \quad (18)$$

where  $T_0$  and  $B$  are constants.

Combining equations (2), (17) and (18) we find

$$\eta_e = \eta_0 \exp \left( \frac{B}{T - T_0} \right) \exp (E_\eta/RT) \quad (19)$$

This is the so called "hybrid representation" of  $\eta_e(T)$ . Some authors prefer the Fulcher-Vogel representation, which equals equation (19) with  $E_\eta = 0$ . There has been some discussion on this subject in the literature (refs. 26 and 29). As reliable experimental data on  $\eta_e(T)$  are available only for a very limited number of metallic glasses in a rather narrow temperature range (30 K at most), so far the question has not been settled beyond doubt.

For the study of the approach to free volume equilibrium, relatively stable metallic glasses are required. Equilibrium must be attained prior to the onset of crystallisation. A number of Pd based glasses like PdCuSi and PdNiP meets this requirement. For these glasses, the difference between  $T_g$  and the crystallisation temperature  $T_x$  in a linear heating experiment is of the order of 40 K. Measurements on the behaviour of viscosity in this range were reported by Tsao and Spaepen<sup>26</sup> on Pd<sub>77.5</sub>Cu<sub>6</sub>Si<sub>16.5</sub> and by Volkert and Spaepen<sup>27</sup> on Pd<sub>40</sub>Ni<sub>40</sub>P<sub>19</sub>Si<sub>1</sub>. An example from the latter work is presented in figure 12.

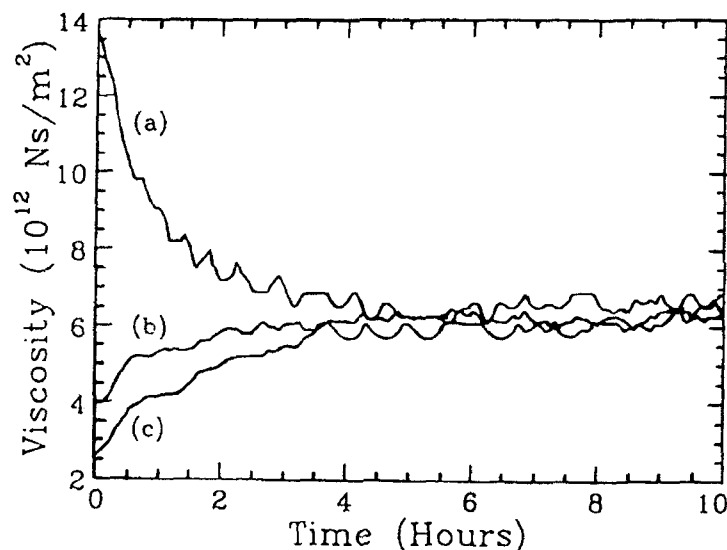


Figure 12. Change of viscosity vs time of amorphous Pd<sub>40</sub>Ni<sub>40</sub>P<sub>19</sub>Si<sub>1</sub> at 573 K (a) after equilibration at 563 K (b) after equilibration at 583 K (c) as-quenched. From ref. 27.

It is seen that here  $\eta(t)$  is no longer linear, but saturates to a constant equilibrium value which is the same in all three cases, because the measuring temperature was the same (573 K). Curve (a) shows  $\eta$  as a decreasing function of time. This specimen was, prior to the measurement, equilibrated at 563 K. Upon annealing at 573 K, free volume increases to a new equilibrium value (equation (18)). In these experiments the reversible behaviour of free volume with temperature is clearly visible.

Analogous experiments on  $\eta(t)$  near equilibrium have been recently carried out by Duine et al.<sup>30</sup> on  $\text{Pd}_{40}\text{Ni}_{40}\text{P}_{20}$ . The observed kinetics could be well described by equations (15) to (18).

When all the data are taken into account, the fit parameters  $B$ ,  $T_0$ ,  $E_\eta$ ,  $E_f$ ,  $C_0$  and  $\eta_0$  appear to be restricted to a rather narrow range. The 95% confidence interval of the fit parameters as determined from parameter  $B$  is represented in table 2. In particular, it is satisfactory that the values of  $E_\eta$  and  $E_f$ , obtained in this way, agree well with those determined in an independent manner from structural relaxation data far from equilibrium<sup>31</sup>. Further, the evaluation of the data showed a clear preference for equation (14) to alternative propositions to describe the variation of free volume near equilibrium. Finally, the result  $E_\eta = 193 \text{ kJ mol}^{-1}$  (where  $E_\eta$  was a free fit parameter) clearly points to a preference of the hybrid representation of  $\eta_c(T)$  (equation (19)) to the Fulcher-Vogel representation. In the latter case  $E_\eta$  should have been close to zero.

Table 2. Estimation of the 95% confidence interval of the fit parameters

$\eta_0$	$(4.2 \pm 0.6) \cdot 10^{-23}$	$\text{Ns m}^{-2}$
$C_0$	$(5 \pm 4) 10^{24}$	$\text{s}^{-1}$
$E_\eta$	$193 \pm 1$	$\text{kJ mol}^{-1}$
$E_f$	$155 \pm 5$	$\text{kJ mol}^{-1}$
$B$	$6650 \pm 150$	$\text{K}$
$T_0$	$357 \pm 2$	$\text{K}$

Recently, Koebrugge<sup>15</sup> performed measurements of the change of Young's modulus due to structural relaxation close to free volume equilibrium. An example is presented in figure 13, where the change of Young's modulus (again represented as  $\Delta v^2$ ) of as-

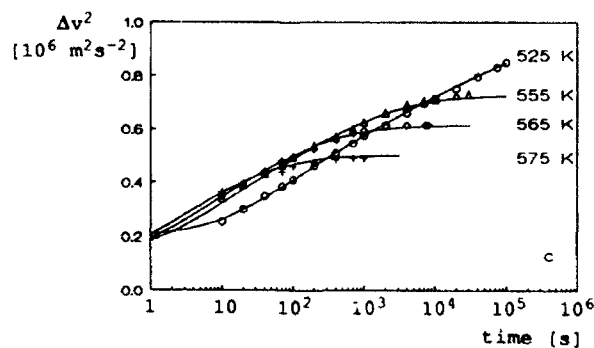


Figure 13. Saturation behaviour of  $\Delta v^2(t)$  in  $\text{Pd}_{40}\text{Ni}_{40}\text{P}_{20}$  upon annealing at the temperatures indicated. Drawn curves: From model calculations. From ref. 15.

quenched specimens of  $\text{Pd}_{40}\text{Ni}_{40}\text{P}_{20}$  is shown in the temperature range 525 - 575 K. For the higher temperature isotherms the approach to equilibrium is clearly visible. For a quantitative calculation of the effects, equation (10) as to be used, where  $\Delta x$  can be found from equations (2) and (15). The parameters used are within the limits given in table 2, as obtained from Duine's<sup>30</sup> analysis of the viscosity data. The drawn curves in figure 13 show the results of the calculations. The agreement with the data points is good.

Finally, Koebrugge<sup>15</sup> performed several cycling experiments on  $\text{Pd}_{40}\text{Ni}_{40}\text{P}_{20}$  in the vicinity of free volume equilibrium. An example is presented in figure 14. First the sample was equilibrated at 565 K, and subsequently annealed at 575 K and 555 K. The observed  $\Delta v^2(t)$  is represented in figure 14 by the data points labeled 1, 2 and 3 respectively. Note the sign of the observed variations: going from 1 to 2 (increasing temperature) and from 2 to 3 (decreasing temperature) should give rise to production and annealing out of free volume, respectively. This corresponds to the negative esp. positive sign of the observed  $\Delta v^2$ . The drawn curves are the results of model calculations, based on the same equations and parameter values as discussed before. Again the agreement with the data points is satisfactory.

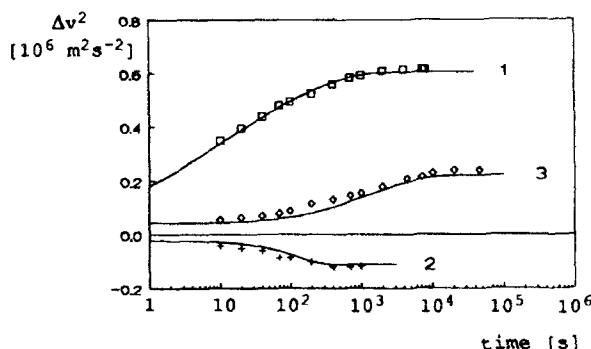


Figure 14.  $\Delta v^2$  vs time of  $\text{Pd}_{40}\text{Ni}_{40}\text{P}_{20}$  upon cycling a specimen from 565K (1) to 575K (2) and 555K (3). Drawn curves: From model calculations. From ref. 15.

### 2.5. The Glass Transition as a Free Volume Related Kinetic Phenomenon

The glass transition in amorphous materials is a phenomenon observed in DSC experiments, where the sample is warmed up at a constant heating rate. It shows up as a rather sudden increase of the specific heat  $c_p$ , followed by a maximum. Beyond the maximum  $c_p$  levels off to a constant value.

In the literature (e.g. ref. 28) it has often been suggested that this observation does not represent a thermodynamic phase transition, but that it has a kinetic origin. The main reason is that in isothermal measurements of the change of physical properties, the glass transition (in contrast to crystallisation) does not show up. This viewpoint was adopted by Van den Beukel and Sietsma<sup>32</sup> who considered the glass transition as the result of a specific aspect of structural relaxation, viz. the kinetic process due to free volume being out of equilibrium and continuously approaching (metastable) equilibrium during the continuous heating in a DSC experiment.



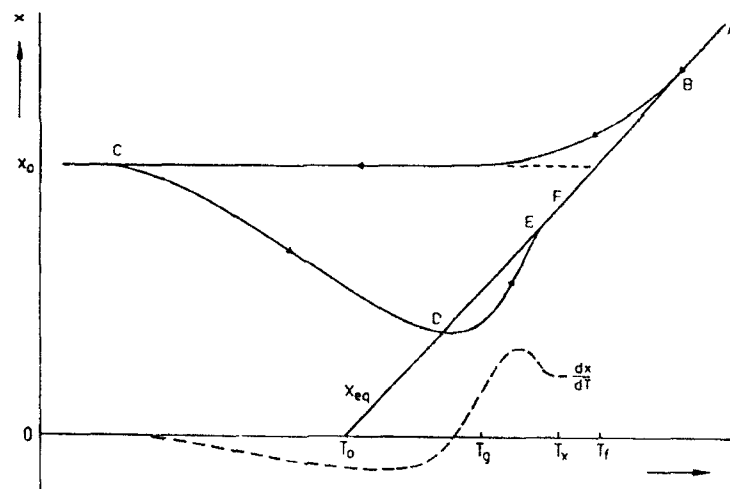


Figure 15. Schematic picture of the free volume history of a specimen during quenching (ABC) and subsequent warming up (CDEF). Dashed curve:  $\frac{dx}{dT}$ , showing both structural relaxation and the glass transition. From ref. 32.

The idea is sketched in figure 15, representing the free volume history of a glass during its production by rapid quenching and subsequent warming up until crystallisation occurs. The straight line AB represents the reduced free volume in thermodynamic equilibrium, as described by equation (18). During the rapid quench which produces the glass from the melt, in the high temperature region (AB) the kinetics of free volume annihilation is fast enough to maintain equilibrium. At lower temperatures (BC) this is no longer the case and an excess (non equilibrium) amount of free volume  $x_0$  is frozen in.  $x_0$  corresponds to the equilibrium value of  $x$  at temperature  $T_f$ , the so called "fictive temperature". When subsequently the specimen is put into a DSC and warmed up at a constant heating rate, the excess free volume anneals out and  $x$  will move into the direction of the equilibrium line (CD). This process, which we earlier called TSRO, gives rise to a release of energy. At D,  $x$  crosses the equilibrium line AB, because the kinetics is still too slow to follow the increase of  $x_{eq}$  due to the continuous increase of temperature. From now on  $x$  is smaller than the equilibrium value  $x_{eq}$ . This means that from D on new free volume is produced in order to attain equilibrium; this is an endothermic process. This is what happens in the range DEF. At E equilibrium is attained. On EF the production of free volume is fast enough to keep up with the linearly increasing  $x_e(T)$ . Finally in F, at temperature  $T_x$ , crystallisation occurs.

It is noted that the fact that  $x < x_{eq}$  beyond D is entirely due to the nature of the DSC experiment. In an isothermal experiment this will never occur, and that is the reason why the glass transition (in contrast to crystallisation) does not show up in isothermal experiments.

In the DSC experiment (CDEF in figure 15), the amount of heat released c.q. absorbed by the specimen per unit time will be proportional to  $dx/dt$  and therefore to  $dx/dT$ , as  $t \sim T$ .

in figure 15,  $dx/dT$  vs  $T$  is represented (dashed curve). It shows the structural relaxation (TSRO,  $dx/dT < 0$ ) followed by the glass transition. It is very similar to the observed  $\Delta c_p(T)$  in DSC experiments.

As the kinetics of the processes involved is well known for several metallic glasses (see previous section), the program sketched above can be carried out numerically. This has been performed by Van den Beukel and Sietsma<sup>32</sup> and yielded satisfactory agreement with the experimentally observed glass transition in several metallic glasses.

### 3. Concluding Remarks

The model described in this paper in general provides a consistent quantitative description of the observed changes in physical properties during structural relaxation. This is true both for properties which are "defect controlled" (viscosity, diffusion coefficient and diffusion related phenomena like chemical and stress induced ordering) as for properties which depend on the average free volume (density, electrical resistivity, elastic constants, etc.). The model also provides a quantitative description of the glass transition.

Three main problems wait for further clarification:

1. A more convincing separation of irreversible and reversible processes in the pre-TSRO range and a physical interpretation of the former.
2. The physical meaning of the second order reaction kinetics observed in the annealing out of flow defects.
3. A physical interpretation of the relation between the concentrations of diffusion defects and flow defects,  $c_d \sim c_f^{1/2}$ , which has to be postulated in order to connect the diffusion and viscosity data.

### Acknowledgement

Thanks are due to Drs. J. Sietsma and P.A. Duine for critically reading the manuscript.

### References

1. A. van den Beukel, in *Rapidly Quenched Metals*, eds. P.W. Lee and S. Carbonera (ASM 1986) p. 193.
2. T. Egami, *Ann. N.Y. Acad. Sc.* **371** (1981) 238.
3. A.I. Taub, F. Spaepen, *Acta Metall.* **28** (1980) 1781.
4. F. Spaepen, *Acta Metall.* **25** (1977) 407.
5. D. Turnbull, M.H. Cohen, *Journ. Chem. Phys.* **29** (1958) 1049.
6. D. Turnbull, M.H. Cohen, *Journ. Chem. Phys.* **34** (1961) 120.
7. A. van den Beukel, E. Huizer, A.L. Mulder, S. van der Zwaag, *Acta Metall.* **34** (1986) 483.
8. A.I. Taub, *Acta Metall.* **30** (1983) 2117, 2129.
9. E. Huizer, J. Melissant, A. van den Beukel, in *Liquid and Amorphous Metals*, eds. W. Gläser et al. (München, 1987) vol. 2, p. 335.
10. A. van den Beukel, S. van der Zwaag, A.L. Mulder, *Acta Metall.* **32** (1984) 1895.
11. E. Huizer, A.L. Mulder, A. van den Beukel, in *Rapidly Quenched Metals*, eds. S. Steeb and H. Warlimont (North Holland, 1985) p. 639.
12. E. Huizer, A. van den Beukel, *Acta Metall.* **35** (1987) 2843.
13. A. van den Beukel, *Journ. Non Cryst. Sol.*, **83** (1986) 134.
14. M.R.J. Gibbs, J.E. Evetts, J.A. Leake, *Journ. Mat. Sc.*, **18** (1983) 278.

15. G.W. Koebrugge, *On the kinetics of structural relaxation in some metallic glasses* (Thesis, Delft, 1991).
16. E. Kokmeyer, E. Huizer, B.J. Thijsse, A. van den Beukel, *Phys. Stat. Sol. (a)*, **105** (1988) 235.
17. J. de Vries, G.W. Koebrugge, A. van den Beukel, *Scripta Metall.*, **22** (1988) 637.
18. J. Horvath, H. Mehrer, *Cryst. Latt. Def. and Amorph. Mat.*, **13** (1986) 1.
19. A. van den Beukel, *Scripta Metall.*, **22** (1988) 887.
20. A. van den Beukel, *Isr. Journ. Techn.*, **24** (1988) 101.
21. A. van den Beukel, *Acta Metall. et Material.*, 1991, in press.
22. P.A. Duine, unpublished data.
23. G.W. Koebrugge, A. van den Beukel, *Scripta Metall.*, **22** (1988) 529.
24. G.J. Leusink, A. van den Beukel, *Acta Metall.*, **36** (1988) 3019.
25. G.W. Koebrugge, J. Sietsma, A. van den Beukel, *Journ. Non Cryst. Sol.*, **117/118** (1990) 601.
26. S.S. Tsao, F. Spaepen, *Acta Metall.*, **33** (1985) 881.
27. C.A. Volkert, F. Spaepen, *Mat. Sc. Eng.*, **97** (1988) 449.
28. M.H. Cohen, G.S. Grest, *Phys. Rev.*, **B20** (1979) 1077.
29. A. van den Beukel, S. Radelaar, *Acta Metall.*, **31** (1983) 419.
30. P.A. Duine, J. Sietsma, A. van den Beukel, accepted for publication by *Acta Metall. et Material.*.
31. A.I. Taub, F. Spaepen, *Acta Metall.*, **28** (1980) 1781.
32. A. van den Beukel, J. Sietsma, *Acta Metall. et Material.*, **38** (1990) 383.

## COOPERATIVITY OF MOLECULAR MOTION IN LIQUIDS NEAR THE GLASS TRANSITION

J. JÄCKLE

*University of Konstanz, Fakultät für Physik  
D 7750 Konstanz, Germany*

### ABSTRACT

The dynamical properties of the hard-square lattice gas with diffusion are shown to correspond to the physically attractive ideas about cooperativity in supercooled glass forming liquids near the glass transition. The model exhibits dynamical size effects, which are governed by a characteristic length of cooperativity, suggesting that analogous size effects should be observable in geometrically confined liquids close to their glass transition.

### 1. Introduction

The intuitive physical idea that the slow molecular motions in liquids near the glass transition are strongly cooperative<sup>1</sup> is very plausible. One expects that the geometrical and energetic conditions in a dense liquid well below the melting temperature require a coordinated motion of a larger number of molecules for a molecular rearrangement to be possible. Indirect evidence for such cooperativity is given by the experimentally observed temperature dependence of the viscosity, or relaxation time. In the case of pure fused quartz, e. g., the temperature dependence of the viscosity follows the Arrhenius formula<sup>2</sup>, but both the prefactor and the activation energy are much too large to be explained in terms of single defects of the covalent SiO<sub>2</sub> network<sup>3,4</sup>. The discrepancies are rationalized as an effect of cooperativity. At present, however, there is no direct experimental information about cooperativity, nor is there a theory for it. In this situation, simplified models with cooperative dynamics arising from kinetic constraints are of great interest. Such models are lattice gases with extended hard-core interaction and diffusion dynamics<sup>5-10</sup>, or kinetic Ising models with an isotropic<sup>11-13</sup> or directed<sup>14,15</sup>

constraint requiring a certain number of up-spin neighbours for a spin to be allowed to flip. The models

- help to give the intuitive concept of cooperativity a concrete meaning,
- reproduce qualitative features of the glass transition, in particular the rapid and unlimited slowing down in the absence of a sharp blocking transition,
- suggest the existence of size effects in the relaxational or transport properties of confined liquids near the glass transition.

In these notes I restrict myself to the two-dimensional hard square lattice gas as a model for cooperative dynamics.

## 2. Cooperativity in the hard-square lattice gas

The hard-square lattice gas model<sup>5-10</sup> is a special case of a general class of lattice gas models. The particles populating the lattice sites have an extended hard core which excludes the simultaneous occupation of nearest neighbour sites. There are no other interactions apart from this hard-core repulsion. A particle jumps to a nearest-neighbour site with a constant jump rate (which defines the unit of time) provided that the nearest neighbours of the site of destination are also empty. The hard-square lattice gas is obtained for the two-dimensional square lattice. As a result of the exclusion of pairs of nearest neighbours, the particles behave like hard squares which are allowed to touch, but not to overlap one another. The diffusion process in this model resembles a sliding-piece puzzle with square pieces which can move only in the direction of their diagonals. The maximum particle concentration  $c$  for the hard-square lattice gas is  $c_{\max} = 0.5$ . At the highest concentration one sublattice is fully occupied, the other is completely empty. At higher particle concentrations, for  $c > 0.35$ , say, a particle usually can jump only in one of the four directions, and many particles are completely blocked. For a blocked particle to become mobile again, certain neighbouring particles have to jump first into particular directions. This process, by which an initially blocked particle regains mobility, represents what we mean by "cooperativity" in the model.

The complexity of the process is illustrated by the example<sup>16</sup> shown in Fig. 1, where crosses mark particles, circles are vacancies. The squares drawn around the central site, which is occupied by a blocked particle, represent the different shells of neighbour sites on the sublattice to which the central site belongs. (Note that a particle can be blocked only by particles on the same sublattice, since the nearest neighbour sites around a particle are always free.) The arrows and numbers in the figure mark a sequence of jumps, which is the shortest process after which the central particle has become mobile again. In the configuration shown the central particle

is hindered to jump upwards by a single particle on the next nearest neighbour site above it. This particle, however, is blocked, too, and becomes mobile only after a sequence of nine particular jumps of other particles on the outer neighbour shells has taken place. The first of these jumps is from the fourth neighbour shell, from where the sequence proceeds inwards to shells number three and two and outwards to the fourth shell again, before turning towards the centre and reaching the blocking particle.

The number  $l$  of the outermost shell occurring in the process defines a length which is a measure of the degree of cooperativity involved: Particles up to the  $l$ th shell must "cooperate" to unblock the particle considered. If, e. g., the particles on the outermost shell were permanently blocked by a rigid boundary, the particle in the centre would also remain permanently blocked. I therefore propose to call it the "cooperativity length". Averaging over different configurations at a given particle concentration  $c$ , we obtain the average cooperativity length  $\langle l \rangle$ . The concentration dependence of this length is shown by the lower curve <sup>16</sup> in Fig. 2. The abscissa is the inverse of the concentration of holes, which is given by  $c_h = 1 - 2c$ . For small values of  $c_h$  the average cooperativity length increases rapidly. However, it remains finite for any non-zero hole concentration, i. e. for all particle concentrations below  $c_{\max} = 0.5$ . Consequently, there is no sharp blocking transition at any lower particle concentration. To prove this <sup>6,9</sup>, the blocking problem needs to be treated in a more global way.

We consider a lattice of finite size  $L \times L$ , randomly occupied by particles of concentration  $c$ , and ask for the probability  $p_l$  that none of the particles is permanently blocked. (It is appropriate to express  $L$  in units of the lattice spacing of a sublattice of the square lattice.) For reasons which are not explained here, this probability has also been called the probability of "rectangular-cluster percolation" <sup>6</sup> or of a particular type of "bootstrap percolation" <sup>9</sup>. A lower bound to this probability can be shown to converge to one for  $L \rightarrow \infty$  at any particle concentration  $c < 0.5$ , from which the proof follows. The probability  $p_L$  of absence of permanently blocked particles in  $L \times L$  lattices can be calculated by simulation <sup>7</sup>. The length for which the probability is 50 %, say, defines another characteristic length  $\xi_{50}$  of the blocking problem. The concentration dependence of this length has been calculated up to a length of 20 000. For shorter values, it is shown by the upper curve in Fig. 2 (data from ref. 9). Apparently, the two lengths  $2 \langle l \rangle$  and  $\xi_{50}$ , which are defined by the individual and by a global blocking problem, converge asymptotically for large values. (The factor of 2 in  $2 \langle l \rangle$  takes into account that the edge length of the  $l$ th neighbour shell is  $2l$ , again in units of the lattice constant of a sublattice.)

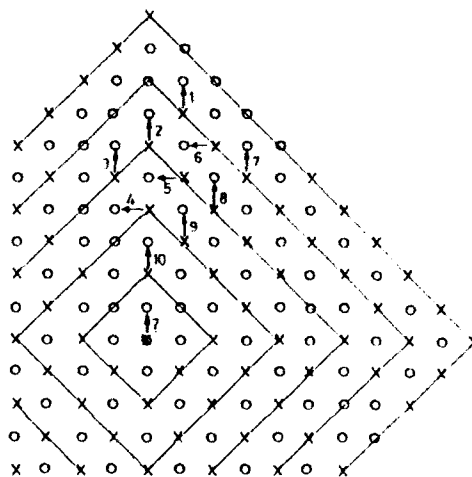


Fig. 1:

Sequence of particle jumps, after which the initially blocked particle in the centre is allowed to jump in the upward direction (see text; the particle concentration is  $c = 0.42$ ).

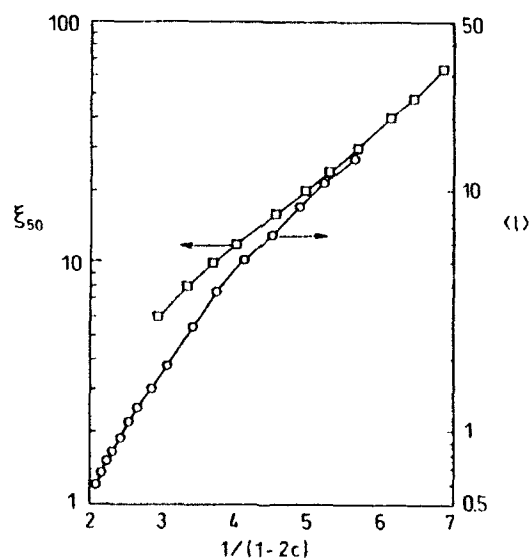


Fig. 2:

The two characteristic lengths defined by the blocking problem in the hard square lattice gas as a function of particle concentration  $c$ . Lower curve:  $\langle l \rangle$ . Upper curve:  $\xi_{50}$ . Both lengths are given in units of the lattice constant of a sublattice.

The appearance of a characteristic length in the blocking problem (I assume that  $2\langle l \rangle$  and  $\xi_{50}$  are identical at high particle concentrations) immediately implies a size dependence of dynamical properties of the lattice gas. For linear lattice dimension  $L$  smaller than the characteristic length, a substantial fraction of particles is permanently blocked. Expressed in more general terms, in this case part of the lattice gas is frozen and can never relax. Studying the self diffusion of particles in the hard square lattice gas by Monte Carlo simulation, we found a size effect which is more surprising than this<sup>9</sup>. Fig. 3 shows the mean square displacement of the particles in lattices of different size at concentration  $c = 0.415$ . In small lattices  $L < 100$  the mean square displacement is reduced enormously as compared with the largest lattices. Most striking is the fact that the size dependence occurs already at relatively short times, when the mean distance travelled by a particle is much smaller than  $L$ . For illustration of this fact, the points where the root-mean-square displacement amounts to only a twentieth of  $L$  are marked on three curves in Fig. 3. Fig. 4 demonstrates that the observed size effect correlates strongly with the probability  $p_L$  for the absence of permanently blocked particles. Accordingly, the size effect is governed by the characteristic length  $\xi_{50}$  of the blocking problem, which has a value of 40 for the concentration considered. The effect disappears for  $L \gg \xi_{50}$ , as can be seen also from the curves of Fig. 3.

### 3. Conclusion

It has been shown that the diffusion dynamics of the hard-square lattice gas has features which correspond to our intuitive ideas about cooperativity as proposed by Adam and Gibbs. The process of unblocking of an initially immobile particle as well as the problem of the existence of permanently blocked particles in finite lattices define a characteristic length, which can be interpreted as a measure of the range of cooperative interactions. In finite lattices with periodic or blocking boundary conditions, the existence of such a length inevitably leads to a size dependence of dynamic properties, as demonstrated for self-diffusion. Our study of this model strongly suggests that cooperativity of molecular motion in undercooled liquids close to the glass transition should cause a similar size dependence of relaxation or transport properties. Experimental efforts to discover such size effects in geometrically confined liquids are highly desirable.



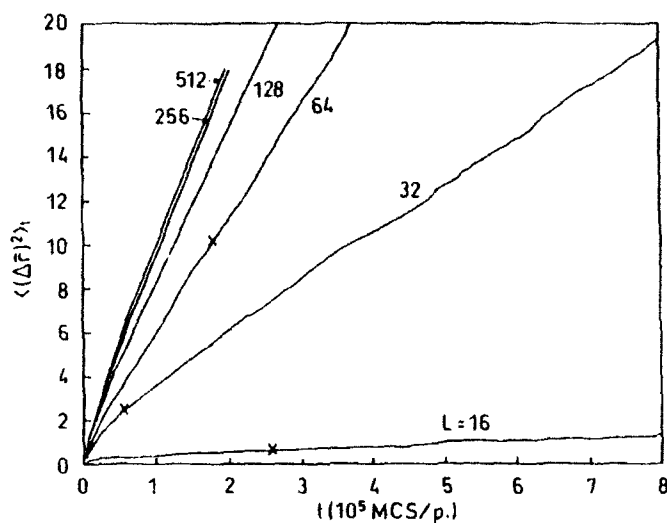


Fig. 3:  
The size-dependent mean-square displacement versus time for the hard square lattice gas ( $c = 0.415$ ) (from ref. 9).

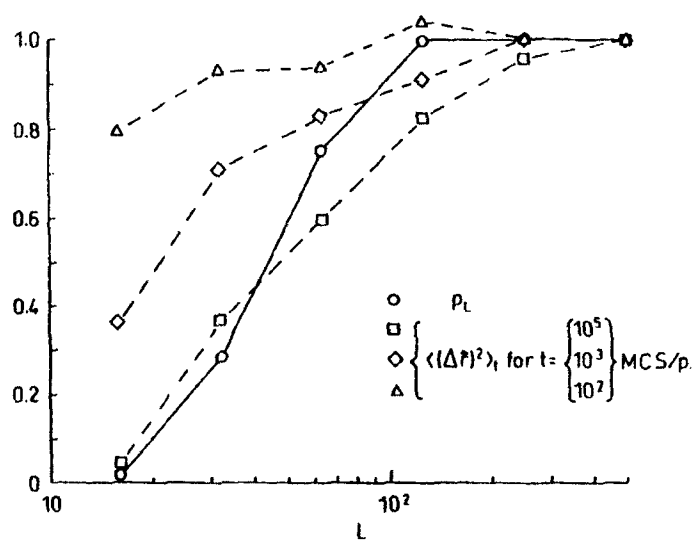


Fig. 4:  
Comparison of the size dependence of mean-square displacements at different times (dashed) with that of the probability  $p_L$  for the absence of permanently blocked particles (full line). For each time the mean-square displacements are normalized relative to the value for the largest size  $L = 512$  ( $c = 0.415$ ) (from ref. 9).

### References

1. G. Adam and J.H. Gibbs, *J. Chem. Phys.* **43** (1965) 139.
2. G. Hetherington, K.H. Jack, and J.C. Kennedy, *Physics Chem. Glasses* **5** (1964) 130.
3. N.F. Mott, *Phil. Mag.* **B56** (1987) 257.
4. J. Jäckle, *Phil. Mag.* **B56** (1987) 113.
5. G.E. Murch, *Phil. Mag.* **A44** (1981) 699.
6. W. Ertel, K. Froböse, and J. Jäckle, *J. Chem. Phys.* **88** (1988) 5027.
7. K. Froböse, *J. Stat. Phys.* **55** (1989) 1285.
8. R. Pitis, *Phys. Rev.* **B41** (1990) 7156.
9. J. Jäckle, K. Froböse, and D. Knödler, *J. Stat. Phys.* **63** (1991) 249; **65** (1991) 415.
10. J. Jäckle, *Mat. Res. Soc. Symp. Proc.* **215** (1991) 151.
11. G.H. Fredrickson and H.C. Andersen, *J. Chem. Phys.* **83** (1985) 5822.
12. G.H. Fredrickson and S.A. Brawer, *J. Chem. Phys.* **88** (1986) 3351.
13. J. Reiter, *J. Chem. Phys.* **95** (1991) 544.
14. J. Jäckle and S. Eisinger, *Z. Phys.* **B84** (1991) 115.
15. J. Reiter, F. Mauch, and J. Jäckle, subm. to *Physica A*.
16. D. Sappelt, private communication, and unpublished results.

# STUDIES OF STRUCTURE AND GLASS TRANSITION IN LIQUID CRYSTALLINE COPOLYESTERS BY MEANS OF SYNCHROTRON RADIATION AND RELATED METHODS

H. G. Zachmann, S. Thiel

*Institut für Technische und Makromolekulare Chemie, University of Hamburg,  
Bundesstr.45, 2000 Hamburg 13, Germany*

## ABSTRACT

Binary and ternary copolyesters of poly(ethyleneterephthalate) (PET), poly(ethylene-naphthalene-2,6-dicarboxylate) (PEN) and p-hydroxybenzoic acid (PHB) were synthesized. These materials are liquid crystalline (LC) if they contain more than about 30 mol% PHB. The glass transition was studied by dynamic mechanical analysis and the crystallization kinetics by wide angle x-ray scattering employing synchrotron radiation. The transition LC-isotropic state was investigated by means of differential scanning calorimetry. It was shown that in some of the copolyesters different fractions of the LC phase (from 0 to 100%) can be frozen in. Thus it became possible to compare the glass transition, molecular motion and crystallization kinetics of the LC phase to that of the isotropic phase. In the LC phase the glass transition temperature is lower than in the isotropic phase, the molecular motion above  $T_g$  does not include conformation changes, and crystal growth is linear instead of three-dimensional.

## 1. Introduction

In polymers the following states may be observed:

- *The state of the melt*, obtained by heating in all polymers except the few ones which degrade before melting
- *The semicrystalline state*, obtained in all polymers composed of chains with a regular chemical structure. It must be pointed out, that polymers never crystallize completely. There always remain small amorphous regions between the crystals. The crystalline fraction may reach values between 20 and 80% depending on the molecular structure and thermal pretreatment.
- *The glassy state*, which is obtained by cooling below the glass transition temperature  $T_g$  in all polymers which are not able to crystallize. The glassy state may also be obtained in some crystallizable polymers in which crystallization proceeds slowly enough so that it can be prevented by quenching the melt.
- *The liquid crystalline (LC) state*, which can be obtained in polymers which contain a fraction of stiff, rod like units. In addition, these polymers may or may not be able to crystallize.
- *The glassy liquid crystalline state*, which may be obtained in some LC polymers by rapid cooling below  $T_g$ . In this state the molecular order of the LC state is preserved while the molecular motion is frozen in to a large extent.

LC polymers become more and more important and many investigations of the structure and phase transitions in such polymers have been performed<sup>1</sup>. In this paper some on the glass transition and crystallization of LC polymers will be presented. In particular, the corresponding properties of the LC phase will be compared to those of the isotropic melt. For such investigations it is necessary to have polymers available in which the state of both the LC phase and the isotropic melt can be frozen in by quenching and which are able to crystallize. We have synthesized such polymers in our laboratory<sup>2,3</sup> and performed the corresponding investigations by means of dynamic mechanical analysis (DMA), differential scanning calorimetry (DSC), microscopy, wide angle x-ray scattering (WAXS) employing synchrotron radiation, and small angle neutron scattering (SANS).

## 2. Investigated Materials

The polymers investigated are composed of the following structural units (Fig. 1): poly(ethyleneterephthalate) (PET), poly(ethylenenaphthalene-2,6-dicarboxylate) (PEN) and p-hydroxybenzoic acid (PHB). The polymer chains either may be built up by a

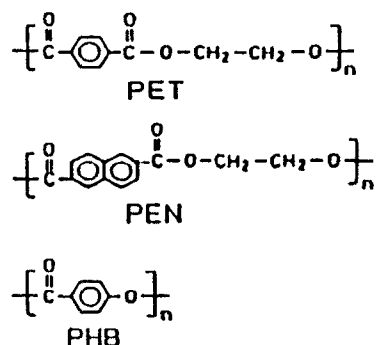


Fig. 1: Structural units of the polymers investigated

single kind of units, let us say PET. In this case the material is called a homopolymer. Or, the chains may consist of two or all three kinds of units randomly linked together. In this case one calls the material a binary or ternary copolymer, respectively.

Due to the CH<sub>2</sub> groups, the PET and PEN chains are flexible. Therefore, these homopolymers and their copolymers do not form liquid crystalline states. In contrast, the PHB units are stiff rods. As a consequence, if about 30 to 40 mol% of PHB-units are added to the chains containing PET or/and PEN the material may form a nematic liquid crystalline phase.

An overview of the properties of the materials in relation to their compositions is shown<sup>3</sup> in Fig. 2. The corners of the triangle represent the three homopolymers PET, PEN, PHB. The lines connecting two points represent the corresponding binary

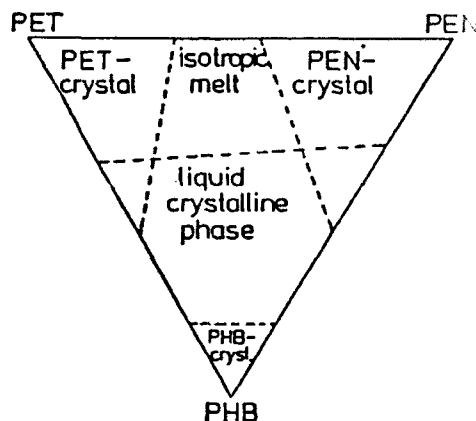


Fig. 2: Phase diagram of binary and ternary copolyesters of PET, PEN and PHB

copolymers. The area within the triangle stays for the ternary copolymer. One can see, for example, that in the binary copolymers PEN/PHB, crystals of PEN can be obtained if the PEN content is larger than 50 mol%, whereas PHB crystals are only formed if the PHB content is larger than 80 mol%. The same is true for the PET in the PET/PHB copolymer. All binary and ternary copolymers can be brought into the liquid crystalline state if the PHB content exceeds about 30 mol%.

Some further details concerning phase transitions of the binary copolymer PEN/PHB are shown<sup>4</sup> in Fig. 3. One can recognize that the melting point of PEN decreases if the PHB content is raised. At about 70 mol% PEN, the material becomes liquid crystalline upon melting. An isotropic melt is obtained at a higher temperature which usually is

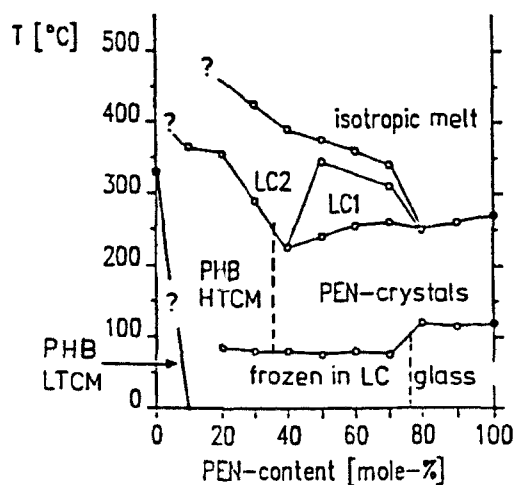


Fig. 3: Phase diagram of the binary copolyester PEN/PHB

called clearing point. The glass transition temperature, as determined by DSC is decreased when one goes over from the isotropic glass to the liquid crystalline glass. This is a very interesting effect which was investigated by us more intensively.

### 3. Glass Transition

The glass transition can be determined more reliable by means of dynamic mechanical analysis than by means of DSC. While only a small step is observed in the DSC curve, the loss modulus  $G''$  and the loss factor  $\tan \delta$ , plotted as a function of temperature show an intensive peak at the glass transition temperature<sup>2</sup>. Figs. 4a, b and c show the DMA curves for the homopolymers PET and PEN as well as for two copolymers of this material. The peak in  $G''$  and the one in  $\tan \delta$  at temperatures of about 100°C represent the glass transition. Fig. 4d shows the glass transition temperature as a function of the PET content as obtained from the position of the maximum of the  $G''$  curve. A linear relation between  $T_g$  and the PET content is obtained.

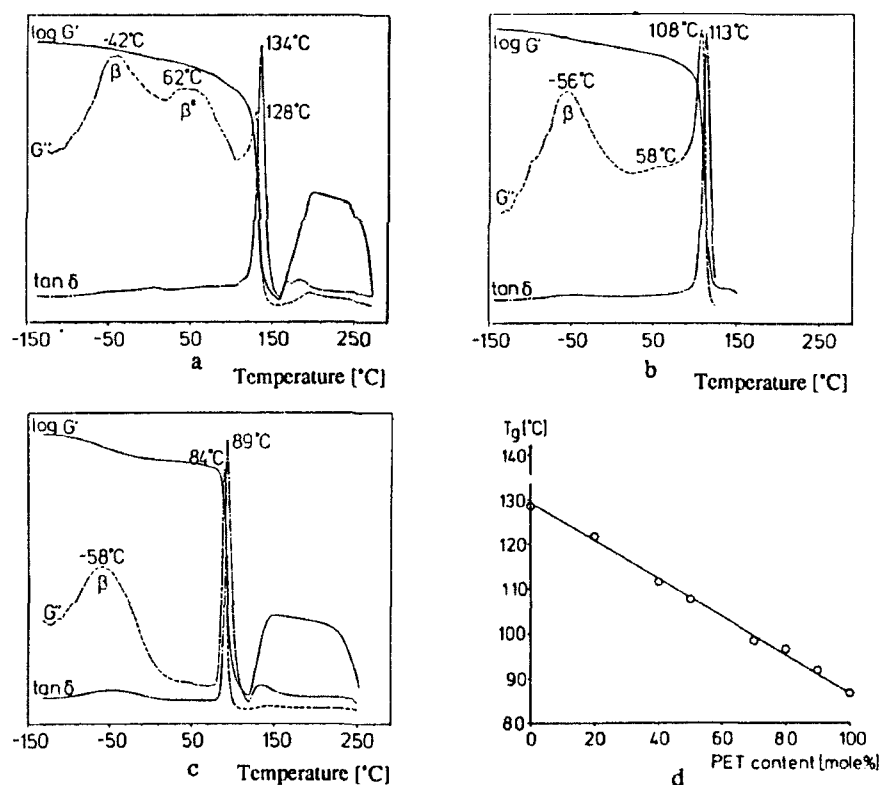


Fig. 4: Storage modulus  $G'$ , loss modulus  $G''$  and  $\tan \delta$  as a function of temperature of the copolyester PET/PEN at the composition 0/100 (a), 50/50 (b) and 100/0 (c)  
Glass transition temperature as a function of composition (d)

Fig. 5a shows  $G''$  as a function of temperature for the PET/PHB copolymers with different compositions. With decreasing content of PET, the maximum representing the glass transition shifts from 80°C to higher temperatures. At a content of 60 mol% PET a second maximum appears at about 60°C. When the fraction of PET further decreases, the intensity of this maximum becomes larger while the maximum at the higher temperature disappears. As it is known from microscopic investigations<sup>5</sup> that the material becomes partially liquid crystalline at the PET content of about 60 mol% and completely liquid crystalline at smaller PET contents, we attribute the maximum at the lower temperature to the glass transition of the material in the liquid crystalline state.

In Fig. 5b the glass transition temperatures of the isotropic phase and of the liquid crystalline phase are plotted as a function of the PET content. The glass transition temperature of the isotropic phase increases linearly with decreasing PET content. When the PET content becomes smaller than about 60 mol% no glass transition peak of the isotropic phase appears.

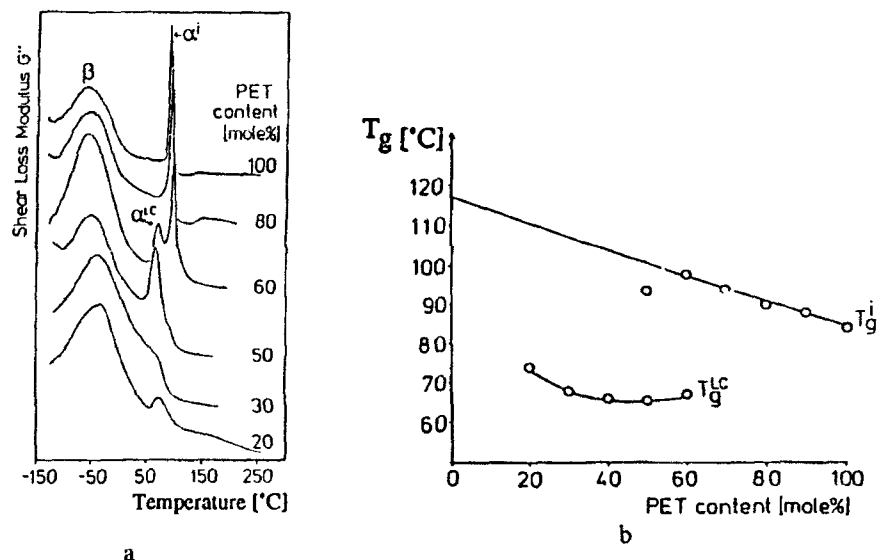


Fig. 5: Results for the copolyester PET/PHB. (a) Loss modulus  $G''$  as a function of temperature. (b) Glass transition temperature as a function of composition

By extrapolation of the straight line a value of about 120°C is obtained for an hypothetical isotropic amorphous PHB phase. The glass transition temperature of the liquid crystalline phase is not as strongly depending on the composition as the other one.

Similar results are obtained for the PEN/PHB copolymer. The corresponding curves of  $G''$  and the glass transition temperatures  $T_g$  are shown in Fig. 6. By extrapolating the straight line representing the glass transition temperature of the isotropic phase to 0% PEN the same temperature is obtained as in Fig. 5b. This result supports our conclusion, that for isotropic amorphous PHB  $T_g$  is approximately 120°C. This value is also supported by measurements on other copolyesters<sup>6</sup>.

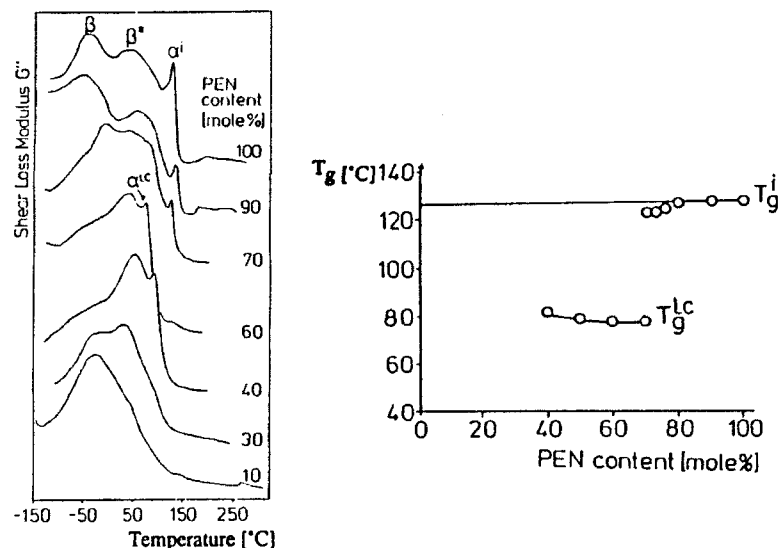


Fig. 6: Results for the copolyester PEN/PHB. (a) Loss modulus  $G''$  as a function of temperature. (b) Glass transition temperature as a function of composition.

Why is the glass transition temperature of the liquid crystalline phase lower than that of the isotropic phase? We believe that this is a consequence of the fact that, above  $T_g$ , in the LC phase only rotation of the chain around their axis is possible while in the isotropic phase changes in conformation have to take place. Rotation obviously becomes possible at lower temperatures than changes of chain conformation. For some polymers it is reported<sup>7</sup> that the LC phase has a higher glass transition temperature than the isotropic phase. In this case the restriction of mobility due to the higher density of the LC phase seems to prevail over the lower chain mobility which has to be attained.

Interesting results are obtained<sup>2</sup> with the ternary copolyester PEN/PET/PHB (35/35/30). The sample quenched from 110  $^{\circ}\text{C}$  is turbid, which is obviously due to the fact that it is

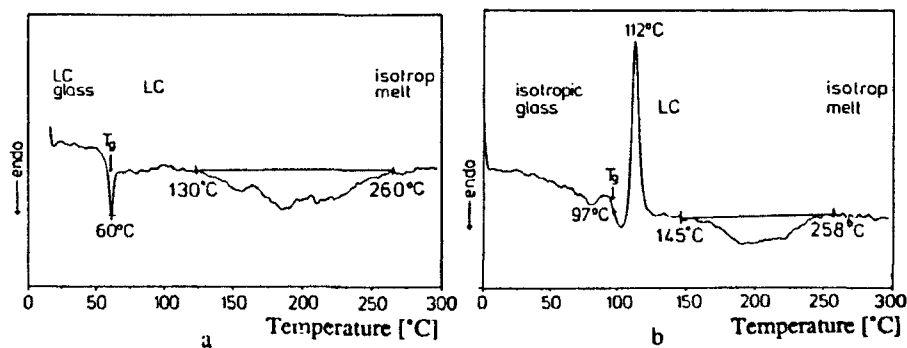


Fig. 7: DSC plot of PEN/PET/PHB (35/35/30) obtained after quenching from (a) 110  $^{\circ}\text{C}$  and (b) 290  $^{\circ}\text{C}$



in the state of a liquid-crystalline glass. The DSC curve obtained during heating of this sample is shown in Fig. 7a. A glass transition is observed at 60°C. Between 130°C and 260°C, a broad endothermic peak appears, indicating the transition to the isotropic melt. At 260°C the sample becomes transparent. In contrast, if the sample is quenched from 290°C in ice-water, it remains transparent; the state of the isotropic melt has been frozen in. The DSC curve obtained during heating of this sample is represented in Fig. 7b. A glass transition is observed at 97°C followed by an exothermic peak at 112°C, which indicates the transition from the isotropic into the liquid-crystalline state. When heated up further, again the transition into the isotropic melt is observed.

#### 4. Fraction of LC-Phase

By different thermal treatment it is possible to freeze in different fractions of the liquid crystalline phase. Fig. 8 shows the loss modulus  $G''$  as a function of temperature of the copolymer PEN/PET/PHB (40/30/30) after different thermal treatments. The upper curve represents the result for the material quenched from 290°C to room temperature. The following curves were obtained from materials which, after quenching from 290°C, were annealed at different temperatures for 70 s and then quenched again. For the sample quenched from 290°C a comparatively strong peak at about 110°C is observed.

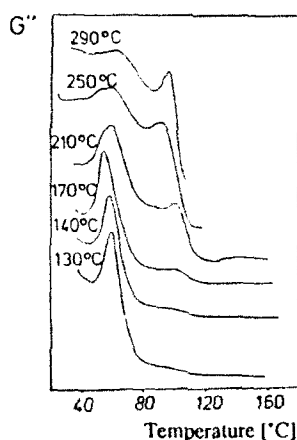


Fig. 8: Loss modulus  $G''$  as a function of temperature for the copolyester PEN/PET/PHB (40/30/30) after quenching from 290°C (upper curve) and after annealing of this sample at different temperatures for 70s and quenching again. The annealing temperature is written at each curve.

This peak can be attributed to the isotropic phase. By the subsequent annealing and quenching this peak decreases and another one at about 60°C appears which corresponds to the LC phase. This indicates that the isotropic phase is partially transformed into the LC phase. The lower the annealing temperature the more complete the transformation into the LC phase.

An attempt was made to determine the fraction of the liquid crystalline phase. Three different methods were applied:

- (i) It was assumed that the fraction of liquid crystalline phase is proportional to the area under the peak of the  $G''$  curve at 60°C.
- (ii) It was assumed that the fraction of the liquid crystalline phase is proportional to the height of the peak of the  $G''$  curve at 60°C.
- (iii) The LC fraction was calculated from density measurements by means of the equation

$$x_{LC} = \frac{\rho - \rho_a}{\rho_{LC} - \rho_a}$$

In this equation  $\rho_{LC}$  is the density of the liquid crystalline phase measured on the completely liquid crystalline sample obtained by annealing at 130°C.  $\rho_a$  is the density of the amorphous isotropic phase measured at a sample of the composition (35/35/30) after quenching from 290°C. The value was corrected in order to take into account that the composition was slightly different from (40/30/30).  $\rho$  is the measured density.

Fig. 9 shows the fractions of the LC phase as a function of annealing temperature as determined by the three different methods. Good agreement is obtained. The fraction of the LC phase does not change if annealing times longer than 70s are applied. Therefore one has to conclude that the fraction of the LC phase is mainly determined by the annealing temperature. It is obvious that different fractions of the LC phase can be frozen in as a consequence of the broad temperature range in which the transition from the LC phase into the isotropic phase occurs (see Fig. 7). We believe that this broad temperature range is due to a distribution in molecular weight and/or structural composition.

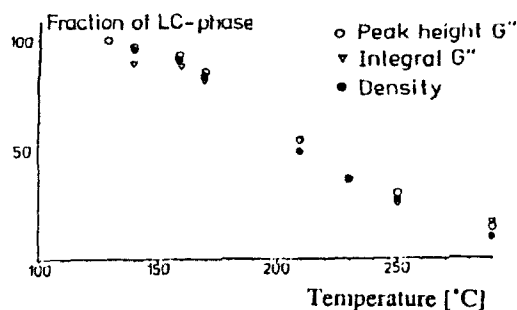


Fig. 9: Fraction of LC phase as a function of annealing temperature for PEN/PET/PHB (40/30/30) as determined by different methods

### 5. Crystallization

One of the main questions is the following one: What is the difference in the mechanism of crystallization from the isotropic state and from the liquid crystalline state? In order to investigate this question we wanted first to bring a sample into the amorphous state and then crystallize this state. In a second experiment we wanted to bring the same sample into a liquid crystalline state and then start the crystallization

from this phase. We tried to perform this experiment on the copolymer PEN/PET/PHB (40/30/30) which can be brought into both states almost completely by quenching from different temperatures. In order to crystallize the sample from the isotropic phase we quenched the material from 290°C. The sample obtained in this way contained about 90% isotropic and only 10% LC phase. The DMA curve and the x-ray scattering curve are represented by the curves A in Fig. 10. From the WAXS curve we see that the

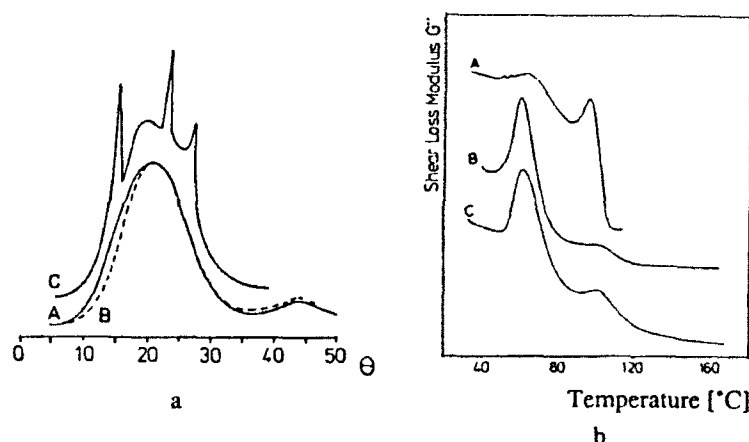


Fig. 10: WAXS (a) and loss modulus  $G''$  as a function of temperature (b) for the copolyester PEN/PET/PHB (40/30/30) quenched from 290°C (curves A), annealed for 70s at 170°C (curves B) and annealed for 7h at 170°C (curves C).

material is completely amorphous. From the DMA curve we can recognize that it is almost completely in the isotropic state because only the peak at 110°C appears. Next we annealed the sample at 170°C for 70s. The corresponding WAXS curve and the DMA curve are represented by the curves B in Fig. 10. We clearly recognize from the DMA curve that the sample is almost completely (95%) transformed into the liquid crystalline state. According to the WAXS curve the sample is still not crystallized. Finally we annealed the same sample for 7h at 170°C. The corresponding curves are denoted by C in Fig. 10. We see that after this treatment the material is crystallized.

This result shows that it is impossible to crystallize this material from the isotropic state. Before crystallization starts, a transformation into the liquid crystalline state occurs. Therefore the comparison of the process of crystallization from the two different states cannot be performed using the same material.

As a consequence, the kinetics of crystallization from the isotropic phase was investigated on a material which does not form liquid crystalline states. We have chosen the copolymer PEN/PET/PHB (65/20/15). Fig. 11 shows the change of WAXS with time during crystallization at 167°C. On the left hand side the change of the patterns are shown, on the right hand side one can see the increase of the intensity of the 100-reflection with time. The corresponding Avrami plot is shown on the left hand side in Fig. 12. A straight line with the slope  $n=2.95$  is obtained, indicating a three-dimensional growth of the morphological units.

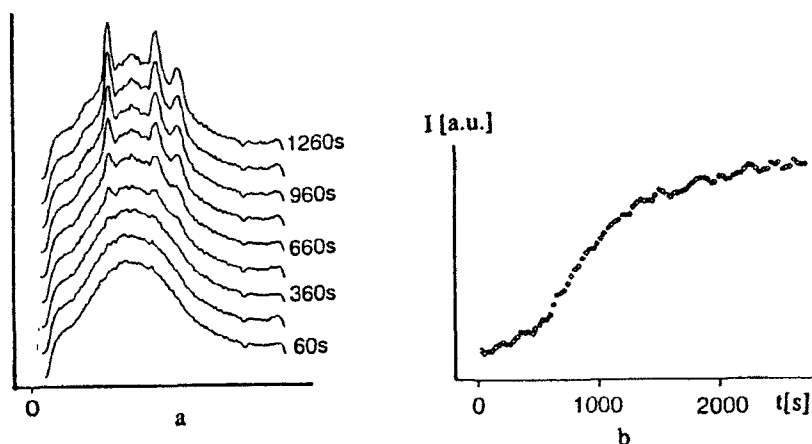


Fig. 11: Change of WAXS (a) and integral intensity  $I$  of the crystal reflection (b) as a function of time  $t$  during isothermal crystallization of the copolyester PEN/PET/PHB (65/20/15) at 167°C

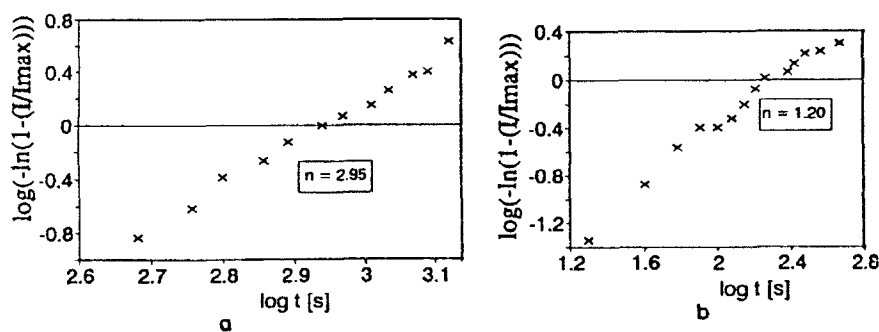


Fig. 12: Avrami plots of the copolyesters PEN/PET/PHB (65/20/15) annealed 167°C (a) and PEN/PET/PHB (50/10/40) annealed at 160°C (b)

For comparison the kinetics of crystallization of the copolyester PEN/PET/PHB (50/10/40) were investigated. This copolyester is almost completely liquid crystalline when the crystallization starts. Fig. 13 shows the change of WAXS with time during crystallization at 160°C. On the left hand side we see the WAXS patterns and on the right hand side the increase of the intensity of the 100-reflection with time is shown. We see that in contrast to Fig. 11 the increase of the intensity of the crystal reflections is already at the beginning of crystallization. In agreement with this, in the Avrami plot shown on the right hand side of Fig. 12 the straight line obtained has a slope of approximately 1 corresponding to linear growth. It must be pointed out, however, that crystallization proceeds very quickly at all temperatures, so that it is difficult to define the time zero.

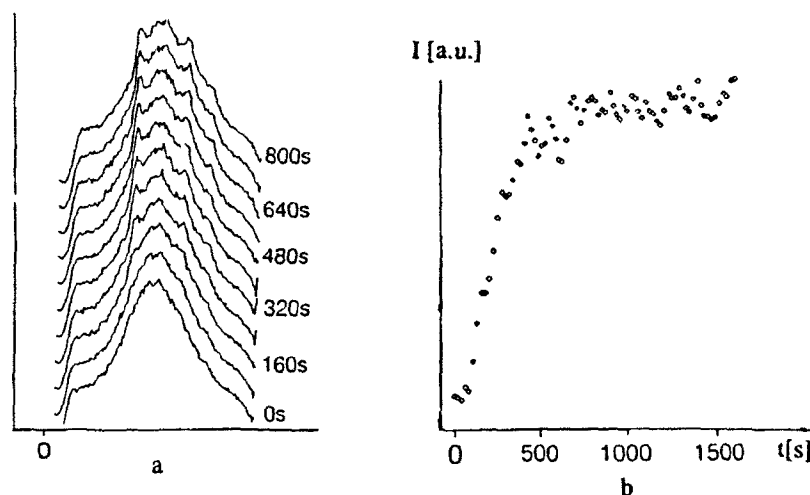


Fig. 13: Change of WAXS (a) and integral intensity  $I$  of the crystal reflection (b) as a function of time  $t$  during isothermal crystallization of the copolyester PEN/PET/PHB (50/10/40) at 160°C

## 6. Chain Conformation

When one considers the structure of the nematic LC phase one tends to assume that the molecules must be almost completely elongated in this state. From studies of small angle neutron scattering (SANS) it was shown that this is not the case<sup>8</sup>. The radius of gyration is the same as in the isotropic state. This proves that the molecules are only in parts elongated and that there must be found bends as discussed by other authors<sup>9</sup>, or larger parts of the molecules oriented more or less perpendicular to the director characterizing the main orientation.

## 7. Conclusion

In the copolyesters investigated the glass transition temperature of the LC phase is lower than the  $T_g$  of the isotropic phase. This is due to the lower mobility of the chains in the LC phase namely rotation instead of segmental motion in the isotropic phase.

By quenching from different temperatures different fractions of LC phase can be frozen in. The fraction of LC phase can be determined from the intensity of the loss modulus glass transition peak and from density.

The polymers which are able to form LC phases cannot be transformed from the isotropic state directly into the crystalline state. Before crystallization they are always transformed into the LC state.

If crystallized from the LC state linear growth was found (Avrami exponent  $n=1$ ) while three-dimensional growth ( $n=3$ ) was observed for the crystallization from the isotropic state.

### 8. Acknowledgement

The investigations by synchrotron radiation were funded by the German Federal Minister for Science and Technology (BMFT) under contract number 05405 HXB. One of the authors (S. Thiel) is grateful for a fellowship from the Fonds der Chemie.

### 9. References

1. A. Ciferri (Editor), *Liquid Crystallinity in Polymers* (VCH Publishers, Inc. 1991)
2. D. Chen and H.G. Zachmann, *Polymer* **32** (1991) 1612
3. D. Chen, PhD thesis, University of Hamburg (1990)
4. S. Buchner, D. Wiswe and H.G. Zachmann, *Mol. Cryst. Liq. Cryst.* **155** (1988) 357
5. W.J. Jackson and H.F. Kuhfuß, *J. Polym. Sci.* **4** (1976) 2043
6. R. Rosenau-Eichin, M. Ballauf, J. Grebowicz and E.W. Fischer, *Polymer* **29** (1988) 518
7. B. Wunderlich and J. Grebowicz, *Adv. in Pol. Sci.* **60/61** (1984) 1
8. E. Olbrich and H.G. Zachmann, *Macromolecules* **24** (1991) 4364
9. P.D. De Gennes, *Mol. Cryst. Liq. Cryst. Lett.* **34** (1977) 177

**ELECTRICAL RESISTIVITY AND YOUNG'S MODULUS CORRELATIONS  
DURING STRUCTURAL RELAXATION IN AMORPHOUS  $\text{Fe}_{75}\text{TM}_{25}\text{B}_{20}$   
(TM=Cr, Mn, Ni)**

M. BARICCO<sup>+</sup>, G. KOEBRUGGE<sup>++</sup>, G. RIONTINO<sup>+</sup>, J. SIETSMA<sup>++</sup>

<sup>+</sup> Dipartimento di Chimica dei Materiali, Università di Torino, Via P.Giuria 9, 10125 Torino (Italy)

<sup>++</sup> Laboratory of Materials Science, Delft University of Technology, Rotterdamseweg 137, 2628 AL Delft (the Netherlands)

**ABSTRACT**

Electrical resistivity and Young's modulus changes in isothermal conditions have been considered to analyze their possible correlations during structural relaxation. The coupling factor between the observable changes and relaxation processes is discussed.

**1. Introduction**

Various models have been proposed to interpret the changes of physical properties during structural relaxation in metallic glasses<sup>1-4</sup>. In all models, the property change  $\Delta P$  is related to the occurring relaxation processes by means of a coupling factor, which is often considered constant. In the Activation Energy Spectrum (AES) model<sup>1</sup>, the total property change  $\Delta P$  is related to the occurring relaxation processes by the relation:

$$\Delta P = \int_0^{\infty} c(E_a) \cdot q_t(E_a) dE_a \quad (1)$$

in which  $c(E_a)$  is the coupling factor between relaxation phenomena and the property, and  $q(E_a)dE_a$  is the number of processes with an activation energy between  $E_a$  and  $E_a+dE_a$ . In most applications of the AES model,  $E_a$  is connected with the time by a monotonous function. This allows to express the time dependence of  $\Delta P$  by:

$$\Delta P = \int_0^t c(t') q(t') dt' \quad (2)$$

It is not possible to detect the energy dependence of  $c(E_a)$  from the measurement of a single property. Instead, if different properties are considered, the ratio  $\Delta P_1(t)/\Delta P_2(t)$  rules out possible energy influences on coupling factors.

Aim of this paper is to study the effect of composition on electrical resistivity and Young's modulus changes during isothermal treatments in  $\text{Fe}_{75}\text{TM}_{25}\text{B}_{20}$  amorphous alloys (TM=Cr,Mn,Ni). Possible correlations between the measured properties will be discussed.

## 2. Experimental

The resistance of the melt-spun amorphous ribbons was measured in situ in a 280 Hz AC Thompson bridge. The annealing temperature was held constant within 0.5 K, and the warming-up time for the specimens was about 10 s.

Under the assumption of very small changes in the density, the relative changes in Young's modulus are represented as the relative changes in the squared velocity of sound ( $v^2$ ), since Young's modulus is proportional to  $v^2$ . The velocity of sound is measured by a pulse-echo technique<sup>5</sup>, at room temperature.

## 3. Results and discussion

In Fig.1 the Young modulus changes  $\Delta E = (E - E_0)/E_0$  ( $E_0$  = value for the as-quenched sample) and the electrical resistance changes  $\Delta R = (R - R_0)/R_0$  ( $R_0$  = value at the beginning of isothermal treatment) are reported as a function of annealing time. It can be observed that while  $\Delta E$  is always positive,  $\Delta R$  is positive or negative, depending on the composition and on the temperature.

In order to describe the relationship between the two examined properties, the ratio  $\Delta E/\Delta R$  has been calculated as a function of annealing time (Fig.2).

A strong correlation between electrical resistance and Young's modulus is observed in the Ni-containing alloy (Fig.2). For both the considered temperatures,  $\Delta E$  is positive and  $\Delta R$  is negative and their ratio is quite constant. A similar behaviour is observed for the Mn-containing alloy, but positive  $\Delta R$  values are evidenced. A different trend is observed for the Cr-containing alloy, for which an always positive  $\Delta E$  is associated to a positive (at 250°C) or a negative (at 280°C) resistance change.

Taking constant the coupling factor "c" between the measured property changes  $\Delta P$  and the parameter describing the relaxation processes (eqs. 1 or 2), a constant ratio



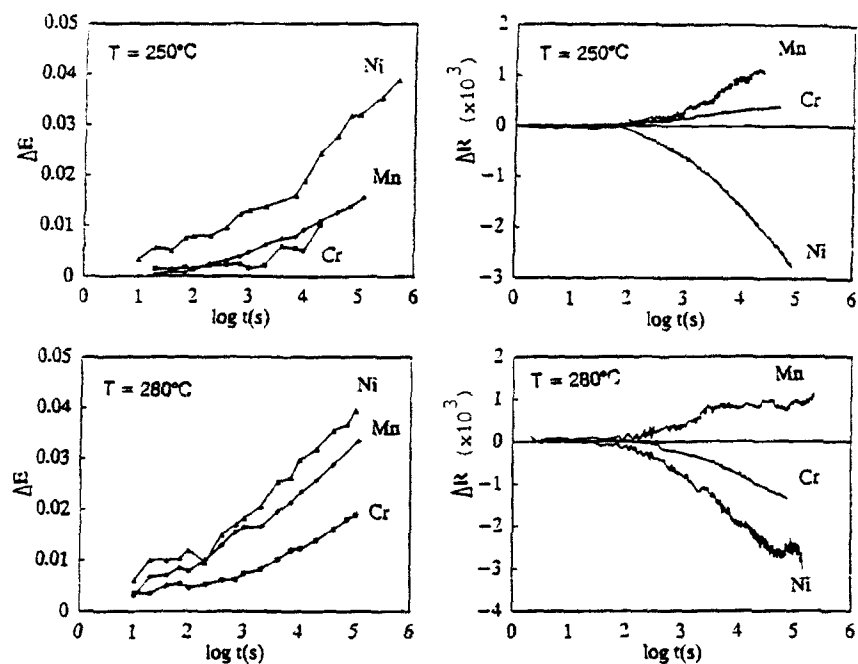


Fig. 1 - Young modulus variations  $\Delta E$  and electrical resistance variations  $\Delta R$  as a function of annealing time. Annealing temperatures and compositions are indicated.

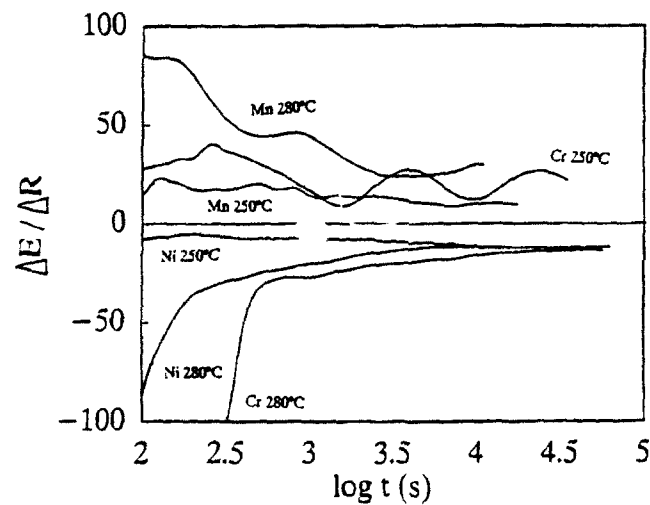


Fig. 2 - Ratio between  $\Delta E$  and  $\Delta R$  at the same annealing time for the indicated temperatures and compositions.

between two  $\Delta P$  is to be expected for the same thermal treatments. In effect, present results obtained for the Ni-containing alloy, show the validity of this assumption. An opposite sign for "c", relative to  $\Delta R$  for Ni- and Mn-containing alloys, is observed in the same temperature range.

Whereas the temperature dependence of "c" seems to be weak, upon changing the composition from 5% Ni to 5% Mn, its value for  $\Delta R$  turns out to be strongly changed.

The behaviour of the Cr-containing alloy, however, is different in this respect. The "c" factor for  $\Delta R$ , which changes in sign in the range 250÷280°C, seems to be in accordance with the occurrence of a maximum in  $R(t)$  in Cr-containing glasses<sup>6,7,8</sup>.

The investigated alloys contain substitutional elements (Cr, Mn, Ni) of similar atomic volume, but different chemical behaviour. Since the observed  $\Delta E$  values are very similar for these three alloys, topological effects might be the dominant influence on the relaxation behaviour of Young's modulus. The tendency of Cr and Mn clustering during structural relaxation may be responsible for the resistance increase<sup>8</sup>.

#### 4. Conclusions

Electrical resistance and Young's modulus changes cannot be considered uncorrelated during structural relaxation in  $\text{Fe}_{75}\text{TM}_{25}\text{B}_{20}$  (TM=Cr, Mn, Ni). In the Cr-containing system, the coupling factor between property changes and relaxation processes cannot be considered constant.

#### 5. References

1. M.R.J.Gibbs, J.E.Evetts, J.A.Leake, J.Mat.Sci. **18** (1983) 278
2. K.F.Kelton, F.Spaepen, Phys.Rev.B **30** (1984) 5516
3. A.Van den Beukel, S.Radelaar, Acta Met. **31** (1983) 419
4. A.Inoue, H.S.Chen, T.Masumoto, S.A.Ajuria, Sci. Rep. RITU **32** (1985) 116
5. A.Van den Beukel, S.van der Zwaag, A.L.Mulder, Acta Met. **32** (1984) 1895
6. O.Haruyama, N.Asahi, J.Mat.Sci. **26** (1991) 1851
7. M.Baricco, G.Riontino, P.Allia, F.Vinai, Mat.Sci.Eng. **27** (1988) 537
8. G.Riontino, F.Marino, Scripta Met. **18** (1984) 13

## RELAXATION BEHAVIOUR OF CURIE TEMPERATURE OF AN FE-BASED GLASS

C.F. CONDE and A. CONDE.

*Departamento de Física de la Materia Condensada. Instituto de Ciencia de Materiales (C.S.I.C.). Universidad de Sevilla. Spain.*

### ABSTRACT

Curie temperature variations upon isothermal annealing of a  $\text{Fe}_{79}\text{Si}_{13}\text{B}_8$  glass was studied by calorimetric (DSC) methods. The  $T_c$  value for as-quenched samples is 695 K and the crystallization onset is 835 K. The Curie temperature increases with annealing temperature and time and the saturation value is inversely proportional to the annealing temperature. As in other analogous Fe glasses containing two metalloids, an uniformly linear logarithmic kinetics with time is found.

### 1. Introduction

Metallic glasses with a high Fe content are ferromagnetic, their Curie temperatures being generally lower than those of crystalline alloys with analogous compositions. Annealing of these glasses below glass temperature causes changes in the glassy state, the so-called structural relaxation. These changes affect many physical properties and one of the most sensitive to relaxation is the Curie temperature,  $T_c$ . Reported experimental results indicate that  $T_c$  of Fe-based glasses rises to a saturation value when the glass is isothermally annealed. However, the time response of  $T_c$  and the dependence of its saturation value on the annealing temperature is not unique and compositional dependence of these features is not well established.

In this paper we report results on the relaxation behaviour of Curie temperature of a metallic glass of nominal composition  $\text{Fe}_{79}\text{Si}_{13}\text{B}_8$ , in the hypoeutectic region of the Fe-Si-B system (1).

### 2. Experimental

The alloy studied was prepared by the melt-spinning technique from a master alloy with nominal composition. The ribbons were 10 mm wide and 30  $\mu\text{m}$  thick. Curie temperature of the glass was determined from specific heat anomaly associated with the

ferro-paramagnetic transition, using a differential scanning calorimeter Perkin Elmer DSC-7. Temperature calibration was checked by using lead and  $K_2SO_4$  standards. Isothermal annealings were performed in the DSC chamber using a heating rate of 320 K/min from room temperature to the annealing temperature and, after the anneal, the sample was cooled abruptly (by selecting the maximum rate of 320 K/min).  $T_c$  was well defined and could be determined within  $\pm 0.5$  K.

### 3. Results

The alloy crystallizes in two stages: in the first, a precipitation of  $\alpha$ -Fe phase occurs; the second stage consists of a polymorphic crystallization to give  $\alpha$ -Fe and  $Fe_2B$  type phases. Crystallization onset occurs at 835 K (at 10 K/min) and the Curie temperature of the as-quenched samples is 695 K.

Fig. 1 shows changes in  $T_c$  after isothermal annealing of as-quenched samples at various temperatures. Isochronal curves indicate the rise in Curie temperature for different annealing times. As can be observed,

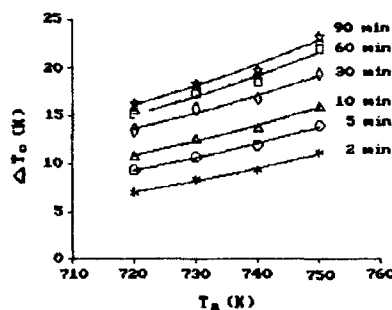


Fig. 1

$T_c$  increases upon structural relaxation in agreement with previous results (2-5) in some FeB glasses but is significantly different from those obtained in other cases, such as  $Fe_{81.5}B_{14.5}Si_4$  (6). The value of  $\Delta T_c$  is a monotonic function of annealing time and temperature. The saturation value  $T_{c(\infty)}$  of Curie temperature increases with annealing temperature in the temperature range explored (720-765 K). Fig. 2 shows plots of  $\Delta T_c(t)/\Delta T_{c(\infty)}$  against annealing time for the different annealing temperatures and, as observed, the plots collapse in a single curve. The equilibrium or saturation value is found to be inversely proportional to the annealing temperature,

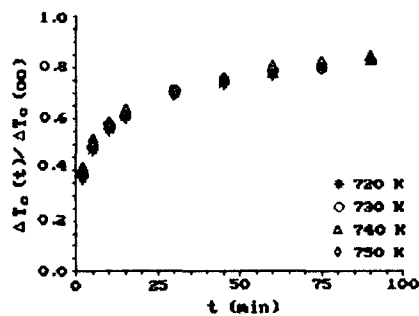


Fig. 2

in agreement with previous results (4,5,7) for analogous glasses. Experimental values can be

roughly fitted by the equation  $T_c(\infty) = 209.7 - 137082.1/T_s$  (correlation coefficient  $r = 0.98$ ).

Values of  $\Delta T_c$  for the different annealing temperatures obey, approximately, a  $\ln t$  law (Fig. 3). This logarithmic behaviour, habitually found in the relaxation kinetics of amorphous alloys, is interpreted as an indication of a continuous change in the apparent activation energy, which is proportional to the relaxing quantity itself (8). Similar behaviour is found for other glasses containing B and Si (4,5,9) but, in contrast, a rapid change in the slope of the

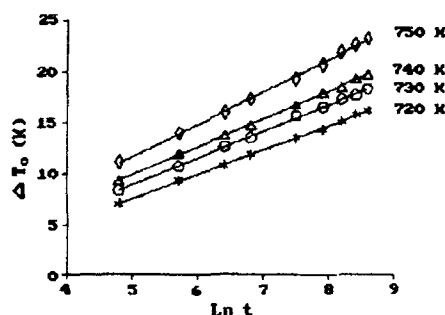


Fig. 3

$T_c - \ln t$  plots is reported for glasses with B as the only metalloid (10,11). As suggested by Davies and Gregan (11), this different behaviour may result from the presence of two metalloids species, Si either diluting the effect of B diffusion or impairing it.

The experimental data of time variation of  $T_c$  were analysed in terms of a spectrum of relaxation times  $Q(\tau)$  such as  $\int_0^\infty Q(\tau) d\tau = 1$ . Assuming first order kinetics, the rate equation for change of a physical property  $x$  becomes

$$\frac{x - x_{eq}}{x_0 - x_{eq}} = \int_0^\infty Q(\tau) \exp(-t/\tau) d\tau$$

A useful equivalent of this expression (12) is

$$\frac{x - x_{eq}}{x_0 - x_{eq}} = \exp(-t/\tau)^n$$

where  $n$  is an exponent which is temperature dependent and  $\tau$ , also temperature dependent, is an effective relaxation time for the overall process.

In our case, by plotting  $\ln [\ln \Delta T_c(\infty) / [\Delta T_c(\infty) - \Delta T_c(t)]]$  against  $\ln t$  (Fig. 4) we obtain, by a linear fit, the values of  $n$  and  $\tau$  included in Table 1. Values of the exponent  $n$  are near the usual value 0.4 for ordering. As can be expected, the relaxation time decreases with increasing atomic mobility with temperature favouring a more efficient packing of atoms. From

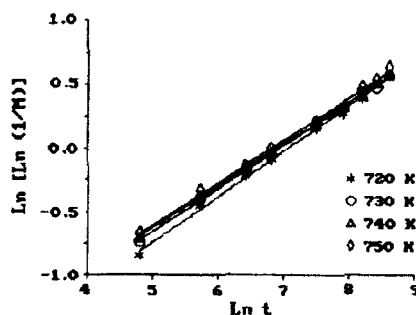


Fig. 4

**Table 1.** Curie temperature relaxation parameters

$T_a$ (K)	$T_c(\infty)$ (K)	$n$	$\tau$ (s)
720	715	0.36	1152
730	717	0.34	1013
740	719	0.33	976
750	723	0.33	903

the exponential temperature dependence of  $\tau$  we can derive an effective activation energy of 34.6 kJ/mol for the process. This value is lower than that observed in other metallic glasses (10,12) for which a higher decrease of  $\tau$  is reported.

#### 4. Acknowledgments

This work was supported by the CICYT of the Spanish Government (Project MAT88-301) and by the Junta de Andalucía.

#### 5. References

1. V.R.V. Raman and G.E. Fisch. *J. Appl. Phys.* **53** (1982) 2273.
2. A.L. Greer and J.A. Leake. *J. Non-Cryst. Solids* **33** (1979) 291.
3. R. Gerling and R. Wagner. *Scripta Metall.* **17** (1983) 1129.
4. C.F. Conde, H. Miranda and A. Conde. In: *Basic Features of the Glassy State (Procc. of the Second Int. Workshop on Non-Crystalline Solids)*. Eds. by J. Colmenero and A. Alegria. World Scientific, Singapore (1990).
5. C.F. Conde, H. Miranda and A. Conde. *Mat. Lett.* **10** (1991) 501.
6. A.L. Greer. *J. Mat. Sci.* **17** (1982) 1117.
7. P.J. Flanders, N. Morito and T. Egami. *IEEE Trans. Mag.* **MAG-19** (1983) 1910.
8. T. Egami. *J. Mat. Sci.* **13** (1978) 2587.
9. T. Jaglilinski and T. Egami. *J. Appl. Phys.* **57** (1985) 3578.
10. A.L. Greer and F. Spaepen. *Ann. N.Y. Acad. Sci.* **371** (1981) 218.
11. H.A. Davies and G.P.J. Grogan. *J. Non-Cryst. Solids* **61/62** (1984) 218.
12. M.G. Scott and A. Kursumovic. *Acta Metall.* **30** (1982) 853.

**POSITRON LIFETIME AND X-RAY DIFFRACTION MEASUREMENTS DURING  
STRUCTURAL RELAXATION IN METALLIC GLASSES  $\text{Fe}_{78-x}\text{Co}_x\text{Si}_9\text{B}_{13}$**

J. FILIPECKI

*Institute of Physics, Pedagogical University,  
Al. Armii Krajowej 13/15, 42 201 Częstochowa, Poland*

**ABSTRACT**

The isothermal annealing of metallic glasses gives rise to changes in many physical properties together with transition to the crystalline state at higher temperatures of annealing. The process is caused by atomic rearrangements in the amorphous structure and is generally called "structural relaxation". Investigated specimens of metallic glasses  $\text{Fe}_{78-x}\text{Co}_x\text{Si}_9\text{B}_{13}$  ( $x=0,30,50,78$ ) were first preannealed for  $10^5$  s at 530K and next the same specimens were further annealed at 578K and 778K (for  $10^5$  s respectively). The positron lifetime and X-ray diffraction measurements show that annealing below the crystalline temperature (530K and 578K) causes changes in chemical and topological short range ordering. At the same time isothermal annealing at 778K causes an increase in the number of positron voids and existence of  $\alpha$ -Fe and  $\beta$ -Co crystalline phases.

**1. Introduction**

Annealing of metallic glasses below the crystallization temperature gives rise to a change in many physical properties. The process is caused by atomic rearrangements in the amorphous structure, and is generally called "structural relaxation". In a series of previous publications <sup>1,2,3</sup> it was shown that the property changes can be separated into contributions of two processes :

- 1) Chemical short range ordering (CSRO), describing reversible changes in the local surroundings of given atom. It was shown <sup>4</sup> that this part of the structural relaxation process can be described by the activation energy spectrum (AES) model of Gibbs and co-workers.
- 2) Topological short range ordering (TSRO), describing an irreversible decrease in the free volume. This process can be quantitatively described in terms of the free volume model <sup>5</sup>.

The crystallization process is caused by the structural change which

results from annealing in higher of temperatures. These changes resulted from the short range ordering to the long ordering after crystallization.

## 2. Experimental

Measurements of positron lifetimes were carried out on a ORTEC spectrometer of resolution FWHM = 270 ps. A  $^{22}\text{Na}$  isotope of  $3.7 \times 10^9$  Bq activity was used as a positron source. The metallic glasses were made by the Institute of Materials Engineering of Warsaw Technical University. Each specimen consisted of ribbons 15 mm wide and 0.04 mm thick and were made up of a system layers of total size 15 mm  $\times$  15 mm  $\times$  0.25 mm. The source was situated between two identical investigated samples, forming a "sandwich" system. The investigated samples of metallic glasses  $\text{Fe}_{78-x}\text{Co}_x\text{Si}_9\text{B}_{13}$  ( $x=0, 30, 50, 78$ ) were first preannealed for  $10^5$  s at 530 K and next the same specimens were further annealed at 578 K and 778 K (for  $10^5$  s respectively). The process of isothermal annealing was carried out in the atmosphere of gaseous argon. Measurements of X-ray diffraction (by means of spectrometer DRON 2.0) were carried out before and after processes of annealing. The X-ray diffraction measurements show that after preannealing at 530 K and 578 K the amorphous structure of investigated specimens does not change. However, after annealing at in  $10^5$  s at 778 K after preannealing at 530 K and 578 K (in  $10^5$  s respectively) crystallization in all investigated samples was obtained (Fig. 1).

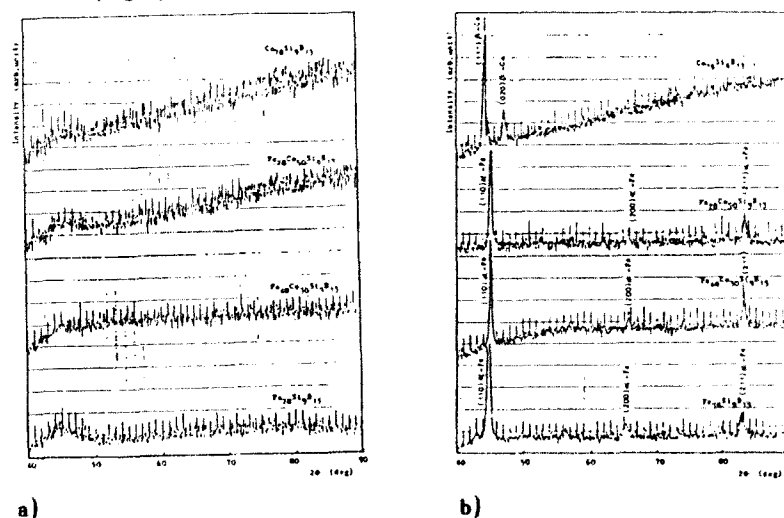


Fig. 1 X-ray patterns of investigated metallic glasses  $\text{Fe}_{78-x}\text{Co}_x\text{Si}_9\text{B}_{13}$ :  
a) amorphous; b) after crystallization



### 3. Results and discussion

The POSITRON program was used to calculate mean values of the positron lifetimes  $\tau_1$ . The results of calculation of the mean values of positron lifetimes in the investigated metallic glasses before and after the process of isothermal annealing showed the existence of two components  $\tau_1$  and  $\tau_2$ . According to theory <sup>7,8</sup> the  $\tau_1$  component is responsible for positron annihilation with free electrons, whereas, component  $\tau_2$  occurs as the result of positron trapping. The values of positron lifetimes  $\tau_1$  for as-quenched specimens isothermally annealed at 530K ( $10^5$  s) and also annealed at 578K after pre-annealing for  $10^5$  s at 530K practically are constant ( $\tau_1 = 160$  ps). Simultaneously changes of values of positron lifetimes  $\tau_2$  are insignificant and irregular, hence, it is difficult, at the present stage of study, to explain these changes. However, we can conclude from the change of intensity values  $I_2$  ( $I_2 = 100 - I_1$ ) connected with positron trapping in voids that they are due to atomic rearrangements in the amorphous structures as a result of annealing. The values  $I_2$  for as-quenched specimens annealed at 530K changed insignificantly in the whole range of annealing (Fig. 2). This fact suggests the changes in the local surroundings of a given atom (CSRO). For the values  $I_2$  in specimens annealed at 578K after pre-annealing for  $10^5$  s at 530K in all cases a minimum was observed (after  $10^3$  s of annealing - Fig. 2). Identical minimum was observed for the same process

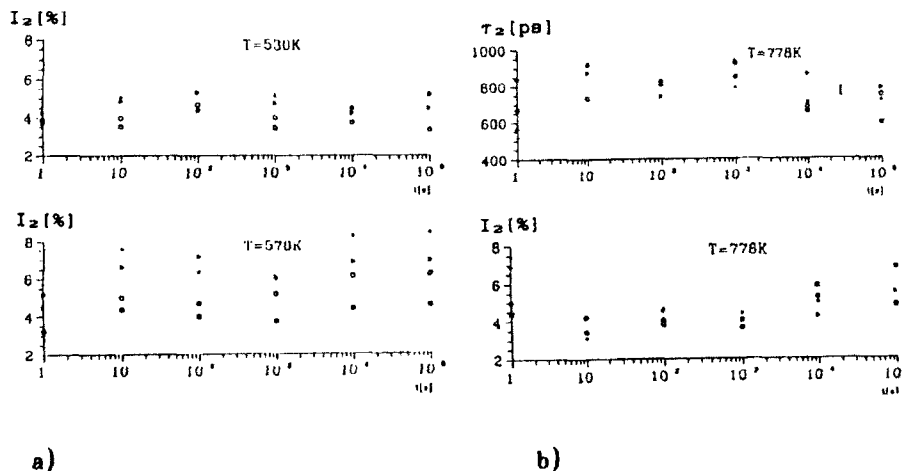


Fig. 2 Isothermal changes of intensities  $I_2$  and positron lifetimes  $\tau_2$  in metallic glasses  $\text{Fe}_{78-x}\text{Co}_x\text{Si}_9\text{B}_{13}$  :

a) - annealed at 530K and 578K after preannealing for  $10^5$  s at 530K;

b) - after crystallization;

$\text{Fe}_{78}\text{Si}_9\text{B}_{13}$  - ○ ○ ○

$\text{Co}_{78}\text{Si}_9\text{B}_{13}$  - △ △ △

$\text{Fe}_{48}\text{Co}_{30}\text{Si}_9\text{B}_{13}$  - □

$\text{Fe}_{28}\text{Co}_{50}\text{Si}_9\text{B}_{13}$  - \*

of annealing in investigations of change of Young's modulus <sup>9</sup>. Such behaviour of values  $I_2$  for all specimens annealed at 578K is connected with the changes of topological ordering of the amorphous structures.

Simultaneously for measurements after annealing at 778K the value of component  $\tau_1$  after crystallization is constant ( $\tau_1 = 160\text{ps}$ ). The lifetime component  $\tau_2$  decreases during the time of annealing at 778K (Fig. 3). We can recapitulate that for investigated metallic glasses  $\text{Fe}_{78-x}\text{Co}_x\text{Si}_9\text{B}_{13}$  ( $x = 0, 30, 50, 78$ ) the process of crystallization does not change the concentration of free electrons but on the other hand increases the concentration of electrons in positron-trapping areas (voids) (concentration of electrons annihilated with positrons is inversely proportional to the value of positron lifetimes <sup>7</sup>). At the same time the process of crystallization resulted in increase of intensity  $I_2$ , at the cost decreasing values of intensity  $I_1$ , hence, we can conclude that the number of positron-trapping voids increased.

Recapitulating, we can conclude from results of the observed measurements of positron lifetimes and earlier changes of Young's modulus during structural relaxation in metallic glasses  $\text{Fe}_{78-x}\text{Co}_x\text{Si}_9\text{B}_{13}$  ( $x = 0, 30, 50, 78$ ) that the preannealing process at 530K is connected with the chemical short range ordering (CSRO) and the next annealing process at 578K is connected with topological short range ordering (TSRO). Simultaneously the process of crystallization starts the process of ordering from short range ordering to long range ordering and cause existence of  $\alpha$ -Fe and  $\beta$ -Co crystalline phases.

#### 4. References

1. J. Filipecki and A. Van den Beukel, *Scripta Metall.* **21** (1987) 1111.
2. A. Van den Beukel, in *Rapidly Solidified Materials*, ed. by P.W. Lee and S. Corbonera (ASM New York 1986).
3. E. Huizer and A. Van den Beukel, *J. Phys.* **C8** (1985) 561.
4. M.R.J. Gibbs, J.E. Evetts and A. Leake, *J. Mat. Sci.* **18** (1983) 278.
5. F. Spaepen, *Acta Metall.* **25** (1977) 407.
6. P. Kirkegaard and M. Eldrup, *Comp. Phys. Commun.* **23** (1981) 307.
7. R.N. West, *Adv. Phys.* **22** (1973) 263.
8. J. Filipecki, B. Calusński and Z. Mandecki, *Phys. Stat. Sol. (a)* **79** (1983) 585.
9. J. Filipecki and A. Van den Beukel, *J. of Mater. Sc. Lett.* **9** (1990) 1169.

# AN IMPROVED METHOD FOR THE CALCULUS OF ACTIVATION ENERGY SPECTRA (AES) IN THE ANALYSIS OF RELAXATION EXPERIMENTS

F.L. CUMBRERA & F. GUIBERTEAU

*Dpto. de Física, Fac. de Física, Univ. de Extremadura  
Avda. de Elvas s/n, Badajoz, Spain*

and

A. MUÑOZ

*Dpto. de Física Materia Condensada, Facultad de Física,  
Univ. de Sevilla, Avda. Reina Mercedes s/n, Sevilla, Spain*

## ABSTRACT

Much past work associated with the structural relaxation in amorphous materials was based on the Gibbs activation energy spectrum (AES) model. These early works made the starting assumption of replacing the annealing function,  $\phi(E, T, t)$ , by a step function. However, the inadequacy in many cases of such approximation lead us to propose a more sophisticated method to calculate the detailed shape of the spectrum. The method is applied to the enthalpic relaxation in amorphous Se as well as to the mechanical stress relaxation in CoO single crystals.

## 1. Introduction

Analysis of relaxation experiments has often employed the theoretical AES model introduced by Primak<sup>1</sup> and Gibbs<sup>2</sup>. In this method, the change during relaxation at temperature  $T$  of a measured property,  $\Delta P$ , is expressed by means of a Volterra integral equation of the first kind

$$\Delta P(t) = \int_0^\infty P_0(E) \phi(E, T, t) dE \quad (1)$$

with kernel the characteristic annealing function,  $\phi(E, T, t)$ , and where  $p_0(E)$  is the total property change in the energy range  $E$  to  $E+dE$ .

Following Primak<sup>1</sup>, the annealing function can be expressed as

$$\phi(E, T, t) = 1 - \exp[-\nu_0 t \exp(-E/kT)] \quad (2)$$

$\nu_0$  being an attempt frequency and  $k$  the Boltzmann constant. In fact, the functional form of  $\phi(E, T, t)$  versus  $E$ , for given experimental values of  $T$  and  $t$ , is that of a sharp step at an energy  $E_0 = kT \ln \nu_0 t$ . Therefore, if

we have to deal with broad and smooth AES we can replace the  $\theta$ -function by a step function: for  $E \leq E_0$  the function has value unity and zero for  $E > E_0$ . This assumption for  $\theta(E, T, t)$  is equivalent to assuming that during an isothermal anneal, at time  $t$ , all processes with energy  $E \leq E_0$  have contributed to the relaxation whereas processes with  $E > E_0$  have yet to contribute.

In the frame of this step-like approximation (the Primak's energy derivative method) one can easily prove that  $p_0(E)$  is given by

$$p_0(E) = - \frac{1}{kT} \frac{d \Delta P}{d \ln t} \quad (3)$$

Unfortunately, it is no longer possible in practice to support the drastic assumption about  $\theta(E, T, t)$  and there is a need into develop a better and more general procedure of calculus.

## 2. Description of the Method

Instead of calculating a continuous spectrum  $p_0(E)$  we will calculate a discrete spectrum: i.e. a discrete number of points  $p_{0j}$  at certain energies  $E_j$

$$p_{0j} = (1/\Delta E) \int_{E_j - \Delta E/2}^{E_j + \Delta E/2} p_0(E) dE \quad (4)$$

By means of this step-wise approximation the Volterra integral equation can be replaced by a set of linear equations which in matrix notation becomes

$$\Delta \tilde{P} = A \tilde{p} \quad (5)$$

where  $\Delta \tilde{P}$  and  $\tilde{p}$  are column matrix with  $n$  rows ( $n$  is the number of data points) and  $A$  is a  $n$ -th order square matrix of the form

$$A_{ij} = \int_{E_j - \Delta E/2}^{E_j + \Delta E/2} \theta(t_i, E) dE \quad (6)$$

Eqn. (5) has the solution

$$\tilde{p} \approx A^{-1} \Delta \tilde{P} \quad (7)$$

It turns out however that eqn. (5) forms a so-called "ill conditioned" system resulting in very unstable solutions. In practice, resort to the variational Cook's "least structure analysis"<sup>3,4</sup> allow us to get smooth and stable solutions. In this method a structure function

$S(\tilde{p})$  is defined as a fourth difference operator satisfying our intuitive concepts of a structureless function. Thus, our purpose is to find the solution which minimizes  $S(\tilde{p})$  under the  $\kappa^2$  constraint

$$\kappa^2 = \sum_{i=1}^n (\Delta P_{it} - \Delta P_{ie})^2 / \sigma_i^2 = n \quad (8)$$

$\Delta P_{it}$  and  $\Delta P_{ie}$  being the calculated (via eqn. (5)) and the experimental (at time  $t_i$ ) values of  $\Delta P_i$ , respectively, and  $\sigma_i$  is its standard deviation.

Using methods of variational calculus the following result is obtained

$$\tilde{p} = [A + \lambda(\tilde{A})^{-1}(W)^{-1}S]^{-1} \Delta \tilde{P} \quad (9)$$

where  $\lambda$  is a Lagrangian multiplier,  $W$  is a diagonal matrix with elements  $W_{ii} = 1/\sigma_i^2$ ,  $\tilde{A}$  is the transposed of matrix  $A$  and  $S$  is the smoothing matrix associated to the  $S(\tilde{p})$  operator.

In order to assess the performance of the method we consider two different experimental cases:

i) the broad spectrum corresponding to the enthalpic relaxation of amorphous Se around  $T_g$ . We have in this case  $\beta = 0.41$ ,  $\beta$  being the non-exponential decay parameter of the Williams-Watts law. Note that the value of  $\beta$  ( $0 < \beta \leq 1$ ) is inversely proportional to the AES width.

ii) a narrow and sharp spectrum obtained from mechanical stress relaxation experiments on CoO single crystals at 77 K. The choice of experimental conditions was directed in order to ensure that the Peierls mechanism is the only operative one. Then we have  $\beta = 0.83$ .

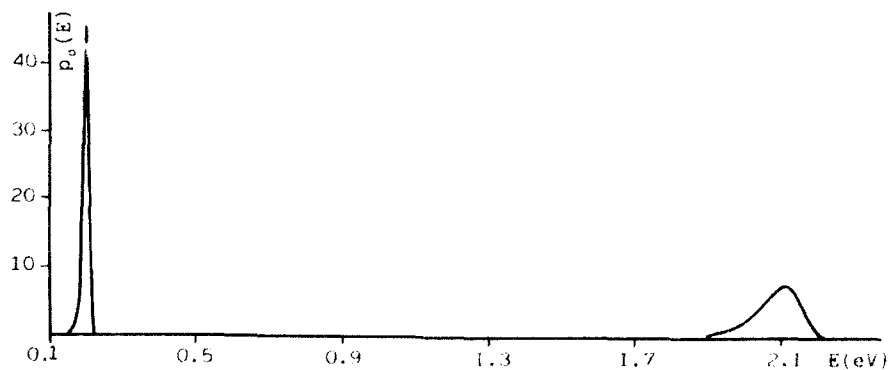


Fig. 1. Normalized AES evaluated by the approximate method. Note the differences between the broad spectrum (Se) and the narrow one (CoO).

Fig. 1 displays on the same scale both AES which were calculated by the approximate method. It is expected to find less reliable values for the narrow AES where the step-like approximation for  $\phi(E, T, t)$  is more drastic: the width of the spectrum is only slightly larger than the narrow range where the  $\phi$ -function drops abruptly. In Fig. 2 ((a) and (b)) we have replotted the approximate AES versus the exact ones. Both kind of spectra are in fair agreement but it may be remarked the following comments:

- The approximate spectra are skewed toward the low-energy side, while the 'exact' ones are more symmetric.
- The reliability of the approximate AES appears inferior for the narrow spectrum. In fact, it may be appreciated for this case a slight shift between the maxima of both distributions.

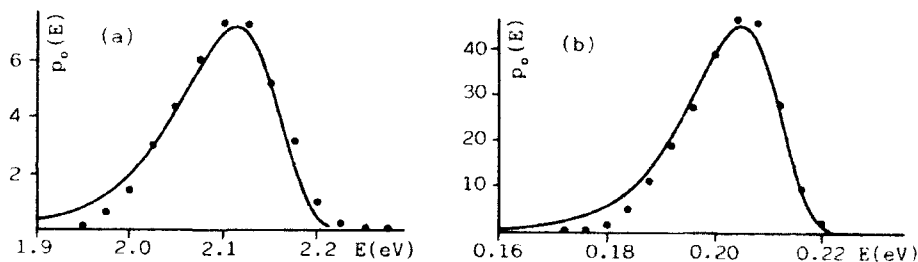


Fig. 2. A comparison of the approximate AES (solid lines) versus the exact ones. a) enthalpic relaxation of Se. b) mechanical stress relaxation of CoO.

Otherwise, the calculus complexity is by far superior for the new method. Thus, resort to the Primak's approximation appears widely justified if we are dealing with a broad and smooth spectrum and we are mainly interested in its general shape.

### 3. References

1. Primak, *Phys. Rev.* **100** (1955) 1677.
2. M. R. Gibbs, J. E. Evetts and J. A. Leake, *J. Mat. Sci.* **18** (1983) 278.
3. B. C. Cook, *Nuc. Inst. and Met.* **24** (1963) 256.
4. W. Ceuninck, Z. Ruyan, G. Knuyt, L. Schepper and L. M. Stals, *Mat. Sci. and Eng.* **97** (1988) 545.

# SPECIFIC HEAT MEASUREMENTS OF Ge DOPED $\text{Te}_{0.15}\text{Se}_{0.85}$ GLASSES IN THE GLASS TRANSITION REGION

E. ILLEKOVÁ

*Inst. Physics, Slovak Academy of Sciences, Dúbravská cesta 84228-Bratislava,  
Czechoslovakia*

and

M. T. CLAVAGUERA-MORA, M. D. BARÓ, S. SURIÑACH

*Física de Materials, Departament de Física,  
Universitat Autònoma de Barcelona, 08193 Bellaterra, Spain*

## ABSTRACT

Accurate measurements of the apparent heat capacity below and through the glass transition in  $\text{Ge}_x(\text{Te}_{0.15}\text{Se}_{0.85})_{1-x}$  glasses were performed by differential scanning calorimetry. The enthalpy released by the glasses when annealed near the glass transition was deduced. The observed behaviour may be explained by assuming first order relaxation kinetics and the rate constant with a spectrum of activation energies ranging from 1.2 to 1.5 eV.

## 1. Introduction

A liquid which has been undercooled to a temperature between the melting point and the glass transition temperature is in a metastable state of equilibrium called "undercooled liquid state" (ULS). When the liquid is undercooled into the glass transition region the relaxation times for molecular movements become comparable to the experimental time scale. At temperatures low enough below glass transition, molecular movements are completely frozen and one can consider the glass as being in a metastable solid state<sup>1</sup>. On heating the glass the molecular movements become thermally activated at temperatures near the glass transition giving rise to relaxation phenomena.

In this work we present accurate measurements of the apparent specific heat capacity below and during the glass transition performed by differential scanning calorimetry (DSC) on  $\text{Ge}_x(\text{Te}_{0.15}\text{Se}_{0.85})_{1-x}$  glasses with  $x=0.00$ , 0.02 and 0.10.

## 2. Experimental procedure

Bulk glasses were obtained by the melt-quenching technique. To avoid any significant uncontrolled relaxation, slowly cooled glasses were prepared directly in the DSC

apparatus from the initial melt-quenched glasses by heating them up to the ULS and subsequent by cooling them at 20 K/min to room temperature. The glassy nature of the samples was confirmed by X-ray diffraction. The calorimetric experiments were performed in a Perkin Elmer DSC 2 apparatus on about 10 mg of material under argon flow. The estimated error in heat capacity measurement was 0.5 % for the samples in the ULS and <2% in the glassy form, using a synthetic sapphire standard for calibration. The accuracy of the temperature measurements was within  $\pm 0.5$  K.

### 3. Results

The glass with  $x = 0.10$  is very stable against crystallization and shows only the glass transition on heating. The glass with  $x = 0.02$  shows also partial crystallization followed by melting. The glass with  $x = 0$  exhibits glass transition, crystallization and melting. Another characteristic of the studied glasses is that they have glass transition temperatures rather close to room temperature and, therefore, relaxation occurs even at room temperature.

To study the relaxation, the excess heat capacity  $\Delta C_p$  induced by the annealing was measured as the difference between the apparent heat capacity of the annealed sample and that of the slowly cooled sample. The relaxation enthalpy,  $\Delta H_r$ , was calculated as the area under the curve of the excess heat capacity versus temperature. Isothermal anneals were performed and after annealing the sample was quickly brought to 270 K and its heat capacity measured from there to the ULS. As an example Fig. 1 shows the apparent heat capacity of a glass with  $x = 0.10$  previously annealed at  $T_a = 320$  K as a function of annealing time  $t_a$ .

### 4. Discussion

For the description of structural relaxation processes the Activation Energy Spectrum (AES) model<sup>2</sup> was used. It is assumed that the spectrum of activation energies  $p_0(E)$  is proportional to the total density of processes available for relaxation for each activation energy  $E$ . Further the distribution of processes available is assumed to change with time following a first order kinetics with an Arrhenius form of the rate constant. Therefore the dependence on annealing temperature  $T_a$  and annealing time  $t_a$  of the relaxation enthalpy  $\Delta H_r$  is given by:

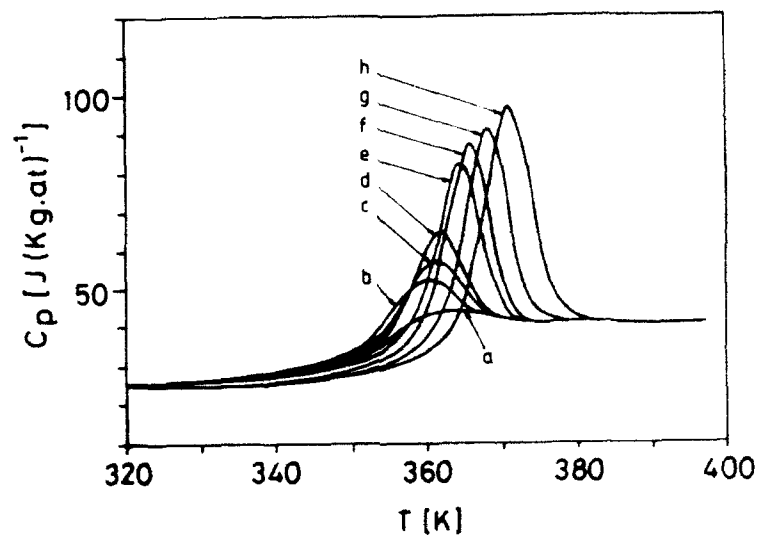
$$\Delta H_r(T_a, t_a) \propto \int_0^{E_0(T_a, t_a)} p_0(E) dE \quad (1)$$

where

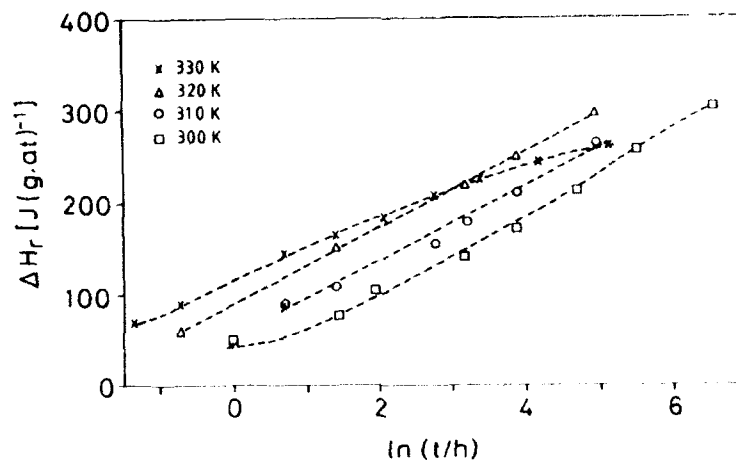
$$E_0 = RT_a \ln(At_a) \quad (2)$$

Fig. 2 shows the values of  $\Delta H_r$  as a function of  $\ln t_a$  at different annealing temperatures for the sample with  $x = 0.10$ . In order to calculate the form of  $p_0(E)$  the frequency factor  $A$  has to be known. If we take a value of the order of that obtained for  $\text{Ge}_{0.10}\text{Se}_{0.90}$  glasses<sup>3</sup>, that is  $A = 1 \cdot 10^{17} \text{ s}^{-1}$ , then we obtain for all three investigated samples activation energy spectra, which show a bell-shaped distribution from 1.2 to 1.5 eV.





**Fig.1-** Apparent heat capacity of  $\text{Ge}_{0.1}(\text{Te}_{15}\text{Se}_{85})_{0.9}$  glass previously annealed at  $T_1 = 320$  K (annealing time being the parameter: a-0, b-1, c-2, d-4, e-16, f-24, g-48, h-143h)



**Fig.2-** Relaxation enthalpy of  $\text{Ge}_{0.1}(\text{Te}_{15}\text{Se}_{85})_{0.9}$  glass as a function of annealing time

## 5. Conclusions

Experimental determination of the apparent heat capacity as a function of temperature in the glass transition range has been performed for  $\text{Ge}_x(\text{Te}_{0.15}\text{Se}_{0.85})_{1-x}$  glasses with  $x=0.00, 0.02$  and  $0.10$  using a DSC equipment. The enthalpy released by the glass when annealed near the glass transition temperature, called relaxation enthalpy, was calculated from the measurement of the apparent heat capacity of the annealed sample by heating it up to the undercooled liquid state and compared to the apparent heat capacity of the slowly cooled sample in the same temperature interval. The observed isothermal relaxation behaviour of all investigated glasses at temperatures just below the glass transition can be explained by assuming first order kinetics and a spectrum of activation energies for linear relaxation times. Further modelization of the annealing behaviour will be undertaken in the near future.

## 6. Acknowledgements

This work has been supported by CICYT project No MAT-90-0454 which is acknowledged. E.I. is grateful to UAB for financial support during the course of this work.

## 7. References

1. J. Jäckle, *Phil. Mag.* **B56** (1987) 113.
2. M.R.J. Gibbs, J.E. Evetts and J.A. Leake, *J. Mater. Sci.* **18** (1983) 278.
3. M.T. Clavaguera-Mora, M.D. Baró, S. Suriñach, J. Saurina and N. Clavaguera, *J. Non-Cryst. Solids* **131&133** (1991) 479.

# CHARACTERIZATION OF Se BASED CHALCOGENIDE ALLOYS BY MEASUREMENT OF T<sub>g</sub> VARIATIONS

A. HAMOU\*

and

J.M. SAITER, J. BAYARD, J. GRENET

*Laboratoire d'Etude et de Caractérisation des Composés Amorphes et des Polymères  
U.F.R. Sciences, BP 118, 76134 Mont-Saint-Aignan Cédex, France*

## ABSTRACT

In this paper we show that, for different vitreous selenium based alloys such as Se-Te, Se-As and Se-Ge, the variations of T<sub>g</sub> with heating rate measured by differential scanning calorimetry, follow an Arrhenius law. For a given alloy, the activation energy does not depend on thermal history and is weakly dependent on preparation method. Finally, we show that this energy is characteristic of the nature of the atoms added to selenium as well as the alloy composition.

## 1. Introduction

Researches of physical parameters which could describe the structure and classify the properties of glasses are always a large topic of investigation. It is known that glasses can be classified according to bond types (metallic, ionic, covalent) and that they often exhibit the glass transition phenomenon. Many works attempt to link the glass transition temperature (T<sub>g</sub>) to different physical parameters. For a large variety of covalent glasses, K. Tanaka [1] has linked the values of T<sub>g</sub> with an average coordination number ( $\bar{m}$ ) and shown that a simple relationship given by  $\ln(T_g) = 1.6 \bar{m} + 2.3$  could be obtained. In an other hand, J.P. De Neufville et al [2] have shown that for covalent glasses the relationship  $T_g = 340 \pm 20 + \beta E_g$  ( $E_g$  is the optical gap and  $\beta$  a function of  $\bar{m}$ ) could be obtained. It is also known that for a given glass, the glass transition temperature is not constant but depends on many parameters such as : preparation method, ageing, method of measurement of T<sub>g</sub>... In order to shake off these T<sub>g</sub> dependences, we propose to use a parameter obtained from the variations of T<sub>g</sub> with the heating rate instead of the value of T<sub>g</sub> for characterize the Se chalcogenide alloys.

## 2. Experimental and results

Samples are prepared by water quenching (=100 K/s) of a mixture of Ge and Se or As and Se melted in a vacuum-sealed quartz tube, heated at a temperature of 1273 K during period of 10 hours. Measurements of the glass transition temperature have been performed using a D.S.C. (Perkin-Elmer system 4).

Figure 1 shows the dependence of T<sub>g</sub> on heating rate ( $r$ ), in an Arrhenius plot, obtained on vitreous selenium in bulk form with different ageing duration.

\* Permanent adress : Universitéès-Sénia, Oran, Algérie

In each case, the data exhibit a linear behaviour. Moreover, the activation energy values  $E$  are independent of the age of the samples. The ageing dependence is pointed out by the shift of the curves toward the highest temperatures.

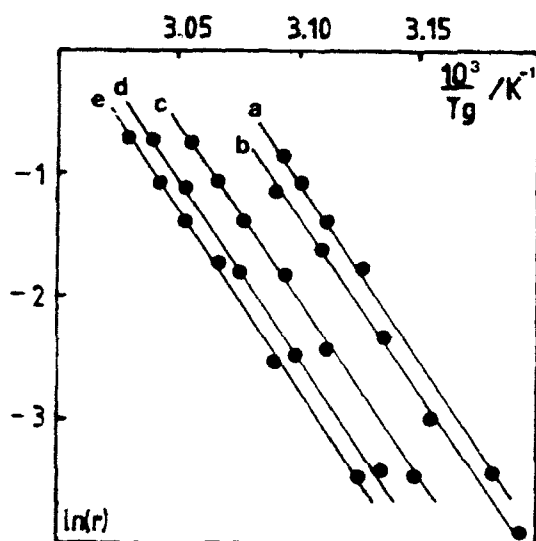


Figure 1 :  
Arrhenius plot of  
the variations of  
 $T_g$  with  $r$  for  
vitreous Se with  
different ageing  
duration  
a: 28h at 294K  
b: 1 week at 294K  
c: 7 weeks at  
294K  
d: 1 year at 294K  
e: 54 days at  
279K

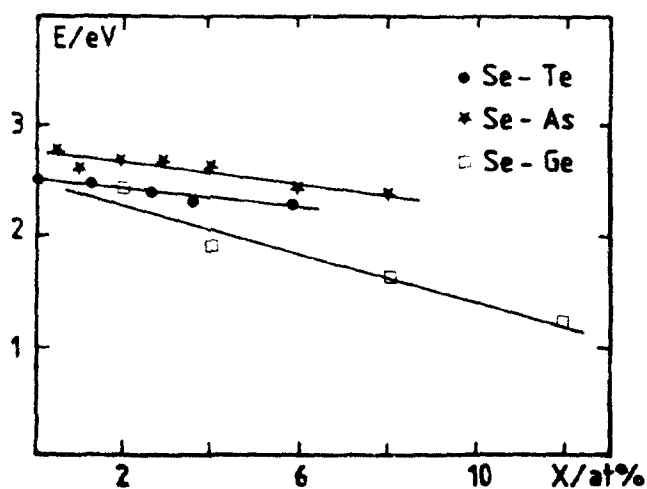


Figure 2 :  
Variations of the  
activation energy  
 $E$  with the  
composition for  
SeTe (Ref 3) Se-  
Ge and Se-As  
vitreous alloys.

Figure 2 shows the variations of  $E$  with the composition  $x$  for vitreous Se-Te (from ref. 3), Se-As and Se-Ge alloys. We remark that  $E$  varies linearly with the composition :

$$E = x E' + E_0 \quad (1)$$

The values of  $E'$  and  $E_0$  are reported in table 1.

	SeTe	SeAs	SeGe
$E'/\text{ev per atom fraction}$	-4,1	-4,9	-10,7
$E_0/\text{eV}$	2,5	2.8	2.5

Table 1: Variations  $E'$  and  $E_0$  versus the composition for three Se-chalcogenide alloys.

Although the values of  $E$  obtained by S.O. Kasap et al [3] on SeTe are lower than that we obtained on Se-As (probably due to the sample elaboration).  $E'$  decreases as coordination number  $N_c$  of the element added to Se increases. The values of  $E_0$  lie between 2.5eV (SeTe and SeGe) to 2.8eV (SeAs). Within experimental errors these values correspond to the activation energy of  $T_g$  versus heating rate for pure Se [4].

### 3. Discussion

During heating or cooling at different rates of samples of the same age, we can assimilate the continuous change of temperature to a series of instantaneous small variations  $\Delta T$  followed by an isothermal hold of time duration  $\Delta t$ .

Then, the structure will be readily relax to its equilibrium state if the relaxation time  $\tau$  is smaller than  $\Delta t$ ; when  $\tau$  is larger than  $\Delta t$ , the structure will remain in the glassy state.

The relaxation phenomena is governed by :

$$\frac{\partial H}{\partial t} = - \frac{H - H_e}{\tau} - C_{pg} \cdot r \quad (2)$$

where  $H$  is the current enthalpy,  $H_e$  the equilibrium enthalpy,  $t$  the time,  $C_{pg}$  the heat capacity in the glassy state.

The relaxation time is given by [5,6,7]

$$\ln \tau = \ln a + \frac{E_r}{kT} - c (H - H_e) \quad (3)$$

where  $a$ ,  $E_r$  and  $c$  depend on material.

Moreover the difference  $\Delta C_p$  between the specific heats in the liquid and in the glassy states may be supposed independent of the annealing temperature, annealing duration and heating rate ; then a linear relationship exists between enthalpy and temperatures variations.

$$H - H_e = \Delta C_p (T_f - T) \quad (4)$$

where  $T_f$  is a fictive temperature (for which the curve  $H(T)$  followed during heating reaches the extrapolated equilibrium curve  $H_e(T)$ ).

Then, the glass transition temperature may be defined as the temperature for which the relaxation time becomes comparable to the isothermal hold time and therefore the quantity  $r \cdot \tau(T_g)$  is constant. Thus

$$\ln r = - \frac{E_r}{kT_g} - c \Delta C_p T_g + c \Delta C_p T_f + \text{Constant} \quad (5)$$

The quantity  $c \Delta C_p T_f$  depends on ageing duration, but  $T_f$  is constant for a same ageing duration. So that

$$\frac{d \ln r}{d 1/T_g} = - \frac{E_r}{k} + c \Delta C_p T_g^2 \quad (6)$$

The second term of the right hand part of this equation is of second order compared to the value of the first term. Then the quantity  $-E_r/k$  is approximately equal to the slope of the  $\ln r = f(1/T_g)$  curves.

The experimental values of activation energy  $E$  may be identify to the relaxation time activation energy  $E_r$ .

Therefore the experimental results show that this relaxation time activation energy decreases as the coordination number of the atoms added in the selenium matrix increases.  $E_r$  may be considered as the energy required to reach the equilibrium state. This state would be reached all the faster because the chain lengths are shorter. Moreover for the same at % of added element the connectivity increases with coordination number. These two phenomena may explained the decrease of  $E_r$  from SeTe to SeGe.

## REFERENCES

1. K. Tanaka, Solid St. Commun. 54 (1985) 867.
2. J.P. Deneufville and H.K. Rockstad, Proceeding of the Fifth International Conference on Amorphous and Liquid Semiconductors, Edited by J. Stuke and W. Brening (London: Taylor and Francis) (1974) p.425.
3. S.O. Kasap and C. Johasz, Journal of Materials Science, 21 (1986) 1329.
4. J. Grenet, J.P. Larmagnac, Thin Solid Film, 110 (1983) 139.
5. C.T. Moynihan, A.J. Easteal, J. Wilder and J. Tucker, J.Phys. Chem. 78 (1974) 2673.
6. A.J. Kovacs, J.M. Hutchinson and J.J. Alkonis, Structure of Non-Crystalline Materials, Edited by P.H. Gaskell, Taylor and Francis, London (1977) p.153.
7. A.Q. Tool, J.Am.Ceram.Soc., 29 (1946) 240.

# IS THE SOFT POTENTIAL MODEL ABLE TO EXPLAIN THE GLASSY ANOMALIES?

M.A. RAMOS \*, L. GIL, and U. BUCHENAU

*Institut für Festkörperforschung, Forschungszentrum Jülich  
Postfach 1913, D-5170 Jülich, Federal Republic of Germany.*

*\* Present address: Lab. Bajas Temperaturas, Dept. de Física de la Materia  
Condensada, C-III, Universidad Autónoma de Madrid, E-28049 Madrid, Spain*

## ABSTRACT

The soft-potential model is an extension of the tunnelling model. It assumes a fixed effective mass and a random distribution of potentials for the tunnelling or vibrating entities. We present numerical calculations of low-temperature specific heat and acoustic attenuation using this model in order to discuss the question to which extent it enables a unified description of the glassy anomalies.

## 1. Introduction

An important progress towards the understanding of "glassy anomalies" was achieved after the introduction of the *tunnelling model*<sup>1</sup>, which provides an explanation for the main features of the physical properties of glasses below typically 1 K<sup>2,3</sup>. Inelastic neutron-scattering measurements in vitreous silica<sup>4</sup> have given clear evidence for additional vibrational states for temperatures typically ranging from 1 to 10 K, which are in turn directly responsible of the large excess in specific heat over the Debye contribution. These questions are addressed by the *soft-potential model*<sup>5,6</sup>, which describes both tunnelling and soft vibrational motion in terms of an effective potential with locally varying parameters. Starting from a recent reformulation<sup>7</sup> of the soft-potential model, we present here the main results of numerical calculations of low-temperature specific heat<sup>8</sup> and acoustic attenuation<sup>9</sup>.

Within this model, the effective potential energy of a single-mode can be written as<sup>6,7</sup>

$$V(x) = \mathcal{E}[h(x/a) + \eta(x/a)^2 + (x/a)^4] \quad (1)$$

where  $\mathcal{E}$  is an energy of atomic scale,  $x$  is some generalized spatial coordinate and  $a$  is a distance of the order of the interatomic spacing. At the distance  $a$  the fourth-order term is as high as the harmonic term for an unsoftened mode at a crystal-like frequency  $\omega_c$  (which can be estimated<sup>7</sup> from neutron-scattering data).  $h$  and  $\eta$  are random parameters.

From the invariant properties of the Schrödinger equation for the potential of Eq. 1 it can be seen that only two parameters enter the final results:  $\mathcal{E}$  (or  $\omega_c$ ) and  $W$  defined by

$$W = \mathcal{E}^{1/3}(h^2/2M_Sa^2)^{2/3} \quad (2)$$

In other words, the typical atomic energy  $\mathcal{E}$  can be related<sup>7</sup> to the two material-parameters  $W$  and  $\omega_c$  via  $\mathcal{E} = (\frac{1}{2}h\omega_c)^4/W^3$ .

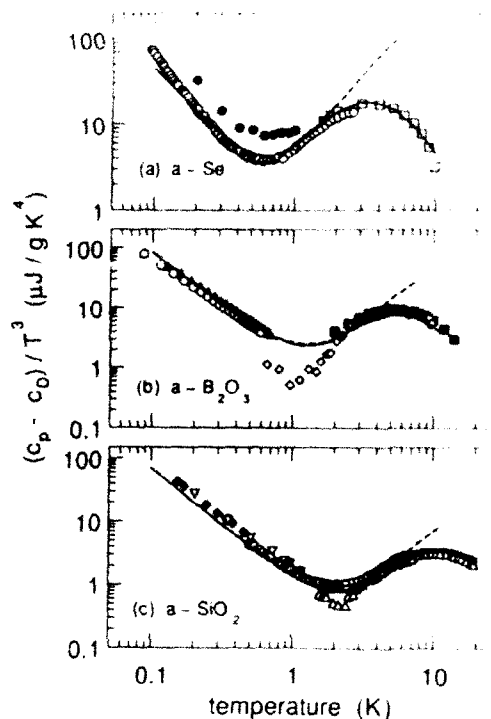


Figure 1: Specific heat at low temperatures for  $\text{SiO}_2$ ,  $\text{B}_2\text{O}_3$  and  $\text{Se}$ , numerically calculated following the soft potential model. Sources of experimental data are given elsewhere<sup>7,8</sup>. Dashed lines: using  $P(h, \eta) = 2P_0$ . Solid lines: using a gaussian distribution of the  $h$ -parameter.

For symmetrical potentials ( $h = 0$ ) the crossover from double- to single-well ones occurs just at  $\eta = 0$ . Hence the typical situation at the crossover is the well-known case of a particle moving in a quartic potential, whose two first energy levels are  $E_0 = 1.06W$  and  $E_1 = 3.80W$ . It is clear then why  $W$  is the important energy scale in this model.

## 2. Results and discussion

The universal properties of soft potentials represented by Eq. 1 enable a straight determination of  $W$  (our second material-parameter) from specific-heat ( $C_p$ ) data. All glasses exhibit a minimum in  $C_p/T^3$  at a certain temperature  $T^*$  of the order of 1K, that is, the crossover from the two-level system regime to another one where low-lying vibrational excitations dominate the specific heat. Simple approximations<sup>7</sup> for a constant distribution of the potential-shape parameters ( $P(h, \eta) = 2P_0$ ) yield a specific heat behaviour passing from  $(C_p - C_D) \propto T$  below  $T^*$  to  $(C_p - C_D) \propto T^5$  just above  $T^*$  ( $C_D$  is the Debye contribution), in rather good agreement with experiments, and giving  $W \approx 1.6k_B T^*$ . We have performed more rigorous numerical calculations (shown in Fig. 1), which support this picture, though



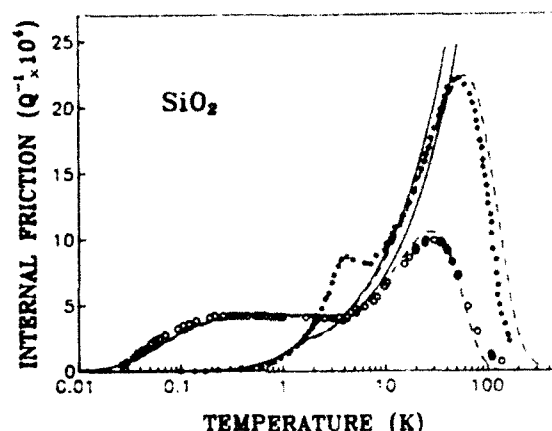


Figure 2: Internal friction<sup>10</sup> of SiO<sub>2</sub> for 4KHz and 45MHz. Solid lines: numerical calculations based in the soft-potential model using constant distributions ( $P(h, \eta) \approx 2P_0$ ). Dashed lines: the same but using a distribution of the  $\eta$ -parameter as to give a gaussian distribution in barrier heights

indicating a slightly supralinear dependence on temperature for  $T < T^*$  and a relationship  $W \approx 2k_B T^*$ . For instance, for vitreous silica ( $\alpha$ -SiO<sub>2</sub>) we use  $\omega_c/2\pi \approx 3$ THz (from neutron data) and  $W = 3.8$ K (from the experimental value of  $T^*$ ), finding a density of soft modes of  $P_0 = 1.3 \times 10^{29} \text{ m}^{-3}$  to fit the quasilinear contribution to the specific heat at the lowest temperatures. These are the parameters of the model for  $\alpha$ -SiO<sub>2</sub> that we must use to calculate its acoustic attenuation. If we relax the assumption of an unbounded distribution of the linear coefficient  $h$  in Eq. 1, the only difference occurs at the highest temperatures (see Fig. 1). Very interestingly, it can explain both the magnitude and position of the hump in  $C_p/T^3$ , though obviously the chosen distribution is by no means unique.

At low temperatures and frequencies ranging from Hz to GHz (below 1 K and around 1 GHz or above, resonant absorption is also important), acoustic loss is dominated by *relaxational absorption*. The interlevel spacing is changed and the corresponding thermal equilibrium of the tunnelling states disturbed by the strain field produced by the sound wave. A relaxation process assisted by thermal phonons occurs then, which restores the equilibrium after a relaxation time  $\tau$ , attenuating in this way the propagating sound.

The *crossover temperature*  $T_c$ , separating the quantum regime from the classical relaxation processes dominant at higher temperatures<sup>2,3,9,10</sup>, remains basically constant throughout the whole frequency range (around 4K for  $\alpha$ -SiO<sub>2</sub>). Above  $T_c$  a sudden rise in  $Q^{-1}$  is observed until a large peak is reached at some tens of Kelvin. In other words, above  $T_c$  *thermal-assisted* jumping over the barrier is a more favourable process than tunnelling.

An important question is how to handle the interaction between phonons and tunnelling states. The tunnelling model makes the simplification of considering a constant phonon coupling, independent of the shape of the potential, but such a relationship should exist. Moreover, it can be traced within the framework of the soft-potential model. The external strain  $u$  changes the potential seen by the tunnelling entity. Following the ideas of the tunnelling

model, we will assume that only the change in the *depth* of the wells is relevant, and then we obtain<sup>9</sup>  $\gamma \approx \mathcal{E} H_0 \sqrt{|\eta|/2}$ , where  $H_0$  is a dimensionless constant.

To calculate the internal friction, we use an expression similar to that of the tunnelling model<sup>2,3,9,10</sup>, but integrating over the random and independent variables of the soft potential model,  $h$  and  $\eta$ , and using as inverse relaxation time the sum of the inverses of quantum and classical relaxation times<sup>2,3,9,10</sup>.

In Fig. 2 we show our numerical calculations of acoustic loss for  $\alpha$ -SiO<sub>2</sub> at 4 KHz and 45 MHz, with a constant distribution  $P(h, \eta) = 2P_0$ , whose magnitude is deduced from specific heat data, as explained above. Therefore, *only* the constant factor  $H_0$  can be used as a free parameter in these calculations and was simply determined as to fit the magnitude of  $Q^{-1}$  at the plateau for 4 KHz. A number of the experimental features are well accounted for, even quantitatively: the onset temperature of the plateau, the crossover temperature  $T_c$  from tunneling to activation around 4K, and the magnitude and steepness of its rise at temperatures above  $T_c$ . Moreover, the calculation at much higher frequencies (with no scaling parameter) is in good agreement with experimental data, with exception of the crossover region, where the attenuation is underestimated and the corresponding small peak is missing, likely due to the omission of mixed tunnelling-activation or Raman processes<sup>9,10</sup>.

Following a derivation rather parallel to that made in the tunnelling model<sup>2,3,10</sup> it can be shown<sup>9</sup> that at low temperatures the soft potential model agrees with the tunnelling model, through the transformation  $\gamma^2 P \Leftrightarrow (\hbar\omega_c) H_0^2 P_0$ , where  $P$  is the constant density of tunnelling states as defined<sup>2,3,10</sup> in the tunnelling model. It also can be shown that the transition from tunnelling to thermal activation takes place at a crossover temperature given by  $k_B T_c \approx W$ . This estimate implies a fundamental and close relationship between the crossover tunnelling-activation and that of tunnelling states-soft vibrations in thermal properties: in particular, the former shall occur at a temperature approximately twice that of the minimum in  $C_p/T^3$ , i.e.  $T_c \approx 2T^*$ . Confirmation of this relationship in other glasses would give substantial support to the present approach of the soft-potential model.

### 3. References

1. W.A. Phillips, *J. Low. Temp. Phys.*, **7** (1972) 351; P.W. Anderson, B.I. Halperin, and C.M. Varma, *Phil. Mag.*, **25** (1972) 1.
2. W.A. Phillips, *Amorphous Solids: Low temperature properties*, (Springer, Berlin, 1981).
3. S. Hunklinger and W. Arnold, in *Physical Acoustics*, Vol. XII, ed. W.P. Mason and R.N. Thurston (Academic Press, New York, 1976).
4. U. Buchenau, H.M. Zhou, N. Nücker, K.S. Gilroy, and W.A. Phillips, *Phys. Rev. B* **60** (1988) 1318.
5. V.G. Karpov, M.I. Klinger, and F.N. Ignat'ev, *Sov. Phys. JETP*, **57** (1983) 439.
6. Yu.M. Galperin, V.G. Karpov, and V.I. Kozub, *Advances in Physics*, **38** (1989) 669.
7. U. Buchenau, Yu.M. Galperin, V.L. Gurevich, and H.R. Schober, *Phys. Rev. B* **43** (1991) 5039.
8. L. Gil, M.A. Ramos, A. Bringer, and U. Buchenau (to be published).
9. U. Buchenau, Yu.M. Galperin, V.L. Gurevitch, D.A. Parshin, M.A. Ramos, and H.R. Schober (to be published).
10. S. Hunklinger, in *Disorder Systems and New Materials*, ed. M. Borisssov, N. Kirev, and A. Vavrek (World Scientific, Singapore, 1989).

## Monte-Carlo simulation of the glass transition in dense three-dimensional polymer melts

J. Baschnagel, W. Paul and K. Binder  
Institut für Physik, Universität Mainz, Staudinger Weg 7  
D-6500 Mainz, Germany

and

H. P. Wittmann, Department of Chemical Engineering, University of California  
Santa Barbara, CA 93106, USA

### Abstract

This Monte-Carlo simulation studies the glass transition of a dense three-dimensional polymer melt using a lattice model (bond-fluctuation model) which was highly optimized for a vector super-computer. If one includes in this a priori athermal model a suitable hamiltonian which favours the bond-vectors from the class  $[3,0,0]$ , it is possible to create a competition between the energetic and geometric constraints of the system which results in a glassy behaviour of the melt, i.e., the static quantities become cooling rate dependent and the correlation functions obey the time-temperature superposition principle.

## Introduction

Although a lot of experimental and theoretical work on the glass transition of polymers has already been done [1], many questions concerning the structure in the glassy state and the nature of the glass transition are unsolved. In such a situation computer simulations can be useful to complete the experimental and analytical studies. Starting from a well defined microscopic model it is possible to calculate virtually all interesting macroscopic quantities, which might be difficult or even impossible to measure in an experiment, without resorting to uncontrollable approximations, as it is often necessary in analytical work. There have already been several attempts to study the static and dynamic properties of glassy polymers by computer simulation methods [2-3]. Whereas all these calculations use chemically realistic models for the polymer chains, we propose to investigate the glass transition by a Monte-Carlo simulation of a lattice model for a dense polymer melt.

## Model and simulation method

In this Monte-Carlo simulation the polymer chains are modelled by self and mutually avoiding walks on a simple cubic lattice where each monomer occupies a whole unit cell. The monomers are connected by bond vectors whose lengths were set to vary between 2 and  $\sqrt{10}$  with the exclusion of  $\sqrt{8}$ . This choice guarantees the local self-avoidance of the chains and prevents them from crossing each other in the course of their motion. Using these restrictions on the bond lengths six basic classes of bond vectors can be constructed by lattice symmetry operations, allowing 108 different bond vectors and 87 bond angles [4]. The basic bonds are:  $[2,0,0]$ ,  $[2,1,0]$ ,  $[2,1,1]$ ,  $[2,2,1]$ ,  $[3,0,0]$ ,  $[3,1,0]$ . In the course of the Monte Carlo simulation a monomer is selected at random and moved for one lattice constant in an arbitrarily chosen direction, if the neighbouring lattice sites in direction of the attempted move are empty (self-avoidance) and if the resulting new bond vectors belong to the classes of vectors enumerated above. Note that self-avoidance and uncrossability of the walks are the only conditions which govern the chain dynamics up to now. No hamiltonian has yet been introduced to contribute to the control of the monomer moves and thus the model is still independent of temperature. Motivated by the research on spin glasses [5], the hamiltonian should be designed in such a way that a competition arises between the trial of a bond to adopt its energetically preferred state and the structural constraints that the surrounding monomers exert on that bond. If this competition prevents the system from satisfying the energetic and geometric constraints simultaneously, the melt will be frozen in an amorphous structure which depends on the quench rate of the cooling process. A cooling rate that tends to zero should allow the system to arrange suitably so that each bond can reach the ground state which corresponds to the possibility of crystallization in simple liquids. In order to realize these requirements we choose a simple hamiltonian which only favours the bond vectors from the class  $[3,0,0]$  irrespective of their direction and thus leads to a highly degenerate and disordered ground state.

$$\mathcal{H}(\vec{b}) = \begin{cases} 0 & \text{if } \vec{b} \in [3,0,0] \\ \epsilon & \text{else} \end{cases} \quad (1)$$

Concerning the implementation of the bond fluctuation model on a computer we work with a highly vectorizable algorithm which was carefully optimized for the use on a CRAY YMP [6] so that also long time studies of correlation functions should be feasible.

## Results

Starting from well equilibrated athermal configurations the polymer melt was cooled down from  $T = \infty$  to  $T = 0.05$  ( $= \beta_{\text{max}}^{-1}$ )<sup>1</sup> by linearly changing the reciprocal

<sup>1</sup>The temperature and all energies are measured in units of  $\epsilon$ . All lengths are measured in units of the lattice constant.

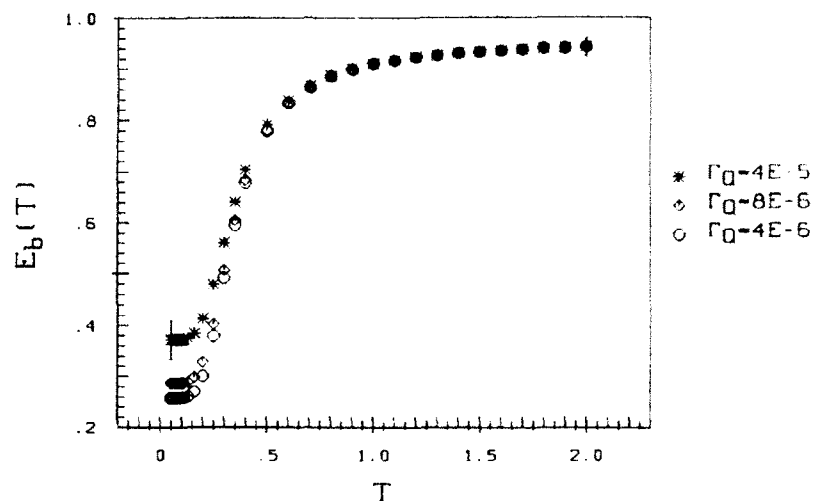


Figure 1: Temperature variation of the mean bond-length energy for different cooling rates

temperature  $\beta$ .

$$\beta(t) = \beta_{max} \cdot \Gamma_Q \cdot t \quad (2)$$

Three different cooling rates, i.e.,  $\Gamma_Q = 4 \cdot 10^{-5}$ ,  $\Gamma_Q = 8 \cdot 10^{-6}$  and  $\Gamma_Q = 4 \cdot 10^{-6}$ , were used. Fig. 1 shows as a typical result of this cooling process the temperature variation of the mean bond-length energy. This energy depends only slightly on temperature for  $T$ -values well above one which means that the melt is mobile, i.e., it is in the liquid state. Decreasing the temperature increases the number of bonds in the ground state and thus decreases the mean bond-length energy, until the energy starts to level off at a temperature below  $T = 0.2$  and finally loses its dependence on temperature totally around  $T = 0.15$ . In that temperature range the melt freezes in at an energy value which is the higher, the higher the cooling rate is, as expected from the discussion of the previous section. A glance at the global static structure function reveals that the frozen melt is amorphous, i.e., glassy.

Besides the dependence of the physical quantities on the cooling rate and the invariance of the amorphous structure at the glass transition other features which a glass model must have are that the diffusion coefficient virtually vanishes in the glassy state and that the correlation functions follow the time-temperature superposition principle. Fig. 2 shows that the diffusion coefficient, defined by,

$$D = \lim_{t \rightarrow \infty} \frac{g_3(t)}{6 \cdot t} \approx \frac{g_3(t)}{6 \cdot t} \Big|_{t=400000mc\tau} \quad (3)$$

indeed becomes very small in the glass transition region ( $T < 0.2$ ). In the upper equation  $g_3(t)$  stands for the mean square displacement of the center of mass of a

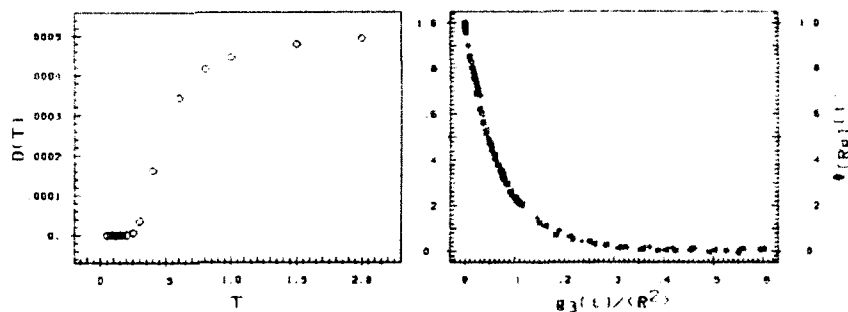


Figure 2: Diffusion coefficient for  $\Gamma_Q = 4 \cdot 10^{-8}$  and  $\Phi_{[R_G]}(t)$  for  $T = 0.05$  ( $\circ$ ),  $0.1$  ( $\square$ ),  $0.2$  ( $\diamond$ ),  $0.6$  ( $*$ ),  $1.0$  ( $+$ ) and  $2.0$  ( $<$ )

chain. Additionally, Fig. 2 presents the data for the correlation function of the radius of gyration which is given by

$$\Phi_{[R_G]}(t) = \frac{\sum_{n=1}^N \langle (\vec{r}_n(t) - \vec{R}_{CM}(t)) \cdot (\vec{r}_n(0) - \vec{R}_{CM}(0)) \rangle}{\sum_{n=1}^N \langle (\vec{r}_n(0) - \vec{R}_{CM}(0))^2 \rangle} \quad (4)$$

where  $\langle \bullet \rangle$  represents the average over all bonds in the system and  $\vec{r}_n(t)$  and  $\vec{R}_{CM}(t)$  are the positions of the monomers and of the center of mass at time  $t$ . Motivated by the Rouse-model [7] one expects that this function decays with a time constant  $\tau_R \propto \langle R^2 \rangle / D$  which can be generalized to  $\tau_R \rightarrow \langle R^2 \rangle \cdot t / g_3(t)$ . If one uses  $g_3(t) / \langle R^2 \rangle$  as a scaling variable, the data for all temperatures should collapse on a single curve and Fig. 2 shows that this is indeed the case.

**Acknowledgement:** This work was supported by SFB262.

## References

- [1] G.B. McKenna, in *Comprehensive Polymer Science*, Vol.2, (Pergamon Press, NY 1989)
- [2] D. Theodorou, U.W. Suter, *Macromolecules* **19**, 379 (1986)
- [3] D. Rigby, R.J. Roe, *Macromolecules* **22**, 2259 (1989)
- [4] H.P. Deutsch, K. Binder, *J. Chem. Phys.* **94**, 2294 (1991)
- [5] K. Binder, A.P. Young, *Rev. Mod. Phys.* **58**, 801 (1986)
- [6] H.P. Wittmann, K. Kremer, *Comp. Phys. Comm.* **61**, 309 (1990)
- [7] M. Doi, S.F. Edwards, *Theory of Polymer Dynamics*, (Clarendon Press, Oxford 1986)

## GLASS TRANSITION AND PHYSICAL AGING IN AMORPHOUS POLY(ETHYLENE TEREPHTHALATE).

G. VIGIER, J. TATIBOUET, J. PEREZ  
INSA Bat. 502 (UA341) GEMPPM F69621 Villeurbanne Cedex

### ABSTRACT

Thermal properties of poly(ethylene terephthalate) are found to depend on aging effects occur below  $T_g$ . DSC results can be described through a physical model assuming diffusion and annihilation of quasi-point defects. The distribution in the mobility of these defects is able to take into account all the observed phenomena.

### Introduction

The purpose of this work is to understand the DSC results, obtained after agings carried out below  $T_g$ , through a physical model of quasi-point defects. The kinetics of the glass transition being most important, simulations have to be made in the same conditions as experiments. Therefore the latter have been performed with cooling rates, aging times and temperatures well controlled.

### Experimental

PET films were supplied by Rhône-Poulenc Films (molecular weight : 20000g/mole) with no detectable crystallinity. DSC scans were done with a 10K/min heating rate. The PET samples were annealed to a temperature just above  $T_g$  ( $T=368K$ ) for 15 min to erase any previous aging. Thereafter specimens were quenched below  $T_g$  (with a rate of about 0.5K/s) in a liquid nitrogen bath, then maintained at a sub  $T_g$  annealing temperature ( $T_a$ ) for different aging times ( $t_a$ ).

### Experimental results

DSC thermograms are shown in fig.1 for different  $T_a$  and  $t_a$ . For low temperature annealing ( $T_a=303K$ ), aging effect is only visible for aging time over  $10^5$  s and the peak appears well below  $T_g$ . This fact is in agreement with the results of Monserrat and al. 1. As aging temperature increases, the usual peak appears later, this one shifts firstly towards lower temperatures for short ageing time and towards higher temperatures as ageing time increases. The amplitude of the peak increases as aging time increases.

### Molecular interpretation

A physical interpretation of structural relaxation, based on the general theory presented earlier 2,3, is proposed. The model is developed on the main assumption that density microfluctuations in a glassy material can be considered as quasi-point defects

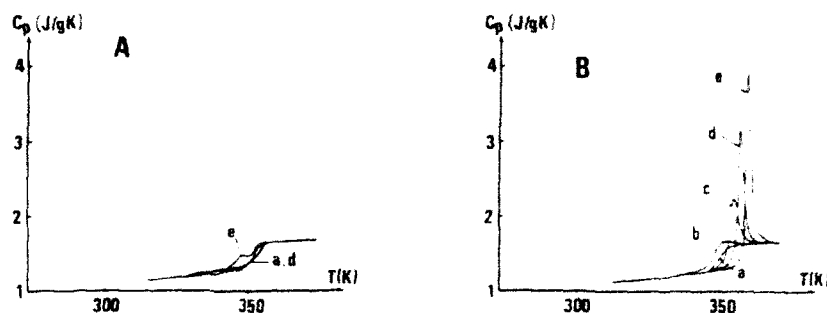


Fig 1 A) Aging at 303K B) Aging at 333K ta: a) Reference curve (0s) b)  $10^{-3}$ s c)  $10^{-4}$ s d)  $10^{-5}$ s e)  $10^{-6}$ s

(qpd). The defect concentration,  $C$ , above  $T_g$  increases with temperature according to a Boltzmann distribution. During quenching, most qpd are frozen-in and the structural relaxation at  $T_a < T_g$  could be interpreted in term of diffusion aided annihilation of qpd until a new thermodynamic (metastable) equilibrium is reached at this temperature. Based on the hierarchically constrained nature of molecular dynamics, a parameter  $b$  has been defined to characterize correlation effects. Since the reorganization of each defect depends on its own environment, it is thus reasonable to define a distribution in the value of the correlation parameters. Then a molecular motion time is associated to

$$\text{each kind of defects : } \tau_i = t_0 \left( \frac{\tau_B}{t_0} \right)^{(1/b)_i} \quad (1)$$

where  $t_0$  is the characteristic time for the elementary molecular motions and  $t_0$  is a scaling time factor.  $(1/b)_i$  is assumed to be distributed around  $1/b$  according to a Gaussian distribution. The total concentration of defects is given as the summation of each kind of defects,  $C_i$ , corresponding to various degrees of molecular mobility  $(\tau_i, b_i)$ . Then the time dependence of  $C$  can be obtained from a set of differential equations such as:

$$\frac{dC_i(t, T)}{dt} = - \frac{C_i(t, T) - C_i(\text{equi}, T)}{\tau_i(t, T)} \quad (2)$$

where  $C_i(\text{equi}, T)$  represents the metastable equilibrium concentration at  $T$ . Using equations (1,2) and assuming that  $C$  and  $b$  are related 2, it is possible to determine the defect concentration during any thermal cycle.

Numerical calculations have been made with 21 classes of defects with the parameters determined and given in the ref. 4. So it is possible to simulate DSC experiments (fig.2) as  $C_p \propto dC/dT$  (with adding phonon contribution). A very good agreement is found for high temperature aging (333K). The agreement is not so good for aging at low temperature (303K) but curves exhibit a sub- $T_g$  peak close to experiments. From considerations about the equations (2), it is possible to explain the displacement of the peak when aging time increases. In effect aging treatment produces two dual effects:

- an increase of the difference  $(C_i(\text{equi}) - C_i(t))$  at the temperatures as the peak can occur.



- a decrease of the correlation factor  $b_i$  (movement becomes more difficult as defects are annihilated). This last effect corresponds to an increase of  $\tau_i$ .

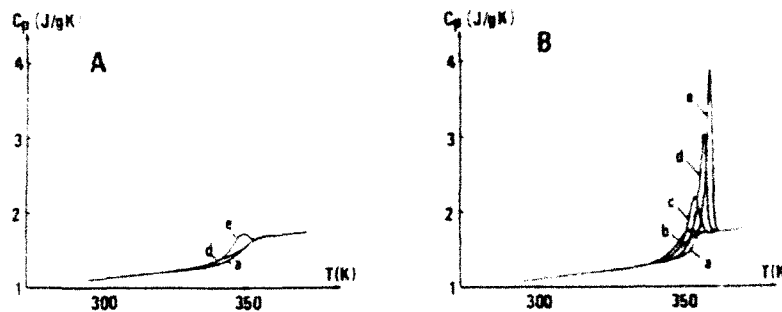


Fig.2 Simulations of DSC experiments (same notations as Fig.1).

These two effects are opposed, so we can understand the displacement toward the low temperatures for short aging times (first effect is preponderant) but when aging times becomes longer the maximum of  $C_p$  is observed at higher temperature as the effect on mobility becomes then preponderant.

It is possible also to obtain the histograms of the defect concentrations all along the thermal treatments (quenching, aging treatments, heating at the same rate as in DSC experiments). An example is given in fig.3 when quenching from 368K to aging temperature of 333K is simulated. From the initial state where defects have a gaussian

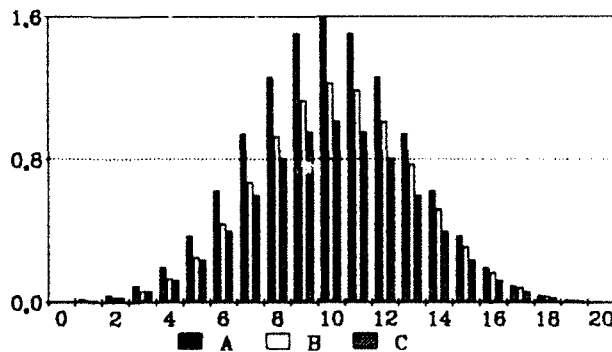


Fig.3 Histograms of defects concentrations in %.

0=>the most mobile defects  
20=>the least mobile defects

A: at 368K (before quenching)  
B: just after quenching at 333K  
C: equilibrium at 333K

distribution in their mobility, it appears that quenching leads to a non-symmetrical distribution for which less mobile defects are far from the equilibrium concentration at 333K. During aging at 333K, an evolution towards the equilibrium occurs and higher the defect mobility, shorter the time to reach this equilibrium. (fig.4). At the temperature just before the DSC peak, all the defect concentrations are lower than their equilibrium concentration, but as the temperature increases, the defect mobility increases also, then the defects tend to reach their equilibrium concentration, therefore their number increa-

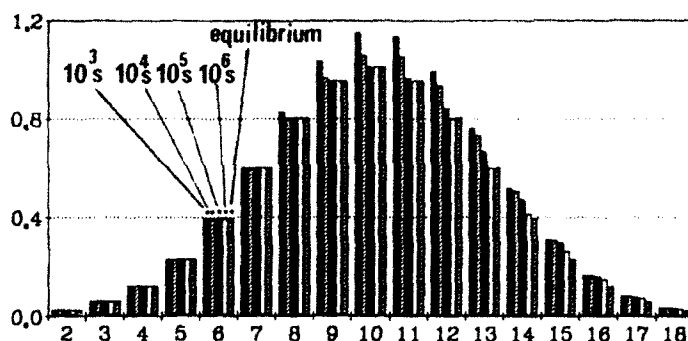


Fig. 4 Evolution of histograms of defects concentrations during an aging at 333K

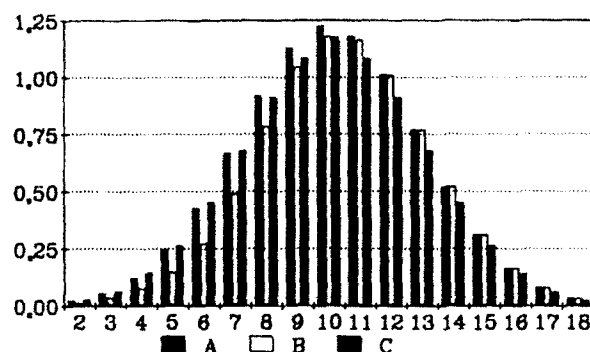


Fig. 5 Influence of aging at 333K (DSC sub-Tg peak) on histograms of defects.

A: histogram after quenching  
B: histogram after aging ( $10^6$ s)  
C: histogram corresponding to the equilibrium just before the sub Tg peak (348K).

ses and that increases also the mobility and so on : an "avalanche" phenomenon occurs, leading to a very sharp peak. When aging occurs at low temperature, only the more mobile defects are annihilated (fig.5); during DSC scans at the temperature just before the sub-Tg peak (348K for aging at 303K) the more-mobile defects concentrations are lower than their equilibrium concentration, whereas the less-mobile defects concentrations are slightly higher than their equilibrium concentration. Then, as the temperature increases, only the former recovers their equilibrium, leading to the sub-Tg peak.

### Conclusion

A quasi-point model, improved by a distribution in the mobility of the defects, is able to describe the structural relaxation and to simulate DSC experiments. Considerations on the histograms of defects populations give explanations of the different aspects of the phenomenon (displacement of the endothermal peak, sub-Tg peak...).

### References

1. S. Monserrat and P. Cortes, *Anales de Quimica* 82 (1986) 499.
2. J. Perez, *Polymer* 29 (1988) 483.
3. J. Perez, J.Y. Cavallé, R. Diaz-Calleja, J.L. Gomez-Ribelles, M. Monleon-Pradas, A. Ribes-Greus, *Makrom. Chem* (1991).
4. A. Benatmane, Thesis Lyon (1991)

## X-RAY DIFFRACTION IN GLASSY POLYMERS AROUND $T_g$

**J. J. del Val and J. Colmenero**

Departamento de Física de Materiales, Fac. Química, Univ. País Vasco, Apdo. 1072, 20080 San Sebastián, SPAIN

and

**B. Rosi and G. R. Mitchell**

J. J. Thomson Physical Laboratory, Univ. Reading, Whiteknights, Reading RG6 2AF, U. K.

### ABSTRACT

X-ray diffraction patterns have been obtained at different temperatures between  $T_g - 50K$  and  $T_g + 50K$  for two amorphous polymers: Poly(Vinyl Acetate) and Poly(2-hydroxypropylether of bisphenol A). Attention has been paid to the evolution with the temperature of the position and the intensity of the wide diffraction maxima corresponding to interchain correlations in the polymers. The temperature evolution of these parameters shows a marked discontinuity just in the glass transition temperature for each material.

### 1. Introduction

For many years the "Glass Transition" phenomenon has been well known and has been widely studied for glasses, specially for glassy polymers: the different behaviour of the volume or the enthalpy of a given glassy material at the two sides of a given temperature zone defines a temperature value characteristic of each material called the Glass Transition Temperature ( $T_g$ ). Up to now, few studies have been carried out in order to know if the structural parameters of a glassy polymer vary with temperature through its glass transition.

By using Small Angle X-ray Scattering (SAXS), Fischer and Dettenmaier<sup>1</sup> have measured the mean square value of the density fluctuations  $\langle \Delta \rho^2 \rangle$  of PMMA, PC and PET showing in the three cases that the temperature behaviour for  $\langle \Delta \rho^2 \rangle$  is linear, with a higher slope in the liquid ( $T > T_g$ ) region than in the glassy ( $T < T_g$ ) one; the change in the slope was located at the respective  $T_g$  value. Later, Curro and Roe<sup>2,3</sup> have obtained very similar results for PS, PMMA and PC using the same technique; moreover, they have measured the isothermal relaxation of the density fluctuations frozen at temperatures below  $T_g$  for each polymer. More recently, Mitchell and Windle<sup>4</sup> and Song and Roe<sup>5</sup> have tried to study by means of Wide Angle X-ray Scattering (WAXS) the structural changes against the temperature in amorphous PC and PS respectively.

Nevertheless, up to now no systematic studies have been developed through WAXS in order to know how the medium range order of polymeric glasses changes with the temperature specially around  $T_g$ . In this work, we show some preliminary results concerning the variation of diffraction patterns of two particular amorphous polymers around their respective  $T_g$  values.

## 2. Experimental

Two commercial polymers, previously purified, were used in this work:

a) Poly(vinyl acetate) (PVAc) of low molecular weight, from Aldrich. It contains a side chain with methyl and carbonyl groups.

b) Poly(2-hydroxypropylether of bisphenol A) from Union Carbide (PKHH) currently known as Phenoxi (Ph) ( $M_n=25000$ ). The residue of bisphenol A makes this polymer structurally similar to PC.

$T_g$  values are 313K and 373K for PVAc and Ph respectively.

WAXS measurements were carried out on a fully automatized transmission diffractometer (provided with a cell with temperature variation, graphite monochromator and a proportional detector) using Cu wavelength ( $1.54\text{\AA}$ ) in a scattering vector region between  $0.2\text{\AA}^{-1}$  and  $6\text{\AA}^{-1}$ .

Diffraction patterns were obtained for the two polymers at temperatures between  $T_g+50\text{K}$  and  $T_g-50\text{K}$  in order to cover wide temperature ranges in both liquid and glassy states of the materials. Prior to each  $T < T_g$  measurement, the sample was heated up to  $T_g+50\text{K}$  and then cooled the temperature of measurement at around  $10\text{K/min}$  in order to assure the material had the same prior thermal history. Prior to the comparison of the different patterns, these ones were corrected for background, polarization and multiple scattering<sup>6</sup>.

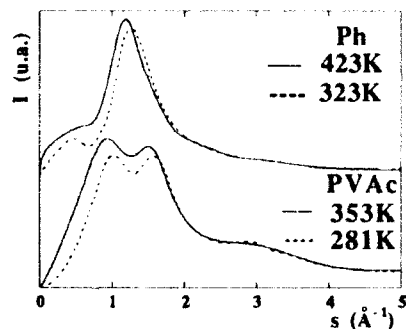


Fig. 1- WAXS patterns for PVAc and Ph at temperatures below and above  $T_g$ .

## 3. Results and Discussion

Fig. 1 shows diffraction patterns for PVAc and Ph in liquid and glassy states. In the two polymers, the intensity and the position of the diffraction maxima corresponding to interchain structural correlations<sup>7</sup> (obtained at scattering vector values  $s < 2.5\text{\AA}^{-1}$ ) vary appreciably while the intrachain correlations<sup>7</sup> related maxima do not. In glassy polymers, the position of a diffraction maximum at  $s < 2.5\text{\AA}^{-1}$  indicates a certain average correlation distance between structural units belonging to different chains.

PVAc shows two wide diffraction maxima located around  $1\text{\AA}^{-1}$  and  $1.5\text{\AA}^{-1}$ . Fig. 2 shows the evolution with the temperature of the first one. Within the scatter of the points, a clear discontinuity can be observed just at  $T_g$ ; different linear behaviours are found below and above  $T_g$ . The fitting of certain points from the  $T < T_g$  region by the  $T > T_g$  linear behaviour could be attributed to a recovery process during the experiment where the

glassy material evolves from an out of equilibrium configuration to a more stable one in the thermodynamic equilibrium, that is the well known physical aging process in glassy materials. The position of the second maximum changes with the temperature too; nevertheless, one cannot find a clear discontinuity around  $T_g$ . The different temperature evolution of the two peaks indicates different types of structural interchain correlations. Moreover, WAXS measurements carried out onto oriented PVAc

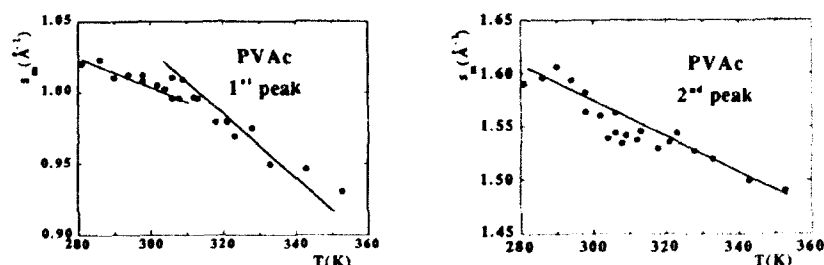


Fig. 2- Variation of the position of the WAXS maxima of PVAc with the temperature.

at room temperature show that the second peak is isotropic although the first one shows a marked meridional character<sup>7</sup>. In order to elucidate what is the structural origin of the two peaks, simulations of the scattering by molecular models of PVAc chains will be performed. On the other hand, Radial Distribution Functions (RDF) of PVAc have been calculated for each temperature and no differences were found in the two peaks obtained at around 1 Å and 5 Å (only a widening of the RDF peaks at higher temperatures is observed but this is also evident in the diffraction patterns).

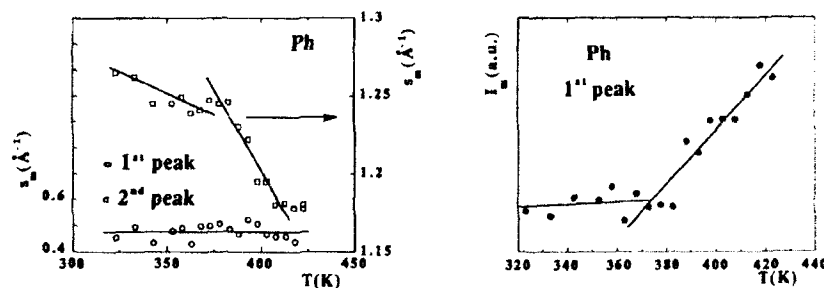


Fig. 3- Variation of the positions of the two WAXS maxima of Ph with the temperature.

Fig. 4- Variation of the intensity of the first WAXS maximum of Ph with the temperature.

Ph shows a high intensity diffraction peak located around  $1.25\text{Å}^{-1}$  (see Fig. 1) and a low intensity one at  $0.5\text{Å}^{-1}$ . The position of the first peak does not vary with the temperature (see Fig. 3) although the second one shows a clear variation with a marked discontinuity around the  $T_g$  value of Ph, in the same sense as shown in Fig. 1 for the first peak of PVAc. Now, we have paid attention to the intensity of the two peaks, which is a parameter related to the density of the material. The second peak intensity varies with the temperature but the scatter of the results does not present any clear conclusion on the influence of the liquid-glass transition; surprisingly, it is the first low intensity peak that

shows a very clear variation between the glassy and liquid regions in the material (see Fig. 4). Some similar feature has been found for PC, structurally very similar to Ph because the existence of the bisphenol A group in the repeating unit, in the evolution of the area of a low intensity diffraction peak at  $0.7\text{\AA}^{-1}$  with the temperature<sup>5</sup>.

The main conclusion of these preliminary WAXS measurements around  $T_g$  in glassy polymers is that, although the structure of glass-forming liquids does not change in general through the glass transition, in the case of polymers the temperature behaviour of interchain correlations changes noticeably. The study of these changes would allow us to learn more about the physics behind these interchain correlations. Another important point, which is now investigated, is whether interchain correlations change with time at isothermal conditions below  $T_g$  (physical aging processes).

#### 4. Acknowledgements

This work has been carried out in the frame of "Acciones Integradas Hispano Británicas" 34 and 96A and is supported in part by CICYT project MEC MAT89-0186. Two of us (JJdV and JC) are grateful to the Gipuzkoako Foru Aldundia for partial financial support.

#### 5. References

1. E. W. Fischer and M. Dettenmaier, *J. Non-Crystalline Solids* **31** (1978) 181.
2. R. J. Roe and J. J. Curro, *Macromolecules* **16** (1983) 428.
3. J. J. Curro and R. J. Roe, *Polymer* **25** (1984) 1424.
4. G. R. Mitchell and A. H. Windle, *Colloid & Polym. Sci.* **263** (1985) 280.
5. H. H. Song and R. J. Roe, *Macromolecules* **20** (1987) 2723.
6. H. P. Klug and L. E. Alexander, *X-ray Diffraction Procedures* (Wiley, New York, 1974) p. 791.
7. G. R. Mitchell, in *Comprehensive Polymer Science*, eds. G. Allen, J. C. Bevington, C. Booth and C. Price (Pergamon Press, London 1989).

## QUASIELASTIC NEUTRON SCATTERING STUDY OF THE DYNAMICS OF THE $\alpha$ -RELAXATION IN POLYMERS.

J. COLMENERO, A. ARBE A. ALEGRIA and B. FRICK<sup>1</sup>.

Departamento de Física de Materiales, Universidad del País Vasco, Facultad de Química, Apdo. 1072, 20080, San Sebastián, SPAIN.

<sup>1</sup>Institute Laue-Langevin, 156X Av. des Martyrs, F-38042 Grenoble, FRANCE.

### ABSTRACT

The dynamics of the  $\alpha$ -relaxation in three glass-forming polymeric systems has been studied by means of quasielastic neutron scattering as well as by relaxation techniques. All data have been interpreted in terms of a Havriliak-Negami relaxation function,  $\Phi^*_{HN}$ . The results obtained indicate that the dynamics of the  $\alpha$ -relaxation in a wide timescale can be well described by means of the same spectral shape, i.e. the same Havriliak-Negami parameter values. Moreover, the Havriliak-Negami characteristic times deduced from the fitting of the experimental data can also be described using only one Vogel-Fulcher functional form. Then, this implies a self-consistent description of the dynamics of the  $\alpha$ -relaxation obtained by very different probes.

### 1. Introduction

During recent years, a great deal of effort has been made in the study of the dynamics of the  $\alpha$ -relaxation in very different glass-forming systems. From an experimental point of view, the main magnitudes characterizing the dynamics of the  $\alpha$ -relaxation are the different relaxation times associated to the different probes as well as the shape of the relaxation function. Nowadays, it is well experimentally established that the relaxation times follow a non-Arrhenius temperature behavior which can be parametrized by means of different functional forms. Moreover, the shape of the relaxation function shows a clear non-Debye behavior. Almost of these results have been obtained by means of standard relaxation techniques, like dielectric and mechanical spectroscopies or in some cases by means of Photon Correlation Spectroscopy, a light scattering technique in the time domain. All of these techniques cover a timescale ranging from about  $10^{-5}$  s to  $10^2$  s, i.e., a macroscopic range. Then a first question open to discussion is whether the results obtained by the abovementioned techniques can be extended or not to a more microscopical time scale, like the mesoscopic range ( $10^{-11}$ - $10^{-7}$  s). This time scale can be covered by Incoherent Quasielastic Neutron Scattering (QENS). In addition, this technique allows us to learn about how the magnitudes characterizing the dynamics of the  $\alpha$ -relaxation depend on  $Q$  (where  $Q$  is the modulus of

the change of the wavevector in a scattering experiment) in a Q-range roughly  $0.2 < Q < 5 \text{ \AA}^{-1}$ .

In this work we summarize the results obtained by means of QENS on the dynamics of the  $\alpha$ -relaxation of three different polymeric systems. These results are compared to the corresponding ones obtained by relaxation techniques in the same polymers.

## 2. Experimental

The samples investigated were poly(vinyl methyl ether) (PVME), poly(vinyl chloride) (PVC) and poly(bisphenol A, 2-hydroxypropylether) (PH). The glass-transition temperatures were determined by differential scanning calorimetry (DSC) resulting to be:  $T_g = 250 \text{ K}$  (PVME),  $T_g = 350 \text{ K}$  (PVC) and  $T_g = 358 \text{ K}$  (PH).

QENS measurements were carried out by means of the neutron backscattering spectrometers IN10 and IN13 at the Institute Laue Langevin (ILL) in Grenoble. The incident wavelengths used by us were  $\lambda = 6.28 \text{ \AA}$  (IN10) and  $\lambda = 2.23 \text{ \AA}$  (IN13), giving an energy resolution of  $\delta E \sim 1 \mu\text{eV}$  and  $\delta E \sim 8 \mu\text{eV}$  respectively. The Q-range covered was roughly between  $0.2$ – $2 \text{ \AA}^{-1}$  on IN10 and  $0.2$ – $5.4 \text{ \AA}^{-1}$  on IN13. The samples (thickness:  $0.15 \text{ mm}$ ) were filled in a cylindrical Al-container yielding a transmission of about 85 %. Typical measuring time at each temperature was 24 hours for IN10 and 36 hours for IN13. Initial data treatment was carried out in the normal way, correcting for effects of detector efficiencies, scattering from sample container, and instrumental background. The experimental curve for the incoherent scattering function  $S(Q, \omega)$  was finally obtained at each temperature as a function of the frequency change on scattering,  $\omega$ , and the modulus of the change of wavevector,  $Q$ .

## 3. Results

In the  $\alpha$ -relaxation range, the dynamics of the polymers investigated was detected by neutron scattering as a quasielastic broadening by IN10 and by IN13 at temperatures higher than  $T_g + 50 \text{ K}$ . The spectral shape for the three polymers was found to be clearly non-Lorentzian. In order to fit the QENS data we have followed the procedure previously developed for PVME [1]. We express the scattering function  $S(Q, \omega)$  in terms of the imaginary part of the Havriliak-Negami (HN) relaxation function  $\Phi_{\text{HN}}^*(\omega)$ ,

$$S_{\text{HN}}(Q, \omega) \propto -\frac{1}{\omega} \text{Im} [\Phi_{\text{HN}}^*(\omega)] = -\frac{1}{\omega} \text{Im} \left\{ \left[ 1 + [i \omega \tau_{\text{HN}}(Q, T)]^\alpha \right]^{-\gamma} \right\} \quad (1)$$

Here,  $\alpha$  and  $\gamma$  are two parameters in the range  $(0 < \alpha, \gamma < 1)$  characterizing the spectral shape and  $\tau_{\text{HN}}$  is a characteristic time of the relaxation process.

Constant spectral shape parameters ( $\alpha, \gamma$ ), i.e. independent of  $T$  and  $Q$ , were found to describe well the neutron scattering data within the experimental limitations. For each polymer, the spectral shape parameters obtained by QENS were similar to the values



measured by relaxation techniques [1,2,3]. Thus, the only Q- and T-dependent parameter seems to be the relaxation time  $\tau_{HN}(Q,T)$ . The values of  $\tau_{HN}(Q,T)$  were determined from the fitting of the experimental data of IN10 and IN13 by means of Eq. (1), allowing in addition for a flat background (FBG). Possible explanations for the latter are widely discussed in Ref. [1].

#### 4. Discussion

The Q-behavior of  $\tau_{HN}(Q,T)$  found is almost independent of the temperature for the three polymers investigated. This implies that the Q- and T- dependence of  $\tau_{HN}$  may be factorized as  $\tau_{HN}(Q,T) = a(T) \tilde{\tau}(Q)$ . Within the experimental errors, we may describe the Q-dependence of the relaxation times by a power law  $\tilde{\tau}(Q) \propto Q^{-n}$  with a n value depending on the system ( $n=4.6$  for PH,  $n=3.8$  for PVME, and  $n=9.5$  for PVC). A possible explanation of this "anomalous" Q-dependence of the relaxation time is discussed elsewhere (Ref. [4]).

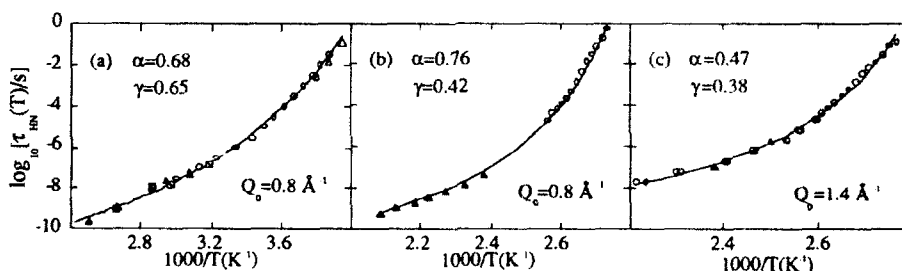


Figure 1 Temperature behavior of the HN relaxation times obtained from QENS ( $\blacktriangle$ ), dielectric ( $\circ$ ), mechanical ( $\Delta$ ), and NMR ( $\blacksquare$ ), for the  $\alpha$ -process of PVME (a), PH (b), and PVC (c). The corresponding shape parameters are also shown.

The temperature dependence of  $\tau_{HN}(Q,T)$  has been plotted in Fig. 1, for the three polymers, in comparison to the temperature behavior of the HN relaxation times obtained from relaxation techniques  $\tau_{HN}(T)$ . In this figure, we have plotted for each polymer the values of  $\tau_{HN}(Q,T)$  corresponding to the Q-value,  $Q_0$ , at which  $\tau_{HN}(Q,T)$  is similar to  $\tau_{HN}(T)$ , i. e., similar to the relaxation time at the same temperature obtained from relaxation techniques. It is clear that the values of  $\tau_{HN}(T)$  obtained by relaxation techniques have a temperature behavior very different from the corresponding one to an activated relaxation which can be well fitted by the Vogel-Fulcher (VF) law ( $\tau(T) \propto \exp[A/(T-T_0)]$ ). The same law fits the QENS data. The  $Q_0$ -values obtained allow us to define a spatial scale,  $\xi$ , associated to the  $\alpha$ -relaxation, as  $\xi \sim 2\pi/Q_0$ . The resulting  $\xi$  values were:  $\xi \approx 4.4 \text{ \AA}$  for PVC,  $\xi \approx 7.5 \text{ \AA}$  for PVME, and  $\xi \approx 9 \text{ \AA}$  for PH. These values are

in the range one can expect for the local conformational changes which can be considered as the "primitive" molecular motion of the  $\alpha$ -relaxation in the framework of the Coupling model [5]. However, this is only a speculation and more theoretical work is needed in order to clarify what is the physics behind these spatial scales.

## 5. Conclusions

Therefore, the main conclusion of this paper is that the dynamics above the glass-transition in a wide time scale ( $10^{-10}$ - $10^1$  s) can be well described by using similar "spectral shape", i.e. similar Havriliak-Negami parameters. Moreover, the characteristic time scale  $\tau_{HN}$  deduced from these fits can also be described by using only one Vogel-Fulcher functional form. Then, this implies a self-consistent description of the dynamics obtained by very different probes.

## 6. Acknowledgments

This work has been supported by the CICyT (project: MEC MAT89-0816) and by Gipuzkoako Foru Aldundia. One of us (A. Arbe) acknowledges the grant of the Basque Government.

## 7. References

- [1] J. Colmenero et al. *Phys Rev B* **44** (1991) 7321
- [2] J. J. del Val et al. *Makromol Chem* **190** (1989) 7321
- [3] A. Alegría et. al. (1991) being prepared
- [4] J. Colmenero et al. (1991) *Phys Rev Lett* (submitted)
- [5] K. L. Ngai and R. W. Rendell, *J. of Non Crystalline Solids* **131-133** (1991) 942

## PHYSICAL AGING AND DIELECTRIC RELAXATION IN A POLAR GLASSY POLYMER.

A. ALEGRIA, E. GUERRICA-ECHEVARRIA, I. TELLERIA  
and J. COLMENERO

Departamento de Física de Materiales, Universidad del País Vasco UPV/EHU  
Facultad de Química, Apdo. 1072, San Sebastián E-20080, Spain.

### ABSTRACT

The influence of physical aging on the dielectric  $\alpha$ -relaxation of poly(bisphenol A, 2-hydroxypropylether) was investigated. The dielectric  $\alpha$ -relaxation in the range  $T_g$  to  $T_g-30K$  was well described by means of the KWW law. The dependence of the characteristic time and the stretching exponent on temperature and physical aging was found. Comparison of these results with enthalpy recovery measurements allows the interpretation of some of the results obtained.

### 1. Introduction

Nowadays it is well known that a glassy system below its glass-transition temperature,  $T_g$ , is an unstable system which will have a slow decay towards the supercooled liquid-like equilibrium state.<sup>1</sup> This process is frequently known as physical aging and has usually been monitored by means of thermodynamic magnitudes as volume or enthalpy.<sup>2</sup> However, while this process is going on, other physical properties as the dielectric response in the case of polar systems, are also affected.<sup>3</sup>

In this work we have investigated the physical aging process just below  $T_g$  on poly(bisphenol A, 2-hydroxypropylether) (phenoxy). We have measured the dielectric relaxation below  $T_g$  as function of both the temperature and the physical aging. The enthalpy recovery during physical aging has also been measured. Results from both dielectric and enthalpic measurements are found to be consistent.

### 2. Experimental

The polymer studied was supplied by Union Carbide (grade PHKK). For this polymer the calorimetric  $T_g$  was determined from the middle point of the DSC scan at 10 K/min heating rate resulting to be 370 K.

For the dielectric measurements, a parallel plate capacitor filled with the sample was first heated above  $T_g$  and then cooled down at a constant rate (10K/min) until the temperature of measurement was reached. After a given waiting time  $t_w$  at this temperature, a constant d.c. voltage was applied during a polarization time  $t_p$ . Then, the

electric field was removed and the depolarization current as a function of time was measured by means of a Keithley 642 electrometer. The isothermal depolarization procedure (ID) described above can be used in the temperature range  $T_g$  to  $T_g - 40$  K.

A Perkin-Elmer DSC-4 set-up was used in order to study the enthalpy recovery in the  $T < T_g$  range. The relative enthalpy as function of the temperature was determined by integration of the  $C_p(T)$  curves as measured during a temperature scan at 10 K/min. The enthalpy recovery during the physical aging of the sample was obtained from the difference between two consecutive DSC-scans corresponding to the annealed and non-annealed samples respectively.

### 3. Results

As it was mentioned in the experimental section, the ID procedure involves that the pooling field should be applied during a finite interval of time  $t_p$ . In this conditions, the isothermal depolarization current is given by:

$$I(t) \propto -\frac{d}{dt} [\psi(t) - \psi(t+t_p)] \quad (1)$$

where  $\psi(t)$  is the time decay function corresponding to the dielectric relaxation.

The experimental  $I(t)$  behaviour was found to be very different from the corresponding to a Debye relaxation [ $\psi(t) = \exp(-t/\tau)$ ], however it was successfully described assuming a Kohlrausch-Williams-Watts (KWW) law<sup>4</sup> for  $\psi(t)$ :

$$\psi(t) = \exp\left[-\left(\frac{t}{\tau_{WW}}\right)^\beta\right] \quad (2)$$

Here  $\tau_{WW}$  is a characteristic time scale of the relaxation process and  $0 < \beta < 1$  is a parameter describing the stretching of the decay. Eqs. (1) and (2) allow to fit the  $I(t)$  data and to obtain the values of  $\tau_{WW}$  and  $\beta$  characterizing the dynamics of the dielectric  $\alpha$ -relaxation. Figure 1a shows the values of  $\tau_{WW}$  and  $\beta$  as a function of temperature for experiments performed on both, non-annealed samples cooled down at 10K/min from  $T > T_g$  (empty points) and samples annealed for long time at the measurement temperature (filled points). As can be seen, near  $T_g$  values of  $\tau_{WW}$  corresponding to annealed and non-annealed samples are very close each other, however, further below  $T_g$ ,  $\tau_{WW}$  values of the non-annealed samples are much more lower than the corresponding ones to the well annealed samples. On the other hand,  $\beta$  values corresponding to well annealed samples are close to 0.4 which corresponds to the  $\beta$  value measured above  $T_g$ ,<sup>5</sup> i.e. at equilibrium, while for the non-annealed samples  $\beta$  is in the range 0.45-0.55. The systematic differences between annealed and non-annealed samples make evident the influence of the physical aging in the dielectric relaxation and suggest the ID technique to be adequate to investigated such influence. We have performed a careful study of the influence of physical aging on the dielectric relaxation at 363 and 358 K. At these temperatures the effects of physical aging are clear and the

fully annealed state of the sample can be obtained in a reasonable time say, a week. As it is shown in Figs. 1b and 1c,  $\beta$  value continuously decreases as the physical aging is going on and achieves a nearly constant value for very long annealing times. On the other hand,  $\tau_{ww}$  values increase monotonously following a log-time kinetics until the limit value corresponding to the well annealed sample is reached. This last kind of kinetics has usually been found in the recovery behaviour of both enthalpy and volume during physical aging.<sup>2</sup>

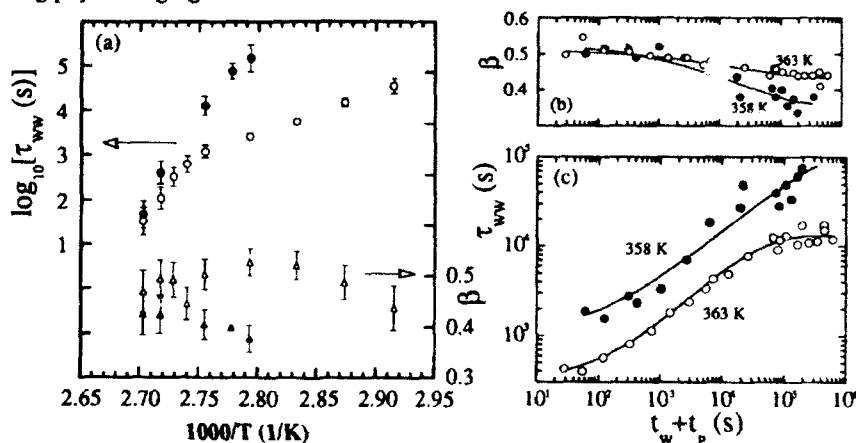


Figure 1. Behaviour obtained for  $\tau_{ww}$  and  $\beta$  below  $T_g$ , as function of  $T$  (a) and as function of annealing time (b) and (c). (see the text)

#### 4. Discussion

The physical aging influence on the time scale of the dielectric relaxation shown above can be qualitatively understood in the frame of the free-volume ideas. It is well established that physical aging leads to a decreasing of the free-volume in the sample, so assuming the Doolittle relationship between the relaxation time  $\tau_{ww}$  and the fractional free-volume  $V_F$

$$\tau_{ww} = \tau_0 \exp \frac{1}{V_F} \quad (3)$$

an increasing of the relaxation time with the aging process follows. However, there is no hint of how  $\beta$  can be affected by physical aging and by the glass transition itself.

On the other hand, Eq. 3 allows to obtain the  $V_F$  value from the dielectric relaxation experiments. To do this we have assumed  $\tau_0$  to be  $10^{-13}$  s of the order of magnitude of the reciprocal Debye frequency. Values obtained for  $V_F$  have been plotted in Fig. 2 as function of the aging time and compared with the enthalpy recovery data measured at the same temperatures. The aging time involved in the dielectric experiments has been estimated to be of the order of  $t_w + t_p + \tau_{ww}$ .<sup>6</sup> Figure 2, clearly shows that, in the

temperature range investigated, both set of data,  $V_F$  and  $\Delta H$ , overlaps perfectly within the experimental uncertainty supporting the relationship given by Eq. (3).

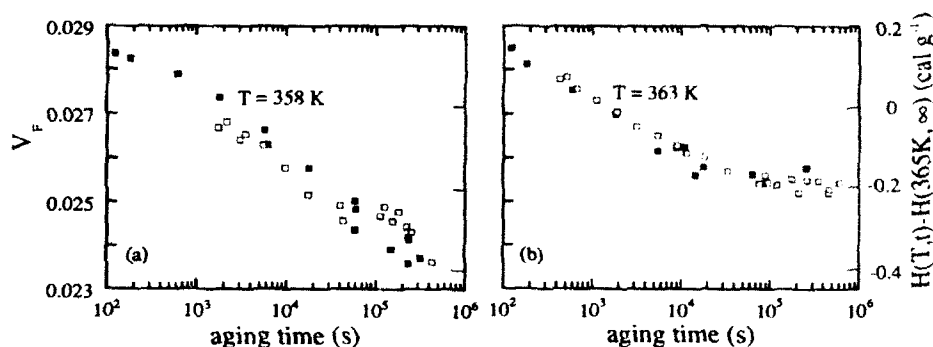


Figure 2. Comparison between the aging behaviour corresponding to recovery of both enthalpy (filled points) and fractional free volume obtained from the dielectric relaxation time (empty points).

## 5. Conclusions

The results presented above confirm previous ones obtained on other polymers.<sup>3,6</sup> The comparison between enthalpic recovery and dielectric results allows to rationalize only some of the observed behaviours. Therefore, more insight effort from both, experimental and theoretical points of view, is needed for a whole understanding of the dielectric behaviour around and below the glass transition.

## 6. Acknowledgments

This work has been supported by the CICyT (project: MEC MAT89-0816) and by Gipuzkoako Foru Aldundia. One of us (EG) acknowledges the grant of the Spanish Ministry of Education.

## 7. References

1. Struik L.C.E., *Physical Aging in Amorphous and Other Materials*, (Elsevier, Amsterdam, 1980).
2. *Physical Aging Processes in Molecular and Atomic Glasses*, NATAS conference, September 1983, *Pol. Eng. Sci.*, **24** (1984)
3. Alegría A., Goitiandía L., Tellería I. and Colmenero J.; in *Basic Features of the Glassy State*, eds. J. Colmenero and A. Alegría, (World Scientific, Singapore, 1990) p. 245.
4. Kohlrausch F., *Pogg. Ann. Phys.* **119** (1863)352. Williams G., Watts D.C., *Trans. Faraday Soc.* **66** (1970)80
5. To be published
6. Alegría A., Goitiandía L., Tellería I. and Colmenero, *J. Non-Cryst. Solids* **131-133** (1991)457.

## TEMPERATURE DEPENDENCE OF ENTHALPY RELAXATION PARAMETERS IN A FULLY CURED EPOXY RESIN

S. Montserrat Ribas

Laboratori de Termodinàmica i Físico-química

E.T.S.Enginyers Industrials de Terrassa, Universitat Politècnica de Catalunya

C. Colón 11, E-08222-Terrassa (Barcelona), Spain

### ABSTRACT

Various enthalpic relaxation experiments at different ageing temperatures  $T_a$  were conducted on a fully cured epoxy resin with a constant crosslinking density by differential scanning calorimetry. The enthalpy relaxation was found to increase gradually with ageing time  $t_a$  to a limiting value according to the loss of segmental mobility. The dependence of temperature was analysed in terms of the function of relaxation  $\phi(t)$  and the effective relaxation time  $\tau$ . Assuming that  $\tau$  is a function of  $T$  and enthalpy excess, three characteristic parameters of the enthalpic relaxation process can be determined ( $\ln A = 409.8$ ,  $C = 2.6$  g/J, and  $E_a = 1249$  kJ/mol).

### 1. Introduction

A fully cured epoxy resin has two characteristic aspects: its crosslinked nature and its glassy state. The chemical crosslink between functional groups gives the network structure and the thermosetting properties of the material. As a consequence of their glassy nature, epoxy resins can undergo structural relaxation or physical ageing<sup>1</sup> at annealing temperatures below  $T_g$ , despite its network structure<sup>2,3</sup>.

The main goal of this work is to study the temperature dependence of the ageing parameters in the enthalpic relaxation process of a fully cured resin, with a constant crosslinking density. The ageing parameters studied are enthalpy relaxation, relaxation function and the effective relaxation time.

### 2. Experimental Part

The epoxy resin used in this study was of the diglycidyl ether of bisphenol-A type (CIBA-GEIGY Araldite CY225) cured with a derivate of phthalic anhydride with accelerator (CIBA-GEIGY HY225). The curing conditions were 130°C for 8 h in order to obtain a fully cured epoxy resin. The calorimetric study of the curing process has been reported in a previous paper<sup>4</sup>.

The samples were submitted to the following thermal history: Annealing at  $T_0 = 130^\circ\text{C}$  for 5 minutes, quenched to ageing temperature ( $T_a$ ), kept at this temperature for time  $t_a$  and quenched in air down to  $T_1 = 20^\circ\text{C}$ . The aged sample was then scanned in a Mettler TA 4000 equipped with a DSC 30 Differential Scanning Calorimetry module at a heating rate of  $10^\circ\text{C}/\text{min}$  from 20 to  $130^\circ\text{C}$ . In order to measure enthalpy relaxation  $\Delta h$ , the sample was submitted to a quenching from 130 to  $20^\circ\text{C}$  and reheated at the same rate of  $10^\circ\text{C}/\text{min}$  without ageing (reference DSC scan). The difference between both scans

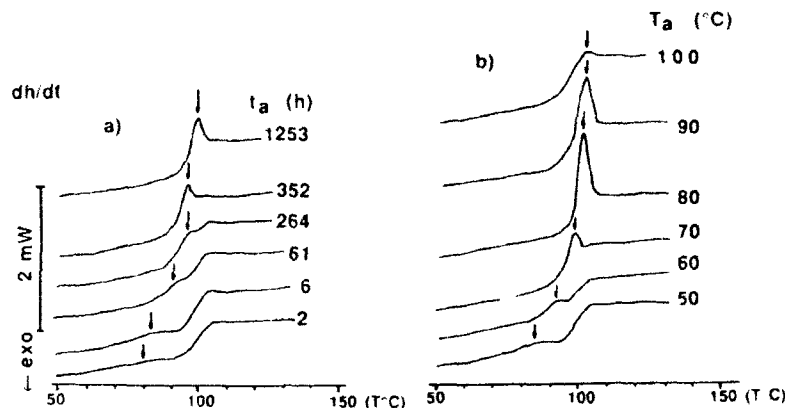


Figure 1. DSC curves of epoxy resin: (a) aged at  $T_a=50^{\circ}\text{C}$  for various ageing times; (b) aged 10 h for various  $T_a$ .

allows us to determine  $\Delta h$ :

$$\Delta h = \int_{T_1}^{T_0} (c_{p, \text{aged}} - c_{p, \text{ref}}) dT \quad [1]$$

where  $c_{p, \text{aged}}$  and  $c_{p, \text{ref}}$  are the specific heat capacities of the aged sample and of the sample in the reference DSC scan respectively. The glass transition temperature was  $98.5^{\circ}\text{C}$  measured as the halfpoint of the  $\Delta c_p$  value in the reference DSC scan,  $\Delta c_p$  being the difference between the specific heat of glassy state ( $c_{p, g}$ ) and liquid state ( $c_{p, l}$ ) respectively.

### 3. Results and Discussion

At low ageing temperatures ( $T_a = 50$  or  $60^{\circ}\text{C}$ ) an endothermic peak appears well below the glass transition whose position, size and intensity are strongly dependent on ageing time (Fig. 1). This peak grows like a shoulder within the glass transition region, increases in magnitude with  $t_a$ , and finally appears clearly as a peak superposed on the high part of  $T_g$ . At higher ageing temperatures ( $70$  to  $90^{\circ}\text{C}$ ) the peak appears superposed on  $T_g$  for practically all the ageing times. This *sub- $T_g$*  or *main peak* has been reported both in thermoplastic<sup>5-7</sup> and thermosetting<sup>2,3</sup> polymers. The behaviour of this peak can be described by phenomenological models taking into account a distribution of relaxation times.

For each  $T_a$ , the enthalpy relaxation  $\Delta h$  increases with the annealing time and tends to have a limiting value which depends on  $T_a$  (Fig. 2). This behavior is similar to that observed in thermoplastic polymers as a consequence of the segmental mobility decrease when the system approaches the metastable equilibrium state. The segmental mobility in thermosets can be located mainly on chain segments between crosslinks and end-chain segments. The possible presence of non-reticulated polymer or excess of hardener can have a plasticizer effect, and increase the segmental mobility.



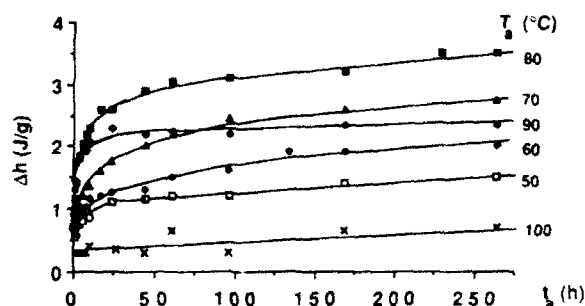


Figure 2. Dependence of enthalpy relaxation on the ageing time for various  $T_a$ .

Theoretically, the limiting value of enthalpy relaxation ( $\Delta h_\infty$ ) should decrease with  $T_a$ , but experimentally we found that this limiting value tends to increase with  $T_a$  till a maximum, and to further decrease when  $T_a$  approaches  $T_g$ . This increase observed at low  $T_a$  (50, 60 and 70°C) is due to the limitation of ageing periods used. The maximum extent of the relaxation process has been observed at  $T_a=80^\circ\text{C}$ .

An analysis of temperature dependence on enthalpy relaxation can be made by the effective relaxation time concept  $\tau$ :

$$\phi(t_a) = \exp\left(-\frac{t_a}{\tau}\right) \quad [2]$$

where  $\phi(t_a)$  is the relaxation function defined by the equation:

$$\phi(t_a) = 1 - \frac{\Delta h}{\Delta h_\infty} \quad [3]$$

$\Delta h_\infty$  being the limiting enthalpy relaxation which can be obtained by an extrapolation of the liquid enthalpy curve of the reference unaged sample from the equation:

$$\Delta h_\infty = \int_{T_a}^{T_o} (c_{p,l} - c_{p,ref}) dT \quad [4]$$

The parameter  $1/\tau$  is a measure of the rate of relaxation of the system as it approaches metastable thermodynamic equilibrium. For each  $T_a$ , the parameter  $1/\tau$  can be obtained from rearrangement of Eq. 2 with the relaxation function  $\phi(t_a)$  previously calculated from Eq. 3, which yields:

$$\frac{1}{\tau} = -\frac{1}{t_a} \ln[\phi(t_a)] = -\frac{1}{t_a} \ln\left[1 - \frac{\Delta h}{\Delta h_\infty}\right] \quad [5]$$

Figure 3 shows the dependence of  $\ln(1/\tau)$  on the excess of enthalpy defined as  $\delta = \Delta h_\infty - \Delta h$ . The effective recovery time  $\tau$  increases with the extent of the relaxation process because the segmental chains lose mobility. The variation of  $\tau$  with  $\phi(t)$  decreases when  $T_a$  approaches  $T_g$ .

Assuming that  $\tau$  is a function of both temperature and excess of enthalpy via:

$$\ln(1/\tau) = \ln A + c\delta - E_a/RT_a \quad [6]$$

three characteristic parameters of the enthalpic relaxation process can be determined:

$$\ln A = 409.8 \quad c = 2.6 \text{ g/J} \quad E_a = 1249 \text{ kJ/mol}$$

where  $E_a$  is an apparent activation energy which is in good correspondence with other values of  $E_a$  calculated by this method in thermoplastics.  $E_a$  value calculated in this epoxy resin is higher than that calculated in amorphous poly(ethylene terephthalate) (860 kJ/mol)<sup>6</sup> and in polystyrene (1192 kJ/mol)<sup>9</sup>, probably due to the network structure.

However, this method assumes a single relaxation time, and some discrepancies are found when these values are compared with the experimental ones (Fig. 3). A better fit to ageing data can be obtained when an equation of the Williams-Watts type is applied, but this is the subject of a separate publication.

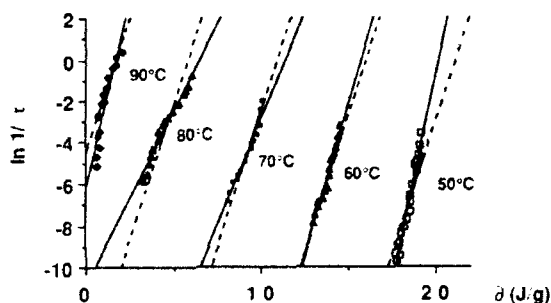


Figure 3. Representation of  $(\ln 1/\tau)$  vs. excess of enthalpy ( $\delta$ ) for different ageing temperatures calculated by Eq. 2 and 3 (solid line), and by Eq. 5 (broken line).

#### 4. Acknowledgements

Financial support has been provided by the "Plan Nacional de Nuevos Materiales" of the CICYT (Project num. MAT 89/0282 ).

#### 5. References

1. L.C.E. Struik, *Physical Aging in Amorphous Polymers and other Materials*(Elsevier, Amsterdam, Oxford, New York, 1978).
2. Z. H. Ophir, J. A. Emerson and G L Wilkes, *J. Appl. Phys.* **49** (1978) 5032.
3. E. S. Kong, *Adv. Polym. Sci.* **80** (1986) 125.
4. S. Montserrat, in *Basic Features of Glassy State*, ed. J.Colmenero and A.Alegria (World Scientific, Singapore, 1990) p. 371.
5. A.R. Berens and I.M. Hodge *Macromolecules* **15** (1982) 756.
6. S. Montserrat and P. Cortés, *Makromol. Chem. Macromol. Symp.* **20/21** (1989) 389.
7. M. Rudy and J.M. Hutchinson, *Polym. Commun.* **29** (1988) 132.
8. A.J. Kovacs, J.J. Aklonis, J.M. Hutchinson and A. R. Ramos, *J. Polym. Sci., Polym. Phys. Ed.* **17** (1979) 1097
9. S.E.B. Petrie, *J. Polym. Sci. Part A-2* **46** (1972) 1255.

## MOLECULAR DYNAMICS IN PVAc STUDIED BY RELAXATION TECHNIQUES AND PHOTON CORRELATION SPECTROSCOPY.

F. ALVAREZ, A. ALEGRIA, J. M. ALBERDI and J. COLMENERO

Departamento de Física de Materiales, Universidad del País Vasco UPV/EHU  
Facultad de Química, Apdo. 1072, San Sebastián E-20080, Spain.

### ABSTRACT

A comparative study of the  $\alpha$ -relaxation of poly(vinyl acetate) PVAc by means of different relaxation techniques (dielectric and mechanical spectroscopies and nuclear magnetic resonance, NMR) and quasielastic light scattering (photon correlation spectroscopy, PCS) is presented here. As in other glass-forming systems, the results obtained indicate a clear non-Debye behaviour of the  $\alpha$ -relaxation. However in this case, the dynamical behaviour observed does not show universality. Moreover, the shape of the relaxation depends on temperature implying a breakdown of the principle of time-temperature superposition.

### 1. Introduction

The dynamics of the  $\alpha$ -relaxation in glass-forming systems above and near their glass-transition temperature has been a subject of increasing interest over the last years. Now, it is well experimentally established that the relaxation times associated to the different probes follow a non-Arrhenius temperature behaviour which can be parametrized by different functional forms. Moreover, the shape of the relaxation functions show a non-Debye behaviour. However, in spite of these results, several questions still remain unclear. One interesting point is if the dynamics of the  $\alpha$ -relaxation shows universality, i.e., if the results obtained by different probes behave in a similar way. Another point open to controversy is whether the shape of the relaxation is temperature dependent or not. With these ideas in mind we have investigated the dynamics of the  $\alpha$ -relaxation in poly(vinyl acetate) PVAc, by combining several relaxation techniques and a time-domain light scattering technique, photon correlation spectroscopy, P.C.S.

### 2. Experimental

A PVAc, purchased from Aldrich-Chemie (ref. 18.949-9), was studied by the different techniques mentioned above. The glass transition temperature  $T_g$  of the sample as measured by Differential Scanning Calorimetry was 40 °C. The sample was made optically pure by preparing it by freeze-drying.

The PCS measurements were performed with an argon ion Spectra Physics laser operating at a wavelength of  $\lambda = 488$  nm. Intensity autocorrelation functions,  $g(t)$ , were measured in the time range  $10^{-6}$  -  $10^2$  s on a ALV-3000 correlator. The temperature range measured was from 35 to 70 °C. Dielectric spectroscopy measurements of the susceptibility,  $\chi^* = \chi' - i\chi''$  were performed by means of a lock-in amplifier EG&G PAR 5208 scanning the frequency in the range 5 -  $10^5$  Hz at isothermal conditions between 40

and 90 °C. The transient currents, a dielectric time domain technique, was also used in order to cover the time range 1 - 10<sup>5</sup> s. Dynamic mechanical measurements were carried out on a DMTA Polymer Lab. apparatus. The complex mechanical modulus,  $E^* = E' + iE''$ , was recorded in the frequency range 10<sup>-2</sup>-10<sup>2</sup> Hz at isothermal condition between 35 and 50°C. On the other hand, NMR experiments were carried out by means of a Varian VXR-300 spectrometer. Carbon spin-lattice relaxation times  $T_1$  and  $T_{1\rho}$  were measured at 75.4 MHz in the temperature range 145 to 190°C.

### 3. Results

PCS data have been analyzed by assuming a Kohlrausch-Williams-Watts (KWW) stretched exponential form for the autocorrelation function of the scattered field, i.e.

$$\psi(t) = \exp[-(t/\tau)^\beta]; \quad 0 < \beta < 1 \quad (1)$$

where  $\beta$  is a shape parameter and  $\tau$  is a characteristic time scale. Equation (1) has also been assumed to describe the time decay of the electric polarization. On the other hand, all the relaxation data in the frequency domain were fitted assuming a Havriliak-Negami (HN) functional form for the normalized relaxation function:

$$\Phi^*(\omega) = \frac{1}{[1 + (i\omega\tau_{HN})^\alpha]^\gamma} \quad 0 < \alpha, \gamma < 1 \quad (2)$$

Here  $\alpha$  and  $\gamma$  are also shape parameters and  $\tau_{HN}$  the HN relaxation time. We have shown in a previous paper<sup>1</sup> that the HN relaxation function could be considered as a good analytical approximation of the Fourier transformation of the KWW function. In that paper we obtained some empirical relationship between the HN parameters and the KWW ones. Then, we have interpreted all of our results in terms of the KWW dynamical parameters  $\beta$  and  $\tau$ .

Figure 1a shows the intensity correlogram obtained by PCS and corresponding to the 50°C temperature. The contribution of the  $\alpha$ -relaxation has been described by means of the KWW law (Eq. 1). The line in Fig. 1a stands for the fitting with the shown KWW parameters.

The isothermal dielectric curves have been fitted by means of the HN description as was mentioned above [ $\chi^*(\omega) - \chi(\infty) \propto \Phi^*(\omega)$ ]. An extra imaginary term, inverse in frequency, was also used to account for the d.c. conductivity. Fig 1b shows an example of the fitting of dielectric losses corresponding to 73°C. The analysis for the mechanical data was similar but in this case the relation  $E(\infty) - E^*(\omega) \propto \Phi^*(\omega)$  is the one to be applied. Fig. 1c shows an example of the fitting of the loss modulus at 45°C.

The NMR  $T_1$  relaxation times were also analyzed in terms of HN function following the procedure described in ref. 2. In Fig. 1d the experimental  $T_1$  are plotted versus temperature. In this case HN shape parameters were chosen to account for the experimental value of  $T_1$  at the minimum. Then, fixing the  $\alpha$  and  $\gamma$  parameters, a  $\tau_{HN}$  value can be straightforwardly obtained from  $T_1$  or  $T_{1\rho}$  experimental data.

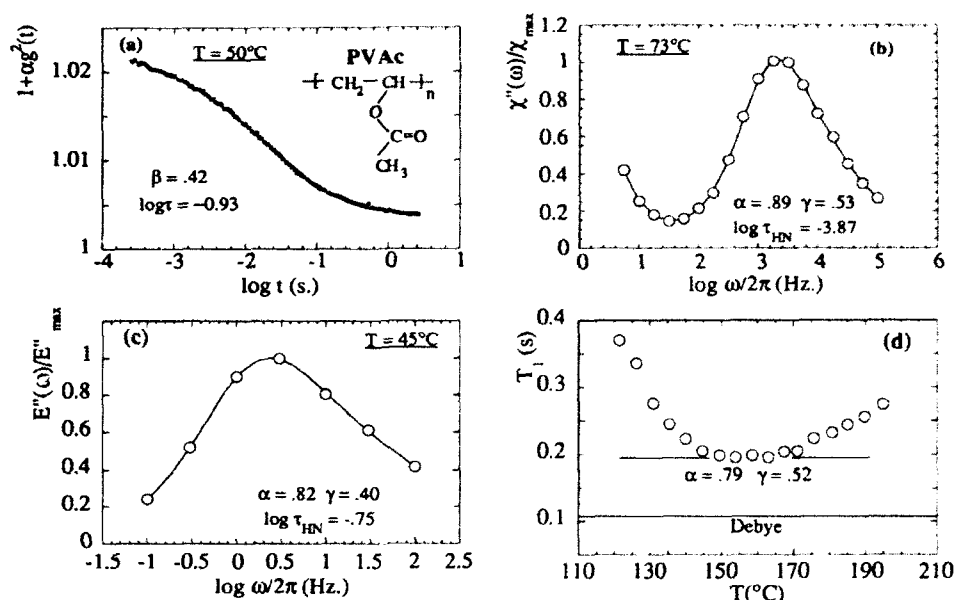


Figure 1. Some examples of the experimental data and their fitting by using KWW (a) and HN (b), (c), and (d) equations. For more details see the text.

As abovementioned, all the HN parameters corresponding to the fitting of relaxation data were converted to the KWW ones. The values of the KWW parameters  $\tau$  and  $\beta$  so obtained are shown in Fig. 2 as a function of the inverse of temperature. The main features shown in this figure are: i) PCS and dielectric  $\tau$  values overlap perfectly within the experimental uncertainty, while the mechanical and the NMR data fall aside. Moreover, it appears that the mechanical data could be extrapolated to the NMR ones. ii) There is a systematic temperature dependence of the dielectric  $\beta$  values which are higher than one could expect from the PCS, mechanical and NMR ones. However, the temperature dependence obtained for the dielectric  $\beta$  behaviour agrees with recent studies of the dielectric  $\alpha$ -relaxation<sup>3</sup> on a wider frequency and temperature range but on a PVAc sample of a different source.

#### 4. Discussion

It appears that, opposite to results corresponding to other glass-forming polymeric systems,<sup>2</sup> the dynamics of the  $\alpha$ -relaxation in PVAc does not show universality. Both, the temperature behaviour and the shape of the relaxation obtained by different probes, are different. Moreover, the measured shape parameter values are temperature dependent. This implies a breakdown of the principle of time-temperature superposition. Possible explanations of this behaviour are now being outlined. First of all, the quite

long side group of the monomer of PVAc could imply that two different local molecular processes were involved in the  $\alpha$ -relaxation. On the other hand, in the framework of the coupling-model ideas,<sup>4</sup> the  $\beta$  parameter is directly related to the interchain cooperativity involved in the  $\alpha$ -relaxation. Then, our results could suggest two different interchain interactions. This would be in agreement with the results obtained by X-ray diffraction as a function of temperature around  $T_g$ . The static structure factor  $S(q)$  of PVAc shows two clear interchain peaks which display different temperature behaviour around  $T_g$ .<sup>5</sup> These speculations, i.e., different molecular processes and different interchain correlations, could also explain the found temperature behaviour of  $\beta$ .

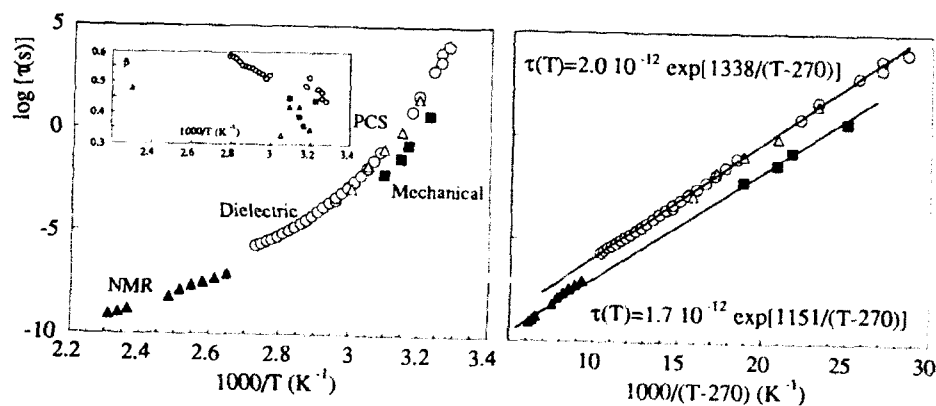


Figure 2. a) Temperature dependence of the KWW parameters. b) Vogel-Fulcher plot of  $\tau(T)$  [ $\tau(T) \propto \exp[A/(T-T_0)]$ ]. All the data can be fitted by using the same  $T_0$ .

## 6. Acknowledgments

This work has been supported by the CICyT (project: MEC MAT89-0816) and by Gipuzkoako Foru Aldundia. One of us (FA) acknowledges the grant of the Basque Department of Education and thanks the MPI für Polymerforschung for the allowance to perform the PCS measurements.

## 7. References

1. Alvarez F., Alegria A. and Colmenero J., *Phys. Rev. B* **44** (1991) 7306.
2. Colmenero J., Alegria A., Alberdi J.M. and Alvarez F., *Phys. Rev. B* **44** (1991) 7321.
3. Schönhals, Kremer F. and Schollosser E., *Phys. Rev. Lett.* **67** (1991) 999.
4. Ngai K. L., Plazek D., *J. Polym. Sci. Part B: Polymer Physics*, **24** (1986) 619.
5. del Val J.J. et al. *X-ray diffraction in glassy polymers around  $T_g$* . This Workshop.

## INFLUENCE OF THE STRETCHING ON THE MOLECULAR DYNAMICS OF GLASSY POLY(VINYL CHLORIDE)

A. Elicegui, J. J. del Val and J. Colmenero

Departamento de Física de Materiales, Univ. País Vasco, Apdo. 1072,  
20080 San Sebastián, SPAIN.

V. Bellenger and J. Verdu

ENSAM, 151 Bvd. de l' Hôpital, F75640 Paris, FRANCE.

G. Martinez and J. L. Millán

Instituto de Ciencia y Tecnología de Polímeros, C. S. I. C., Juan de la  
Cierva 3, 28006 Madrid, SPAIN.

### ABSTRACT

We present some results concerning the molecular mobility of Poly(Vinyl Chloride) (PVC) in different stretched and non-stretched PVC samples. Two relaxation modes,  $\beta$  (local motions) and  $\alpha$  (cooperative motions), have been studied by means of a dynamic dielectric spectroscopy. The raw results do not show a strong influence of the stretching but an analysis of data in terms of Havriliak-Negami empirical distribution and William-Watts relaxation function show that both the macroscopic relaxation times and their distribution are slightly changed with the stretching in the two relaxation process.

### 1. Introduction.

In the last years, the conformational microstructure of Poly(Vinyl Chloride) (PVC) has been shown to play an important role in a great part of its physical and chemical properties<sup>1</sup>; moreover, the microstructure of PVC has been correlated to the molecular dynamics in the Glass Transition temperature ( $T_g$ ) region<sup>2,3</sup>.

On the other hand, irreversible local conformation changes produced by the orientation of PVC chains (mainly, isotactic GTTG- triads are transformed in isotactic GTTT triads) have been recently determined by means of infrared spectroscopy<sup>4</sup>.

In this way, we have begun to study the influence of these conformational changes, induced by the stretching, on the molecular dynamics of PVC. We show here the first results obtained by means of dynamic dielectric spectroscopy.

### 2- Experimental

PVC used was polymerized at 70°C with molecular weight  $M_n = 29300$  and slightly isotactic character (22.4% of isotactic triads). PVC films were oriented by stretching above  $T_g$  at elongation ratios of 1.5 and 2.5 and quenched under tension. Prior to all measurements stretched samples were heated at 386K during one hour under vacuum in order to eliminate the deformation produced during the orientation process; however, the length of the samples is not completely recovered after this high temperature treatment (they remain some 9% larger).

Calorimetry measurements, performed on a Perkin Elmer DSC4 calorimeter, showed that the  $T_g$  value was not changed with the stretching. Wide Angle X-ray Scattering (WAXS) measurements, carried out at room temperature in a Philips powder

diffractometer with a vertical goniometer and a graphite monochromator using  $1.54\text{\AA}$  ( $\text{Cu K}\alpha$ ) radiation, show that there is some structural difference between non-stretched and recovered stretched PVC samples: in addition to the interchain structural correlations<sup>5</sup> shown by PVC at scattering vector values of  $s=1.75\text{\AA}^{-1}$  and  $s=1.35\text{\AA}^{-1}$ , stretched samples present a new low intensity peak at longer distances corresponding to  $s=0.5\text{\AA}^{-1}$ . This structural change and the remanent deformation in the samples could, but it is not sure up to date, be a consequence of the irreversible local conformational changes above mentioned.

Molecular motions were studied by means of dynamic dielectric spectroscopy by measuring the real  $\epsilon'$  and imaginary  $\epsilon''$  parts of the complex dielectric constant

$$\epsilon^* = \epsilon' - i\epsilon'' \quad (1)$$

The measurements were carried out between 100K and 400K with a frequency range between 1Hz and  $10^5$ Hz in an experimental set-up described elsewhere<sup>3</sup>.  $\alpha$  (cooperative mobility) and  $\beta$  (local mobility) relaxation processes are measured with these conditions.

### 3- Results

Fig. 1 shows the frequency evolution of the imaginary part  $\epsilon''$  of the dielectric constant at different temperatures corresponding to  $\alpha$  and  $\beta$  relaxations of PVC. The same type of isothermal evolutions have been obtained for 1.5 and 2.5 stretched PVC samples.

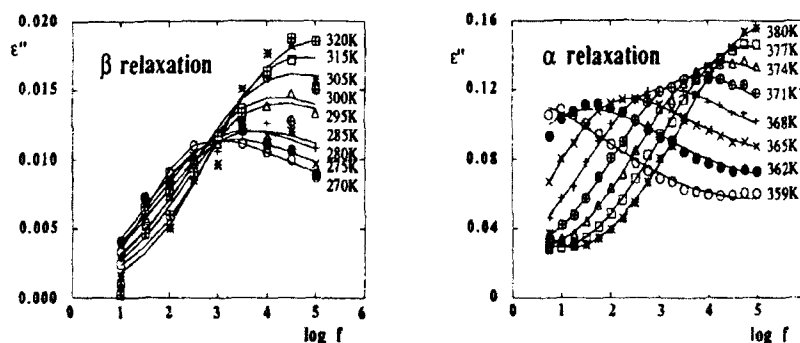


Fig. 1. Isothermal results obtained for non-stretched PVC in  $\beta$  and  $\alpha$  relaxations. Solid lines show the respective fittings to a HN distribution function.

$\alpha$  relaxation, corrected from AC conductivity and from the influence of the  $\beta$  process which is very broad and overlapped to the  $\alpha$  one, and  $\beta$  relaxation  $\epsilon''$  data have been fitted to the Havriliak-Negami (HN) empirical distribution function

$$\frac{\epsilon^*(\omega) - \epsilon_\infty}{\epsilon_s - \epsilon_\infty} = \phi^*(\omega) = \left[ 1 + (i\omega\tau)^\alpha \right]^{-\gamma} \quad (2)$$

where  $\epsilon_s - \epsilon_\infty$  is the relaxation strength,  $\alpha$  and  $\gamma$  are two parameters characterizing the shape of the relaxation ( $0 < \alpha, \gamma < 1$ ) and  $\tau$  is the characteristic relaxation time. In a recent paper<sup>6</sup>, it has been shown that HN relaxation function can be considered as a good analytical approximation of the numerical Fourier transformation of the Kolrausch-Williams-Watts (WW) time domain relaxation function where  $\tau_{ww}$  is the WW relaxation time and  $\beta$  ( $0 < \beta < 1$ ) a parameter giving account of the separation from a Debye process.



$$\psi(t) = \exp \left[ - \left( \frac{t}{\tau_{ww}} \right)^\beta \right] \quad (3)$$

In the above mentioned reference, a procedure was developed for transforming  $\alpha$ ,  $\gamma$  and  $\tau_{HN}$  parameters into  $\tau_{ww}$  and  $\beta$  ones. Here, we follow this procedure and discuss all of our results in terms of  $\tau_{ww}$  and  $\beta$  values.

#### 4- Discussion

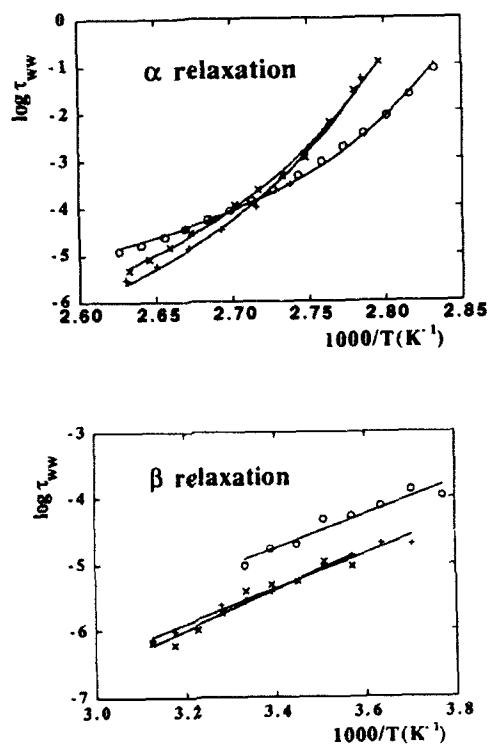


Fig.2. Variation of the macroscopic relaxation time in  $\alpha$  and  $\beta$  relaxations for non-stretched (+), 1.5(x) and 2.5(o) stretched PVC. Solid lines show the respective fittings to Vogel-Fulcher and Arrhenius equations.

Fig. 2 shows the evolution of  $\tau_{ww}$  values against the reciprocal temperature for all the polymers. The temperature behaviour of  $\tau_{ww}$  is Vogel-Fulcher type

$$\tau_{ww} = \tau_0 \exp[A/(T-T_0)] \quad (5)$$

in the  $\alpha$  region and Arrhenius type

$$\tau_{ww} = \tau_0 \exp(E/KT) \quad (6)$$

in the  $\beta$  region.

In any case,  $\beta$  values indicate a marked non-exponential character of the two dielectric relaxation processes in the three samples. Nevertheless, one can find some variation between non-stretched and stretched PVC. The values of the parameters obtained from the respective fittings of  $\tau_{ww}$  to Eqs. 5 and 6, as well as the respective  $\beta$  values are shown in Table I.

One can observe that both,  $\alpha$  and  $\beta$  dielectric relaxation processes of PVC, are altered after elongation (see Table I).

In the case of  $\beta$  relaxation no drastic changes are found for  $\beta$  parameter and for the activation energy, but the time scale for the molecular motion is markedly altered, nearly by one decade, in the case of the highest elongation ratio.

In  $\alpha$  relaxation region,  $\beta$  parameter is appreciably increased in the case of the highest elongation ratio. The  $\tau_{ww}(T)$  behaviour is linearized by the same  $T_0$  value of 334K; this is in accordance with the fact that  $T_g$  value does not show appreciable changes within the non-stretched and stretched samples. On the other hand,  $\tau_0$  and  $A$  values show marked differences between the 2.5 elongated sample and the two other ones.

elongation rate	$\alpha$ relaxation				$\beta$ relaxation		
	$\log \tau_0(s)$	$A(K^{-1})$	$T_0(K)$	$\beta$	$\log \tau_0(s)$	$E(eV)$	$\beta$
x1.0	-10.6	527	334	0.220	-14.4	0.53	0.182
x1.5	-9.9	486	334	0.223	-15.8	0.61	0.168
x2.5	-7.5	286	334	0.265	-13.4	0.51	0.182

Table I. Values of  $\beta$  parameter and of fitting parameters for macroscopic  $\tau_{ww}$  relaxation times to Vogel-Fulcher and Arrhenius laws in  $\alpha$  and  $\beta$  relaxations respectively.

Before a definite conclusion for these relaxation results, a very careful characterization, now in progress, of the tacticity and the distribution of GTTG- isotactic triads in the stretched polymers is needed in order to correlate the structural change from WAXS and the changes in the relaxation processes to the above mentioned conformational changes, even if the samples do not recover their initial length with the high temperature treatment.

## 5. Acknowledgements

Three of us (AE, JdV and JC) thank Gipuzkoako Foru Aldundia for partial financial support.

## 6. References

1. J. L. Millán, G. Martinez, C. Mijangos, A. Mendez, J. M. Gomez-Elvira and M. Gomez-Daza, *Makromol. Chem., Macromol. Symp.* **20/21** (1988) 49.
2. J. J. del Val, J. Colmenero, C. Mijangos, G. Martinez and J. L. Millán, *Makromol. Chem.* **190** (1989) 893.
3. J. J. del Val, A. Alegría, J. Colmenero, C. Mijangos, G. Martinez and J. L. Millán, *Makromol. Chem.* **190** (1989) 3257.
4. V. Bellenger, J. Verdu, G. Martinez and J. L. Millán, *Polym. Degrad. and Stab.* **28** (1990) 53.
5. G. R. Mitchell, in *Comprehensive Polymer Science*, eds. G. Allen, J.C. Bevington, C. Booth and C. Price (Pergamon Press, London 1989).
6. F. Alvarez, A. Alegría and J. Colmenero, *Phys. Rev. B* **44** (1991) 7306.

## DYNAMIC MECHANICAL RELAXATIONS OF AN AMORPHOUS COPOLYESTER

R. BENAVENTE, J.M. PEREÑA, E. PEREZ, A. BELLO

Instituto de Ciencia y Tecnología de Polímeros (CSIC)

Juan de la Cierva, 3. 28006 Madrid. Spain

and

V. LORENZO

E.T.S. de Ingenieros Industriales

José Gutiérrez Abascal, 2. 28006 Madrid. Spain

### ABSTRACT

Differential scanning calorimetry (DSC) and dynamic mechanical thermal analysis (DMTA) have been employed in order to study the influence of a plasticizer agent on the relaxations of an amorphous copolyterephthalate (COP). The results show that the higher temperature relaxation can be identify with the glass transition and the secondary relaxation, which location is diluent content ( $w_1$ ) independent, tends toward being suppressed when  $w_1$  increases.

### 1. Introduction

The addition of low molecular weight diluents to polymers (plasticization) alters to a greater or lesser extent their physical properties depending on the nature of the interactions between polymer and solvent and on the plasticizer content. Because of the fundamental and technological implications of relaxations in polymers, the influence of the plasticizers on these transitions have been deeply investigated by using different experimental techniques. In line with this, the aim of this paper is to report and discuss some results about the mechanical relaxations of an amorphous plasticized copolyterephthalate.

### 2. Experimental part

The polymer used in this work was a commercially available amorphous copolyester that was supplied by Eastman. The composition of this copolymer was 3:1

(weight ratio) of poly (ethylene terephthalate) and poly (1,4 cyclohexylenedimethylene terephthalate). Tricresylphosphate (mixture of isomers, supplied by Bayer), TCP, was selected as plasticizer.

The details of sample preparation and DSC measurements have been reported elsewhere<sup>1</sup>.

Viscoelastic relaxations were measured with a MK II Dynamic Mechanical Thermal Analyser manufactured by Polymer Laboratories. The complex modulus and the loss tangent of each sample were determined at 3, 10 and 30 Hz over a temperature range from -140 to 150°C with a heating rate of 2°C/min. The maximum values of the loss modulus and the loss tangent are considered to measure the intensity of the relaxations. The apparent activation enthalpy values were calculated from the slopes of the straight lines log frequency vs reciprocal absolute temperature, according to an Arrhenius type equation.

### 3. Results and discussion

Dynamic mechanical analysis shows that the neat copolymer and the plasticized samples present two viscoelastic relaxations that are affected to a great extent by the addition of plasticizer (Fig. 1). The temperature of appearance of the  $\alpha$  relaxation is higher than that of the  $\beta$  dispersion and the former decreases monotonically with the increase of the plasticizer concentration. The Tg values that were previously obtained by means of DSC measurements<sup>1</sup> are compared with the  $\alpha$  peak temperature in Fig. 2. The excellent agreement between these two sets of data allows one to identify the  $\alpha$  relaxation with the glass transition. Even more, the broadening and lowering of the  $\alpha$  peak with the increasing plasticizer content, and the apparent activation enthalpy for this relaxation (it ranges from 300 to 380 kJ/mole, depending on the diluent content) are features of a glass transition.

The  $\beta$  dispersion for the unplasticized COP, which takes place around -70°C (3 Hz), is a complex relaxation that has been previously studied<sup>2</sup>. The addition of TCP does not shift this relaxation to a lower temperature even for plasticizer content as great as 29 %wt. Regression methods indicate that the apparent activation enthalpy for this peak (60 kJ/mole) does not depend on the diluent content. These facts seem to indicate the intramolecular nature of the  $\beta$  relaxation. It is important to point out that the intensity of the  $\beta$  peak decreases linearly when TCP content increases (Fig. 3 and 4) and this relaxation almost vanishes for the highest diluent concentration. Similar behaviours have been reported for secondary relaxations in other polymer-solvent

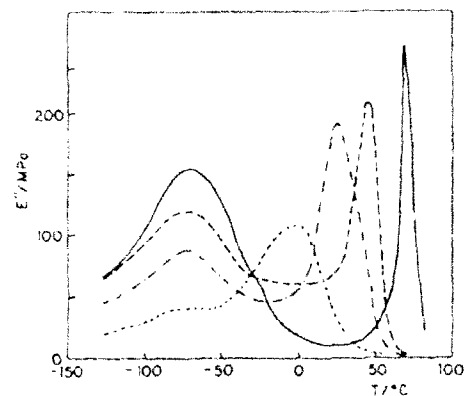


Fig. 1: Temperature dependence of the loss modulus  $E''$  at 3 Hz for some plasticized samples (plasticizer content: — 0%, - - 8%, - · - 16% and · · · 29%).

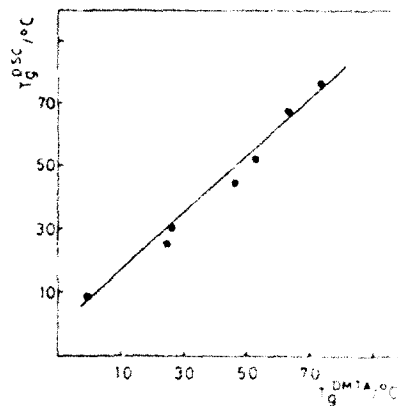


Fig. 2: Comparison between the calorimetric glass-transition temperature,  $T_g^{\text{DSC}}$ , and the mechanical relaxation temperature,  $T_g^{\text{DMTA}}$ .

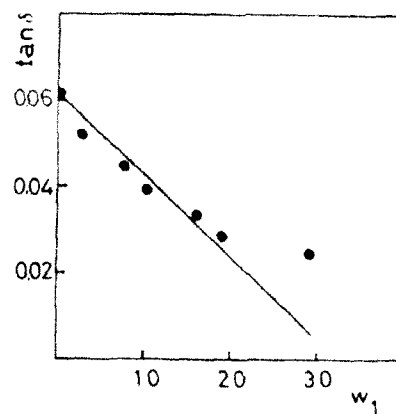
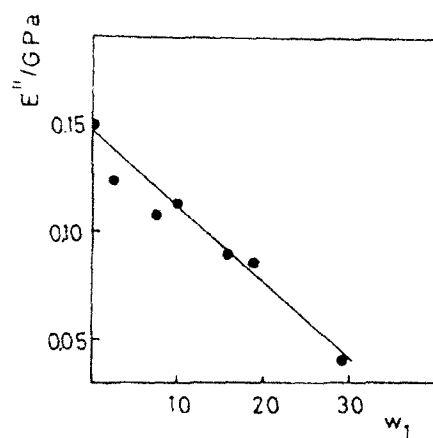


Fig. 3 and 4: Relationships between the diluent content,  $w_1$ , and the loss modulus,  $E''$  (left), and the loss tangent,  $\tan \delta$  (right).

systems and were related to antiplasticization. Several authors have discussed this phenomenon and different explanations for the hindrance of the local motions that are responsible of the sub-T<sub>g</sub> transition have been proposed: increase of the cohesive energy density or filling of polymer free volume by diluent molecules. The insensitivity of the temperature of the  $\beta$  peak maximum to the variation of the TCP content and the constancy of the apparent activation enthalpy seem to point out that the decrease in the intensity with the increasing diluent concentration is mainly due to the diminishing concentration of the groups participating in the local motions.

#### 4. Conclusions

The  $\alpha$  relaxation of plasticized COP corresponds to the glass transition. The  $\beta$  relaxation can be assigned to intramolecular movements because its location and activation energy do not depend on diluent content. The decrease of the intensity of this relaxation when TCP concentration increases can be explained in terms of a dilution effect.

#### 5. Acknowledgement

The financial support of the CICYT is gratefully acknowledged (Projet: MAT91-0380).

#### 6. REFERENCES

- 1.- R. Benavente, J.M. Pereña, E. Pérez, A. Bello and V. Lorenzo, in *Basic Features of the Glassy State*, ed. J. Colmenero and A. Alegría (World Scientific, Singapore, 1995) p. 494.
- 2.- R. Benavente and J.M. Pereña, *Makromol. Chem.* **189** (1988) 1207.
- 3.- W.J. Jackson and J.R. Caldwell, *J. Appl. Polym. Sci.* **11** (1967) 211.
- 4.- L.M. Robeson and J.A. Faucher, *J. Polym. Sci. Part B* **7** (1969) 59.

## DYNAMIC MECHANICAL BEHAVIOUR OF VINYL ALCOHOL-ETHYLENE COPOLYMERS

M.L. CERRADA, J.M. PEREÑA, R. BENAVENTE, E. PÉREZ, A. BELLO

Instituto de Ciencia y Tecnología de Polímeros

Juan de la Cierva 3, 28006-Madrid.

### ABSTRACT

Dynamic mechanical analysis is carried out on vinyl alcohol-ethylene copolymers with high content in the former component, capable of being used for gas barrier applications. Three relaxation have been found, which temperature locations and activation energies have been studied and compared with those of the corresponding homopolymers, poly(vinyl alcohol) and low-density polyethylene.

### 1. Introduction

The copolymers of vinyl alcohol and ethylene (VAE) with molar fraction of the former component ranging from 0.6 to 0.8, are used increasingly as barrier layers for packaging foods and pharmaceutical. These recent applications of those materials, which were firstly synthesized long time ago, have prompted the study of the structure-dependent properties of the VAE copolymers. The gas barrier properties of these materials are strongly affected by both vinyl alcohol and water contents, which can be studied by using different approaches, one of the most sensitive being dynamic mechanical analysis. Thus, the aim of the paper is to study the influence of the copolymer composition on the mechanical relaxations.

### 2. Experimental

VAE copolymers are obtained by hydrolizing the corresponding vinyl acetate-ethylene copolymers. Three commercial VAE samples, coded B, C and D, have been

studied. In addition to these, the two homopolymers, poly(vinyl alcohol) and low-density polyethylene (samples A and E, respectively), have been also studied for comparative purposes. Similar thermal histories were reproduced in a differential scanning calorimeter Perkin-Elmer DSC-7.

The determination of the molar fraction of vinyl alcohol was carried out by  $^1\text{H}$  and  $^{13}\text{C}$  NMR in a Varian XL-300 spectrometer, in solutions of DMSO at  $90^\circ\text{C}$ .

Polymer granules were placed in a Collin press fitted with smooth-polished plates and hot-pressed at 1 MPa and  $210^\circ\text{C}$  for 5 min. The cooling process, under the same pressure, was carried out following two different routes, either by quenching the molten copolymer with water or by slowly cooling it to room temperature (average cooling rate  $1.5^\circ\text{C min}^{-1}$ ). The samples thus obtained are named quenched and crystallized, and coded Q and S, respectively.

The complex modulus, resolved into its storage and loss components, has been measured over the temperature range from  $-150$  to  $150^\circ\text{C}$ , by using a Dynamic Mechanical Thermal Analyser MK II, manufactured by Polymer Laboratories, working in the tensile mode at 3, 10 and 30 Hz. Activation energies were calculated from the shift of the relaxation temperatures with frequency, according to the usual Arrhenius-type equation. The absolute error of the activation energy value is obtained by assuming a maximum variation of  $\pm 0.5^\circ\text{C}$  in the location of the relaxation temperatures, operating with loss modulus vs. temperature plots.

### 3. Results and Discussion

VAE copolymers display two clear relaxations, taking place about  $-20^\circ\text{C}$  and  $50^\circ\text{C}$ , respectively. Moreover, low-density polyethylene shows relaxations around  $-120^\circ\text{C}$  and  $-20^\circ\text{C}$  and poly(vinyl alcohol) at  $-60^\circ\text{C}$  and  $70^\circ\text{C}$ . The actual values are listed in Table I, following the greek alphabet convention for naming the relaxations in decreasing temperature order.

The  $\alpha$  relaxation is considered as the glass transition of the two VAE copolymers and the poly(vinyl alcohol) sample, due to its sharpness, to the correspondingly strong



decrease of the storage moduli at the relaxation maximum and to the high value of the activation energy. Moreover, the temperature of this  $\alpha$  relaxation increases with the vinyl alcohol content, approaching the glass transition temperature of poly(vinyl alcohol).

The crystallization process of the samples has no apparent consequences on the material, considering the DSC results. However, dynamic mechanical analysis show an increase of the temperature location of the  $\alpha$  relaxation when the samples are crystallized, together with a slight widening of the maximum. The latter effect can be due to the overlapped presence of the enhanced  $\alpha$  relaxation of low density polyethylene, which takes place in the same temperature interval for the crystallized samples<sup>1</sup>.

TABLE I

Temperatures ( $^{\circ}\text{C}$ , at 3 Hz, E" basis) and activation energies ( $\text{kJ mol}^{-1}$ ) of the different relaxations, for samples with various vinyl alcohol contents ( $f_{\text{VA}}$ ).

Sample	$f_{\text{VA}}$	$T_{\gamma}$	$\Delta H_{\gamma}$	$T_{\beta}$	$\Delta H_{\beta}$	$T_{\alpha}$	$\Delta H_{\alpha}$
A	1	-	-	-64.5	37	71.5	> 400
B-Q	0.77	-	-	-26.5	146	40	> 400
B-S	0.77	-	-	-25	68	49.5	> 400
C-Q	0.73	-	-	-26	122	36.5	> 400
C-S	0.73	-	-	-17	280	44	> 400
D-Q	0.62	-130*	42	-35	82	34	> 400
D-S	0.62	-130*	42	-42	54	39	> 400
E	0	-120	50	-20	40	50	100

\*Weak maximum

The  $\beta$  relaxation is very broad for all the samples studied. In the case of pure poly(vinyl alcohol) (sample A), the temperature location and activation energy of the  $\beta$  relaxation are typical of a small amount of absorbed water. A similar water-sensitive

relaxation is also displayed by other polymers as polyamides and polyimides<sup>2</sup>. However, the  $\beta$  relaxation of the VAE copolymers is not so broad as that of poly(vinyl alcohol), it appears at higher temperature and its activation energy is also higher. Due to these facts, the  $\beta$  relaxation of the VAE copolymers can be considered more akin to the corresponding of low-density polyethylene, produced by motions in the interfacial region, which is mainly showed by branched polymers and copolymers at nearly constant temperature for similar interfacial contents.

The samples DQ and DS also display a weak maximum around -125°C. This temperature value and the low activation energy of the relaxation are features of the relaxation, produced by crankshaft movements of chains containing sequences of three or more methylenic units. Due to the requirement of polymethylenic sequences, the  $\gamma$  relaxation is only displayed by the sample with the highest ethylene content.

Summing up, VAE copolymers display three relaxations. The  $\gamma$  one only appears for samples with the highest ethylene content. The  $\beta$  relaxation seems to be produced by motions in the interfacial content. Finally, the  $\alpha$  one is the glass transition of the copolymers and it tends to the  $T_g$  of poly(vinyl alcohol). The presence of a water-sensitive relaxation in this polymer makes feasible, that the  $\beta$  relaxation of VAE copolymers can be affected by absorbed water and this possibility is presently investigated.

#### 4. Acknowledgement

The financial support of the CICYT (project IN89-0066) is gratefully acknowledged.

#### 5. References

- 1.- R. Benavente, J.M. Pereña, A. Bello, E. Pérez, C. Aguilar, M.C. Martínez, *J. Mater. Sci.* **25** (1990) 4162.
- 2.- J.M. Pereña, *Angew. Makromol. Chem.* **106** (1982) 61.

LOCAL DEFORMATION INHOMOGENEITY IN DYNAMIC MECHANICAL  
BEHAVIOUR OF BLOCK COPOLYMERS

A.D.VILESOV\*, V.P.VOLODIN, I.V.KENUNEN

Institute of Macromolecular Compounds, Academy of Sciences,  
St.Petersburg, Russia

\*Present address: Institute of Technical and Macromolecular  
Chemistry, University of Hamburg, Germany

N.STRIBECK, H.G.ZACHMANN

Institute of Technical and Macromolecular Chemistry  
University of Hamburg, Germany

ABSTRACT

Models which describe the relationship between macroscopic complex modulus and the spatial inhomogeneities of the properties of block copolymers are presented. Both the inhomogeneity of the composition of the interfacial layers and the distribution of local deformations were investigated. The structures of block copolymer samples were studied by X-ray scattering employing synchrotron radiation at HASYLAB in Hamburg.

1. Introduction

The temperature dependence of the loss modulus  $G''(T)$  of block copolymers (BC) forming domain structures cannot be described within the models which only take into account the homogeneous properties of the components. In this paper we propose an approach which also considers the inhomogeneities of the properties. The calculations are compared with the experimental data obtained for butadiene-styrene block copolymers.

2. Results and Discussion

In the previous publications<sup>1,2</sup> the role of the interfacial layers was investigated. The composition of the layer where the components were mixed varied in space<sup>2</sup> and hence its dynamic mechanical properties were spatially inhomogeneous. The interfacial layer was presented as a composition

of  $n$  phases. There was obtained:

$$G^*(T) = G'(T) + iG''(T) = (G_a^* G_b^*)^{1/2} \quad (1)$$

$G_a^* = (\sum_i^n f_i / G_i^*)^{-1}$ ,  $G_b^* = \sum_i^n f_i G_i^*$  are complex moduli of the regions of the sample where domains are oriented to the external force perpendicular or parallel,  $n$  is number of phases,  $f_i$ ,  $G_i^*$  are the volume fraction and the modulus of  $i$ -phase. In the model and in the experiment we varied the absolute and relative fractions of the interfacial layer. Good description of the relative changes of  $G'(T)$  and  $G''(T)$  was obtained<sup>3</sup>. However the experimental values of  $G''(T)$  in the range between  $T_g$  of the components were much higher.

Next we investigated the role of the spatial distribution of stresses. Each inclusion of a certain component acts as a stress concentrator in the medium of another component<sup>4</sup>. It produces different amplitudes of deformation in different volume elements. Assuming that we can write the modulus of the composite:

$$G_k'' = G'' \sum_i (e_i / e)^2 V_i / V \quad (2)$$

$G''$  is modulus for a given component,  $e_i$  is amplitude of deformation for  $i$ -th volume element,  $V_i / V$  is volume fraction of  $i$ -element.  $B_i^{-1} = e_i / e$  characterises the change of the amplitude of deformation.

The values of  $G_k'$  and  $G_k''$  measured by torsional pendulum at frequency of 1 Hz are presented in Fig.1. Calculated values are denoted by points. The corresponding values of  $B_i$  are indicated by numbers.

From these data one can conclude that in the temperature range between  $T_g$  of the components the mechanical model of the type (1) with constant  $B_i$  is quite good for quantitative description of the experimental data.

The domain structures of the BC were studied by small angle X-ray scattering employing synchrotron radiation at HASYLAB in Hamburg. The data concerning with the structure

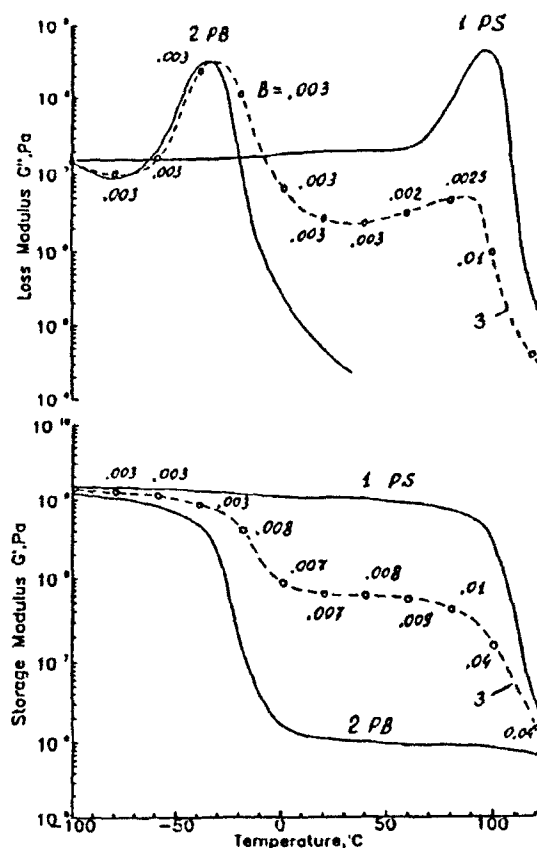


Fig.1. Dynamic storage modulus and loss modulus vs temperature for polystyrene (curve 1), polybutadiene (2) and styrene-butadiene BC (3). Calculated values are denoted by points with  $B_i$  values numbers.

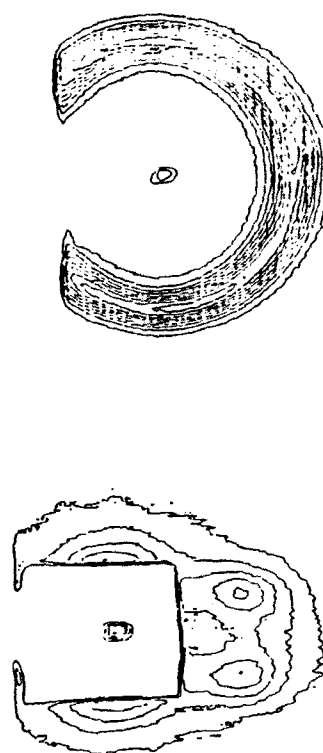


Fig.2. Two-dimensional scattering pattern of three-block copolymer sample as obtained by the VIDICON detector (HASLAB)  
1 - without elongation  
2 - 100% elongation.

are necessary to choose the proper parameters for the mechanical model. Using the Vidicon system<sup>5</sup> it is possible to obtain a two-dimensional scattering pattern. The stretching of the sample which causes the orientation of the domains enables one to get a detailed information about the struc-

ture. Typical scattering patterns of three-block copolymer sample forming the domain structure of hexagonally packed cylinders are presented in Fig.2. The long period of the structure is  $285\text{\AA}$ .

### 3. Conclusions

The model which takes into account the spatial distribution of the interfacial layer composition allows to obtain a quite good description of the relative changes of the storage and loss moduli due to variation of the relative fractions of the interfacial layer. Complete quantitative description of these moduli is possible if one takes into account the spacial distribution of the amplitudes of deformation in the sample.

Acknowledgment: This work was in part supported by the German Federal Minister of Science and Technology (BMFT) under the contract number 05405HXB. One of the authors (A.V.) thanks the Deutsche Forschungsgemeinschaft for financial support.

### 4. References

1. Ju.S.Lipatov, Physical Chemistry of Filled Polymers (Nauka, Moscow, 1977).
2. N.M.Khasilov, A.D.Vilesov, V.P.Volodin and et.al., Vysokomol.soed. 31(1989)1745.
3. N.M.Khasilov, A.D.Vilesov, V.P.Volodin and et.al., Vysokomol.soed.32(1990)19.
4. K.Zener, Elasticity and anelasticity of metals (Chicago, 1948).
5. G.Elsner, C.Riekell and H.G.Zachmann, Adv.Pol.Sci. 67(1985).

## STUDY OF THE MOLECULAR DYNAMICS IN PVME/PH MISCIBLE BLENDS BY MEANS OF NUCLEAR MAGNETIC RESONANCE

J. M. ALBERDI, M. F. LORENZO and J. COLMENERO

Departamento de Física de Materiales, Universidad del País Vasco UPV/EHU  
Facultad de Química, Apdo. 1072, San Sebastián E-20080, Spain

### ABSTRACT

In this work we have investigated how the dynamical behaviour of one homopolymer in a mesoscopic time scale changes when this homopolymer is blended with another one. The miscible system investigated has been PVME / PH. The technique used by us was NMR. We have measured  $^{13}\text{C}$  spin-lattice relaxation time  $T_1$ . The results obtained have been interpreted in the framework of the coupling model.

### 1. Introduction

We have investigated the molecular dynamics in a miscible (only one glass-transition process) glass-forming polymer system Poly(vinyl methyl ether) / Poly(2-hydroxypropylether of Bisphenol A) (PVME/PH) by means of  $^{13}\text{C}$  nuclear magnetic resonance, i.e., in a mesoscopic time scale ( $10^{-7}$ - $10^{-10}$ s). The magnitude measured was the temperature behaviour of the  $^{13}\text{C}$  spin-lattice relaxation time  $T_1$  at a frequency of 75.4 MHz. The main advantage of NMR technique over other relaxation techniques is that  $^{13}\text{C}$  NMR allows us to follow the relaxation behaviour of a given carbon. In our case we have followed the relaxation behaviour of both, the CH group of PVME and the protonated carbons of the phenyl groups of PH. This procedure gives the opportunity to study how the dynamics of one of the components of the blend is affected by the presence of the other component.

### 2. Experimental

The homopolymers used by us were: PH from Union Carbide (PKHH), average molecular weights  $\bar{M}_n = 18000$  and  $\bar{M}_w = 50600$ , and PVME from Aldrich Chemical Co.,  $\bar{M}_n = 6520$  and  $\bar{M}_w = 21900$ , previously purified. Blends of these two homopolymers were prepared by solution casting with dioxane as the solvent. The polymer concentration in the solution was about 20%. Dioxane evaporation was conducted first in air at room temperature and then in a vacuum oven at 50 °C. Final preparation of the NMR samples included heating in the vacuum oven at a temperature 80-100 °C above the glass transition of the corresponding blend.

The following compositions were worked out (by PVME/PH weight percentage): 100/0, 80/20, 65/35, 50/50, 35/65, 20/80 and 0/100.

NMR measurements were carried out on bulk blends by means of a Varian VXR-300 spectrometer. Carbon spin-lattice relaxation times  $T_1$  were measured at 75.4 MHz with a 10-mm probe by using the technique of the inversion-recovery of the magnetization. Values of the relaxation times were obtained from exponential regression of the magnetization as a function of the recovery time. The highest temperature covered in this study was 200 °C.

### 3. Results

Figure 1 shows the temperature evolution of  $T_1$  experimental values corresponding to the abovementioned carbons in PVME (Fig. 1a) and in PH (Fig. 1b).

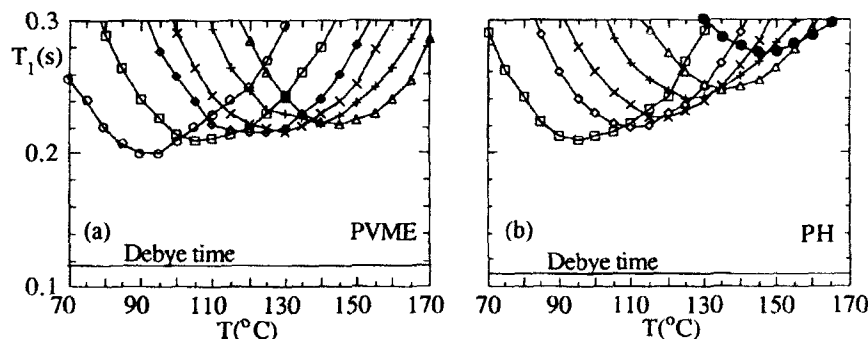


Fig. 1. Experimental values of  $T_1$ , (a) PVME and (b) PH, as a function of the composition of the blends, O 100/0, □ 80/20, ◇ 65/35, × 50/50, + 35/65, Δ 20/80, ● 0/100 (by PVME / PH weight percentage).

With the assumption of a purely  $^{13}\text{C}$ - $^1\text{H}$  dipolar relaxation mechanism  $T_1$  is given by<sup>1</sup>

$$\frac{1}{T_1} = \frac{\hbar^2 \gamma_C^2 \gamma_H^2}{r_{CH}^6} [3J(\omega_C) + 6J(\omega_H + \omega_C) + J(\omega_H - \omega_C)] \quad (1)$$

where  $\omega_C$  and  $\omega_H$  are the Larmor frequencies for carbon and proton respectively,  $\gamma_C$  and  $\gamma_H$  are the gyromagnetic ratios and  $r_{CH}$  is the carbon-proton internuclear distance; we have used  $r_{CH} = 1.09 \text{ \AA}$  for PVME<sup>2</sup> and  $r_{CH} = 1.076 \text{ \AA}$  for PH.

$J(\omega)$  is the spectral density function which is defined as the Fourier transform of the self correlation function  $G(t)$  of the C-H relative orientation. Fig. 1 represents the values (Debye time) predicted by a single exponential correlation function which turns out to be much lower than the experimental ones.

Taking into account recent experimental results on the dynamics of  $\alpha$ -relaxation in glass-forming systems<sup>3</sup>, we have assumed a stretched exponential form for  $G(t)$ ,  $G(t) = \exp[-(t/\tau_{ww}(T))^\beta]$ . Here  $\tau_{ww}$  is a characteristic time scale and  $\beta$  is a parameter  $0 < \beta < 1$  which accounts for the separation of  $G(t)$  from a single exponential decay. In previous papers<sup>3,4</sup> we have shown that the Fourier transformation of this  $G(t)$  can be well analytically described by means of a Havriliak-Negami spectral density function. Then, by



using this Havriliak-Negami  $J(\omega)$  and following the procedure described in ref. 3 we have obtained the  $\beta$  and  $\tau_{ww}$  values which fits the experimental minima of  $T_1$  shown in Fig. 1 to Eq. 1.  $\beta$  values found for both, CH group of PVME and the protonated carbon of the phenyl group of PH, are plotted in Fig. 2 as a function of the blend composition.

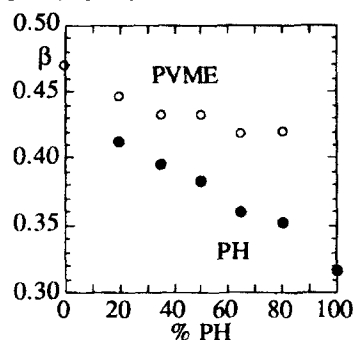


Fig. 2. Evolution of the  $\beta$  parameter as a function of the blend composition.

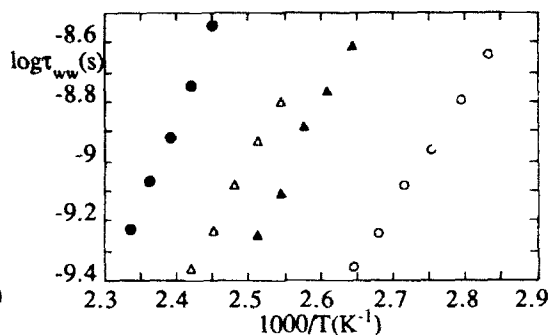


Fig. 3. Temperature evolution of the characteristic time  $\tau_{ww}$  in the homopolymers ( $\blacktriangle$  PH,  $\triangle$  PVME), and in the 50/50 blend ( $\bullet$  PH,  $\circ$  PVME). See the text.

It has been recently reported<sup>5</sup> that the  $\beta$ -values could be temperature dependent in polymer blends. Then, in order to avoid this problem, we have obtained the temperature dependence of  $\tau_{ww}(T)$  only in a narrow temperature window (20 °C) around the temperature of the minimum of  $T_1$  corresponding to each blend. The corresponding  $\beta$ -value can be considered approximately constant in such a range. Fig. 3 shows the temperature behaviour of  $\tau_{ww}(T)$  around the minimum of  $T_1$  corresponding to the two homopolymers and the 50/50 blend. Fig. 4 shows the dependence of the apparent activation energies,  $E_a$ , on the composition.  $E_a$  was calculated from the temperature behaviour of  $\tau_{ww}$  around the temperature of the minimum of  $T_1$ .

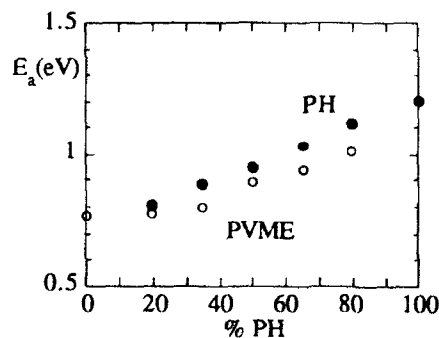


Fig. 4. Apparent activation energy,  $E_a$ , as a function of the blend composition.

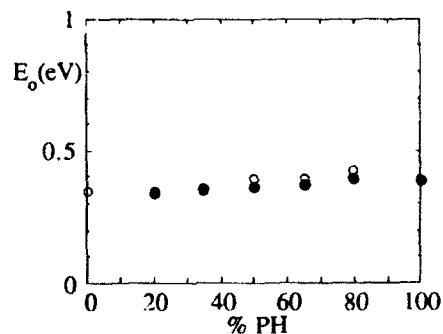


Fig. 5. Microscopical activation energy,  $E_o$ , as a function of the blend composition.

#### 4. Discussion

First of all from the data shown in figures 2-4 we can conclude that blending of two homopolymers clearly modify the dynamical behaviour of each of ones at the time scale investigated. The  $\beta$  value of pure PVME (0,47) is higher than the  $\beta$  value of pure PH (0,32). Fig. 2 shows that  $\beta$  value of PVME decreases with the PH content in the sample, while  $\beta$  value of PH increases with the content of PVME. The temperature behaviour of  $\tau_{ww}$  shown in figures 3 and 4 evolves in a similar way, for example the activation energy of PVME increases with the content of PH while the activation energy of PH decreases with the PVME content. With this respect we can speak about the dynamical miscibility in a mesoscopic time scale.

On the other hand, we can try to interpret the results obtained in the framework of the coupling model proposed by Ngai <sup>6</sup>. In this framework  $\beta$  is a measure of the degree of intermolecular (interchain in the case of polymers) cooperativity associated with the relaxation processes. The measured relaxation time,  $\tau_{ww}$ , is related to the coupling parameter,  $n = 1 - \beta$ , as

$$\tau_{ww} = [(1 - n) \omega_c^n \tau_0]^{\frac{1}{1 - n}} \quad (2)$$

where  $\tau_0$  is a "microscopical relaxation time" and  $\omega_c$  is a cut-off frequency ( $\sim 10^{10} \text{ s}^{-1}$ ). Then, following this model we can calculate the activation energy corresponding to the microscopical process,  $E_0$ , from the apparent activation energy measured ( $E_0 = E_a \cdot \beta$ ). The results obtained are shown in Fig. 5. As can be seen  $E_0$  is almost independent of the composition for both PVME and PH, as one can expect for the microscopic (primitive) process in the framework of the coupling model.

#### 5. Acknowledgments

We thank J. J. Irui for doing molar mass measurements in PVME. This work has been supported by the UPV 206.215-E032/90 Project. We thank Gipuzkoako Foru Aldundia for partial financial support. M. F. Lorenzo also acknowledges the grant of the Basque Department of Education.

#### 6. References

1. M. Mehring, *Principles of High Resolution NMR in Solids* (Springer-Verlag, Berlin, 1983) Chap. 8.
2. R. Dejean de la Batie, F. Lauprêtre and L. Monnerie, *Macromolecules* **21** (1988) 2045
3. J. Colmenero, A. Alegría, J. M. Alberdi, F. Alvarez and B. Frick, *Phys. Rev.* **B44** (1991) 7321, and references therein.
4. F. Alvarez, A. Alegría and J. Colmenero, *Phys. Rev.* **B44** (1991) 7306.
5. C. M. Roland and K. L. Ngai, *Macromolecules* (in press).
6. K. L. Ngai, *Comm. Solid State Phys.* **9** (1980) 127.

## NON-LINEAR CREEP AND THE EFFECT OF FREE VOLUME.

J. MAIA <sup>1</sup>, A. M. VELHO <sup>1</sup>, and A. C. DIOGO <sup>1,2</sup>

<sup>1</sup> Centro de Física da Matéria Condensada (INIC), Av. Gama Pinto 2,  
1699 Lisboa Codex, Portugal

<sup>2</sup> Dep. Eng. Materiais, Instituto Superior Técnico, Av. Rovisco Pais,  
1096 Lisboa Codex, Portugal

### ABSTRACT

It is shown that, through the generalization of the Cohen-Grest free volume theory performed before by the authors, it is possible to compute the creep compliance  $J(t)$  of a polymer by assuming that the free volume depends on the applied stress. As the stress increases, the creep compliance becomes stress-dependent, and this dependence can be computed. These results are compared to experimental data on polypropylene.

### 1. Introduction.

In recent work <sup>1</sup>, it has been shown that, by a suitable generalization of the Cohen-Grest free volume theory <sup>2</sup>, one could compute the order parameter and temperature dependence of a complete set of nematic viscosities for nematic polymers, either in equilibrium <sup>1</sup>, or in the out of equilibrium region close to the glass transition temperature <sup>3</sup>. An interesting feature of the model is that it tends asymptotically to the well known W.L.F. behaviour without showing the unphysical divergence below  $T_g$ . Another one is that, in general, time-temperature superposition is only approximately valid in the high temperature region.

In this paper we consider the situation where the free volume depends on the applied stress. In the next section, the main theoretical results will be presented. According to the parameters of the model, as the stress increases there is a departure from linear behaviour and the creep compliance starts to exhibit a stress dependent behaviour. It shall be noticed that this behaviour is an intrinsic feature of the model and there is no need to consider additional free parameters. In section 3, these results are discussed and compared to experimental data on polypropylene. At last, in section 4, the main conclusions are presented.

### 2. Main theoretical results.

The main arguments of the model are the following ones. It is assumed that for every segment there is associated a cell of volume  $v$  which is the sum of the segment volume  $v_c$  and the free volume  $v_f = v - v_c$ . The exchange of free volume within a cluster of contiguous liquid-like cells (i.e. cells for which  $v_f > 0$ ) is assumed to be free, and the motion of one segment is only possible provided there is available a minimum free volume  $v_m$  within the cluster it belongs. The average free

volume  $\bar{v}_f$  may be computed by considering the free energy as a functional of the distribution function of free volume  $\rho(v_f)$ , normalized to the fraction of liquid-like cells,  $p$ . For  $p > p_c$  an infinite liquid-like cluster is present so the material shows liquid behaviour;  $p = p_c$  yields the glass transition where an infinite solid cluster appears, and the corresponding temperature shall be  $T_0$ ; for  $p < p_c$ , ( $T < T_0$ ), the segment motion is strongly hindered but yet possible up to  $0^\circ\text{K}$  where  $\bar{v}_f = 0$ . In equilibrium,  $\bar{v}_f$  can be related to  $p$  by solving numerically an autoconsistent equation, and the temperature dependence of  $\bar{v}_f$  may then be computed. We assume<sup>3</sup> that the relationship between  $\bar{v}_f$  and  $p$  remains valid even in non-equilibrium, so the temperature  $T$  now becomes a parameter which can be used for relating  $\bar{v}_f$  and  $p$ .

In adimensional variables, the relevant equations needed are the following ones:

$$2.\bar{v}_{fr}.\zeta_{or} = (T_r - 1) + [(T_r - 1)^2 + 4.T_r.(1 - T_{lr})]^{0.5} \quad (1)$$

$$1 - T_{lr} = v_{ar}.\zeta_{or} \quad (2)$$

Here  $\bar{v}_{fr} = \bar{v}_f/v_0$ , where  $v_0$  is the segment volume at  $T_0$ ,  $T_r = T/T_0$ ,  $\zeta_{or} = \zeta_o.v_0/kT_0$ , where  $\zeta_o$  is a parameter equal to the derivative of the free energy density in order to free volume at  $0^\circ\text{K}$ ,  $v_{ar} = v_a/v_0$ , where  $v_a$  is related to the pressure ( $P$ ) dependence of  $T_0$  by  $v_a = k.dT_0/dP$ . The characteristic relaxation time is

$$\tau(T) = \tau_{oo} \cdot \exp [v_{mr} / \bar{v}_{fr}(T)] \quad (3)$$

and its temperature dependence can be simply summarized as follows:

$$[\tau(T)]^{\bar{v}_f(T)} = [\tau(T_0)]^{\bar{v}_f(T_0)} \quad (4)$$

where

$$\tau(T_0) = \tau_{oo} \cdot \exp [v_{mr} \cdot (1 - T_{lr})^{0.5} / v_{ar}] \quad (5)$$

The preceding expressions allow the computation of the temperature dependence of the characteristic time  $\tau(T)$ . It can easily be proven that for  $T > T_0$  one gets an asymptotic W.L.F. behaviour, and for  $T < T_0$ ,  $\tau(T)$  only diverges as  $T$  goes to  $0^\circ\text{K}$ .

It has been shown<sup>2</sup> that the effect of pressure can be taken into account by performing the following substitution:  $kT_0 \rightarrow kT_0 + v_a.P$ . An analogous argument leads to a more general expression to account for simultaneous pressure and stress effects. It is:

$$kT_0(P, \sigma) = kT_0(0, 0) + v_a.[P - (1/3) \cdot \text{Tr}(\sigma)] \quad (6)$$

where  $\sigma$  is the stress tensor. Eqs. (4) and (6) allow the computation of the stress dependence of the characteristic time  $\tau$ . It should be noticed that no additional free parameters are needed, because  $v_a$  ( or  $v_{ar}$ ) can be determined in an independent way.

### 3. Discussion.

The simplicity of models like the W.L.F. one <sup>4</sup>, brings back some drawbacks which have been recognized for a long time. First, time-temperature superposition is only an approximation, for most of the cases. Second, there is an unphysical divergence for  $T = T_g - c_{2g}$ , which prevents the utilization of this kind of expression near the glass transition temperature. The present model does not increase substantially the number of free parameters ( in practice only two parameters can be varied *ad libitum* ), but does not suffer from the inconvenients quoted above. Moreover it can be useful at least in some non-equilibrium situations <sup>3</sup>, as shown before.

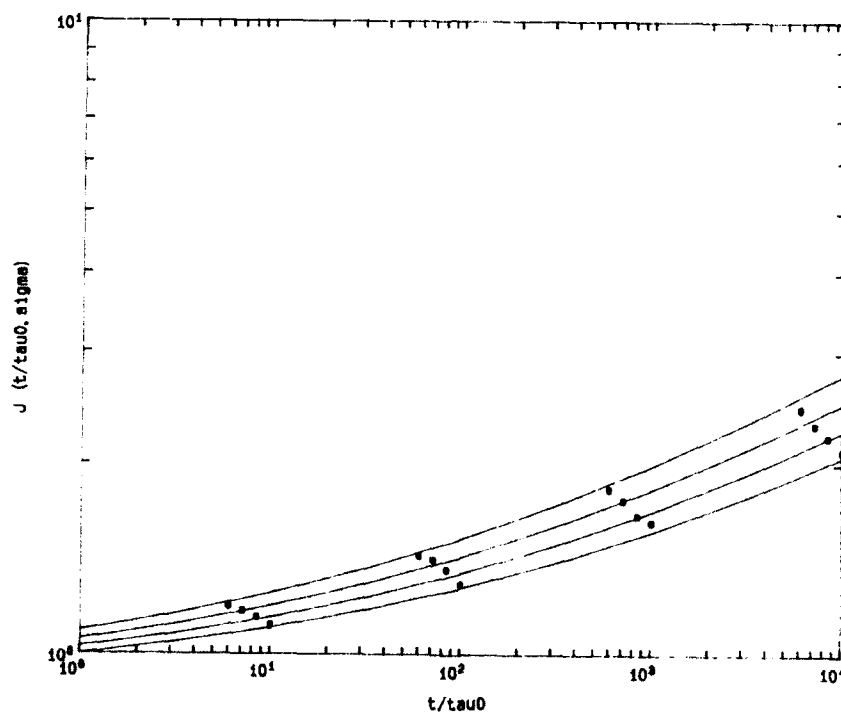


Fig. 1. Simulation of the stress dependence of the creep compliance.

Fig. 1 displays a simulation of  $J(t, \sigma) / J_g$  for an elongation experiment. The full curves were computed by assuming a retardation spectrum of the Havriliak-Negami type, with exponents  $\alpha = 0.5$  and  $\beta = 0.46$ , and the remaining parameters were  $T_r = 1.045$ ,  $v_{mr} = 10$ ,  $v_a = 1.6 \text{ cm}^3$ , and  $\zeta_{or} = 8.0$ . The following stresses were chosen: 1.0, 5.0, 9.0 and 13.0 MPa. Superposed to these curves are represented some experimental points corresponding to elongation experiments on a polypropylene copolymer. The agreement found is quite good, taking into account the experimental errors, and the lack of knowledge of some of the parameters of the samples.

#### 4. Conclusion.

It has been shown that the non-linear stress dependent creep compliance of polymers can be computed in the framework of the free volume model presented above, without the introduction of any additional free parameter. The agreement found with experimental data suggests that it is worth to do a more deeper analysis of the existent data. This is left as a suggestion for further work.

#### 5. References.

1. A. C. Diogo and A. M. Velho, *Mol. Cryst. Liq. Cryst.* **153** (1987) 231
2. M. H. Cohen and G. S. Grest, *Phys. Rev. B* **20** (1979) 1077
3. A. C. Diogo and A. M. Velho, in *Molecular Structure and Rheology of Polymers*, *Suppl. Rev. Port. Hemorr.* (1990) (in press)
4. J. D. Ferry, *Viscoelastic Properties of Polymers*, (J. Wiley & Sons, New York, 3rd ed., 1980), ch. 11.

**Acknowledgements:** This work was partially supported by Junta Nacional de Investigação Científica e Tecnológica under R.&D. contract n° 87/627. One of us (A. C. D.) benefited from helpful discussions with Prof. J. J. Cruz-Pinto.

## DETERMINATION OF TRAP PARAMETERS IN POLYMERS

JÓZEF ŚWIĄTEK

*Institute of Physics, Pedagogical University,  
ul. Armii Krajowej 13/15, 42-200 Częstochowa, Poland*

and

ARKADIUSZ MANDOWSKI

*Institute of Physics, Pedagogical University,  
ul. Armii Krajowej 13/15, 42-200 Częstochowa, Poland*

## ABSTRACT

Thin polybutadiene and polyisoprene films were investigated using TSC (thermally stimulated currents) technique. The spectra were analysed in terms of 'kinetics order' model with the use of computer fitting of some theoretical parameters to the data. The applicability of the 'kinetics order' model to the analysis of TSC in polymers is briefly discussed.

## 1. Introduction

Thermally stimulated relaxation processes such as thermally stimulated currents (TSC), thermoluminescence (TL), thermally stimulated electron emission (TSEE) and many others (e.g. see Chen and Kirsh<sup>1</sup>) are frequently used to study trapping parameters in solids. The great advantage of these methods is its experimental convenience. Typical experiment consist of the following steps: a sample is cooled down to the temperature  $T_0$  and excited in any way, then the excitation is removed and the sample is heated with a constant rate  $\beta$ . Carriers thermally released from traps change the values of conductivity (TSC) and/or luminescence (during its radiative recombination - TL) of the sample. Since the probability of releasing of an electron from a trap is proportional to  $\exp(-E/kT)$ , where  $E$  is the activation energy,  $k$  is the Boltzmann constant and  $T$  is the temperature of the sample, each peak on TSC spectrum should contain an information about trap parameters in the solid. Some particular models will be presented later.

## 2. Experimental

The material under study were thin polybutadiene and polyisoprene films with metallic (gold and aluminium) electrodes. The measurements were performed in a vacuum of  $10^{-5}$  Pa.

The temperature was controlled using a cooper - constantan thermocouple.

For TSC experiments the thermal cycle consisted of the following steps: a) polarization in d.c. electric field of the order of  $10^6$  V/m for 1800 s at temperature 350 K; b) cooling with the applied electric field to the liquid nitrogen temperature; c) linear heating of the sample at different rates. Details of the experimental technique were described by Świątek<sup>2</sup>, Świątek *et al.*<sup>3</sup> and Tkaczyk *et al.*<sup>4</sup>

### 3. Theory

In contrast to the experimental convenience, methods for analysis of the obtained spectra are not so easy. This is so, first of all, because of nonlinearity of the basic differential equations describing these phenomena. Even for the simplest model consisting of one type of traps and recombination centers there are no analytical solutions for TSC and TL. One of the most often used approximate expressions is so called Randall - Wilkins' equation, valid for slow retrapping range:

$$I(T) = I_0 \exp \left[ - \frac{E}{kT} - \frac{\nu_0}{\beta} \int_{T_0}^T \exp \left( - \frac{E}{kT} \right) dT \right]; \quad (1)$$

although, it does not describe properly the whole variety of all possible kinetic phenomena. For this purpose a different model was proposed<sup>1</sup> based on the kinetic theory of chemical reactions. In this model the intensity  $J$  (TSC or TL) is defined as:

$$J \propto - \frac{dn}{dt} = \nu (n)^b \exp \left( - \frac{E'}{kT} \right), \quad (2)$$

where  $b$  is so called 'kinetic order'. For  $b=1$  the model coincide with Eq.1. Although all the cases  $b \neq 1$  (except  $b=2$ ) do not correspond to any physical reality, it was shown by many authors, that for more physically important cases  $E'$  calculated from Eq.2 differs from the 'true' value  $E$  only a few per cent.

### 4. Results and Discussion

The above approximate equations were applied to determine trap parameters in polybutadiene and polyisoprene thin films using computer curve fitting analysis. Typical TSC spectra as well as calculated theoretical curves are shown on Figs. 1 and 2. One can see that the fit is satisfactory. The polybutadiene spectrum consists of a few almost isolated peaks at 185 K, 272 K and 365 K. The respective estimated values of activation energy  $E'$  and kinetic order  $b$  were the following:

$$\begin{array}{lll} E = 1.22 \text{ eV}; & 1.48 \text{ eV}; & 0.76 \text{ eV}; \\ b = 1.9; & 1.2; & 1.0; \end{array}$$

The polyisoprene TSC spectrum is much more complex, but it was possible to decompose the spectrum, by using a computer, on four Randall-Wilkins type (i.e. with  $b=1.0$ ) having maxima at 217 K, 229 K, 246 K and 250 K.



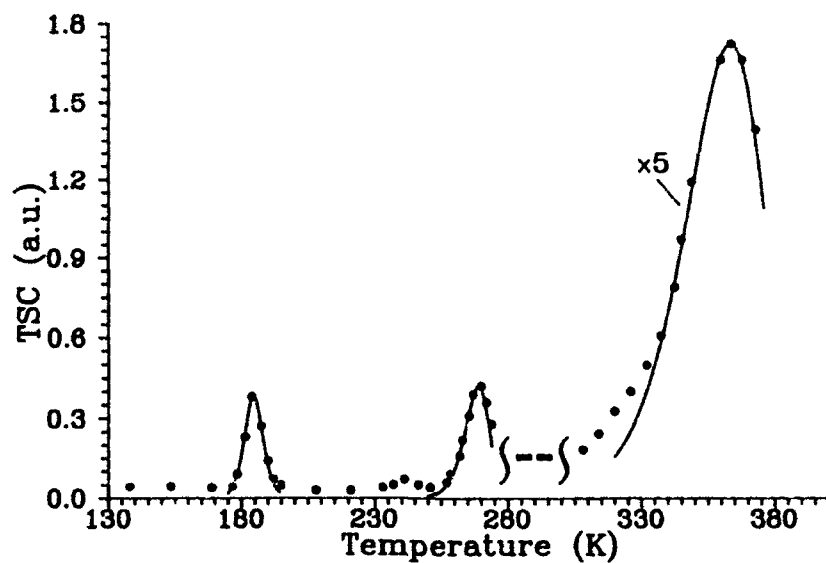


Fig.1. TSC spectrum of polybutadiene (.....) and calculated theoretical curves (——).

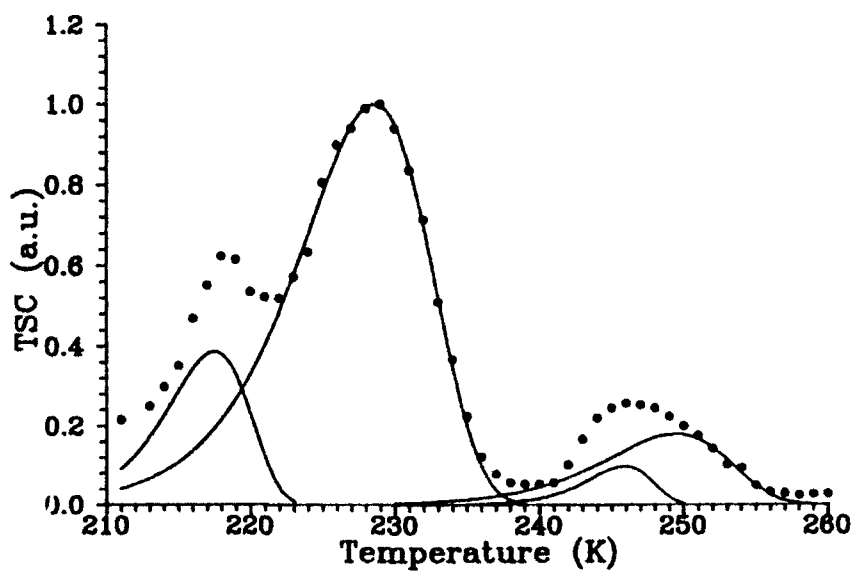


Fig.2. TSC spectrum of polyisoprene (.....) and calculated theoretical curves (——).

Calculated values of the respective activation energies were the the following:

$$E = 1.42 \text{ eV}; \quad 0.98 \text{ eV}; \quad 2.33 \text{ eV}; \quad 1.23 \text{ eV};$$

However the 'general order' kinetics model described by Eq.2, as applied to TSC spectra, was questioned by some authors<sup>6</sup>, it can be shown, that it very good qualitatively describes TSC spectra in polymers. This may be due to some specific kind of kinetics of carriers trapping in these materials - e.g. it was demonstrated, using Monte Carlo technique, that TSC spectra in systems with strongly correlated traps and recombination centers (e.g. containing small separated groups of traps and recombination centers) should obey the 'general order' equation, even for such values of trap parameters, where classical solutions are perfectly of Saunders type (a peak with a broad high-temperature tail). Nevertheless, because there is still lack of analytical solutions for such cases of kinetics, the problem of exact determining of activation energy from TSC spectra (or at least knowledge of accuracy) remains still open.

## 5. References

1. R. Chen and Y. Kirsh, *Analysis of Thermally Stimulated Processes* (Pergamon Press, Oxford, 1981).
2. J. Świątek, *Trap states and electrical conductivity in polycrystalline p-phenyl layers* (Politechnika Łódzka - Zeszyty Naukowe, Monografie nr 13, Łódź, 1980).
3. J. Świątek, S. Tkaczyk and A. Kwiatkowska, *Progr. Colloid Polym. Sci.* **78** (1988) 123.
4. S. Tkaczyk, J. Świątek and A. Kwiatkowska, *Progr. Colloid Polym. Sci.* **78** (1988) 136.
5. J. T. Randall and M. H. F. Wilkins, *Proc. Roy. Soc. (London)* **A184** (1945) 366.
6. J. Vanderschueren and J. Gasiot, in *Thermally Stimulated Relaxation in Solids*, ed. P. Braunlich (Springer-Verlag, Berlin, 1979)
7. A. Mandowski and J. Świątek, *Phil. Mag.* **B** (in press)
8. I. J. Saunders, *J. Phys.* **C2** (1969) 2181.

#### **IV. PROPERTIES AND APPLICATIONS**

NON-CRYSTALLINE ALUMINIUM ALLOYS :  
FUNDAMENTALS AND APPLICATIONS

Jean-Marie DUBOIS

*Laboratoire de Science et Génie des Matériaux Métalliques (CNRS URA 159)*

*Ecole des Mines, Parc de Saurupt, F-54042 NANCY*

ABSTRACT

The formation of aluminium-based glasses is reviewed with emphasis put on structural aspects. A comparison is made with quasicrystalline phases. Information available on the structure, the crystallization and glass formation is discussed with the aim to distinguish to which extent the metastable glasses and the supposedly stable quasicrystals are related. A few potential applications that follow are evoked.

1. Introduction

Our understanding of the structure of metallic glasses was based on random packing algorithms until P.H. Gaskell greatly clarified the view when he introduced stereochemical models in the late 70's. He first demonstrated that a  $\text{Pd}_{80}\text{Si}_{20}$  glass may be built by connecting well defined structural units of the kind that exist in the  $\text{Pd}_3\text{Si}$  crystalline counterpart<sup>1</sup>. This so-called cementite structure type gathers many crystalline compounds such as  $\text{Fe}_3\text{C}$  (the cementite carbide),  $\text{Ni}_3\text{B}$ ,  $\text{Pd}_3\text{B}$ ,  $\text{Y}_3\text{Ni}$ ,  $\text{Yb}_3\text{Pd}$ , etc ... and  $\text{Al}_3\text{Ni}$ . It consists of a parallel stacking of flat sheets formed by edge and vertex connected triangular prisms having six large atoms lying on the vertices and one small atom in their centre.

The computer-built model that Gaskell designed at that time was able to reproduce the available diffraction data<sup>1</sup>. Gaskell was also in a position to show that polymorphism observed in various crystalline types was reflected as well in the scattering functions of the corresponding amorphous alloys<sup>2</sup>. More specifically, the  $\text{Fe}_3\text{P}$  tetragonal compound constructed by vertex-sharing prisms produces a signature on pair distances that is different from that of  $\text{Pd}_3\text{Si}$ . It so happens that the same distinct signatures are observed on the Fourier transform of the interference functions of  $\text{Fe}_{80}\text{P}_{20}$  and  $\text{Pd}_{80}\text{Si}_{20}$  glasses. Thus, the atomic structure of metallic glasses reproduces the local order of polymorphous crystals, in support of stereochemical models.

Furthermore, macroscopic properties, such as the specific mass, which are dominated by the arrangement of atoms, should reflect the above trends. For instance, Gaskell pointed out that the atomic density, or equivalently the packing fraction  $\eta$  of transition metal atoms in transition metal-metalloid amorphous alloys varies linearly with the atomic size ratio  $p = R_X / R_M$  ( $R_X$  is the covalent radius of the metalloid atom and  $R_M$  the Goldschmitt radius of the transition metal).

The figure 1 shows the correlation diagram proposed by Gaskell<sup>3</sup> for cementite crystals superimposed on the correlation line obtained for several glasses of composition M75X25. At that time, this figure was not a surprise to Gérard Le Caër and myself since we were already tackling the problem of the structure of metallic glasses in terms very similar to Gaskell's approach (and inspired by it)<sup>4</sup>. We thought that we could add a new point to the figure above by measuring the specific mass of the Al<sub>80</sub>Ni<sub>20</sub> glass because the radius ratio of the Al<sub>3</sub>Ni cementite structure was clearly apart the ones retained by Gaskell. Thus, we wanted to see if the Al-Ni glass would breakdown Gaskell's correlation or not.

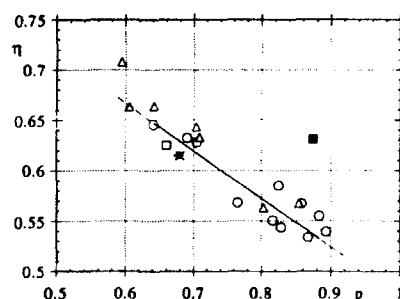


Figure 1 - Packing fraction  $\eta$  of the metal atoms versus atomic size ratio  $p$  for amorphous alloys containing 25 at% metalloid atoms (circles) and cementite crystals (triangles). The filled square is for Al<sub>3</sub>Ni with  $p$  defined according to Gaskell<sup>3</sup> and the empty square with  $p$  defined according to section 3.2. The correlation for  $\tau$ -Al<sub>7</sub>NiSi<sub>2</sub> is represented by a star with  $p$  according to section 2.2.

If we had been successful at this stage, we had stopped, I am afraid. Fortunately, our melt spinning machine was not efficient enough to produce bulk quantities of the Al<sub>80</sub>Ni<sub>20</sub> glass suitable for a specific mass measurement. We then turned back to the idea on polymorphism and thought of adding copper to the Al-Ni alloy. The reason is that the Al<sub>2</sub>Cu tetragonal compound is isotypic with Fe<sub>2</sub>B, a periodic stacking of Archimedean antiprisms with eight Al (respectively Fe) atoms on vertices and a Cu (respectively B) atom in the centre. Meanwhile, we designed a strict parallel between Al-Cu-Ni and Fe-B-C alloys, the latter one being known as an easy glass former. As a matter of fact, we immediately obtained ribbons with an amorphous fraction exceeding 80%, the remaining fraction being occupied by a fcc supersaturated solid solution  $\underline{\text{Al}}-(\text{Ni},\text{Cu})$  that exhibited very broad Bragg peaks (figure 2a). Addition of minor quantities of refractory metals and/or silicon produced fully amorphous ribbons (figure 2b) in large quantities. Upon heating, the thermal response of

the alloys, as studied by electrical resistivity and Differential Thermal Analysis (figure 3) was typical of an amorphous metal.

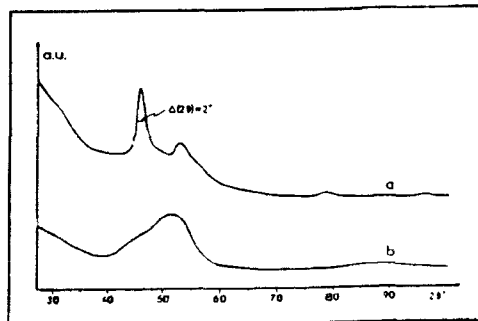


Figure 2 - X-ray diffraction pattern of two rapidly solidified alloys : a -  $\text{Al}_{81}\text{Cu}_{12}\text{Ni}_7$  consisting of an amorphous phase and a supersaturated fcc solid solution with very broad diffraction lines ; b - amorphous  $\text{Al}_{80}\text{Cu}_{10}\text{Ni}_8\text{Mo}_2$ .

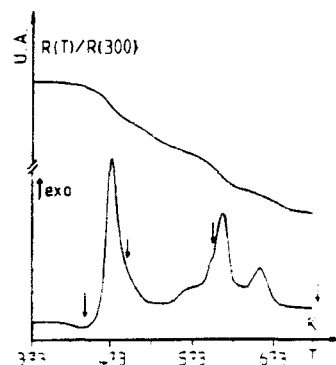


Figure 3 - Reduced electrical resistivity (top curve) and Differential Thermal Analysis (bottom) of the amorphous  $\text{Al}_{80}\text{Cu}_{10}\text{Ni}_8\text{Mo}_2$  alloy.

The discovery of aluminium amorphous alloys was submitted for publication in 1982 in a sealed note, which did not prevent us of patenting<sup>5</sup>, and was disclosed only in 1985<sup>6</sup>. In the mean time, we found many other amorphous alloys, basically by trial and error composition variations (e.g. the Al-Cu-V glasses to which we will come back to in a forthcoming section). The existence of a bulky amorphous alloy in the Al-Fe-Si system was reported on in 1983<sup>7</sup> which opened the way to the discovery of the very easy glass forming Al-Ni-Si alloys<sup>8</sup>. Many results discussed in the present paper will be taken from this study<sup>9</sup>.

At the end of 1984, D. Shechtman and his colleagues published their famous paper on quasicrystals<sup>10</sup>. This discovery, which first shook the foundations of crystallography, has opened a fascinating field of research on condensed matter. Specifically, attention was focused in many groups on finding new quasicrystalline alloys and, by the way, a very important class of amorphous aluminium alloys was pointed out independently in the States and in Japan<sup>11,12</sup>. This family of alloys, with composition Al-TM-X (TM = Fe, Ni or Co ; X = some of the rare earths, Y, Zr, Nb or Hf) may contain up to 90 at% Al. The reader is referred to an extensive review of the subject by Inoue et al<sup>13</sup> which supplies up to date data on the physical and mechanical properties of the aluminium-based glasses. Accordingly, there is no need to recapitulate all the experimental data and I shall focus in the present review to those pieces of information that are pertinent to glass formation in aluminium alloys. Most of

the quasicrystalline alloys known so far are aluminium-based too, a relationship to the aluminium amorphous alloys that is important enough to deserve discussion in this review. However, the connection between both types of non-crystalline aluminium alloys goes much deeper and will be analysed herein to some extent, including their applied properties.

This is, briefly summarized, how amorphous aluminium alloys, that may be produced in bulk quantities, were discovered during the past decade. For the sake of completeness, I should mention also that amorphous thin films (more precisely, thin areas) were produced in Al-Cu, Al-Cr, Al-Si, etc ... alloys (for references, see 13), well before this period of time. To conclude on this introductory section, I would also like to emphasize that a deliberate ignorance of the (French) literature by some groups involved in the subject does not suffice to support the claim that all aluminium amorphous alloys were invented in one single place. For instance, the ductile Al-Ni-Si glass is introduced in a paper of 1990<sup>13</sup> as having appeared in a scientific journal for the first time in 1987<sup>14</sup> despite the patent that was specifically devoted to this glass system was published already in 1986<sup>8</sup>. More surprising is the insistence on claiming<sup>13</sup> that the first amorphous alloy with Al as the majority constituent to be reported on was Al-Fe-B in 1981<sup>15</sup>, a straightforward extrapolation from the iron-rich side of the amorphous range, whereas no diffraction data nor calorimetric measurement were published then (nor since) to substantiate this discovery.

## 2. Experimental

Many experimental data to be discussed in the present paper were obtained by the group working in Nancy. The alloys were prepared by RF melting of the pure constituents under rare gas atmosphere. The amorphous specimens were produced by melt spinning on a copper wheel according to a now classical technique. This holds true also for the metastable quasicrystalline alloys discussed latter on. In contrast, stable quasicrystals and their so-called approximant crystals were prepared by conventional solidification.

A variety of experimental techniques were employed to investigate the samples : X-ray diffraction ( $\lambda = K\alpha_{\text{Co}} = 1.7889 \text{ \AA}$ ), electron microscopy, large and small angle neutron diffraction, calorimetry and resistivity measurements.

## 3. Aluminium-based amorphous alloys

### 3.1. Structural characteristics

What actually distinguishes aluminium amorphous alloys (AAA), on a structural standpoint, is their diversity of structure factors or equivalently total pair distribution functions. In contrast, structure factors of metallic glasses made of metalloids and transition

metals are much more resembling each other, even with constituents that carry different scattering factors. To exemplify this point of view, the figure 4 shows the Bhatia-Thornton total structure factor  $S(q)$ , ( $q = 4\pi \sin \theta / \lambda$ ), measured by neutron diffraction) of four different AAA (for a definition of  $S(q)$ , see 16). The last one (d) has a rather narrow first peak and is reminiscent of conventional  $S(q)$  curves. The other ones exhibit a double component first peak. The one of Al-Co-Si(c) is clearly split and resembles nearly to what is measured for Al-Ce-Fe glasses<sup>17</sup>. Upon Fourier transform of the data to real space, the difference may become even more obvious. For instance, the comparison is made in figure 5 between the reduced total pair correlation functions  $G(r)$ <sup>16</sup> of amorphous Al<sub>70</sub>Ni<sub>15</sub>Si<sub>15</sub> (a) and Al<sub>70</sub>Fe<sub>13</sub>Si<sub>17</sub> (b).

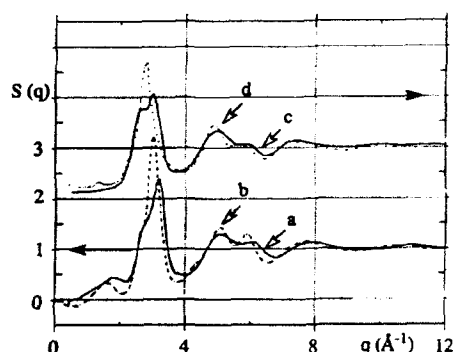


Figure 4 - Bhatia Thornton total structure factors of Al<sub>70</sub>Ni<sub>15</sub>Si<sub>15</sub> (a), Al<sub>70</sub>Fe<sub>13</sub>Sr<sub>17</sub> (b), Al<sub>75</sub>Co<sub>13</sub>Si<sub>12</sub> (c) and Al<sub>72</sub>Cu<sub>15</sub>V<sub>10</sub>Mo<sub>1</sub>Si<sub>3</sub> (d) measured by neutron diffraction at room temperature.

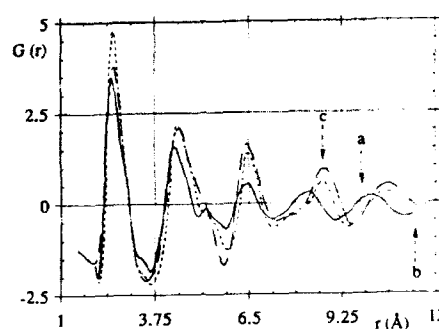


Figure 5 - Reduced total pair correlation functions  $G(r)$  of amorphous Al<sub>70</sub>Ni<sub>15</sub>Si<sub>15</sub> (a) and Al<sub>70</sub>Fe<sub>13</sub>Sr<sub>17</sub> (b). Comparison is made to a calculated function (c) typical of an icosahedrally ordered material (see text).

Furthermore, the  $G(r)$  of Al-Fe-Si may be reproduced to a very satisfactory extent by calculating a  $G(r)$  function (c) from the partial pair functions measured in quasicrystalline Al-Mn alloys<sup>18</sup> after suitable broadening by a gaussian line shape to simulate the effect of disorder. The agreement between calculated and experimental data strongly supports the assumption that this glass is icosahedrally ordered at short distances<sup>19</sup> as was also reported for Al-Mn glassy films<sup>20</sup>. However, this picture does not fit at all with the  $S(q)$  measurements for Al-Ni-Si. We will come back to the structure of this latter glass in the next subsection but, clearly enough, we can already conclude that some aluminium glasses show no sign of icosahedral order whereas some others do.

Interpreting the origin of the nearly split first peak of  $S(q)$  is a difficult task. A crude, and actually wrong interpretation is that of a two-phase system having distinct compositions and therefore different first pair distances<sup>14</sup>. As a matter of fact, the relative



amplitude of the two components of the first peak changes with composition (figure 6). The low- $q$  side component is more important when the Ni content is the smallest, irrespectively of the Si concentration. Conversely, this component is weakened when the aluminium content is decreased, which just rules out the possibility of a two-phase system. Meanwhile, the prepeak at about  $1.8 \text{ \AA}^{-1}$  is enhanced with increasing Ni content. Nickel carries the strongest scattering factor whereas Al and Si, which are not distinguishable by neutron nor X-ray diffraction, contribute to the scattering function by a factor about 2.5 times smaller. It is then tempting to assign the prepeak to chemical ordering of Ni atoms (the first peak of the  $S_{CC}$  partial function<sup>16</sup>). This is presumably going too fast since the large difference between atom sizes may also contribute to the prepeak through the  $S_{NC}$  partial<sup>16</sup>. Nevertheless, since Co is about equivalent to Al and Si as far as neutron scattering is considered, the absence of a

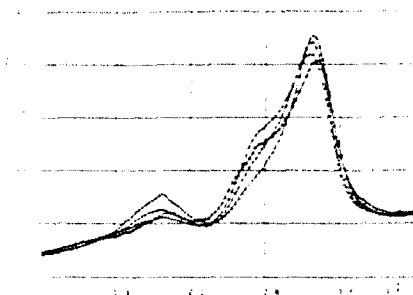


Figure 6 - Low- $q$  region of the total structure factor of  $\text{Al}_{67}\text{Ni}_{11}\text{Si}_{22}$  (o),  $\text{Al}_{75}\text{Ni}_{12.5}\text{Si}_{12.5}$  ( $\blacklozenge$ ),  $\text{Al}_{70}\text{Ni}_{15}\text{Si}_{15}$  (x) and  $\text{Al}_{60}\text{Ni}_{20}\text{Si}_{20}$  ( $\blacktriangle$ ) glasses (neutron diffraction).

prepeak on  $S(q)$  of amorphous Al-Co-Si (figure 4) confirms that a very significant contribution to  $S(q)$  in the  $1.4$  to  $2 \text{ \AA}^{-1}$  range comes from short range chemical ordering. Accordingly, we may conclude that transition metal atoms avoid neighbouring each other in these glasses (and are separated by an average distance of the order of  $2\pi/1.8 = 3.5 \text{ \AA}$ ).

It is more difficult to assess the origin of the two components of the main peak of  $S(q)$ . In real space, the first peak of  $G(r)$  contains also two components which may be deconvoluted in two gaussian lines<sup>9</sup>. The first line is located at roughly  $2.5 \text{ \AA}$  and slightly shifts to shorter distances with increasing Ni content while its area increases a little. The other component is at about  $2.8 \text{ \AA}$  and its area markedly decreases with increasing Ni concentration. At this stage, it is tempting to assign the  $2.5 \text{ \AA}$  pair distance to the radius of the neighbour shell of Ni atoms and the  $2.8 \text{ \AA}$  one to the Al-Al pairs (with the assumption that Si and Al species may be confused due to their nearly equal scattering factors). Then, coordination numbers are obtained : nickel atoms have 8 nearest neighbours and there are 10 Al-Al pairs at  $2.8 \text{ \AA}$ . We will see in the next sub-section that this picture is not accurate enough for Al-Ni-Si glasses. However, it emerges clearly from it that Ni atoms do not occupy the centre of

icosahedral units, which would have raised  $Z_1$  to about 12, nor belong to an icosahedron characterised by  $Z_1 = 10-11$  as Frank-Kasper compounds tell us. Comparing the first peaks of  $G(r)$  in  $\text{Al}_{70}\text{Fe}_{13}\text{Si}_{17}$  and  $\text{Al}_{75}\text{Ni}_{15}\text{Si}_{15}$  (figure 5) immediately shows that the balance between TM-(Al,Si) and (Al,Si)-(Al,Si) is not identical in the two alloys (TM = Fe or Ni). There are now more neighbours around Fe atoms if the same type of weighting is adopted as previously. A more precise conclusion was reached<sup>17</sup> for the Al-Ce-Fe glasses : Fe atoms have 10 Al neighbours, 6 of them being in close contact with Fe in this glass.

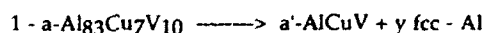
The distance between transition metal atoms and aluminium is short (2.49 to 2.51 Å) and significantly smaller than the sum of the Goldsmitt radii (1.25 and 1.43 Å, respectively). The same situation is encountered in crystalline counterparts where distances as short as 2.3 Å may be found<sup>21</sup>. The 2.8 Å distance assigned to Al-Al pairs looks slightly shorter than in the fcc metal, thus confirming the network densification effect due to a strong hybridization between the 3d metal and  $\text{sp}^3$  Al bands. Up to now, I have not mentioned a small supplementary shoulder situated at about 3.4 Å on the right side of the first peak of  $G(r)$  (see figure 5). This component is much more visible with Al-Fe-Ce glasses<sup>17</sup> and is appropriately assigned to Al-Ce distances owing to the large size of the rare earth atom. However, as we deal in the present paper only with atoms having size smaller than Al, we see that part of this component may as well originate from other pairs. I already pointed out the occurrence of Ni-Ni pairs at 3.5 Å and will show in the next section that Al-Al pairs may also contribute.

### 3.2. Crystallization products

My opinion is that more may be learnt on AAA by looking carefully at their crystallization products than by a direct study of the amorphous structure. To substantiate this point of view, I shall in this sub-section focus on the study of the crystallization of two alloys : Al-Cu-V and Al-Ni-Si, which produce quasicrystals and conventional crystals, respectively.

The crystallization sequence of amorphous  $\text{Al}_{83}\text{Cu}_7\text{V}_{10}$  was studied in situ by neutron real time powder diffraction (technical details are given in ref. 22). An overview of the sequence is shown in figure 7. This figure is a pseudo three dimensional view showing the diffraction angle  $\theta$  along the X-axis, the temperature along the Y-axis and the neutron counting intensity along Z. Each waving line represents one diffraction pattern accumulated during a temperature increase of 1.8 K (heating rate 0.6 K  $\text{mn}^{-1}$ ).

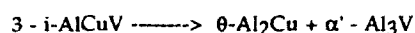
The material is initially amorphous and is characterized by a very broad diffraction peak with a well visible shoulder on the low-angle side. The crystallization begins at  $T_1 = 520\text{K}$  and is completed through three stages

$$T_1$$


where  $a'$  labels an intermediate amorphous phase with shifted composition owing to the precipitation of a fraction  $y$  of fcc aluminium (in fact, presumably a solid solution)

$$T_2$$


where  $i$  is now for the icosahedral phase, still of unknown composition.

$$T_3$$


which leads to the equilibrium mixture of crystalline compounds. With the present heating rate, the successive transformations begin at  $T_1 = 520\text{K}$ ,  $T_2 = 575\text{K}$  and  $T_3 = 630\text{K}$ . Above  $T = 820\text{K}$ , the  $\text{Al}/\theta\text{-Al}_2\text{Cu}$  eutectic becomes liquid and the corresponding Bragg-lines vanish as may be seen in the background of figure 7. Meanwhile, a small fraction of  $\text{Al}_{45}\text{V}_7$  shows up in the mixture of intermetallic compounds.

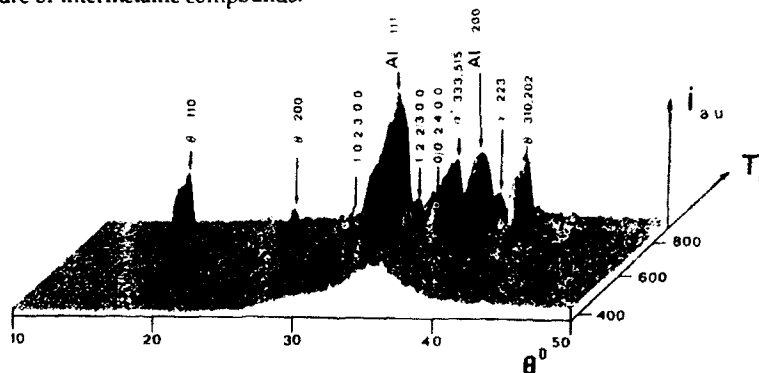


Figure 7 - Perspective view to the crystallization of amorphous  $\text{Al}_{83}\text{Cu}_7\text{V}_{10}$ . The foreground pattern shows the diffraction response of the amorphous alloy and the background that of liquid  $\text{Al}/\theta\text{-Al}_2\text{Cu}$  plus vanadium containing compounds ( $\alpha\text{-Al}_3\text{V}$ ,  $\text{Al}_{45}\text{V}_7$ ). Indexing of the transient pseudo-Bragg lines of the icosahedral phase is according to ref. 23.

Another sequence is observed with alloy  $\text{Al}_{78}\text{Cu}_{15}\text{V}_7$  having a larger  $\text{Cu}/\text{V}$  ratio<sup>24</sup>. The tetragonal compound  $\theta\text{-Al}_2\text{Cu}$  precipitates first, then a small amount of fcc-Al solid solution. It is only after these two steps that the icosahedral phase appears before transforming itself to equilibrium crystals. By following the amount of  $\theta\text{-Al}_2\text{Cu}$  precipitated at each step (i.e. the intensity change of one of its well defined Bragg lines) allows us to estimate the composition of the intermediate amorphous phase to be close to  $\text{Al}_{82}\text{Cu}_8\text{V}_{10}$  and that of the icosahedral phase close to  $\text{Al}_{82}\text{Cu}_7\text{V}_{11}$ . The resemblance between the two compositions strongly suggests that the icosahedral phase is a polymorphous product of the

residual amorphous phase. A better example of such a polymorphic crystallization producing an icosahedral phase is known in Pd-U-Si glasses<sup>26</sup>. Comparable results were also deciphered from the study of the crystallization of amorphous  $\text{Al}_{70}\text{Fe}_{13}\text{Si}_{17}$ <sup>25</sup>: the growth of fcc Al proceeds before the residual amorphous phase transforms to crystalline compounds which exhibit a strong icosahedral order. The best case known to date however is that of amorphous  $\text{Pd}_{60}\text{U}_{20}\text{Si}_{20}$  which transforms directly into an icosahedral phase before turning into the equilibrium crystal mixture<sup>26</sup>. All these examples converge appropriately in favour of icosahedral ordering in the AAA, in agreement with both the presence of quasicrystals in the phase diagram and theoretical arguments<sup>27</sup>.

Nevertheless, this is not all the story. A polymorphous crystallization also takes place in Al-Ni-Si glasses, in the vicinity of the  $\text{Al}_{67}\text{Ni}_{11}\text{Si}_{22}$  composition<sup>9</sup>. As a matter of fact, a truly amorphous sample of this specific composition is rather difficult to produce (i.e. requires a very efficient melt-spinning process), in contrast with other alloys of a different Ni/Si content. The crystallization sequences which were pointed out in the Al-Ni-Si amorphous system are summarized in the figure 8. They involve the metastable crystalline compounds  $\tau$ - $\text{Al}_7\text{Si}_2\text{Ni}$ , to be discussed later on in this section,  $\eta$ - $\text{Al}_9\text{Ni}_2$ , isotypic with  $\text{Al}_9\text{Co}_2$ <sup>28</sup> and the equilibrium mixture of fcc Al, cubic Si and orthorhombic  $\text{Al}_3\text{Ni}$ .

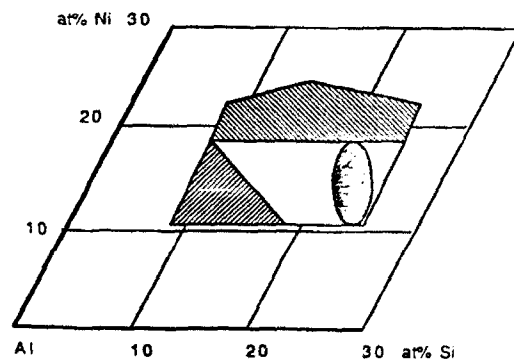


Figure 8 - Amorphous range in Al-Ni-Si alloys. The different areas of the diagram correspond to the following crystallization sequences:

- $\text{am1} \rightarrow \text{am2} + \tau \rightarrow \text{am3} + \tau + \text{Al} \rightarrow \text{equilibrium}$
- ▤  $\text{am} \rightarrow \tau$  (polymorphous crystallization)
- ▥  $\text{am1} \rightarrow \text{am2} + \tau + \text{Al} \rightarrow \text{equilibrium}$
- ▧  $\text{am} \rightarrow \tau + \eta + \text{Al} \rightarrow \text{equilibrium}$

Again, the structure of the compound labelled  $\tau$  above is of great significance for it is produced with no composition change from the amorphous state. It is straightforward to

identify the Bravais lattice from the indexation of the X-ray diffraction pattern. Identifying the space group and determining the atomic positions is a much more difficult matter, simply because the crystallization mechanism produces so small crystals that they are even below the minimum size acceptable for an electron diffraction single crystal study. However, this goal may be performed if one is able to fit the powder diffraction pattern to an appropriate model. This was successfully achieved<sup>29</sup> by using entry parameters to the fit defined along the following line.

The Nickel and Silicon atoms have low solubility at equilibrium in fcc aluminium but supersaturated solid solutions are known to exist<sup>30</sup>. In such solid solutions, Ni occupies a volume which is intermediate between that of Al and the space offered by an interstitial, octahedral, site. It will therefore distort the fcc lattice in a way that will depend on which site is occupied, either in substitution on an Al site or as an interstitial. From the cementite  $\text{Al}_3\text{Ni}$  structure, which at least formally is a distorted interstitial solid solution<sup>31</sup>, the Ni atoms were assigned to the octahedral sites. Reasonably, it was assumed that the chemical order was maximum, i.e. the partition of the Ni atoms was then univocally determined.

The case of Si is more complicated to fix up. Nevertheless, it was known from Si-containing compounds such as  $\text{Al}_7\text{Si}_4\text{Cr}_4$  that Si occupies the same type of sites than Al. Accordingly, Si was located on Al sites in the fcc lattice with furthermore avoiding close contact with Ni atoms (owing to the Ni concentration, this maximises the chemical order of the ternary mixture). Then, the relevant distortion was applied to the fcc lattice in order to offer more room to the Ni atoms, i.e. remove the atomic stresses introduced by the atom size mismatch effect already dealt with in the introduction.

The lattice transformation, called chemical twinning<sup>31</sup>, is perfectly defined. The motivation for doing so is discussed in detail elsewhere<sup>32</sup>. Altogether, the entry parameters were obtained in a straightforward way and it was then an easy matter to converge the fit to a residual factor of 4%<sup>29</sup>. The resulting structure (figure 9) appears very simple. It is a trigonal arrangement (hexagonal cell,  $a = 6.61 \text{ \AA}$ ,  $c = 3.82 \text{ \AA}$ , space group  $P6_3/m$ ) of aluminium triangular prisms housing a Ni atom in their centre. Silicon atoms occupy distorted and enlarged octahedral sites in between (sites I and II in figure 9). Depending on the stoichiometry of the compound, Ni atoms may also be located on those sites<sup>39</sup>.

This structure raises a few comments. First of all, it is based on tri-capped triangular prisms of aluminium atoms which host the transition metal. This is also the case in  $\text{Al}_3\text{Ni}$  as well as in the  $\eta\text{-Al}_9\text{Ni}_2$  compound (bi-capped prisms). In these compounds, the Ni-Al distance is (not surprisingly) shorter than the sum of the Goldschmidt radii:  $2.55 \text{ \AA}$  instead of  $2.68 \text{ \AA}$  (see table 1). The Al-Al distances appear very much distributed. Close contact

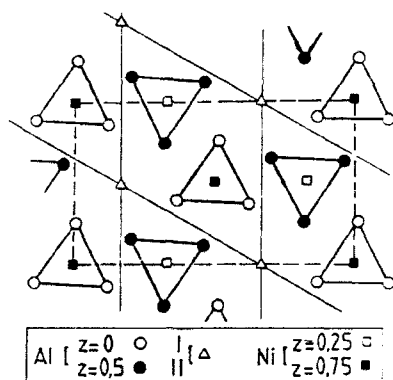


Figure 9 - Projection on the basal plane of the structure of the  $\tau$  compound produced by polymorphous crystallization of the  $\text{Al}_{67}\text{Ni}_{11}\text{Si}_{22}$  glass.

distances are at about 2.81 Å, like in the fcc metal, but second "first" pair distances are split between 3.12 Å (4 atoms) and 3.82 Å (2 atoms) for both distances are found in each, well defined, tri-capped unit. These distances contribute to the small shoulder visible on the right hand side of the first peak of  $G(r)$  (cf. previous section) and to the peak of second distances. A numerical simulation, which considered the crystalline structure of the  $\tau$ -compound as a model for the glass after suitable broadening of  $G(r)$  to mimic the effect of disorder, appeared rather successful<sup>29</sup>. Taking also the sites I and II into account, an effective atomic size ratio may be defined as  $p = (\langle d_{\text{Ni-A}} \rangle - \langle d_{\text{A-A}} \rangle / 2) / (\langle d_{\text{A-A}} \rangle / 2) = 0.63$  (where A stands for both Al and Si atoms). This brings the  $\tau\text{-Al}_7\text{NiSi}_2$  compound sharply on Gaskell's correlation introduced in figure 1. Alternatively, the same definition of  $p$  also brings the  $\text{Al}_3\text{Ni}$  back to the correlation line (figure 1).

Table 1. First pair distances found up to 3.82 Å in the  $\tau\text{-Al}_7\text{Si}_2\text{Ni}$  compound (in Å units).

Sites	Al	Ni	I	II
Al	2.72 (2)	2.54 (2)	2.66	2.61
	2.90 (2)	2.58	-	2.82
	3.12 (4)	-	-	2.89
	3.82 (2)	-	-	3.07
Ni	2.54 (6)	3.82 (2)	3.42	3.42 (3)
	2.58	-	-	-
I	2.66 (6)	3.42	3.82 (2)	2.86 (2)
II	2.61	3.42	2.86 (2)	3.82 (2)
	2.82	-	-	-
	2.89 (2)	-	-	-
	3.07 (2)	-	-	-

The situation about the atomic structure of the parent amorphous alloy is more contrasted now. Indeed, looking at figure 9 shows no sign of icosahedral order around Ni atoms

nor around sites I and II. The Al sites have 15 neighbours (table 1) which also rules out the existence of an unbroken icosahedral order. They accordingly represent a distinct class of amorphous alloys, as compared to the previously examined Al-Fe-Si and related alloys. This point of view is confirmed by the rapid increase in crystallization temperature observed with increasing iron content in Al-(Ni<sub>1-x</sub>Fe<sub>x</sub>)-Si glasses (figure 10). Obviously, the crystallization behaviour of the glasses is not the same at each end of the Ni/Fe range : icosahedrally ordered glasses happen to be more stable. This, however, does not mean that 5-fold symmetry, the signature of icosahedral order, does not occur in Al-Ni-Si glasses. Actually, there are six, nearly perfect, rings of atoms per tri-capped prism that exhibit 5-fold symmetry (figure 11) because of the height  $H$  of the unit ( $H = c = 3.82 \text{ \AA}$  in  $\tau\text{-Al}_7\text{NiSi}_2$ ) which ensures close contact between Al atoms on the triangular facets of the prism<sup>33</sup>. This is possibly related with the existence of a decagonal phase, basically a two-dimensional tiling of five-fold units, in Al-Ni alloys<sup>34</sup>.

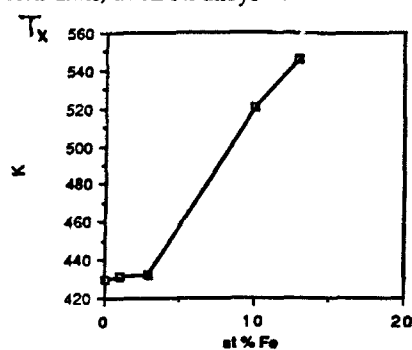


Figure 10 - Temperature  $T_x$  at which crystallization begins in  $\text{Al}_{70}\text{Ni}_{13-x}\text{Fe}_x\text{Si}_{17}$  glasses versus iron content  $x$ .

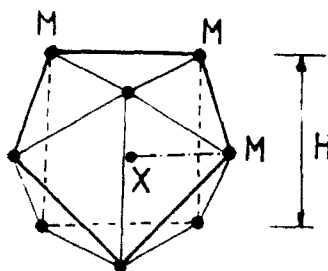


Figure 11 - Non-regular tri-capped prism made of a trigonal prism elongated along its threefold axis and three capping atoms (only two of which are drawn). One of the six fivefold rings of atoms is shown as a bold line to guide the eyes. M sites are occupied by Al and X by Ni in  $\tau\text{-Al}_7\text{NiSi}_2$ .

To conclude on this section, it is observed from the crystallization products that AAA, depending on their composition, may show evidence either of icosahedral order or of another, more conventional, type of order. The order which is quenched-in influences drastically the thermal stability of the glass. I will show in the next section that it has also a strong impact on the experimental conditions for glass formation. Nevertheless, it must be stressed that

both types of order may coexist, or that a smooth transition from one to the other is conceivable with continuously varying composition within a given alloy range.

### 3.3. Formation criteria

The formation of AAA was recently revisited by Bechet and Regazzoni<sup>35</sup>. When studying only static parameters, i.e. composition and atom size effect, they showed (figure 12) that binary alloys favourable to glass formation are split in two groups : those with a solute element much smaller than Al and those in which it is much bigger. In between are found both the solid solutions and the quasicrystals. I will come back to this point in the next section. Other important parameters are discussed in 35, especially the requirement of a cooling rate larger than a certain critical level beyond which nucleation of the crystalline phases is by-passed. The non-existence of deep eutectics, which is a common feature in aluminium-based alloys, is emphasized. This is of special significance in Al-TM-RE glasses which manifest very high reduced glass transition temperatures of the order of 0.7 and no eutectic point so that the eutectic line does not plunge deeply in the phase diagram<sup>36</sup>.

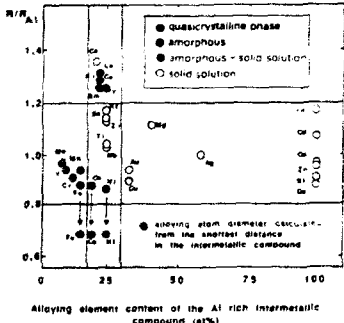


Figure 12 - Rapid solidification modes on a static parameters map. The rapid solidification behaviour of binary alloys can be plotted on a two-parameter map : the difference in atomic size and the alloying element content of the aluminium-richest intermetallic compound (e.g. in the case of Al-Ni system, the aluminium-richest intermetallic compound is  $\text{Al}_3\text{Ni}$  and the value 0.25 is plotted). Intermetallic compound stoichiometries are from equilibrium data, except for  $\text{AlFe}$ . White data have not been studied yet or let to common phase formations (from ref. 35).

It is now widely recognized that the most important criterion for glass formation is the atomic size mismatch between constituent species. We used this approach as a guide line to discover the first AAA (see introduction) before Egami and Waseda have put it to a firm analytical basis by considering several tens a binary alloys<sup>37</sup>. It was further on extended to ternary alloys with apparently acceptable success. In AAA however, a comprehensive view at the amorphous domain limit is not obtained as long as an effective atom size, comparable to the one adopted in the previous section, is not considered<sup>17</sup>.

Yet, the view at glass formation in AAA is not so clear. Indeed, consider the figure 13 which presents the minimum amount of silicon atoms to add to an  $\text{Al}_{86-x}\text{Si}_x\text{TM}_{14}$  alloy ( $\text{TM} = \text{Cr, Mn, Fe, Co, Ni}$ ) to obtain a fully amorphous specimen<sup>38</sup>. This amount decreases by a factor



3 when going from TM = Cr to M = Ni. Meanwhile, the Goldschmitt radius of the TM atoms is nearly the same throughout the series ( $R_{Cr} = 1.3 \text{ \AA}$ ,  $R_{Ni} = 1.25 \text{ \AA}$ ) and therefore the atom size mismatch criterion does not apply to this type of AAA. This holds true as well for the ratio  $p$  defined above which does not vary very much in crystals of the Al-TM serie. It must furthermore be emphasized that Al-Cu-Si glasses have not been discovered so far (whereas  $R_{Cr} < R_{Cu} < R_{Ni}$ ).

It is presumably important to realize (figure 13) that, by rapid solidification, an  $Al_{86}Cr_{14}$  or an  $Al_{86}Mn_{14}$  alloy are entirely transformed to an icosahedral phase. Similarly,  $Al_{86}Fe_{14}$  grows a decagonal phase in the same conditions whereas  $Al_{86}Co_{14}$  and  $Al_{86}Ni_{14}$

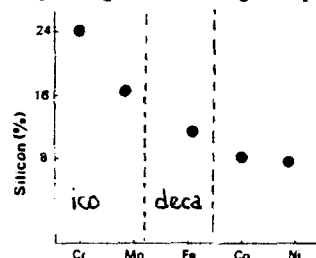


Figure 13 - Minimum silicon content necessary to achieve amorphisation in an  $Al_{86-x}Si_xTM_{14}$  alloy (from ref. 38).

do not form easily quasicrystals. Glass forming ability is then much more related in these systems to the ability of silicon to break down the establishment of long range order, either orientational or translational, rather to lattice instability effects. This is apparently easier to promote in crystals with a small unit cell than in quasicrystal forming liquids which lead to compounds with large size atomic clusters. The discovery that Al-Mn amorphous films already contain all the nuclei needed for crystal growth upon heating<sup>39</sup> reinforces this point of view. A more advanced discussion of the role of silicon may be found in ref. 40. Unusually large incubation time and activation energy for crystallization are measured in rare-earth containing AAA<sup>41</sup>. The crystallization proceeds first through a nucleation step and then growth like in other metallic glasses. Since the structure of these glasses appears rather reminiscent of icosahedral ordering, the effect of the large rare earth atoms is presumably to reduce the coherence length associated to the order parameter and to damp the atomic mobility. Both effects are in favour of an enhanced glass formability, in accordance with observation.

#### 4. Quasicrystals and AAA : a comparative view

##### 4.1. Formation

The conditions for forming an aluminium-based quasicrystal (AQC) are not completely clear yet. It is recognized that the atom size difference is weaker than for AAA

formation (see previous section) and the most important factor is apparently related to electron negativities, thus leading to an extension to AQC of the Hume-Rothery rule<sup>42</sup>.

For a long time, it was believed that AQC (more generally, quasicrystals) were intermediate between crystals and glasses because they were produced by rapid solidification techniques. To some extent, this is true for many AQC systems exhibit characteristics that are the privilege of metallic glasses : they may be prepared by solid state techniques as well, for instance ball milling<sup>43</sup>, they return to the crystalline state either by primary<sup>44</sup>, eutectic or polymorphous crystallization<sup>45</sup>, they show electronic density of states, specific heat, conductivity, spin glass, etc ... behaviour which are not basically different from what is measured in corresponding glasses<sup>46-48</sup>. However, the discovery of stable quasicrystals such as Al-Cu-Fe<sup>49</sup>, able to grow faceted single crystals by slow solidification from the melt, has changed this view. It has become more evident that quasicrystals are much closer to conventional intermetallics of aluminium : they form with comparable composition and according to similar phase diagrams, most often by peritectic reaction<sup>50</sup>. In several AQC, but not all of them, a reversible phase transition relates the quasicrystal to its closely resembling crystalline counterpart<sup>50</sup> but the quasicrystalline state is in equilibrium at high temperature. It is still a matter of debate to know whether the QC high temperature state is stabilized by the configurational entropy of the tiling<sup>51</sup> but there is converging evidence in favour of this hypothesis. In this case, the main difference between AAA and AQC would arise from entropy which promotes the metastability of the glass while enhancing the stability of AQC. An illustration of this effect may be found in the electrical conductivity behaviour upon thermal annealing. In AAA, annealing destroys the amorphous lattice and, due to precipitation of crystalline phases, the resistivity decreases as figure 3 shows. In stable AQC alloys, it is just the reverse that is observed. Annealing improves the lattice perfection and a drastic enhancement of the resistivity is observed<sup>52</sup>. It is deduced from this that a better ordered quasicrystal, i.e. that has sharper Bragg peaks, increases the effect of localization of the electronic transport.

If the reasons why an aluminium-based alloy forms a quasicrystal rather than a glass or a crystal are still obscure, it is even more difficult to understand which atomic rearrangements take place during the growth process. It was observed however that AQC formation is very often encountered in the presence of a CsCl-type phase with superstructure ordering. Lattice orientation relationships between this phase and different types of quasicrystals were determined. The tiling patterns of the AQC phases, as visualized by high resolution electron microscopy, were related to the atomic site position in the cubic structure<sup>53</sup>. More relevant to the purpose of the present paper is the following model<sup>54</sup>.

The Cs-Cl cubic phase is in fact a solid solution ordered according to which kind of atomic species is substituted on one or the other site. Because of the small but non-zero atom size difference between constituents, this solid solution may become topologically unstable in the sense already introduced in this paper for AAA and elsewhere<sup>32</sup>. This idea is demonstrated in figure 14 where a twinning, with plane (113) as the twinning plane, is applied to the CsCl structure projected along the  $[\bar{1}10]$  direction. On the atomic layer  $z = 0$  (the atomic positions are shown by open circles in figure 14), this twinning operation produces a distorted pentagon ABCDE which contains another small distorted pentagon abcde.

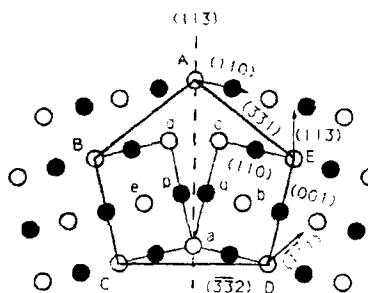


Figure 14 - Distorted pentagon formed by twinning on the (113) atomic plane of the CsCl phase. The CsCl structure is projected in direction  $[\bar{1}10]$ . Open and black circles correspond to atoms on layers  $z = 0$  and  $z = \sqrt{2}/2 a_c$ , respectively. Twinning plane (113) is marked by a dotted line. Two unit cells are outlined by thin solid lines. This pentagon can be further multiplied by mirror operations (reflection twinning), either on edge planes (332), (001) and (331) or on planes  $(\bar{1}\bar{1}1)$ , (113) and (110) to produce an infinite planar tiling with 5-fold symmetry (from ref. 54).

This atomic configuration is quite close to that of the Al-Cu-Co decagonal phase resolved by Steurer and Kuo<sup>55</sup>. The inter-atomic distances after the twinning are the same as in the original CsCl structure with the exception of that between atoms d and e. This distance is  $d_{dc} = 4/9 \sqrt{3} a_c$  ( $a_c$  is the unit cell parameter of the CsCl phase), about 11% shorter than the closest inter-atomic distance (e.g.  $d_{ac} = \sqrt{3}/2 a_c$ ). Thus, this distorted pentagon is not stable unless it undergoes a reconstructive transformation in order to satisfy the smallest inter-atomic distances. This kind of transformation has been described in the case of the Al-Mn-Si icosahedral phase<sup>56</sup>. Take the Al-Cu-Co decagonal phase<sup>55</sup> for example. The CsCl phase in this system has a parameter  $a_c = 2.875 \text{ \AA}$ . Thus, the edge lengths can be calculated:  $AB = BC = 4.768 \text{ \AA}$ ,  $AE = CD = 4.067 \text{ \AA}$ ,  $ED = 5.534 \text{ \AA}$ . Their average value is  $4.641 \text{ \AA}$ , quite close to the edge length of the basic pentagon in the Al-Cu-Co decagonal phase ( $4.684 \text{ \AA}$  at room temperature).

The atoms on the atomic layer  $z = \sqrt{2}/2 a_c$  have their positions (black circles in figure 14) projected onto centres of the parallelograms defined by atoms on the layer  $z = 0$ . Note that atom p near the centre of the pentagon and its twinning image q are so close to each other that the two positions can not be occupied together, i.e. one vacancy must be introduced. Since vacancy concentration increases with temperature, this twinning can only take place at high temperature. The role that vacancy ordering on the CsCl lattice plays in the formation of quasicrystals was already pointed out on the basis of an electron microscopy study<sup>57</sup>.

This distorted pentagon can be further multiplied to construct the cluster structure by mirror operations (reflection twinning). The twinings on edge planes (332), (001) and (331) will give two pentagons connected by a common edge; the twinings on planes ( $\bar{1}\bar{1}1$ ), (113) and (110) will give two pentagons separated by an angle close to  $36^\circ$ . Moreover, the CsCl structure along direction  $\langle 110 \rangle$  is stacked by two atomic layers with periodicity of  $\sqrt{2} a_c = 4.067 \text{ \AA}$ , whereas the Al-Cu-Co decagonal phase is also constructed by stacking two atomic layers along the 10-fold direction with periodicity of  $4.184 \text{ \AA}$ <sup>55</sup>. Thus, chemical twinning based on the CsCl type of unit cell can be used to describe the cluster structure of the decagonal phase while cluster twinning serves to multiply these clusters in such a way that the quasiperiodicity is preserved. Obviously, the built-in hierarchy of this mechanism is able to reconcile the micro-twinning point of view of Pauling<sup>58</sup> with the now widely accepted description of quasicrystals which rules out the presence of twins on a macroscopic length scale. In the scope of the present paper, chemical twinning or more appropriately, topological instabilities<sup>32</sup> of alloy lattices appears to play a central role in the formation of non-crystalline aluminium alloys.

#### 4.2. Properties

In many respects, AAA and aluminium-based quasicrystals look similar from the point of view of applied properties. I mentioned already such properties in the previous section. However, they differ greatly as far as mechanical properties are concerned: several AAA are ductile at room temperature whereas quasicrystals known so far are brittle. A list of a few ductile AAA is reported in table 2. It appears today that these two aspects, which apparently are conflicting, carry an interesting potential of applications and therefore deserve some comments. The reader is referred to papers<sup>11,13</sup> for more information on the subject of applied properties of AAA.

The family of AAA made of Al, lanthanides and transition metals offers the most exciting mechanical characteristics (table 2). A fracture strength as high as  $\tau = 1140 \text{ MPa}$  was pointed out in  $\text{Al}_{87}\text{Y}_8\text{Ni}_5$ <sup>13</sup>, in association with a fracture elongation  $\epsilon$  of 1.6%. Typical values of the fracture strength for other materials of this AAA family are found in the range of 800-900 MPa with Young modulus  $E$  scaling between 55 and 85 GPa<sup>11,13</sup>. Other AAA made with early and late transition metals have fracture strength and Young modulus rather in the vicinity of 600 to 800 MPa and 50 to 80 GPa, respectively. A clear correlation is observed between crystallization temperature, fracture strength and Vickers hardness (the higher the first, the better the others). Vickers hardness, also reported in table 2, reaches values as high as 600 in brittle amorphous alloys but is rather of the order of 280-320 in ductile AAA.

Table 2. Digest of a few measurements of mechanical properties at room temperature in ductile AAA<sup>11,13,59</sup> and quasicrystals<sup>60</sup> ( $\sigma$  : fracture strength, E : Young modulus,  $\epsilon$  : fracture elongation, Hv : Vickers hardness,  $\mu$  : friction coefficient).

Composition at%	Material	$\sigma$ MPa	E GPa	$\epsilon$ %	Hv	$\mu^*$ $\pm 0.03$
Al <sub>75</sub> Si <sub>15</sub> Ni <sub>10</sub>	AAA	440		1.4	370	-
Al <sub>85</sub> Zr <sub>5</sub> Ni <sub>10</sub>	AAA	800	80.4		340	-
Al <sub>87</sub> Y <sub>8</sub> Ni <sub>5</sub>	AAA	1140	71.2	1.6	300	-
Al <sub>86</sub> Ce <sub>4</sub> Ni <sub>10</sub>	AAA	810	54.6	1.5	300	-
Al <sub>87</sub> Ce <sub>4.3</sub> Ni <sub>8.7</sub>	AAA	500	46	-	-	-
Al <sub>90</sub> Fe <sub>5</sub> Gd <sub>5</sub>	AAA	735	50.7	-	-	-
Al <sub>90</sub> Fe <sub>5</sub> Gd <sub>5</sub>	partially crystallised	1010	48.6	-	-	-
Al <sub>63.5</sub> Cu <sub>24.5</sub> Fe <sub>12</sub>	icosahedral (as-cast)	250	68.0	0.35	715	0.12
Al <sub>63.5</sub> Cu <sub>24.5</sub> Fe <sub>12</sub>	icosahedral (annealed)	688	61.0	1.10	715	-
Al <sub>67</sub> Cu <sub>9</sub> Fe <sub>10.5</sub> Cr <sub>10.5</sub> Si <sub>3</sub>	decagonal approximant	595	8.9	0.65	670	0.17
Al <sub>63.5</sub> Cu <sub>8.5</sub> Fe <sub>10</sub> Cr <sub>10</sub> Si <sub>2.5</sub> B <sub>5.5</sub>	decagonal approximant	1060	105	1.0	560	
Al <sub>61.3</sub> Cu <sub>23.6</sub> Fe <sub>11.6</sub> B <sub>3.5</sub>	icosahedral	1010	118	0.85	850	

\* Diamond indenter, tip radius : 0.2 mm, applied load 40N.

Indeed, the most promising alloys appear ductile under bend testing up to an angle of 180°. Annealing the samples very carefully may even improve the mechanical properties. For instance (table 2), the Al<sub>90</sub>Fe<sub>5</sub>Gd<sub>5</sub> amorphous alloy shows  $\sigma = 735$  MPa, E = 50,7 GPa in the as-cast state. After annealing for 20 mn at 445K, the same alloy gives rise to  $\sigma = 1010$  MPa and E = 48,6 GPa and no embrittlement is observed<sup>59</sup>. Similarly, extrusion techniques are suitable for producing bulk specimens after compaction of AAA powders. The mechanical properties thus obtained appear rather outstanding as compared to values typical of conventional materials of the same specific mass<sup>13</sup>. Applications, for instance in aero-space industry, are in progress.

At first glance, quasicrystalline alloys show no sign of ductility and behave like many intermetallics : they are brittle at room temperature. For instance, an alloy of composition Al<sub>63.5</sub>Cu<sub>24.5</sub>Fe<sub>12</sub>, which forms a pure icosahedral phase<sup>49</sup>, breaks at 250 MPa and 0.35% elongation during compressive testing at room temperature<sup>60</sup>. Nevertheless, the situation may be most significantly improved either by heat treatment or by alloying to minority additions such as boron<sup>60</sup>.

Annealing the previous alloy at 650°C during 3 hours rises the fracture strength to 690 MPa and the deformation at rupture to 1.1%. Meanwhile, the Young modulus and Vickers hardness keep unchanged (table 2), the latter value being as high as 715.

Similarly, an alloy of composition  $\text{Al}_{67}\text{Cu}_9\text{Fe}_{10.5}\text{Cr}_{10.5}\text{Si}_3$  produces a crystalline phase, with giant unit cell, which closely resembles the decagonal phase<sup>61</sup>. In the as-cast state, it was measured :  $\sigma = 595$  MPa,  $E = 89$  GPa and  $H_v = 670$ <sup>60</sup>. These values may be significantly enhanced by addition of 5.5 at% boron. Then,  $\sigma = 1060$  MPa,  $E = 1060$  GPa,  $\epsilon = 1\%$  and  $H_v = 560$  (table 2). After addition of boron, the previous  $\text{Al}_{63.5}\text{Cu}_{24.5}\text{Fe}_{12}$  alloy gives  $\sigma = 1010$  MPa,  $E = 118$  GPa,  $\epsilon = 0.85\%$  despite the Vickers hardness turns to a value as high as 850. Furthermore, all the alloys that we have tested so far exhibit a marked superplastic behaviour at high temperature (figure 15).

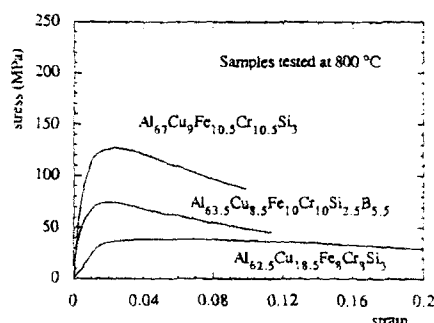


Figure 15 : Compressive stress-strain curves measured at 800°C for three quasicrystalline alloys. Note that the applied stress was removed before fracturing the specimen.

Finally, let me mention that fairly low friction coefficients were observed between various types of indenters and coatings of quasicrystalline structure prepared by plasma spraying of powders of appropriate composition as reported in table 2. This has recently opened a field of applications for quasicrystalline alloys<sup>62</sup> but many others should follow.

## 5. Conclusion

Amorphous aluminium-based alloys present a great variety of structures, of crystallization mechanisms, of properties. They are in many respects similar to the fascinating quasicrystalline alloys that were more recently discovered. Conversely, they are not stable and should not fit to the same types of applications. Despite the size of the atomic constituents plays an important role in the formation of both kinds of materials, it is rather clear that the conditions for their formation are still to be understood in detail. Understanding the mechanisms that promote the growth of quasicrystal might be of great help along this line but it must be stressed that aluminium glasses specially focus attention to the non-uniqueness of the metallic glass nature. They form therefore probably the most

exciting class of metallic glasses to tackle. No need to say that several groups are on the track and that good science, both fundamental and applied, is expected to continue to flow in next future.

## 6. References

1. P.H. Gaskell, *Nature* **276** (1978) 484 ; *J. Non Cryst. Sol.* **32** (1979) 207.
2. P.H. Gaskell, *Nature* **289** (1981) 474.
3. P.H. Gaskell, *Acta Metall.* **29** (1981) 1203.
4. J.M. Dubois and G. Le Caër, *Nucl. Inst. Meth.* **199** (1982) 307.
5. G. Le Caër and J.M. Dubois, French patent n° 82/12404, 6 July 1982.
6. J.M. Dubois and G. Le Caër, *C.R. Acad. Sci. Paris* **301-2** (1985) 73.
7. R.O. Suzuki, Y. Komatsu, K.F. Kobayashi and P.H. Shingu, *J. Mater. Sci.* **18** (1983) 1195.
8. S. Dermakar, French patent n° 85/03318, 27 February 1985.
9. B. Chenal, Thesis, Nancy 1988, unpublished.
10. D. Shechtman, I. Blech, D. Gratias and J.W. Cahn, *Phys. Rev. Lett.* **53** (1984) 1951.
11. Y. He, S.J. Poon and G.J. Shiflet, *Science* **241** (1988) 1640.
12. A. Inoue, K. Ohtera, A.P. Tsai and T. Masumoto, *Jap. J. Appl. Phys.* **27** (1988) L479.
13. A. Inoue, K. Ohtera and T. Masumoto, *Sci. Rep. RITU A-35* (1990) 115.
14. A. Inoue, T. Masumoto, H.M. Kimura and T. Masumoto, *J. Mat. Sci. Lett.* **6** (1987) 194.
15. A. Inoue, A. Kitamura and T. Masumoto, *J. Mater. Sci.* **16** (1981) 1895.
16. E. Nold, P. Lamparter, H. Olbrich, G. Rainer-Harbach and S. Steeb, *Z. Naturforsch.* **36a** (1981), 1032.
17. H.Y. Hsieh, B.H. Toby, T. Egami, Y. He, S.J. Poon and G.J. Shiflet, *J. Mater. Res.* **5-2** (1990) 2807.
18. J.M. Dubois and C. Janot, *J. Phys. (Paris)* **48** (1987) 1981.
19. J.M. Dubois, K. Dehghan, P. Chieux and M. Laridjani, *J. Non Cryst. Sol.* **93** (1987) 179.
20. J.L. Robertson, S.C. Moss and K.G. Kreider, *Phys. Rev. Lett.* **60-20** (1988) 2062.
21. M. Cooper and K. Robinson, *Acta Cryst.* **20** (1966) 614.
22. J. Pannetier, J.M. Dubois, C. Janot and A. Bildé, *Phil. Mag. B* **55-4** (1987) 435.
23. J.W. Cahn, D. Shechtman and D. Gratias, *J. Mater. Res.* **1** (1986) 1.
24. J.M. Dubois, M. de Boissieu, A. Pianelli, J. Pannetier and C. Janot, *Scripta Metall.* **23** (1989) 1069.
25. J.M. Legresy, M. Audier, J.P. Simon and P. Guyot, *Acta Metall.* **34-9** (1986) 1759.
26. S.J. Poon, A.J. Drehman and K.R. Lawless, *Phys. Rev. Lett.* **55-21** (1985) 2324.
27. S. Sachdev and D.R. Nelson, *Phys. Rev. Lett.* **53-20** (1984) 1947.
28. A.M.B. Douglas, *Acta Cryst.* **3** (1950) 19.
29. J.M. Dubois, B. Malaman, B. Chenal and G. Venturini, *C.R. Acad. Sc. Paris* **304** (1987) 641.
30. H. Matyja, K.C. Russel, B.C. Giessen and N.J. Grant, *Met. Trans. A* **6** (1975) 2249 ;  
B. Cantor and R.W. Cahn, *J. Mat. Sci.* **11** (1976) 1066.
31. S. Andersson and B.G. Hyde, *J. Sol. St. Chem.* **9** (1974) 92.
32. J.M. Dubois, *J. Less Common Met.* **145** (1988) 309.
33. J.M. Dubois and C. Janot, *Phil. Mag B* **61-4** (1990) 649.
34. X.Z. Li and K.H. Kuo, *Phil. Mag. Lett.* **58** (1988) 167.
35. D. Bechet and G. Regazzoni, *Mat. Sc. Eng.* **A134** (1991) 1120.
36. Y. He, S.J. Poon and G.J. Shiflet, *Scripta Metall.* **22** (1988) 1813.
37. T. Egami and Y. Waseda, *J. Non-Cryst. Solids* **64** (1984) 113.
38. R.A. Unlap and K. Dini, *J. Mater. Res.* **1(3)** (1986) 415.
39. L.C. Chen and F. Spaepen, *Nature* **336** (1988) 366.

40. L.C. Chen, F. Spaepen, J.L. Robertson, S.C. Moss and K. Hiraga, *J. Mater. Res.* 5(9) (1990) 1671.
41. Y. He, H. Chen, G.J. Shiflet and S.J. Poon, *Phil. Mag. Lett.* 61-5 (1990) 297.
42. J. Friedel, *Helv. Phys. Acta* 61 (1988) 538.
43. A. Eckert, L. Schultz and B. Urban, *Europhys. Lett.* 13(4) (1990) 349.
44. J. Pannetier, J.M. Dubois, C. Janot and A. Bildé, *Phil. Mag.* ...
45. U. Köster, Mospoq Conference, Balatonzeplaq, Hungary (1991) to appear in *Phase Transitions*.
46. E. Belin, J. Kojnok, A. Sadoc, A. Traverse, M. Harmelin, C. Beyer and J.M. Dubois, *J. Phys : Cond. Matter.*, in press.
47. J.C. Lasjaunias, C. Berger, K. Hasselbach, C. Paulsen, G. Fourcandot and J.C. Grieco, *Quasicrystalline Materials*, eds C. Janot and J.M. Dubois, World Scientific, Singapore (1988) 389.
48. A. Gozlan, C. Berger, G. Fourcandot, R. Omari, J.C. Lasjaunias and J.J. Préjean, *Phys. Rev. B* 44 (1991) 575.
49. A.P. Tsai, A. Inoue and T. Masumoto, *Jap. J. Appl. Phys.* 26-9 (1987) L1587
50. J.M. Dubois, C. Dong, C. Janot, M. de Boissieu and M. Audier, *Phase Transitions* 32 (1991) 3.
51. M. Widom, K.J. Strandburg and R.H. Swendsen, *Phys. Rev. Lett.* 58-7 (1987) 706.
52. T. Klein, A. Gozlan, C. Berger, F. Cyrot-Lackman, Y. Calvayrac and A. Quivy, *Europhys. Lett.* 13(2) (1990) 129.
53. C. Dong, J.M. Dubois, S.S. Kang and M. Audier, *Phil. Mag.*, in press.
54. C. Dong and J.M. Dubois, *Phys. Rev. B* 1. submitted.
55. W. Steurer and K.H. Kuo, *Phil. Mag. Lett.* 62 (1990) 175.
56. V.P. Dmitriev, S.B. Rochal, Y.M. Gufan and P. Toledano, *Phys. Rev. Lett.* 60 (1988) 1958.
57. K. Chattopadhyaya, S. Lele, N. Thangaraj and R. Ranganathan, *Acta Metall.* 35-3 (1987) 727.
58. L. Pauling, *Phys. Rev. Lett.* 58 (1987) 365.
59. H. Chen, Y. He, G.J. Shiflet and S.J. Poon, *Scripta Metall. Mater.* 25 (1991) 1421.
60. S.S. Kang and J.M. Dubois, *Phil. Mag.* submitted.
61. C. Dong and J.M. Dubois, *J. Mater. Sc.* 26 (1991) 1647.
62. *Advanced Materials and Processes* 139-6 (1991) 6.

Acknowledgement : The neutron diffraction work reported on in this paper was performed at Institut Laue Langevin (Grenoble) and Laboratoire Léon Brillouin (Saclay). It has benefited from help of R. Bellissent, P. Chieux, C. Janot, A. Menelle and J. Pannetier.



# MAGNETOELASTIC INTERACTIONS IN AMORPHOUS FERROMAGNETS: THEORY AND APPLICATIONS

H.T. SAVAGE and M. VÁZQUEZ\*

Instituto de Magnetismo Aplicado of the Universidad Complutense and RENFE  
Apartado 155, Las Rozas (Madrid), 28230, Spain

\*Instituto de Ciencias de Materiales, Serrano 144, 28006 Madrid, Spain

## ABSTRACT

In this paper we survey applications of magnetoelastic amorphous ribbons and wires. The applications exploit the extremely high figures of merit caused by the low anisotropy obtained from the magnetic annealing. The applications include torque sensors, accelerometers and counters. The bistable magnetization of wires is considered in detail, covering recent experimental data in the inverse Wiedemann and Matteucci effect.

## 1. Introduction

The decrease in the value of Young's modulus  $E(H)$  caused by rotation of the magnetic moment in a solid is called the  $\Delta E$  effect. The externally applied magnetic field  $H$  is used to rotate the magnetic moment. The  $\Delta E$  effect has become important because it has recently become possible to reversibly change the value of  $E(H)$  by a factor of 10 in certain amorphous ferromagnetic materials with a field three times the earth's field<sup>1</sup>. This has led to quite definitive experiments in the field of nonlinear dynamics where important nonlinear phenomena, chaotic and nonchaotic, have been observed for the first time<sup>2</sup>. Several significant efforts exist to exploit the new materials in ribbon material in applications such as accelerometers, pressure sensors, strain gages, torque sensors and security devices<sup>3</sup>. Wire material, in spite of being the same amorphous composition, shows quite different characteristics because of the cylindrical geometry. Large amplitude Barkhausen jumps will be reviewed in theory and experiment. This is a phenomenon not seen in the ribbon material because in wires a hierarchy of coercive fields determines the kind of magnetization process. Counters and threshold devices are possible applications of large amplitude Barkhausen jumps. Wire material can also have superior characteristics for torque sensors and magnetometers. Some magnetoelastic theory will be presented for cylindrical geometries. We begin by describing the  $\Delta E$  in ribbon material. The result is a large amplitude stress-strain theory<sup>4</sup>.

## 2. Review of the $\Delta E$ Effect

A sample of transversely field-annealed amorphous ribbon material which is shown with its domain structure in Fig. 1. In this simplified model the domain walls play no role in the generation of longitudinal magnetization  $M$ . The total magnetization

is the sum of equivalent longitudinal components in each domain due to moment rotation. We therefore just have to consider what goes in one domain when the applied magnetic field is in the usual (longitudinal) direction.

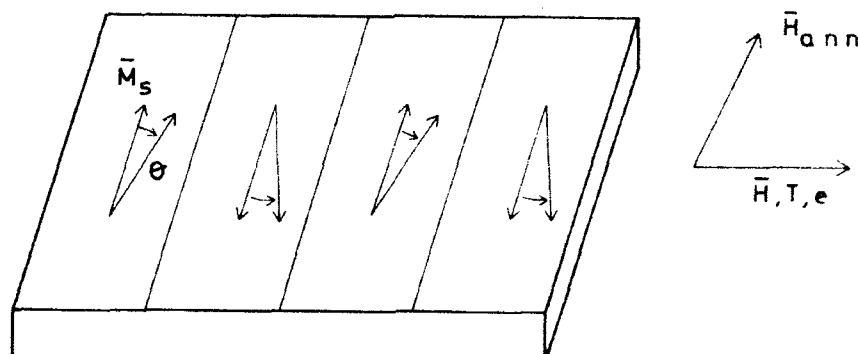


Fig. 1. The magnetic structure of transversely-field annealed amorphous material of approximate composition  $\text{Fe}_{80}\text{B}_{15}\text{Si}_5$ . The annealing field (not the applied field) is in the plane of the ribbon and perpendicular to the longitudinal axis. The ribbon is held in the annealing field at  $\approx 475^\circ\text{C}$  for ten minutes. As the temperature is lowered below the Curie point the presence of exchange forces and the transverse-annealing field of  $10^3 \text{ A/m}$  or more generates a magnetic anisotropy  $K$  of about  $40 \text{ J/m}^3$ . The value of  $K$  represents the magnetic energy necessary to rotate the moment from the transverse to the longitudinal direction. A simplified domain pattern is shown. We ignore the closure domains that exist on the edges. The longitudinal variables are the moment  $M$ , applied field  $H$  (not the annealing field), stress  $T$  and strain  $e_{zz}$ . The saturation moment is  $M_s$ . As  $H$  is increased from zero the moments in each domain rotate and the sample becomes longer (shorter) with positive (negative) magnetostriction. The change in length per unit length at magnetic saturation ( $M = M_s$ ) is  $3\lambda_s/2$ . In the composition listed above the value of  $\lambda_s$  is  $\approx 35 \times 10^{-6}$ .

In the derivation of an expression for Young's modulus in a linear elastic solid we simply write down the elastic energy and minimize it with respect to the strains  $e_{ij}$ . The differentials of the energy with respect to the strains are set equal to zero except for the differential with respect to the longitudinal strain  $e$  which is set equal to the applied longitudinal stress  $T$  (Fig. 1). The result is Hooke's law,  $T = E_0 e$ .  $E_0$  is an expression for Young's modulus in terms of the elastic constants,  $c_{ij}$ , of the solid. For our derivation of the  $\Delta E$  effect we do the same thing except that now there are more terms in the energy. We must include the Zeeman energy  $-MH$  (due to the forces tending to align the magnetic moment with the field), the anisotropy energy  $K$  (due to atomic forces tending to align the magnetic moment with a certain material axis) and the magnetoelastic energy (due to atomic forces resulting from the interaction between the magnetic and elastic systems). We assume there is no nonzero component of the magnetization out of the plane of the ribbon. Then  $M = M_s \cos \theta$  where  $\theta$  is the angle between the longitudinal axis and the magnetic moment vector

$\underline{M}_z$  (Fig. 1). With this assumption the Zeeman energy is  $-H M_z \cos \theta$ , the anisotropy energy is  $K \cos^2 \theta$ , and the magnetoelastic energy<sup>5</sup> becomes:

$$E_{me} = -(3\lambda_s/2)(c_{11} - c_{12})(e_{xx}(\sin^2 \theta - 1/3) + e_{zz}(\cos^2 \theta - 1/3) - e_{yy}/3 + e_{xz} \sin \theta \cos \theta),$$

with the elastic energy

$$E_e = c_{11}(e_{xx}^2 + e_{yy}^2 + e_{zz}^2)/2 + c_{12}(e_{xx}e_{yy} + e_{yy}e_{zz} + e_{zz}e_{xx}) + (1/2)(c_{11} - c_{12})(e_{xy}^2 + e_{xz}^2 + e_{yz}^2)/2 - e_{xz}T.$$

After minimizing the total energy with respect to the  $e_{ij}$  we obtain:

$$e_{zz} = T/E_0 + (3\lambda_s/2)(\cos^2 \theta - 1/3) \quad (1).$$

We can call (1) Hooke's law for our isotropic magnetoelastic solid. The result contains the usual expression for Young's modulus  $E_0$  in an isotropic solid. The usual strain  $T/E_0$  is incremented by the magnetostrictive strain  $(3\lambda_s/2)\cos^2 \theta$ , the change in length of the sample caused by rotation of the magnetic moment. In Eq. (1) we can see the cause of the  $\Delta E$  effect. When a small stress  $\delta T$  is imposed on the sample with  $H = \text{constant} > 0$ , the moment rotates to lower the energy. Thus an additional strain to  $\delta T/E_0$ , a magnetostrictive strain, is observed and since Young's modulus  $E(H) \equiv (\delta T/\delta e)_H$ , a lower or "softer" modulus is observed.

The energy must also be minimized with respect to the direction of the moment, i.e., with respect to  $\theta$ . The slope is called the susceptibility  $\chi$  and in our materials has almost the same value as the permeability  $\mu$ . We simulate defects by imposing a small shear stress  $T_{xz} = S$  on the sample. This adds a term  $-Se_{xz}$  to the elastic energy. The result is:

$$M_z H = \cos \theta (2K - 3\lambda_s T + 6\lambda_s S \cot 2\theta) \quad (2).$$

The sample never truly saturates no matter how high the field. The moment only rotates close to the longitudinal direction when  $T$  or  $H$  are large. The stress appears as a magnetic anisotropy. The stress is externally applied so that we now have an externally controllable susceptibility or permeability. Later we will show how this can be exploited in devices. The  $\Delta E$  effect or the determination of the field dependence of  $E = \delta T/\delta e$  at constant  $H$  around  $e = e_0$  can now be determined. The results are shown in Fig. 2. The excellent agreement with experiment is also shown.

The coupling factor  $k_{33}$  can now be defined by the relationship  $E(H) = E_0(1 - k_{33}(H)^2)$ . Large values of  $k_{33}$  imply a large  $\Delta E$  effect. In fact, if  $k$  is the maximum value of  $k_{33}$  then, in the simple rotational model ( $S = 0$ ),  $D = (3\lambda_s)^2 E_0/2K = k^2/(1 - k^2)$ . Values of the  $\Delta E$  effect and coupling factor are shown in Table I for different materials. The large values of  $k_{33}$  in amorphous ribbons occur because values of  $K$  are so small. Large values of  $k_{33}$  are desired in applications.

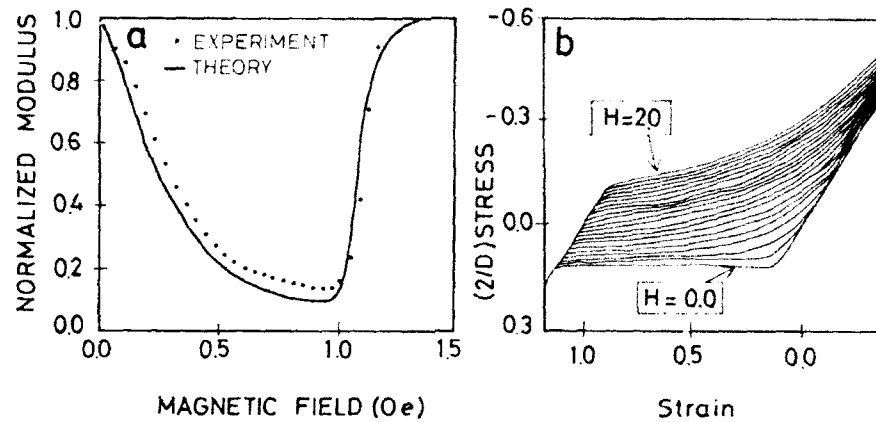


Fig. 2. (a) Normalized modulus  $E(H)/E_0$  vs  $H$  from the theory (line) given later in the text and the experimental results (dots).  $E_0$  is Young's modulus without magnetoelastic interactions. The decrease is caused by the stress rotating the magnetic moment. (b) Stress-strain curves for the theory with  $D = (3\lambda_s)^2 E_0 / 2K$ . The material is described in caption of Fig. 1.

Table I

Ferromagnetic Material		Maximum Coupling Factor, $k_{33}$	$(E_0 - E(H)_{min})/E(H)_{min}$
Fe		approx. 0	approx. 0
Ni		.32	.11
Amorphous Ribbon	$Fe_{67}Co_{17}B_{14}Si_2$	.72	1.08
Amorphous Ribbon	$Fe_{78}B_{12}Si_{10}$	.82	2.03
Amorphous Ribbon	$Fe_{81}B_{13.5}Si_{3.5}C_2$	.95	9.25
Amorphous Ribbon	$Fe_{81}B_{13.5}Si_{3.5}C_2$	.97	10.0
Amorphous wire	$Fe_{77.5}Si_{7.5}B_{15}$	.95	$\approx 10$

The coupling factor and  $\Delta E$  effect in various ferromagnetic materials.  $E(H)_{min}$  is the minimum value measured of Young's modulus. In the amorphous ribbon material the large values of  $k_{33}$  are highly dependent on composition, annealing conditions and surface quality. The addition of  $Co$  leads to a higher magnetic anisotropy energy, hence lower values of  $k_{33}$ . The higher value in the last ribbon entry is due to an improvement in surface quality.

### 3.- Large Barkhausen Jumps in Amorphous Wires.

The study of magnetic properties of wire shaped amorphous wires is a topic of growing interest. Like amorphous ribbons, wires exhibit very good properties as soft magnetic materials (i.e. coercive fields are of the order of magnitude of tens of mOe depending on composition and magnetostriction constant). First peculiarity distinguishing wires and ribbons is of course their different shape. Cylindrical symmetry of wires makes their treatment more difficult from a theoretical point of view but makes them suitable for some particular applications. One of the most attractive magnetic features is the possibility of getting bistable behavior (i.e. Wiegand wire like magnetic behavior) without any heat treatment<sup>6</sup>.

In the case of Fe-rich wires, after applying and removing a saturating axial field, magnetization remains at the remanent state with a value close to one half of saturation. Upon application of a field in the opposite direction, axial magnetization slightly decreases until a critical or switching field is reached. Then a single Barkhausen jump is observed and magnetization takes on a negative value. A further increase of the field leads to a reversible increase of magnetization that reaches saturation value.

It should be noticed that the unmagnetized state cannot be reached for these wires. For comparison, hysteresis loops of ribbon and wire shaped alloys with similar compositions are shown in Fig. 3. The bistable magnetic behavior (Fig. 3) can be understood by considering the domain structure of the wires. It consists of two regions (a) the inner core and (b) the outer shell where the magnetization spontaneously lies roughly along axial and transverse directions respectively<sup>7,8</sup>. This domain structure is determined by the energetic contributions from intrinsic magnetoelastic anisotropies and demagnetizing effects as we will discuss later. Consequently, when an a.c. magnetic field larger than the switching field is applied along the axial direction, pulses can be detected on a pick-up coil wound around the wire. Similar pulses can be obtained when measuring the voltage induced between the ends of twisted wire (Matteucci effect). In short, this bistable behavior is the basis of a number of applications such as pulse generator elements, proximity sensors, etc., which can be used in the robotic and automobile industries for example<sup>9</sup>.

On the other hand, the switching field depends on applied stresses (tensile, compressive and torsional) as a consequence of the additional magnetoelastic anisotropies introduced by them. Moreover microstructural changes produced by treatment activated either thermally or by cold drawing also give rise to modified magnetic behavior. All these dependences are reviewed below since they are important not only for designing particular applications but also to get further information about the fundamental magnetism underlying the excellent properties of the wires.

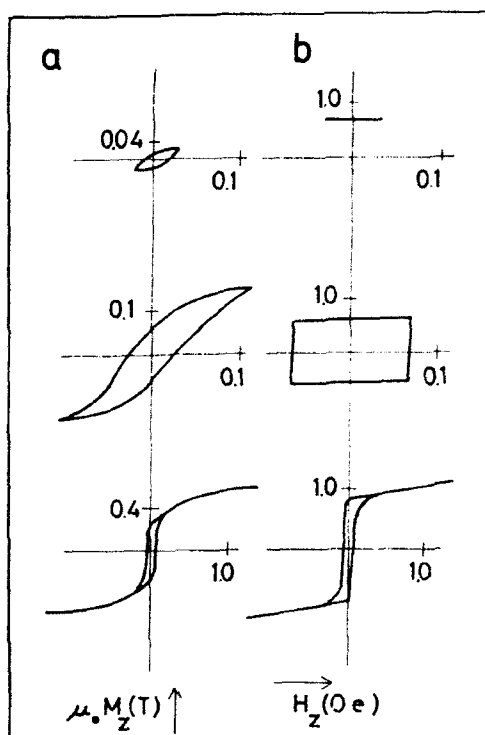


Fig. 3. Typical hysteresis loops of Fe-base ribbon (a) and wire (b) amorphous alloys with similar compositions.

#### A. Axial Bistable Behavior and Domain Structure.

The origin for bistability in amorphous wires with large magnetostriction is their characteristic domain structure. Domain structure at the surface of as-cast wires has been observed by means of the Bitter technique<sup>10</sup>. Patterns are interpreted as showing the existence of a transverse easy axis for the magnetization as well as random helical easy axes. By polishing the sample, it is possible to observe an inner part of the wire where the easy axis is roughly parallel to the axial direction<sup>11</sup>. Owing to the lack of long range atomic periodicity magnetocrystalline anisotropy can be neglected so that magnetoelastic anisotropies play the dominant role in determining such domain structure. In the as-cast state, internal stresses frozen-in during the fabrication couple with the magnetostriction constant creating large magnetoelastic anisotropies that fix the easy magnetization direction.

When fabricating the wires by the in-water-quenching technique<sup>12</sup>, the molten alloy plunges into water so that, the cooling process gives cylindrical symmetry. In

this way, the surface solidifies before the inner part of the wire. As a consequence of the thermal gradient along the radial direction, distributed internal stresses are quenched. Several efforts were made in order to obtain the actual distribution of internal stresses<sup>13,14</sup>. Considering the wire as formed by superimposed narrow cylindrical tubes, according to theory of elasticity, the radial thermal gradient gives rise to three components of internal stresses namely, radial, azimuthal and axial, determined by the elastic constants, dilatation coefficient and temperature inside each tube. Integration of these local stresses along the radial coordinate results in the global expression for the internal stresses once the heat conduction equation is solved to evaluate the radial dependence of temperature. The detailed procedure has been reported elsewhere<sup>15,16</sup>. The resultant radial distribution of the stress components is shown in Fig. 4.

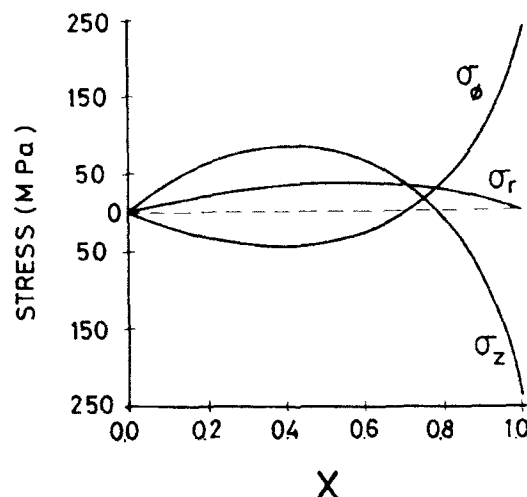


Fig. 4. Radial distribution of internal stress.  $X$  is the distance to the axis normalized to the wire radius.

Considering the coupling between internal stresses and magnetization through the magnetostriction constant, the easy axis for the magnetization can be obtained. Fig. 5 shows that angle between easy magnetization direction and the wire axis as a function of the reduced radial coordinate,  $r$ . Two regions are then distinguished, an inner core up to  $r \approx 0.7$  with almost axial magnetization and an outer shell with transverse easy axis. It is important to notice that easy magnetization direction has

also an azimuthal component in the whole radial range.

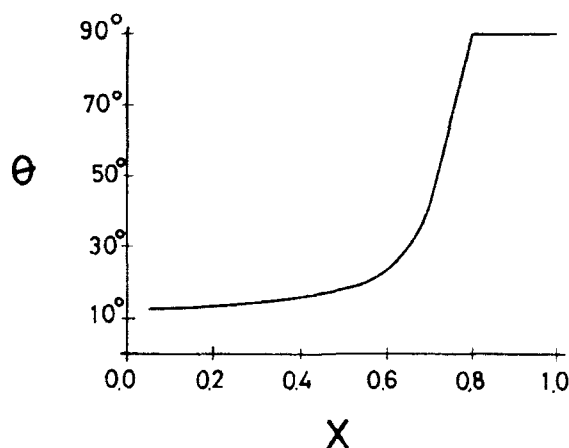


Fig. 5. Polar angle of easy magnetization direction as a function of the radial coordinate.

Very recent results examining the influence of the sample's length<sup>17</sup>, complex susceptibility<sup>18</sup>, and hysteresis loops<sup>19</sup>, as a function of the distance to the wire end, give valuable information on the actual internal domain structure of wires. Fig. 6 shows the hysteresis loops for a 10 cm long  $Fe_{77.5}Si_{7.5}B_{15}$  wire at distances  $d$  of 1 cm and 5 cm from the end of the wire.

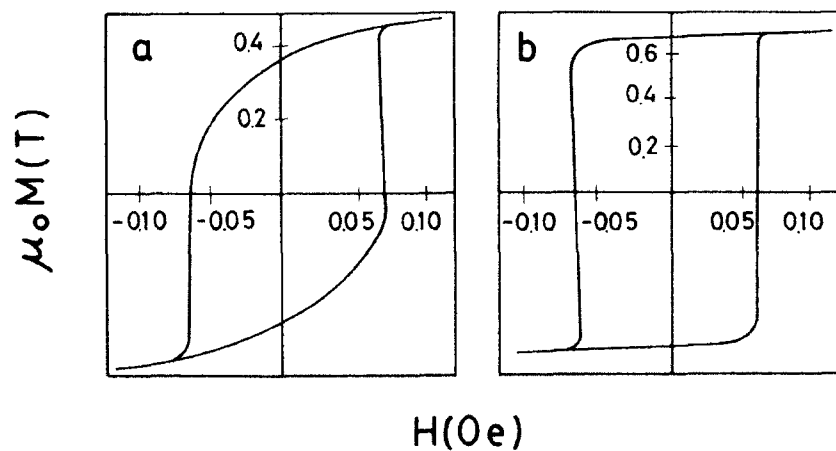


Fig. 6. Axial hysteresis loops of  $Fe_{77.5}Si_{7.5}B_{15}$  wire at 1 cm (a) and 5 cm (b) distance to the end.



Assuming that only the inner core contributes to the switching process, the squareness ratio,  $m_r = M_r/M_s$ , of the loop gives us information on the fractional volume of such a core. Considering the dependence of  $m_r$  on  $d$  it is possible to deduce the existence of a kind of closure domain, probably conical or trumpet-shaped, at the wire end (with reversed magnetization). This closure domain extends over a distance of 3 to 4 cm along the wire. The energy required to form the limiting wall should come from the decrease in magnetostatic energy at the wire end.

On the other hand, the demagnetizing field of the inner core plays a very important role in determining the domain structure and the hysteresis loops. Fig. 7 shows the loops of samples having different lengths. It is observed that for lengths less than around 6 or 7 cm no bistability appears. In fact, this critical length seems to be related to the length of the closure domains discussed above.

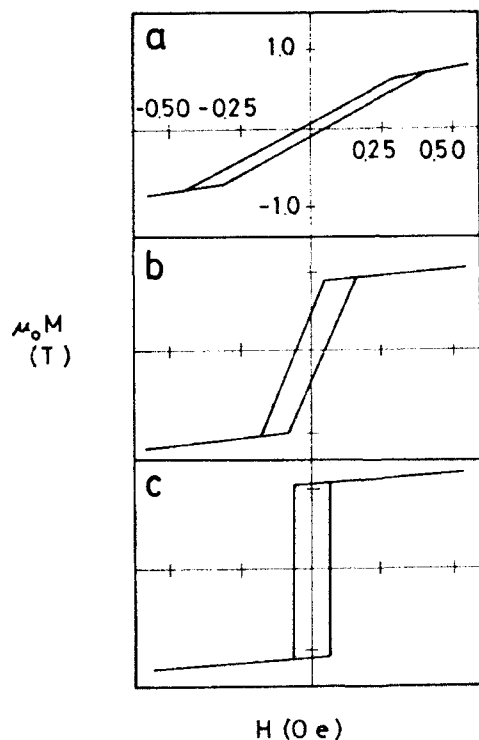


Fig. 7. Axial hysteresis loops of  $F_{77.5}Si_{7.5}B_{15}$  wires having different length: (a) 3 cm, (b) 6 cm and (c) 9 cm.

Up to now, the switching field has been associated with the field necessary to nucleate a small domain with reversed magnetization inside the inner core. This nucleation, being larger than the propagation field, would produce a quick reversal of

magnetization in the whole inner core. Nevertheless, in accordance with the suggested results, it seems likely that the switching field should be related to the wall pinning associated with the pole density at the wire end or just with the increase of wall surface during the switching process. A general expression for the switching field  $H^*$ , has been suggested<sup>17</sup>:

$$H^* = aE_g - bM_s \quad (3)$$

$E_g$  is the energy density of the wall inside the inner core,  $a$  is a parameter denoting the shape of the wall and  $b$  is the effective demagnetizing factor of the inner core which becomes less important as the length of the wire increases. It should be noticed that after switching, the same domain structure is kept but with reversed magnetization inside the core and the closure domains.

#### B. Influence of Applied Stress on the Switching Process.

The influence of applied tensile, compressive and torsional stresses has been reported in a series of works<sup>17,20-24</sup>. In the following, we summarize some of the most interesting results regarding such dependences. We will focus on two parameters namely the switching field  $H^*$ , and the squareness ratio,  $m_r$ . Fig. 8a and 8b, show the applied tensile stress,  $s_a$ , dependence of  $H^*$  and  $m_r$  respectively as measured at the middle of wires with different lengths.

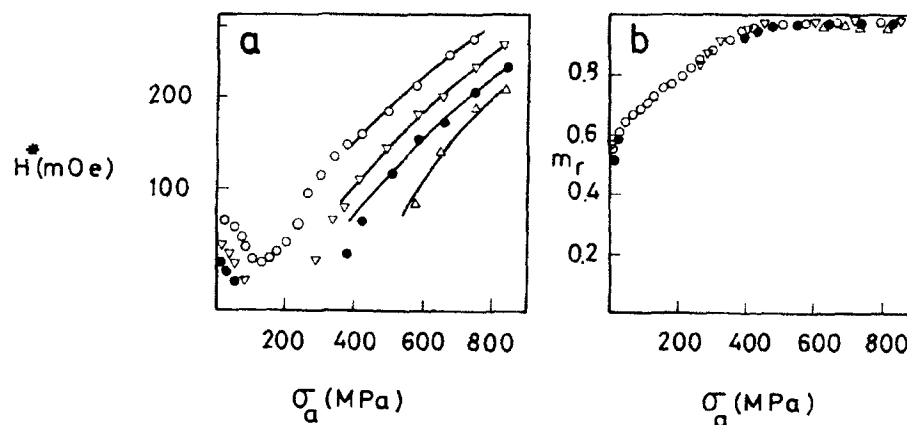


Fig. 8. Applied tensile stress dependence of switching field (a) and squareness ratio (b) for  $F_{77.5}Si_{7.5}B_{15}$  wires having different lengths: 12 cm (o), 10 cm ( $\nabla$ ), 8.5 cm ( $\bullet$ ), and 6 cm ( $\Delta$ )

Assuming again that  $m_r$  corresponds to the fractional volume of the inner core, it can be observed that this volume increases with stress and saturates for an applied stress close to 400 MPa. Such an increase is interpreted as arising from magnetoelastic anisotropy  $K_s$  induced by the applied tensile stress,  $s_a$ , with axial easy axis:

$$K_s = 3/2\lambda_s s_a \quad (4)$$

As stress increases, it overcomes internal stresses at the outer shell thereby in-

creasing the core volume and for the largest values of applied stress the whole wire has the same domain structure as the core. Accordingly, when compressive stresses are applied, remanence of the loops decreases progressively up to a negligible value.  $H^*$  decreases with decreasing length as a consequence of the larger demagnetizing field (Eq. 3). The stress dependence of  $H^*$ , after an initial reduction, increases monotonically with a phenomenological linear dependence on  $s_a^{1/2}$  for the largest  $s_a$ . For the shortest wire no bistability appears at zero applied stress but bistability is observed after applying a large enough stress. Fig. 9 shows the dependence of  $H^*$  and  $m_r$  on applied torsional strain,  $z$ .

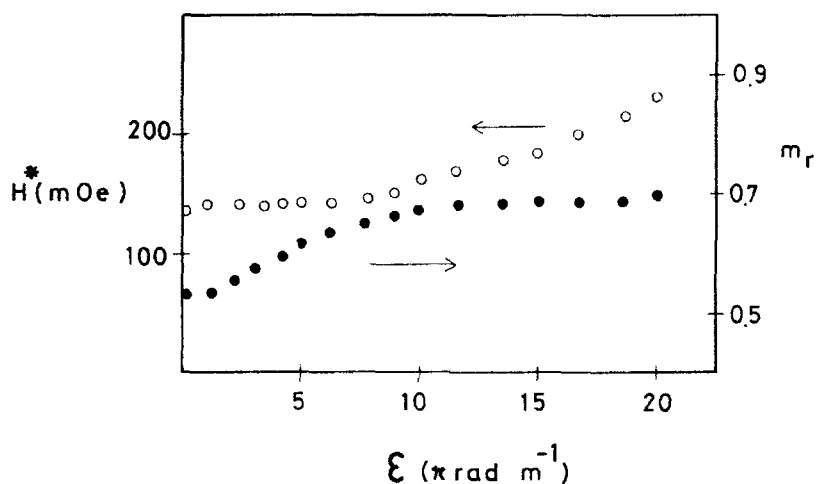


Fig. 9. Dependence of switching field and squareness ratio on applied torsional strain.

This strain induces a helical magnetoelastic anisotropy  $K_t$  with easy axes at 45 deg with the axis of the wire and magnitude:

$$K_t = 3/2\lambda_s m_z r \quad (5)$$

$m$  being the shear modulus and  $r$  the distance to the axis. For large enough applied twist, the magnetization follows a helical path in the whole wire so that, the remanence is expected to be  $m_r = \cos \pi/4 = 0.71$  as shown in Fig. 9. The switching field shows a slight dependence on twist at low applied twists, while for the torsional strains at which  $m_r = 0.71$ ,  $H^*$  shows (experimentally) a linear increase with  $z^{1/2}$ . When applying saturating stresses,  $m_r = 1$  for tensile stresses and  $m_r = 0.7$  for torsional stresses. Further increases in stress do not produce any change of domain structure at the remanent state so that no influence of the demagnetizing field in Eq. (3) has to be considered. Therefore  $H^*$  can be rewritten as  $H^* = \alpha E_g - H_d$ , where the demagnetizing field  $H_d$  is constant for a given length of wire. The wall energy density  $E_g$ , in the range of applied stresses larger than the internal stresses, can be expressed as  $E_g = g(AK)^{1/2}$ , where  $g$  is a constant,  $A$  the exchange constant and  $K$

the magnetoelastic energy density introduced by the applied stresses. Taking into account Eq. 4 and 5, we obtain for  $H^*$  the stress dependence  $H^* = as_s^{1/2}$  for tensile or torsional stresses. The constant  $a$  is related to the wall shape during the switching process.

### C. Switching Process and Induced Anisotropies.

It is well known that thermal treatments of metallic glasses relax the internal stresses frozen in during the fabrication process. Moreover when annealing is performed under the action of magnetic fields or applied stresses, macroscopic magnetic anisotropies are induced. The influence of various thermal treatments on the switching process of large magnetostriction amorphous wires has been reported in several works<sup>24-29</sup>. A consequence of the relaxation of internal stresses produced by single thermal treatment is the disappearance of bistable behavior. In this case the spontaneous formation of the inner core can be destroyed and only when large magnetoelastic anisotropies are induced by applying stress is bistability recovered<sup>17</sup>. When the treatment is performed at the presence of a transverse field, a transverse induced anisotropy can be detected. Transverse fields can be provided by an electromagnet or by making a current flow along the wire. In these cases perfect squareness of the loops are lost. Fig. 10 shows the hysteresis loops of a wire annealed in a 7.8 KOe transverse field for various applied torsional strains.

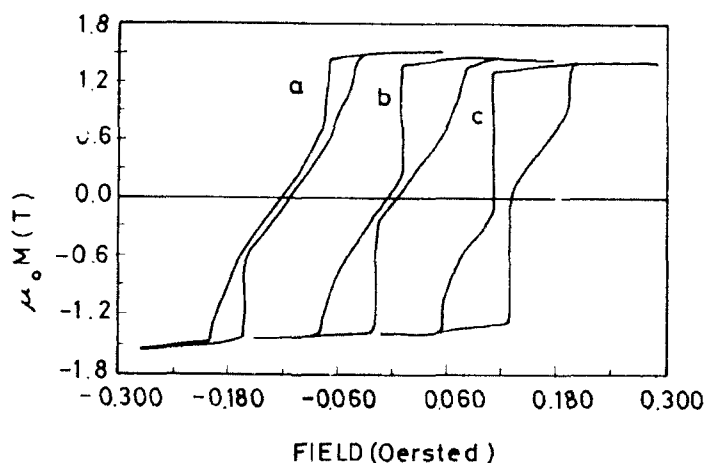


Fig. 10. Axial hysteresis loops of  $F_{77.5}Si_{7.5}B_{15}$  wire after annealing in transverse field with various torsional strains: (a) 15 deg, (b) 19 deg and (c) 23 deg.

Annealing under torsion gives rise to induced helical anisotropies. In Fig. 11, the helical anisotropy induced by current annealing under a torsional strain of 20 rad/m

is shown for an as-cast wire and after full relaxation.

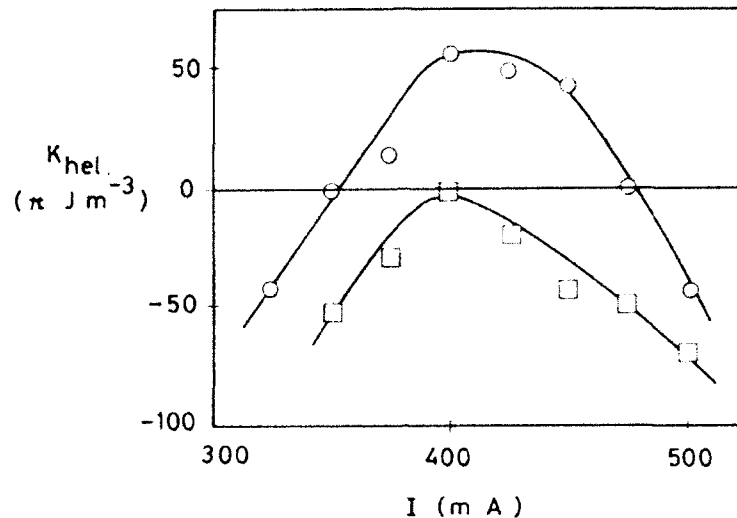


Fig. 11. Helical anisotropy induced by current annealing under twist for as-cast and relaxed wire.

Here, positive and negative values indicate the different helix of preferred magnetization. Quite recently<sup>29</sup>, it has been shown that bistable behavior can be obtained also for a Co-rich non-magnetostrictive wire after annealing at the presence of a tensile stress. Magnetic behavior of wires can be also modified by cold drawing. In this way the diameter of the wire can be greatly reduced. Consequently, large stresses are induced in such a way that bistability is lost and coercive fields reach values up to tens of Oe<sup>25,30</sup>. Nevertheless, bistability can be recovered after stress-field annealing. In this case, bistable behavior is found for wires 2 cm in length (Fe-Si-B wire) and 1 cm (Co-Fe-Si-B wires).

#### D. *Mattlucci and Inverse Wiedemann effects*

Shear stresses introduced by a torque on a wire are equivalent to the combination of tensile and compressive stresses of equal strength, mutually perpendicular, and making an angle of 45° with the wire axis. Consequently, a twist induces easy magnetoelastic directions following a helical path and non-diagonal terms appear in the susceptibility tensor

$$\begin{pmatrix} M_x \\ M_f \end{pmatrix} = \begin{pmatrix} \chi_{xx} & \chi_{xf} \\ \chi_{fx} & \chi_{ff} \end{pmatrix} \begin{pmatrix} H_x \\ H_f \end{pmatrix}$$

that leads to a net axial magnetization  $M_x$  when applying an azimuthal field  $H_f$  (inverse Wiedemann effect, IWE), or to a net azimuthal magnetization  $M_f$  when applying an axial field  $H_x$  (Mattlucci effect, ME). The helical stress  $t$  can be expressed in a

first approximation as  $t = m \cdot r$  that results in the helical magnetoelastic anisotropy given by Eq.5 (see Fig. 12). One has to keep in mind that neither the IWE nor the ME appear for purely axial or transverse magnetization processes.

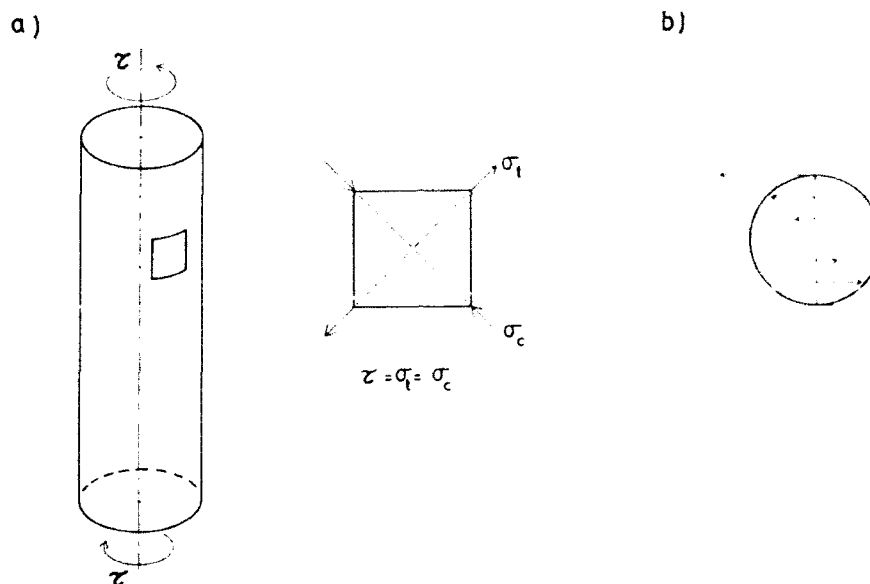


Fig. 12 Schematic view of the stress distribution in a wire under torsion: (a) tensile and compressive stresses acting on a surface element and (b) projection of resulting stress on the cross section of the wire.

Fig. 13 shows the spontaneous IWE and ME for a  $Fe_{77.5}Si_{7.5}B_{15}$  wire. As stated above, internal stresses give rise to easy magnetoelastic directions having axial and azimuthal components. Accordingly, such IWE and ME reflect the existence of a net helical component of magnetization in the as-cast wire. Both non-diagonal effects have been previously studied because they are important in applications<sup>10,15,23,31-34</sup>. In the case of IWE, the azimuthal field can be achieved with an a.c. current,  $I$ , through the wire (the intensity has to be small in order not to increase the sample temperature) yielding  $H_t = Ir/2\pi R^2$ ,  $R$  being the radius of the wire. The axial component of magnetization is obtained by integrating the induced signal of a pick-up coil surrounding the wire. When measuring the ME, the axial field is provided by a solenoid and the azimuthal magnetization can be obtained by integrating the voltage induced at the ends of the wire. As a consequence of the bistable behavior, even for non-diagonal effects, a well defined pulse can be detected either by a pick-up coil (IWE) or at the ends of the wire (ME) when the magnetization switches. In fact, it has been shown that such pulses are sharper and have less voltage jitter than either twisted

amorphous ribbons or Wiegand wires<sup>32</sup>.

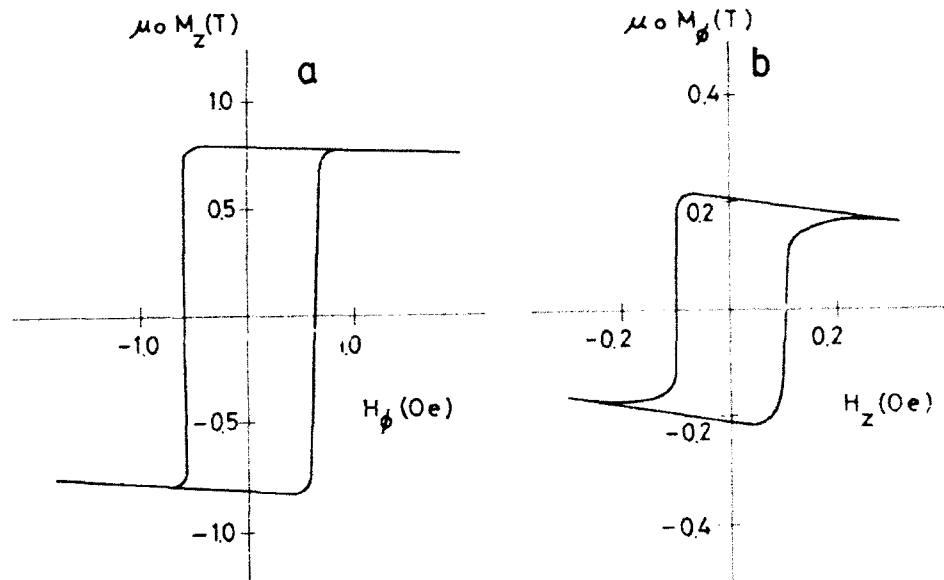


Fig. 13-Spontaneous inverse Wiedemann and Matteucci effects for the  $F_{77.5}Si_{7.5}B_{15}$  wire.

#### 4. Applications in Ribbon Material

The magnetic permeability in the simple rotational model ( $S=0$  in Eq. 3),  $\mu = \mu_0 + \chi$ ,  $\chi = (\partial M / \partial H)_T = M_s^2 / (2K + 3\lambda T)$ , is a function of the applied stress as seen in denominator of the  $\chi$ . Because the magnetic anisotropy energy  $K$  is very small the effects of small stresses are very large. This is equivalent to saying that effects of small strains are very large because we can replace  $T$  by its equivalent in Eq. 1. This characteristic has been exploited in the construction of a magnetoelastic strain gage. In ordinary resistive strain gages where one measures  $R$ , the resistance of the strain gage, the figure of merit is  $R^{-1} \partial R / \partial \epsilon \approx 2$ . With this device<sup>35</sup> strains are measured by measuring values of  $\mu$ . Therefore the figure of merit<sup>36</sup> is  $\mu^{-1} \partial \mu / \partial \epsilon = 3\lambda_s E_0 / 2K$ . Values of the figure of merit of around  $4 \times 10^5$  were observed. This is three orders of magnitude higher than in present strain gages (Wun-Fogle et al, 1987, Savage et al, 1988). Good temperature characteristics are expected because  $\lambda_s / K$  is roughly temperature independent. Accelerometers and pressure sensors can be built using a strain gage type construction. Fe based material has the highest figure of merit. Although the figure of merit in Co based material is lower, the negative magnetostriction of the Co based material has a big advantage when it is desired to have the device material in tension. A longitudinal tensile stress orients the moment normal to the long axis of the ribbon. The measuring field is along the long axis of the ribbon. Although the response will

be nonlinear large stresses will not saturate the device and a measurement can be effected<sup>3</sup>.

Sputtered amorphous materials can have the same properties as the bulk materials. A non-contacting torque sensor could be made for example by sputtering materials on a rotating shaft. Again the torque is measured by simply measuring the permeability with a coil placed about the shaft. We will say more about torque sensors when we talk about wires.

Suppose we impose a magnetic field  $H = H_0 + h_{ac}\sin\omega t$  on a sample like that of Fig. 1. Because the field is varying,  $E(H)$  is varying. This is equivalent to having a time dependent spring constant. With a system like this we expect a subharmonic bifurcation, i.e., the appearance of a response with period two (a frequency of  $\omega/2$ ) if the  $\Delta E$  effect is large enough. This experiment has been done by placing a pickup coil around the sample and observing the induced voltage. As  $h_{ac}$  is increased the period two voltage suddenly appears at a threshold value of  $h_{ac}$ . The threshold value of  $h_{ac}$  was in good agreement with the theory presented here<sup>36</sup>. This experiment forms the basis for acoustic parametric amplification at sonic frequencies.

##### 5. Applications in Wire Material

Wires have a more robust geometry than ribbons. In the construction of ribbon torque sensors glue must be used to fix ribbons to a shaft. The glue introduces unwanted hysteresis and temperature effects. With wires no glue is necessary. A wire torque sensor<sup>37</sup> is shown in Fig. 14. The wire is mounted on the shaft at a 45 deg angle with a twist (torsional strain) and a tensile stress. The combination of the two determines the magnetic anisotropy thus determining the dynamic range and resolution of the device. The torque is measured by measuring the magnetic permeability with an external coil. Thus a noncontacting torque sensor is achieved.

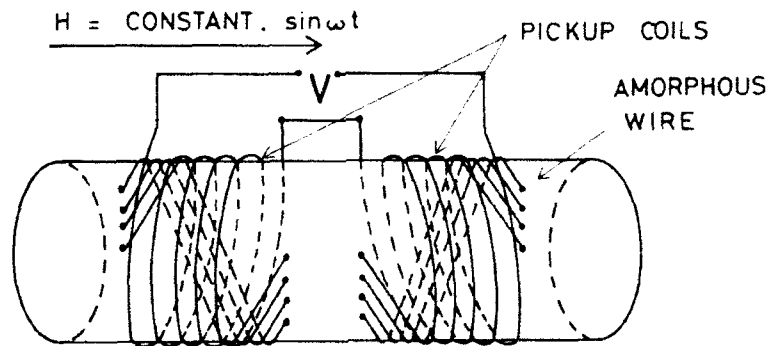


Fig. 14- Torque sensor using wire material. No glue is used. The wires are attached with an imposed twist and tensile stress in a complimentary arrangement.

Wire material also has advantages in magnetometers. The lower surface to volume ratio means that surface defects are less important in domain wall pinning.



Therefore lower Barkhausen noise can be expected. Barkhausen noise near the knee of the hysteresis curve is the worst source of noise in fluxgate magnetometers. A unique magnetometer (described in Ref. 38) uses the Wiedemann effect. A current is passed through a wire that has a helical anisotropy induced by twisting. The polarity of the current switches the magnetization sharply so that the voltage of a pickup coil detecting changes in the longitudinal moment exhibits large spikes. The presence of an external field changes the time-symmetry of the spikes, causing a second harmonic to appear in the pickup coil voltage. This second harmonic voltage is a measure of the external field.

#### 6. Summary

The ideas presented have just begun to be exploited in physics and engineering. In physics an experiment that controls chaos has been effected.<sup>39</sup> A chaotic system, in some respects, can be thought of as a system randomly exhibiting a series of unstable periodic motions that are at frequencies equal to the driving frequency divided by integers. With the experiment of a ribbon in chaotic motion it is possible, by appropriately varying the driving field, to lock the system onto one of the unstable periodic motions. Thus unstable, chaotic motion can be transformed to a (possibly desired) stable motion. Wire may be used as actuators in the future for extremely precise control of delicate instruments. We have shown that "bang-bang" control is possible in some cases. We hope to present more on this subject<sup>40</sup> in the future.

This work has been partially supported by the Spanish C.I.C.Y.T. under project MAT89/0508.

#### References.

1. M. Wun-Fogle, A.E. Clark and K.B. Hathaway, *J. Magn. Magn. Mat.* 54-57(1986) 893-894
2. H.T. Savage, W.L. Ditto, P.A. Braza, M. L. Spano, S. N. Rauseo, W. C. Spring III, *J. Appl. Phys.* 67 (1990) 5619-5623
3. A. Hernando, M. Vázquez, J. M. Barandearán, *J. Phys. E:Sci. Instrum.* 21 (1988) 1129-1139
4. H.T. Savage and M.L. Spano, *J. Appl. Phys.* 53(1982) 8092-8097
5. S. Chikazumi, 1978 *The Physics of Magnetism*, Robert E. Krieger Publishing Company, Huntington, New York, page 167.
6. T. Masumoto. Proc. I. Int. Workshop on non-crystalline solids, S. Frelin de Guixols, 1986. Ed. M.D. Baró and N. Clavaguera (World Scientific, Singapore, 1986) 73.
7. F.B. Humphrey, K. Mohri, J. Yamasaki, H. Kawamura, R. Malmhäll and I. Ogasawara, *Magnetic Properties of Amorphous Metals* Ed. A. Hernando et al. (Elsevier, Amsterdam, 1987) 110.

8. M. Vázquez, C. Gómez-Polo, J. González, E. Pulido and A. Hernando,  
*Magnetic Materials and their applications*  
Ed. by F. Leccabue (I.O.P. London, in press)
9. K. Mohri, IEEE Trans. Magn. 20 (1984) 942.
10. K. Mohri, F.B. Humphrey, J. Yamasaki and F. Kinoshita,  
IEEE Trans. Magn. 21 (1985) 2017.
11. D.G. Lord (private communication).
12. T. Masumoto, I. Ohnaka, A. Inoue and H. Hagiwara, Scripta Mat. 15 (1981) 293.
13. V. Madurga and A. Hernando, J. Phys.: Condens. Matter 2 (1990) 2127.
14. J. Liu, R. Malmhäll, L. Arnberg and S.J. Savage, J. Appl. Phys. 67 (1990) 4238.
15. J. Velázquez, M. Vázquez, H.T. Savage, A. Hernando  
and M. Wun-Fogle, J. Appl. Phys. (in press).
16. J.L.Costa and K.V.Rao in *Physics of Magnetic Materials*  
Ed. W.Gorzkowski, et al, (World Scientific, Singapore 1991) p.279
17. A.M.Severino, C.Gómez Polo, P.Marin and M.Vázquez,  
J. Magn. Magn. Mat. (in press)
18. D.X.Chen, M.Vázquez and C.de Julian, J. Magn. Magn. Mat. (to be published)
19. M.Vázquez, C.Gómez Polo and D.X.Chen, (to be published)
20. F.Kinoshita, R.Malmhäll, K.Mohri, F.B.Humphrey and J.Yamasaki,  
IEEE Trans. Magn. 22 (1986) 445
21. M.Wun-Fogle, H.T.Savage, L.T.Kabacoff, M.L.Spano, J.R.Cullen, G.A. Jones  
and D.G.Lord, IEEE Trans. Magn. 25 (1989) 3617
22. V.Madurga, J.L.Costa, A.Inoue and K.V.Rao, J.Appl. Phys. 68 (1990) 1164
23. M.Vázquez, J.González, J.M.Blanco, J.M.Barandearán, G.Rivero  
and A.Hernando, J.Magn. Magn.Mat. 96 (1991) 321
24. A.Mitra and M.Vázquez, J.Phys. D:Appl. Phys. 23 (1990) 228
25. R.Malmhäll, K.Mohri, F.B.Humphrey, T.Manabe, H.Kawamura, J.Yamasaki  
and I.Ogasawara, IEEE Trans.Magn. 23 (1987) 3242
26. M.Wun-Fogle, H.T.Savage, L.T.Kabacoff, K.B.Hathaway, J.M.Merchant  
and B.Beihoff, J.Appl. Phys. 64 (1988) 5405
27. V.Madurga, L.Ortega, J.L.Costa and K.V.Rao, Sec. Int. Workshop Amorphous  
Materials, Ed. J.Colmenero and A.Alegre (World Scientific, Singapore, 1990) 570

28. J.González, J.M.Blanco, J.M.Barandeiáran, M.Vázquez, A.Hernando, G.Rivero and D.Niarchos, IEEE Trans Magn. 26 (1990) 1798
29. C.Gómez Polo, T.Reininger, M.Vázquez and H.Kronmller, (this workshop)
30. I.Ogasawara and K.Mohri, IEEE Trans Magn. 26 (1990) 1795
31. K.Mohri and S.Takenchi, J.Appl. Phys. 53 (1982) 8386
32. K.Mohri, F.B.Humphrey, J.Yamasaki and K.Okamura, IEEE Trans Magn. 20 (1984) 1409
33. J.L.Costa, Y.Makino and K.V.Rao, IEEE Trans. Magn. 26 (1990) 1792
34. K.Mohri, F.B.Humphrey, K.Kawashima, K.Kimura and M.Mizutani, IEEE Trans. Magn. 26 (1990) 1789
35. M.Wun-Fogle, H.T. Savage and A.E. Clark, Sensors and Actuators 12 (1987) 323-331.
36. H.T. Savage and C.L. Adler, Science and Engineering 99 (1988) 13-18.
37. M. Wun-Fogle, H. T. Savage and Stuart A. Antman, Anales de Fisica B 86 (1990)277.
38. E. Pulido, R.P. del Real, F. Conde, G. Rivero, M. Vázquez, E. Ascasibar, and A. Hernando, INTERMAG Conference, Pittsburgh, 1991, to be published.
39. W.L. Ditto, S.N. Rauseo and M.L. Spano, Phys. Rev. Ltrs. 65 (1991)3211.
40. J. Macki and A. Strauss, 1978 Introduction to Optimal Control Theory, Springer-Verlag Publishing Company, New York.

## IONICALLY CONDUCTING GLASSES

MALCOLM D. INGRAM

Department of Chemistry, University of Aberdeen,  
Meston Walk, Aberdeen AB9 2UE, Scotland, U.K.

## ABSTRACT

The field of "glassy ionics" encompasses practical developments in new batteries and electrochromic systems, and theoretical questions concerning the relationship between ion mobility and glass structure. It is argued here that the crucial step (in theory and in practice) is to identify the pathways for ion migration, and to understand how these are influenced by chemical composition, temperature, and other factors including thermal history and even electrochemical pretreatment procedures.

### 1. Introduction

The birth of solid state ionics some twenty years ago coincided with the search for Na<sup>+</sup>-ion-conducting glasses for use in sodium/sulphur batteries,<sup>1-4</sup> and interest in glassy conductors was boosted by the discovery<sup>5-8</sup> of the class of AgI-containing glasses which have high ionic conductivities (ca.  $2 \times 10^{-2}$  S cm<sup>-1</sup>) at ambient. It was soon appreciated that glasses have a number of advantages over corresponding crystalline conductors, such as the absence of grain boundaries and preferred orientation effects, the possibilities of working with glassy films or hollow fibres, and the opportunity of improving the behaviour of devices containing glassy electrolytes by appropriate thermal or pressure treatments. At the present time, lithium batteries based on Li<sup>+</sup>-conducting glasses are fully commercialised,<sup>9</sup> and prototype electrochromic devices are under investigation<sup>10</sup> which contain amorphous films of tungsten oxide, whose electrochromic activity depends on the simultaneous injection of ions and electrons.

The field of "glassy ionics" has also come of age. At the 2nd International Workshop on Relaxation in Complex Systems held in Crete in 1990<sup>11</sup> and more recently at the International Conference on the Physics of Non-Crystalline Solids held at Cambridge in 1991, these practical developments were subsumed into a discussion of the wider aspects of the physics of such materials including conductivity

dispersions, mixed-cation effects, and the structural relaxations occurring in the glass-transition region.

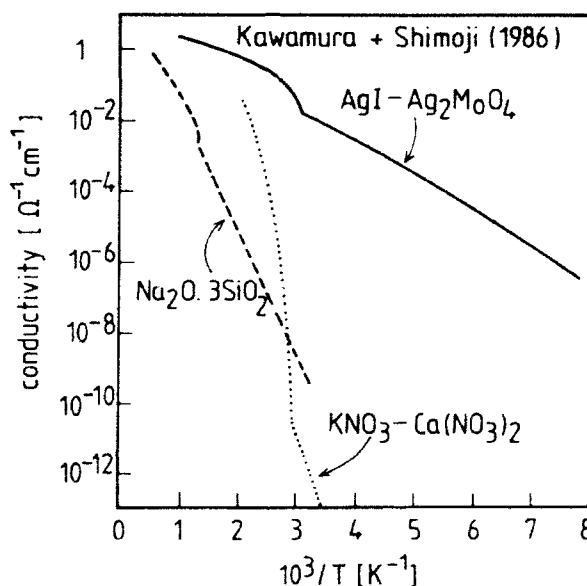


Fig. [1] Arrhenius plots, showing conductivity dependence of three typical glass-forming systems. Note the curvature above  $T_g$  and linearity below  $T_g$ . (After Kawamura and Shimoji, reference [12]).

What emerges is the need for a better knowledge of glass structure and how this can influence the ionic mobilities. In particular, the need to explain the huge variations in ionic conductivity - see Fig. [1]<sup>12</sup> - from materials such as the  $\text{KNO}_3-\text{Ca}(\text{NO}_3)_2$  glasses, which are virtually insulators even at  $T_g$ , through the more "conventional" silicate glasses with conductivities around  $10^{-3} \text{S cm}^{-1}$  at  $300^\circ\text{C}$ , to the silver idomolybdate glasses (mentioned above) which are "superionic" conductors at room temperature. The question is which features of glass structure are responsible for such variations in conduction.

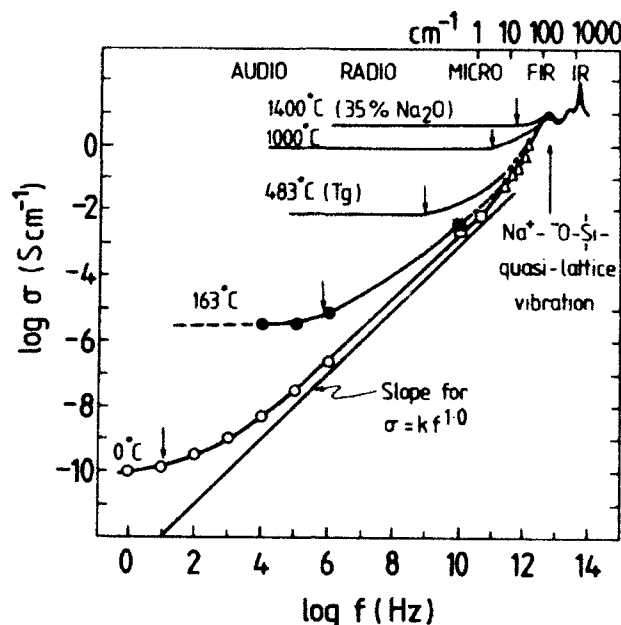


Fig. [2] The conductivity spectrum for sodium trisilicate glass at various temperatures. (After Wong and Angell, reference [13]).

## 2. Basic Phenomenology

### 2.1 The Conductivity Spectrum

The conductivity spectrum of sodium trisilicate glass as presented originally by Wong and Angell<sup>13</sup> is shown in Fig. [2]. The essential features of this figure are confirmed by the additional measurements in the microwave region by Burns *et al.*<sup>14</sup> The "d.c." conduction plateaux appear on the low-frequency side of the graph, but increase in importance and extent as the temperature increases. On the high-frequency side, the limit is set by the cation vibrations in the far infrared region. In effect, the infrared conductivity sets the upper limit<sup>15</sup> for the d.c. conductivities, which can be encountered only at high temperatures ( $> 1400^\circ\text{C}$  in this case).

The essential idea behind most theoretical interpretations is that ionic conductivity in glass is a "rattle and jump process",<sup>16</sup> where only a tiny fraction of possible ionic hops actually contribute to the d.c. conductivity. As the time scale for electrical measurement increases (*i.e.* as the frequency decreases), there is a

smooth progression from localised to long-range ionic motions. In between the rattling region (*i.e.* the far infrared) and the d.c. conductivity, there is a region of conductivity dispersions, which is still poorly understood.

## 2.2 Activation Energies and Activation Volumes

Quite empirically, the ionic conductivities of glass are usually fitted to the Arrhenius equation (where temperature is varied):

$$\ln \sigma \text{ (or } \sigma T) = \ln \sigma_0 - E_A/RT \quad [1]$$

or (when pressure is varied) to the equation:<sup>17</sup>

$$RT \ln \sigma = RT \ln \sigma_0 - P\Delta V_A \quad [2]$$

where  $\sigma_0$  and  $\sigma_0'$  refer either to conductivities at infinite temperatures or zero pressures, and  $E_A$  and  $\Delta V_A$  are activation energies and volumes, respectively. Very generally ionic conductivity decreases as the activation energy decreases. The relationship between conductivity and activation volume remains to be established.

## 3. Some Fundamental Concepts and Special Problems in Glassy Conductors

### 3.1 The Anderson-Stuart Model

Some effort has gone in recent years<sup>18</sup> into developing further the classical Anderson-Stuart model (1954), which enables the activation energy to be calculated from "glass" parameters, some of which can be determined directly, some must be inferred from other measurements, and others are estimated quantities. The activation energy is written as the sum of two terms,<sup>19</sup> referring respectively to a coulombic contribution  $E_C$  (involving ions being taken out from their sites), and an elastic contribution  $E_S$  (involving the opening up of the glass structure as the ions move between sites). Thus:

$$E_A = E_C + E_S \quad [3]$$

where

$$E_C = \beta z_+ z_- e^2 / \gamma (r_+ + r_-) \quad [4]$$

and

$$E_S = 4\pi G r_D (r_+ - r_D)^2 \quad [5]$$

Here,  $z_+$  and  $r_-$  are the charge and radius of the anion respectively,  $\beta$  is a lattice parameter depending on the distance between neighbouring cation sites,  $r_+$  is the cation radius,  $r_D$  is the radius of 'doorways' already existing in the glass,  $G$  is the elastic modulus, and  $\gamma$  is a covalency parameter usually identified with the relative permittivity or dielectric constant.

One viewpoint (see *e.g.* ref. [18]) is that the activation energy - especially for smaller cations like  $\text{Li}^+$  and  $\text{Na}^+$  - is dominated by the electrostatic or coulombic contribution. A difference in  $E_A$  between one glass system and another thus depends mainly on differences in the covalency parameter,  $\gamma$ , and variations in  $E_A$  within one system will depend on variations in the intersite distance. Arguments based on the covalency parameter will certainly explain why the iodide-containing glasses are

better conductors than the oxide glasses (see Fig. [1]); also, if intersite distance is important, it is easy to see why cationic conductivity in many oxide glasses (silicates, borates, etc.) is such a strong function of the total cation content.

Yet, two interesting questions remain. These are:

- (i) Why is the elastic strain energy apparently so unimportant in many glassy conductors? and
- (ii) What actually controls the inter-site separation in glass?

Both these questions are related in some way to glass structure and to the possible existence of preferred pathways for ion-migration. These are presently two issues central to the theory of glassy ionics.

### 3.2 The Mixed Cation Effect

One "special problem" which arises in the discussion of ionic motion in glass is the mixed cation or mixed mobile ion effect.<sup>20-22</sup> This involves, see Fig. [3], *massive* decreases in ionic conductivity in glasses which contain two or more mobile ions. In the example given<sup>20</sup> the conductivity of mixed lithium/potassium disilicate glasses at 150°C is seen to be about four powers of ten less than in either single-cation disilicate glass.

This effect is not to be confused with much smaller effects seen in molten salts,<sup>22</sup> where conductivity may fall by approx. 50% and "chemical" interpretations such as complex formation, or *quasi*-thermodynamic arguments involving the friction coefficient formalism, have been involved. The effect in glass is qualitatively different. It is large enough to turn a "conducting" glass into an insulator.



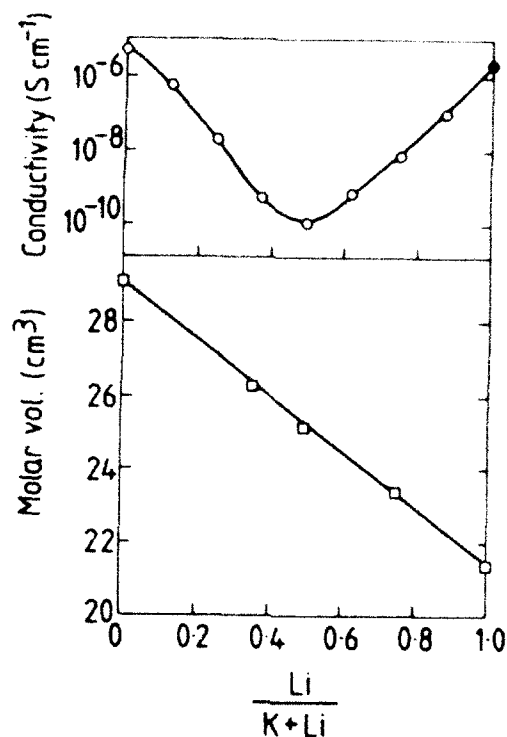


Fig. [3] The mixed cation effect in sodium/lithium disilicate glasses at 150°C. (After Day, reference [20]).

This phenomenon is still a source of on-going controversy and no theory has yet won general acceptance. The only point which does seem clearly established is that the minimum in glass conductivity is *not* associated with some specially stabilised or "compacted" version of the glass structure. This also emerges from Fig. [3], and the observed linear variation of molar volume with glass composition. It is also clear from the variation of  $\text{Na}^+$  and  $\text{Cs}^+$  diffusion coefficients in the mixed Na-Cs trisilicate glass system, see Fig. [4], that individual ionic mobilities do not reach a minimum value at the conductivity minimum. Rather, the  $\text{Na}^+$  ion has its lowest mobility in the Cs glass, and *vice versa*. The implication is that  $\text{Na}^+$  ions do not move easily in a glass containing only sites for  $\text{Cs}^+$  ions, and that the same is true in reverse.

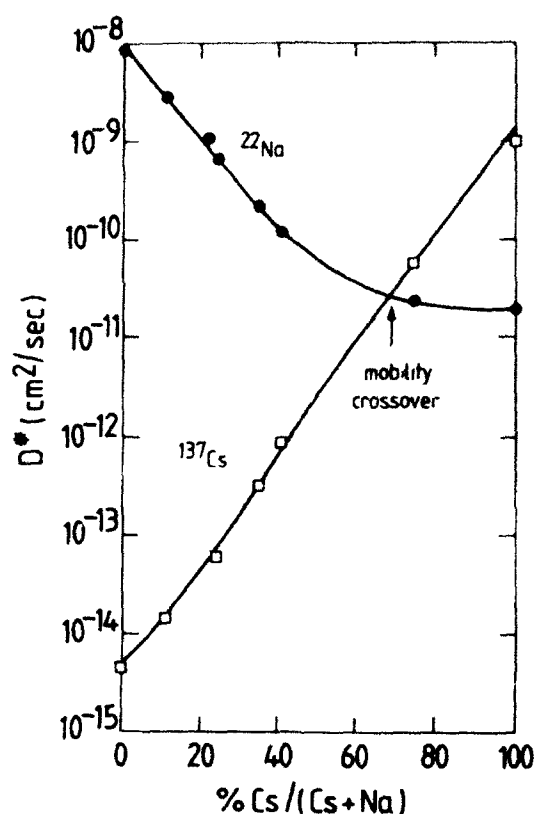


Fig. [4] The "mobility crossover" seen in the diffusion coefficients of  $\text{Na}^+$  and  $\text{Cs}^+$  ions in sodium/caesium disilicate glasses at  $396^\circ\text{C}$ . (After Jain *et al.*, reference [22]).

### 3.3 Memory Effects in Glass

It is generally accepted that glasses show memory effects in relation to macroscopic properties, and that certain of these properties such as volume and enthalpy<sup>23-25</sup> depend on the thermal history. Insofar as the glass structure is fixed at  $T_g$ , then glass properties will also reflect some "memory" of liquid state behaviour.

Pursuing this argument a stage further, ionic conductivity may also be regarded as a liquid-state property, which in some way is carried over (below  $T_g$ ) into the glassy phase. The question is whether or not this latter kind of memory

effect is related to some feature of the microscopic glass structure, and whether such structures can be identified, or indeed be introduced deliberately.

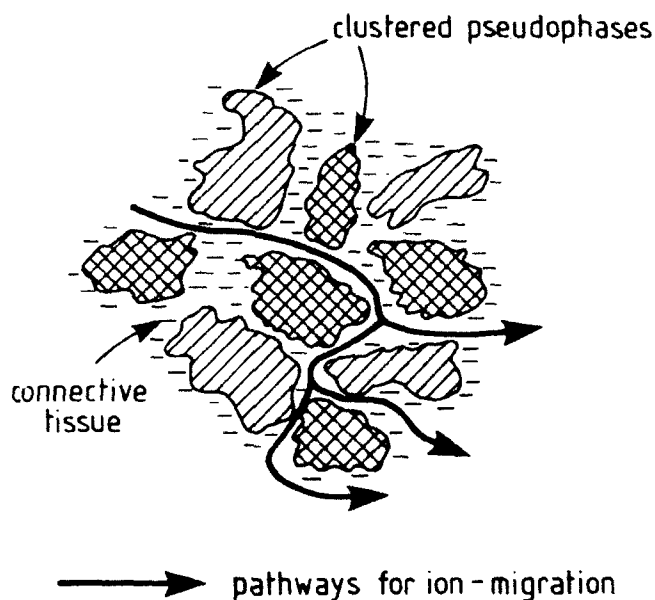


Fig. [5] The cluster-tissue model showing clustered pseudophases and preferred pathways for ion migration located in the connective tissue. (After Ingram *et al.*, reference [30]).

### 3.3.1 The Cluster-Tissue Model

According to the cluster-tissue models<sup>24-30</sup> of glass structure, all melts will tend to vitrify inhomogeneously, and the glass transition will mark the appearance of space-filling networks of "solid-like" clusters. On subsequent cooling, the "residual liquid" converts gradually into a connective tissue, which is relatively more disordered and less densely packed than the clusters.

Indeed, it is argued that the effect of glasses contracting further, *i.e.* below  $T_g$ , is to put the clusters under compression and to subject the connective tissue to tensile stresses, which further accentuate the differences between cluster and tissue phases.<sup>29</sup> The result is illustrated schematically in Fig. [5].<sup>30</sup> The relevance to the present discussion is that the connective tissue provides *preferred pathways* for ion-migration to occur in glass.

In very simple terms, it would be argued that insulating glasses, like those derived from the  $\text{KNO}_3\text{-Ca(NO}_3)_2$  melts, see Fig. [1] above, contain very little

connective tissue. On the other hand, highly conductive, AgI-based glasses (also shown in Fig. [1]) should have a strongly developed *biphasic* structure, with conduction pathways tracked largely by iodide ions.<sup>31</sup>

The information so far available on glass structure tends to support this simple viewpoint. Thus, the far infrared spectroscopy of lithium borate glasses<sup>30</sup> points up the presence of two cation vibration bands corresponding to two differing cation environments as in Fig. [6]. The relatively narrow high-frequency band has been associated with cations in the clustered pseudophases, while the relatively broad low-frequency band has been assigned to cations in the tissue. Neutron scattering experiments on silver iodophosphate<sup>32</sup> and silver iodoborate glasses<sup>33</sup> show strong evidence of the emergence of a silver iodide "pseudophase" and of structure on the scale of 10-15Å.

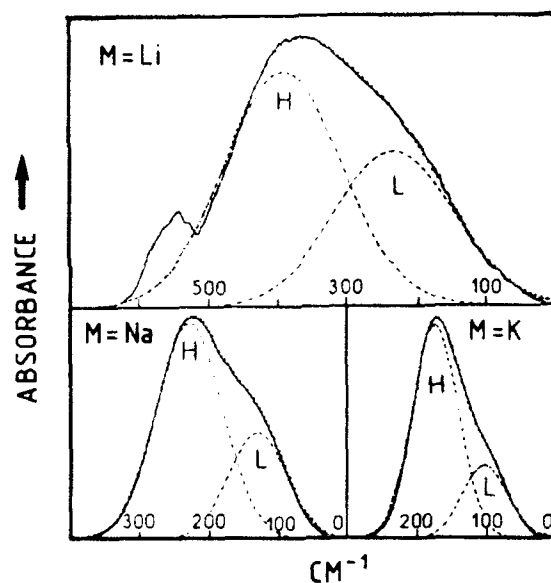


Fig. [6] Far infrared spectra of selected alkali borate glasses ( $0.3 M_2O : 0.7 B_2O_3$ ) showing the "high" and "low" bands (H and L) corresponding to cations in different environments. (After Kamitsos and coworkers, see reference [30]).

However, to some extent the cluster/tissue model as discussed above says nothing about the sites which are available to cations in the tissue, and how far these sites are influenced by the cations themselves. In this sense, it offers no microscopic

interpretation of the mixed cation effect or of other compositional variations in conductivity.

### 3.3.2 The Site Memory Effect

The site memory effect of Bunde, Ingram and coworkers<sup>34-37</sup> is based on the simple notion that cations create their own distinct sites or chemical environments in glass. This idea stems directly from early results on vibrational spectroscopy<sup>38</sup> and the more recent EXAFS data<sup>39</sup> for mixed-cation systems.

The added ingredient now is the assumption that *after* a  $\text{Na}^+$  ion (for example) has left its site, its presence is still remembered for some relaxation time  $\tau$ . During this time interval, it can be *reoccupied* quite readily by  $\text{Na}^+$  ions, but less readily by other kinds of cation.

This process is illustrated schematically in the upper half of Fig. [7], where "triangular" cations are shown hopping readily into "triangular" sites, but less readily into "square" sites. The same is true in reverse for the migration of "square" cations into these sites.

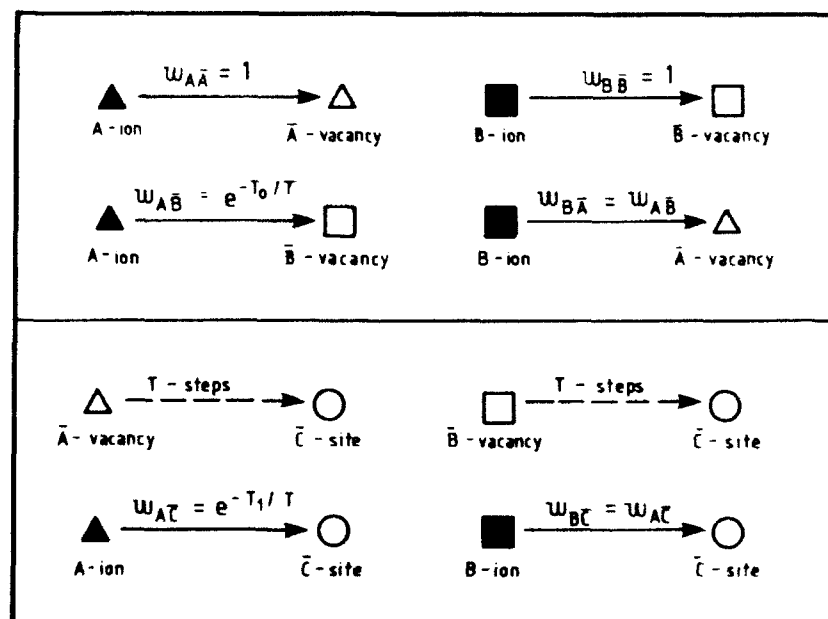


Fig. [7] The "mismatch" and "site memory" effects in mixed cation glasses. This model distinguishes cation vacancies  $\bar{\text{A}}$  and  $\bar{\text{B}}$  appropriate to A and B cations both from each other and from interstitial C sites where cations can enter less easily. (After Bunde et al., reference [35]).

Intuitively, one can see that this "mismatch effect" could be the origin of the mobility crossover, Fig. [4], which results in both  $\text{Cs}^+$  and  $\text{Na}^+$  cations being immobilised in each of the dilute foreign alkali regions.

Fig. [7] also shows the process of cation vacancies (designated here as A or B sites) relaxing into normal "interstitial" C sites after the time  $\tau$ . This process will tend to "shut off" some of the possible conducting pathways, and thus (regardless of freezing out by clustering) to direct the mobile ions along preferred pathways. These pathways in turn will be kept open by the continuing movement of the ions and by the consequent beneficial operation of the memory effect.

Very simply, highly conducting glasses are those where this synergism operates most effectively. On the other hand, sharp falls in conductivity, as seen in the mixed cation effect, reflect the loss of synergy (A sites being unavailable for A cations to hop into and likewise for other cations).

Fig. [8] shows a recent Monte Carlo simulation by Bunde and Maass<sup>40</sup> of the crossover effect in a mixed cation glass, based on this simple model. It is apparent that the correct shape of Fig. [4] is reproduced successfully, and it seems reasonable to conclude that the quantitative theory must therefore be capturing some of the essential physics of ion transport processes in glass.

#### 4. Ongoing Problems

##### 4.1 Structural Order in Glass

One area of continuing interest concerns the question of short, medium and long-range order (SRO, MRO and LRO) in glass. Greaves for example has remarked<sup>41</sup> that the existence of good short-range in glass implies (*via* the fixing of bond angles, for example) some medium range order.

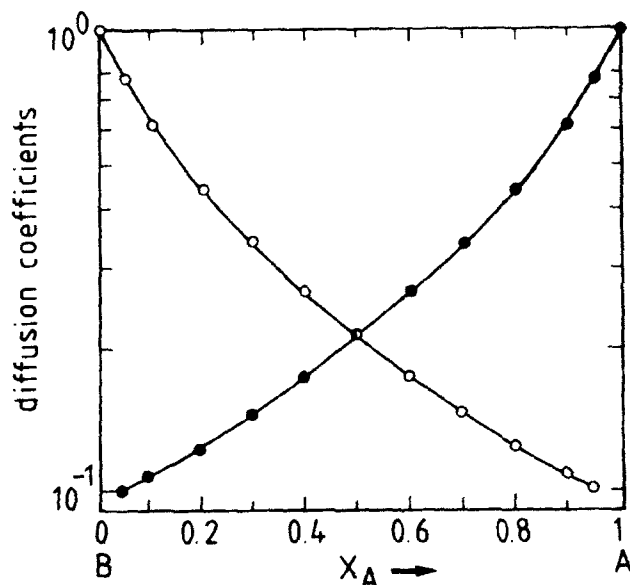


Fig. [8] The "mobility crossover" - compare Fig. [4] - in a simulated mixed cation glass. The Monte Carlo simulation is based on simple cubic lattice and reasonable assumptions relating to site occupancy levels, mismatch effects and memory relaxation times. (After Bunde and Maass, reference [40]).

However, it emerges from the account of the site memory effect given in Section 3.3.2 above that cation migration could create site ordering *over much larger distances*. This novel idea could provide a new basis for mechanistic discussions of the "long-range structures" to be found in highly conducting glasses.

#### 4.2 Enhanced Ionic Diffusion in Glass

Until now, it has always been assumed that ionic mobility in glass is very largely a function of chemical composition. However, in terms of the above discussion, the ion mobility could be just as strongly influenced by structural features dependent upon the existence of long-range "memory" effects.

There is some very recent evidence from work in our laboratory<sup>42</sup> that this is so. Thus thin films of amorphous  $\text{WO}_3$  incorporated into electrochromic devices were found to be impermeable to protons until they had been "activated" by previous electrochemical colouration and bleaching cycles. It seemed as if the untreated  $\text{WO}_3$  material simply did not contain the pathways to enable proton migration, and so the electrochromic reaction was inhibited.

#### 4.3 Pressure Effects

In Section 2.2, reference has already been made to measurement of both activation energies and volumes, yet with few exceptions<sup>17,43-46</sup> little attention has been given to the latter and to the effects of pressure in general. As a result, a large body of data is missing, but urgently needed to test the models and theories under discussion.

#### Acknowledgements

The author wishes to thank the Science and Engineering Research Council (U.K.) for financial support, and the many co-authors cited herein for helpful discussions and shared ideas.

#### 5. References

1. F.Y. Tsang, *U.S. Patent* (1974) 3 829 331.
2. S. Susman, C.J. Delbecq, J.A. McMillan and M.F. Roche, *Solid State Ionics* 9-10 (1983) 667.
3. C.C. Hunter and M.D. Ingram, *Solid State Ionics* 14 (1984) 31.
4. C.C. Hunter and M.D. Ingram, *Phys. Chem. Glasses* 27 (1986) 51.
5. D. Kunze, p.495 in *Fast Ion Transport*. Edited by W. von Gool, North Holland, Amsterdam (1973).
6. A. Schiraldi, *Electrochim. Acta* 23 (1978) 1039.
7. E. Robinel, B. Carette and M. Ribes, *J. Non-Cryst. Solids* 57 (1983) 49.
8. S.W. Martin and A. Schiraldi, *J. Phys. Chem.* 89 (1985) 2070.
9. J.R. Akridge and H. Vourlis, *Solid State Ionics* 28-30 (1988) 841.
10. A.M. Andersson, C.G. Granquist and J.R. Stevens, *Applied Optics* 28 (1989) 3295.
11. Proceedings of II International Workshop on Relaxation in Complex Systems, Heraklian (Crete) 1990, *J. Non-Cryst. Solids* 131-133 (1991).
12. J. Kawamura and K. Shimoji, *J. Non-Cryst. Solids* 88 (1986) 281, 295.
13. J. Wong and C.A. Angell, *Glass Structure by Spectroscopy* (Dekker, New York, 1976) p.750.
14. A. Burns, G.D. Chryssikos, E. Tombari, R.H. Cole and W.M. Risen, *Phys. Chem. Glasses* 28 (1987) 215.
15. C.A. Angell, *Chem. Revs.* 90 (1990) 523.
16. C.A. Angell, P.A. Cheeseman and S. Tamaddon, *J. Physique* 43, C9, 381.
17. K. Ari, K.L. Kumata, K. Yamamoto, H. Namikawa and S. Saito, *J. Non-Cryst. Solids* 13 (1973/74) 131.
18. S.W. Martin and C.A. Angell, *J. Non-Cryst. Solids* 83 (1986) 185.
19. O.L. Anderson and D.A. Stuart, *J. Am. Ceram. Soc.* 37 (1954) 573.
20. D.E. Day, *J. Non-Cryst. Solids* 21 (1976) 343.
21. M.D. Ingram, *Phys. Chem. Glasses* 28 (1987) 215.



22. H. Jain, N.L. Peterson and H.L. Downing, *J. Non-Cryst. Solids* **55** (1983) 283.
23. C.T. Moynihan, A.J. Bruce, D.L. Gavin, S.R. Loehr and S.M. Opalka, *Polym. Engng. Sci.* **24** (1984) 1117.
24. J.M. Hutchinson, p.172 In *Molecular Dynamics and Relaxation Phenomena in Glasses*. Lecture Notes in Physics **277** (1987) Springer Verlag, Berlin.
25. M.D. Ingram, J.M. Hutchinson and A.J. Pappin, *Phys. Chem. Glasses* **32** (1991) 121.
26. C.H.L. Goodman, *Phys. Chem. Glasses* **26** (1985) 1.
27. M.C.R. Shastry and K.J. Rao, *Solid State Ionics* **37** (1989) 17.
28. K. Yamamoto and H. Namikawa, *Jap. J. Appl. Phys.* **27** (1988) 1845.
29. M.D. Ingram, M.A. Mackenzie, W. Mueller and M. Torge, *Solid State Ionics* **40/41** (1990) 671.
30. M.D. Ingram, G.D. Chryssikos and E.I. Kamitsos, *J. Non-Cryst. Solids* **131** (1991) 1089.
31. T. Minami, K. Imazawa and M. Tanaka, *J. Non-Cryst. Solids* **42** (1980) 469.
32. C. Rousselot, M. Tachez, J.P. Malugani, R. Mercier and P. Chieux, *Solid State Ionics* **44** (1991) 151.
33. L. Boerjesson, L.M. Torrell and W.S. Howells, *Phil. Mag.* **B59** (1989) 105.
34. A. Bunde, M.D. Ingram, P. Maass and K.L. Ngai, *Phys. A: Math. Gen.* **24** (1991) L881.
35. A. Bunde, P. Maass and M.D. Ingram, *Ber. Bunsenges. Phys. Chem.* (in press).
36. M.D. Ingram, P. Maass and A. Bunde, *Ber. Bunsenges. Phys. Chem.* (in press).
37. M.D. Ingram, W. Mueller and M. Torge, Proceedings of VII International Conference on the Physics of Non-Crystalline Solids, Cambridge, 1991 (to be published by Taylor and Francis).
38. G.B. Rouse, P.J. Miller and W.M. Risen, *J. Non-Cryst. Solids* **28** (1978) 193.
39. G.N. Greaves, C.R.A. Catlow, B. Vessal, J. Charnock, C.M.B. Henderson, R. Zhu, S. Qiao, Y. Wang, S.R. Gurmon and S. Houde-Walter, Int. Phys. Conf. Ser. No. 111, Paper presented at Int. Conf. on New Materials and their Applications, University of Warwick, 1990.
40. A. Bunde and P. Maass, Proceedings of VII International Conference on the Physics of Non-Crystalline Solids, Cambridge, 1991 (to be published by Taylor and Francis).
41. G.N. Greaves, *J. Non-Cryst. Solids* **71** (1985) 203.
42. J.A. Duffy, M.D. Ingram and P.M.S. Monk, to be published.
43. S.D. Hamann, *Aust. J. Chem.* **18** (1965) 1.
44. M.J. Ryan and S.I. Smedley, *J. Non-Cryst. Solids* **65** (1984) 29.

45. H. Senapati, G. Parthasarathy, S.T. Lakshmikamar and K.J. Rao, *Phil. Mag.* **B47** (1983) 291.
46. J.M. Hutchinson, M.D. Ingram and J.M. Robertson, to be published.

# MAGNETIC PROPERTIES OF TERNARY Co-B-C MELT SPUN ALLOYS AMORPHIZED OVER AN EXTENDED CONCENTRATION RANGE

M. Pont

*Electromagnetism Group, Dept. of Physics  
Autonoma University of Barcelona, 08193 Bellaterra, Spain*

R. Puzniak and K.V. Rao

*Dept. of Condensed Matter Physics, Royal Inst. of Technology, Stockholm, Sweden*

and A. Inoue

*Institute for Materials Research, Tohoku University, Japan*

## ABSTRACT

*The field dependence of the magnetization at 4.2 K, and the temperature dependence of the spontaneous magnetization for two series of ternary Co-based alloys, namely  $\text{Co}_{76-x}\text{B}_{24}\text{C}_x$  and  $\text{Co}_{88-y}\text{B}_y\text{C}_{12}$  have been measured. The metalloid content in these series ranges from 24 to 44 at.%, and extends almost to the critical concentration for the disappearance of ferromagnetism.*

*The thermal demagnetizing process at low temperatures has been analyzed in terms of Bloch's Law and the stiffness constant has been determined.*

## 1 INTRODUCTION

The magnetic properties of soft magnetic amorphous materials have been widely studied in recent years not only because of their technical interest for applications already in use, but also because of the scientific interest to understand magnetism in amorphous structures. Several reviews have been published<sup>1,2,3,4</sup>.

However until recently, a systematic study of the composition dependence of the magnetic properties in metal-metalloid alloys produced by melt-spinning was inhibited because amorphization in these systems was only possible close to the eutectic points in the phase diagram. Recently, amorphous ternary Co-B-C alloys with metalloid content as high as 50 at.% have been produced by melt-spinning<sup>5</sup>. These new materials provide us the opportunity to study systematically, for the first time, the magnetic properties of Co-based alloys close to the ferromagnetic-paramagnetic transition in the magnetic phase diagram.

## 2 EXPERIMENTAL METHOD

Amorphous ribbons of  $\text{Co}_{76-x}\text{B}_{24}\text{C}_x$  with  $x = 4, 12, 16$  and  $20$  and  $\text{Co}_{88-y}\text{B}_y\text{C}_{12}$  with  $y = 12, 24, 28$  and  $32$  were produced on a single roller by melt-spinning at 4000

rpm. All the alloys studied were confirmed to be at least x-ray amorphous. Magnetization measurements as a function of applied fields up to 5 T were carried out on a VSM (PAR Model-155). The accuracy of our measurements was better than  $10^{-4}$  emu at low magnetic fields and better than  $10^{-3}$  emu at 2 T. The temperature ranged from 5 K to 200 K.

In order to achieve sufficient precision in the measurements, the total mass of the sample used was around 10 mg. The magnetic field was applied parallel along the longest axis of the piece of the ribbon and the data have been corrected for demagnetizing field effects. To obtain the saturation magnetization at 4.2 K a hysteresis loop was recorded in fields up to 2 T.  $M_s$  was determined by linear extrapolation of the magnetization to zero magnetic field.

### 3 EXPERIMENTAL RESULTS

Fig 1 shows the average magnetic moment, determined from the  $M_s$  data at 4.2K, as a function of the Co content for the studied ternary alloys. For comparison, data on other Co-based amorphous alloys<sup>6</sup> as well as crystalline Co-B alloys<sup>7</sup> are also included. Notice that from our experimental data the disappearance of ferromagnetism is observed to be around 54 at.% of Co. The same critical concentration, was obtained from an analysis of the composition dependence of the Curie temperatures<sup>8</sup>.

For the sake of brevity only results for the  $\text{Co}_{76-x}\text{B}_{24}\text{C}_x$  series are shown graphically. The figures for the other series are very similar. Fig 2 shows the magnetization, normalized to its zero temperature value, versus the reduced temperature,  $T/T_C$ . It is observed that the curves become flatter in the intermediate temperature range, as expected, with decreasing Co content.

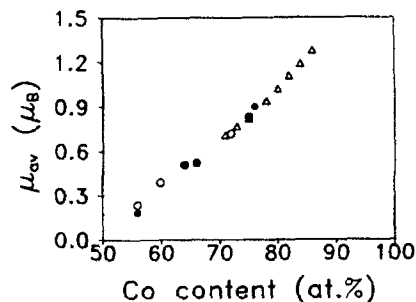


Fig 1 Average magnetic moment versus the Co content for (○)  $\text{Co}_{76-x}\text{B}_{24}\text{C}_x$  (●)  $\text{Co}_{88-x}\text{B}_{12}\text{C}_{12}$  (△)  $\text{Co}_{1-x}\text{B}_x$  (Ref 6) and (■) c-Co-B (Ref 7)

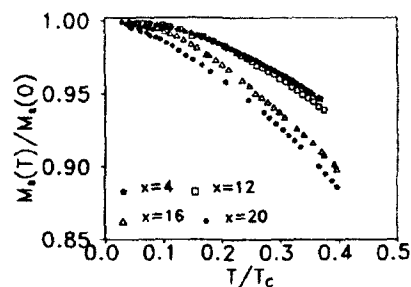


Fig 2 Normalized saturation magnetization versus  $T/T_C$  for  $\text{Co}_{76-x}\text{B}_{24}\text{C}_x$

### 4 DISCUSSIONS

Although transition metal based systems must be considered as itinerant systems of electrons, spin wave excitations have been observed in these systems, for a review

see O'Handley<sup>4</sup>, and thus, the temperature dependence of the spontaneous magnetization is given, in general, by,

$$M_s(T) = M_s(0) - M_{sw}(T) - M_{st}(T) \quad (1)$$

where  $M_s(T)$  is the saturation magnetization at absolute zero,  $M_{sw}(T)$  the deviation arising from the collective spin wave excitations and  $M_{st}(T)$  that arising from the single particle Stoner excitations.

The deviation due to spin wave excitations is given by Bloch's Law,

$$M_s(T) = M_s(0) [1 - BT^{3/2}] \quad (2)$$

with,

$$B = \frac{2.612 \mu_B g}{M_s(0)} \left( \frac{k_B}{4\pi D} \right)^{3/2} \quad (3)$$

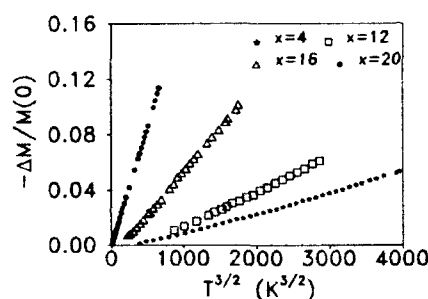


Fig 3  $-\Delta M(T)/M(0)$  as a function of  $T^{3/2}$  for  $\text{Co}_{76-x}\text{B}_{24}\text{C}_x$

where  $D$  is the spin wave stiffness constant. Fig 3 shows a plot of  $-\Delta M(T)/M(0)$  versus  $T^{3/2}$  to determine the stiffness of the spin wave excitations and at the same time to detect the possible presence of other contributions like magnon-magnon interaction or Stoner single particles. As observable in Fig 3 a simple  $T^{3/2}$  behaviour is found over a considerable temperature range. Table I gives the main results for the studies carried out in this work.

In the case of the 56 at.% Co-based alloys, i.e. the concentration closest to the percolation limit where we have data through the magnetic transition we observe

in Fig 4, as expected, the deviation from a  $T^{3/2}$  law above  $T/T_C = 0.4$ .

Figure 5 is a plot of the stiffness constant  $D$  as a function of the Curie temperature for the alloys studied in this work, together with data obtained from neutron scattering measurements in  $\text{Co}_{70}\text{P}_{10}\text{B}_{20}$  ( $T_C = 452$  K)<sup>9</sup> and  $\text{Co}_4\text{P}$  ( $T_C = 622$  K)<sup>10</sup>. There appears to be a good agreement between the two sets of data, indicating that any other contribution to the thermal demagnetization must be very small. The ratio  $D/T_C$  is a measure of the range of the exchange interaction<sup>11</sup>. For Fe-Metalloid amorphous alloys its value has been found to be smaller than that for pure Fe, indicating a shorter range of the exchange interactions<sup>12</sup>. However, for Co-Metalloid amorphous alloys we found  $D/T_C \approx 0.28 \text{ meV} \cdot \text{\AA}^2 \cdot \text{K}^{-1}$  to be compared with the value of  $0.25 \text{ meV} \cdot \text{\AA}^2 \cdot \text{K}^{-1}$  for pure crystalline cobalt<sup>13</sup>. The agreement between these two values is consistent with the findings that the magnetic properties of amorphous Co-Metalloid alloys differ little from those of their crystalline counterparts.

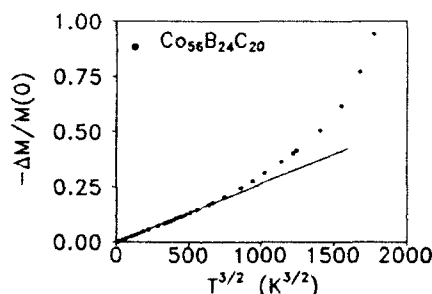


Fig 4  $-\Delta(T)/M(0)$  versus  $T^{3/2}$   
for  $\text{Co}_{56}\text{B}_{24}\text{C}_{20}$

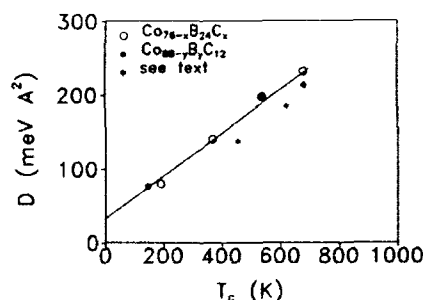


Fig 5 Stiffness constant versus  $T_c$   
for Co based alloys

Table I

Alloy	$T_c$ (K)	$M_s$ (G)	$D$ (meV Å <sup>2</sup> )
$\text{Co}_{72}\text{B}_{24}\text{C}_4$	680	657	232
$\text{Co}_{64}\text{B}_{24}\text{C}_{12}$	539	479	198
$\text{Co}_{60}\text{B}_{24}\text{C}_{16}$	366	364	140
$\text{Co}_{56}\text{B}_{24}\text{C}_{20}$	190	226	80
$\text{Co}_{76}\text{B}_{12}\text{C}_{12}$	681	806	213
$\text{Co}_{64}\text{B}_{24}\text{C}_{12}$	539	479	198
$\text{Co}_{56}\text{B}_{32}\text{C}_{12}$	145	178	76

## 5 CONCLUSIONS

In this work we have carried out a systematic study of the magnetic properties for two different series of Co-B-C amorphous alloys. These alloys have been quenched beyond the eutectic regime and the metalloid concentration extends from 24 to 44 at.%, i.e. almost at the critical concentration for the disappearance of ferromagnetism, which takes place when more than 46 at.% of the material are metalloids.

Analyses of the thermal demagnetization for all the alloys studied can be understood in terms of the well known Bloch-spin wave excitations. The stiffness constant

obtained from our analyses of the data and its linear dependence on the ferromagnetic transition temperature is consistent with the predictions by Wohlfarth<sup>11</sup> for itinerant systems.

## Acknowledgments

The financial help of the Swedish Nat. Board for Technical Development and of CICYT (MAT-88-605) is gratefully acknowledged.

## References

- 1 R.C.O'Handley in *Amorphous Metallic Alloys* (Ed. F.E.Luborsky, Butterworths Mon. in Materials, London, 1983) p.257
- 2 K.Moorjani and J.M.D.Coe, in *Magnetic Glasses* (Elsevier, Amsterdam, 1984)
- 3 T.Egami, Rep. Prog. Phys. **47**, 1601 (1984)
- 4 R.C.O'Handley J. Appl. Phys. **62**, R15 (1987)
- 5 A.Inoue, T.Nakamura and T.Masumoto, J. Mat. Scien. Lett. **5**, 1178 (1986)
- 6 R.Hasegawa and R.Ray, J. of Appl. Phys. **50**, 1586 (1979)
- 7 M.C.Cadeville and E.J.Daniel, J. Phys. (Paris) **27**, 447 (1966)
- 8 M.Pont, K.V.Rao and A.Inoue in *Basic Features of the Glassy State* (World Scien. 1990) pp. 544
- 9 Mc Coll et al. AIP Conf. Proc. **29**, 172 (1976)
- 10 H.A.Mook, N.Wakabayashi and D.Pan, Phys. Rev. Lett. **34**, 1029 (1975)
- 11 A.Katsukiy and E.P.Wohlfarth, Proc. Roy. Soc. A **295**, 182 (1966)
- 12 R.Hasegawa and R.Ray, Phys. Rev. B **20**, 211 (1979)
- 13 V.Jaccarino, Bull. Am. Phys. Soc. Bull. **4**, 461 (1959)

## MAGNETIC PROPERTIES OF RAPIDLY QUENCHED NdDyFeB ALLOYS

*J.S. Muñoz, M. Pont and J. Reverter*

*Grup D'Electromagnetisme, Dept. de Física,  
Universitat Autònoma de Barcelona, 08193 Bellaterra, Spain*

### ABSTRACT

The effects of wheel speed on the magnetic properties of melt-spun  $\text{Fe}_{75}\text{Nd}_{13.5}\text{Dy}_{3.7}\text{B}_{7.8}$  alloys have been studied. For the different samples we have determined the Curie temperature, the dependence of the coercive field on the applied magnetic field and the low field ac-susceptibility.

### 1 INTRODUCTION

Since the discovery of the hard magnetic phase on the ternary alloy system Fe-Nd-B<sup>1,2</sup> a great research effort has been devoted to the problems of increasing the Curie temperature and the coercivity of the tetragonal  $\text{Nd}_2\text{Fe}_{14}\text{B}$  phase. It is well known that Co addition<sup>3</sup> enhances linearly the Curie temperature above 583 K and many other heavy rare earth substitutions have been tried with different degree of success. Among these, dysprosium seems to be a good candidate for enhancing the coercivity. Experimentally it has been found that the larger Nd atoms tend to occupy the 4g sites while the smaller Dy atoms go into the 4f sites in the structure<sup>4</sup>.

The broad aim of our work is to investigate some of the effects of substitution of Nd through the processing variables and its effect on the microstructure and the magnetic properties. Substitution of Nd enlarges the intrinsic coercivity due to the increase in the anisotropy field. However, there might be other variables that could enhance  $H_C$ , probably due to the formation of other phases, and the identification of these secondary magnetic and non-magnetic phases or the strong temperature dependence of the magnetocrystalline anisotropy are still problems to be solved. In this paper the effect of the wheel speed on the basic magnetic properties is reported.

### 2 EXPERIMENTAL METHOD

Samples of nominal composition  $\text{Fe}_{75}\text{Nd}_{13.5}\text{Dy}_{3.7}\text{B}_{7.8}$  were melt spun at 11, 15, 23, and 32 m/s at the Demokritos Research Centre (Athens). Similar speeds have

been already studied<sup>5</sup> by our group with the expected result that the underquenched ribbons are almost fully crystallized while the overquenched, above 25 m/s, are largely amorphous. Their coercivity was substantially increased up to 18 kOe upon heat treating them to 1023 K for 20 minutes in argon atmosphere to avoid oxidation.

X-ray diffraction patterns for all the samples have been taken in both sides of the ribbons. SEM pictures of freshly broken ribbons were taken, showing a granular microstructure, with a gradient in the grain size that ranged from 0.01 to 1.2  $\mu\text{m}$ , in almost all the samples but the one melt spun at 32 m/s which appears mostly amorphous.

The low field thermogravimetric measurements were carried out in a commercial Perkin Elmer TGA-7 in the temperature ranges from 323 to 1173 K and 323 to 623 K. The magnetization, as weight loss in arbitrary units, was recorded as a function of temperature with heating rates of 10 and 20 K/min.

The coercivity dependence on the applied magnetizing field was measured with a home made magnetometer, that enable us to measure  $H_C$  up to a field of 3.5 T. The great advantage of this magnetometer is that it does not need much amount of material. Prior to the measurements the samples were premagnetized in a field of 5 T.

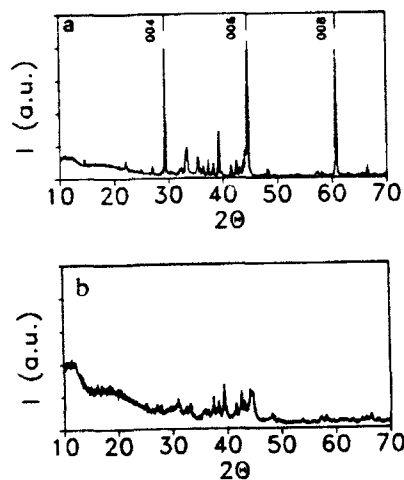


Fig 1 x-ray diffraction pattern of the free side for  $\text{Fe}_{75}\text{Nd}_{13.5}\text{Dy}_{3.7}\text{B}_{7.8}$  quenched at a) 15 m/s and b) 32 m/s

The ac-susceptibility was measured with a Lake Shore 7000 susceptometer, at a driving field of  $10^{-4}$  T and at a frequency of 111.1 Hz, in the temperature range of 4.2 K to 300 K.

Fig 2 shows the result of heating the sample to 623 K, cooling down in zero field, measuring again, then cooling in the presence of the magnetic field and measuring once more. All the samples show an abrupt decrease of the magnetization at around 600 K irrespectively of the wheel speed, which clearly corresponds to the ordering temperature of this alloy.

We have also observed, as is evident from Fig 2, that there is a secondary magnetic

3 RESULTS AND DISCUSSION

The x-ray diffraction patterns given in Fig 1a and 1b show that the sample spun at 32 m/s is almost fully amorphous, while the one spun at 15 m/s is crystallized. The peaks have been identified as belonging to the tetragonal  $\text{Nd}_2\text{Fe}_{14}\text{B}$  phase. We also observe that the  $(0,0,2l)$  reflections, indicated by the short lines in Fig 1a, are largely enhanced indicating that texturing has occurred during the solidification process and the c-axis is perpendicular to the surface of the ribbon.



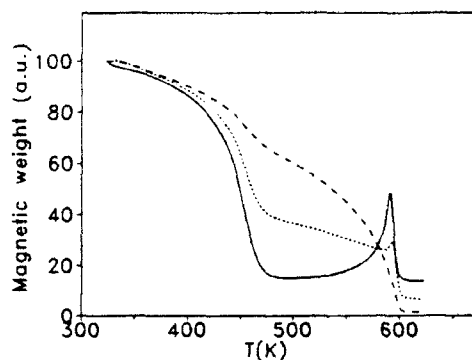


Fig 2 TGS-scans for the  $\text{Fe}_{75}\text{Nd}_{13.5}\text{Dy}_{3.7}\text{B}_{7.8}$  sample spun at 23 m/s. The solid line corresponds to the as-quenched sample, the short dashed line to the ZFC procedure and the long dashed line to the FC procedure.

low sensitivity, do not give us a clear picture of the presence of other phases. Nevertheless the small slope of the coercivity at low magnetizing fields is a clear indication that we are under a nucleation mechanism rather than another hardening process. Even at the highest field we could reach with our magnet, around 3.5 T

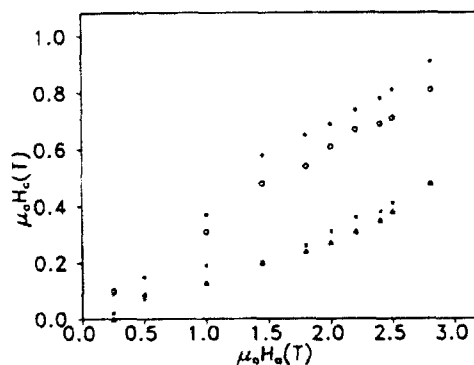


Fig 3 Coercivity as a function of magnetizing field for  $\text{Fe}_{75}\text{Nd}_{13.5}\text{Dy}_{3.7}\text{B}_{7.8}$  spun at (o) 11 m/s, (o) 15 m/s, ( $\Delta$ ) 23 m/s and ( $\times$ ) 32 m/s

there are not indications of saturation. These results are given in Fig 3. We have also measured the ac-susceptibility as a function of temperature in the range between 4 K and 300 K with a driving field of  $10^{-4}$  T. Fig 4 shows the results for the samples spun at 15 and 32 m/s. The results are presented in units of mass susceptibility  $\text{emu/gr/Oe}$  and no correction for the demagnetizing factor has been performed. The inflection point on the right side of the peak is around 112 K for all the samples and is an indication of a spin reorientation transition. It should be noticed that the Dy substitution has lowered the spin reorientation transition that is known to happen in the hard  $\text{Nd}_2\text{Fe}_{14}\text{B}$  phase at 135 K<sup>6</sup>. In similar studies it has already been found that  $T_{\text{RS}}$  decreases when Nd is substituted by other rare earth elements<sup>7</sup>. Table I shows the main results obtained in this study.

phase with a  $T_{\text{C}}$  around 453 K. This phase is mainly present in the samples spun at 23 and 32 m/s and disappears when the sample is heated to 1173 K. It should be noticed that the thermo-gravimetric measurements have a very high sensitivity revealing magnetic features that usually are missed in other conventional magnetic measurements. Moreover, since the x-ray diffractograms do not give other peaks than the ones corresponding to the tetragonal hard phase we are led to believe that we have an additional amorphous ferromagnetic phase, that upon heating to 1173 K crystallizes.

The measurements with the magnetometer, due to its relatively low sensitivity, do not give us a clear picture of the presence of other phases. Nevertheless the small slope of the coercivity at low magnetizing fields is a clear indication that we are under a nucleation mechanism rather than another hardening process. Even at the highest field we could reach with our magnet, around 3.5 T

there are not indications of saturation. These results are given in Fig 3. We have also measured the ac-susceptibility as a function of temperature in the range between 4 K and 300 K with a driving field of  $10^{-4}$  T. Fig 4 shows the results for the samples spun at 15 and 32 m/s. The results are presented in units of mass susceptibility  $\text{emu/gr/Oe}$  and no correction for the demagnetizing factor has been performed. The inflection point on the right side of the peak is around 112 K for all the samples and is an indication of a spin reorientation transition. It should be noticed that the Dy substitution has lowered the spin reorientation transition that is known to happen in the hard  $\text{Nd}_2\text{Fe}_{14}\text{B}$  phase at 135 K<sup>6</sup>. In similar studies it has already been found that  $T_{\text{RS}}$  decreases when Nd is substituted by other rare earth elements<sup>7</sup>. Table I shows the main results obtained in this study.

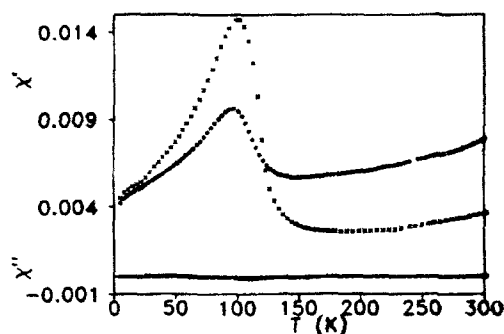


Fig 4 Ac-susceptibility as a function of temperature for  $\text{Fe}_{75}\text{Nd}_{13.5}\text{Dy}_{3.7}\text{B}_{7.8}$  spun at (○) 15 m/s and (×) 32 m/s.

#### 4 CONCLUSIONS

Melt spun ribbons of the alloy  $\text{Fe}_{75}\text{Nd}_{13.5}\text{Dy}_{3.7}\text{B}_{7.8}$  indicates that for speeds below 30 m/s there is a microcrystallization of the hard magnetic  $\text{Nd}_2\text{Fe}_{14}\text{B}$  phase, as shown by the x-ray diffraction patterns.

The bulk magnetization as function of temperature measured on the TGA reveals the presence of an amorphous secondary magnetic phase that could contribute to the increased coercivity observed in this alloy system, in addition to the increase in the anisotropy field produced by the Dy substitution.

It has been found that there is an increase in the coercivity with the magnetizing field and a lowering of the spin reorientation transition temperature from 135 to 112 K.

Table I

Speed (m/s)	$T_{C1}$ (K)	$T_{C2}$ (K)	$T_{SR}$ (K)	$\mu_0 H_C$ (T) at 2.5T
11	--	598	118	0.7
15	--	596	109	0.8
23	451	596	112	0.4
32	455	594	112	0.4

#### Acknowledgments

We would like to thank the EEC-EURAM for financial help under contract MA1-0052, and the CICYT for the support given under the Spanish Materials Programme MAT-88-603. We also express our thanks to Dr. G.Nikolaides for making the ribbons.

#### References

- 1 J.J.Croat, J.F.Herbst, R.W.Lee and F.E.Pinkerton, *J.Appl. Phys.* **55** 2078 (1984)
- 2 M.Sagawa, S.Fujimura, M.Togawa, H.Yamamoto and Y.Matsuura, *J. Appl. Phys.* **55** 2083 (1984)
- 3 M.Sagawa, S.Fujimura, H.Yamamoto, Y.Matsuura and K.Hiraga, *IEEE Trans. Mag* **20** 1584 (1984)
- 4 W.B.Yelon and F.F. Herbst, *J.Appl. Physics* **59** 93 (1986)
- 5 L.Puig, M.T.Aurell, D.X.Chen and J.S.Muñoz, *CEAM Report*, M41, (1991)
- 6 K.Tokuhara, Y.Ohsu, F.Ono, O.Yamada, M.Sagawa and Y.Matsuura, *Solid Stat. Comm.* **56** 333 (1985)
- 7 E.B.Boltich, A.T.Pedziwat and W.E.Wallace, *J.Mag. and Mag. Mat.* **66** 317 (1987)

## ANISOTROPY FIELD DISTRIBUTION IN AMORPHOUS Co-P ALLOYS

A. García-Arribas, J. Herreros\*, J. M. Barandiarán

Dpto. de Electricidad y Electrónica and (\*) Dpto. de Física Aplicada I

Facultad de Ciencias, UPV/EHU, Apdo. 644, 48080 Bilbao (Spain)

### ABSTRACT

Studies of the evolution of the magnetic anisotropy with the annealing temperature has been performed in Co-P alloys. The samples were prepared by electrodeposition technique with variable conditions, such as current density and temperature of the electrolytic bath.

Results points to two different behaviours in the crystallization process that yields to strong differences in the final state: while one of the sample develops a huge perpendicular anisotropy at crystallization, the others show softer magnetics properties. This can be related with the appearance of different phases in the two groups of samples.

### Introduction

As it is well known, the amorphous Co-P alloys obtained by electrodeposition show high magnetic anisotropy with its easy axis perpendicular to the deposition surface. Such

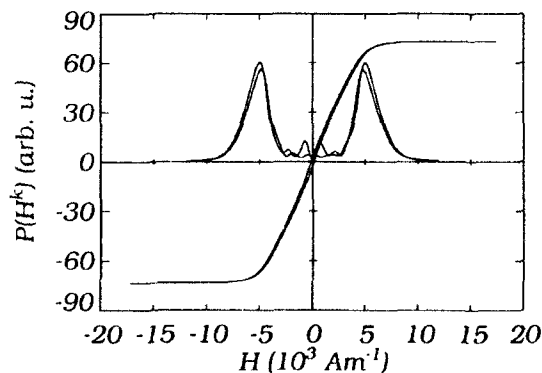


Fig 1. Anisotropy distribution of sample 1

anisotropy has been related to the columnar growth of a Co rich phase during the alloy formation<sup>1,2</sup>. It is of interest to study the evolution of that anisotropy with the annealing temperature in order to determine the evolution of the Co rich phase. Apart from a low field rectangular zone, the hysteresis loop shape is fixed by the anisotropy field distribution present in the sample.

To obtain this distribution in ferromagnetic amorphous alloys we use a procedure that has been recently developed<sup>3</sup>. It is based on the numerical calculation (directly on the hysteresis loop) of the second derivative of the magnetization with respect to the field. Figure 1 shows the typical aspect of an anisotropy distribution.

In this work we report the evolution of the anisotropy distribution with the annealing temperature for a series of  $\text{Co}_{1-x}\text{P}_x$  ( $0.1 < x < 0.2$ ) samples prepared under different conditions.

### Experimental

Four samples were prepared by an electrolytic procedure from baths based on those described by Brenner<sup>4</sup>. Depositions were carried out in small vessels of 125 cc, using a cobalt rod as anode and a polished 0.1 mm copper foil as substrate for the deposition. Sample 1 was prepared at  $150 \text{ mA/cm}^2$  and  $70^\circ\text{C}$ . The other three samples were prepared at  $50^\circ\text{C}$  and with increasing density currents: 200, 350 and  $480 \text{ mA/cm}^2$ . The phosphorus content was about 20, 11, 10 and 9% respectively (with an estimated error of  $\pm 2\%$ ). After deposition the copper substrates were chemically removed in a chromium sulphuric solution that does not attack the films. *Before removing the copper foil*, the samples were cut with a cooled diamond saw in ribbons of 2 mm wide. The thickness inhomogeneity of the samples was less than 7%. Compositions of the samples were deduced mainly from comparison of magnetic and calorimetric measurement with those found in the literature<sup>5</sup>. Besides chemical wet analyses were performed. The method used was a complexometric EDTA titration of the cobalt present in the sample<sup>6</sup>. The results obtained by this imprecise technique roughly confirm the compositions found before.

Saturation magnetization ( $M_s$ ), anisotropy distribution ( $P(H^k)$ ) and magnetostriction ( $\lambda_s$ ) of the samples were measured before the annealing;  $M_s$  from the hysteresis loop and  $\lambda_s$  from the evolution of the maximum of the anisotropy distribution with the applied stress.

Thirty minutes annealing of the samples was performed in a furnace in controlled argon atmosphere. The annealing temperatures were varied from  $100^\circ\text{C}$  to  $300^\circ\text{C}$  with  $25^\circ\text{C}$  steps. The evolution of the magnetic parameters with the annealing can be observed in figure 2 for the two different behaviours. Sample 1 has a high, decreasing anisotropy energy until crystallization takes place. At this point, the anisotropy increases hugely. The full width at the half maximum of the anisotropy distribution starts decreasing to reach a finite value at crystallization. In contrast, in the other three samples, the anisotropy energy decreases to nearly zero while the anisotropy distributions get rapidly wider and

asymmetrical until crystallization takes place. The aspect of the hysteresis loops after crystallization can be seen in figure 3.

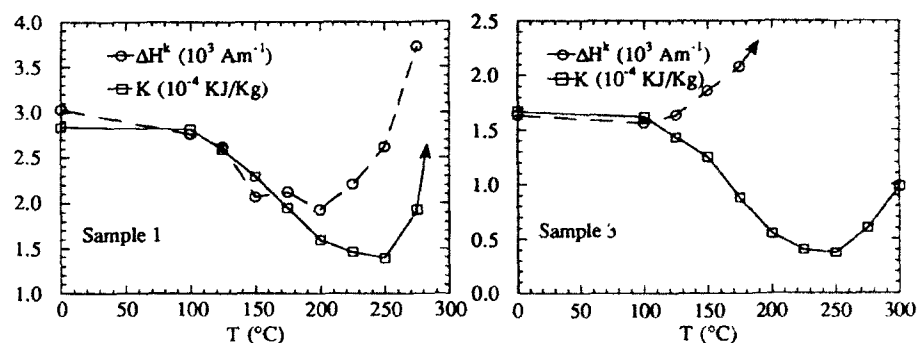


Fig.2. Evolution of anisotropy energy ( $K$ ) and full width at the half maximum of anisotropy distribution ( $\Delta H^K$ ) for samples 1 and 3.

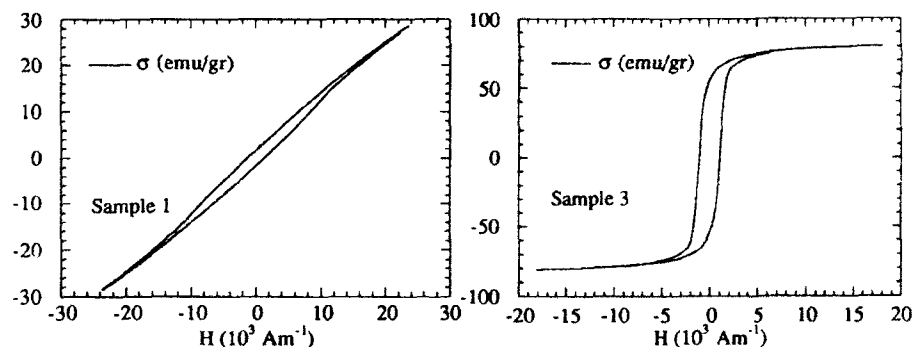


Fig.3. Hysteresis loops of samples 1 and 3 after crystallization.

### Discussion

Relaxation and crystallization processes are markedly different in sample 1 and in the three others. Sample 1 exhibits, during the whole treatment, a high anisotropy field which, although decreasing, does not vanish. At crystallization, a very great anisotropy is developed. This behaviour shows that cobalt rich phases, the ones that contribute mainly to the perpendicular anisotropy and determine the magnetic properties, grow up directly from the as prepared amorphous alloy and, when crystallization takes place, an easy axis

of magnetization perpendicular to ribbon surface is preserved. The narrowing of the anisotropy distributions in the first stages of the annealing implies that the process tends to group all the anisotropy fields  $H^k$ , in the sense that all of them converge to a definite value. This contrasts with the behaviour of the other three samples in which the anisotropy field values spread very fast as can be seen in the broadening of the anisotropy distributions. These samples evolve with rapidly decreasing anisotropy which implies that the columnar cobalt rich phases homogenize as a result of structural relaxation losing its columnar structure. At crystallization, the soft loops these samples present show that no easy axis perpendicular to the surface remains in the sample. There must be a random distribution of easy axis in the crystallized state.

The marked differences found in the evolution of the samples could be due to either a particular composition of sample 1 or to the differences in the preparation or both. More complete studies are being done to understand the role of temperature and other parameters of the deposition process in the properties of the Co-P electrodeposited amorphous alloys.

#### Acknowledgments

The authors wish to thank Dr. Hernández Bocanegra for DSC measurements. This work has been supported by the Spanish CICyT under grant nº MAT90-0877.

#### References

1. C.G.Chi and G.S.Cargill III. *AIP Conf. Proc.* **29** (1975) 147
2. J.M.Riveiro, M.C.Sánchez and G.Rivero. *IEEE Trans. on Magn.* **17** (1981) 1282
3. J.M.Barandiarán, M.Vázquez, A.Hernando, J.González and G.Rivero. *IEEE Trans. on Magn.* **25** (1989) 3330
4. A.Brenner. *Electrodeposition of Alloys* (Academic, New York, 1963), Vol II, p. 457
5. G.Rivero, I.Navarro, P.Crespo, E.Pulido, A.García-Escorial, A.Hernando, M.Vázquez, M.Vallet and J.Gonzalez-Calbet. *J.Appl. Phys.* **69** (8) (1991) 5454
6. C.W.Wilson and D.W.Wilson Eds. *Comprehensive Analytical Chemistry*. (Elsevier Publishing Company, 1960), Vol IB p. 350.

## UNIDIRECTIONAL MAGNETIC ANISOTROPY IN THE $\text{Fe}_{80}\text{B}_{20}$ METALLIC GLASS

J. M. Riveiro, J. Flores and M. J. Bernal,  
*Departamento de Física Aplicada, Facultad de CC. Químicas,  
 Universidad de Castilla-La Mancha, Ciudad Real, SPAIN.*

### ABSTRACT

In some metallic glasses a unidirectional magnetic anisotropy (UMA) can be observed when weak magnetic fields are applied. An experimental method to measure the UMA is described. This investigation is conducted on the simple metallic glass  $\text{Fe}_{80}\text{B}_{20}$ . It may be observed that the unidirectional anisotropy is, at least, one order of magnitude larger in samples which present clear indications of microcrystallinity. UMA phenomenon in metallic glasses is therefore associated with the presence of this kind of defect in the amorphous matrix.

### 1.- Introduction

In a great variety of metallic glasses it is possible to detect some anomalies in the magnetization process which occur in low magnetic fields. These anomalies are produced by a weak UMA whose direction can be changed by applying a strong magnetic field in the correct direction. Riveiro<sup>1</sup> associates this anomalous behaviour with the presence of crystalline-like nuclei in the metallic glasses. He considers that the nuclei are defects which are more or less always present in the structure of metallic glasses. Other scientists have reached a similar conclusion<sup>2</sup>. The possible relationship between the crystalline-like nuclei and the UMA is as follows: these nuclei are usually in a metastable phase and there are sufficient proofs that they can undergo reversible structural transformations at a certain temperature ( $T_s$ )<sup>3,4,5,6</sup>. At the stable phase below  $T_s$ , the nucleus can be very anisotropic, and if it is magnetic, it may have a great magnetic anisotropy. This local anisotropy field could anchor the magnetization of the corresponding nuclei. In this case, if a weak magnetic field is applied, the magnetization of the amorphous matrix could orientate itself towards the applied magnetic field  $H$ , while the magnetization of the nuclei remains still. This could be the cause of a local UMA. A macroscopic unidirectional effect, which appears if this local UMA effect is distributed non randomly, is UMA.

In order to observe the UMA, the magnetization of the crystalline-like nucleus must be weakly coupled to the magnetization of the amorphous matrix. The reason

that this weak coupling exists can be as follows. Let us suppose that a metallic glass of transition metal-metalloid type (TM-M) has been obtained by rapid quenching. Presumably the suggested magnetic nuclei have been formed during the cooling process, by the segregation of some TM atoms from amorphous matrix. This is more likely to occur in binary systems, such as Co-B, Fe-B, etc, since they are difficult to amorphize by rapid quenching. The matrix region next to the interface (TM depleted zone) would be enriched with metalloid atoms forming an alloy, probably a non magnetic alloy. Thus the exchange coupling between the magnetization of the nucleus and the magnetization of the amorphous matrix could be interrupted, or at least dramatically reduced.

It is possible to check the proposed model in the following way: when a metallic glass is obtained by rapid cooling, it is usually seen that there are some zones in the sample that are closer to the "ideal amorphous" state than others, due to misfits in the contact between the melt and the cooling wheel, during the sample growth. The ideal state would be that which did not have any microcrystal. This can not be experimentally ensured, but we can check if the sample is farther or closer to the ideal state. The idea we propose is to establish two kinds of samples (coming from the same original ribbon) very different in closeness to the ideal state, then to study its UMA and, repeating successive times, to try to obtain support for the proposed model.

## 2.-Experiment

An amorphous  $\text{Fe}_{80}\text{B}_{20}$  ribbon  $\approx 0.7\text{mm}$  wide and  $24\mu\text{m}$  thick was prepared by the single roller quenching method. This sample shows the described UMA in a very marked manner. The experimental set-up is shown in Figure 1. This set-up is mainly a typical inductive device with which to measure  $M-H$  hysteresis loops. While the sample is heated a single pulsed magnetic field can be applied ( $\sim 200$  Oe). The thermocouple is constructed from a non magnetic alloy (Cu-Constantan). The presence of magnetic material within the surrounding area of the sample can create a similar UMA phenomenon, so it is very important to avoid the possibility of this occurrence. The  $M-H$  hysteresis loops are obtained by applying an alternating magnetic field (50 Hz). With weak alternating magnetic fields ( $H_{\text{max}} < 10^2 \text{Am}^{-1}$ ) the following phenomena may be observed:

- a) First, a DC pulse on the primary coils (enough to reach technical saturation) is applied.
- b) Next, a weak alternating magnetic field is applied, and the oscilloscope registers the corresponding  $M-H$  loop.
- c) Then, the continuous pulsed magnetic field is applied again, but this time in the opposite direction to the originally applied pulse.
- d) Finally, the alternating magnetic field is once more applied and the corresponding  $M-H$  loop is registered.

Both the  $M-H$  loops are superimposed on the oscilloscope screen. A shift of the  $M-H$  loops is observed along the  $H$  axis. This shift can be easily measured and an effective unidirectional anisotropic field  $H_k \approx d/2$  can be defined.



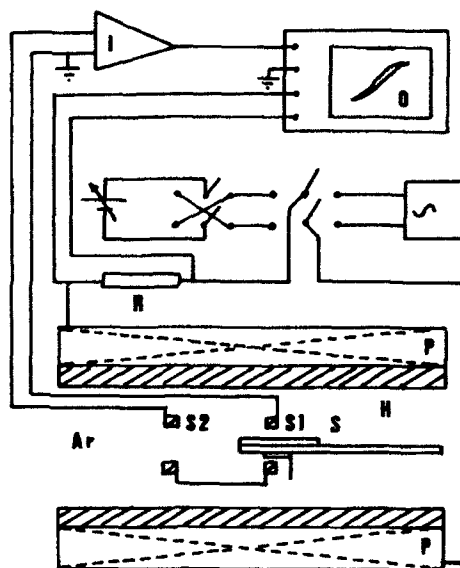


Figure 1: Experimental set-up: H, heater; I, integrating fluxmeter; O, digital oscilloscope; P, primary coil; R, resistor; S1 and S2, secondary coils; S, sample.

In order to study the greater or lesser proximity of the samples to the ideal state, an X-ray diffractometer (Cu  $K_{\alpha}$  radiation) has been used.

### 3.-Results and discussion

The UMA at room temperature was analyzed for 50 samples consisting each one of a piece of  $\approx 60\text{mm}$  long of the original ribbon. A first group (approximately 80% of the samples) showed an UMA that we will consider small, included between  $[4 - 1]\text{Am}^{-1}$ . The second group had a marked larger value, included between  $[40 - 20]\text{Am}^{-1}$ . Three samples of any of the mentioned groups were chosen. Those of the first group corresponded to those three which exhibited the smaller UMA. Those of the second, to those which exhibited the larger UMA. The X-ray diffraction diagrams of the three samples belonging to the first group were completely similar, as with the samples of the second group. The detail of both kind of diffractograms is shown in Figure 2. While in the first group it is not possible to see any sign of microcrystallinity, in the second one it is shown clearly the presence of microcrystals of Fe corresponding to the bcc structure.

In case that our model about the origin of the UMA in the metallic glasses was correct, a lower cooling velocity would give rise to a larger density of microcrystalline defects in the amorphous matrix. This larger density must result in a marked larger macroscopic perturbation (UMA), which matches the results obtained in this work.

This evidence, together with other recent works which show the behaviour of the UMA with the temperature in metallic glasses<sup>7</sup>, allow us to establish in a definitive

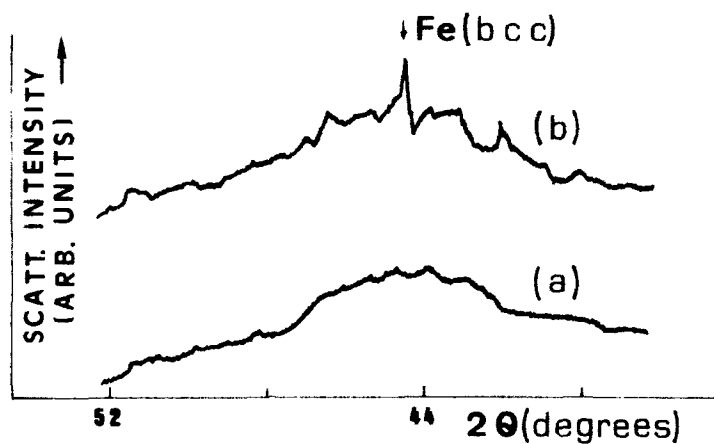


Figure 2: X-ray diffractograms (Cu K $\alpha$  radiation) for a Fe<sub>80</sub>B<sub>20</sub> amorphous alloy: (a) First group; (b) Second group.

way that the crystalline nuclei which are present in the amorphous matrix are the defects causing the UMA phenomenon.

### References

1. J. M. Riveiro, J. Phys.:Con. Matter. (to be published).
2. A. S. Schaafsma, H. Snijders, F. van der Woude, J. W. Drijver and S. Rade-  
laar, Phys. Rev. B **20**, 4423 (1979).
3. B. W. Corb, R. C. O'Handley, J. Megusar and N. J. Grant, Phys. Rev. Lett.  
**51**, 1386 (1983).
4. J. M. Riveiro and R. Pareja, Phys. Rev. B **34**, 2029 (1986).
5. J. M. Riveiro, Phys. Rev. B **37**, 7731 (1988).
6. J. M. Riveiro, V. Madurga and A. Hernando, Phys. Rev. B **39**, 11950 (1989).
7. J. M. Riveiro, J. Flores and M. J. Bernal, J. Mag. Mag. Mat. (to be  
published)

## SELECTION AND PROCESSING OF METALLIC GLASS MATERIALS FOR FLUXGATE APPLICATIONS

O.V. Nielsen<sup>1</sup>, F. Primdahl<sup>2</sup>, J.R. Petersen<sup>1</sup> and B. Hernando<sup>1\*</sup>

<sup>1</sup> Department of Electrophysics, The Technical University of Denmark, Dk-2800 Lyngby, Denmark

<sup>2</sup> Danish Space Research Institute, Dk-2800 Lyngby, Denmark

**ABSTRACT.** Noise levels as a function of hysteresis effects on a series of sensitive fluxgate sensors with non-magnetostrictive metallic glass ribbons as core materials have been studied. Correlation between noise and local occurrence of hysteresis has not been observed, showing that Barkhausen jumps do not seem to be the main source of noise. Analysis and measurement of some other possible sources of noise like eddy currents, geometrical and end defects are in progress.

### 1. INTRODUCTION

Many fluxgate magnetometers use as the magnetic sensing element the ringcore fluxgate shown in fig. 1. The sensing mechanism is based on the ability of the ferromagnetic core material to be fully AC magnetized by a moderate AC current flowing in the toroidally wound excitation coil. The classical material used in the magnetic core consists of sheets or ribbons of the permalloy type.

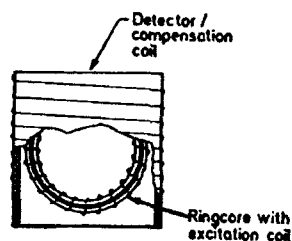


Fig. 1. Ringcore fluxgate sensor

A serious drawback for this material is its high sensitivity to small mechanical stresses which makes a heat treatment necessary after the sensor production.

In recent papers it has been demonstrated that non-magnetostrictive metallic glass ribbons, suitable heat treated, compete favourably with traditional core materials of the permalloy type. In the present work we make a systematical study with the purpose of further reducing the low noise level (about 17 pT, RMS 0.06-10.0 Hz) normally obtained as a standard for sensors from our present method of production. The lowest noise level we have obtained up to now is 12 pT for a sensor like those discussed below.

### 2. EXPERIMENTAL SET-UP AND RIBBON PRODUCTION

The magnetometer used to test the various sensors has been described previously<sup>1</sup>. The output from the detector coil, which works in a short-circuited condition, is sampled by means of a switch which is controlled by the driving 15 kHz excitation signal. The sampled signal is integrated and used in a feedback loop to compensate the field to be measured. For details see Nielsen et al.<sup>1</sup>, and references therein. The ringcore sensors used in the present work are like that shown in fig. 1. A metallic glass ribbon, about 0.8×0.02 mm<sup>2</sup> in cross section, is wound with about 20 wraps to form a 0.27 mm<sup>2</sup> cross section core in a groove inside a ring-shaped support made of MACOR<sup>®</sup> or of polycarbonate. The dimensions of the support are: outer/inner diameter=18.2/15.0 mm, length=2.9 mm, groove depth=1.0 mm giving a core outer diameter=17.0 mm. MACOR, which is a machinable glass material stable up to high temperatures (1000°C), has a thermal expansion (9.4×10<sup>-6</sup>°C<sup>-1</sup>) which matches that of the metallic glass (8.97×10<sup>-6</sup>°C<sup>-1</sup>). The ring is supplied with a toroidal excitation coil which has about 200 windings of 0.2 mm Cu wire. For further details see ref. 1. The metallic glass ribbons, all of them with the composition Co<sub>46.5</sub>Fe<sub>3.5</sub>Si<sub>12</sub>B<sub>18</sub>, were produced (quenched) in vacuum using the single roller quenching technique (Fe-roller). The ribbons were given an annealing treatment in argon atmosphere consisting of a 1 hour pre-annealing (stress relief) at 340°C followed by a 1 hour stress annealing at the same temperature with applied tensile stress=200 or 300 MPa.

\* On leave from: Departamento de Física, Universidad de Oviedo, 33007 Oviedo, Spain.

This treatment induces a hard ribbon axis anisotropy, promoting a domain rotation rather than domain wall movement in the AC magnetization process. The resulting magnetization curve is shown in fig. 2. The susceptibility (slope in fig. 2(b)) is inversely proportional to the stress applied during the annealing process.

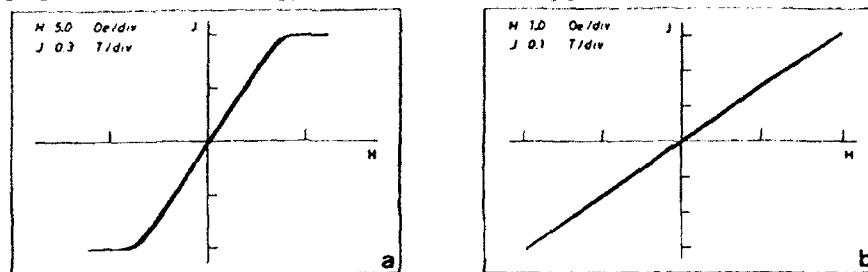


Fig. 2. Axial magnetization curves of the stress annealed ribbon

### 3. RESULTS

#### 3.1. Hysteresis effects

A series of 17 sensors (C1-C17) were produced from one ribbon. Fig. 3 shows the results of noise measurements performed in the frequency band 0.06-10 Hz. The sensors (cores) are divided in two series, C1-C6 and C7-C17, of which the first series is used for further investigations. Fig. 3 does not reveal any systematic dependence of noise. The sensors are labelled arbitrarily according to decreasing noise level within each series.

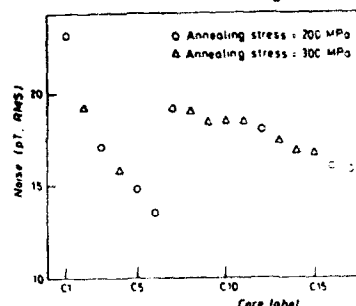


Fig. 3. Noise measurements performed in the frequency band 0.06-10 Hz for two series of arbitrarily labelled sensors

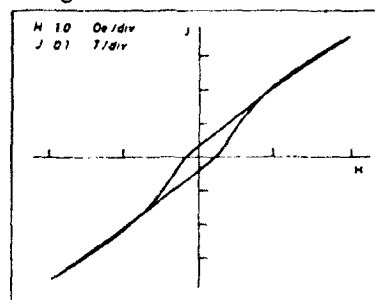


Fig. 4. Axial hysteresis loop of the stress annealed ribbon

The noise for the 17 sensors ranges from 13.5 to 23.2 pT with a mean value of 17.6 pT. The figure further confirms a previously obtained result, that the dependence of noise on annealing stress (susceptibility) has a broad almost constant minimum level in the range 200 (o) to 300 ( $\Delta$ ) MPa. As mentioned above the stress annealed ribbon has a magnetization curve as shown in fig. 2. In places on the ribbon, however, the magnetization curve shows up a shape like fig. 4 i.e. a small hysteresis occurs when the ribbon has been exposed to fields above 1 Oe (80 A/m). Further inspection along the ribbon reveals that all loops close at field values about 1 Oe. We may therefore take the remanence as a good measure for the magnitude of the hysteresis. Fig. 5 shows the position dependence of the remanence measured for a selected part of the ribbon from which cores C2 and C8 were prepared. The mean values of the remanence along the ribbons for C2 and C8 are 2.9 and 4.6 mT respectively. All the ribbon was analysed in this way before the sensors were produced.

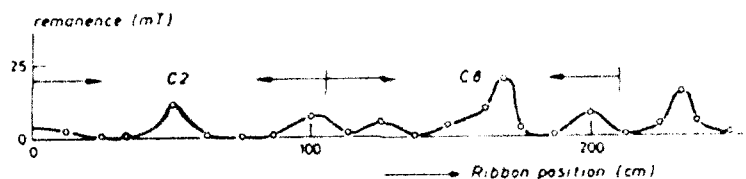


Fig. 5. Position dependence of the remanence measured for a select part of the ribbon of C2 and C8 cores

The original hypothesis, leading to the induction of a hard ribbon axis anisotropy, was to get rid of the domain wall motion (hysteresis, Barkhausen noise), thereby reducing the total noise level. In a previous paper it was demonstrated that this hypothesis was very fruitful<sup>2</sup>. Therefore we expect that the noise can be correlated with the local occurrence of hysteresis effects. Because the remanence is proportional to the total movement of the domain walls, a reasonable assumption is that the noise is proportional to, or at least increasing with, the mean value of the remanence measured at all positions along the ribbon. This assumption, however, seems not to be valid in our case, as illustrated in fig. 6 which shows the noise as a function of the mean remanence. An analogous analysis of the noise dependence on the peak value of the remanence shows a similar lack of correlation.

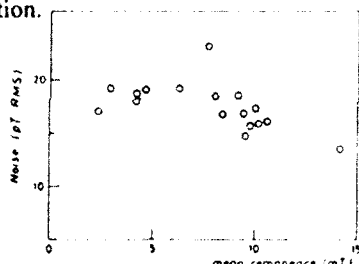


Fig. 6. Sensors noise as a function of the ribbon mean remanence

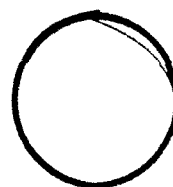


Fig. 7. Possible geometrical defect of the innermost wrap

### 3.2. Other effects

The (negative) results from fig. 6 may be explained by assuming that there exist some other sources of noise which mask the noise from Barkhausen jumps. We therefore make some technical modifications of the sensors C1-C6. After 3 months storage at normal laboratory conditions (room temperature, Earth's field) the noise measurements on C1-C6 were repeated as above. Using the core ribbons from C1-C6 in a modified sensor we could estimate the effects of various potential sources of noise. Fig. 8 shows the result of noise measurement for one of the sensors.

#### 3.2.1. Geometrical effects

As described above, the ribbon is wound inside a groove in the ring-shaped support. The ribbon length is adjusted to make an integer number of wraps which are kept in position by means of the elastic spring force. The innermost wrap, however, is not quite circular because the end of the ribbon more or less forms a chord in the circle as illustrated in fig. 7. Cores C1 and C2 were mounted in a two-part support designed so that an inner circular part fits with the inner diameter of the ribbon core, thereby bending the end of the ribbon. Noise measurements showed the following results:

	C1	C2
Before modification (fig. 3)	23.2 pT	19.2 pT
Before modification, after 3 months	17.1 pT	19.8 pT

After modification

15.5 pT

18.7 pT

## 3.2.2. Effect of end defects

The ribbons in C1-C17 are shortened to their suitable lengths by simple cutting. This may introduce defects which could destroy the induced anisotropy, thereby promoting domain wall movements. Cores C3 and C4 were shortened one wrap by etching both ends in a mixture of concentrated HCl and  $H_2O_2$  in the ratio 4:1. Noise measurements showed the following results:

	C3	C4
Before modification (fig. 3)	17.1 pT	15.8 pT
Before modification, after 3 months	16.6 pT	16.7 pT
After modification	22.9 pT	17.1 pT

## 3.2.3. Eddy current effects

Although the magnetization process for the ribbon is almost pure rotational, some delay ("viscosity") is present due to the occurrence of eddy currents in the material. Some eddy currents may pass through the surfaces in contact between neighbouring wraps. If the contact resistance changes from cycle to cycle (as it probably does) this will introduce an additional source of noise. The ribbons from cores C5 and C6 were spray-painted on one side with a thin layer of teflon suspension (trade mark: Acoflon) in order to insulate the individual wraps from one another. Noise measurements showed the following results:

	C5	C6
Before modification (fig. 3)	14.4 pT	13.5 pT
Before modification, after 3 months	15.3 pT	14.3 pT
After modification	15.0 pT	11.8 pT (fig. 8)

## 4. CONCLUSIONS

Due to the proportionality between remanence and movement of domain walls, noise was expected to be proportional to the mean value of the remanence measured at all positions along the ribbon. But this correlation has not been observed in our results. So, it seems that Barkhausen jumps are not in these sensors the main source of noise and there must exist other sources which mask them. Other possible noise sources like eddy currents, geometrical and end defects also studied till now in this work have not produced significant improvements as can be seen in the RMS noise values obtained after modifying the sensors, showing that these sources can be discarded at these noise levels and other magnetic and/or electronic sources must be investigated for the improvement of our sensors.

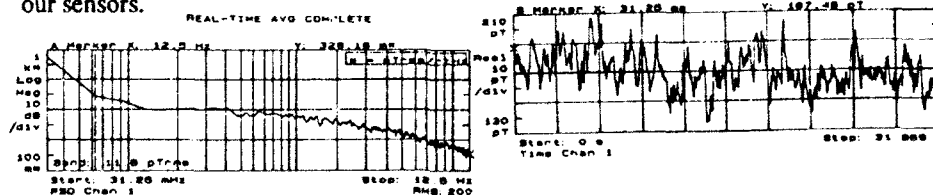


Fig. 8. Noise power spectral distribution and noise time series for the C6 core sensor

## 5. ACKNOWLEDGMENTS

B.H. has been supported, in part, by the Spanish CICYT under project ESP90-0670.

## 6. REFERENCES

1. O.V. Nielsen, J.R. Petersen, A. Fernández, B. Hernando, P. Spisak, F. Primdahl and N. Moser, *Meas. Sci. Technol.* **2** (1991) 435.
2. O.V. Nielsen, J.R. Petersen, B. Hernando, J. Gutiérrez and F. Primdahl, *An. Fis. R 86* (1990) 271.

## BISTABLE BEHAVIOUR IN STRESS-ANNEALED NON-MAGNETOSTRICTIVE AMORPHOUS WIRE

C. GOMEZ-POLO, M. VAZQUEZ  
*Inst. de Ciencia de Materiales (C.S.I.C.).  
 Serrano 144, 28006 Madrid. Spain.*

and

T. REININGER, H. KRONMULLER  
*Max-Planck Institut für Metallforschung, Institut für Physik,  
 Heisenbergstrasse 1, 7000 Stuttgart 80. Germany.*

### ABSTRACT

Non-magnetostrictive Co-rich amorphous wires do not present in as-cast state the striking bistable behaviour observed in high-magnetostrictive wires. However, under certain annealing conditions, it has been possible to reproduce such behaviour. The anisotropy induced by thermal treatments has been interpreted as the origin of the occurrence of bistability. Moreover, the temperature dependence of DC hysteresis loops (from 10 K to 300 K) has been evaluated. The decrease in the corresponding switching field (field at which a large Barkhausen jump occurs) has been related to the change in anisotropy.

### 1. Introduction

Large magnetostriction amorphous wires exhibit a quite interesting magnetization process characterised by a single large Barkhausen jump that makes them suitable for a number of applications<sup>1</sup>. Nevertheless, this unique property, attributable to the anisotropy caused by the interaction between magnetostriction and internal stresses quenched-in during solidification, has been only observed in large magnetostriction amorphous wires. Non-magnetostrictive amorphous wires do not present bistable behaviour in the as-cast state.

However, as in the case of amorphous ribbons, it is possible to induce macroscopic magnetic anisotropies by thermal treatments under the action of a magnetic field or/and an applied stress. In the present work, a nearly non-magnetostrictive ( $\lambda_s \sim -0.40 \cdot 10^{-7}$ ) Co-rich amorphous wire has been annealed under an applied tensile stress by means of flowing a current through the sample. With this treatment it was possible to achieve bistable behaviour in non-magnetostrictive amorphous wires. Hysteresis loops and changes in magnetostriction are studied as a function of applied stress during annealing. Moreover, the temperature dependence (from 10 K to 300 K) of the corresponding switching field (field at which a large Barkhausen jump takes place) is shown.

## 2. Experimental techniques and results

Amorphous wires obtained by the in-water quenching technique with composition  $(\text{Fe}_{0.06}\text{Co}_{0.94})_{72.5}\text{Si}_{12.5}\text{B}_{15}$  were kindly supplied by UNITIKA Inc. The diameter of the samples was  $125\text{ }\mu\text{m}$ . Pieces of 10 cm in length were cut from the same roll.

Thermal treatments were performed by means of the current annealing technique under an applied tensile stress<sup>2</sup>. Isochronal treatments (6 min) were performed for a series of different annealing stresses (319, 439, 559 and 679 MPa) with a fixed current density  $28.5\text{ A/mm}^2$  flowing through the samples. This current density corresponds to an annealing temperature of 550 K (Curie point at 568 K).

Axial DC hysteresis loops were obtained with a Förster coercimeter, where the temperature of the samples could vary from 10 K to 300 K. That allowed us to determine the temperature dependence of magnetic parameters such as saturation magnetization, remanence, coercive field and initial susceptibility. The hysteresis loops at room temperature of as-cast (a), 319 (b) and 679 (c) MPa stress annealed wires are plotted in fig.1. It can be seen that the as-cast wire presents a similar behaviour to that of non-magnetostrictive amorphous ribbons. However, the shape of the hysteresis loops for the stress-annealed wires is completely different, since a large Barkhausen jump can be observed (mainly in case (b)).

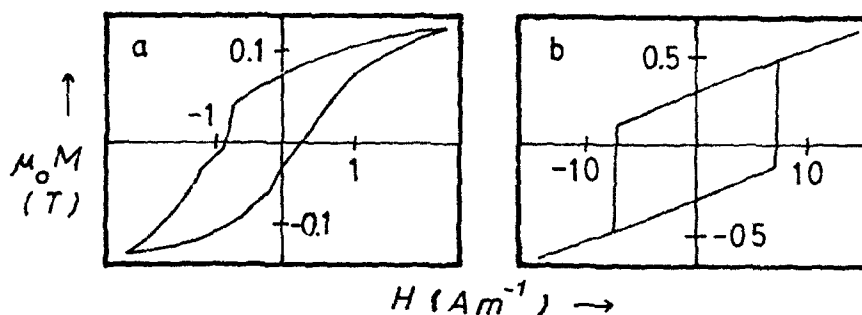
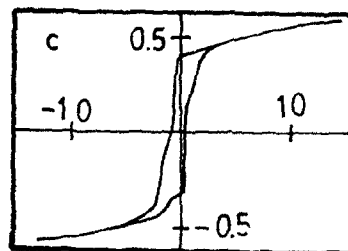


Fig 1. DC hysteresis loops at room temperature of (a) as-cast (b) 319 and (c) 679 MPa stress annealed wires.

On the other hand, the small angle magnetization rotation (SAMR) technique has been used to measure the linear magnetostriction,  $\lambda_s$ , in as-cast and stress-annealed samples at room temperature (see table 1). As in the case of nearly non-magnetostrictive Co-rich ribbons,  $\lambda_s$  is found





to depend on applied stress and follows the law:

$$\lambda_s = \lambda_0 - \alpha \sigma \quad (1)$$

Table 1

$\sigma_{\text{ann}}$	as-cast	319 MPa	439 MPa	559 MPa	679 MPa
$\lambda_0 (10^7)$	-0.40	0.48	0.52	0.50	0.53
$\alpha (10^{10} \text{ MPa}^{-1})$	1.7	1.7	1.6	1.6	1.7

Fig. 2a shows the temperature dependence of the switching field,  $H^*$ , for the stress annealed wires. A remarkable feature is that at a given temperature,  $H^*$  decreases with increasing annealing stress. Nevertheless, the bistable behaviour is deteriorated for the largest annealing stress.

The thermal evolution of the remanence reduced to the saturation magnetization at each temperature is shown in fig 2b. Note that  $m_r$  can be correlated to the fractional volume of the core.

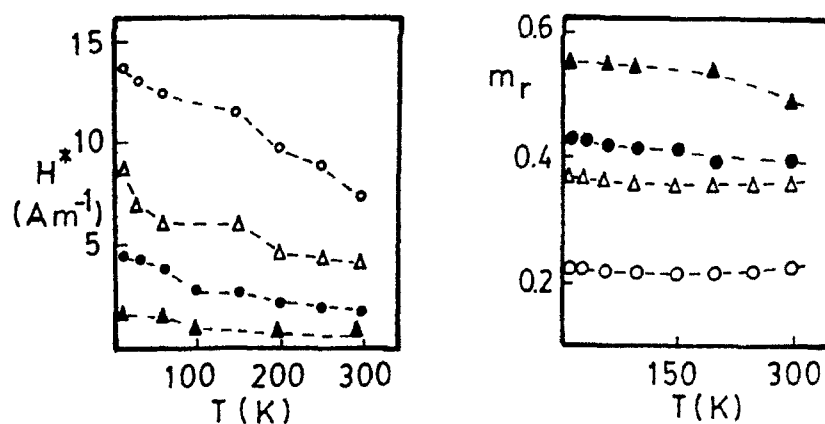


Fig 2. Temperature dependence of the switching field,  $H^*$ , and reduced remanence,  $m_r$ , for the stress annealed wires. ((o) 319, ( $\Delta$ ) 439, ( $\bullet$ ) 559 and ( $\blacktriangle$ ) 679 MPa).

Domain structure at the surface of the wires has been observed by Bitter technique. Particularly for the case when perfect bistability is obtained (see fig. 1b), nice bamboo-like patterns are observed as in the case of large magnetostriction Co-rich wires. It suggests us that induced anisotropy plays the same role as the intrinsic magnetoelastic anisotropies in these Co-rich wires.

### 3. Discussion and conclusions

As previously established for large magnetostriction wires, the interpretation of the squareness of the present hysteresis loops can be done considering two main regions in the wire. Within an inner core, magnetization lies spontaneously along the axial direction, while at the outer shell it is transversely oriented. Moreover, closure domains with reversed magnetization should appear at the ends of the wire to minimize the stray field energy<sup>3</sup>. While the magnetization process in the shell can be ascribed to reversible magnetization rotations, wall displacements have to be taken into account within the core. Whether we have prevailing reversible domain wall displacements or rotations at applied fields  $H < H^*$  strongly depends on the pinning force and anisotropy<sup>4</sup>. For  $H \sim H^*$  the applied field overcomes the pinning of the closure domain walls and we get a large Barkhausen jump. That means the switching field  $H^*$  and its temperature dependence are governed by pinning.

Annealing with the smaller stress promotes larger transverse anisotropy at the shell and accordingly the fractional volume of the core is reduced and perfect bistability is observed. For larger annealing stress, anisotropy at the shell is reduced and the volume of the core increases. In this case, it seems likely that the initial magnetization process is mainly determined by wall displacements that gives rise to distorted bistability.

After analyzing the present experimental data, we can conclude that stress-annealed nearly non-magnetostrictive wires can exhibit bistable behaviour. The appearance of such behaviour has been explained for large magnetostriction wires to be a consequence of the intrinsic magnetoelastic anisotropy. In the present case, the anisotropy induced by stress annealing, plays the same role as those magnetoelastic anisotropies (note that magnetostriction takes two order of magnitude less than in Fe-rich wires). However, in both cases the occurrence of bistability is determined by the correlation between anisotropy, pinning forces and domain structure. A more detailed work regarding the relationship between switching field and induced anisotropy is in progress.

#### Acknowledgments

This work has been carried out within the framework of "Acciones integradas hispano-alemanas" under project HA-27A, 1991.

### 4. References

1. K. Mohri, *IEEE Trans. Mag.* **20** (1984) 942.
2. M. Vázquez, J. González and A. Hernando, *J. Magn. Magn. Mat.* **53** (1986) 323.
3. M. Vázquez, C. Gómez-Polo and D.X. Chen. (to be published).
4. H. Kronmüller and T. Reininger, *SMM 10* Dresden (1991).

## Large Barkhausen effect and coupling factors in iron rich amorphous wires

J.D.M.Carey, M.D.Hickmott and H.T.Savage  
*Instituto de Magnetismo Aplicado, Laboratorio 'Salvador Velayos',  
Universidad Complutense / RENFE, Las Rozas 28230, Madrid, SPAIN.*

C.Gomez-Polo and M.Vazquez  
*Instituto de Ciencias de Materiales (C.S.I.C.) 28006, Madrid, SPAIN.*

J.B.Blanco and J.Gonzalez  
*Dpto. Fisica de Materiales, Univ. Pais Vasco, San Sebastian, SPAIN.*

### Abstract

The effect of various current annealing conditions has been examined for iron rich Fe<sub>77.5</sub>Si<sub>7.5</sub>B<sub>15</sub> amorphous wires with a view to establishing optimum magnetomechanical coupling. An anomalous minimum in the coupling factor is specifically investigated. We find that the wires current annealed for 90 seconds at 0.50 amps yield the highest minimum coupling factor  $k_{33}$  of 0.22. Larger or smaller values of current yield lower values of coupling factor. From hysteresis loops the switching field and squareness ratio of  $M_r/M_s$  were examined as functions of length of wire and under different applied tensile stresses. We find that the switching field is proportional to the square root of the applied stress, above a certain stress irrespective of the annealing conditions carried out on the wires. Below this limit the as-cast wire exhibits a larger switching frequency of 80 mOe whereas a wire annealed for one minute at 0.55 amps has a switching frequency of 50 mOe. We also show that the switching frequency depends linearly on the length of the wire up to a limiting length of 11 cm. No bistability was observed for wires less than 7 cm. Above this length the switching frequency remains constant at 90 mOe.

### Introduction

Iron rich amorphous wires produced by quenching techniques are known to exhibit outstanding soft magnetic properties. However the magnetic behavior of such wires, has a considerable dependence upon the internal stresses found in the wire. Such stresses can originate in the solidification process as the wire cools at different rates during manufacture and as it is cooled through its Curie temperature, both leading to the formation of an outer sheath and an inner core<sup>1</sup>. Non-simultaneous cooling gives rise to the formation of uniaxial anisotropy which results in the magnetisation of the core by a large Barkhausen jump. Application of tensile stress or a magnetic field as well as preparatory annealing treatments may all be used to enhance magnetic properties as coupling factor and switching field.

### Experimental

Wire samples (diameter 125  $\mu\text{m}$ ) were obtained from Unitika Co., Japan. Hysteresis loops of the amorphous wires were obtained by the conventional 15 Hz induction technique. From these the switching field (field at which the large Barkhausen jump occurs) and the squareness ratio of  $M_r/M_s$  have been examined. The study was carried out for different length samples (3-15 cm) in both their as-cast (unannealed) state and after the samples were current annealed. Furthermore specimens were examined under tensile stress for switching field response. A variety of wire samples have been annealed at a series of different currents. Each wire was subsequently examined for its coupling factor using the dynamic technique<sup>2</sup> based upon the response of the wire to a change of the frequency of the ac magnetic field in a given bias field.

### Results and discussion

Figure 1 shows a typical response of a wire to varying the frequency of the excitation ac field. Reading the resonant  $f_R$  and anti-resonant  $f_A$  frequencies gives a value of the coupling factor  $k_{33}$  at a given bias field using the expression shown.

In figure 2 the effect of increasing the bias field is seen on the position of the frequencies and on the amplitude of the voltage. As the bias field becomes dominant the resonant voltage decreases and the position of both resonant frequencies moves up in frequency which leads to a change in the coupling factor.

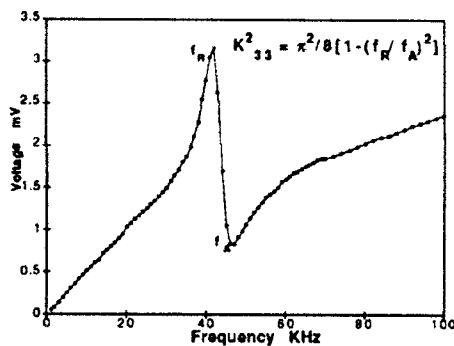


Figure 1 shows a typical response of a wire to varying the frequency of the exciting field for a given bias field.

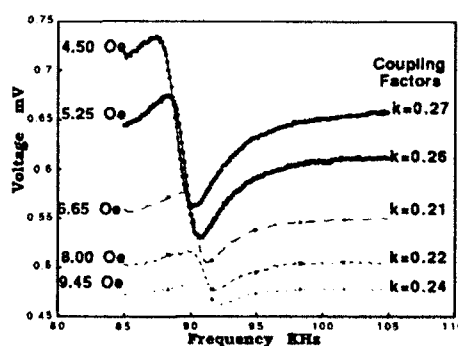


Figure 2 shows the effect of increasing the bias field on the resonant frequencies.

Figure 3 shows how the coupling factor  $k_{33}$  varies as a function of bias field for five wires annealed for 90 seconds at different annealing currents. The minimum point on the curve, which gives the minimum coupling factor  $k_{min}$ , changes depending on the wire's annealing conditions. The highest minimum  $k_{33}$  value occurred for the wire annealed at 0.50 amps.

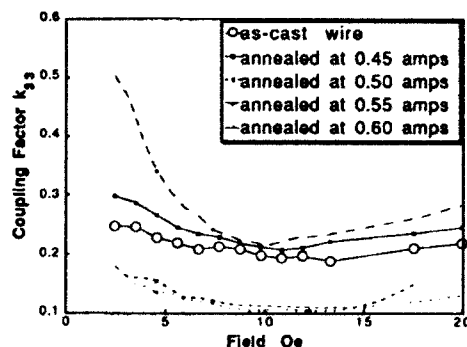


Figure 3 shows the effect on the coupling factors of the different annealing conditions.

Figure 4 shows explicitly the effect of increasing the annealing current on the minimum coupling factor. Note that after the highest coupling found at 0.50 amps, a sharp reduction of the coupling is found for 0.55 and 0.60 amps due to the onset of crystallisation.

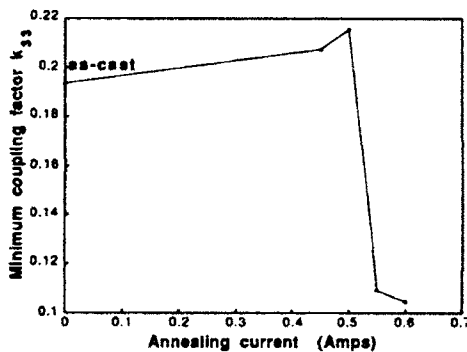


Figure 4 shows the effect of different annealing currents on the minimum coupling factor.

Figure 5 shows the dependency of the switching field as a function of wire length. No bistability is observed for wires less than 7 cm and a saturation value of 90 mOe is found for the switching field for 10 cm and longer. In Between the switching field proceeds roughly linearly with length.

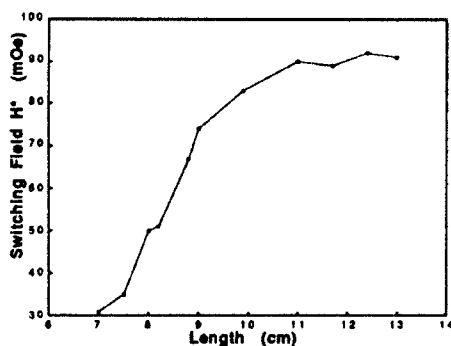


Figure 5 shows the effect of the length of the sample has on switching field.

Figure 6 highlights the applied tensile stress effect on the switching field. Results for an as-cast wire and an annealed wire (0.55 amps, 60 seconds) are given. A linear behavior is seen for applied stresses less than 300 MPa for which the remance is saturated even in the as-cast state.

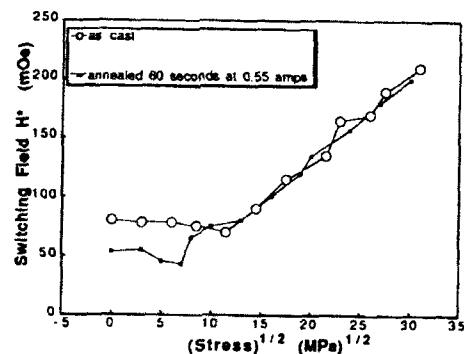


Figure 6 shows the effect applied stress has on the switching field for two samples which were annealed differently.

### Conclusion

From figure 3 it is quite clear that the wire annealed at 0.50 amps gives the highest coupling. This can be interpreted in terms of the core and sheath model as being the most stress relaxed sample. In the incompletely annealed samples (as cast and 0.45 amp annealed) the residual stresses still overwhelms the interaction between the core and sheath thus reducing the anisotropy of the sheath. The sample annealed at 0.50 amps represents the point where the core/sheath interaction becomes more apparent - the best coupling. Increased annealing currents result in more substantial crystallisation and hence less coupling, as seen. Instead of the conventional maximum in coupling<sup>2</sup> we find a minimum. This anomalous behavior can be regarded as the existence of an inhomogeneous magnetic structure and is a result of inefficient current annealing due to variations in the diameter of the wire. Dependence of the switching field upon wire length seems to arise from different demagnetising factors of the sample<sup>3</sup>. While the linear dependency of the switching field upon applied stress above 300 MPa can be interpreted when wall energy propagation at the switching field is considered.

### References

1. A. Mitra et al J. Magn. Magn. Mat., **83** (1990) 339
2. H.T. Savage et al IEEE Trans. Magn., **MAG-11** (1975) 1355
3. A.M. Serertno et al J. Magn. Magn. Mat., unpublished.

## VARIATION OF THE MAGNETIC ANISOTROPY OF AMORPHOUS RIBBONS BY REDUCTION IN THICKNESS BY MECHANICAL POLISHING.

M. Tejedor, J. A. Garcia and J. Carrizo

Departamento de Fisica, Universidad de Oviedo, Oviedo, Spain

### ABSTRACT

Magnetic anisotropy of low magnetostrictive Co-based alloys (VC-6150) has been measured by torque magnetometry for different thicknesses obtained by mechanical polishing of the as-quenched sample. The results allow us to evaluate the contribution to the whole anisotropy of the different possible origins such as surface roughness or induced anisotropies produced during the quench.

### 1. INTRODUCTION

Amorphous state that has not periodic arrangement of atoms exhibit nevertheless magnetic uniaxial anisotropies. Several explanations of the as-quenched anisotropy observed were proposed: shape anisotropy<sup>1</sup>, structural<sup>2</sup> and directional order<sup>3</sup>.

The magnetic anisotropy present in the amorphous ribbons is one of the most important properties that affect the magnetic behaviour of these materials. The study and analysis of the anisotropies in the as-quenched samples is very important and after their knowledge it is possible to vary them, in a controlled way with different treatments, in order to get suitable materials for every application.

The surfaces, with their roughness and striations, and the bulk contribute in a different way to the whole anisotropy. In this paper we use torque magnetometry to disclose the different contributions to the in-plane anisotropy decreasing the thickness of the as-quenched samples by both sides by means of mechanical polishing, that is the best way for removing the surface roughness. For this purpose in a first attempt we have chosen the Co-based alloy VITROVAC-6150 (Co,Mn,Fe)<sub>80</sub>(Si,B)<sub>20</sub>, due to its low magnetostriction that allow us to suppose that internal stresses produced during the polishing do not affect its anisotropy significantly.

### 2. EXPERIMENTAL PROCEDURE

For measuring magnetic anisotropy we used torque magnetometry which is the most direct method to measure in-plane anisotropy. The torque magnetometer employed was a model developed in our laboratory named Compact Torque Magnetometer<sup>4</sup>.

Discs were cut out from the amorphous Co-based ribbon VITROVAC-6150 manufactured by the German Vacuumschmelze. In order to produce very perfect circular samples (for avoiding demagnetizing anisotropy effects

in the plane of the sample) we started by cutting a near circular sample and then we completed the process by a mechanical polishing of the sample edge by fixing the sample to a lathe axis, and when turning we approached a grind-stone by and by to the sample edge. The width of the ribbon allows us to produce discs larger than one centimeter diameter, enough for reliable in-plane measurements by torque magnetometry.

Mechanical polishing of the samples was performed with 0.1 microns size grain alumina, taking care that the polishing were at random along all directions.

### 3. RESULTS AND DISCUSSION

We have prepared two samples of VITROVAC-6150 40 microns thickness named samples A and B.

Sample A was reduced in thickness by polishing in various steps onto the contact surface until a total layer of 19.4 microns was removed. After every step torque measurements were performed.

The thickness of sample B was reduced from the free surface in 14.6 microns by the same procedure.

THICKNESS REMOVED ( $\mu\text{m}$ )	$K_0$ ( $\text{Jm}^{-3}$ )	VOLUME ( $\text{mm}^3$ )	ZONE VOLUME ( $\text{mm}^{-3}$ )	ZONE ANISOTROPY CONSTANT ( $\text{Jm}^{-3}$ )	$k_i/K_0$
0	496	9.19	-	-	-
2.0	390	8.68	$V_1 = 0.51$	$K_1 = 2304$	4.64
4.5	400	8.17	$V_2 = 0.51$	$K_2 = 225$	0.45
7.5	400	7.47	$V_3 = 0.70$	$K_3 = 400$	0.81
11.1	430	6.64	$V_4 = 0.83$	$K_4 = 163$	0.33
14.5	451	5.87	$V_5 = 0.77$	$K_5 = 266$	0.54
19.4	530	4.73	$V_6 = 1.14$	$K_6 = 123$	0.25

TABLE I. Anisotropy constants along the ribbon axis and volumes of sample A, as-received and after successive reductions in thickness from its contact surface.

THICKNESS REMOVED ( $\mu\text{m}$ )	$K_0$ ( $\text{Jm}^{-3}$ )	VOLUME ( $\text{mm}^3$ )	ZONE VOLUME ( $\text{mm}^{-3}$ )	ZONE ANISOTROPY CONSTANT ( $\text{Jm}^{-3}$ )	$k_i/K_0$
0	384	9.07	-	-	-
1.4	322	8.75	$V_1 = 0.32$	$K_1 = 2081$	5.42
3.2	300	8.34	$V_2 = 0.41$	$K_2 = 792$	2.10
5.7	290	7.78	$V_3 = 0.56$	$K_3 = 434$	1.13
11.9	223	6.37	$V_4 = 1.41$	$K_4 = 592$	1.54
14.6	210	5.77	$V_5 = 0.60$	$K_5 = 348$	0.91

TABLE II. Anisotropy constants along the ribbon axis and volumes of sample B, as-received and after successive reductions in thickness from its free surface.

Tables I and II show the results obtained for samples A and B respectively. The magnetic anisotropy constant was measured at an applied magnetic field of  $9.55 \cdot 10^4 \text{ Am}^{-1}$  (1200 Oe).

The anisotropy constant data of Tables I and II were processed in order to obtain the anisotropy constant for every thickness in the



sample :

In a simple model, if we suppose the sample divided into  $n$  regions, the anisotropy constant of the whole sample can be expressed as the volume average of the anisotropies of each region, then

$$K_o = 1/V (k_1 v_1 + k_2 v_2 + \dots + k_n v_n), \quad (1)$$

where  $v_1, v_2, \dots$  are the volumes of each region,  $V$  is the total volume and  $k_1, k_2, \dots$  are the anisotropy constants of each region at a certain deepness in the sample.

If we remove the  $n^{\text{th}}$  region we will obtain another anisotropy constant  $K'_o$  and in the same way we can write

$$K'_o = \frac{1}{(V-v_n)} (k_1 v_1 + k_2 v_2 + \dots + k_{n-1} v_{n-1}). \quad (2)$$

If we subtract the expression 2 from 1 we find the value  $k_n$  as:

$$k_n = \frac{VK_o - (V-v_n)K'_o}{v_n}. \quad (3)$$

In our case  $v_n$  is the volume removed in each polishing operation. We can repeat this calculation for each region and obtain the values of the anisotropy constant corresponding to every zone in the sample, being each zone characterized by its deepness in the ribbon.

We have calculated this anisotropy constants and the values of them are collected in Tables I and II as  $k_i$ 's. Thus in Table I  $k_1$  is the anisotropy constant of the region between 0 and 2 microns deep from the contact surface of sample A and  $v_1$  is the volume of this region.

As it is known amorphous magnetic ribbons in the as-quenched state have non-uniform physical properties. If we are dealing with macroscopical in-plane anisotropy it means that the measured anisotropy constant fluctuates from one sample to another in about 10-20 %, being this the typical range of deviation from the average value. In our case the as-received sample A has  $496 \text{ Jm}^{-3}$  and sample B  $384 \text{ Jm}^{-3}$ .

With the aim of compare the results obtained on both samples we take the rough approximation of assuming that the total anisotropy is divided proportionality through the thickness for the two samples in the same way. Then we can define normalized anisotropy constants as the relations between the anisotropy constants of each zone and the whole anisotropy constant of the sample  $k_i/K_o$ . These normalized anisotropy constants are shown in Tables I and II and represented in Figure 1 versus the deepness through the ribbon.

Looking at Figure 1 there is possible to highlight two principal aspects:

1. The anisotropy near the surfaces is the largest and it can be ten times greater than the inside anisotropy.
2. The anisotropy increases gradually from the contact surface to the free one.

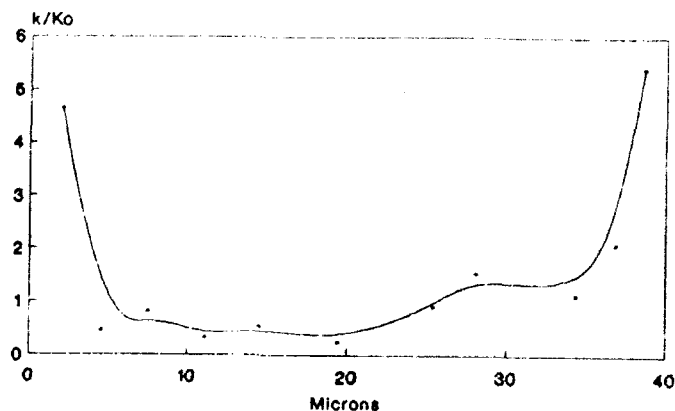


Figure 1. Normalized magnetic anisotropy through the thickness of VITROVAC 6150

We interpretate the high anisotropy near the surfaces as due to the shape anisotropy produced by the surface roughness.

The interpretation of the second point we think that goes through the realization of the possible differences between the layers of material that form the sample from one surface to the other. We think that one of the most important differences between them is the different cooling rate undergone during the manufacturing process; while contact surface is cooled at a greater rate due to its direct contact with the wheel, the rest of the layers are cooled at smaller rates because they are at longer distances apart from the cold wheel. The zone cooled at the lowest rate is the region near the free surface.

Taking into account the above considerations and the fact that this alloy exhibits a relatively high Curie Temperature ( $T_c = 485^\circ\text{C}$ ) we could explain this behaviour as due to an effect of a directional order anisotropy induced along the ribbon during the quench. The driving force that would produce the directional order would be the shape anisotropy that would align the magnetization along the ribbon axis during the cooling process.

#### 4. ACKNOWLEDGEMENTS

This work was supported in part by the C.I.C.Y.T. under the Grant n° MAT 90-0861 (Madrid, Spain)

#### 5. REFERENCES

- 1 L. Kraus, I. Tomas, E. Kratochvilova, B. Springmann and E. Mller, Phys. Stat. Sol. (a) **100**, 289 (1987)
- 2 M. Takahashi and S. Ishio, Jap. J. Appl. Phys., Vol. **16**, n° 12 (1977).
- 3 H. Morita, H. Fujimori and Y. Ohi, Jap. J. Appl. Phys. **18**, 683 (1979).
- 4 M. Tejedor, J.A. Garcia and J. Carrizo, J. Phys. E: Sci. Instrum., **22**, 362 (1989).

CORROSION BEHAVIOR OF  $\text{Fe}_{60}\text{Ni}_{20}\text{B}_{20}$  AMORPHOUS  
ALLOY AND PARTIALLY CRYSTALLIZED

A.R. PIERNA and A. LORENZO

Dpto. Ing. Química y Medio Ambiente. Apto. 1.379  
UNIVERSIDAD DEL PAIS VASCO. San Sebastián (Spain)

and

J. GONZALEZ

Dpto. de Física de Materiales. Fac. Ciencias Químicas  
UNIVERSIDAD DEL PAIS VASCO. 20009 San Sebastián (Spain)

ABSTRACT

Metallic glass  $\text{Fe}_{60}\text{Ni}_{20}\text{B}_{20}$ , both as-quenched and partially crystallized, has been studied by cyclic voltametry in aqueous KOH solution. The formation and growth of a redox oxide layer was observed. The influence of electrochemical variables (sweep rate of potential, anodic and cathodic limit of potential and number cycles) and chemical variables (pH) were studied on this metallic glasses. These results show a different behavior at the corrosion resistance.

Introduction

The study of the corrosion in amorphous metallic alloys has an increasing interest during the last years, because of amorphous alloys are also potentially attractive materials for electric motors, audio and video recording heads, magnetic shielding sheets and for building various electric and electronic devices <sup>1,2</sup>.

The thermal stability of the metallic glasses is a subject of considerable interest <sup>3,4</sup>. The properties of these engineering materials may be significantly changed by the onset of crystallization. The amorphous alloys crystallized lead to significant changes in their oxidation behavior. Thus the metallic glasses

$\text{Fe}_{40}\text{Ni}_{40}\text{P}_{14}\text{B}_6$  and  $\text{Co}_{50}\text{Ni}_{10}\text{Fe}_5\text{Si}_{11}\text{B}_{14}$  show better oxidation resistance after crystallization. On the other hand the metglas  $\text{Fe}_{78}\text{Si}_9\text{B}_{13}$  and  $\text{Fe}_{40}\text{Ni}_{40}\text{B}_{20}$  exhibit a poorer oxidation resistance after crystallization. The aim of our present work is to clarify the effect of the partial crystallization on the electrochemical and corrosion behavior of the  $\text{Fe}_{60}\text{Ni}_{20}\text{B}_{20}$  amorphous alloy.

### Experimental

The amorphous ribbon of nominal composition  $\text{Fe}_{60}\text{Ni}_{20}\text{B}_{20}$  was crystallized by means of a flow of electrical current. The percentage of crystallinity was evaluated from the initial magnetic susceptibility.

The specimens were chemically analyzed with the help of an atomic absorption spectrophotometer. The amorphous structure of the alloy was confirmed by X-ray diffraction.

Prior to the electrochemical measurements, the samples were degreased in methanol, rinsed in the electrolyte, and then they were treated by repeated cathodic and anodic polarizations to achieve a practically constant corrosion current density.

The electrochemical behavior of the ribbons with different degrees of crystallinity was determined by linear sweep voltammetry. An aqueous solution of KOH was employed as the electrolyte.

### Results

Thick oxide layers were obtained when the ribbons were subjected to consecutive potential sweeps between different anodic and cathodic potential limits. The oxide growth was evaluated after stopping consecutive sweeps of potential and then checking voltammetric response when the electrode was submitted to

potential sweeps between +200 and -1200 mV at 200 mV/s. The electrode treatment was evaluated and checked again after each treatment. The influence of other electrochemical and chemical variables was estimated using the same sequence.

From the experimental results obtained in 1N, 2N KOH at 20°C, +100mV of anodic limit, 1 V/s of sweeps rate, and using sample with 0,20,40,60 and 80% of crystallinity, it can be deduced that the crystallized amorphous alloys show greater corrosion resistance than the amorphous at potentials near to the hydrogen release. The oxide layers are clearly of high activity with a maximum of charge oxidation in the anodic voltammogram.

The potentiodynamic behavior of the oxide layers was checked at low sweep rate of potential. It can be concluded that this behavior was quite similar to that obtained for  $\text{Fe}_{40}\text{Ni}_{40}\text{B}_{20}$  amorphous alloy and AISI 316L stainless steel<sup>6</sup>.

When the anodic limit of potential for treatment periods was shifted, keeping constant the cathodic limit (-2200 mV, vs S.C.E.) the oxide layer was not developed until more anodic limits than -900 mV were reached. Between 0 and +200 mV, depending of the KOH concentration, appears a maximum of treatment efficiency. At higher anodic limits this efficiency is greater in the amorphous state than in the crystallized one.

All these facts point out the great influence of the electric potential on the formation of active or passive oxide layers. The concentration of the electrolyte also plays an important role when we try to obtain thick oxide layers by an electrochemical method.

On the other hand, the treatment efficiency is practically constant when the number of cycles is above 200, and is even independent of the KOH concentration. Moreover,  $\text{Fe}_{60}\text{Ni}_{20}\text{B}_{20}$  amorphous alloy shows poorer

oxidation resistance (fig.1) than that partially crystallized.

When the crystallinity degree of the samples was greater than the 20%, it is worth noting that the electrochemical behavior was similar. An independence similar to the above mentioned has been observed when the magnetic properties were followed.

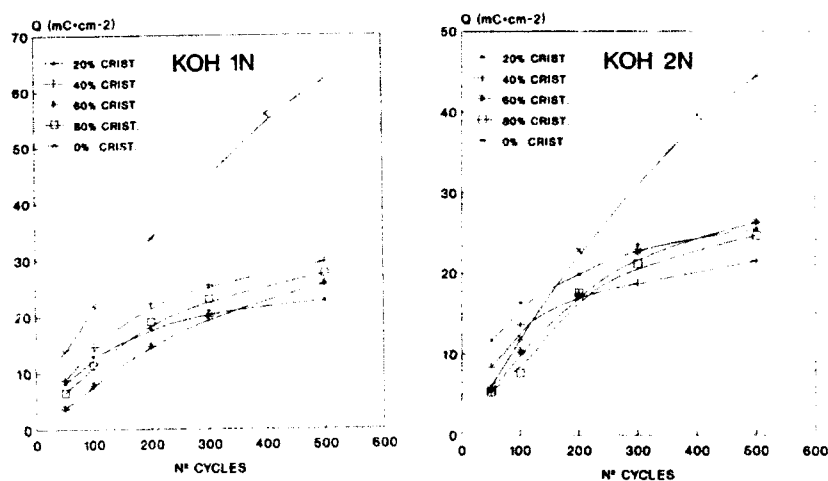


Fig.1.- Influence of the crystallization on the behavior of electrochemical growth of oxide layer in the metallic glasses  $\text{Fe}_{60}\text{Ni}_{20}\text{B}_{20}$ . The variation of the anodic-charge with time of treatment in 1N, 2N KOH aqueous solutions.

#### Acknowledgment

The authors are grateful to the Excma. Diputacion Foral de Guipuzcoa for financial support for this work.

1. N.D. Cristofaro et al., *J. Metals* **38**, p. 1, (1986).
2. H. Warlimont, as Ref. 1. p. 1599 (1985).
3. R.S. Biasi, A.A.R. Fernandes. *J. of Mat. Sci.* (1989).
4. Gao Wei and B. Cantor. *Acta Metall. Scriptae* **23** p. 649-654 (1989).
5. Gao Wei and B. Cantor. *Proceeding of the first int. workshop on non crystal.* p.353-360 (1986).
6. A.R. Pierna, T.F. Otero, J.M. Blanco and J. Gonzalez Proc. 40th ISE Meeting **1** p.637-638 (1989).

## ON CURRENT CONTROLLED NEGATIVE DIFFERENTIAL RESISTANCE IN CHALCOGENIDE GLASSY SEMICONDUCTORS

M. Domínguez, E. Márquez, P. Villares and R. Jiménez-Garay

*Departamento de Estructura y Propiedades de los Materiales  
Facultad de Ciencias, Universidad de Cádiz  
Apartado 40, 11510 Puerto Real, Cádiz, Spain*

### ABSTRACT

Current Controlled Negative Differential Resistance (CCNDR) effect has been studied in bulk glassy chalcogenide semiconductor  $\text{Cu}_{0.05}\text{As}_{0.50}\text{Te}_{0.45}$ . This physical phenomenon has been explained in terms of a thermal model, where non-ohmic effects are excluded. The key lies on the balance of Joule self-heating, with the heat loss due to temperature difference with the ambient. In this work, the relationship between turnover voltage and interelectrode distance has been studied, confirming the thermal nature of this physical process, and the absence of non-ohmic effects in the mechanism of electrical conduction.

### 1. Introduction

Glassy semiconductors exhibit some interesting electrical properties, the most important of which is the reversible switching effect<sup>1,2</sup>. The doping of chalcogenide glassy semiconductors with metallic elements has also been analyzed<sup>3</sup>. In fact, copper has been used as a chemical modifier in arsenic selenides, showing a marked influence on electrical conductivity<sup>4</sup>. As an extension of the previous work made on the analysis of the electrical characteristics of the bulk glassy semiconductor  $\text{Cu}_{0.05}\text{As}_{0.50}\text{Te}_{0.45}$ <sup>5</sup>, in this work, the influence of interelectrode distance on CCNDR effect was studied, from the point of view of the thermal model.

### 2. Experimental

The bulk glassy semiconductor was obtained by the usual melt-quench method<sup>2</sup>, from the elements of 99.999% purity, which were introduced into a quartz ampoule, that was held into a rotary furnace at 950°C for 4 h. The ampoule was quenched in an ice-water bath. The non-crystallinity of the ingot thus obtained, was checked by X-ray Diffraction<sup>6</sup> and by Differential Scanning Calorimetry<sup>5</sup>.

The samples were prepared for electrical measurements by embedding the fragments of the glassy ingot in an epoxy-type resin, and polishing them until mirror-like surfaces were obtained. The electrode arrangement consisted of two copper discs of 2.2 mm diameter, adhered with silver paste to the same surface. The electrical

measurements took place in air and a reflected light microscope was used to observe the material surface, and to photograph it, in order to measure the interelectrode distance.

### 3. Results and discussion

#### 3.1. The dependence of electrical resistance on temperature

The dependence of electrical resistance on temperature of the bulk glassy semiconductor under study, was analyzed elsewhere<sup>5</sup>, showing an acceptable fit to the known Arrhenius-type relationship

$$R(T_a) = R_0 \cdot \exp(\Delta E / k_B \cdot T_a) \quad (1)$$

where  $T_a$  is the ambient temperature,  $R_0$  is a constant for each interelectrode distance,  $k_B$  is the Boltzmann constant and  $\Delta E$  is the activation energy for the electrical conduction process<sup>7</sup>, which showed a value of 0.38 eV from  $R$  versus  $T_a$  regression analysis. This value is lower than those found for Cu-free chalcogenide semiconductors (0.4 - 0.5 eV). The presence of copper also leads to a decrease in electrical resistance.

#### 3.2. Current - Steady State Voltage Characteristics

The CCNDR effect is showed by those materials which exhibit a negative coefficient of electrical resistance on temperature, i.e. when temperature increases, the resistance decreases. By this way, when current applied to the semiconductor is increased step by step, allowing the sample to reach the thermal equilibrium at every

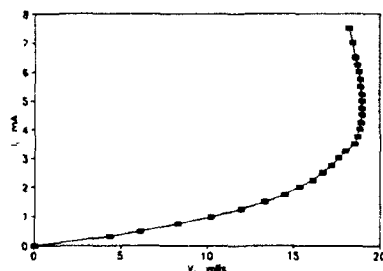


Fig. 1. Steady State I-V characteristics for an interelectrode distance of 0.85 mm, showing the CCNDR region.

step, the temperature of the sample increases for each stage, decreasing the semiconductor electrical resistance as well. The voltage measured at steady state will be lower than the one predicted by the application of Ohm's Law, until a maximum value is reached. This maximum voltage is called "turnover voltage", because beyond this point, the steady-state voltage turns down to lower values (the differential resistance is negative), although current increases<sup>8,9</sup>. Fig. 1 shows the typical I-steady state V characteristics of  $\text{Cu}_{0.05}\text{As}_{0.50}\text{Te}_{0.45}$ , including the CCNDR Region.

This zone is electrically unstable and the external circuit must limit the current passing through the material, to prevent electrical switching of the semiconductor in a thermal avalanche-type process<sup>10</sup>. In fact, to obtain the experimental results, a constant current source was used, and sample was allowed to achieve thermal equilibrium before readings were taken.

The CCNDR region has a well-established limit, as was shown in a previous work<sup>5</sup>. When a certain transitional current is reached, a sudden change in electrical



conductivity of the material occurred: the semiconductor pass to a permanent low resistance or memory state, appearing a crystalline conductive filament between the electrodes<sup>5,10</sup>. This behaviour is typical of a negative differential resistance device with memory<sup>11</sup>.

### 3.3. Dependence of turnover voltage on temperature and interelectrode distance

The theoretical deduction of the turnover voltage-ambient temperature relationship comes from the assumption of the thermal balance equation, in steady state conditions, based on Newton's Law of cooling, i.e. the generation of heat by Joule effect, equals the loss of heat due to the temperature difference between the sample and the ambient

$$I \cdot V_s = K_{th} \cdot (T_s - T_a) \quad (2)$$

where  $I$  is the current,  $V_s$  is the voltage at steady state conditions,  $K_{th}$  is the thermal conductance,  $T_s$  is the sample temperature at steady state, and  $T_a$  is the ambient temperature. The electrical resistance for each pair of values  $I, V_s$  can be derived from eq. (1)

$$R(T_s) = \frac{V_s}{I} = R(T_a) \cdot \exp \left[ \left( \frac{1}{T_s} - \frac{1}{T_a} \right) \cdot (\Delta E / k_B) \right] \quad (3)$$

Deriving eq. (2) and (3) with respect to  $I$  and considering that  $dV/dI=0$  and  $T_s=T_m$  at turnover point, one obtains the approximate relationship

$$V_m^2 \approx (K_{th} \cdot R_0 \cdot k_B \cdot T_a^2 / e \cdot \Delta E) \cdot \exp(\Delta E / k_B \cdot T_a) \quad (4)$$

As  $R_0$  is proportional to interelectrode distance through the relationship with conductivity

$$R_0 = K_r \cdot d \quad (5)$$

The relationship between turnover voltage,  $V_m$ , and interelectrode distance,  $d$ , is

$$V_m^2 = (K_{th} \cdot K_r \cdot k_B \cdot T_a^2 / e \cdot \Delta E) \cdot \exp(\Delta E / k_B \cdot T_a) \cdot d \quad (6)$$

Considering eq. (6), fig. 2 shows the experimental values of  $V_m$ , normalized at an unique temperature by application of eq. (4), versus  $d^{1/2}$ , obtaining a good agreement with this expression ( $r=0.997$ ). Also, fig. 3 shows the experimental values of electrical resistance, corrected through eq. (1) to 293 K, versus  $d$ , in order to verify the relationship in eq. (5) ( $r=0.996$ ), confirming the validity of the assumption of the absence of non-ohmic effects.

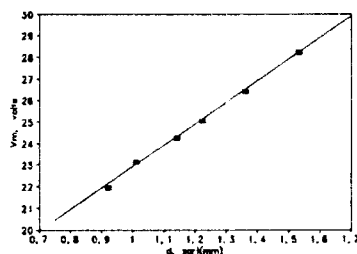


Fig. 2. Turnover voltage, normalized at 293 K, versus square root of interelectrode distance.

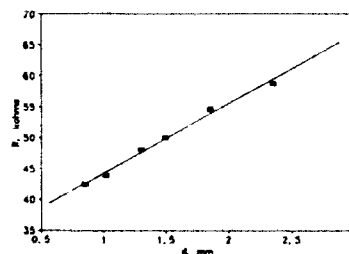


Fig. 3. Plot of electrical resistance, normalized at 293 K, versus interelectrode distance.

#### 4. Conclusions

Together with the experimentally verified relationship of turnover voltage with ambient temperature<sup>5</sup>, the good agreement of turnover voltage dependence on interelectrode distance, deduced from the thermal model, confirm the validity of this one to explain the physical nature of CCNDR phenomenon. The absence of marked non-ohmic effects is also proved for the studied voltage range.

Finally, the possibility of predicting the electrical behaviour of the semiconductor in the range of temperature below transition to crystalline state ( $T_g = 130^\circ\text{C}$ ), from easily determination of certain physical parameters as mobility gap, interelectrode distance and thermal conductance, makes this glassy semiconductor material suitable for NTC thermistor applications.

#### 5. References

- (1) S.R. Ovshinsky *J. Non-Cryst. Solids* **73** (1985) 395.
- (2) E. Márquez, P. Villares and R. Jiménez-Garay *J. Non-Cryst. Solids* **74** (1985) 195.
- (3) Z.U. Borisova, B.V. Kobrin, V.P. Shantarovich, T.I. Kim and M.D. Mikhailov *J. Non-Cryst. Solids* **89** (1987) 263.
- (4) E. Márquez, P. Villares and R. Jiménez-Garay *Mat. Letters* **5** (1987) 296.
- (5) M. Domínguez, E. Márquez, P. Villares and R. Jiménez-Garay *Semicond. Sci. and Technol.* **3** (1988) 1106.
- (6) J. Vázquez, E. Márquez, N. de la Rosa-Fox, P. Villares and R. Jiménez-Garay *J. Mat. Sci.* **23** (1988) 1709.
- (7) N.F. Mott *Conduction in Non Crystalline Materials* (1987) New York, Oxford University Press.
- (8) N. Popescu and N. Croitoru *J. Non-Cryst. Solids* **8-10** (1972) 531.
- (9) B.K. Ridley *Proc. Phys. Soc.* **82** (1963) 954.
- (10) E. Márquez, P. Villares and R. Jiménez-Garay *Phys. Stat. Sol.* **102** (1987) 741.
- (11) H. Fritzsche *IBM Journal R&D* **13** (1969) 515.

## ELECTRICAL CONDUCTIVITY IN THE IONIC AMORPHOUS SOLID



M. OLIVA, J. L. ROJAS, E. MARQUEZ, P. VILLARES, R. JIMENEZ-GARAY

*Departamento de Estructura y Propiedades de los Materiales. Universidad de Cádiz. Puerto Real. Cádiz.*

## ABSTRACT

The a.c. conductivity,  $\sigma_{ac}$ , of chalcogenide glass  $\text{As}_{42}\text{Se}_{41}\text{Ag}_{17}$  has been measured, and reveal polarization phenomena that point to the presence of an ionic component of the conductivity. The  $\sigma_{ac}$  of this material varies as  $\sim \omega^{\beta}$  in the frequency range studied. The d.c. conductivity was estimated by using the complex impedance method.

## 1. INTRODUCTION

D.C. electrical measurements at room-temperature, show a gradual increase in the resistance with elapsed time, where that the time dependence of  $\Delta R$  has the form  $\Delta R = A \exp(-t/\tau)$ , with a constant time,  $\tau$ , which is higher than 30 hours; too large to be interpreted only by an electronic process.

Studies of this chalcogenide glasses show that the contribution of ionic conduction due to  $\text{Ag}^+$  exists[1-4], thus the conductivity has been measured in a.c. The curves obtained in the complex plane ( $Z^*$ ,  $\sigma^*$ ,  $\epsilon^*$ ,  $M^*$ ) are semi-circles, more or less skewed, the form and the center of which lead to information about the distribution of the conductivity relaxation times, hence the disorder within the system. According to the Fourier transform of the Kolhrausch[5] decay function,  $\phi(t) = \exp(t/\tau)^{\beta}$ , if the observed values of  $\beta$  differs from 1, that point does not exhibit a single relaxation time.

## 2. EXPERIMENTS

## 2.1 PREPARATION

The sample was prepared from stoichiometric mixtures of the elements. The mixtures were melted at 825°C for one week in evacuated quartz ampoules, and then quenched in water at room temperature.

The samples were checked to be in the glassy state by means of X-ray diffraction.

The samples used for measurements were cut from the ingot and polished into parallel sided platelets, graphite paste was painted on both sides of it as electrodes.

## 2.2 IMPEDANCE MEASUREMENTS

The impedance measurements for the cell C/glass/C were determined using the impedance spectroscopy method [6-7]. The ac frequency range 50 Hz to 50 kHz was covered by a lock-in amplifier as phase sensitive detector, model 5104.

The complex-impedance spectrum (i.e.,  $Z''(\omega)$  versus  $Z'(\omega)$ ) at various temperatures, reveal an arc; the low frequency tail it could be due to the existence of chemical inhomogeneity. The centers of the observed arc fall below the real-axis for all temperatures, that is to say, with a non-zero relaxation time distribution parameter. This behavior is referred to as "non-Debye" behavior [8].

Fig 1. shows a.c. impedance data for one selected temperature, similar plott were obtained for several temperatures of range 30°C - 100°C.

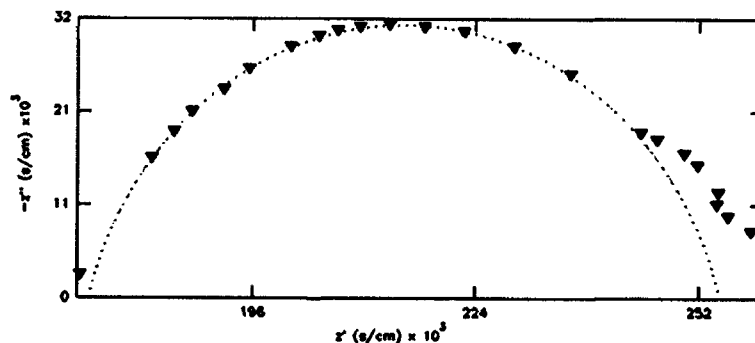


Fig. 1. Complex plane for sample at 303

## 2.3 CONDUCTIVITY MEASUREMENTS

The extrapolation of the low and high frequency of the impedance data to the real-axis, indicates of the average conductivity of the sample and it is necessary to separate the bulk contribution.

The absence of an electrode "spike", indicative of blocking electrode behaviour, suggests that the conduction in the glass is largely electronic [9].

The conductivity  $\sigma^*$  and the conductivity  $\sigma_\infty$  were obtained by extrapolating to their intersections with the real axis the low frequency portions of the complex-

impedance arcs corresponding to the bulk conduction. The best fit calculations were carried out by using the non-linear least square fitting program, making use of the well known Newton method.

The complex impedance is related to the complex conductivity

$$\sigma^*(\omega) = \sigma'(\omega) + i\sigma''(\omega)$$

by the following equations

$$\sigma^* = (d/S)Z^{*-1}$$

where  $S$  is the electrodes area and  $d$  the sample thickness.

The dispersion of conductivity with frequency was a consequence of the non-exponential nature of relaxation in the time domain [10]. According to J. Kawamura et al.[11], for the non-exponential relaxation, the complex conductivity  $\sigma^*$  can be written as

$$\sigma^*(\omega) = \sigma(0)[1 + (i\omega\tau_c)]^n$$

where  $\sigma(0)$  is the  $\sigma_{dc}$  conductivity, being the real part

$$\sigma'(\omega) = \sigma(0)[1 + (\omega\tau)^n \cos(n\pi/2)] \quad (1)$$

Also the power-law frequency dependence of the a.c. conductivity is very often expressed as

$$\sigma'(\omega) = \sigma(0) + A\omega^s \quad (2)$$

where  $A$  and  $s$  (in this case  $n=s<1$ ), are related to polarization conductivity. Therefore, it could written the parameter  $A$  in terms of the  $\sigma(0)$  and  $\tau_c$ :

$$A = \sigma(0)\tau_c^n \cos(n\pi/2)$$

The d.c. conductivity,  $\sigma_{dc}$ , was obtained from a least-squares fit to the equations (1),(2).

The temperature-dependence of the d.c. conductivity fig.[2], obeys to the Arrhenius conventional equation

$$\sigma T = \sigma_0 \exp(-E_a/kT)$$

and the activation energy,  $E_a = 0.27$  eV, was determined from a least-squares fit.

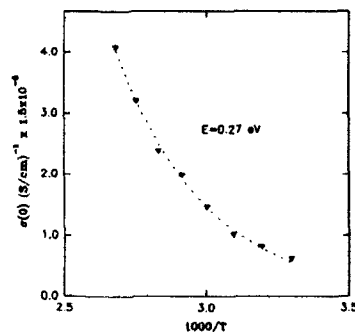


Fig. 2. The temperature dependence of the d.c. conductivity at various temperatures.

The angle of the arcs depressed and the d.c. conductivity shown in the table I.

Tabla I

T(°K)	303	313	323	333	343	353	363	373
$\sigma(0)(\times 10^{-5} \text{ S/cm})$	0.9	1.2	1.5	2.2	3.0	3.7	4.1	6.0
$\alpha(\text{grad.})$	0.3	0.3	0.1	0.1	0.3	0.1	0.1	0.2

#### References

- [1] K. Shimakawa, S. Nitta and M. Mori, Phys. Rev. B18 (1978) 4348
- [2] M. Kitao, K. Hirata and S. Yamada, J. de Physique, 42 (1981) c4-927.
- [3] C. Carcaly and D. Houphouet-Boigny, J. Non-Cryst. Solids 86 (1986) 271.
- [4] Z. U. Borisova. "Glassy Semiconductors". Plenum Press, New York. 1981.
- [5] R. Kolhrausch, Ann. Phys 12 (1947) 353.
- [6] J. Bauerle, J. Phys. Chem. Solids 30 (1969) 2975.
- [7] J. M. Hodge, M.D. Ingram and A. R. West, J. Electroanal. Chem. 74 (1976) 125.
- [8] P.P. Macedo, C.T. Moynihan and R. Bose. J. Phys. Chem. Glasses 18 (1977) 27.
- [9] R. D. Armstrong, T. Dickinson and R. Willis, J. Electroanal. Chem. (1973)
- [10] A. K. Jonscher. "Dielectric Relaxation in Solids". Chelsea. Dielectric Press, 1983.
- [11] J. Kawamura and M. Shimoji, J. Non-Crystalline Solids 79 (1986) 367.

OPTICAL PROPERTIES OF  $a\text{-Ge}_{(1-x)}\text{Sb}_x$  THIN FILMS

J. M. DEL POZO

and

L. DIAZ

*Instituto de Optica, C.S.I.C.  
Serrano 121. 28006. Madrid. Spain.*

**Abstract**

The optical constants of  $a\text{-Ge}_{(1-x)}\text{Sb}_x$  films ( $x = 0.68, 0.73, 0.84$ ) have been determined from reflectance and transmittance measurements at normal incidence. Absorption coefficient dependence on stoichiometry has been found. The films show a semiconductor behaviour with indirect optical band gap, that decreases when Sb concentration increases.

**1. Introduction**

Multicomponent materials with variable physical properties, which can be obtained by varying the relative concentrations of the constituent elements, have played an important role in solid state physics and technology. The binary compounds have been frequently studied and many of them are used in electronics and optoelectronics applications. Most of the few studies of the simple eutectic  $\text{Ge}_{(1-x)}\text{Sb}_x$  binary system have been carried out on liquid or crystalline phase.<sup>(1-3)</sup> Nevertheless, studies on amorphous  $\text{Ge}_{(1-x)}\text{Sb}_x$  seem to show interesting applications of this material on electronics technology<sup>4</sup>, and is also expected to have good properties as optical recording media.

Although electrical, thermodynamic and structural properties of  $\text{Ge}_{(1-x)}\text{Sb}_x$  have been studied, in our knowledge no optical properties have been reported so far. The aim of the present work is to give experimental data on optical constants of  $a\text{-Ge}_{(1-x)}\text{Sb}_x$  thin films ( $x = 0.68, 0.73, 0.84$ ).

**2. Experimental details**

Three  $a\text{-Ge}_{(1-x)}\text{Sb}_x$  and one  $a\text{-Ge}$  films were grown in a dc-magnetron sputtering system onto quartz and glass substrate respectively. The system base pressure was  $3 \times 10^{-6}$  Torr and sputtering was carried out in gettered Ar at a pressure of

$4 \times 10^{-3}$  Torr. The growth temperature ranged from 25 to 35°C. The reflectance and transmittance measurements at normal incidence in the 0.4 – 2.5  $\mu\text{m}$  region were obtained by a Cary 17D spectrophotometer. Diffuse reflectance measurements showed that scattering in these films is negligible. The optical constants and thickness were calculated by the OCS method<sup>5</sup>. The composition of the  $a\text{-Ge}_{(1-x)}\text{Sb}_x$  films was measured by EDX, resulting  $x = 68, 73$  and 84 at.% with film thicknesses  $d = 63.5, 44$  and 65 nm respectively. The thickness of the  $a\text{-Ge}$  film was 57.4 nm. Optical microscopy showed that the films are macroscopically homogeneous.

### 3. Results and Discussion

We have calculated the optical constants ( $n, k$ ) for the three  $a\text{-Ge}_{(1-x)}\text{Sb}_x$  films and for the  $a\text{-Ge}$  film. In fig.1 we show the refractive index vs. wavelength for the four films. We plot also the values of  $n$  for crystalline  $\text{Sb}$  taken from Cardona and Greenaway<sup>6</sup>. We can see in this figure that the refractive index depends on the stoichiometry, though no clear correlation is observed. Fig.2 shows the absorption coefficient obtained for the same films. The absorption coefficient for  $\text{Sb}$  is that obtained by Fox, Howson and Emmony<sup>7</sup> for an evaporated thin film. In this figure,

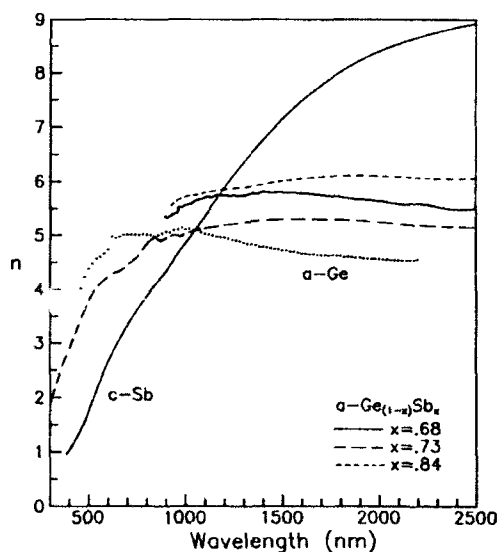


Fig.1. Refractive index for the  $a\text{-Ge}_{(1-x)}\text{Sb}_x$ , and  $a\text{-Ge}$  films, and for  $c\text{-Sb}$ .

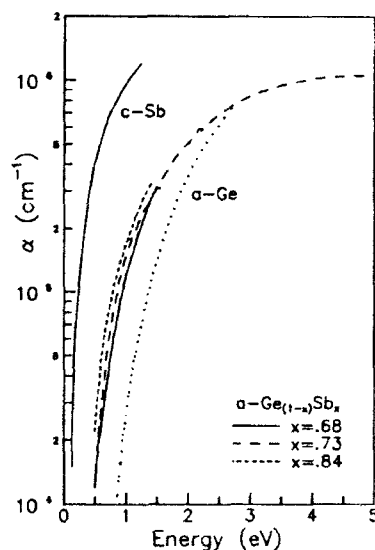


Fig.2. Absorption coefficient for the  $a\text{-Ge}_{(1-x)}\text{Sb}_x$ , and  $a\text{-Ge}$  films, and for a  $c\text{-Sb}$  film.



it can be observed that  $\alpha$  is correlated with the stoichiometry. The higher the concentration of *Sb* is, the higher the absorption is, as one could expect. On the other hand, we can see in both figures 1 and 2 that the behaviours of  $n(\lambda)$  and  $\alpha(h\nu)$  for  $a\text{-Ge}_{(1-x)}\text{Sb}_x$  are intermediate between those for *a-Ge* and *Sb*. However, although the films have a larger fraction of *Sb* than *Ge*, the behaviour of  $n(\lambda)$  and  $\alpha(h\nu)$  is closer to that of the *a-Ge* film, showing semiconductor characteristics.

In the vicinity of the absorption edge  $\alpha$  can be described by the relation

$$h\nu\alpha \propto (h\nu - E_g)^2 \quad (1)$$

The optical gap  $E_g$ , was determined by Tauc's method. The linear relationship between  $(h\nu\alpha)^{1/2}$  and  $h\nu$  in a Tauc's plot was extrapolated to yield the optical gap at  $(h\nu\alpha)^{1/2} = 0$ . This shows the presence of an indirect band gap in the  $a\text{-Ge}_{(1-x)}\text{Sb}_x$  films. The values of  $E_g$  are shown in table 1. It can be seen that these values show a dependence of the optical band gap on the stoichiometry. The higher the concentration of *Sb* is, the smaller  $E_g$  is, and yields to the predicted value, 0.11 eV, of the optical energy gap of *Sb*<sup>7</sup>.

Table 1. Optical band gap for  $a\text{-Ge}_{(1-x)}\text{Sb}_x$  films.

<i>Sb</i> (at.%)	0	68	73	84
$E_g$ (eV)	0.83	0.5	0.4	0.37

On the other hand, effective medium theories of Bruggemann, and Maxwell-Garnett<sup>8</sup> for macroscopically uniform and microscopically heterogeneous media, used to analyse our films, did not provide satisfactory results. This could mean that the films are microscopically homogeneous, although in our case the composition of the samples ranged between 16 and 32 at.% *Ge*, and the maximum equilibrium value of the solid solubility of *Ge* in *Sb* is reported to be 6 at.% *Ge*<sup>1</sup>.

#### 4. References

1. B. C. Giessen and C. Borromee-Gautier, *J. Sol. State Chem.* **4** (1972) 447.
2. S. B. Field and T. F. Rosenbaum, *Phys. Rev. Lett.* **55** (1985) 522.
3. P. Y. Chevalier, *Thermochim. Acta* **155** (1989) 227.
4. N. Croitoru, *Thin Solid Films* **44** (1977) L19.

5. J. M. del Pozo and L. Díaz, (to be published in *Thin Solid Films*)
6. M. Cardona and D. L. Greenaway, *Phys. Rev.* **133** (1964) A1685.
7. T. J. Fox, R. P. Howson and D. C. Emmony, *J. Phys. D* **7** (1974) 1864.
8. D. E. Aspnes, *Thin Solid Films* **89** (1982) 249.

## A.C. CONDUCTIVITY OF AN AMORPHOUS NIOBIUM PHOSPHATE

M. Cantero, M. Martínez-Lara, L. Moreno-Real, S. Bruque  
 Departamento de Química Inorgánica, Cristalografía y Mineralogía.  
 Universidad de Málaga, E-29071 Málaga, Spain.

and

C. Criado, J.R. Ramos-Barrado  
 Departamento de Física Aplicada I. Universidad de Málaga, E-29071  
 Málaga, Spain.

## ABSTRACT

The A.C. conductivity of an amorphous niobium phosphate  $K_{0.5}NbOPO_4 \cdot 2.2H_2O$  and the crystalline compound  $\alpha-NbOPO_4 \cdot nH_2O$  ( $n < 3$ ) is studied by means of the impedance spectroscopy technique in the temperature range 313–473 K. Both compounds shows a similar behaviour with their highest conductivity of  $\approx 10^{-6} \text{ Scm}^{-1}$  near to 373 K. The mechanism of conductivity for the amorphous solid at temperatures higher than 373K is defined by a configurational tunneling model.

## 1. Introduction

Niobium phosphate  $\alpha-NbOPO_4 \cdot nH_2O$  ( $n < 3$ ) is a lamellar solid whose sheets have the  $[NbOPO_4]_{\infty}$  composition. The interlayer space is defined by two types of water molecules and their nature and situation has been investigated using IR and NMR spectroscopy<sup>1,2</sup>.

The compound  $K_{0.5}NbOPO_4 \cdot 2.2H_2O$  is an amorphous solid that is very similar to  $\alpha-NbOPO_4 \cdot nH_2O$  ( $n < 3$ ), and they belong to the extensive family  $MOXO_4$  ( $M = V, Nb, Ta$  and  $X = P, As$ ).

Our purpose is to make conductivity measurement in  $K_{0.5}NbOPO_4 \cdot 2.2H_2O$  in comparison with the crystalline compound  $\alpha-NbOPO_4 \cdot nH_2O$  ( $n < 3$ ).

## 2. Experimental

## 2.1. Preparation of the compounds

The synthesis of  $\alpha-NbOPO_4 \cdot nH_2O$  ( $n < 3$ ) has been made by the method of Chernorukov et al<sup>2</sup> and modified by Bruque et al<sup>1</sup>, and for the synthesis of the amorphous potassium niobium phosphate,  $K_{0.5}NbOPO_4 \cdot 2.2H_2O$  the method described by Hahn<sup>3</sup> with a modification from us was used<sup>4</sup>.

## 2.2. Characterization of the products

The chemical composition of these compounds were determined by dissolving the solids in hot hydrofluoric acid (48% w/w). The niobium was precipitated with cupferron (3%)<sup>5</sup>. Phosphorus content was determined by colorimetric analysis as the molybdo-phosphate complex.

Thermal analysis (TGA and DTA) was carried out in air on a Rigaku Thermoflex apparatus at a heating rate of  $10\text{ K min}^{-1}$  with calcinated  $\text{Al}_2\text{O}_3$  as the internal standard reference.

Surface area of the amorphous potassium niobium phosphate was measured with a Carlo Erba Sorptomatic 1800 instrument. The sample was evacuated at  $10^{-4}$  torr ( $275^\circ\text{C}$ ) overnight; then adsorption-desorption of  $\text{N}_2$  at  $77.4\text{ K}$  was obtained.

X-ray diffraction (XRD) studies were carried out on both the oriented aggregates and the powder diffractograms of the samples with a Siemens D 501 automated diffractometer using graphite-monochromated  $\text{CuK}\alpha$  radiation.

Infrared spectra were recorded on a Perkin Elmer 883 spectrometer with a spectral range of  $4000\text{--}200\text{ cm}^{-1}$ , using dry KBr pellets containing 2 % of the product. In some cases, the sample for IR was prepared as oriented aggregates by evaporating aqueous suspensions on a  $\text{CaF}_2$  crystal. The diffuse-reflectance spectra (UV-VIS-NIR) were recorded on a Shimadzu 3100 spectrophotometer with a integrating-sphere of  $60\text{ mm}$   $\varnothing$  coated with  $\text{BaSO}_4$ ; pressed tablets of  $\text{BaSO}_4$  were used as the reference.

A.C. conductivity measurement between  $313\text{ K}$  and  $473\text{ K}$  were performed using a Solartron 1255 Frequency Response Analyzer controlled by computer.

### 3. Results and discussion

The  $\text{K}_{0.5}\text{NbOPO}_4 \cdot 2.2\text{H}_2\text{O}$  is an amorphous potassium niobium phosphate with a BET surface area of  $234\text{ m}^2/\text{g}$  and a pore size of  $42\text{ \AA}$   $\varnothing$ , this compound is similar to  $\alpha\text{-NbOPO}_4 \cdot n\text{H}_2\text{O}$  ( $n < 3$ ) in its composition and some properties, but with potassium, this ion come in the structure to replace protons from  $\text{P-O-H}$  and/or  $\text{Nb-O-H}$ .

#### 3.1. X-ray diffraction

The  $\alpha\text{-NbOPO}_4 \cdot n\text{H}_2\text{O}$  ( $n < 3$ ) is a lamellar solid, it can be verify in oriented samples by the greater intensity of the 001 reflections whereas the  $\text{K}_{0.5}\text{NbOPO}_4 \cdot 2.2\text{H}_2\text{O}$  is an amorphous solid which diffractogram shows a broad band between  $15^\circ$  and  $39^\circ$  ( $2\theta$ ) with a maximum at  $26^\circ$  ( $2\theta$ ) corresponding to interplanar spacing of  $3.42\text{ \AA}$  near to  $3.19\text{ \AA}$  (200 plane) for crystalline phosphate. This suggests that this amorphous phosphate has a local structure similar to the crystalline phosphate but very distorted.

#### 3.2. Infrared and UV-VIS-NIR diffuse reflectance study

The IR spectrum of  $\alpha\text{-NbOPO}_4 \cdot n\text{H}_2\text{O}$  ( $n < 3$ ) and  $\text{K}_{0.5}\text{NbOPO}_4 \cdot 2.2\text{H}_2\text{O}$  are shown in fig. 1. One of the main zones is located between  $1400$  and  $800\text{ cm}^{-1}$  where appears the stretching vibration  $\nu_3$  corresponding to the phosphate of the layer. The triply degenerate  $\nu_3$  stretching in isolate  $\text{PO}_4^{3-}$  is affected when exist a lowering of the symmetry because to distortion of  $\text{PO}_4^{3-}$  tetrahedron<sup>6</sup> passing of symmetry  $T_d$  to  $C_{2v}$  or

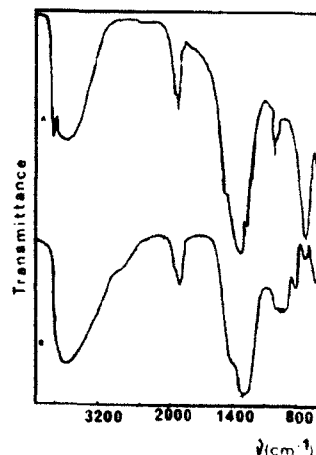


Figure 1. IR spectra of:  
a)  $\alpha\text{-NbOPO}_4 \cdot n\text{H}_2\text{O}$  ( $n < 3$ ),  
b)  $\text{K}_{0.5}\text{NbOPO}_4 \cdot 2.2\text{H}_2\text{O}$ .

even  $C_1$ . Between  $1210\text{--}1120\text{ cm}^{-1}$  and  $1020\text{--}1000\text{ cm}^{-1}$  appear two absorption bands due to splitting of the  $\nu_3$  stretching vibration in  $K_{0.5}NbOPO_4 \cdot 2.2H_2O$ , whereas the  $\alpha\text{-NbOPO}_4 \cdot nH_2O$  ( $n < 3$ ) only shows one band at  $1145\text{ cm}^{-1}$ . The absorption band between  $980\text{--}920\text{ cm}^{-1}$  in  $K_{0.5}NbOPO_4 \cdot 2.2H_2O$  and at  $945\text{ cm}^{-1}$  for  $\alpha\text{-NbOPO}_4 \cdot nH_2O$  ( $n < 3$ ) is due to  $\nu_1$  of  $PO_4^{3-}$ , the low site symmetry makes this band IR-active.

In both compounds between  $750\text{--}550\text{ cm}^{-1}$  approximately appears a band with peaks that are assigned to different  $\nu(Nb\text{--}O)$  stretching vibration. The absorption band at  $520\text{ cm}^{-1}$  with a shoulder at  $540\text{ cm}^{-1}$  in  $K_{0.5}NbOPO_4 \cdot 2.2H_2O$  and at  $560\text{ cm}^{-1}$  in  $\alpha\text{-NbOPO}_4 \cdot nH_2O$  ( $n < 3$ ) can be assigned to  $\delta_{as}(O\text{--}P\text{--}O)$  asymmetric deformation<sup>6</sup>. The bands between  $490\text{--}380\text{ cm}^{-1}$  in both compounds are assigned to  $\delta_s(O\text{--}P\text{--}O)$  symmetric deformation, as the low site symmetry make these bands IR-active. Other important regions of IR spectrum are between  $3800\text{--}2000\text{ cm}^{-1}$  and  $1700\text{--}1600\text{ cm}^{-1}$ , in these zones appear the characteristic bands of hydration water, crystallization water,  $OH^-$ ,  $H_3O^+$ ,  $H_5O_2^+$ ,  $Nb\text{--}OH$ ,  $P\text{--}OH$ , etc. The  $K_{0.5}NbOPO_4 \cdot 2.2H_2O$  has a very broad shoulder at  $2300\text{ cm}^{-1}$  which can be due to  $\nu(PO\text{--}H)$ . This amorphous phosphate lacks an intense band between  $3700\text{--}3650\text{ cm}^{-1}$ , that indicates a low concentration of isolate  $OH^-$  group, being more important the hydrogen-bonded systems and/or by water molecules. The other characteristic band of water is the  $\delta(H\text{--}O\text{--}H)$  deformation that appears at  $1632\text{ cm}^{-1}$  with shoulder at  $1660\text{ cm}^{-1}$  in  $K_{0.5}NbOPO_4 \cdot 2.2H_2O$  and at  $1610\text{ cm}^{-1}$  with a shoulder at  $1635\text{ cm}^{-1}$  in  $\alpha\text{-NbOPO}_4 \cdot nH_2O$  ( $n < 3$ ), due to the existence of two types of water molecules. In the UV-VIS-NIR zone these solids do not exhibit electronic bands due to the  $d^0$  configuration of niobium, only appears a charge transfer band.

### 3.3. Thermal analysis

The  $K_{0.5}NbOPO_4 \cdot 2.2H_2O$  dehydration occurs in two stages defined by a broad endotherm at  $77^\circ\text{C}$  with a shoulder at  $106^\circ\text{C}$  in its DTA-TG curve. In the first stage are lost the water molecules more weakly linked in the structure (1.6 mol per formula) corresponding to hydrogen-bonded water and a small part of the niobium coordinated water. In the second stage is lost the rest of coordinated water (0.6 mol per formula). In the TG curve is observed a inflexion point which defines these two stages.

This compound shows an exotherm effect at  $908^\circ\text{C}$  without mass loss, that is related to an intracrystalline transformation towards a more stable structure. In contrast the  $\alpha\text{-NbOPO}_4 \cdot nH_2O$  ( $n < 3$ ) shows a great thermal stability and it has not any thermal effect after its dehydration.

### 3.4. A.C. Conductivity Measurement

The  $\alpha\text{-NbOPO}_4 \cdot nH_2O$  ( $n < 3$ ) shows a typical behaviour of a proton conductor with its highest conductivity of  $5 \cdot 10^{-6}\text{ Scm}^{-1}$  near to  $100^\circ\text{C}$ ; conductivity increases with the temperature although at

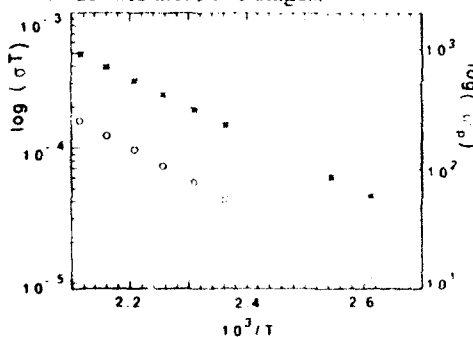


Figure 2. Arrhenius plot of d.c. conductivity ( $\circ$ ) and hopping rate ( $*$ ) for  $K_{0.5}NbOPO_4 \cdot 2.2H_2O$ .

temperatures higher than 373K hydration water is lost and proton conductivity suddenly falls down. Also the amorphous  $\text{K}_{0.5}\text{NbOPO}_4 \cdot 2.2\text{H}_2\text{O}$  shows a similar behaviour (highest conductivity:  $1.2 \cdot 10^{-6} \text{ Scm}^{-1}$  at  $90^\circ\text{C}$ ). The experimental results of  $\text{K}_{0.5}\text{NbOPO}_4 \cdot 2.2\text{H}_2\text{O}$  were fitted to the universal response<sup>7</sup> ( $\sigma(\omega) = \sigma_0 + A\omega^n$ ) where  $\sigma_0$  is the d.c. conductivity, A is a temperature dependent parameter and n is found to take values between 0 and 1.

The hopping rate  $\omega_p$  may be obtained from a. c. conductivity data since it corresponds to the frequency at which  $\sigma(\omega_p) = 2\sigma_0$  (Table 1)<sup>8</sup>. For temperatures higher than 373K the Arrhenius plot of d. c. conductivity and the hopping rate show the same activation energy ( $E_a = 0.174 \text{ eV}$ ) (fig.2), the n fractional exponent is temperature independent ( $n = 0.51$ ), like the tunnelling model. We have applied the Mott law about the variable range hopping and good fits are achieved [ $\sigma = 3.7 \exp(-71.4/T^{1/4})$ ].

The electrical conduction may be carry out by means small transitions occurring in a disordered array, so the sum of many individual and small transitions of ions when they are to take up new disordered positions means the same effect as a single large transition. These small adjustments requiring negligible energies for their induction are known under the name configurational tunnelling<sup>9</sup>.

Table 1. Results of conductivity and hopping rate for  $\text{K}_{0.5}\text{NbOPO}_4 \cdot 2.2\text{H}_2\text{O}$

T(K)	$\sigma_0(\text{S cm}^{-1}) \cdot 10^{-8}$	$\omega_p(\text{s}^{-1})$
313	7.4	2384
333	10.5	2539
363	12.4	2716
383	2.9	60
393	4.8	107
423	9.8	234
433	12.7	433
443	16.3	409
453	20.8	545
473	33.6	955

#### 4. Acknowledgements

We thank the C.I.C.Y.T. (proyect MAT 90-298) support of this work, and one of us M.C.S., is grateful to Dirección General de Universidades e Investigación de la Junta de Andalucía for a grant.

#### 5. References

1. S. Bruque, M. Martínez-Lara, L. Moreno-Real, A. Jiménez-López, B. Casal and Ruiz-Hitzky, *Inorg. Chem.* **26** (1987) 847.
2. N.G. Chernorukov, N.P. Egorov, I.R. Mochalova, *Zh. Neorg. Khim.* **23** (1978) 2931-2934; *Russ. J. Inorg. Chem.* (Engl. Transl.) **23** (1978) 1627-1629.
3. R.B. Hahn, *J. Am. Chem. Soc.* **73** (1951) 5091-5093.
4. M. Cantero, M. Martínez-Lara, S. Bruque, L. Moreno-Real, *Inorg. Chem.* Submitted (1991).
5. A.I. Busev, V.G. Tipsova, V.M. Ivanov, *Analytical Chemistry of rare elements*, ed. Mir Publishers (Moscow, 1978).
6. K. Nakamoto, *Infrared and Raman spectra of inorganic and coordination compounds*, ed. Interscience (New York, 1986).
7. J. Jonscher, *J. Materials Science* **13** (1978) 563.
8. D.P. Almond and A.R. West, *Solid State Ionics* **9/10** (1983) 277.
9. A.K. Jonscher, *Dielectric relaxation in solids*, ed. Chelsea Dielectrics Press (London, 1983).

## AUTHOR INDEX

Alberdi, J.M.	309	Beukel, A. van den	215
	329	Binder, K.	285
Alegria, A.	297	Blanco, J.B.	425
	301	Blanco, E.	69
	309	Bordas, S.	201
Alvarez, F.	309	Bruque, S.	449
Arbe, A.	297	Buchenau, U.	281
Baltá-Calleja, F.J.	127	Cahn, R.W.	3
Barandiarán, J.M.	73	Calventus, Y.	193
	181	Cantero, M.	449
	409	Cantor, B.	161
Baricco, M.	257	Carey, J.D.M.	425
Baró, M.D.	153	Carrizo, J.	429
	177	Casas-Ruiz, M.	209
	193	Cebollada, F.	177
	273	Cerrada, M.L.	321
Baschnagel, J.	285	Clavaguera, N.	153
Bayard, J.	277		193
Belhadji, M.	205		201
Bellenger, V.	313	Clavaguera-Mora, M.T.	153
Bello, A.	317		177
	321		193
Benavente, R.	317		201
	321		273
Bernal, M.J.	413		

Colmenero, J.	293	Filipecki, J.	265
	297	Flores, J.	413
	301	Frick, B.	297
	309		
	313	García, J.A.	429
	329	García-Arribas, A.	409
Conde, A.	165	Gil, L.	281
	169	Gómez-Polo, C.	421
	185		425
	261	González, J.	157
Conde, C.F.	165		425
	261		433
Criado, A.	185	González, J.M.	57
Criado, C.	449		177
Cumbrera, F.L.	269	Grenet, J.	277
		Guerrica-Echevarría, E.	301
Davies, F.J.	85	Guiberteau, F.	269
Díaz, L.	445	Guo, M.M.	97
Diogo, A.C.	333		
Dominguez, M.	437	Hamou, A.	277
Dubois, J.M.	343	Hernando, A.	157
		Hernando, B.	417
Elícegui, A.	313	Herreros, J.	409
Esquivias, L.	65	Hickmott, M.D.	425
	69	Honeybone, P.J.R.	93
	101	Howells, W.S.	81
Evmenenko, G.A.	89		93
Fernández-Gubieda, M.L.	73	Illeková, E.	273



			455
Ingram, M.D.	385	Márquez, E.	437
Inoue, A.	401		441
Ishii, K.	161	Martín, V.E.	57
		Martínez-Lara, M.	449
Jäckle, J.	237	Martínez, G.	313
Jiménez-Garay, R.	209	Matos, J.	101
	437	Matyja, H.	107
	441	Millán, M.	169
			185
Kenunen, I.V.	325	Millán, J.L.	313
Koebrugge, G.	257	Mitchell, G.R.	85
Köster, U.	149		293
Krishnan, R.	173	Monserrat-Ribas, S.	305
Kronmüller, H.	421	Moreno-Real, L.	449
Kulik, T.	107	Morris, M.A.	61
		Muñoz, A.	269
Leal, J.	169	Muñoz, J.S.	405
Lebaudy, P.	205		
Ligero, R.A.	209	Newport, R.J.	93
Lorenzo, A.	433	Nielsen, O.V.	417
Lorenzo, M.F.	329		
Lorenzo, V.	317	Oliva, M.	441
		Orue, I.	73
Maia, J.	333	Otero, A.	153
Málek, J.	197		
	109	Paul, W.	285
Mandowski, A.	337	Pereña, J.M.	317
Marín, P.	157		321

Pérez, E.	317	Saiter, J.M.	205
	321		277
Pérez, J.	289	Savage, H.T.	365
Petersen, J.R.	417		425
Pierna, A.R.	433	Schnitzke, K.	57
Plazaola, F.	73	Schultz, L.	57
Pont, M.	401	Sietsma, J.	257
	405	Smrčka, V.	189
Pozo, J.M. del	445	Spassow, T.	149
Prieto, C.	101	Stribeck, N.	325
Primdahl, F.	417	Strobl, G.R.	37
Pulido, E.	157	Suriñach, S.	153
Puzniak, R.	401		177
			193
Ramírez del Solar, M.	65		273
Ramos, M.A.	281	Sutton, M.	149
Ramos-Barrado, J.R.	449	Świątek, J.	337
Rao, K.V.	401		
Reininger, T.	421	Tatibouet, J.	289
Revell, P.	93	Tejedor, M.	429
Reverter, J.	405	Tellería, I.	181
Riontino, G.	257		301
Riveiro, J.M.	413	Thiel, S.	245
Rojas, J.L.	441	Tichý, L.	197
Rosa-Fox, N. de la	69	Torrelles, X.	201
Rosi, B.	85		
	293	Val, J.J. del	85
Rougier, P.	173		293
			313

			457
Vautier, C.	205	Volodin, V.P.	325
Vázquez, J.	209		
Vázquez, M.	157	Wasylak, J.	77
	365	Wittmann, H.P.	285
	421		
	425	Zachmann, H.G.	97
Velho, A.M.	333		89
Verdú, J.	313		245
Vigier, G.	289		325
Vilesov, A.D.	89	Zarzycki, J.	15
	325		
Villares, P.	437		
	441		